Cranfield University

School of Industrial and Manufacturing Science

PhD THESIS

Academic Year 1994-1997

Elevated temperature oxidation and corrosion of a titanium aluminide alloy

Jonathan Leggett

Supervisor: Professor J.R.Nicholls

October 1997

Abstract

Titanium aluminides are being developed to expand the temperature capability of titanium alloys with maximum service temperatures around 700°C. These materials also have the ability to replace nickel superalloys with potential applications in the high pressure compressor, and in the 4th stages of the low pressure turbine.

The above applications place these alloys in environments not previously considered. Within the compressor hot salt corrosion may be a problem with salt ingested from the atmospheric aerosol. While in the turbine the combination of salt ingestion, and SO_2 from the burning of fossil fuels, results in hot corrosion being a potential problem.

In this study the individual effects of salt and SO_2 were investigated, with corrosion mechanisms being proposed using kinetic, metallographic and thermodynamic data. Understanding these effects enabled both the hot salt corrosion and hot corrosion behaviour of TiAl alloys to be evaluated.

In air alone continuous alumina layers, within a mixed alumina/rutile scale, provide the oxidation resistance of TiAlNb alloys. Logarithmic kinetics operated for 100 hours at 700°C and for 13 hours at 750°C. Parabolic kinetics then operated out to 100 hours at 900°C. Mass gains ranged from 0.06 to 2.1mg/cm^2 after 100 hours at 700 and 900°C respectively. This situation changes in bi-oxidant, air/SO_2, atmospheres where increased growth rates are linked to the formation of a continuous sulphide layer at the scale/substrate interface. Below 800°C logarithmic/parabolic kinetics operate. At and above 800°C initial logarithmic kinetics change to near linear/breakaway kinetics with spallation becoming a problem. Mass gains, after 100 hours, ranged from 0.2 mg/cm^2 at 700°C up to 6.4 mg/cm^2 at 900°C.

The presence of low salt concentrations [<0.05mg/cm^2] resulted in severe substrate degradation, with preferential attack down α2 lathes. The first 10-20 hours were shown

to be the most important with low melting point salt mixtures spreading across the surface, increasing the rate of attack. The evolution of HCl/Cl_2 during initial substrate attack leads to the Vapour Phase Transport of aluminium and manganese chlorides resulting in whisker growth over a porous rutile scale. The presence of salt modified the diffusion controlled kinetics under purely oxidising conditions. Chlorine was shown to promote the vapour phase transport mechanism which resulted in the initial accelerated logarithmic kinetics. A change to parabolic type kinetics occurred due to the loss of chlorine to the atmosphere. The mass gains, after 100 hours, ranged from 0.06 to 1.1mg/cm^2 between 500 and 800°C.

The combination of salt deposits and SO_2 bearing environments resulted in severe substrate degradation. Salt played a dominant role during the early stages of corrosion, whilst low partial pressures of SO_2 affected the later stages of corrosion. Non protective oxide scales were developed with low melting point $MnSO_4$-Na_2SO_4 mixtures forming at salt deposits and a continuous sulphide layer at the scale/substrate interface. Rapid scale growth resulted in severe scale spallation. The initial stages of hot corrosion followed rapid logarithmic type kinetics. Further increases in the corrosion rate where promoted by the formation of continuous sulphide layers at the scale/substrate interface. Parabolic kinetics, at this stage, were followed by linear growth rates once scale spalling occurred. Mass gains, after 100 hours, ranged from 0.52 to 3.89 mg/cm^2 between 650 and 800°C.

Acknowledgments

The author would like to thank Professor J.R.Nicholls for the invaluable discussions throughout the last three years.

The author would also like to thank the DERA and Rolls Royce, and in particular Dr.M.Winestone, S.Kerry, P.Andrews, and W.Voyce without whose support this PhD would not have been possible.

Invaluable assistance was provided by Colin Mathews and Tim Pryor throughout, for which I am extremely grateful.

Table Of Contents

List of Figures

Chapter 1

Chapter 2

Chapter 3

Chapter 4

Chapter 5

Chapter 6

Chapter 7

Chapter 8

Chapter 9

List of tables

LIST OF PHOTOGRAPHS

Nomenclature

A	Cross sectional Area
a	activity
a_M	activity of metal (unit activity in all cases)
a_{MO}	activity of metal oxide (unit activity in all cases)
a_{MCl2}	activity of metal chloride (unit activity in all cases)
c	Concentration gradient
D	Diffusion coefficient
γ	Gamma (TiAl)
H(Ti)	Hydrogen dissolved in titanium
$\alpha 2$	Alpha2 (Ti_3Al)
Kp	Parabolic rate constant ($mg^2/cm^4/h$)
p(Y)	Partial pressure of gas Y
Q	Activation energy (KJ $mole^{-1}$)
R	Universal gas constant (8.134 $J.mole^{-1}.deg^{-1}$)
[Salt]	Salt concentration deposited (mg/cm^2)
T	Absolute temperature (°C and/or °K)
t	Time (hours or seconds)
ppm	Composition of the gas phase (parts per million)
V^{++}_O	Oxygen ion vacancies
V^{++}_{Ti}	Interstitial titanium ions
W	Weight of the specimen (mg)
ρ	Density ($gm.cm^{-3}$)
$\Delta G°_i$	Standard free energy of formation of component I
ΔW	Change in weight of the specimen

Introduction

The aircraft industry has now reached a stage of development where turbine engines are required to provide more thrust to enable larger aircraft to be built. The current nickel based superalloys meet all the mechanical and environmental requirements. However, as the turbine engines become larger their fuel efficiency must be considered. Most superalloys have densities of about 8.0 g/cm^3, so components made from these materials are both expensive and heavy. Fuel economy has thus become an important factor when considering the materials used in the turbine engine. Titanium aluminides are being developed to replace the current superalloys used in the turbine engines, with typical applications being in the later stages of the compressor section and in the third and fourth stages of the low pressure turbine. These materials are typically half the density of most superalloys, thus offering much better specific properties and weight to thrust ratios. Fuel efficiencies are thus improved.

Titanium alloys are currently used in the compressor section. Improvements in engine efficiency are accompanied by higher operating temperatures. There is thus a continuous drive to develop new and improved materials. The titanium alloy IMI 834 was developed so that the nickel superalloys used in the Trent high pressure compressor could be replaced. This was made possible by the improvement in titanium operating temperatures to around 600°C. Titanium aluminides have been developed in a further attempt to replace nickel superalloys at higher operating temperatures and in doing so allowing larger engines to be put into service.

Titanium aluminides alloys are now being developed to operate within the turbine engine at temperatures above 700°C. Previous titanium alloys encountered salt/ air environments. For this reason several investigations were carried out in an attempt to characterise the effects of salt on the life of the material. Salt was shown to cause a reduction in life during laboratory testing. However, these failures were not encountered in cases were titanium alloys were being used in high temperature compressors, even after several million hours

of flight. This may have been due to lower stresses and temperatures operating in service than expected. It was also suggested that salt deposition was minimised due to high airflows over the component. The discontinuous stress and temperature cycles encountered during service may also account for the lack of failures. However, a lack of understanding still existed, with the possibility that as the operating temperatures were continuously being raised hot salt corrosion may eventually have resulted in service failures. This reasoning as to the validity of characterising a material in a particular environment can be followed when suggesting that a hot corrosion study is necessary if titanium aluminides are to be used in salt/sulphur bearing situations. Salt is ingested through the compressor from the atmosphere and sulphur dioxide is generated during the burning of fossil fuels in the combustion chamber.

Extensive research is being completed to determine the best mechanical properties attainable through alloying. However, the environmental behaviour of these materials has not been comprehensively investigated. One of the alloys which is being considered has the composition Ti-45Al-2Nb-2Mn + 0.8%TiB_2 (at%). This alloy has been developed using third and fourth element additions to improve the oxidation resistance of titanium aluminides. From the available studies of this material several oxidation mechanisms have been reported. No studies have so far been published characterising this materials hot salt and high temperature sulphidation behaviour. These areas are important as such environments will be encountered in the applications being considered.

Although extensive research has been carried out on the hot corrosion of nickel based superalloys non has yet been published for titanium aluminides. In order for the hot corrosion behaviour of this material to be understood it was first necessary to understand the individual roles of salt and sulphur dioxide. Continuous thermogravimetric mass gains enabled a detailed understanding of the kinetic behaviour of this material in air and salt environments. The toxic nature of sulphur dioxide prevented continuous mass gains during sulphidation and hot corrosion studies. Individual mechanisms were developed for the corrosion of this material in the various environments studied, using kinetic, metallographic and thermodynamic data.

The aims of of this project have thus been to;

1. Obtain a thorough understanding of the oxidation mechanisms operating in the temperature range of 700-900°C and to evaluate the roles of the third and fourth element additions.

2. Gain an insight into the effect of sulphur dioxide on the corrosion behaviour of this material, over the temperature range of 700-900°C, and to determine whether or not the material is degraded to a greater or lesser extent than in the presence of salt.

3. Evaluate the effects of NaCl deposits on the oxidation behaviour of this material in the temperature range of 500-800°C. A mechanism for the hot salt corrosion was also required.

4. Begin characterising this materials hot corrosion behaviour between 650-800°C, with the aim of proposing a general mechanism to support the observed corrosion.

Chapter 1

Intermetallic materials

1.1 Intermetallics

1.1.1 Introduction

Intermetallic phases are compounds of metals with long range ordered lattice structures which are different from those of their components. Up until the last century intermetallics were used primarily for their high hardness. In modern times they have been exploited for a wider range of attractive properties.

High hardness, coupled with high strength at high temperatures makes these materials promising for high temperature applications. This was realised 30 years ago but serious developments were hindered by the brittle behaviour of intermetallics. Interest has again heightened, with many new applications having been proposed.

1.1.2 Properties of intermetallic phases

The mechanical behaviour of intermetallics is of importance when considering the structural applications being proposed.

The deformation behaviour of structural materials can be described using Hooks law shown below[1].

$$\sigma = E * \epsilon \qquad \textbf{(1.2a)}$$

where σ = stress, ϵ = strain and E = Young's modulus.

Deformation can be described as being either elastic or plastic. The material parameter E characterises the elasticity of a material and is dependent on the atomic bond strengths. Plastic deformation at low temperatures is due to the mobility of dislocations on crystallographic slip planes. Dislocations split into partials with two dimensional antiphase boundaries (APB's) or stacking faults in between creating superdislocations in long range

ordered structures. Dislocation mobility depends on the APB energy, enabling partial substitution of the constituent elements giving some control over the materials deformation behaviour.

At high temperatures plastic deformation is controlled by dislocation movements which are controlled by diffusion mechanisms. An Arrhenius equation is given below to describe the temperature dependence of diffusion.

$$D = D_O \exp (-Q_D / KT) \qquad (1.2b)$$

were D_O = frequency factor, K = Boltzmann constant, T = temperature and Q = activation energy.

At high temperatures the stoichiometric alloy is the most creep resistant. Off stoichiometric phases are mobile and so result in higher diffusion rates.

The brittle behaviour of intermetallics is due to the lack of slip systems and high dislocation energy, preventing stress relaxation at crack tips by plastic deformation.

1.1.3 Material development[1]

The potential of intermetallic phases, based on their outstanding physical and chemical properties, has increased since a number of these phases were made more ductile.

Research has been ongoing in breaching the gap between superalloys, which offer good strength and toughness below 1100°C, and ceramics which can operate at much higher temperatures but are inherently brittle as a consequence of covalent bonding. Intermetallics are expected to have higher specific strengths than superalloys, because of their strong atomic bonding and more ductility than ceramics because of their metallic bonding.

1.1.4 Phase selection [1]

The criteria needed in selecting intermetallic phases for high temperature applications are specific with very few phases meeting all the requirements.

High strength, implying the need for adequate creep resistance, at the proposed service temperatures is a requirement. High melting temperatures are also essential, as the mechanical behaviour of the material is directly related to diffusion and shear modulus, which are both temperature dependent.

Intermetallics are often alloyed with very low density elements, such as chromium and aluminium, giving them much better specific strengths (σ/ρ) than superalloys.

Intermetallics are inherently brittle. However, some phases such as NiAl have been tailored so that their brittle to ductile transitions occur at much lower temperatures than some ceramics. This occurs at 0.4Tm in the case of NiAl and above 0.8Tm for Al_2O_3. NiAl is just one phase which has bridged the gap between metals and ceramics.

The brittle behaviour seen in intermetallics increases with decreasing lattice symmetry and increasing unit cell size. Structural intermetallics are being developed with greater crystal symmetry and smaller unit cells. Figure 1 shows some simple crystal structures, with ordered atom distributions, based on bcc and fcc lattices. The $L1_0$ and DO_{22} structures are slightly tetragonal whereas the others are cubic.

Oxidation resistance at high temperatures is another important parameter and can be achieved by alloying with elements such as Al, Cr and Si, which form protective oxide scales. Chromium and silicon oxides are volatile at low oxygen partial pressures above 1000°C, with silica possibly forming low melting point silicates. Aluminides are thus favoured, because of their high temperature stabilities, for high temperature applications. Oxidation resistance can be improved further by using protective coatings. However, their stabilities decrease with increasing temperature.

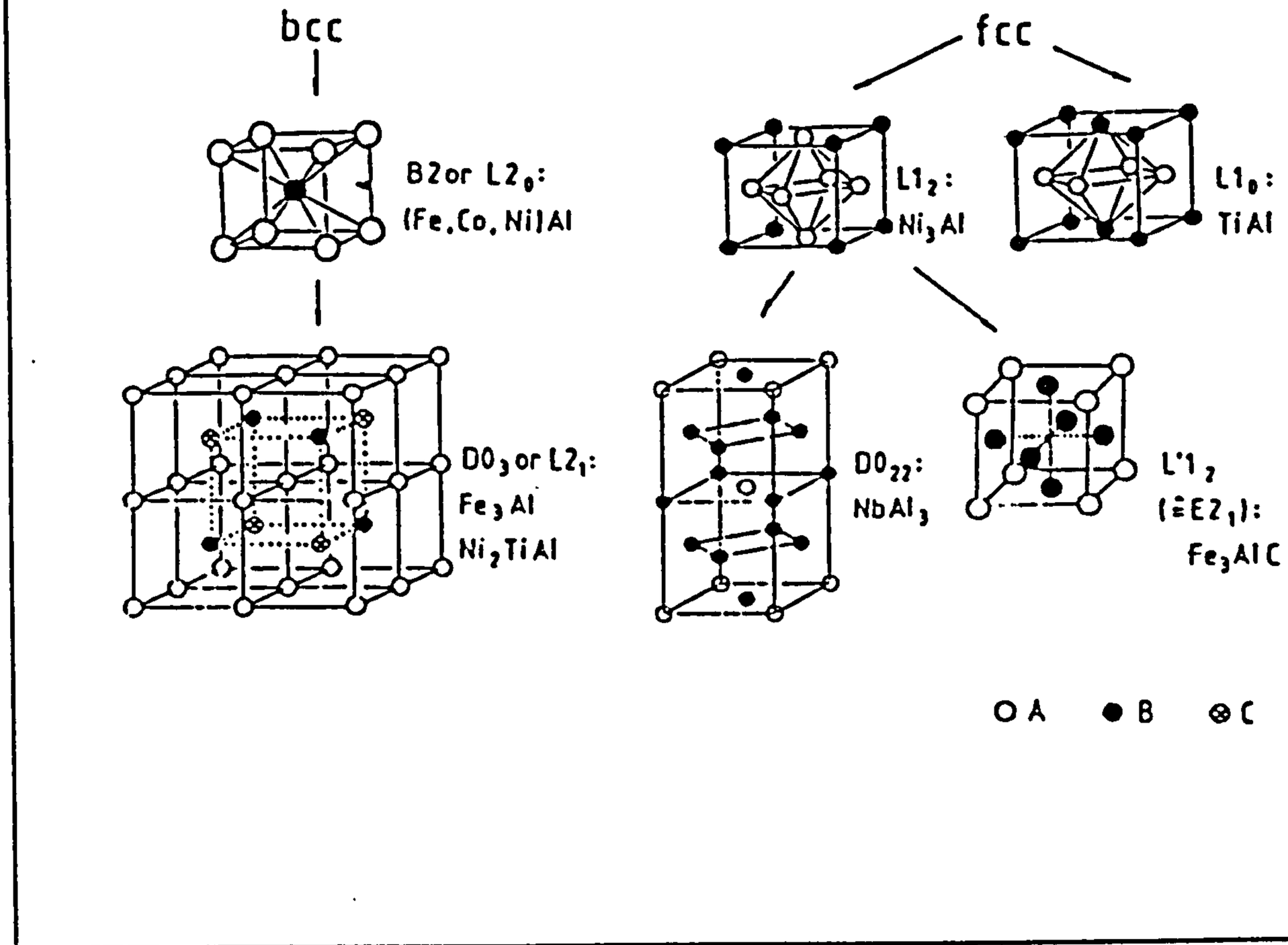

Figure 1: Some simple intermetallic crystal structures, with typical examples [1]

1.2 Titanium Aluminides

1.2.1 Introduction

Interest from the aerospace industry in Gamma titanium aluminides has increased over the last decade, due to their potentially attractive properties at high temperatures. These include low density, good oxidation and burn resistance and high temperature strength retention. Several two phase (TiAl + Ti_3Al) gamma titanium aluminides have been developed which now satisfy some of the high temperature (up to 750°C) property requirements for use in gas turbine engine rotational components. Extensive research has been carried out on the binary alloy based on Ti-(45-48)Al. These investigations highlighted several high temperature property shortcomings[2] which included:

- An inverse relationship between tensile properties and fracture/creep resistance causing unbalanced properties.
- Low strength at high temperature for the structural components used between room temperature and 1000°C.
- A lack of understanding of the mechanisms of scale growth during oxidation at high temperatures but especially at 800°C.

To help overcome these problems several new microstructures, based on lamellar microstructures, have been developed and attempts have been made to understand the oxidation phenomena of this class of material and the effect of alloying elements. Basic properties and structures of a titanium alloy, gamma TiAl and a nickel based superalloy are compared in table 1[3].

Titanium alloys offer substantial weight savings, compared to Nickel and iron base superalloys, enabling reductions in airframe weights and increased thrust to weight ratios of gas turbine engines.

The most advanced titanium alloys (IMI834 and Ti1100) currently in use are limited by strength and oxidation considerations to approximately 600°C. These materials are also limited by creep strength, damage tolerance and fire resistance.

Titanium aluminides are the most promising alloys in meeting the demanding properties now being sought. Table 1 compares TiAl with superalloys. Although TiAl alloys have lower elastic moduli they retain their properties at higher temperatures. Diffusion in TiAl alloys is activated by much higher energies and attributed to the strong A-B bonding. As a consequence TiAl alloys have better high temperature creep strength retention and fatigue resistance.

Several areas of concern remain, with low ductility and toughness at low temperatures,

Table 1: Physical and mechanical properties of titanium, titanium aluminides and superalloys [3,4,5]

Property	Ti-Base	Ti_3Al	TiAl Base	Superalloys
Structure	hcp/bcc	DO_{19}	$L1_0$	fcc/$L1_2$
Density (g/cm^3)	4.5	4.1-4.7	3.7-3.9	7.9-8.5
Modulus (GPa)	96-115	100-145	160-176	206
Y.S (MPa)	380-1150	700-790	400-630	800-1200
U.T.S (MPa)	480-1200	800-11	450-700	1250-1450
R.T Ductility (%)	10-20	2-10	1-3	3-5
H.T Ductility (%)	12-50	10-20	10-90	10-20
Oxidation limit (°C)	600	650	800-950	870-1090
Creep Limit (°C)	600	760	1000	1090

along with poor formability, posing the greatest problems[3,4,5]. However, the temperature capabilities of the present aluminides appears to be limited by their oxidation resistances rather than their creep or strength retention. Advances have been made to improve oxidation resistance through alloy modifications.

1.2.2 TiAl alloy classification[6]

Gamma titanium aluminides consist of titanium, 45-49 at% Aluminium, and 1-10 at% M, where M may be one or more elements from V, Cr, Mn, W, Mo, Nb, and Ta. Depending on the proportion of aluminium gamma alloys exist as single phase (γ) or two phase (γ +α2) alloys. Single phase alloys containing third alloy elements improve strength and oxidation resistance (i.e. Nb), whilst in two phase alloys they improve ductility (i.e. Mn, Cr) and oxidation resistance (i.e. Nb, Ta).

The γ (TiAl) phase has the $L1_0$ ordered f.c.c tetragonal structure. The degree of

tetragonality increases with increasing aluminium content This phase also remains ordered up to its melting point of approximately 1450°C.

The phase diagram for the Ti-Al system is shown in figure 2, with the central region depicting gamma alloys shown in figure 3. Typical heat treatment temperatures are marked on a Ti-48 at%Al alloy line. A lamellar microstructure results if the alloy is cooled from the temperature T_1. Duplex microstructures of lamellar grains and primary γ grains are formed if the alloy is cooled from the two phase fields (T_2,T_3 andT_4). Lamellar structures consist of alternate γ and α2 plates, the thickness of the α2 plates decreasing with increasing aluminium content.

Recent investigations[7] suggested that third element additions shifted the (α2 + γ)/γ phase boundaries. Type N elements (Nb, W, Mo) were believed to replace titanium to form Type I phase field. Type M elements (V, Mn, Cr) were believed to substitute for both titanium and aluminium to form type II or to mainly replace aluminium to form type III phase fields. Figure 4 illustrates the three shifts on a tertiary Ti-Al-X phase diagram. Reducing the aluminium content in the γ-phase is believed to reduce covalency, and to enhance slip activity of ordinary dislocations (1/2[110]) and twinning by 1/6<112] dislocations.

1.2.3 Processing routes and microstructures of γ-TiAl[6]

Two routes are generally used to process γ-TiAl alloys. Ingot metallurgy involves casting and hot isostatically pressing but results in large grain sizes and inferior properties. Superior properties are obtained if the alloy is thermomechanically processed (TMP). The most common hot working routes involve thermal forging and extrusion.

Single phase alloys usually only require stablisation treatments; whilst two phase alloys often require two step heat treatments. The initial heat treatment involves holding the alloy for a period of time at a sufficiently high enough temperature to solutionise and recrystalise the hot worked alloy. The final heat treatments then stablise the

microstructure. Refined lamellar microstructures promote ductility. However, $\alpha 2$ volumes in excess of 20% embrittle the alloy. Optimum ductility results with 10 volume % $\alpha 2$.

The mechanical properties of TiAl alloys can be manipulated through heat treatment. Four Ti-48Al-1V-1Cr-2.5Nb microstructures are outlined below, with the accompanying heat treatments described[6]. Figure 5 shows the micrographs of the accompanying microstructures.

1. Fully Lamellar (diameter of grains around 600μm) : 1,325°C for two hours followed by air cooling.
2. Lamellar + γ grains (~50-100μm in diameter) : same as 1. + 1000°C for 6 hours.
3. Equiaxed Lamellar + γ grains (~10-20μm in diameter) : 1,250°C for 4 hours followed by air cooling + 1000°C for 6 hours followed by air cooling.
4. Fine equiaxed γ grains + small % Lamellar grains : 1,250°C for 3 hours followed by furnace cooling to 900°C + 1000°C for 6 hours followed by air cooling.

The transformation $\alpha 2 \rightarrow \alpha 2^{s} \rightarrow \alpha 2 + \gamma$ is thus temperature and time dependent, with the transformation of $\alpha 2$ to γ grains a sluggish process.

1.2.4 Mechanical properties of TiAl alloys [6]

Ti alloys have so far been used in structural applications resulting in the strengths and ductilities of these alloys being of greatest importance. The effects of some TiAl alloy modifications are outlined below.

1. Ti-52Al has the lowest hardness value at room temperature.
2. At 1000°C strength decreases gradually with increasing aluminium content.
3. Ti-48Al provides maximum elongations under tensile strains.
4. Manganese and chromium improve ductility.
5. Niobium and Zirconium reduce ductility.

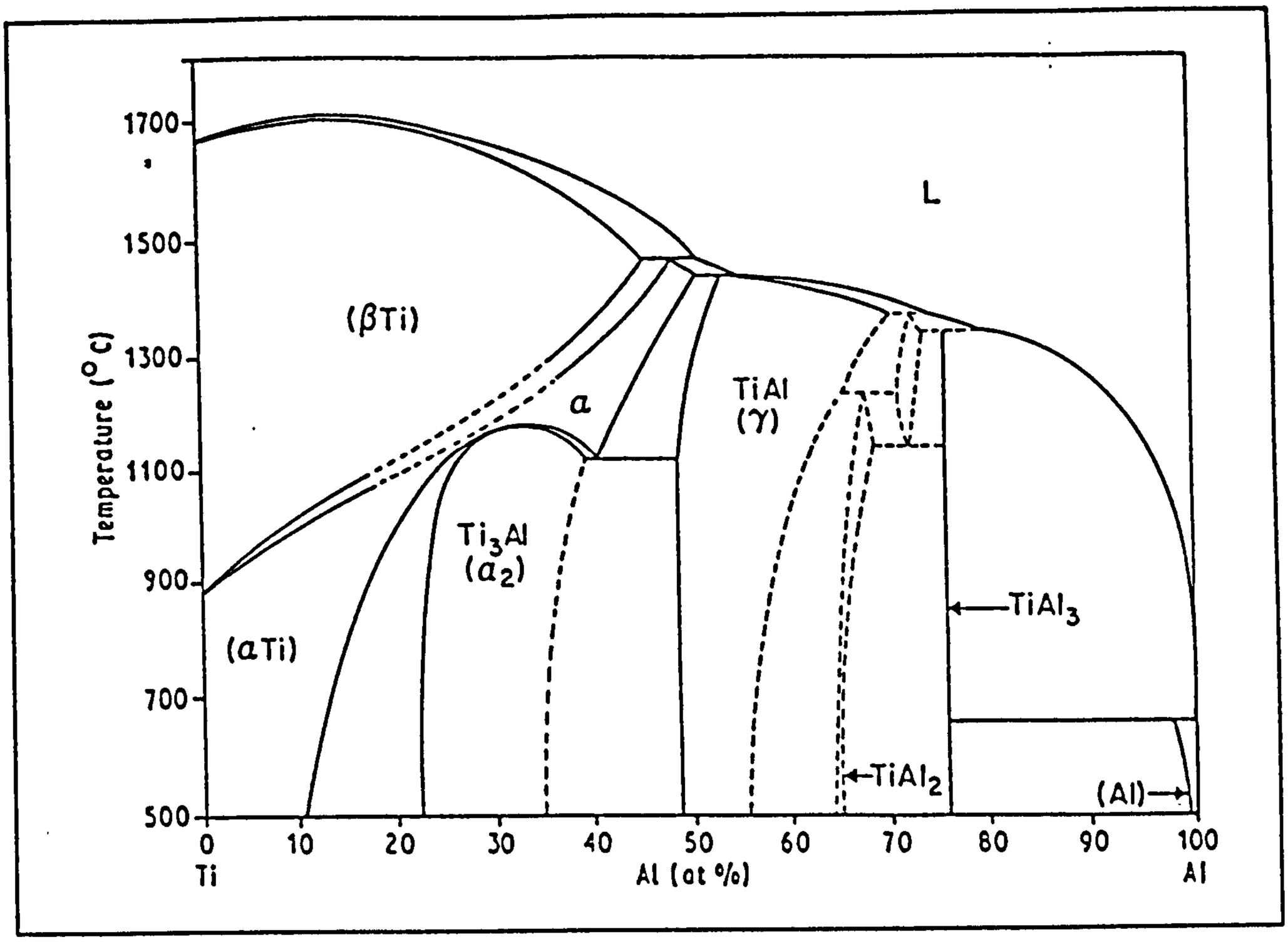

Figure 2: TiAl phase diagram[6]

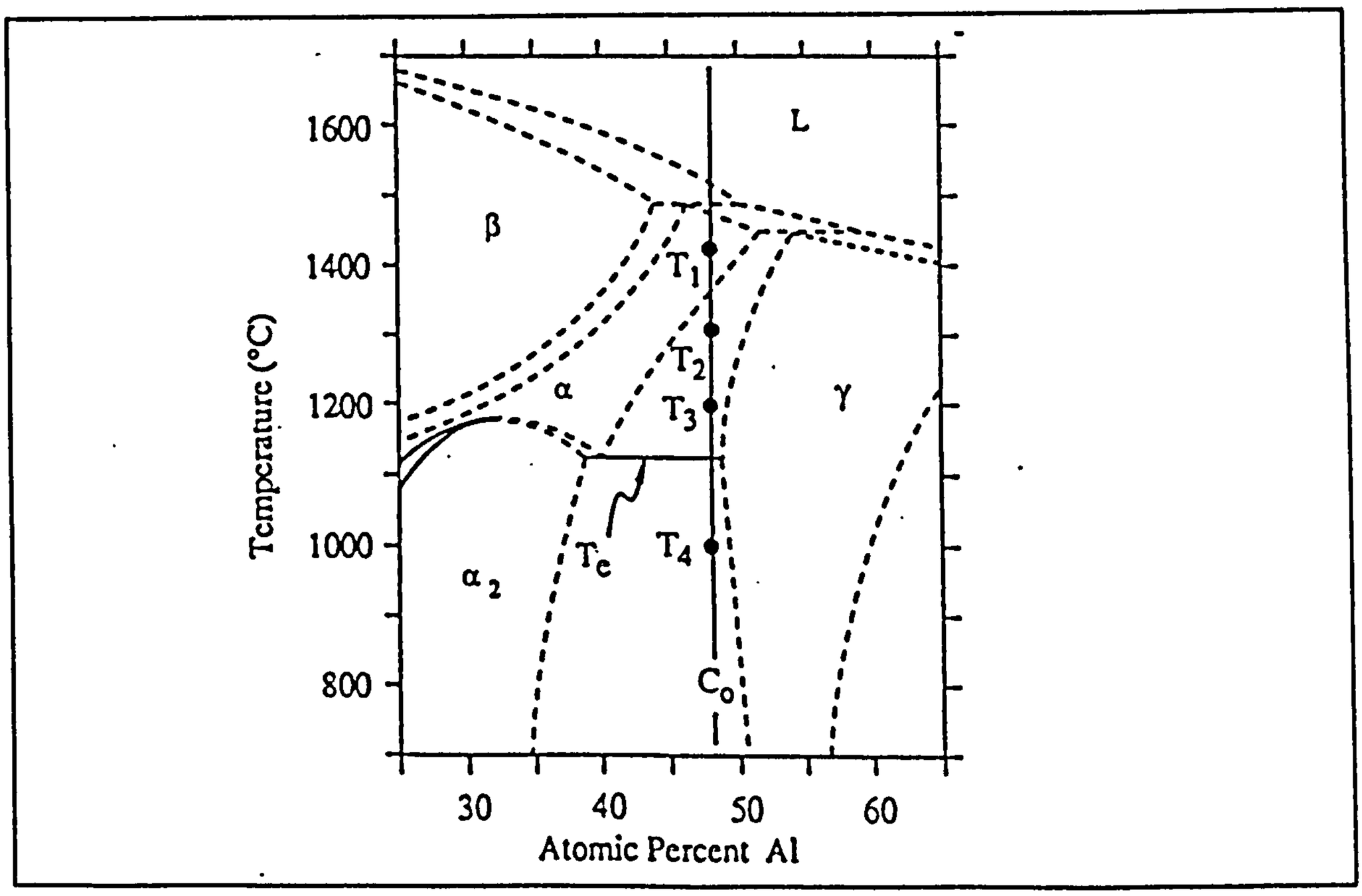

Figure 3: Central region of TiAl phase diagram showing typical heat treatment temperatures used to process γ-TiAl alloys [6]

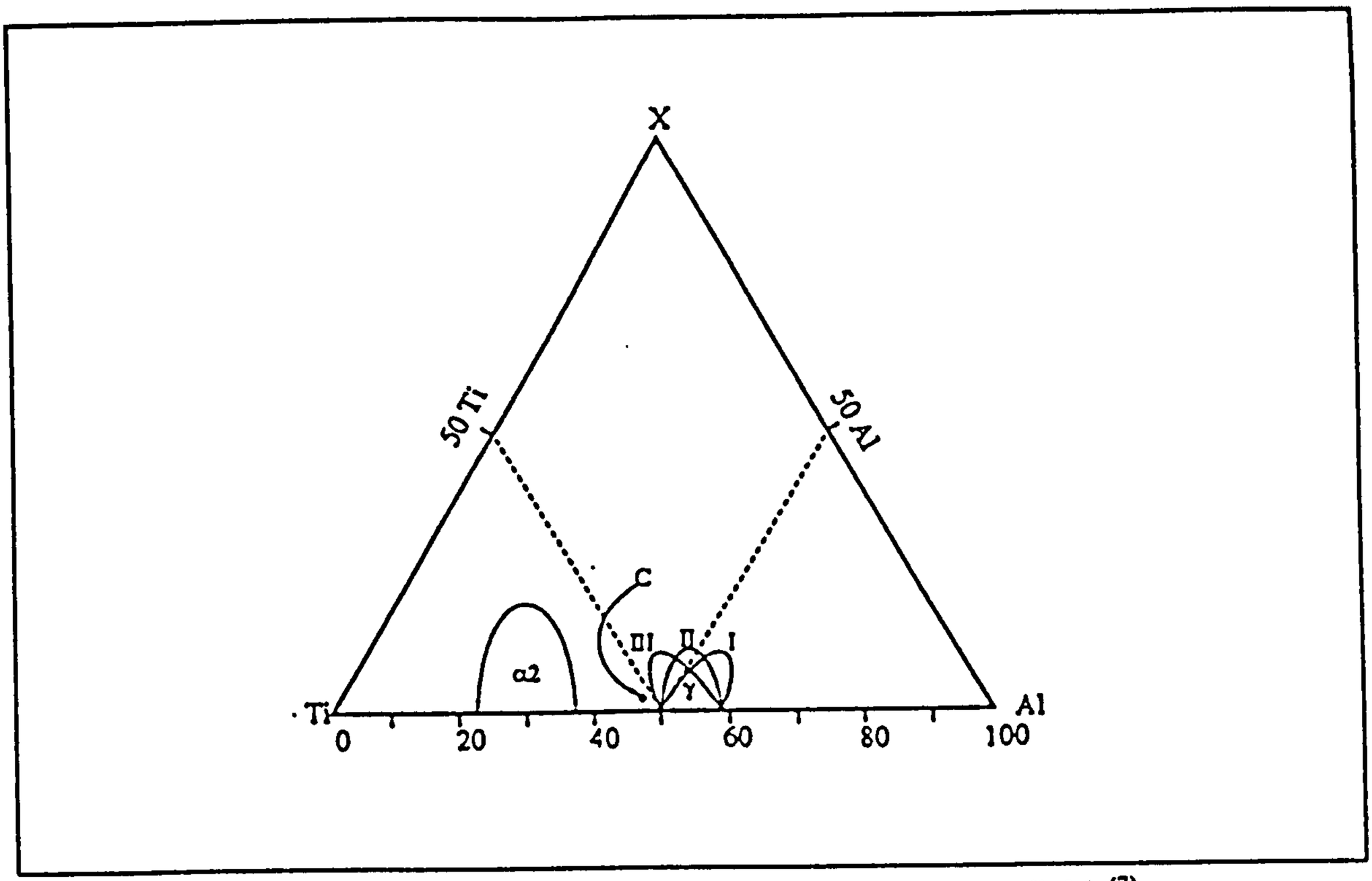

Figure 4: Ternary Ti-Al-X phase diagrams showing the γ phase fields[7]

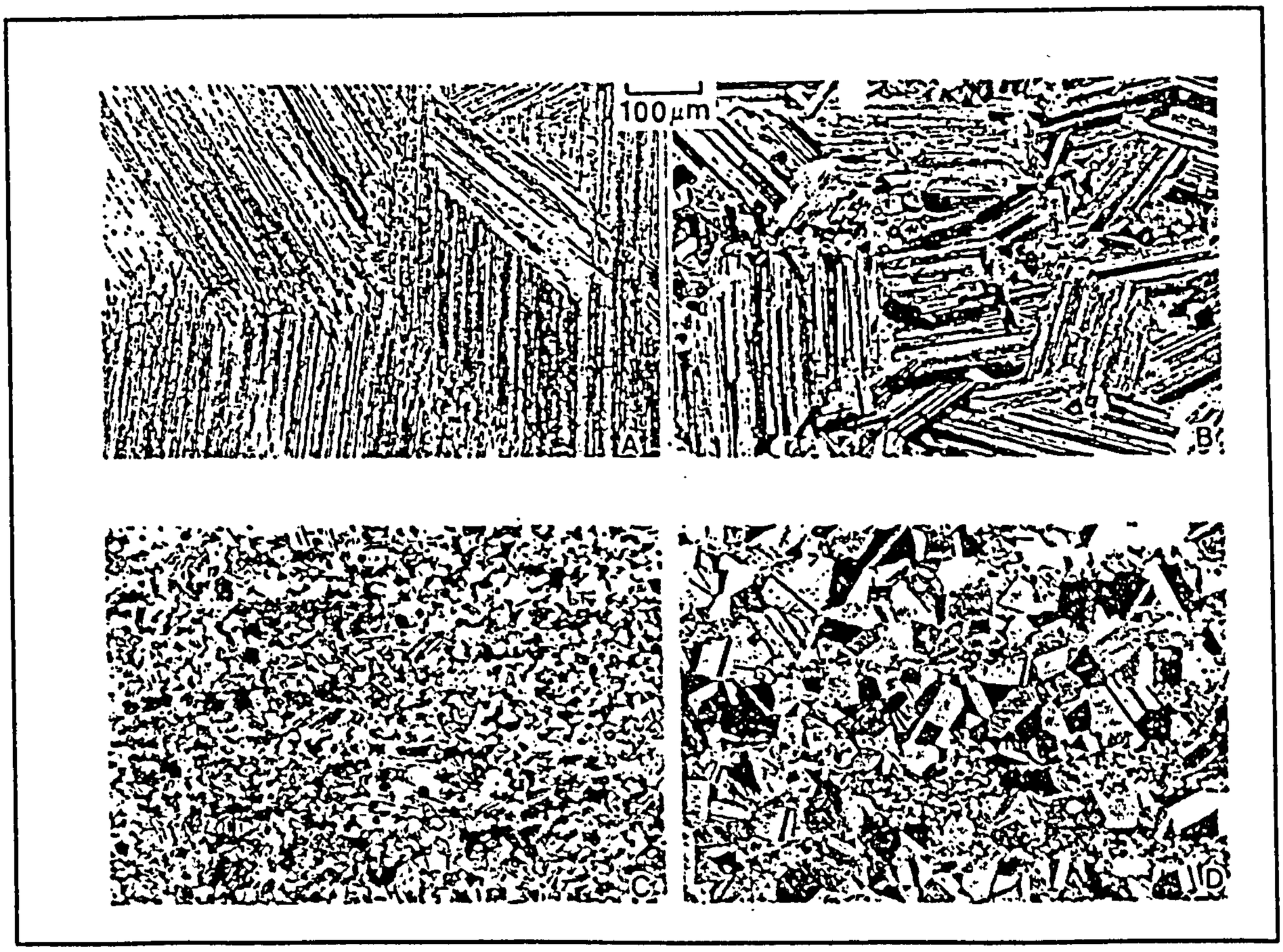

Figure 5: Microstructures of two phase gamma alloys hot worked and then heat treated (a) Fully Lamellar (b) Lamellar+γ (c)Equiaxed Lamellar+γ (d) γ+small%α2 [7]

6. The brittle to ductile transition temperature decreases with decreaseing aluminium content. Ti-54Al has a transition temperature of 700°C.
7. Elastic moduli (160-176GPa) decreases gradually with temperature.
8. Fine grain sizes increase fatigue life below 800°C.
9. Fracture toughness and impact resistance are low at room temperature but increase with temperature.
10. Increasing aluminium content and volume percent lamellar grains increases creep resistance.

Intermetallics are inherently brittle, with deformation being related to the mobility of dislocations through the lattice. Only two types of dislocations exist in the substructure of TiAl[8]. The first type, a/2[110], do not disorder the lattice and move freely as unit dislocations. The second type, a/2[011] and a/2[101], disorder the $L1_0$ superlattice and move in pairs, known as superdislocations. In single phase γ alloys (Ti-(50-56)Al) deformation is limited at room temperature [7]. Ordinary dislocation movement is largely sessile, with superdislocation mobility restricted by the trailing 1/6<112] partials. Yield stress increases with temperature, and peaks at 600°C. This phenomena has been attributed to superdislocation locking, as a result of cross slip creating Kear-Wilsdorf type sessile defects.

In two phase Ti-(47- 50)Al binary alloys superdislocations are pinned by an unknown agent below approximately 630°C[9]. The mobility of the a/6[112] partial dislocations, which are constituents of the a/2[011] superdislocations, controls the plasticity of TiAl. Above 700°C the a/6[112] partials are no longer pinned resulting in twinning, of the type <112>{111}, becoming an increasingly important deformation mode for TiAl. The mode of fracture changes from cleavage at room temperature to intergranular at 700°C. Cleavage fractures result from the pile up of partial superdislocations, during cross slip. The leading partials are forced together and block the movement of the trialing partials. The net result being that wedge shaped cracks are created which rapidly lead to fracture[10].

1.2.5 Factors effecting the ductility of gamma titanium aluminides[6]

Improvements in ductility, gained through alloy modifications, often have detrimental effects on other material properties. By understanding the individual effects it is possible to then develop alloy compositions with optimum mechanical and oxidation properties.

Ductility improvements can be caused by a decrease in lattice tetragonality, a decrease in unit cell volume, a decrease in impurity level, the presence of twins and lamellar microstructure, and a decrease in grain size.

The following points discuss some of the effects alloy additions have on ductility.

1. Decreasing aluminium concentration decreases the c/a ratio of single phase γ-TiAl, improving ductility.
2. In two phase, ternary binary gamma alloys, ductility is not related to c/a ratio. V, Cr, or Mn increase ductility, whilst Nb and W decrease ductility. However, Cr or W decrease the c/a ratio and V, Mn or Nb increase this ratio.
3. Decreases in the unit cell volume are thought to strengthen chemical bonding resulting in improved ductility. Contention exists since V, Cr or Mn decrease the unit cell volume, increasiong ductility, whilst Nb or W also decrease the unit cell volume but result in reduced ductility.
4. Lowering the oxygen content in two phase γ-alloys improves ductility, with the α2 phase expected to have the higher oxygen solubility.
5. Ductility improvements obtained through increasing the proportion of lamellar grains is thought to be as a result of fine uniform deformation of the γ-plates in the early stages of deformation followed by deformation of the α2 plates in the latter stages. This effect appears to be related to lamellar grain orientation.
6. Twinning is enhanced by reducing the aluminium content. Twining, also promoted by V, Mn, or Cr additions, provide a means for deformation which improves ductility.
7. Ternary element additions reduce grain size, increasing the area for grain boundary

deformation, thus improving ductility.

Third alloy additions, such as V, Cr or Mn, may also improve ductility by reducing the aluminium content in the γ phase.

Ductility is dependent on the lamellar/γ (L/γ) grain ratio as well as grain size. Large grain lamellar structures result in the lowest ductilities. Maximum ductilities result if the L/γ ratio is between 0.3 and 0.4.

Alloying additions affect ductility and oxidation resistance of TiAl alloys. Oxidation resistance decreases with decreasing aluminium content or increasing volume fraction α2. A balance has to be reached with neither maximum ductility and oxidation resistance achievable. V, Cr, or Mn additions reduce oxidation resistance but improve ductility. Nb and W improve oxidation resistance but reduce ductility.

Chapter 2

Oxidation of Metals and Alloys

2.1 Principles

2.1.1 The Oxidation of metals

Oxidation can in general be described as the transfer of electrons when any metal combines with an atom or molecular group. In this study oxidation will refer to the formation of metal oxides. All metals and alloys, with the exception of gold, form oxides. The rate of this reaction is generally low at room temperatures, and increases with increasing temperature. Thermodynamic factors determine which reactions take place, whilst the rate of oxidation is governed by kinetic factors, e.g. the rate of diffusional transport through the scale.

A negative change in free energy generally occurs when a metal oxidises. As most materials attempt to reach a state of minimum energy, oxidation will occur in order to form oxides which are thermodynamically more stable than the metal.

Free energy changes can only be used to show which oxides are the most stable. They do not provide information which could be used to predict the final oxide state or at what rate the reactions occur. On this basis of negative free energy changes occurring when the metal oxidises it would be expected for the entire metal to revert to an oxide or oxides. This does not occur as the initial oxidation produces a thin oxide layer (1-4nm thick) which slows further oxidation and helps protect the underlying metal from further oxidation.

The initial stages of oxidation occur as follows;

Oxygen molecules are absorbed onto a metal surface and become loosely bound to metal surfaces during the initial period of contact. The energies associated in the adsorption processes are small (<25kJ/mole)[11]. The oxygen molecules then dissociate and become more strongly bound to the metal through a process of chemisorption which occurs with a much higher energy release(>200kJ/mole). An initial thin film forms over the entire

surface, with a very strong electric field across it. This potential field and/or thermal activation causes metal ions to diffuse to the metal/ metal oxide interface and continue the oxidation process. As the oxide thickness increases the electric field diminishes in strength and the oxidation rate decreases. For the reaction to continue further, sufficient thermal energy is needed, otherwise the oxidation rate may stop.

The defect concentration associated with the formation of these oxide films is important as it determines the transport processes. An important factor in determining the transport processes is whether there is an excess or deficiency in metallic and oxygen ions. Metal oxides with an excess in metal ions or a deficiency in oxygen ions are termed n-type semiconductors. The electronic current is carried by the excess electrons and ionic transport occurs via interstitial metal ions or by oxygen ion vacancies.

P-type semiconductor metal oxides are either deficient in metal ions or have an excess of oxygen ions. Electron conduction occurs via the diffusion of positively charged electron holes and ionic transport occurs via the diffusion of metal vacancies, or oxygen ion interstitials.

A brief summary of these defects found in oxides is given in table 2.

Table 2: Defects found in oxide scales

Type of Semiconductor	Metal excess or deficiency	Oxygen excess or deficiency	Interstitial metal cations or vacancies	Oxygen anions: vacancy or interstitial	+ or - electron
n	excess	-	interstitial	-	+
n	excess	deficiency	-	vacancies	+
p	deficiency	excess	vacancies	-	-
p	-	excess	-	interstial	-

2.1.2 Initial and transient Oxidation of alloys

Initial oxidation of a clean binary A-B alloy results in oxide crystals of both elements forming on the surface. In general the faster growing oxide will then over grow the slower growing oxide. Once a continuous film has formed, atoms of the more reactive element arriving at the scale/metal interface from the alloy will react with the less reactive metal oxide. This results in a displacement reaction,

$$B(\text{in alloy}) + AO = BO + A(\text{in alloy})$$

Thus, as in this case B becomes depleted at the scale/metal interface. Concentration gradients are established in the alloy and scale due to the different activities and diffusivities of the elements in the alloy. The concentration gradients eventually reach a steady state condition.

2.1.3 Rate Equations

Rate equations are used to classify the oxidation behaviour of metals. The rate of oxidation being dependent on temperature, oxygen pressure, reaction time, surface preparation and pretreatment. Rate equations on their own cannot identify the oxidation mechanisms but when correlated with other structural studies narrow down the possible mechanisms.

2.1.3.1 Logarithmic Rate Equations

This type of rate equation is characteristic of metal oxidation at low temperatures. The oxidation rate is initially quite rapid but then drops off to low or negligible values (figure 6).

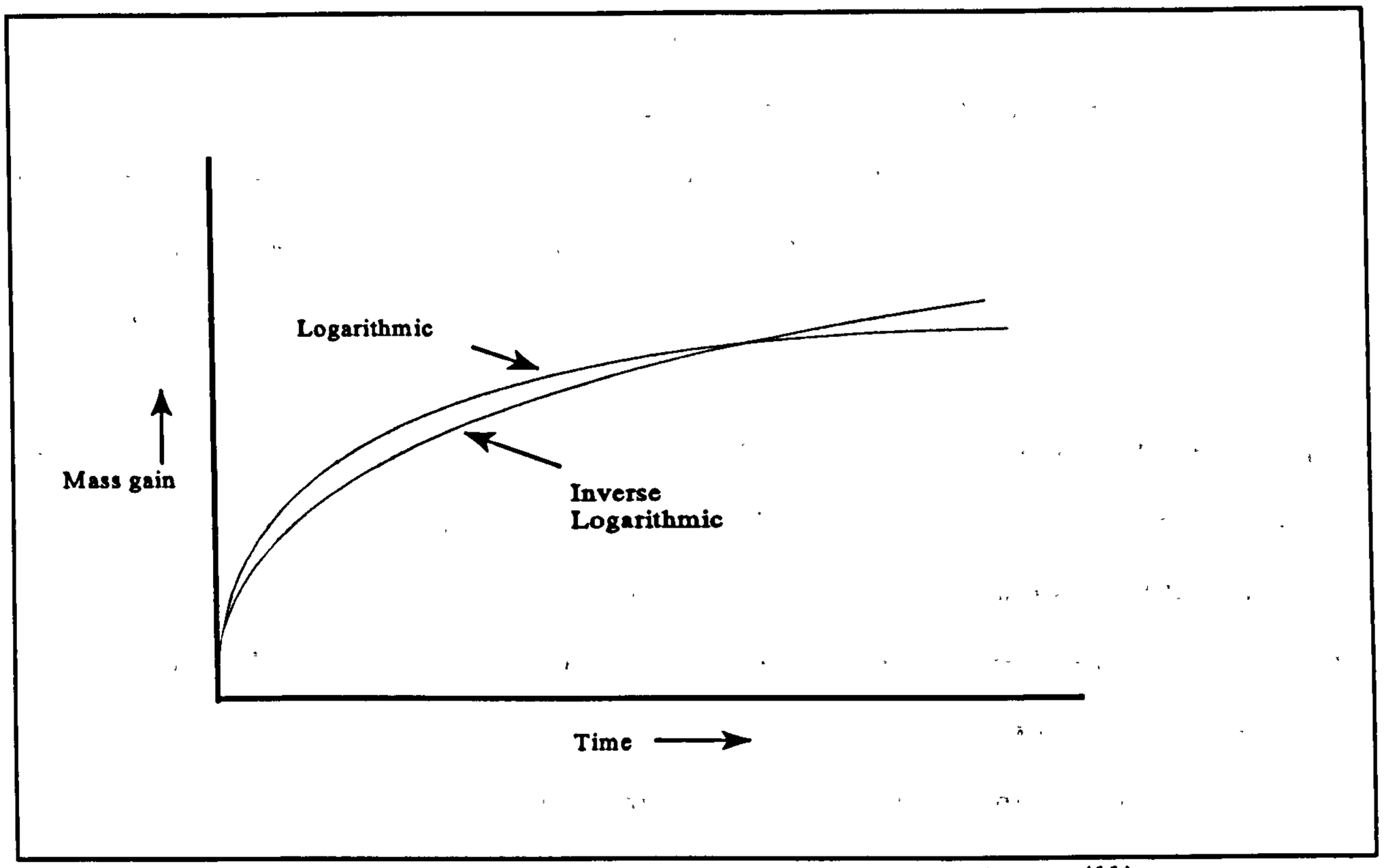

Figure 6: Low temperature Oxidation behaviour[11]

The direct logarithmic rate equation is given by equation 1,

$$X = K_{Log}Ln(t + t_0) + A \qquad (2.1a)$$

where X is the mass gain per unit area, t the oxidation time, K_{log} the rate constant and A a constant.

Many theories have been put forward to explain the kinetics of low temperature oxidation of metals. The validity of the models often being difficult to prove. The most widely accepted theories are reviewed below,

Adsorption of oxygen molecules into the surface is the first step of oxidation. Oxygen molecules collide with the surface, releasing elastic energy resulting in weak physical bonds. Unless these molecules form stronger chemical bonds with the surface they escape back into the atmosphere. The sticking coefficient can give an indication of the type of rate equation. Chemisorption has a coefficient of one, and when a monolayer has formed

the coefficient decreases. For chemisorption to continue at chemisorped sites these species must diffuse into the alloy. Coefficients which remain close to one result in an oxidation rate that is linear with time. Elerlich [12] proposed that the gas is first physically absorbed and that chemisorption continues at sites on the surface where there is a concentration of these physically absorbed molecules.

Once the oxide film covers the whole surface the sticking coefficient falls to low values resulting in very low oxidation rates. Several models predict the reaction rate at this point to be determined by the transport of electrons and ions through the film. At higher temperatures the rate is diffusion controlled. And is caused by the chemical potential established across the scale. At low temperatures an electric field also develops across the film caused by the chemisorption of oxygen. Mott and Cabrera [13] assumed electron tunnelling throughout the oxide maintained equilibrium between the metal and the absorbed oxygen. Thus an electric field is set up which enables the transport of ions across the film. This theory assumes a constant defect concentration and can be represented by an inverse logarithmic rate law. It is only valid for oxide thickness' of less than 2nm.

$$\frac{1}{x} = A - K_{11} \text{Log } t \qquad (2.1b)$$

In this case metal transport into the oxide is rate determining. Mott[14] also derived an alternative rate equation, a direct logarithmic equation, in which electron tunneling through the oxide surface is rate determining.

Grimley and Trapnell [15] later modified Mott and Cabreras thin film theory. They assumed constant field intensity across the film rather than a constant potential difference across the film. For this case, a linear rate equation was derived if metal ions where transported interstitially and a logarithmic equation if this transport occurred via vacancies.

Uhlig[16] also derived a logarithmic rate equation by assuming that the oxidation rate equation to be controlled by the electron flow from the metal to the oxide. The electron

flow being controlled by the space charge which develop at the metal/oxide interface. The space charge changes with time as more electrons are trapped by lattice defect sites

Evans[17], amongst others[18], proposed other models based on the transport of atoms preferentially along grain boundaries, dislocations etc, which are examples of low resistance diffusion paths. Evans[17] derived an asymptotic equation, (2.1c), based on fresh oxide blocking the low resistance diffusion paths and thus oxygen pickup was a function of the number of pores open. This equation follows;

$$X = K_{\alpha}(1 - \exp(K_0 t) \qquad (2.1c)$$

Davies et al [18] also used a pore structure model, but derived a direct logarithmic rate equation assuming new oxides were able to block off neighbouring pores through the formation of compressional stresses.

Evans [17] proposed a further model which also leads to a logarithmic rate equation. In this model film growth is accompanied by an increase in the number of cavities or obstructions. Vacancies may collect at the metal/oxide interface forming cavities resulting in a reduction in the area of film through which transport can occur, this being proportional to the oxidation time.

Finally, Anderson and Gallagher[19] showed that logarithmic kinetics can be linked with internal thermodynamic processes that take place. If the reactions taking place are highly exothermic solid state diffusion is enhanced. This energy may not dissipate fast enough enabling localised atoms to diffuse considerable distances through the solid. This is equivalent to saying that effectively the local temperature rises.

2.1.3.1 Parabolic Rate Equations

These equations describe high temperature oxidation of metals, where thermal diffusion is rate determining. The differential and integral form of the parabolic equation are given

by the following equations[11],

$$\frac{\partial X}{\partial t} = \frac{K_p}{X} \qquad (2.1d)$$

$$X^2 = K_p\, t + C_p \qquad (2.1e)$$

were K_p is the parabolic rate constant, X the mass gain per unit area, t the oxidation time and C_p a constant.

2.1.4 Wagner's Oxidation Theory

Wagner[20] developed a limiting criterion for the transition from internal oxide precipitation to external scale formation which states a critical solute atom fraction, N_B, in an alloy which must be exceeded so that the outward flux of solute is rapid enough for continuous oxide layer formation.

Wagners theory of oxidation assumes ions or electrons to diffuse independently across a compact scale. Equilibrium is also assumed at the oxide/metal and gas/oxide interface.

Wagner[20]showed, if the scale is assumed to be compact and pore free, that the critical concentration N_B (above which only the B oxide is formed) is given by equation 5,

$$N_B = \frac{V}{Z_B M_O} \frac{\Pi K_p}{D_B}^{1/2} \qquad (2.1f)$$

were V is the molar volume of the alloy, Z_B the volume of B atoms, M_O the atomic weight of oxygen, D_B the diffusion coefficient of B in the alloy and K_p the parabolic rate constant for B oxide formation.

Such a reaction in which a metal reacts with oxygen to form an oxide is driven by the change in free energy. As a consequence component concentration gradients are developed across the oxide.

Within oxides containing predominantly metal ion vacancies, the metal ions migrate to the metal oxide/oxygen interface and the vacancies to the metal oxide/metal interface.

Wagners theory of oxidation can also be used to predict oxidation rates. Theoretical predictions are quite accurate at high temperatures but faster oxidation rates and lower activation energies are often observed in practice at intermediate temperatures [21]. Faster oxidation rates can be attributed to short circuit, grain boundary diffusion through fine grained scales which contributes significantly to the outward flux of cations. This may account for the fast oxidation rates observed in Nickel[21] below 1000°C, since lattice diffusion in the oxide is far too slow to explain the oxidation rates.

The parabolic rate constant (K_p) derived from equation 2.1e in section 2.13.1, which describes the parabolic growth of a film thickness (x) with time(t), can be explained using equation 2.1g. The transport properties of the oxide film are incorporated into this equation. The equation relates the parabolic rate constant to the tracer self diffusion coefficients D* of the oxide, where a_o is the molecular oxygen activity (which is equivalent to its partial pressure in atmospheres), *f* is the correlation coefficient for diffusion (close to one) and the limits of integration represent the two interfaces of the film.

$$K_p = \int_I^{II} \left(\alpha \frac{D^*_M}{f_M} + \frac{D^*_O}{f_O} \right) d(\ln a_{O_2}) \qquad (2.1g)$$

2.1.5 Formation of non-planar reaction products

Initial film formation is generally assumed to be non-planar. However, in reality metals are on the whole polycrystalline. Variations in grain size and orientation will, if the anisotropy

of film formation is considered, result in the film thickness's varying according to the individual grain orientation.

Non-planar oxide growth often occurs after a critical scale thickness is exceeded with discrete particles or oxide nuclei growing in the form of polyhedra, particularly at low partial pressures of oxygen and high temperatures.

Whisker, columnar crystal, blade and platelet oxide growth often occurs after longer periods of oxidation. Gulgransen and Capon[22] observed whisker growth in the first few hours of oxidation of iron at 450 C. Blades 10nm thick, and 10^3 - 10^4nm in length, then formed in these areas covering 0.06% of the surface. Blade widths then increased with time, varying from 250-600nm after 23 hours. The presence of water vapour has been observed to enhance whisker and blade formation, as well as their growth rates[23].

The whiskers which grew on multi layered scales are in general higher valence oxides; Fe_2O_3 on oxidation of iron, CuO on oxidation of copper etc, indicating that the oxides where not in contact with the metal when they formed.

Several growth mechanisms have been suggested to explain whisker and blade growth. Depending on the alloy the whiskers could grow from the base (Nb_2O_5 whiskers [24]) or tip (CuO whiskers [25]). One possible mechanism of whisker growth is by chemical vapour deposition (condensation-evaporation processes), but a more common mechanism is thought to be due to short circuit transport. In this case diffusion occurs up through the centre of the whisker. The whiskers may in fact have a hollow core, which act as an easy diffusion path. Such a mechanism explains tip growth of whiskers.

Moist atmospheres increase oxide growth due to water molecules breaking up at a faster rate than oxygen [26] and this is thus the rate determining step. This mechanism does not explain why their are more whiskers in moist atmospheres or their absence in dry oxygen. Water vapour may also effect the plastic properties of scales.

Thick oxide films also show non-planar growth features such as pits and pyramids. In-situ techniques were used to show that scale growth grew from ledges created by screw dislocations at the surface. Kofstad[26] reported that dislocations are important in describing scale morphology. A summary of the morphologies encountered is given below.

- Low Temperatures: Screw dislocations provide mechanism for whisker growth with hollow cores.

- Intermediate Temperatures: The transport process is governed by cation diffusion along dislocations and grain boundaries, causing pyramids and ridges to form due to a broadening of the growth pattern.

- High Temperatures: The transport process is governed by lattice diffusion. The screw dislocations having high surface tension, causing pits to form on the surface.

2.1.6 Stress developed in oxides during oxidation

Stress can be developed via several sources. The dissolution of interstitial oxygen results in lattice expansion and the development of large stresses in the metal. Several factors contribute to the stresses which develop in oxide films[27,28], some of which are sumarised below, while others influence the degree of stress relief.

i. **Volume differences between the oxide and the underlying substrate:** The ratio of the volume of oxide formed per metal ion to the volume of oxide per metal atom, otherwise known as the Pilling and Bedford ratio, can be used to state whether or not compressive or tensile stresses exist in an oxide. Ratios greater than one result in the development of compressive stresses and thus continuous oxide films. Ratios less than one resulted in the development of tensile stresses an discontinuous oxide films. This theory assumes that oxide ions are the only mobile

species in the scale, with the metal ions attempting to expand or contract at the metal./oxide interface to maintain the substrate crystal structure. Volume ratios are useful in predicting the state , but not the magnitude, of the stress in the oxide. This theory fails to take into account oxide plasticity or other stress relieving mechanisms.

ii. **Epitaxial relationships:** Oxide films attempt to adopt the same crystal structure as the substrate at the metal/oxide interface in order to minimise the activation energy for nucleation. The stresses generated by the constraints imposed by the oxides to this growth decrease as the oxide thickens.

iii. Oxide/metal lattice mismatch

iv. **Formation of pores in the oxide, metal, and the metal/oxide interface:** Pores can be developed if cation vacancies, created by the outward migration of cations, coalesce. Pore networks allow oxygen to penetrate into the scale, resulting in oxidation within the scale and a possible build up of compressive stress.

v. **Growth morphology of the oxide:** Preferential oxidation of the substrate that occurs at grain boundaries and other such high energy interfaces results in the development of tensile stresses. The oxide often develops with a buckled morphology

Large stresses may also develop as a result of grain boundaries in polycrystalline materials, as differences in oxidation rates may exist between adjacent grains or because of preferential diffusion and oxide formation along grain boundaries.

The formation of new phases may also act as a source of stress. Preferential oxidation can result in the depletion of an element at the metal/oxide interface with a phase transformation occurring and the possibility of the outer scale breaking down. Scales are generally multi-layered with the different layers having different growth rates, which could

lead to a loss of scale adherence.

In high temperature parabolic oxidation greater stresses are developed by the inward diffusion of oxygen, which occupy consumed metal sites, than the outward diffusion of metal ions which react at the outer free surface.

Stresses are also developed when the oxide is exposed to large temperature changes. This occurs after isothermal oxidation when the oxide is cooled to room temperature. These stresses being the result of differences in thermal expansion between the metal and oxide. Loss of scale adherence and spallation could occur [28]. It was believed that growth stresses dominated at lower temperatures while at higher temperatures stress was relieved by plastic flow in the oxide. Recent investigations by Schutze[29] and many others have shown that it is more likely that stress relief arises from creep in the metal near the metal/oxide interface. The oxide may also sinter at high temperatures through processes such as grain boundary and surface diffusion.

The manner by which stress is relieved is dependent on the mechanical properties of the oxide and substrate. Four mechanisms of stress relief are outlined below [27]. The first two mechanisms result in the formation of discontinuous and thus non-protective oxide scales.

i. **Oxide cracking:** Brittle oxides are weak if put under tension. Hence, oxides with volume ratios of oxide to metal less than one result in cracking.

ii. **Oxide spalling:** Oxides under compressive stresses spall if they have insufficient plasticity. Spallation resistance can be improved by improving scale/metal adherence. The addition of trace elements may improve scale adherence by enhancing oxide plasticity; inhibiting vacancy coalescence at the oxide/metal interface; creating oxide intrusions across the oxide/substrate interface; creating intermediate oxide layers with thermal expansion coefficients closer to that of the substrate; or by tying up sulphur thus preventing it from segregating to the scale/substrate interface.

Scale continuity is critical if the scale is to remain protective. Plastic deformation, leading to stress relief, of the oxide or substrate maintains such scales.

iii. **Plastic deformation of oxide scales:** Cation vacancies are prevented from coalescing and forming voids, during plastic deformation of oxide scales. Scale adherence is also improved. Increasing exposure temperature often increases plasticity, maintaining continuous oxide scales. As the scale thickness increases oxide plasticity often decreases.

Oxide grain size can also effect scale plasticity. At low temperatures oxide deformation occurs through slip mechanisms and is favoured by large grain sizes. At high temperatures oxide deformation occurs through creep mechanisms, but is now favoured by small grain sizes.

iv. **Deformation of the substrate metal:** Stress relief is more likely to arise from deformation or creep of the metal substrate, near the metal/scale interface, especially at low temperatures when oxides are inherently brittle.

Stress relief is often accompanied by oxide cracking[27,28]. Scale continuity and thus protectiveness are affected by the type of crack generated during cooling or oxide growth. Single through thickness oxide scales form during rapid cooling or above a critical scale thickness when large stresses are generated. In this case unstable crack growth often results in scale spallation and rapid corrosion rates. The build up of high energy strain fields results in "tearing " effects.

At slower cooling rates strain energy, due to the differences in coefficients of thermal expansion between oxides and metals, increases at slower rates. Stress reduction occurs as a network of micro-cracks grow at stable rates during cooling[27.28]. On reheating the micro cracks are shortened as a result of rehealing processes. Oxide growth stresses can also lead to micro-crack growth and rehealing. Tensile stresses generated through

preferential oxide growth at the substrate leads to micro-crack formation. Oxygen is then able to penetrate through the network of micro-cracks resulting in crack growth and rehealing.

2.1.7 Oxidation of Titanium and its alloys

Titanium has a high solubility for oxygen, thus the formation of rutile (TiO_2) scale and the solution of oxygen in the titanium alloy are both important to its oxidation. Rutile is an n-type semiconductor due to its excess of metal cations, making the oxide a fast transport route for titanium to the surface. The coexistence of scale formation and oxygen solution makes interpretation of oxidation kinetics for titanium alloys more complicated.

Several rate laws have been put forward to explain the kinetics observed and a lot of discrepancies exist. Most authors are in agreement that more than one law exists, and that the operative law depends on temperature and time of oxidation.

Kofstad et al [26] categorized the different oxidation rate laws according to temperature and time. At 300°C, a logarithmic rate law is obeyed for approximately 5 hours, after which oxidation follows a cubic rate law. At 550°C a cubic rate law operates for a short period of time after which oxidation follows a parabolic rate law. In the temperature range of 600-850°C a sudden change in oxidation rate occurs after long oxidation times. The rate changes from being parabolic to linear. This change occurs after approximately 10 minutes (600s) at 900°C.

During the logarithmic period of oxidation an oxide scale is formed. Kofstad et al [26] found that the dissolution and diffusion of oxygen where small compared to the rate of film formation. Thus while the oxide approaches a limiting thickness, during the logarithmic period of oxidation (<300°C), oxide film formation dominates, with the rate of oxidation decreasing rapidly.

Kofstad et al[26] claimed that the onset of the cubic rate law was related to the diffusion of oxygen into the surface layers of titanium. Thus the duration over which the cubic rate

law dominated decreases as the titanium becomes saturated in oxygen. The main feature distinguishing the cubic rate law from the logarithmic rate law is that the oxygen is continuously diffusing into the alloy. Hence the rate of titanium oxidation changes from being logarithmic to cubic when the rate of oxygen dissolution is much greater than the rate of film formation. At higher temperatures the rate of oxygen dissolution increases shortening the period of cubic controlled oxidation. The cubic rate law can no longer describe titanium oxidation when the metal/scale interface becomes saturated in oxygen. Thus parabolic rate laws operate in the temperature range of 600-850°C, with both scale growth and oxygen solution being diffusion controlled. At these high temperatures the mechanism of oxidation changes abruptly after longer periods of time. The change is associated with a rapid increase in oxidation. A linear rate law describes the increase, which is due to scale cracking. Titanium has a Pilling Bedworth ratio of 1.76 and as a consequence large stresses build up in the scale which ultimately leads to scale failure.

2.2 Oxidation of TiAl and TiAl-Nb

Alloys based on Ti-48Al are predominantly gamma phase (TiAl) with small amounts (<10% by volume) of the alpha 2 phase (Ti_3Al)[30,31,32]. This is shown in the phase diagram in figure 2 in section 1.0. The oxidation behaviour of the binary alloy TiAl has been the subject of a number of investigations. Titanium and aluminium are extremely reactive elements and form oxides with similar stabilities in the presence of oxygen. Aluminium forms a slow growing oxide (α-Al_2O_3), whilst titanium oxides are known to form at much faster growth rates[33,34,35]. In general it has been found that a protective alumina layer does not form on the surface of the TiAl binary alloys [36,37,38]. Instead a layered oxide scale has been observed to form. The kinetics following parabolic growth, as described by equation (2.1e) in section 2.1.3.1.

Rahmel and Spencer[33] used the activities of the Al and Ti in the TiAl system at 700, 900 and 1100°C to calculate the oxygen equilibrium pressures for selected metal/oxide, oxide/oxide equilibria. These are summarised in figure 7 detailed below at 900°C. Both the 700 and 1100°C diagrams were similar.

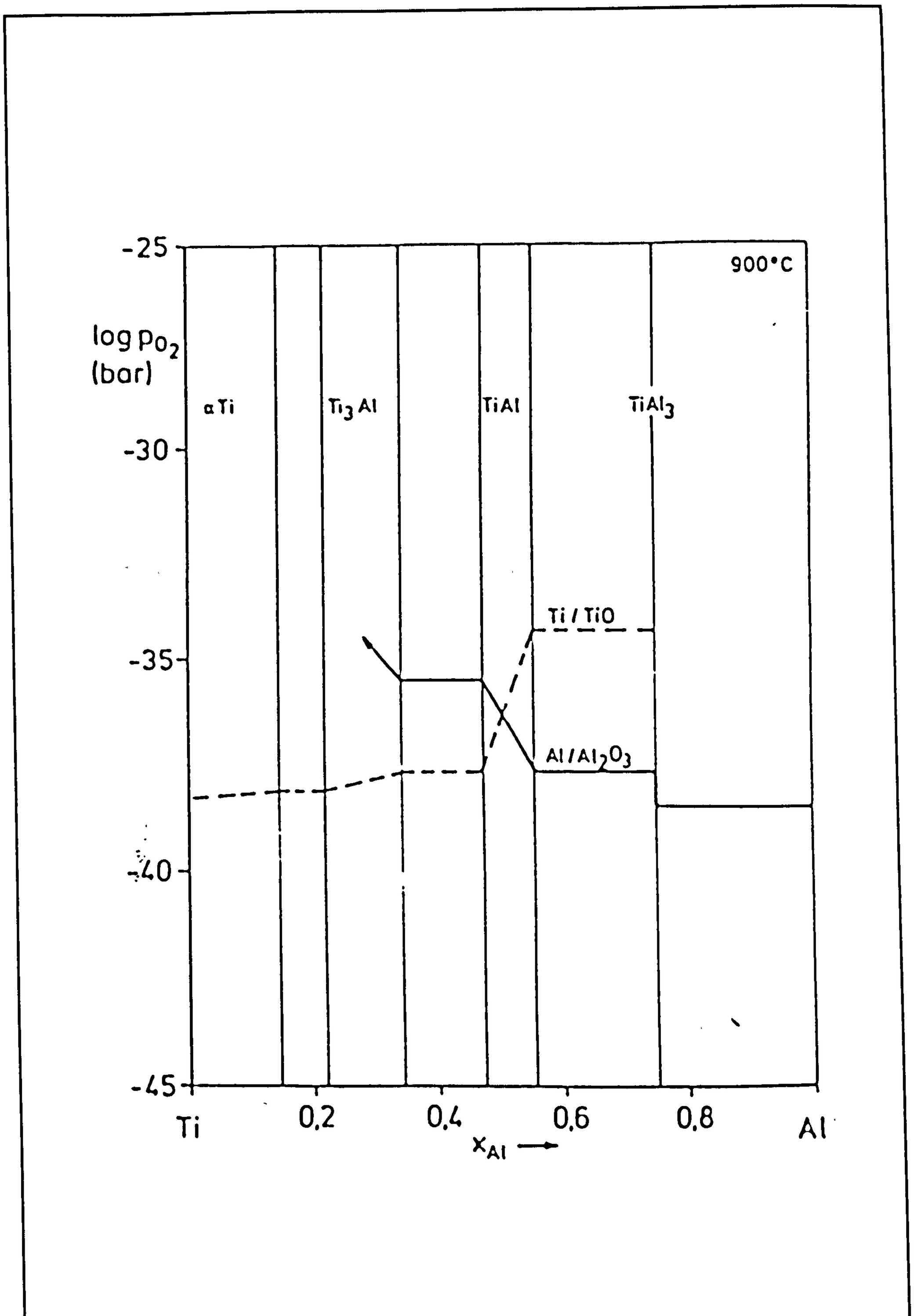

Figure 7: Variation of the metal/oxide equilibrium pressures in the Ti-Al-O system at 900°C[33]

From figure 7 the following can be deduced.

- In the two phase regions Al/$TiAl_3$ and TiAl/$TiAl_3$ the oxygen partial pressure required to stabilise Al/Al_2O_3 is several orders of magnitude below that for Ti/TiO. Hence Al_2O_3 is the more stable oxide.

- In the $TiAl_3$/TiAl phase region the Ti/TiO oxygen pressure decreases with increase in Ti content resulting in the TiO phase being more stable.

- In the TiAl phase region the respective oxygen partial pressures intersect thus indicating that both the oxides will coexist with neither being more stable.

2.2.1 Improving the Oxidation Resistance of TiAl

Oxidation resistance can be improved by the formation of a continuous protective Al_2O_3 scale at the surface. This being favoured by the following.

- Increasing the aluminium content of the binary alloy causing the equilibrium to shift to that favouring the formation of Al_2O_3. However, aluminium depletion can occur below this layer again allowing TiO_2 to become the more stable oxide, later in the oxidation process.

- Alloying with small amounts of elements that will decrease the titanium activity and thus increase that of the aluminium.

Other effects which could aid Al_2O_3 formation are: an increase in aluminium diffusion in the alloy, a decrease in oxygen solubility, a decrease in the diffusion of oxygen into through the scale and a decrease in the extent of transient oxidation[39].

Several papers have reported the beneficial effects of alloying with niobium. Wiedemann[40] among others[41,42,43,44,45,46] confirmed that it promoted the formation of a

protective α-Al_2O_3 scale and as a consequence greatly improved the oxidation resistance. Shida et al [41] found no evidence of internal oxidation at the substrate surface. This resulted from Nb enrichment on the metal side of the metal/scale interface reducing the oxygen solubility in the metal. Third element additions may increase the activity ratio a_{Al}/a_{Ti} so that a larger alumina field is in equilibrium with the alloy. Figge et al [43],among others[44,45], believed that niobium decreased the oxygen vacancy concentration, due to it having a higher valency than titanium. The general effect being to slow the inward diffusion of oxygen. A T.E.M. investigation carried out by Welsch et al[47] on titanium aluminide alloys showed that gamma is oxidized at a faster rate than the alpha 2 phase. The effect of niobium was to increase oxide nucleation but slow long term oxidation as the niobium was observed to form mixed oxides with titanium and aluminium. It was suggested that these oxides acted as possible binder between the insoluble TiO_2 and Al_2O_3 grains.

Bennett et al[48] and many others believed that the addition of Y in Cr_2O_3 forming materials resulted in the segregation of the Y to grain boundaries in the scale blocking grain boundary diffusion, which is often several orders of magnitude greater than lattice diffusion.

Stroosnijder et al[49] found that the oxidation rate of Ti-48Al-2Cr at 800°C was reduced if the surface was ion beam implanted with 10^{17} Nb ions/cm^2 . The improvement in oxidation was similar to that achieved when alloying with a few percent Nb. Although the fundamental corrosion mechanism was not changed it was believed that Nb reduced the period of transient oxidation by decreasing the anion and cation transport through the titania/alumina scale causing the scale to be more protective. This effect occurred without the subsurface composition being modified. Ion implanting with N, C, Al, and Si decreased the ability of TiAl to form continuous protective alumina layers[50].

2.2.2 Oxidation in air

The initial period of oxidation, often referred to as transient oxidation, occurs when there

is a competition between elements forming their respective oxides. A limited understanding of this period of TiAl oxidation exists, but it has been suggested that both TiO_2 and Al_2O_3 form simultaneously and grow laterally[51] or as whiskers normal to the metal surface[52]. After a certain distance the whiskers turn sideways to connect with other whiskers and form a film. The faster growing oxide, in this case TiO_2, overgrows the initial oxide film. Until a continuous alumina layer forms rapid oxidation kinetics are observed.

EDX and metallographic investigations have shown that the surface topography of TiAl changes with increasing oxidation temperature and time. Crystals of TiO_2 grow from being extremely fine to being quite coarse. The surface crystal structure of the Niobium containing alloys remained fine as did the scale thickness.

The scale structure and morphology must first be determined before any oxidation mechanisms can be proposed. This has been done in the literature by comparing TiAl and TiAl-Nb when exposed to air and oxygen. Breakaway oxidation has been identified as being important as the oxidation rate increases rapidly and at a linear rate.

Becker et al [53], along with the majority of investigations which have been made[36-44,47,54], identified the layer compositions seen before and after breakaway oxidation. A three layered scale was observed before this transition in TiAl oxidation. An outer coarse grained TiO_2 layer was proposed to have formed by outward cation diffusion. An inner layer composed of a mixture of TiO_2 and Al_2O_3 was believed to be formed by the inward diffusion of oxygen. Al_2O_3 particles concentrated between these two layers, schematically represented in figure 8a. After breakaway oxidation the scale thickness as increased, and the Al_2O_3 particles were observed to have moved into the outer TiO_2 layer and formed as large particles. It was felt that the Al_2O_3 particles had dissolved and then reprecipitated, signifying the shift to breakaway oxidation. A network of pores was also left behind. Becker et al[53] found that alloying with niobium did not dramatically change the scale

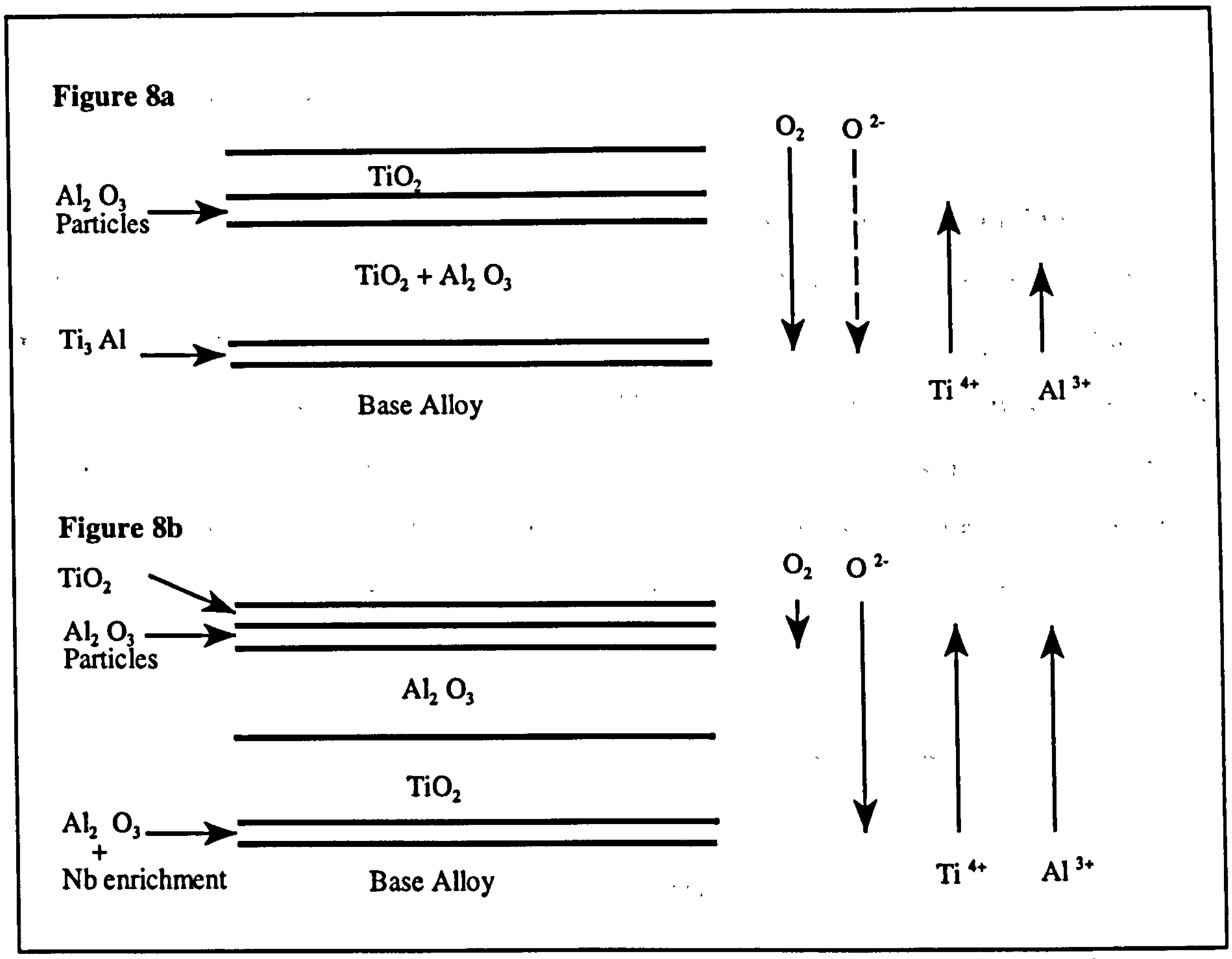

Figure 8: Scale structure after 100 hours oxidation in air a) TiAl b) TiAlNb[53]

structure. However, there were some key differences (figure 8b). After 1000 hours at 900°C two distinct layers could be seen, an Al_2O_3 rich layer above a similarly TiO_2 rich layer. Like the binary alloy a TiO_2 surface layer was present, but just below this a very thin layer of Al_2O_3 particles was seen. The Al_2O_3 layers were believed to act as diffusion barriers. An extremely thin Al_2O_3 layer rich in niobium, which was revealed by EPMA, existed at the metal/ scale interface, and this was thought to be responsible for improving the oxidation resistance. Niobium was also identified in the TiO_2 rich inner layer. No niobium was found in the outer TiO_2 layer. After longer exposure times at 950°C in air, two titanium nitride layers were observed to form directly beneath the scale, together with a niobium rich layer immediately beneath these layers.

Maki et al [55] studied the distribution of each alloying element using EPMA. Profiles on cross sections of the oxides for TiAl and TiAl-Nb at 900°C after 16 hours are reproduced in figure 9. The TiAl distributions confirm previous observations of the formation of a

discontinuous alumina layer, containing voids and pores. The TiAl-Nb alloy formed a more continuous layer with fewer pores and voids.

Figge et al[43] investigated the effect of niobium in air at 800°C and found that a similar scale structure developed. Figure 10 shows how the oxide scale within Ti45Al10Nb and Ti50Al changed with oxidation time. Both alloys developed an alumina scale during the early stages of oxidation at 800 and 900°C. TiN rich zones were also identified below the external oxide layers. A depletion of aluminium occurs in the subsurface zone implying a decrease in aluminium activity. As oxygen activity increases alumina becomes unstable at the metal/scale interface resulting in the outward diffusion of titanium ions.

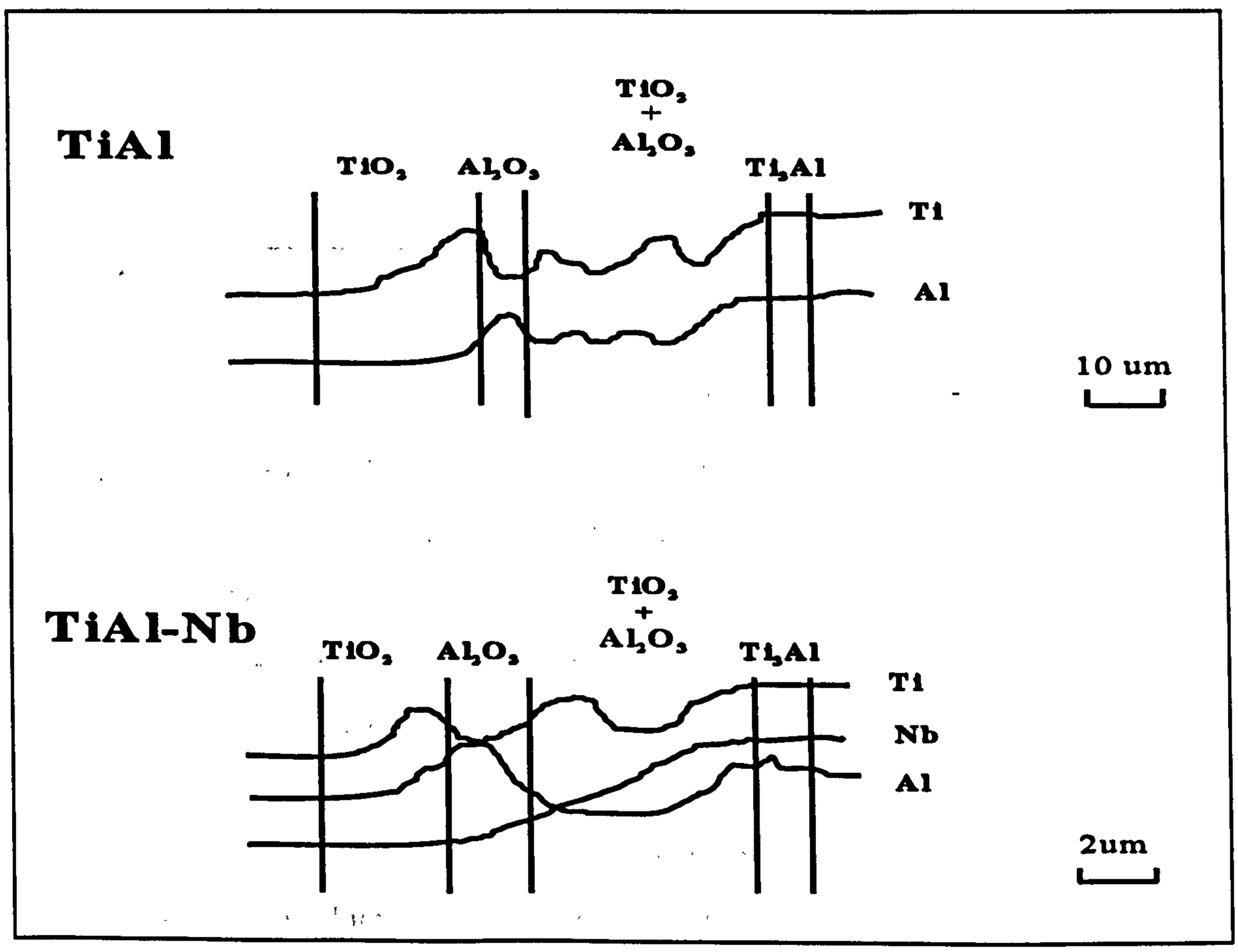

Figure 9: EPMA of TiAl and TiAlNb scale structures[55]

Niobium was identified in the nitride layers and would appear to slow the growth of an external TiO_2. Niobium was not found in the outer oxide layer, although it did occur in

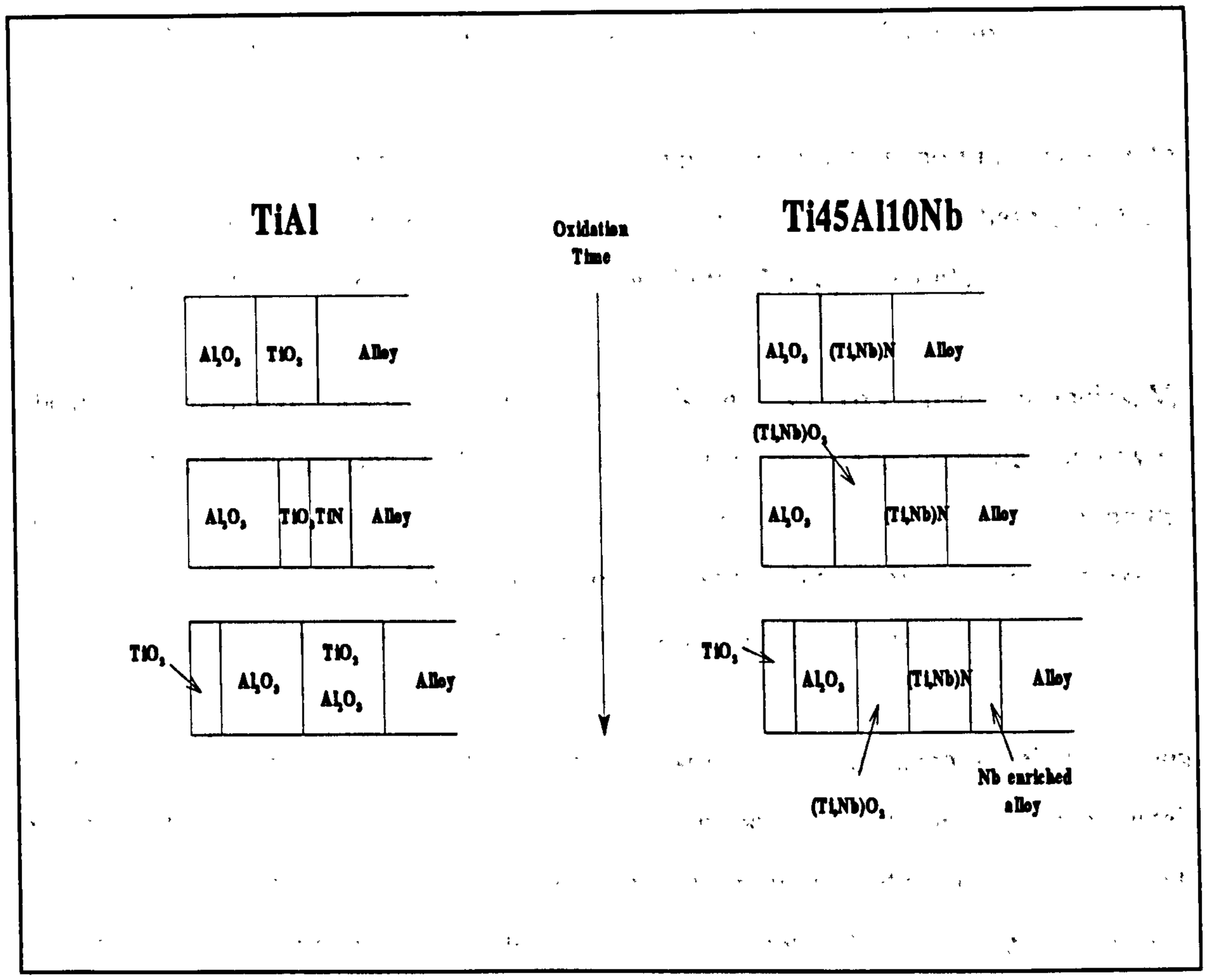

Figure 10: Initial scale growth of TiAl and TiAlNb in air[43]

the inner TiO_2 layer. It was proposed that once in solution in the rutile layer niobium, with a higher valency, reduced the oxygen ion concentration thus slowing the inward diffusion of oxygen. The solution of niobium in TiN may also stabilise the nitride layers, further increasing oxidation resistance. Niobium enrichment directly beneath the nitride rich layers was believed to be the result of an apparent depletion of aluminium and titanium in this region or as a consequence of niobium having a higher solubility in TiN than TiO_2, and no solubility in Al_2O_3. Thus as the nitride layers are oxidized the niobium could itself be oxidized or diffuse through these nitride layers back into the alloy. The oxygen partial pressures beneath the alumina/titania layers were too low for the niobium to be oxidised so niobium appears to have diffused back into the alloy.

2.2.3 Transport processes in oxide scales formed on TiAl alloys

Becker et al[53] made a comprehensive attempt at explaining the transport processes in the scale which forms on TiAl. They assumed that the scale consisted of two phases, TiO_2 and Al_2O_3, and that the transport processes occurred in the TiO_2 phase only.

The defect structure of TiO_2 was suggested to consist mainly of oxygen ion vacancies, V_O, and interstitial titanium ions, Ti^{+++}. The concentration of defects depended on oxygen pressure. From defect concentration formula for the two defect types it was found that titanium ions predominated at low oxygen pressures and high temperatures; whilst oxygen ion vacancies predominated at low temperatures and high pressures.

Parabolic oxidation occurs by the inward diffusion of oxygen accompanied by some outward cation diffusion. The outward diffusion proportion increases to approximately 30% at 900°C, compared with 8% in pure titanium, implying that alumina dissolves into the rutile scale and reprecipitates in the external titania layer. This is thought to cause an increase in titanium interstitial ion content.

A model describing this dissolution of alumina in titania was presented by Becker et al[53] and has been used to explain the following:

1) An increase in the ratio $(cD)Ti^{+++}/(cD)V_O^{-}$ through the scale, where c is the concentration gradient, and D the diffusion coefficient.

2) A decrease of aluminium solubility in titania with increasing oxygen pressure.

Equations 2.2a and 2.2b consider the dissolution of alumina. Equation 2.2a shows the substitutional dissolution of oxygen ion vacancies. Equation 2.2b shows the formula of substitutional dissolution when interstitial titanium ions predominate. The defect concentration increases with dissolved alumina. The majority of alumina would appear to be dissolved interstitially in titania as the Al ions are only mobile in this phase. The

models do not account for the increase in titanium ions or the decrease in oxygen vacancy concentration. The interstitially dissolved Al_2O_3 will decrease the concentration of interstitially dissolved titanium ions. The outer scale therefore grows at a slower rate than the inner.

$$Al_2O_3 = 2Al_{Ti} + V_O^{++} + 3O_O \qquad (2.2a)$$

$$Ti_{Ti}^{*} + 2Al_2O_3 = 4Al_{Ti} + Ti^{+++} + 6O_O^{*} \qquad (2.2b)$$

Oxygen pressure reduces the solubility of alumina in titania. The mechanisms of alumina formation and dissolution can be understood by considering the correlation between the concentration of oxygen ion vacancies and oxygen pressure. Equilibrium was assumed at the gas/scale interface and it was further assumed that oxygen pressure follows a parabolic relationship reaching a maximum at the surface. Becker et al[53] used their model to explain the formation of a protective alumina layer between the outer and inner scale. A large difference in alumina solubility between the two layers, due to a higher flux of oxygen ions in the outer layer causes a steep concentration gradient of oxygen ion vacancies to exist at the interface. Alumina precipitates as a consequence of this discontinuity.

The above model can be used to explain breakaway oxidation as well. Equilibrium is assumed to exist at the gas/scale, external scale/internal scale and scale/metal interfaces. The concentration of oxygen ion vacancies also remains constant across the scale. With increasing oxidation time the scale thickness increases resulting in the alumina solubility gap at the internal/external scale interface narrowing. The alumina particles therefore redissolve and are precipitated at or near the scale surface where the solubility of alumina again decreases with increase in oxygen pressure. The net result is that the oxygen ion flux across the scale increases. Pores within the alumina layer provide experimental evidence for this phenomenon. The scales were also seen to fail in these regions.

2.2.4 Nitride layer formation

Becker et al[53] also believed Ti_2AlN and TiN form beneath the scale by the diffusion of nitrogen along microcracks rather than through the lattice. Once initiated, nitridation would then have been self sustaining as a volume increase of 12% by nitride formation would cause additional scale cracking.

The possible transport processes which could occur in the nitride layers beneath the oxide scale are shown schematically in figure 11. It was believed that initially Ti_2AlN forms and is then transformed into TiN. For this to occur nitrogen must diffuse through the TiN. Additionally Al would have to diffuse from the TiN/Ti_2AlN interface through the Ti_2AlN into the base metal or through the TiN layer into the oxide. The fact that high concentrations of Al existed between the Ti_2AlN and the metal provides evidence to suggest that very little aluminium diffused outwards into the oxide.

Thus a layered structure, TiAl/Ti_2AlN/TiN, develops below the scale . As both Al and Ti form stable nitrides continuous layers are formed. However, it was believed that the nitride layers only formed after long oxidation times and after an alpha 2 layer had formed beneath the scale. This zone will have been oxygen enriched hence alumina precipitates ahead of the nitride zone can be accounted for. Lee at al [31] observed internal oxide precipitation at 1100°C in a two phase (TiAl + Ti_3Al) alloy. Two structures were identified near the scale/metal interface. Dark alumina plates were found within the TiAl plates and finger like TiO_2 structures in the $TiAl_3$ plates. Cracking between the TiAl/Ti_3Al plates was also seen at 1000°C

Nitride formation can affect oxidation kinetics by decreasing titanium activity and increasing that of aluminium favouring the formation of alumina. A detrimental effect may be the embrittling nature of the nitrides that are formed.

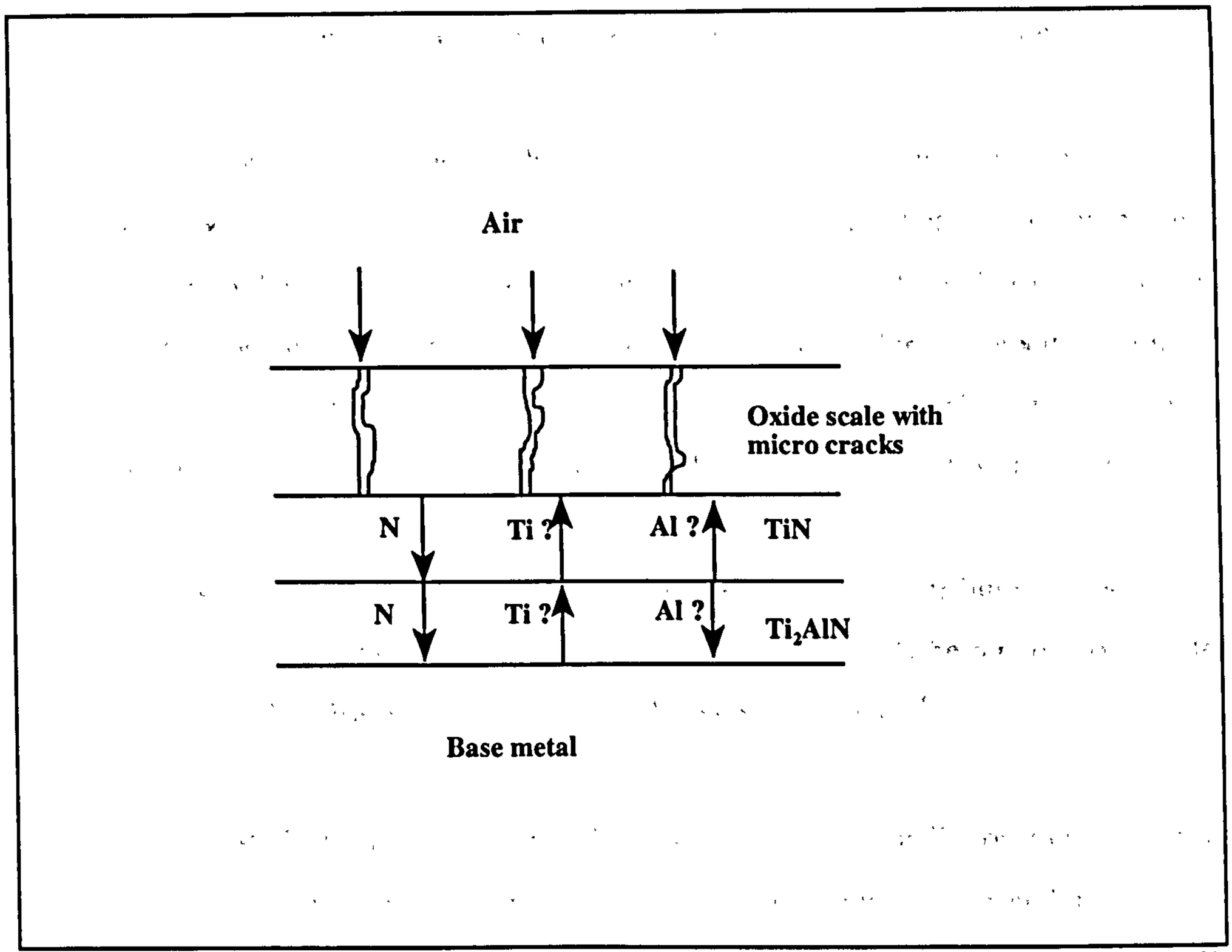

Figure 11: Nitride layer formation beneath oxide layers[53]

2.2.5 Cyclic Oxidation

Isothermal oxidation fails to take into account the severe temperature changes that may occur in service. It is therefore important to know the effect temperature changes have on oxidation behaviour, where component lifetimes are reduced. Becker et al[56] studied the cyclic oxidation of Ti36Al and Ti35Al5Nb0.1C between 800 and 1000°C in air. Negligible scale spallation occurred during cycling from 800°C. At 900°C the TiAl alloy suffered a mass loss of 50mg/cm^2 after 50 cycles, where one cycle involved cooling the specimen down to 40°C after an hour at the test temperature. The TiAlNb alloy showed much better resistance to cyclic oxidation and very little (<3.0mg/cm^2) mass loss was observed up to 1000 cycles at 900°C, or 100 cycles at 950°C. Similar surface scale morphologies were seen compared to those seen under isothermal conditions. Large TiO_2 crystals developed at unspalled areas. Several separate scale layers of similar

thickness occurred where spallation was in evidence, under cyclic conditions.

The results obtained by Becker et al[56]showed that spallation occurred after a critical scale thickness had been reached. Scale failure was associated with a critical strain having been exceeded. Strain develops in the scale during cooling because of the thermal expansion mismatch that occurs between the scale and metal. Scale failure is dependent on the fracture toughness of the scale, size of physical defects in the scale, length of oxide intrusions into the metal, and the Youngs' modulus and Poisson ratio of both the scale and the titanium aluminide. The critical scale thickness was not reached at 800°C. The TiAlNb alloy showed better cyclic oxidation resistance which was attributed to the slower growth rate of the scale leading to the critical scale thickness only being developed after longer times. Similar observations were made by Subrahmanyam[57].

Meier[58] suggested that third element additions may reduce spallation by; preventing vacancies from condensing into interfacial voids; changing the scale growth mechanism and therefore reducing growth stresses; increasing scale plasticity to accommodate stresses generated by creep; or by strengthening the scale-alloy interface.

Chapter 3

High Temperature Sulphidation

3.1 Introduction

Sulphidation can be defined as the corrosive attack experienced by metals and alloys when exposed to sulphur bearing atmospheres at elevated temperatures, leading to the formation of sulphides. The effects of the sulphidation reactions on mechanical properties are important in combustion engines where sulphur containing fossil fuels are used.

The kinetics of sulphidation have received much less attention than high temperature oxidation. Strafford et al [60,61] reviewed the process of sulphidation and found that the sulphidation of metals and alloys is very similar to oxidation. There were however a number of important differences. Sulphidation reactions occur at several orders of magnitude faster than oxidation and the scales produced generally have more complex morphologies. Severe sulphidation attack occurs under conditions of low oxygen potential. The present alloys for service under conditions of high oxygen activity (Partial pressure of oxygen $pO_2 > 10^4$ Pa) are based on iron, cobalt or nickel and titanium. These alloys are generally inadequate when exposed to high sulphur/low oxygen activity gases. Strafford concluded there is therefore a need to develop alloys which are resistant to sulphidation under these low oxygen conditions.

In gasification and liquefaction of coal the partial pressure of oxygen in the processing gases is very very low, of the order of 10^{-20} - 10^{-25} atmospheres, with sulphur pressures several orders of magnitude greater (10^{-6} - 10^{-9} atmospheres). These environments are thus highly sulphidising and therefore extremely aggressive. Combustion gases in marine and airline service differ in that they are highly oxidising, due to the partial pressures of oxygen being several orders of magnitude greater than that of sulphur. Even in environments containing trace amounts of sulphur the majority of oxidation resistant alloys: chromia and alumina formers in particular, undergo rapid and often catastrophic material degradation. Work completed by Mrowec[62] showed that a nickel based alloy (Ni-9Cr-6Al-0.1Y) remained oxidation resistant after 96 hours at 1000°C in air, but that the alloy substrate underwent severe attack when low levels (550ppm) of sulphur were added to the gas flow. Non-protective, heterogeneous, thick scales formed, containing oxides,

sulphides and metallic inclusions.

Mechanisms for the corrosion of materials in oxidising-sulphidising atmospheres are complex and not fully understood. Chromia and alumina forming materials offer very little protection from these environments, as it is only a matter of time before catastrophic alloy degradation occurs. Figure 12 shows that sulphur bearing environments degrade even the most protective oxide scales. An incubation period, which depends on the integrity of the oxide scale, is then followed by the diffusion of sulphur atoms through the oxide layer, reaching the oxide-alloy surface where rapidly growing sulphides form. The oxide scale is then gradually degraded with the inward diffusion of sulphur and the outward diffusion of cations, producing both internal and external sulphides.

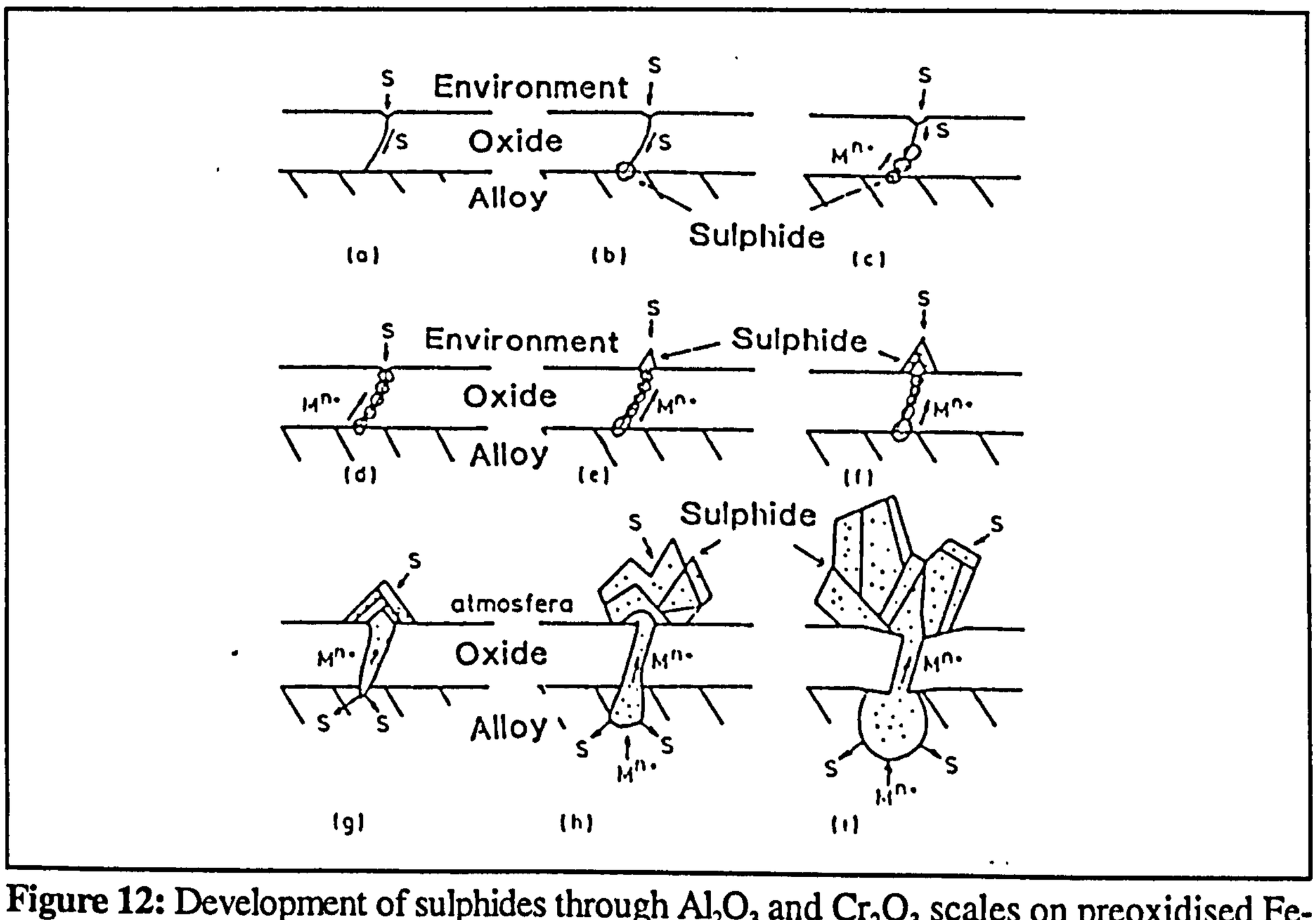

Figure 12: Development of sulphides through Al_2O_3 and Cr_2O_3 scales on preoxidised Fe-Cr-Al alloys[62]

Sulphur vapour is extremely aggressive at high temperatures, attacking all metals including gold and platinum. At these elevated temperatures transport through the metal

sulphides occurs through point defects i.e volume diffusion. The lower melting points of sulphides means that volume diffusion can occur at lower temperatures than in the oxides.

Pure metals undergo extremely rapid sulphidation rates. The sulphidation scales grow in a similar manner to that of the oxide scales, with the outward diffusion of cations. The sulphidation rates of nickel, cobalt and chromium are several orders greater than the corresponding oxidation rates. Although the sulphidation scales grow at parabolic growth rates the accelerated rates of corrosion are believed to be due to the high concentrations of point defects in the sulphide scales.

Mrowec[62,63] showed that alloying with 60 at.% Cr improved the sulphidation resistance of Fe, Co and Ni, with inner barriers of sulfo-spinels being developed. Higher levels of Cr resulted in the formation of Cr sulphide rich scales. However, the sulphidation rates remained up to four orders of magnitude greater than their respective oxidation rates. Aluminium additions of up to 20at.% improved sulphidation resistance to a lesser extent, only reducing the sulphidation rates by two orders of magnitude. Thermodynamic and kinetic factors were used by Mrowec to explain the differences between sulphide and oxide corrosion at high temperatures. Highly protective oxides formed in oxidising atmospheres due to the selective oxidation of Cr and/or Al. In contrast non-protective heterogeneous scales, containing sulphides of all alloying components, formed in sulphidising atmospheres. From a thermodynamic point of view it was found that Al_2O_3 and Cr_2O_3 have much higher free energies of formation than the base metal oxides. Hence stable oxide layers were able to form. Slow oxide growth rates and high enough interdiffusion within the alloy maintained high enough Cr/Al activities, at the scale/substrate interface, for selective oxidation. The situation is different for the sulphidation of Ni, Co and Fe alloys containing Cr and/or Al. The free energies of formation of the base metal sulphides and Cr/Al sulphides are too close, making selective sulphidation of Cr/Al thermodynamically unfavourable. High sulphidation rates of the base metals prevented continuous Al/Cr sulphides from forming

3.2 Principles of Sulphidation resistance

Inhibiting sulphidation could be achieved by

1) developing oxide scales that are stable in low PO_2 environments or

2) using alloy additions to reduce the defect concentration of the diffusing species responsible for parabolic scale growth in the metal sulphide.

Strafford[46] found that large amounts of Molybdenum (10%) when added to Chromium caused the sulphidation rate to decrease. In this case Cr^{3+} ions where substitutionally replaced by Mo^{+} ions. The Mo reduced the quantity of mobile Cr^{3+} cations. This approach of reducing the concentration of diffusing species is limited by the availability of alloying elements with suitable valency and ionic radii.

Sulphidation resistance can also be enhanced by alloying with elements which promote the formation of sulphide barrier layers. Alloys of the type AB, with the concentration of A greater than B, can be made to be sulphidation resistant by choosing element B to undergo selective sulphidation producing a compact and protective inner barrier layer. There are various thermodynamic and kinetic considerations which need to be considered before attempting to produce sulphide barrier layer alloy and are considered in the following section.

Mrowec[64] showed that one of the best solutions in slowing the sulphidation effects was to preoxidise the specimen. However, the specimen is only protected whilst the oxide layer remains intact. This is known as the incubation period. During this period sulphur diffuses through the oxide along grain boundaries and reacts with the substrate forming sulphides. In this manner sulphides build up along the grain boundaries until they breach the surface. Metal ions are thus transported to the surface through the sulphides. This is a much faster transport route than the diffusion of the metal ions through the oxide scale.

The incubation period is dependent on the oxide defect concentration.

3.2.1 Thermodynamic considerations for sulphidation[60]

Using available thermodynamic data it is possible to predict the alloy concentration, temperature and sulphur activity of the atmosphere needed for preferential sulphidation of the alloying element. The free energy data in table 3 would suggest that alloying elements such as aluminium and chromium would be preferentially sulphidised if alloyed to nickel, iron or cobalt. The more negative the free energy of formation of a compound the more energy is needed to dissociate the compound, hence the more stable. These elements must however be present in sufficient concentrations. In the context of titanium aluminide alloys titanium would appear to be preferentially sulphidised. The general reaction between metal and sulphur being,

$$2(x/y)\,M(s) + S_2\,(g) \Rightarrow (2/y)\,M_XS_Y\,(s)$$

Table 3: Free energies of formation of selected sulphides

Element	Sulphide	Free energy of formation ΔG_f	P_S for M/MS equilibrium PS_2
Al	Al_2S_2	-284.3	3.4×10^{-10}
Ti	TiS	-383.4	1.3×10^{-15}
Nb	NbS_2	-289.4	1.0×10^{-10}
Cr	Cr_2S_3	-313.7	5.8×10^{-12}
Fe	FeS	-194.9	8.0×10^{-6}
Co	Co_9S_8	-161.2	5.9×10^{-4}
Ni	NiS	-138.6	1.9×10^{-3}

3.2.2 Reaction Kinetics[60]

Selective sulphide barrier layer formation is governed by thermodynamic considerations whilst the rate of attack is governed by various physio-chemical properties.

The Pilling Bedworth principle states that a protective scale can be predicted if the molar volume of the sulphide is greater than unity. Table 4 examines various volume ratios of sulphides. If the P.B. ratio is large and an adherent scale forms the stress level may become sufficient to cause scale rupture, or for porosity to develop, in which case the scale is no longer protective.

For a sulphide/oxide scale to be protective the growth rates of the secondary and tertiary alloy sulphides must be slower than the base metal sulphides. The growth rate being dependent on the thermodynamic activities at the scale/gas and metal/scale interfaces.

Table 4: Volume ratios of selected sulphides

Sulphide	P-B Ratio	Defect structure	Melting Point (K)
Al_2S_3	2.6	n type	1372
TiS_2	1.11	n type	2272-2372
NbS_2	.....	n type	.....
Cr_2S_3	2.5 (CrS)	n/p type	1823
FeS	2.5	p type	1462
Co_9S_8	2.37	p type	1353
NiS	2.5	p type	1069

Table 5 shows that the self diffusion coefficients in sulphides are several orders of magnitude greater than their corresponding oxides.

The melting point of metal sulphides effects the sulphidation rate. Higher sulphidation

rates occur the closer the melting point is to the actual operating temperature and is due to higher ionic diffusion rates in the sulphides. If this principle is obeyed then aluminium would be expected to have the higher diffusion rates in Al_2S_3, than Ti in TiS_2, when considering TiAl alloys due to the higher melting point of TiS_2. Other factors, such as thermodynamic activities and free energies of formation, must also be considered when predicting the most likely sulphides which form.

Table 5 : Self diffusion coefficients of cations (D_{ME}) in some oxides and sulphides

Sulphide	Temperature (°C)	D_{ME} (cm^2s^{-1})	Oxide	Temperature (°C)	D_{ME} (cm^2s^{-1})
Al_2S_3	600	1.0×10^{-13}	Al_2O_3	1000	1.0×10^{-15}
$Ni_{1-x}S$	800	1.4×10^{-8}	$Ni_{1-x}O$	1000	1.0×10^{-11}
NbS_2	800	1.6×10^{-12}	....	.....	.....

The non-stoichiometry of sulphides affects its defect structure which in turn influences the mechanisms of sulphidation i.e whether it is more likely for the outward diffusion of metal cations or the inward diffusion of sulphur anions via anion defects in the sulphide lattice. This could lead to the condensation of vacancies at the metal/scale interface, with the possibility of the scale adherence being reduced and the loss of scale protectiveness. The inward diffusion of sulphur anions could also cause scale failure due to increased stress at the scale/metal interface.

Selective sulphidation rarely persists as the differences in sulphide free energies or the relative growth rates are not large enough. Interdiffusion and dissolution may also occur between sulphides. A duplex scale generally forms with the outer layer being rich in the base metal and the inner layer rich in the alloying addition.

3.3 Kinetics and mechanisms describing the attack of NiCr alloys in O_2-SO_2 environments

Hot corrosion results when a material is exposed in the presence of both salt and a sulphur dioxide containing atmosphere. Understanding the individual effects of these corrosive environments allows their combined effects to be understood and put into perspective.

No literature is available that covers the effects of salt on titanium aluminides in O_2-SO_2 environments. In depth studies have, however, characterised this behaviour for nickel based alloys. The different alloy systems make direct comparisons difficult, however, understanding the mechanisms which operate during the degradation of these alloys is invaluable as they illustrate the potential interactions between the protective oxides formed, the salt and the sulphur containing atmospheres.

Stafford[65] developed the mechanisms, proposed by S.Mrowec[66], for the attack of Ni25Cr alloys in SO_2 environments, figure 13. This is reviewed and the reactions which occur described.

Sulphide formation was observed at the metal/scale interface, which required the transport of sulphur through an external oxide layer to the metal's surface. The transport process was thought to have occurred down physical defects in the oxide or by being dissolved in the oxide lattice through which the sulphur ions could diffuse to the surface.

At 700°C, and in an atmosphere of O-SO_2, the Ni25Cr alloy formed an external Cr_2O_3 scale during the first 20 hours of exposure. The following two reactions in equations 3.3a and 3.3b can be used to explain the protective scale formation and the accelerated corrosion which occurred after longer times.

$$2NiO(s) + 4/3Cr(s) \rightarrow 2/3\ Cr_2O_3(s) + 2Ni(s) \qquad \Delta G = -257,730 - 23.85T \quad (3.3a)$$

$$3NiO(s) + 2CrS(s) \rightarrow Cr_2O_3(s) + Ni_3S_2(l) \qquad \Delta G = -313,125 + 14.91T \quad (3.3b)$$

Equation 3.3b shows that Cr_2O_3 is more stable than NiO over an extended temperature range and that Cr_2O_3 would overgrow the initial Cr_2O_3/NiO transient oxidation products. Due to the high chromium content, the local Cr content would not be depleted to an extent where Cr_2O_3 could not form. Chromium sulphides form at the metal/scale interface due to sulphur having penetrated the outer oxide scale. In high chromium containing nickel alloys any Ni_3S_2 which forms under the scale is instantly reduced to nickel producing CrS, which is shown in the reaction in equation 3.3c.

$$2Cr(s) + Ni_3S_2(l) \rightarrow 2CrS(s) + 3Ni(s) \qquad \Delta G = -75.476 - 51.09T \quad (3.3c)$$

Ni_3S_2 formation in high chromium containing nickel alloys occurs when sufficient chromium has been used locally to form CrS, resulting in the chromium activity being reduced locally to values of 10^{-4} atmospheres at 700°C. The reaction in equation 11 then proceeds producing Ni_3S_2. At 700°C Ni_3S_2 is a liquid and eventually forces its way to the outer oxide surface, where it reacts with SO_3 and/or O_2 to form NiO as shown in equation 3.3d and 3.3e respectfully.

$$Ni_3S_2(l) + SO_3(g) \rightarrow 3NiO(s) + 3/2S_2(g) \qquad (3.3d)$$

$$Ni_3S_2(l) + 3/2O_2(g) \rightarrow 3NiO(s) + S_2(g) \qquad (3.3e)$$

These reactions occur after longer periods of time producing an outer NiO containing sulphide layer.

Increasing the chromium content in NiCr alloys increases their resistance to attack by sulphur dioxide. More chromium is available for reaction, replenishing the surface layer, without depleting chromium at the alloy's surface appreciably. Hancock[67] showed that these reactions occurred up to 750°C for Ni20Cr alloys, with an outer scale consisting of both NiO and Cr_2O_3, providing some protection as sulphur diffusion is limited. Above 750°C an outer Cr_2O_3 scale develops . Below 750°C little denudation of chromium occurs at the metal's surface as sulphur dioxide oxidises both nickel and chromium. At the higher

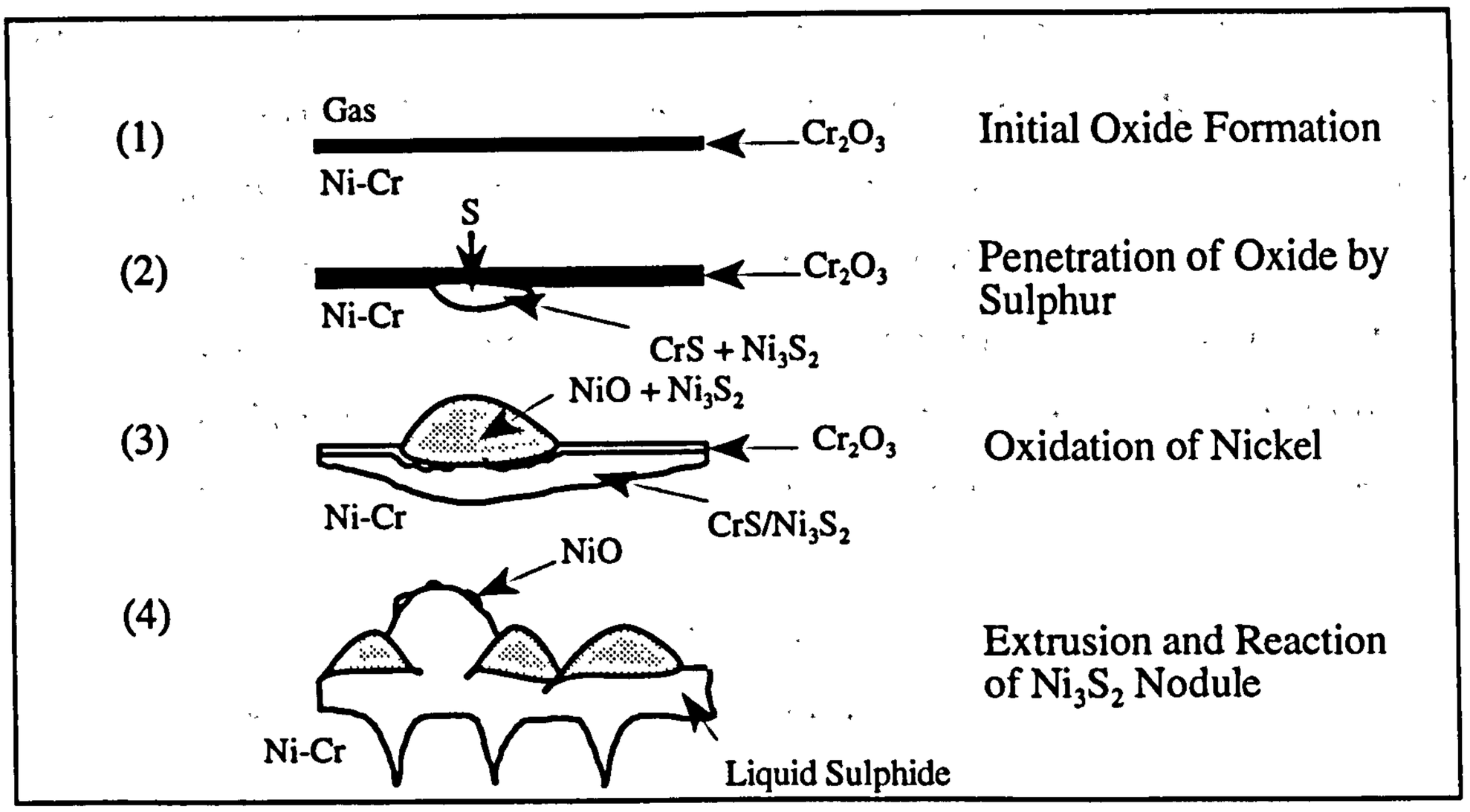

Figure 13: Attack of Ni-Cr alloys in Air-SO_2, 10-25% Cr

temperatures only Cr_2O_3 forms, resulting in chromium depletion at the metals surface causing accelerated corrosion

Accelerated corrosion is promoted by the formation of non protective intermixed oxides and sulphides, providing rapid transport routes for sulphur and any other reaction products. Nickel is the most susceptible alloy base to the formation of these intermixed reaction products followed by cobalt and iron respectively. Mixed oxide/sulphide formation occurs at lower sulphur/oxygen activity ratios with nickel than cobalt or iron. Fe20Cr alloys form internal sulphides at lower rates due to the rapid formation of Cr rich oxides reducing the interdiffusion coefficients. CoCr alloys show better protective properties as the CoS's which form are solid at 700°C, resulting in slower sulphur transport.

Nickel based alloys containing less than 10% Cr behaved in a different manner when exposed to SO_2 atmospheres, figure 14. Wootton and Birks[68] looked at the sulphidation mechanisms operating in alloys containing 2-30at.% Cr between 500-790°C. Initially Cr_2O_3 dissolved in NiO forms on the surface of low Cr containing alloys. Increasing the Cr content resulted in two phase ($NiO + NiCr_2O_4$) oxides forming which eventually becomes a continuous Cr_2O_3 layer as the Cr content is raised further. Once sulphur has

penetrated the initial oxide layer Ni_3S_2 forms at the scale/metal interface of alloys containing less than 5%Cr. Two external layers then develop, NiO + Ni_3S_2 at the surface with a continuous NiO layer sandwiched between the outer duplex layer and the inner Ni_3S_2 layer. After longer times at low temperatures and low Cr levels the displacement reaction in equation 3.3c occurs. This occurs when enough nickel has been depleted from the alloy's surface to increase the activity of chromium, the result being the formation of CrS. This stage of sulphidation occurs at an earlier stage as the Cr content is increased.

The sulphidation behaviour then followed the mechanism proposed by Strafford[65] for the Ni25Cr at 700°C, with the CrS reacting with NiO to form Cr_2O_3 as in equation 3.3b producing a Cr_2O_3 surface layer.

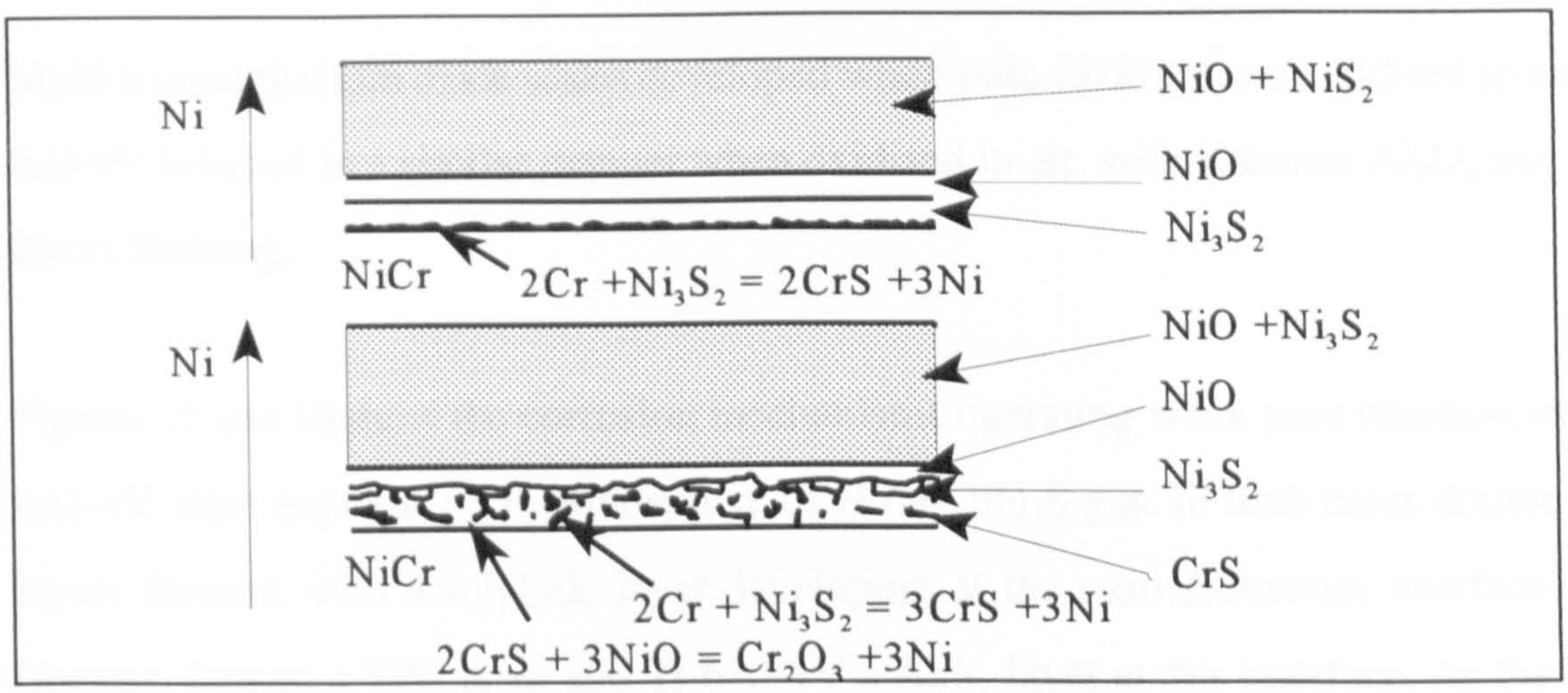

Figure 14: Attack of Ni-Cr (<10%) alloys in Ar-10%SO_2

3.4 Sulphidation and Oxidation of Ti and Ti-6Al-4V

The kinetics and mechanisms for the Sulphidation/Oxidation of Titanium and Titanium-base alloys have not been studied extensively. Very little data exist detailing their behaviour in environments comprising low oxygen/high sulphur partial pressures. Du et al[69] recently studied the behaviour of pure titanium and Ti-6Al-4V at 750°C in an atmosphere comprising $p(O_2) \sim 10^{-18}$ Pa and $p(S_2) \sim 10^{-1}$ Pa.

Table 6 compares the oxidation and sulphidation behaviour of pure titanium and Ti-6Al-4V in terms of kinetics and the mass gains which occurred after 100 hours exposure.

Table 6: Oxidation and Sulphidation behaviour of Ti and Ti-6Al-4V after 100 hours at 750°C

Material	**Environment (Gas)**	**Kinetic rate law obeyed**	**Mass gain (mg/cm^2)**
Pure Ti	Air	Linear-Parabolic	~ 6
Ti-6Al-4V	Air	Linear-Parabolic	~ 8
Pure Ti	$H_2/H_2O/H_2S$	Linear	~ 19
Ti-6Al-4V	$H_2/H_2O/H_2S$	Linear-Parabolic	~ 11

Multi layered titanium oxide scales developed when pure titanium was oxidised in air. Ti-6Al-4V behaved in a similar manner when oxidized in air, with alternate Al_2O_3 and TiO_2 layers forming.

Figures 15 and 16 show the corrosion mechanisms operating when pure titanium and Ti-6Al-4V were exposed to an atmosphere of $H_2/H_2O/H_2S$ gas. In both cases double TiO_2 layers formed, with a sulphide layer developing at the oxide/substrate interface. Pure titanium formed a TiS_2 layer and Ti-6Al-4V a Al_2S_3 layer at this interface. As the oxide scales thickens less sulphur is transported to the oxide/scale interface. This results in the sulphides decomposing allowing Ti and Al to diffuse outwards towards the oxide/gas interface and sulphur to diffuse inwards. The increase in $p(O_2)$ near the oxide/gas interface causes the Al and Ti ions to reprecipitate as oxides. The Al_2O_3 precipitates in the outer TiO_2 layer of the Ti-6Al-4V scale and acts as a partial diffusion barrier, reducing the flux of oxygen inwards and titanium/aluminium outwards.

Du et a[70] attempted to improve the oxidation/sulphidation resistance of Ti and Ti-6Al-4V by applying a HfN coating produced by Physical Vapour Deposition (PVD). The HfN layer, typically 10-15 μm in thickness, suppressed the formation of the duplex oxide

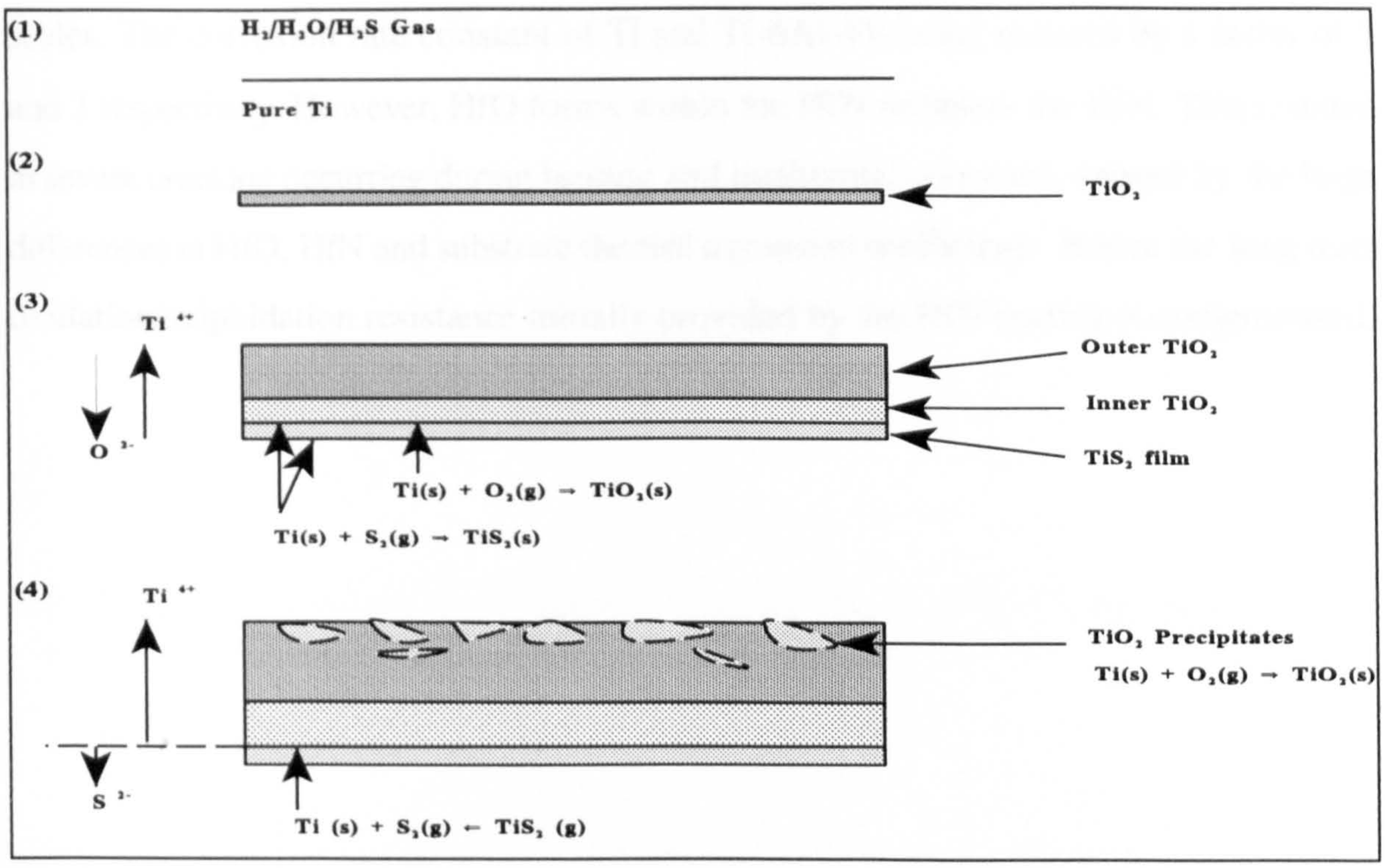

Figure 15: Mechanism for the corrosion of pure titanium in $H_2/H_2O/H_2S$ at 750°C

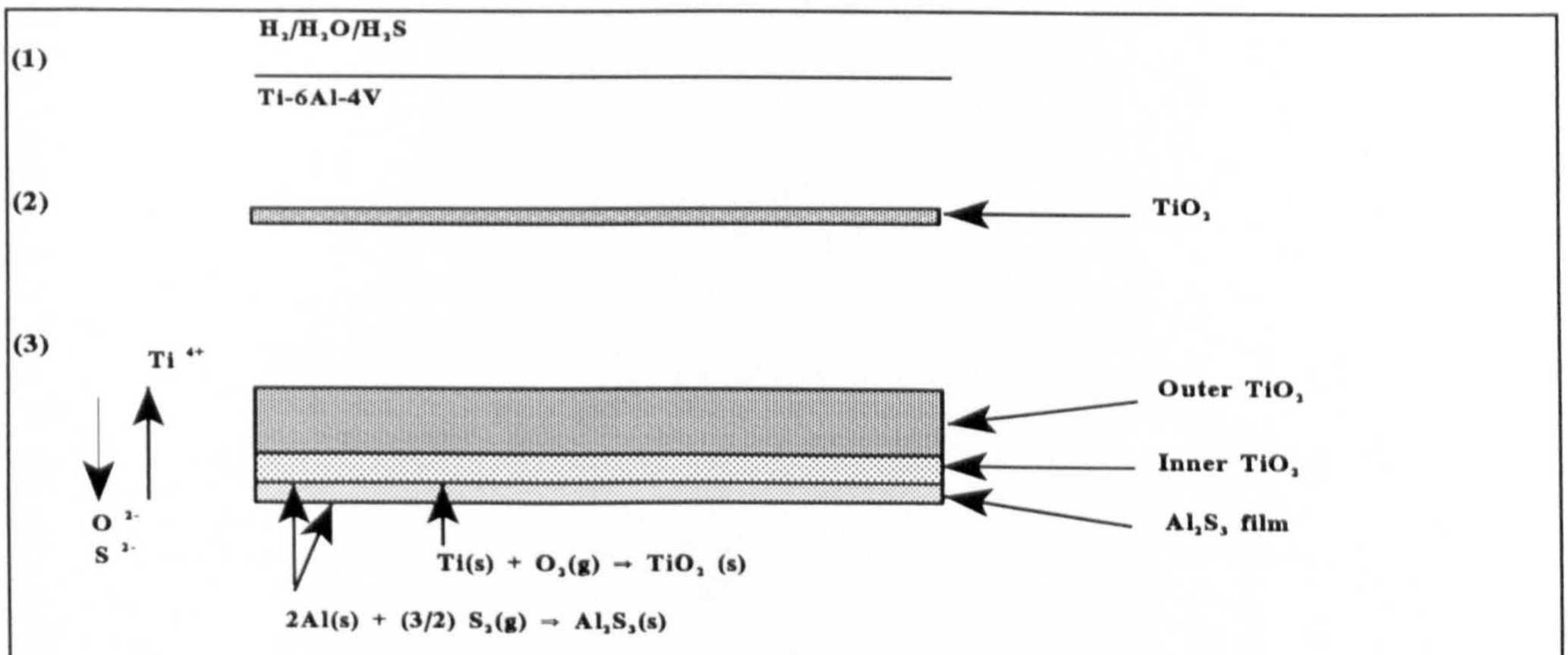

Figure 16: Mechanism for the corrosion of Ti-6Al-4V in $H_2/H_2O/H_2S$ at 750°C

scales. The corrosion rate constant of Ti and Ti-6Al-4V being reduced by a factor of 5 and 3 respectively. However, HfO forms within the HfN or below the HfN. This resulted in severe cracking occurring during heating and isothermal corrosion, caused by the large differences in HfO, HfN and substrate thermal expansion coefficients. Hence the long term oxidation/sulphidation resistance initially provided by the HfN coating is compromised.

Chapter 4

Hot salt corrosion

4.1 Introduction

Hot salt corrosion can be defined as a form of accelerated oxidation. Hot salt corrosion reactions are dependent on temperature, deposit and alloy composition, which change the rate and mechanism of attack[71]. There are two major forms of salt attack. The first involves chlorine in a salt containing atmosphere accelerating the oxidation reactions and is linked to the formation of volatile metal chlorides. This form of corrosion is well understood and has been comprehensively studied for the corrosion of Nickel superalloys. Hannappel[72] summarised this form of corrosion, as detailed below and schematically represented in figure 17.

- The reactants, such as chlorine, diffuse through an outer laminar flow boundary layer and through the oxide layer.

- Volatile metal chlorides are then formed, at the metal/oxide interface.

- The reaction products diffuse outwards via pores in the oxide.

- Metal oxides are deposited on the salt surface whilst the chlorine reforms and diffuses back to the metal/scale interface.

McNallan et al[73] investigated the gaseous chlorination of a Nickel-Cobalt alloy at 1000°K. A similar mechanism to that proposed by Hannappel described the corrosion of this alloy with porous cobalt oxide scales forming. Accelerated oxidation was attributed to the outward transport of volatile $CoCl_2$ from regions of low oxygen potential near the scale /metal interface. Active oxidation, as apposed to passive oxidation in pure oxygen environments, occurs when the vapour pressure of volatile chlorides is high and decreases with increasing pressure of oxygen. In this manner volatile chlorides are transported to the scales surface where they undergo exchange reactions and are redeposited as oxides.

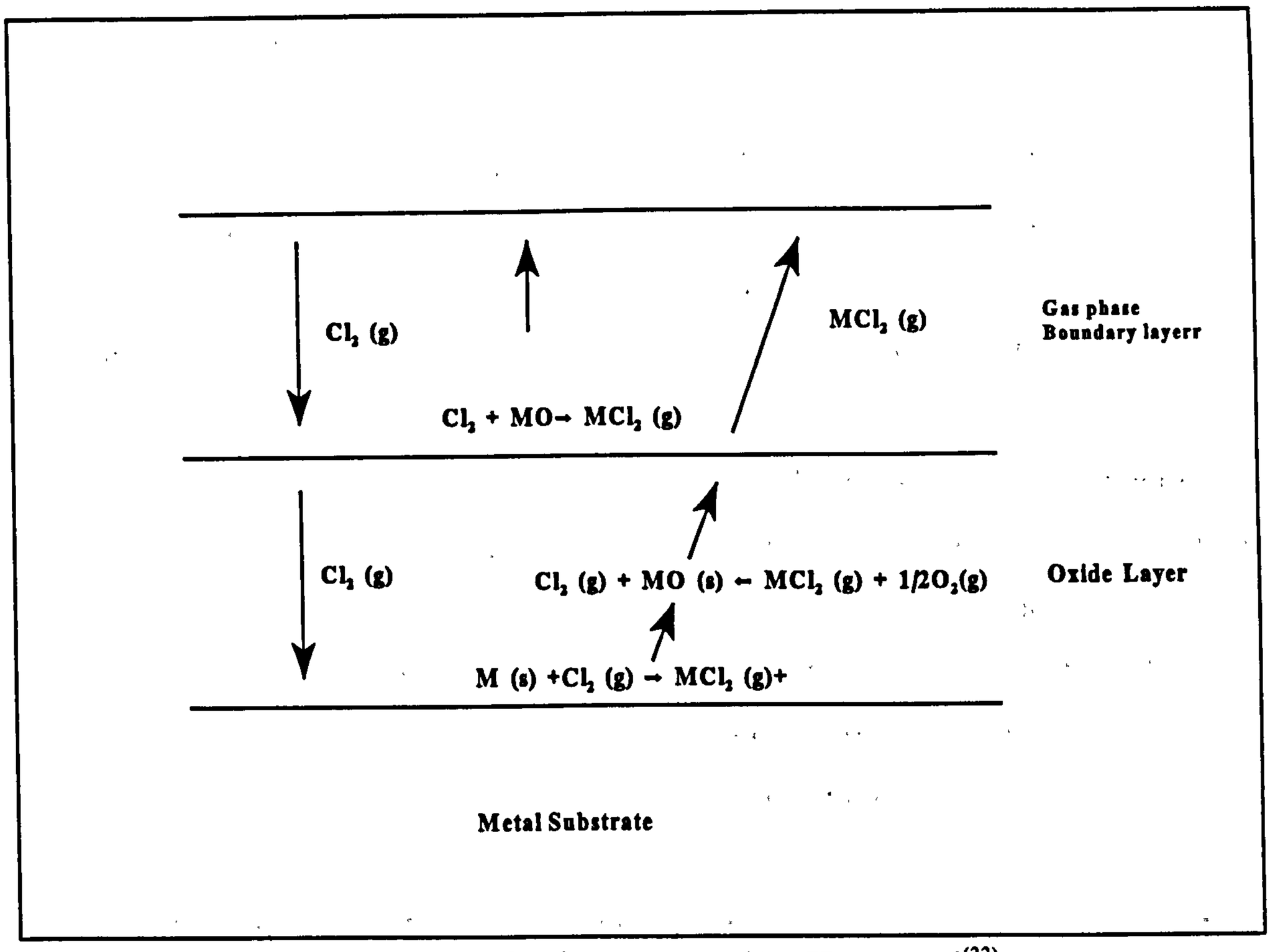

Figure 17: Hot salt corrosion mechanism proposed by Hannappel[33]

Al-Khyatt[74] proposed a similar mechanism for Nickel based alloys tested in chlorine containing atmospheres. His corrosion mechanism is summarised below.

Stage 1: Oxides and chlorides form simultaneously on the specimens surface during a period known as transient oxidation.

Stage 2: The most stable oxide (Cr_2O_3 in the case of most Nickel based superalloys) forms as a continuous layer, overgrowing the other oxides formed during transient oxidation. The transient chlorides are lost as volatile species or converted to more stable oxides.

Stage 3: A healing oxide layer formed below the initial oxide layer. These healing oxides formed preferentially at grain boundaries intersecting the alloys surface. Grain boundaries provide faster diffusion paths. The healing layer spreads laterally giving complete coverage, often trapping chloride species at oxygen ion vacancies. The scale adopts a

wrinkled morphology and is porous in nature.

Stage 4: Internal corrosion occurs beneath the oxide scale. Voids develop at the scales surface and in the underlying alloy. The voids increase in size with both temperature and time, providing access for chlorine to react with the substrate. Volatile chlorides form at the scale/metal interface enhancing the growth of the voids into the substrate.

Void formation was deemed important and relied on chlorine being able to penetrate the surface oxide. The most likely method of chlorine penetration was believed to occur as a result of the initial stages of oxidation, when both oxides and chlorides formed. The chlorides were previously assumed to be lost to the atmosphere. However, it was believed that they also reacted with oxygen in the atmosphere to form oxides, releasing chlorine. Equation 4.1a below shows the general conversion reaction.

$$XMCl_2\,(g) + Y/2O_2(g) \rightarrow M_XO_Y(s) + XCl_2(g) \qquad (4.1a)$$

The free chlorine may then react with elements favouring chloride formation, causing the chlorine to be recycled.

Stage 5: Chloride phases then form beneath the outer scale, particularly $NiCl_2$. The $NiCl_2$ phase exists in molten form due to the high pressures beneath the scale lowering its melting point. High pressures are generated if the vapour chlorides are unable to escape from beneath the oxide scale, resulting in a change in state from gas to liquid. A pool of molten chlorides thus develops at the scale/metal interface reducing the scales adhesion. The likelihood of scale spallation is therefore increased. The liquid pools provide fast transport routes, resulting in their size increasing rapidly. The molten phases volatilize if the scale cracks. The corrosion cycle can only continue if the oxide reforms in these areas.

The effect of chlorine was therefore shown to provide a means of rapid transport for the reactive elements from the bulk material to the scales surface.

The second form of hot salt corrosion involves chlorine within salt deposits causing severe corrosion. Yoshiba et al[75], amongst many others demonstrated this. Chloride ions were incorporated into the close packed anion lattice of the oxide, causing the number of cation vacancies to increase. A continuous alumina layer is prevented from forming as cation diffusion through the oxide occurs at rates which exceed that of inward oxygen diffusion. A porous oxide layer thus develops as the cation vacancies created condense to form pores.

The first hot salt corrosion mechanism proposed that oxidation rates are accelerated by the formation of molten chlorides beneath an external oxide layer. This mechanism is likely to develop at high temperatures where high metal chloride vapour pressures could be generated at rapid rates. However, this mechanism relies on relatively continuous scales. Once spalling occurs this mechanism would breakdown, with the loss of the molten chlorides to the atmospheres as they volatilised. The second hot salt corrosion mechanism, involving the incorporation of chloride ions within the oxide lattice, is likely to operate at relatively low temperatures were the rate of metal chlorides formation below the oxide is too slow to generate high enough vapour pressures for the development of molten chloride phases. Hence, discontinuous porous oxide scales would be expected to form. Molten phases may develop if solid NaCl deposits react with the substrate producing metal chlorides which could then form low melting point eutectics with NaCl.

Chlorides were shown by Hancock[76] to produce a breakdown of normally protective surface oxide scales. This was the case for iron exposed to NaCl vapour[77]. It was suggested that the blistering effect, which often lead to spalling, was caused by the production of volatile oxychlorides at the metal/scale interface. Typical diffusion coefficients (table 7) for typical gaseous, liquid and solid diffusion processes suggested that the rapid corrosion rates observed could only be accounted for by the high diffusion coefficients seen in gaseous media. Gaseous transport of NaCl to the metal surface occurred through scale defects inherent in some surface scales and during thermal cycling during which cracks provide direct access to the metal beneath.

Table 7: Typical diffusion coefficients

Diffusion process	D^0 (cm^2s^{-1})
Gas	10
Liquid	10^{-5}
Solid	10^{-9} - 10^{-12}

4.2 Hot Salt Corrosion of titanium alloys and titanium aluminides

4.2.1 Introduction

TiAl intermetallics are being considered for aerospace applications, and it is for these reasons that their mechanical and oxidation properties have been investigated. Very few investigations have so far been made on the hot corrosion of these alloys.

If TiAl intermetallics are to be used in turbine engines, and in particular turbine discs, studies will be needed to determine what effect salt deposits will have on their corrosion behaviour.

No work has been found to date on TiAl. However, hot salt corrosion and hot salt stress corrosion has been reported[78-85] for titanium alloys illustrating the reactivity that exists between the titanium alloys and halogen salts at high temperatures. A model, electrochemical in nature, best describes the reaction and is dependent on the presence of a halide salt, oxygen, and a titanium alloy. The end product is rutile TiO_2. The kinetics for this reaction can be described in terms of accelerated oxidation.

4.2.2 Kinetics

An investigation into the effects of a 1mg/cm^2 salt (NaCl) deposit on the surface of IMI685 (6Al,5Zr,0.5Mo wt%) thermobalance specimens showed that the hot salt

corrosion reaction increased the oxidation rate by a factor of approximately 100 at 400, 500 and 600°C in an atmosphere of air[78].

The hot salt corrosion curves at these temperatures obeyed a relationship intermediate between cubic and parabolic.

Mass gains of approximately 0.5 mg/cm^2, 1mg/cm^2, and 10mg/cm^2 were observed after 24 hours at 400, 500, and 600 °C respectively.

Chevrot[79] investigated the hot salt corrosion of IMI 834 and was able to make the following observations. The first was that hot salt corrosion does not follow parabolic growth laws, especially during the early stages of salt corrosion. Secondly metallographic and EPMA showed that oxygen was not taken into solution in significant quantities, suggesting that oxygen dissolution did not play a significant role in salt corrosion or the salt corrosion reaction was faster than oxygen solution.

4.2.3 Scale morphology

Dumas et al[78] compared the scale morphologies of titanium alloy specimens purely oxidised to those oxidised after being coated in salt. Simple oxidation resulted in an external scale 1μm thick, and an internal layer, penetrated by oxygen, 5μm thick.

The hot salt corrosion scales were considerably different. Two distinct layers 50μm thick were identified. The external layer contained large pores, whilst the inner layer was more compact.

X-ray analysis identified rutile TiO_2 in both oxidation and hot salt corrosion experiments. At 600°C five faint reflections were detected and attributed to sodium titanate ($Na_2O.TiO_2$).

4.2.4 Corrosion mechanisms for titanium alloys

The range of reactions that are possible during hot salt corrosion are dependent on the alloy, salt and atmosphere composition. Very little is known about a number of possible corrosion products.

X-ray diffraction analyses have shown rutile TiO_2 to be one of the end products. (Logan 1964)[80] This was identified as a flaky blue/gray stain which formed almost immediately.(Rideout 1968)[81].

Garfunkle (1973)[82] and Rideout (1967)[83] among others used EPMA to show that sodium and chlorine ions are absorbed by titanium alloys. Rideout (1967)[83] proposed that chlorine ions diffuse through the surface oxide scales into the base material.

Chevrot[79] analysed the thermogravimetric mass gain curves of IMI 834 hot salt corrosion experiments after 100 hours in air and identified three major zones.

In the first zone, which occurred immediately and up to 2-4 hours, a rapid mass gain was observed . This did not follow a parabolic growth law. The mass gains were up to 6-10 times that of the specimens oxidised isothermally in air. Micrographs of the specimen cross sections, taken after one hour identified an important feature. Long, narrow voids or channels extending from the specimens surface deep into the alloy were observed. These channels provided easy access into the base material for volatile species, and may be a cause of the severe corrosion damage.

In the second zone, which occurred between 4-15 hours extremely low mass gains were observed. This period may be one of transition, as the pores formed in zone one reach a maximum depth of penetration after which stable oxides form.

In zone three, which occurred after 15 hours, the mass gains followed a parabolic rate law similar to that of normal oxidation but at increased rates. The channels produced in the

early stages appear to enhance the diffusion of gases into the base metal accounting for the accelerated mass gains.

4.2.5 Chemical reactions

The possible hot salt corrosion reactions can be classified into four categories: chlorination of titanium metal, oxidation of salt, hydrolysis of both titanium chloride and salt oxides, and exchange reactions between oxygen and chlorine gas. More reactions are possible, with alloying elements being substituted for titanium metal.

The four categories of reactions are illustrated in the equations below.

Chlorination of titanium

$$Ti+2NaCl+1/2O_2+H_2O \rightarrow TiCl_2+2NaOH \qquad \textbf{(Hatch)}^{(84)}$$

Oxidation of salt

$$2NaCl+1/2O_2+TiO_2 \rightarrow Na_2TiO_3+Cl_2 \qquad \textbf{(Crossley)}^{(85)}$$

Hydrolysis

$$TiCl_2+H_2O \rightarrow TiO+2HCl \qquad \textbf{(Hatch)}^{(84)}$$

Exchange reaction

$$TiCl_2+O_2 \rightarrow TiO_2+Cl_2 \qquad \textbf{(Hatch)}^{(84)}$$

Chevrot [79] considered the possible hot salt corrosion reactions proposed by Hatch[84] and

Crossley[85], and deduced the most likely reactions for titanium alloys. These were categorised into three groups;

1) Chlorination of metal species and oxidation of the NaCl deposit. Further reactions between the oxide salts and metal oxides could then result in the formation of sodium titanate and chlorine.

2) Oxides could act as catalysts in the reaction between $TiCl_2$ and water, forming HCl.

3) Halide salts may also act as catalysts during the exchange reaction between the metal chlorides and oxides.

4.3 Hot salt corrosion of TiAlNb alloys

4.3.1 Introduction

Yao[86] investigated the hot salt corrosion of TiAlNb in the temperature range of 500-850°C. His results showed that accelerated oxidation occurred in areas of high salt concentration. The scales where observed to be thicker and more porous when exposed to high temperatures in the presence of salt. Spalling occurred at lower temperatures than in similar oxidation tests, caused by greater stresses in the scale which arise when the scale thickens. NaCl was found to vapourise at 800°C. The highest oxidation slope was seen during hot salt corrosion at 640°C.

4.3.2 Hot salt corrosion above the melting point of NaCl

At 800°C large weight gains were seen. Alumina and Titania dissolved in molten NaCl, causing the underlying alloy to oxidize at a very high rate. These oxides precipitated as non-protective particles within the salt film, allowing further oxides at the oxide/salt interface to be dissolved. The following reactions illustrate dissolution and precipitation

of the oxides.

{Oxide ppt} $Al_2O_3 \leftrightarrow 2Al^{3+} + 3O^{2-}$ *{Oxide dissolution}*

{Oxide ppt} $TiO_2 \leftrightarrow Ti^{4+} + 2O^{2-}$ *{Oxide dissolution}*

4.3.3 Hot Salt Corrosion below the melting temperature of NaCl

Yao[86] observed accelerated oxidation in the presence of salt in the temperature range of 600-800°C. It was believed that this was due to chlorides acting as catalysts for some oxidation reactions, as proposed by Shinata[87]. Yao made several predictions as to what these intermediate products were. The following reactions where proposed by Yao to explain the observed accelerated oxidation.

$$6NaCl + 6Al + 6O_2 = 3Al_2O_3 + 3Na_2O + 3Cl_2$$

$$3Na_2O + 3Cl_2 + 2Al = Al_2O_3 + 6NaCl$$

$$4NaCl + 2Ti + 3O_2 = 2TiO_2 + 2Na_2O + 2Cl_2$$

$$Ti + 2Na_2O + 2Cl_2 = TiO_2 + 4NaCl$$

These reactions show Na_2O to be the major intermediate compound, which then reacts with chlorine and the elemental aluminium or titanium to form the respective oxides and then reforms as NaCl. Hence NaCl is recycled with the only restraints on the corrosion rate being temperature. Above the melting point of NaCl, the deposit will evaporate off the surface leaving less salt to act as a catalyst slowing the overall reaction rate down. All these reactions are exothermic, releasing a large amount of heat further accelerating

the oxidation rate. These reactions, although possible, are unlikely since they assume dry atmospheres. In reality these equations would be modified with water vapour affecting the chlorination of Ti and/or Al resulting in the production of volatile metal chlorides and NaOH, as proposed by Hatch[84]. Yao[86] believed that whiskers developed through oxide growth. Chevrot[79] looked at the thermodynamic stabilities of the chlorides and oxides and showed that at low oxygen partial pressures, which are developed as one traverses the scale towards the scale/substrate interface, $AlCl_3$ becomes the most thermodynamically stable phase. At these temperatures and pressures these metal chlorides volatilise and diffuse out towards the scale/gas interface through pores and channels in the scale, where the chlorides are oxidised or hydrolysed producing thin alumina whiskers. These reactions result in the regeneration of HCl and/or Cl_2 which can either diffuse back through the scale, continuing the vapour transport mechanism, or diffuse into the atmosphere reducing the available chloride species for further reactions.

Chapter 5

Hot Corrosion

5.1 Introduction

Hot corrosion occurs when salt deposits accumulate on the surface of alloys and alter the environment - alloy reactions that would have occurred had the salt been absent. Salt ingested air and sulphur from fuels combine and deposit on components in the turbine engine causing accelerated oxidation. Bornstein and Descrescente[88] categorised the corrosion behaviour of salt deposits into four major steps, summarising as briefly as possible the detrimental effects components are likely to encounter in salt/sulphur bearing environments.

1) Initially a predominantly Na_2SO_4 slag forms on the turbine components.
2) This slag then renders the protective oxide, which forms when exposed at high temperatures, ineffectual.
3) The slag is then able to react with the substrate to form metal sulphides.
4) As a result of the previous three steps the substrate is rapidly oxidized.

It was traditionally thought that Na_2SO_4 deposited directly onto turbine blades and only caused material degradation when the melting point of Na_2SO_4 (884°C) was exceeded. By 1974 the British navy had established that corrosion was often greater at 750°C than at higher temperatures. Two forms of Na_2SO_4 induced hot corrosion of nickel superalloys thus operate.

1. The first form reaches maximum corrosion rates above 880°C
2. The second form reaches maximum corrosion rates around 700°C

5.2 High temperature hot corrosion (Type I), above 800°C

Na_2SO_4 forms when NaCl is exposed to an atmosphere containing SO_2/O_2. The following reactions show the possible conversion processes[89].

$$2NaCl + SO_2 + 1/2O_2 + H_2O = Na_2SO_4 + 2HCl \qquad (5.2a)$$

$$2NaCl + SO_2 + O_2 = Na_2SO_4 + Cl_2 \qquad (5.2b)$$

Na_2SO_4 deposits onto turbine hardware, where it acts as a diffusion barrier for gaseous components in the surrounding atmosphere. By diffusing through this barrier, in order to react with the substrate, the gaseous species create compositional gradients through the deposit. The corrosion behaviour of the salt can change to being more sulphidising, basic or acidic, depending on the diffusing gaseous species.

The acidity or basicity of a Na_2SO_4 melt is determined by the oxide ion concentration and solubility in the deposit.

5.2.1 Sulphidising salts

According to the expression below, if the $p(SO_3)$ does not decrease appreciably, then as the $p(O_2)$ decreases the value of $p(S_2)$ increases and the salt becomes more sulphidising.

$$\frac{p(O_2)^{3/2} \cdot p(S_2)^{1/2}}{p(SO_3)} = K$$

where p is the partial pressure and k the equilibrium constant for $SO_3 = 3/2\ O_2 + ½\ S_2$.

This is illustrated in figure 18 which shows a stability diagram of the Na-S-O system. This figure predicts that a Na_2SO_4 layer would become more sulphidising and hence more acidic as the scale/metal interface was approached.

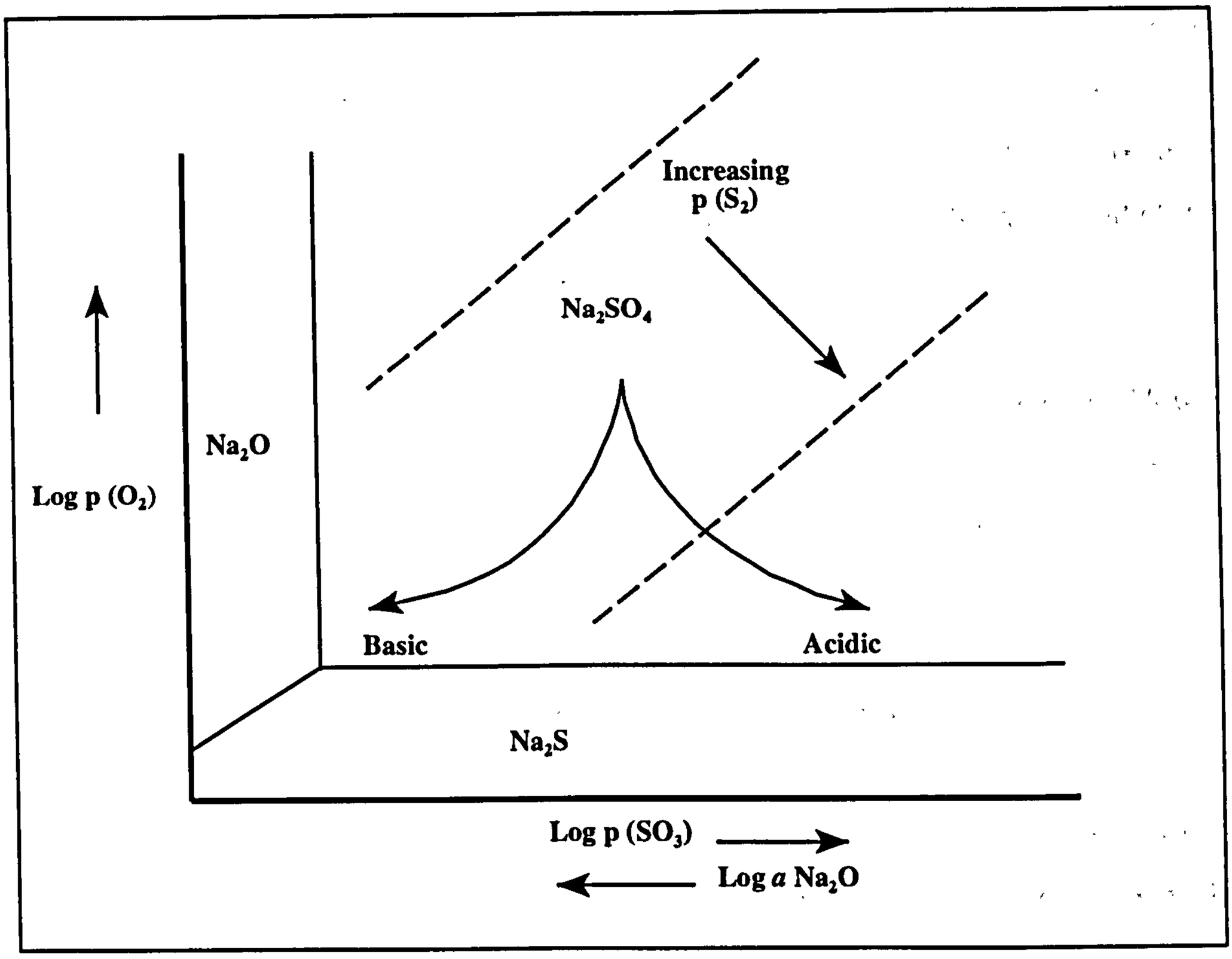

Figure 18: Na-S-O stability diagram, showing the compositional variations that can be developed across a layer of Na_2SO_4 on an alloy[90]

5.2.2 Basic fluxing

Salt deposits become more basic according to the following;

1) SO_4^{2-} (sulphate ions in Na_2SO_4) = S (sulphur) + 3/2 O_2 + O^{2-}(oxide ions)

2) The salt can also be made more basic if the surface oxide below the salt deposit donates oxide ions.

Giggins and Pettit[90] amongst others [91], studied the corrosion of a Na_2SO_4 coated Ni8Cr6Al alloy and associated the mode of attack with basic fluxing. The mechanism is described by the following stages and shown schematically in figure 19.

- An oxygen gradient is set up across the deposit due to the diffusion of oxygen from the atmosphere.

- As a result of the oxygen gradient developed across the deposit and the associated increase in sulphur activity, metal sulphides form within the alloys surface.
- The oxide ion concentration in the Na_2SO_4 deposit increases with the formation of metal sulphides. Eventually the concentration is such that the Al_2O_3 and Cr_2O_3 in the oxide scale dissolve in the Na_2SO_4.

Sulphate ions (SO_4^{2-}) then diffuse to the alloy surface where, because of lower oxygen activities, these ions sulphate elements in the alloy. The oxide ions which are created react with the Al_2O_3 or Cr_2O_3 within the oxide scale to form Na_2SO_4 soluble products. This is shown in the reaction below.

$$\mathbf{Al_2O_3 + O^{2-} = 2AlO_2^{-}\ (aluminate\ ion)}$$

- The aluminate / chromate ions then diffuse outwards from the scale/substrate interface to the gas/scale interface were the oxygen pressures increase to levels causing alumina and chromia to precipitate from the melt.
- The process of sulphate ion transport through the salt deposit continues as long as there is a supply of sulphate ions. The rate of attack will thus decrease if there is a depletion in sulphate ions. The corrosion product will then become more oxygen rich.

This mode of attack via basic fluxing involves Na_2SO_4 induced hot corrosion in air or oxygen. The corrosion process may change if SO_3 is present in the gas, however alloy composition will still affect the corrosion process.

Basic fluxing relies on the production of oxide ions. In this instance they arose from the formation of sulphides. However, Rapp and Goto[92] proposed that oxide ion production could also occur though the reduction which accompanies the oxidation of elements in the alloy ($\underline{½\ O_2} + 2e^- = O^{2-}$) or through the reaction of SO_3 with Na_2SO_4 ($S_2O_7^{2-} + 2e^-. = SO_4^{2-} + \underline{SO_2} + O^{2-}$), where the underlines imply the gases to be dissolved. Substrate degradation

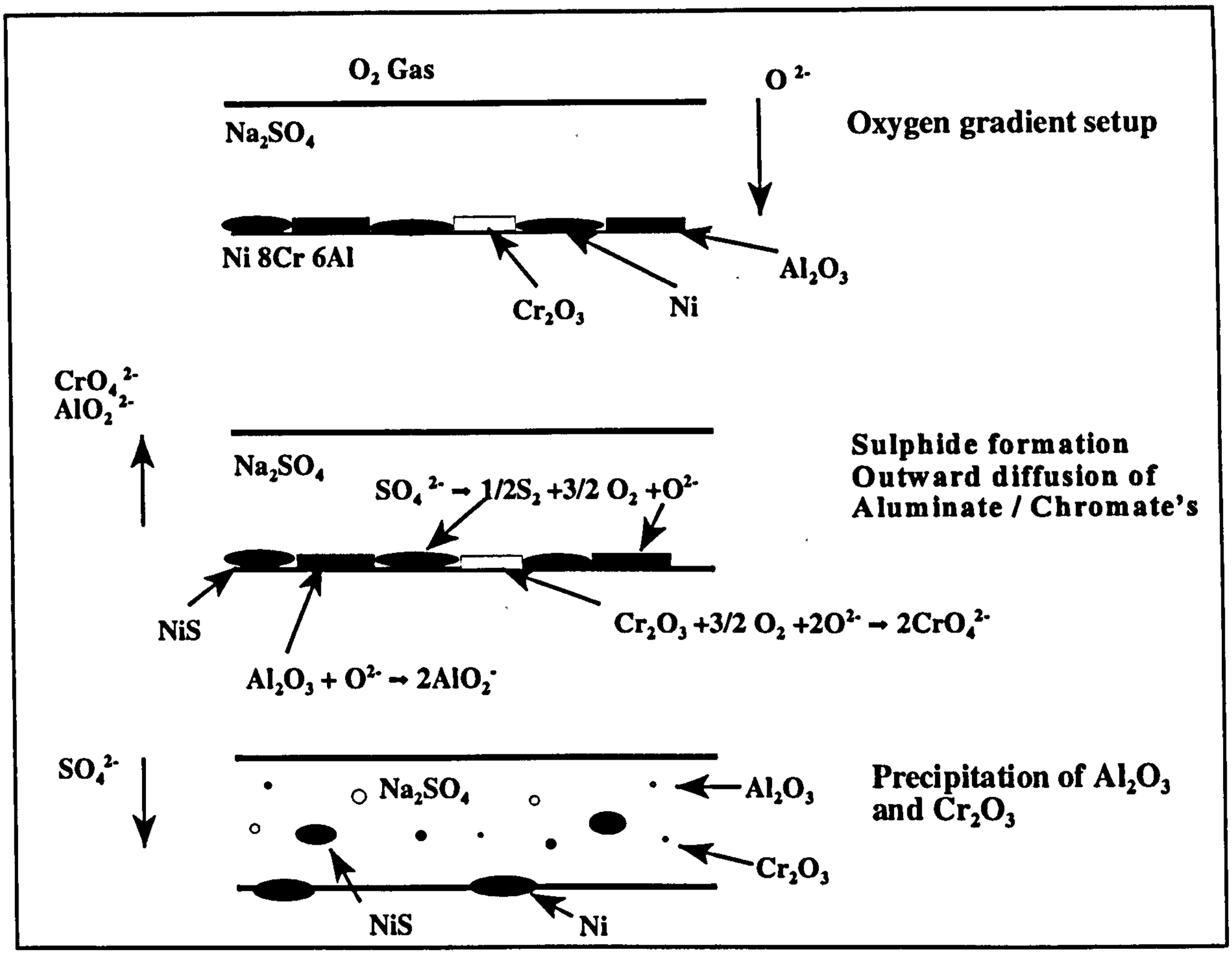

Figure 19: Na_2SO_4-induced hot corrosion of Ni-8Cr-6Al alloy in air illustrating basic fluxing (oxide ion production)

continues in a similar manner as before, with oxides dissolved and reprecipitated within the deposit; the requirement being that a negative gradient of oxide solubility is developed at the salt/oxide interface. As the oxide solubility in the oxide decreases the salt becomes less basic, with the result that oxides are reprecipitated at the gas/salt interface.

During steady state conditions oxide is dissolved in the melt at similar rates as it is reprecipitated at the gas/scale interface. Figure 20 shows this fluxing behaviour schematically. The negative solubility gradient, at the scale/salt interface, derives from the establishment of a gradient in activity of Na_2O. Rapp and Goto[93] believed that this gradient across thin salt films need not have been as a result of the removal of S from Na_2SO_4 (basicity) or the donation of acidic species (acidity). This assumes that the salt composition does not change appreciably with time.

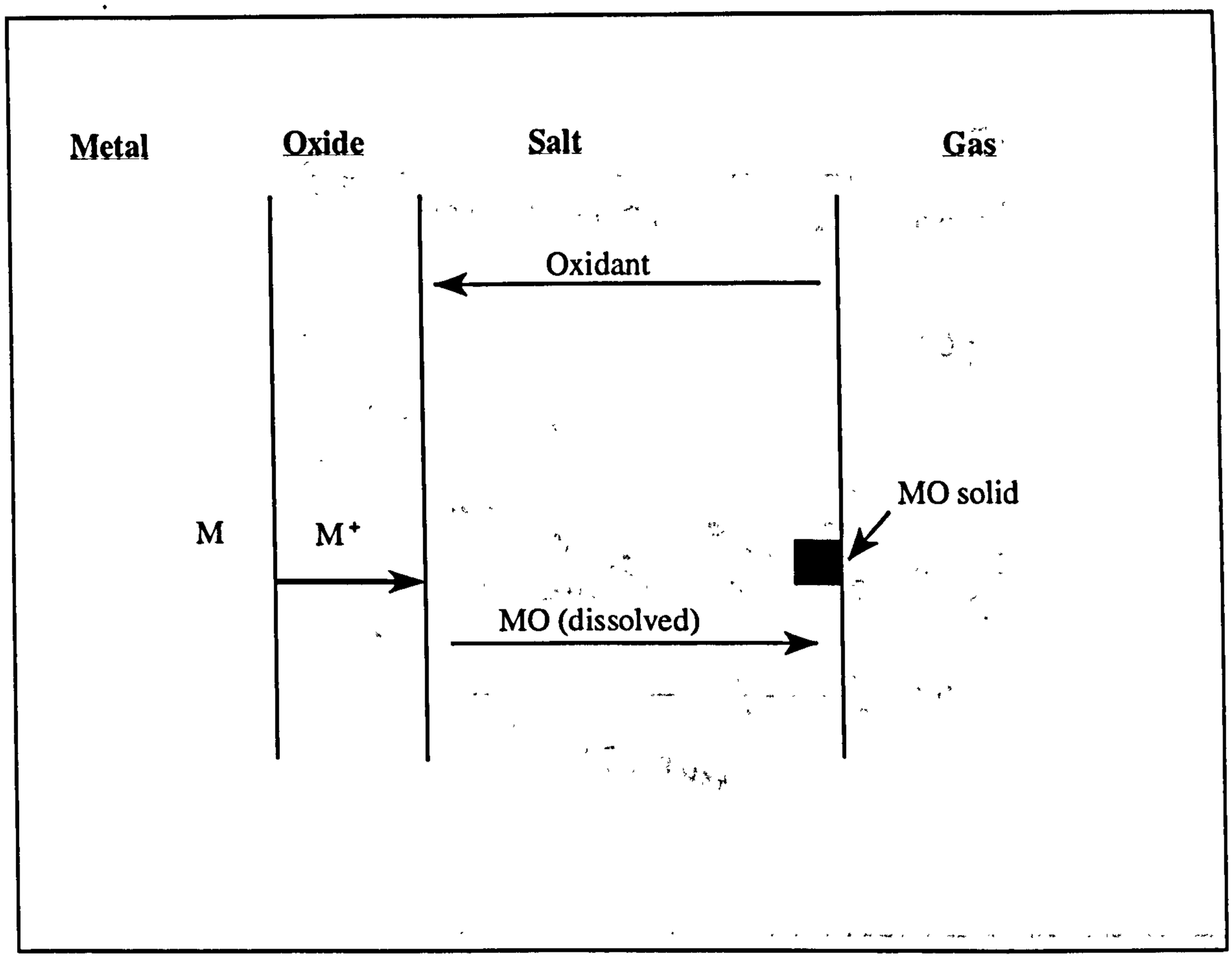

Figure 20: Schematic diagram of salt fluxing

Concentration gradients rely on sources and sinks, for dissolved species in the salt film, to maintain electrical neutrality. Corrosion reactions are driven, with oxidants supplied by the gas phase or the salt itself, by a lower energy state being attained when the metal forms oxides, sulphides or sulphates. The reduction reaction in which pyrosulphate ions ($S_2O_7^{2-}$) are produced is important in oxygen rich, O_2-SO_2-SO_3, environments containing more than a few ppm SO_3, as the concentration of $S_2O_7^{2-}$ will eventually exceed the concentration of dissolved oxygen. Sulphides form through further reduction of SO_3.

Basic dissolution involves a decrease in oxide solubility as the pSO_3 increases (a decrease in the activity of O^{2-}). Figure 21 shows the solubility of NiO as a function of basicity in Na_2SO_4. NiO dissolves in a basic melt as NiO^{2-}. Acidic dissolution of NiO yields Ni^{2+} and O^{2-} and is independent of pO_2.

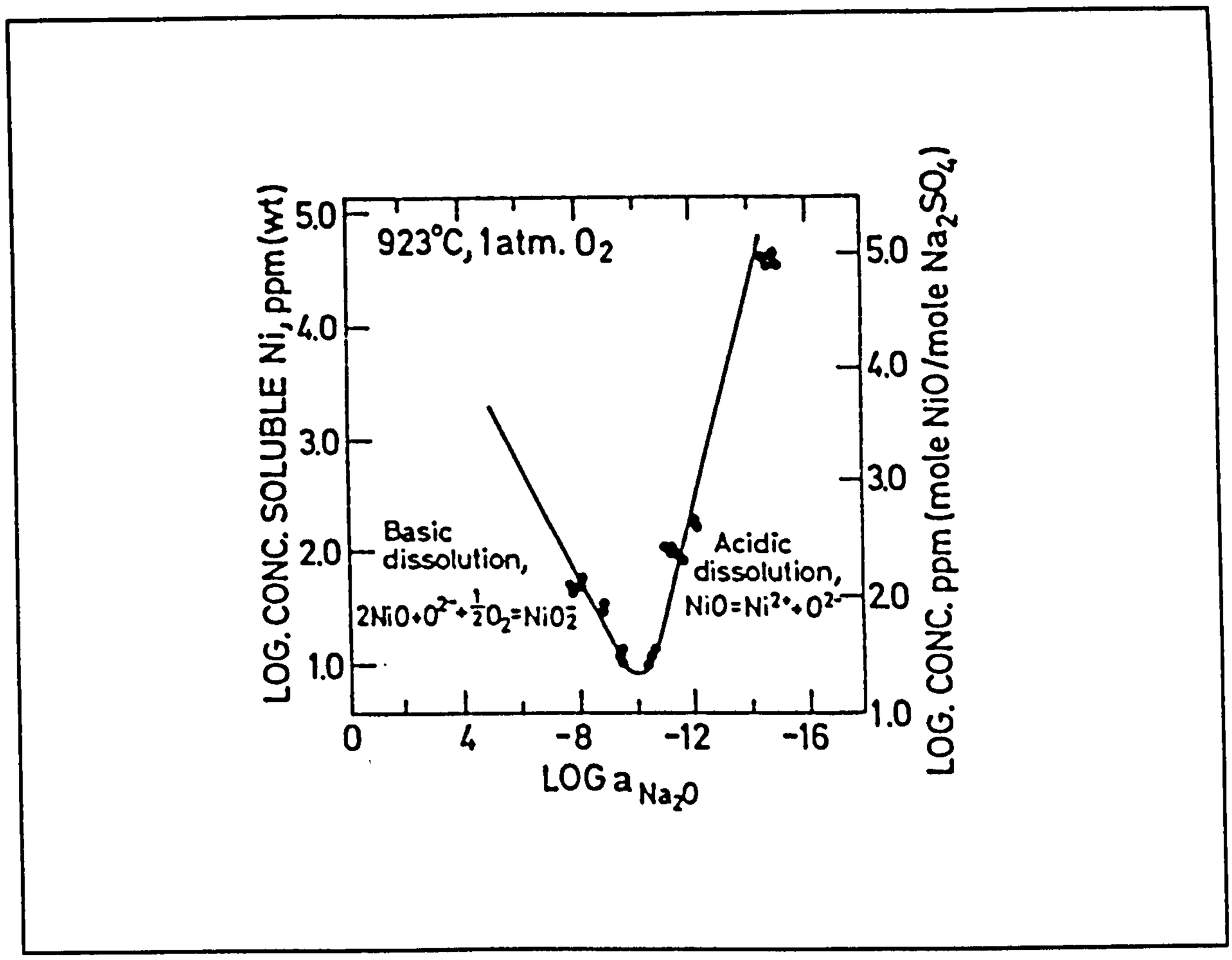

Figure 21: Solubitity curve of NiO in Na_2SO_4 (pO_2=1atm, T=1200K)

Na_2SO_4 may be absorbed by the non protective oxide scale as it thickens. As the salt loses contact with the substrate its detrimental corrosion behaviour decreases.

5.2.3 Acidic fluxing

Acidic fluxing involves the oxide on the alloy reacting with oxide ions in the Na_2SO_4 deposit (equation 5.2.3a).

$$MO + O^{2-} = MO_2^{2-} \text{ (acidifies the deposit)} \qquad \textbf{(5.2.3a)}$$

This form of fluxing is self sustaining and requires smaller amounts of salt deposits to produce more aggressive corrosion rates.

Salt deposits may be made acidic by one of two processes;

1) Alloy induced acidity - This involves the formation of oxides on the alloys surface which have a high solubility for oxide ions.

2) Gas induced acidity - The salt deposit is made acidic by gaseous species such as sulphur oxides.

5.2.3.1 Alloy induced acidic fluxing

Giggins and Pettit[90] proposed the following sequence of events to describe the Na_2SO_4 induced hot corrosion of a Ni8Cr6Al8Mo alloy and is illustrated in figure 22..

- Initially the Na_2SO_4 dissolves oxides of W and Mo, which in the process displace SO_3 from the deposit. Hence the oxide ion concentration within the salt is reduced and the salt becomes acidic.

The dissolution of these oxides depends on the oxidation behaviour of the alloy. The length of time it takes for the oxides to form on the alloys surface, in particular, determines when the oxide interactions can occur and therefore the incubation time.

- Once the Na_2SO_4 is enriched in these oxides, Cr_2O_3 and Al_2O_3 are able to dissolve in the oxide enriched salt. Cr_2O_3 and Al_2O_3 are amphoteric oxides, that is they may behave in an acidic or basic manner.

$$2Al + 3W + 6O_2 = Al_2O_3 + 3WO_3 \rightleftharpoons 2Al^{3+} + 3WO_4^{2-}$$

- The ions donated to the melt diffuse to the gas/scale interface where the lower activity of the W/Mo oxides, caused by their loss to the atmosphere, results in the reprecipitation of Al_2O_3, according to the reverse of the above equation. A non protective and porous oxide scale forms at the gas/scale interface.

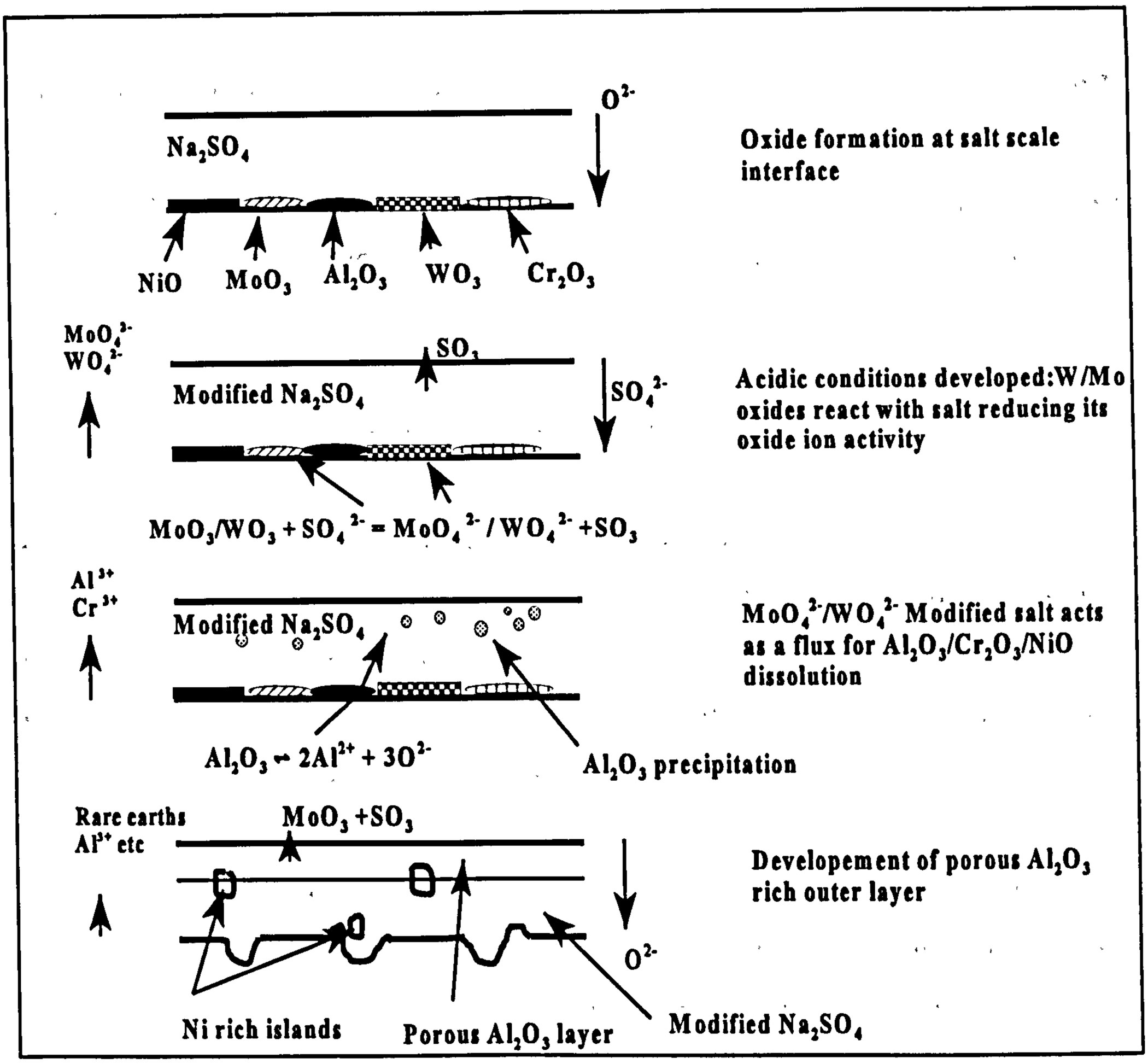

Figure 22: Hot corrosion mechanism of a Ni8Cr6Al8Mo alloy

This process continues as long as W or Mo is dissolved in the Na_2SO_4, resulting in the formation of low melting point Na_2SO_4 eutectics. The resulting liquid phase prevents protective alumina and chromia scales from forming as it acts as a medium for the dissolution and reprecipitation of these oxides.

5.2.3.2 Gas induced acidic fluxing

Giggins and Pettit[90] studied the effect of SO_3 containing gases on the corrosion of a

Na_2SO_4 coated CoCrAlY coating alloy. Shores et al[94] looked at the corrosion of Ni based alloys under similar conditions. Extensive attack occurred at 700°C in the presence of Na_2SO_4/SO_3 but the rate of attack was substantially reduced when SO_3 was removed from the gas. SO_3/O_2 on its own produced fairly insignificant corrosion rates at 700°C.

The following points were made from observing the combined Na_2SO_4/SO_3 attack.

- Na_2SO_4 was incorporated in the corrosion product.
- Co diffused through the deposit to form oxides and sulphates at the gas interface.
- Cr_2O_3 formed at the substrate/scale interface.
- Aluminium was preferentially removed from the alloy and was associated with sulphur and oxygen adjacent to the corrosion front.

The model put forward postulated that at low temperatures a low melting point $CoSO_4/Na_2SO_4$ eutectic formed, with the substrate directly beneath the melt reacting with the melt components. However, this assumes the initial alumina layer which forms has been breached. This mode of attack often leads to pitting due to localised attack. SO_3/O_2 concentration gradients are set up across the melt. SO_3, which is more mobile than oxygen in Na_2SO_4, diffuses to the substrate/melt interface were sulphur and oxygen are able to react with the substrate as well as the Na_2SO_4 reaction products.

Aluminium sulphites form at the substrate/melt interface under low PO_2 conditions and are then converted to oxides in the melt where the PO_2 is higher.

The SO_3 and O_2 pressures are important as they determine the availability of SO, supplying SO^{2-} ions which participate in the acidic fluxing reactions. Increasing the temperature increases the level of $p(SO_3)$ required to form sulphates and sulphites . The proportion of SO_2 in the gas will increase in return lowering the $p(SO_3)$. The acidity of the salt deposit will be reduced, resulting in an increase in the formation of sulphides in the

alloy.

5.2.4 Fluxing developements

Shores[95] refined the fluxing model described by Rapp and Goto[92,93], which states that metal oxide dissolves in salt deposits at the oxide/salt interface and diffuses down a concentration gradient, to regions of lower solubility, where the metal oxide reprecipitates. Shores[95] looked at the transport of oxidants and dissolved oxide through the salt. A Ni-15Co-5Cr-5Al alloy coated with 0.3mg/cm^2 Na_2SO_4 was exposed for 24 hours at 900°C. This resulted in a mass gain of approximately 16mg/cm^2. Porosity within the corrosion product was estimated at approximately 45%. Shores believed that a porous hot corrosion product permeated with a liquid salt developed, rather than a uniform layer of salt on a uniform layer of oxide. At a given corrosion site the rate of oxide growth at the substrate surface was proposed to be equal to the rate of oxidation minus the rate at which oxide is dissolved in the fluxing reactions. Shores believed that a thin oxide layer, approximately tens of angstrons thick, seperates the substrate from the the salt and does not act as a diffusion barrier to further growth. Oxide grain boundaries were also believed to act as rapid diffusion paths. Shores thus identified several areas of work still needed in the understanding of salt fluxing. Comprehensive studies ar required to characterise the oxide corrosion products in terms of pore structure and transport resistance.

5.3 High temperature hot corrosion by chlorides

Turbine engines operating in marine conditions ingest higher proportions of sea salt. Combined with sulphur an aggressive environment is created which causes localised damage on turbine entry vanes and first or second stage turbine blades. NaCl causes accelerated oxidation and sulphidation.

Hancock et al[96] showed that NaCl disrupted the integrity of Nickel based superalloy oxide scales. Johnson[97] noted the following effects of NaCl on the corrosion behaviour of nickel based alloys.

- NaCl is aggressive in a liquid or solid form at both high and low temperatures.
- Gaseous NaCl caused accelerated corrosion at 650°C, whilst solid NaCl caused accelerated corrosion at 450°C.
- The rate of corrosion depended on the integrity of the oxide scales. The severity of attack decreased with increased oxide stability.
- NaCl-Na_2SO_4 eutectic mixtures are more aggressive than either component as the initial incubation periods usually observed do not occur. Thus NaCl disrupts the oxide scale allowing Na_2SO_4 contact with the substrate.

Hancock showed that only small amounts of NaCl is required to accelerate the corrosion rate at 750°C. However, no increase was observed at 850°C . This supports the theory that NaCl accelerated hot corrosion depends on contaminant flux rate.

The mechanism of NaCl induced corrosion is still in doubt due to the variable physical and chemical nature of the corrosion products.

Hancock and Hurst[96] proposed that volatile chlorides, formed when NaCl reacted with Chromium at the metal oxide interface, caused scale cracking due to an increase in pressure. McKee[94] and Hossain [98, 99] focused, in particular, on the role of Cl_2 generated when SO_2 in the environment reacted with NaCl in Na_2SO_4-NaCl mixtures. Rapid rates of attack at high temperatures were attributed to the presence of liquid salts preventing the formation of protective oxide layers. At low temperatures (750°C), in the presence of condensed NaCl, low melting point eutectic mixtures were believed to account for the high corrosion rates observed.

Thermodynamic calculations showed that only $NiCl_2$ and $CoCl_2$, in small amounts, were sufficiently stable to form NaCl eutectic mixtures through the reaction of Cl_2 with components in the oxide scale. The calculated Cl_2 and O_2 partial pressures in O_2-Cl_2 mixtures in equilibrium with liquid NaCl mixtures at 750°C are shown in table 8.

Table 8: pCl_2 and pO_2 values in O_2-Cl_2 gas mixtures in equilibrium with NaCl at 750°C[94]

System	Stable Oxide	Liquid phase	MCl activity in melt	pO_2 (atm)	pCl_2 (atm)
Na-Al-Cl	Al_2O_3	Na_3AlCl_6	0.016	1.2×10^{-9}	1.00
Na-Cr-Cl	Cr_2O_3	Na_3CrCl_6	0.016	8.1×10^{-7}	1.00
Na-Co-Cl	Co_3O_2	NaCl-18.3%$CoCl_2$	0.183	0.89	0.11
Na-Ni-Cl	NiO	NaCl-20%$NiCl_2$	0.021	0.94	0.06
Na-Ti-Cl	TiO_2	-	-	$<10^{-9}$	1.00

Thus NaCl was believed to react with Ni and Co oxides, forming liquid salt mixtures. Subsequent oxide cracking, caused by Cl_2 interactions, provides access for the liquid phase to attack the substrate.

NaCl in NaCl-Na_2SO_4 mixtures was believed to be the cause for the shift in maximum corrosion rates to lower temperatures. For Ni30Al the maximum corrosion rates shifted from 850°C to 700°C when the concentration of NaCl in the salt mixture was increased from 1 to 10%.

The NaCl-Na_2SO_4 phase diagram shows a eutectic temperature of 625°C. Above this temperature some liquid would exist, however there is negligible solid solubility of NaCl in Na_2SO_4. As mentioned above Cl_2 is generated if SO_2 is present in the atmosphere. Table 9 shows that the activity of Cl_2 decreases as the temperature is raised. The potential for scale cracking is thus reduced. The presence of a liquid may also decrease the corrosion rates, by acting as a shield as the diffusion rates of Cl_2 in Na_2SO_4 are thought to be slow. Cr_2O_3 forming scales were found to be more susceptible to Cl-induced hot corrosion than Al_2O_3 forming scales. The evolution of volatile chromium chlorides or oxychlorides lifts and cracks the oxide scale. However, the vapour pressures of the chlorides are less than

1 atmosphere over the temperature range where chlorine effects were observed. The boiling points of $AlCl_3$ and $TiCl_4$ are low, making it feasible that these species would generate considerable pressure if they were to form in regions of low oxygen activity at

Table 9: Effect of temperature on the activity of Cl_2 [94]

Temperature (°C)	Mole fraction NaCl	Pressure Cl_2 (atm)
1000	0.01	5.4×10^{-8}
1000	0.1	5.9×10^{-6}
900	0.01	4.4×10^{-7}
900	0.1	4.8×10^{-5}
800	0.214	2.6×10^{-3}
750	0.3	0.02
700	0.387	0.12

the metal/scale interface. The gaseous chlorides escaping through cracks in the scale, whereupon they are reoxidized at the scale/gas interface leaving very little evidence of chlorine.

5.4 Low temperature (type II) hot corrosion,

5.4.1 Sulphur contamination

Na_2SO_4 induced accelerated hot corrosion of Nickel and Cobalt based superalloys has been comprehensively studied above 884°C. Severe degradation has also been shown to occur in the temperature range of 600-750°C, where Na_2SO_4 is solid[100].

A mechanism has been proposed by Jones[100] for the low temperature hot corrosion of Cobalt based alloys. Initially $CoSO_4$ is formed when SO_3 reacts with the CoO on the alloys surface.

$$CoO + SO_3 = CoSO_4$$

$CoSO_4$ combines with Na_2SO_4 to form a low melting point eutectic. The liquid eutectic allows the transport of reactants and corrosion products.

Nickel based superalloys can corrode in a similar manner with Na_2SO_4 - $NiSO_4$ eutectics providing the transport medium although the eutectic temperatures are higher for Cobalt based salts. Jones et al[100] found that Na_2SO_4-$CoSO_4$ and $NiSO_4$-Na_2SO_4 formed corrosive eutectic mixtures, whilst Al_2SO_4 - Na_2SO_4 did not.

Jones et al showed that $NiSO_4$ and $CoSO_4$ have wide ranges of solid solubilities in Na_2SO_4. This allows large amounts of SO_3 to be absorbed into the salt before a liquid phase is formed. Accelerated corrosion will only proceed if a liquid phase exists.

At higher temperatures the pSO_3 decreases, resulting in a decrease in the likelihood of low melting point eutectic mixtures forming. Above about 750°C hot corrosion will thus proceed via fluxing reactions.

Luthra (NACE -6 1983)[103] showed that a minimum pSO_3 of 1 atm is required to stabilise the Na_2SO_4 -$CoSO_4$ liquid salt below the melting point of Na_2SO_4. Hence, a high pSO_3 and a low oxygen ion activity, is required for such a liquid to exist. In which case basic fluxing cannot occur. Acid fluxing was deemed unlikely at low temperatures as positive gradients in solubilities at the oxide/scale interface are required. Thus Luthra showed that the existing fluxing theories cannot be used to explain low temperature hot corrosion.

Cobalt based alloys coated in Na_2SO_4 and exposed to an SO_3/SO_2 atmosphere formed porous Al/Cr rich oxides. Co-Cr alloys suffered from pitting attack whilst Co-Al alloys from uniform attack. Co was seen to dissolve at the oxide/salt interface and migrate through the salt to form Co_3O_4. A band of sulphides formed at the alloy/scale interface.

Low temperature hot corrosion of nickel and cobalt based alloys, between 600-800°C, has been shown in general to depend on the partial pressure of SO_3 being high enough for the formation of liquid Na_2SO_4-Ni/$CoSO_4$ solutions. Uncertainty still exists concerning detailed corrosion mechanisms. Barkalow and Pettit[102] believed that Na_2SO_4 reacted with the substrate after penetrating the initial alumina layer through cracks. An increase in pSO_2 is believed to occur at the salt/alloy interface as oxide formation results in a reduction in pO_2. O_2 transport through Na_2SO_4 is slow relative to that of SO_2 further increasing the pSO_2, according to the equilibrium equation,

$$\mathbf{SO_3(g) = SO_2(g) + 1/2O_2(g)}$$

The selective removal of aluminium was believed to result in the formation of Na_2SO_4 soluble species such as aluminium sulphites. As the pO_2 increases near the salt/gas interface aluminium oxides were expected to reprecipitate.

5.4.2 Role of liquid salts

This section summarises some of the high temperature corrosion mechanisms, concentrating on the role of liquid salts so that they can be related to low temperature hot corrosion.

Industrial alloys and coatings provide protection from liquid salts. After an initial period of high corrosion rates the salt becomes saturated and a more protective oxide film forms. However, dissolution alone cannot explain the high corrosion rates often seen even when low oxide solubilities exist in the salt. Luthra[101] showed that rapid sustained corrosion occurred when porous oxide films developed. Several processes were proposed for their development and these are discussed below. They refer to chromia forming alloys and also apply to alumina formers.

- **Cr_2O_3 precipitation in the liquid salt:** Cr or CrO dissolves at the scale/salt interface and precipitates as Cr_2O_3 near the gas/salt interface. Due to the rapid

dissolution process discontinuous and thus porous oxides develop.

- **Dissolution of the more noble metal or metal oxide:** This could occur at the scale/salt interface during transient oxidation when a large concentration of the more noble metal oxide (CoO in the case of Co alloys) forms. The liquid salt modifies the corrosion by dissolving the more noble metal oxide at a faster rate than the diffusion of Cr, preventing the formation of a protective Cr_2O_3 layer. The dissolution process undercuts and isolates Cr_2O_3 particles. This process becomes important at low temperatures as the diffusion rates through the oxides decrease. Once the salt becomes saturated a continuous protective Cr_2O_3 layer may form. Sustained corrosion will only occur if the dissolved Cr_2O_3 precipitates away from the scale/salt interface.

Luthra suggested that there were three conditions under which MOy is able to precipitate in the liquid salt.

- **Dissolution and precipitation of MOy:** This can occur if a negative gradient of solubility is set up at the scale/salt interface, with the oxide being dissolved at this interface and being reprecipitated at the salt/gas interface. This is shown in figure 23. An example of this occurs if basic conditions exist at the oxide/salt interface (case a) and acidic conditions at the salt/gas interface (case c) resulting in the oxide solubility decreasing from the oxide/salt interface, passing through a minimum (case b) and increasing again near the salt/gas interface. When the oxide solubilities at the interfaces are spread across the minimum solubility, oxide precipitation and hot corrosion should be favoured.

- **Dissolution and precipitation of its compounds:** MOy dissolution may occur if its activity is one at the scale/salt interface and decreases with distance into the salt. This provides the driving force needed for the precipitation of double oxides (MOy.NOz) near the salt/gas interface.

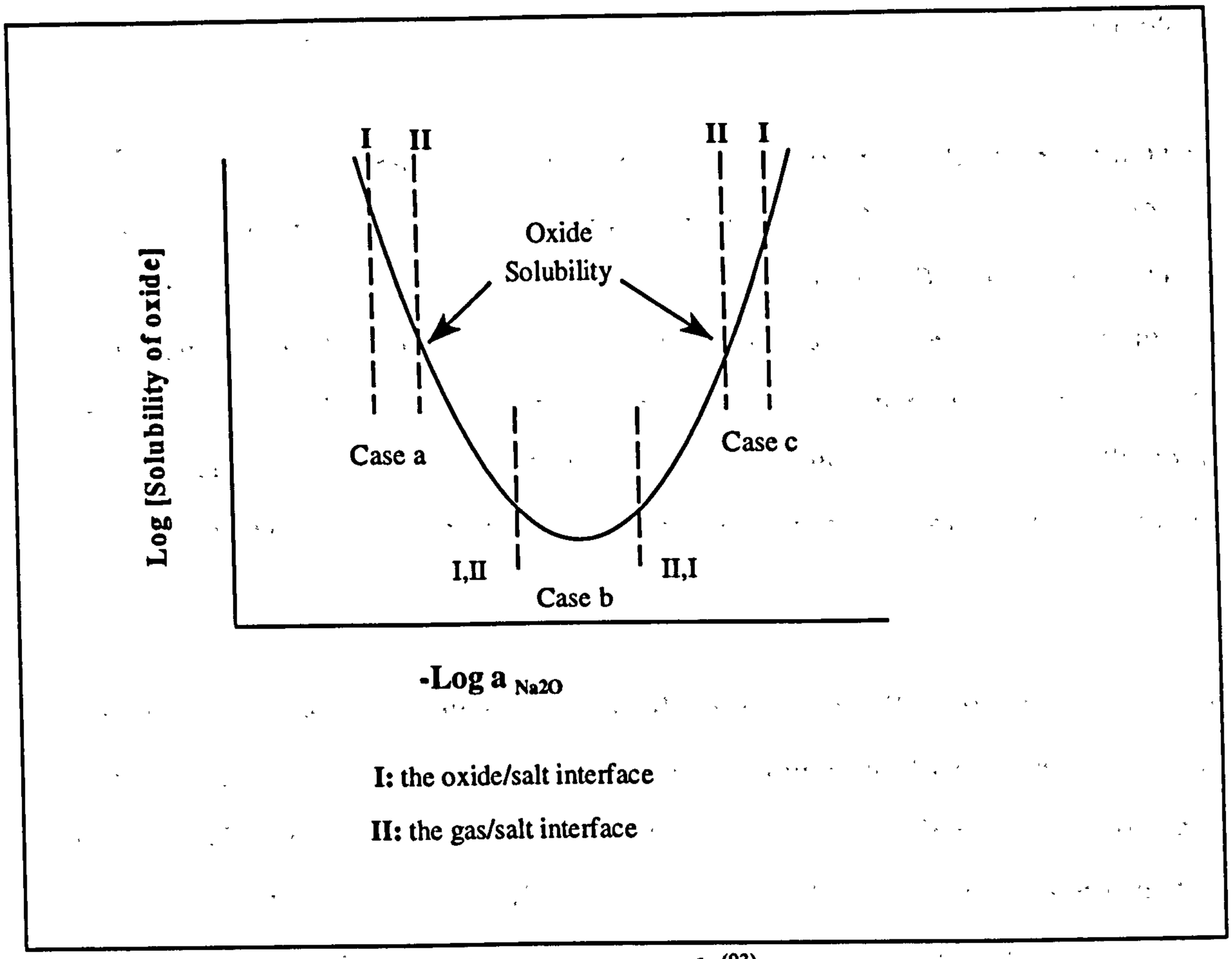

Figure 23: Oxide solubility gradient across a scale[93]

- **Dissolution of M and precipitation of MOy:** A gradient in the activity of M is required if M is to dissolve at the scale/salt interface and precipitate near the salt/gas interface. Within ionic salts there is an outward migration of nMm+ ions to the salt/gas interface and an inward migration of the higher valence mM^{n+} ions to the salt/scale interface.

5.4.3Mechanism of low temperature corrosion, as proposed by Luthra[102]

CoCrAl alloys formed porous oxide films of Cr_2O_3 and Al_2O_3, penetrated with a liquid sulphate when corroded at low temperatures.

It is possible to apply the above three conditions under which MOy is dissolved and precipitated to low temperature conditions. This type of investigation of using known

mechanisms can be applied to other systems so long as the conditions are comparable.

The first mechanism, which relies on a negative oxide solubility gradient, can be eliminated as in this case a positive Cr_2O_3 solubility gradient exists. Cr_2O_3 dissolves as $CrSO_4$ on cobalt based alloys, with its solubility in the salt increasing with pSO_3. Cr_2O_3 precipitaion does not occur as the pSO_3 increases near the salt/gas interface.The second mechnism can also be eliminated as only Cr_2O_3, and not $CoCr_2O_4$ (a higher valence oxide) was identified in the reaction product. Cr_2O_3 and Al_2O_3 do not precipitate out in the salt via the third mechanism as neither Al or Cr exist in multivalent states needed for counter transport of ions.

Luthra came to the conclusion, after systematically eliminating all other mechanisms, that low temperature corrosion of Co alloys occurred through the dissolution of the more noble metal undercutting the surface oxide, resulting in a pitting effect. In the presence of Na_2SO_4 and SO_3 an initial period, in which a liquid is formed, is followed by a propagation stage where SO_3 migrates inwards and Co outwards. Sulphate ions migrate to the salt/gas interface and $S_2O_7^{2-}$ to the oxide/salt interface where oxygen is consumed causing the pSO_2 to be higher at the oxide/salt interface than at the gas/salt interface. SO_2 may then diffuse out as SO_3^{2-} or as dissolved SO_2 . Luthra postulated that CoO dissolution and precipitation occurred via the counter transport of Co^{2+} outwards and Co^{3+} ions inwards with a net outward transport of one cobalt atom.

The pitting effect which often characterises low temperature hot corrosion is not fully understood but could be the result of localised scale failures allowing liquid eutectic mixtures to form at accelerated rates at theses sites. Chiang et al[103] proposed a mechanism, shown in figure 24, for the hot corrosion of Co18Cr6Al at 750°C in oxygen and low partial pressures of SO_2 (~6×10^{-4} atm). The presence of aluminium appeared to increase the severity of attack when compared with a Co-20Cr alloy.

The transport of Co and SO_2 through the salt was explained by Luthra and supported by Chiang et al. Initially liquid salts form through the sulphation of Co oxides at the

salt/substrate interface. High SO_2 and S_2 partial pressures develop at this interface by equations 5.4.3a and 5.4.3b, with further oxide formation lowering the partial pressure of oxygen.

$$SO_3\,(g) \rightleftharpoons SO_2\,(g) + 1/2O_2\,(g) \qquad (5.4.3a)$$

$$SO_2\,(g) \rightleftharpoons 1/2S_2(g) + 3/2O_2(g) \qquad (5.4.3b)$$

The high SO_2 pressures generated could, in principle, be responsible for the formation of phases such as $Cr(SO_4)_3$ by the reaction below;

$$Cr_2O_3(s) + 3SO_3(g) \rightleftharpoons Cr_2(SO_4)3 \text{ (in } Na_2SO_4\text{-}MSO_4) \qquad (5.4.3c)$$

SO_2 diffuses through the salt to the substrate interface where it reacts with alumina producing aluminium sulphites which then dissolve in the liquid sulphate (equation 5.4.3d). The increase in pO_2 near the salt/gas interface causes alumina to reprecipitate as a non protective discontinuous layer. The outward transport of aluminium continues with the preferential attack of aluminium rich CoAl phases.

$$Al_2O_3\,(s) + 3SO_2\,(g) = Al_2(SO_3)_3 \qquad (5.4.3d)$$

5.4.3 NaCl contamination

NaCl may cause accelerated corrosion via a similar mechanism as described in high temperature hot corrosion or through the formation of low melting point (675°C) NaCl - Na_2SO_4 eutectic mixtures. Such mixtures would allow the transport of reactants and corrosion products.

5.5 Hot corrosion of TiAl alloys

No work has been reported for the hot corrosion of titanium aluminide alloys. However,

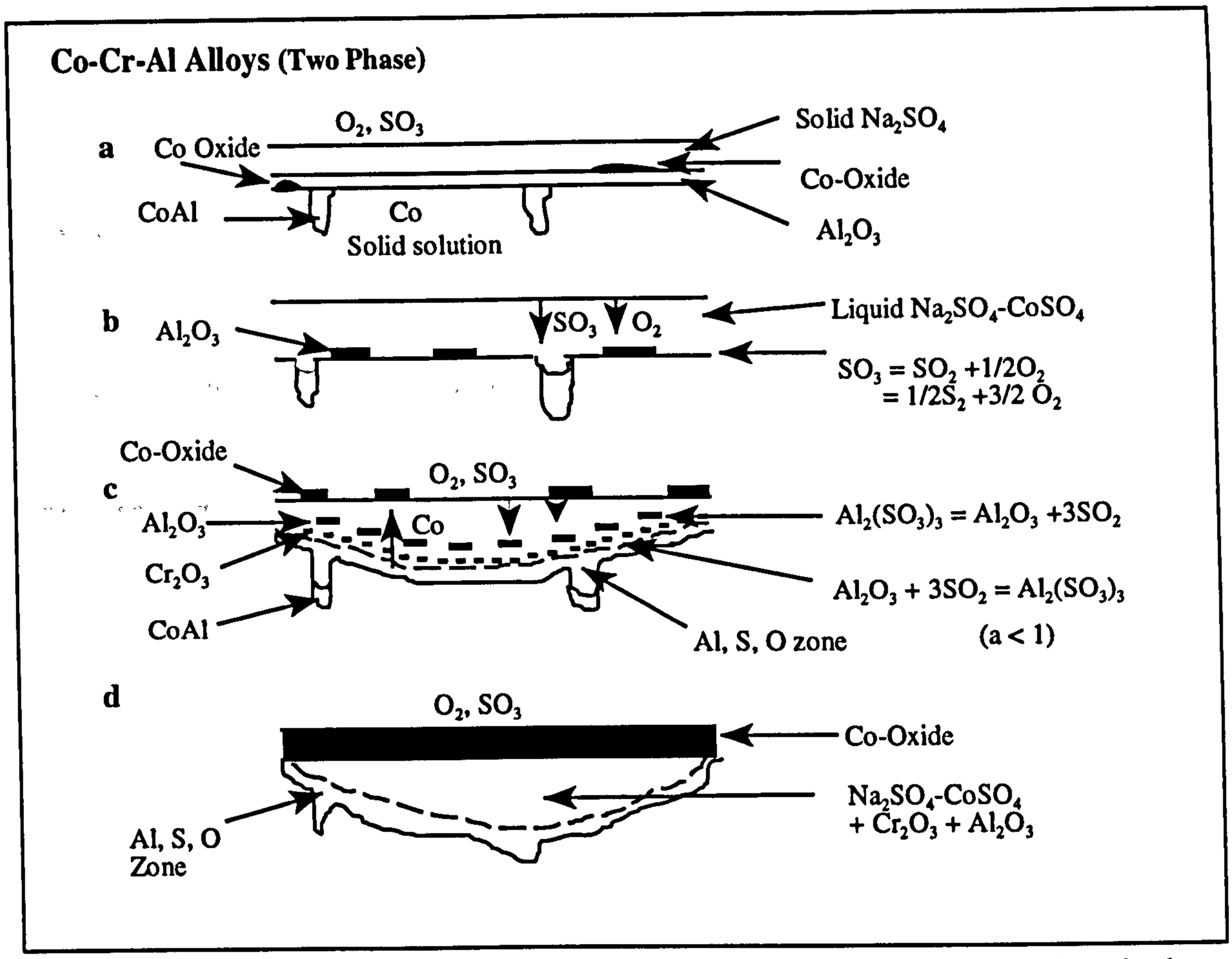

Figure 24: Schematic diagram illustrating the hot corrosion of CoCrAl alloys in the presence of low $p(SO_3)$ at 750°C

it is possible to make some assumptions based on the service conditions expected. If Ti-45Al-2Mn-2Nb was used to replace the current Ni based alloys in the 4th stage of the compressor section, operating temperatures of approximately 700 to 750°C would be expected. During operation low concentrations of salt, NaCl and/or Na_2SO_4, would be expected to be ingested through the compressor section, whilst low partial pressures of SO_2/SO_3 would be present. These temperatures are below the melting temperatures of both forms of salt. This suggests that hot corrosion of TiAl alloys, at these temperatures, would not be controlled by fluxing mechanisms. From these observations it would appear that NaCl may disrupt the initial oxide layer at the substrate, as proposed by Hancock[96] and others[98, 99] and that low melting point Na_2SO_4 eutectic mixtures, suggested by Luthra[102],would form accelerating the oxidation rates at these areas of salt deposits. As in service, complete surface coverage by salt is unrealistic. Dual mechanisms may thus operate with sulphidation type reactions occurring at regions of little salt.

Chapter 6

Phase Stability Diagrams (PSD's)

6.1 Introduction

The thermodynamics of a reaction or reactions can provide further support to the corrosion mechanisms being proposed. Predicting the order in which the corrosion reactions occur is not always simple as metallographic evidence frequently shows the resulting products but not necessarily the intermediate reactions. The following sections build up a thermodynamic know how needed to understand and construct phase stability diagrams (PSD's). These diagrams show the equilibrium conditions under which the possible reaction products form.

6.2 Gas/Metal reactions

This section reviews the simple gas/metal reaction providing the background information needed to understand bi-oxidant/metal reactions.

The general chemical reaction which occurs between a metal and a gas, resulting in the formation of a solid reaction product is shown below;

$$\mathbf{XM(s) + YX(g) = XMX_z(s)} \qquad \mathbf{(6.2a)}$$

where Z=2Y/X

This reaction is only possible if it results in a negative value of free energy of formation (ΔG^0). That is a lower energy state is reached. A positive value implies that the reaction is thermodynamically impossible. Reaction (6.2b) illustrates how the free energy of formation of this reaction can be calculated from tabulated standard free energy of formation data.

$$\begin{aligned}\mathbf{\Delta G^0} &= \mathbf{\Delta G\,(products) - \Delta G\,(reactants)} \\ &= \mathbf{X\,\Delta G\,(MX_z\,(s)) - X\Delta G(M\,(s)) - Y\,\Delta G\,(X_2\,(s))}\end{aligned} \qquad \mathbf{(6.2b)}$$

Reaction (6.2a) can also be characterised by its equilibrium constant (K) given below;

$$K = \frac{a(MX_Z(s))^X}{a(M(s))^X \; x \; a(X_2(s))^X} \qquad (6.2c)$$

where $a(MX_z(s))$, $a(M(s))$ and $a(X_2(s))$ are the activities or effective concentrations of the species involved in the reaction.

Assuming equilibrium it becomes possible to relate the standard free energy of formation with the equilibrium constant by the relationship below;

$$\Delta G^0 = -2.303\ RT \text{ x } Ln\ K \qquad (6.2d)$$

where R = 8.314 J/°K the gas constant and T = the temperature in °K

Substituting K from reaction 6.2c into this expression gives the following;

$$\Delta G = -2.303\ RT\ Ln\ \left(\frac{a(MX_Z(s))^X}{a(M(s))^X \text{ x } a(X_2(s))^X}\right) \qquad (6.2e)$$

This can be simplified if it is assumed that the reactants and products in equation (6.2a) form in there standard states, in which case $a(M(s)) = 1$ and $a(MX_Z(s)) = 1$. The activity of the gas is also equal to its partial pressure. The equation can now be written as;

$$\Delta G^0 = 2.303RT \text{ x } Ln\ (P(X_2\ (g))^Y) \qquad (6.2f)$$

6.3 Bi-oxidant reactions

When a material is exposed to bi-oxidant environments at high temperatures the stability

of the resulting corrosion products is governed by both the standard free energies of formation and the partial pressures of the gas components.

There are three main reactions that occur when a material is exposed to an environment containing oxygen and sulphur dioxide. These are shown in equations 6.2a, 6.2b and 6.2c.

$$XM + 1/2O_2 = M_XO \qquad \Delta G^0_1 \qquad (6.3a)$$

$$SO_2 = 1/2S_2 + O_2 \qquad \Delta G^0_{2a} \qquad (6.3b)$$

$$YM + 1/2S_2 = M_YS \qquad \Delta G^0_{2b} \qquad (6.3c)$$

where M=metal and ΔG^0_1 the standard free energy of formation

Thermodynamic stability diagrams are useful in predicting the most stable reaction products at a given temperature. The stable phases formed depend on the $p(O_2)$ and $p(S_2)$ developed. Minimum values of $p(O_2)$ and $p(S_2)$ exist below which the respective oxides and sulphides are no longer stable. Equations 6.3d and 6.3e can be used to determine these values.

$$pO_2 > \frac{1}{a_M^{2X}} \exp\left(-\frac{2\Delta G_1^0}{RT}\right) \qquad (6.3d)$$

$$pS_2 > \frac{1}{a_M^{2Y}} \exp\left(-\frac{2\Delta G_2^0}{RT}\right) \qquad (6.3e)$$

6.4 M-O_2-Cl_2 Phase stability diagrams (PSD's)

In this section the methodology for constructing phase stability diagrams will be summarised and used to construct a Mn-O_2-Cl_2 PSD (Figure 25 shows an example at

500°C). This example will enable the remaining PSD's to be constructed and used in future discussions. These diagrams provide useful thermodynamic data which shows the likelihood of the phases formed being stable in different partial pressures of the reacting gases. Free energy data on their own only confirms whether or not a reaction is possible. PSD's become useful when predictions need to be made on the reaction products formed within the scale. The partial pressures of the reacting gases can be expected to change in which case the stabilities of the reaction products will also change. A similar methodology may be used to construct $M-O_2-SO_2$ PSD's.

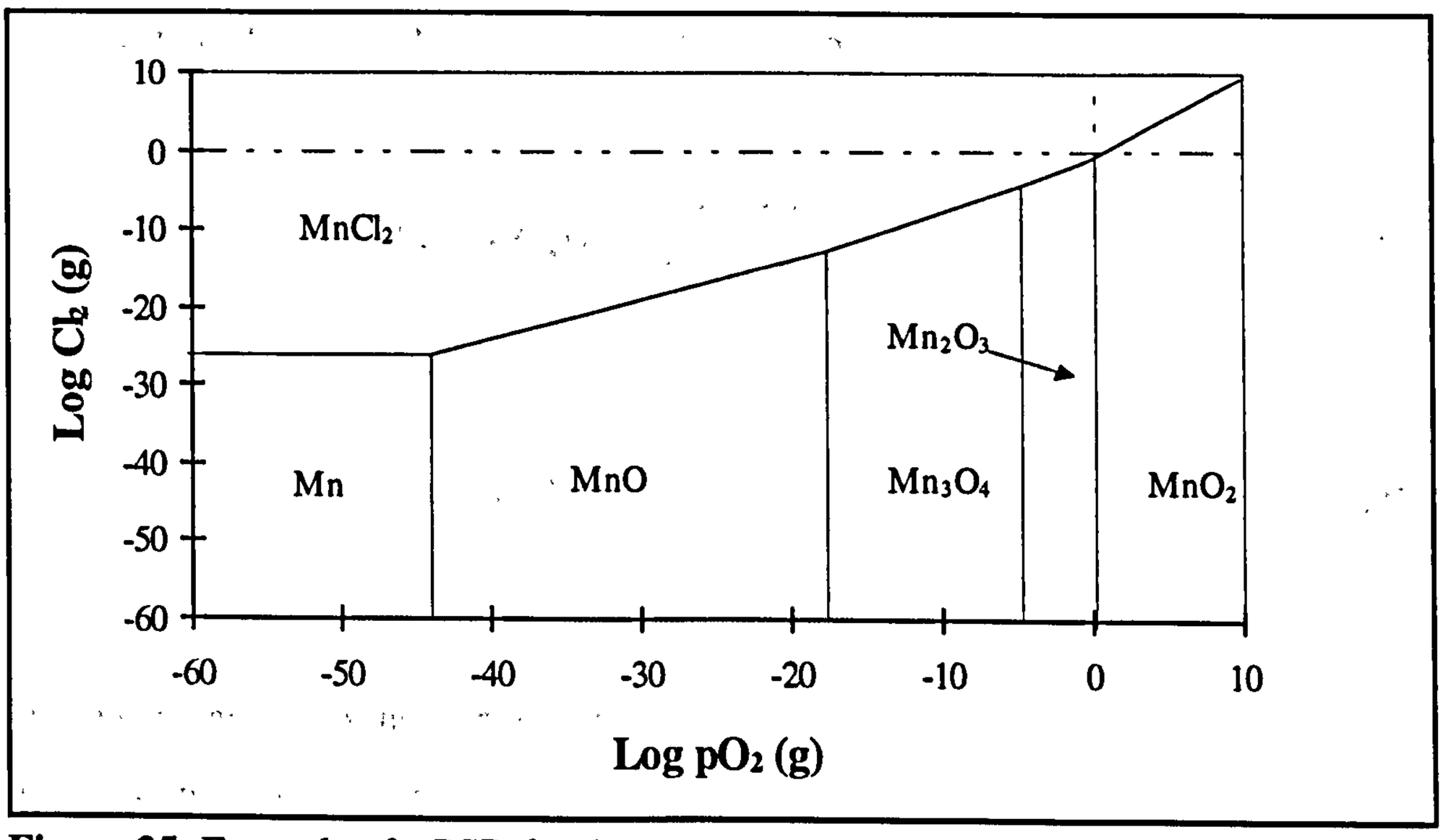

Figure 25: Example of a PSD for the system $Mn-O_2-Cl_2$

Formation of solid Manganese oxides and chlorides

The oxidation and chlorination reactions are shown below;

$$Mn\ (s) + 1/2O_2\ (g) = MnO\ (s) \qquad \text{at temperature T} \qquad \textbf{(6.4a)}$$

$$Mn\ (s) + Cl_2\ (g) = MnCl_2\ (s) \qquad \text{at temperature T} \qquad \textbf{(6.4b)}$$

Assuming equilibrium exists equation 6.2f can be used to write thermodynamic equations

relating the standard free energy of formation to the partial pressures of oxygen and sulphur. These are shown below;

$$\Delta G^0 = 2.303RT \times \text{Ln}\,(p(O_2)^{½}) \qquad (6.4c)$$

$$\Delta G^0 = 2.303RT \times \text{Ln}\,(p(Cl_2)) \qquad (6.4d)$$

These equations can be rearranged to enable ΔG^0 values, calculated from equation (6.2b) using tabulated values, to be used to calculate the partial pressures of oxygen and chlorine at which stable MnO and $MnCl_2$ begin to form at the metals surface.

$$\text{Ln}\,(p(O_2)) = \frac{2\Delta G^\circ}{2.303\ RT} \qquad (6.4e)$$

$$\text{Ln}\,(p(Cl_2)) = \frac{2\Delta G^\circ}{2.303\ RT} \qquad (6.4f)$$

The oxygen and chlorine partial pressures at which the next transitions occur can be calculated in a similar manner.

$$3MnO\,(s) + 1/2O_2\,(g) = Mn_3O_4\,(s) \quad \text{at temperature T} \qquad (6.4g)$$

$$MnCl_2\,(s) + 1/2O_2\,(g) = MnCl_3\,(s) \quad \text{at temperature T} \qquad (6.4h)$$

Oxidation reaction of solid chlorides

The stability of $MnCl_2$ would be expected to decrease as the partial pressure of oxygen increased. This results in the following oxidation or exchange reaction;

$$MnCl_{2\,(s)} + O_2\,(g) = MnO_2\,(s) + Cl_2\,(g) \quad \text{at temperature T} \qquad (6.4i)$$

The free energy of formation for this reaction can be expressed using equation 6.2e. The resulting equation:

$$\Delta G = -2.303\ RT\ Ln\ (\frac{p(Cl_2(g))}{p(O_2(g))}) \qquad (6.4j)$$

can be rewritten as;

$$Ln(p(O_2)) - Ln(p(Cl_2)) = \frac{\Delta G^\circ}{2.303RT} \qquad (6.4k)$$

This can be rearranged to obtain the equation of a straight line:

$$Ln(p(O_2)) = \frac{\Delta G^\circ}{2.303RT} + Ln(p(Cl_2) \qquad (6.4l)$$

A straight line can be derived by calculating $Ln(p(O_2))$ for different $Ln(p(Cl_2))$

Formation of volatile chlorides in equilibrium with solid oxides

In environments containing oxygen and chlorine volatile metal chlorides are able to form alongside stable oxides according to equation .

$$Mn\ (s) + Cl_2\ (g) = MnCl_2\ (g) \qquad (6.4m)$$

Using equation 6.2e enables an expression for the free energy of formation of $MnCl_2$ to be made.

$$\Delta G = -2.303\ RT\ Ln\ (\frac{p(MnCl_2(g))}{p(Cl_2(g))}) \qquad (6.4n)$$

This can be rewritten as:

$$\mathbf{Ln(p(Cl_2)) = \frac{\Delta G^{o}}{2.303RT} + Ln(p(MnCl_2)} \qquad \textbf{(6.4o)}$$

This equation can be used to obtain a straight line on a Ln(p(Cl_2)) versus Ln(p(O_2)) plot by using arbitrary values for the activity of $MnCl_2$.

Chapter 7

Experimental procedures

7.1 Introduction

Although the oxidation of titanium aluminides has been studied very little is known about the oxidation and corrosion behaviour of these materials at their potential service temperatures, 500-750°C. In fact there have been no studies concerning the hot salt corrosion of Ti-45Al-2Nb-2Mn + 0.8%TiB_2 and low temperature (< 700°C) oxidation of this alloy is another aspect of interest which has not been addressed. In attempting to simulate the conditions encountered in service separate studies have been undertaken to determine the effects of oxidation in air, air + sulphur dioxide and salt deposits over this temperature range of interest, 500-900°C. A concluding investigation has investigated the combined effects of solid salt deposits and an atmosphere of air and SO_2 simulating the hot corrosion of γ-TiAl. The studies undertaken are as follows:

7.2 Oxidation

Several oxidation mechanisms have been proposed over the temperature range being considered or at more elevated temperatures for γ-TiAl alloys. This study will assess the performance of Ti-45Al-2Nb-2Mn + 0.8%TiB_2 and compare it to the published data, characterise the materials oxidation behaviour and determine whether or not there is a change in oxidation kinetics with increasing temperature using a thermogravimetric microbalance. In this manner the oxidation behaviour will be investigated over the temperature range of 700 to 900°C.

7.3 Corrosion in air-SO_2 environments

If a true simulation is to be made of the conditions encountered in service then a study using an atmosphere of air + sulphur dioxide must be made. Discontinuous measurements, following the guidelines proposed by Nicholls[104], will be made over a temperature range of 700 to 900°C after 5,10, 20, 50 and 100 hours. Individual specimens are to be used for each time to allow analytical investigations to be made at each exposure time in order to compile valid corrosion mechanisms.

7.4 Corrosion under salt deposits

A thermogravimetric study will be carried out in order to determine the salt corrosion rates over the temperature range of 500-800°C. The oxidation and sulphidation data will provide a useful comparison, enabling the effects of salt to be more clearly seen.

7.5 Hot corrosion studies

Service conditions incorporate a mixture of contaminants. The hot corrosion behaviour of this alloy will be carried out in an atmosphere of air containing low $p(SO_2)$ with the specimens coated with low levels of NaCl. This study will evaluate the materials kinetic behaviour discontinuously over the temperature range of 650-800°C.

7.6 Material

7.6.1 Ti-45-2-2

The titanium aluminide intermetallic used throughout this study contained 45 at%Al, 2 at%Nb, 2 at%Mn, and 0.8 at%TiB_2. This is a gamma plus approximately10 percent, by volume, alpha 2 alloy, with a lamellar microstructure. Figure 26 shows a typical microstructure of this alloy.

7.6.2 Specimens

For the thermogravimetric studies test coupons 1.4-1.9 mm in thickness by 9.7-10 mm in diameter were used. The test coupons were cross-hatch polished using 240 and 1200 grit abrasive papers to remove all EDM (electro-discharge machining) markings and to produce uniform surfaces, eliminating any deep scratches.

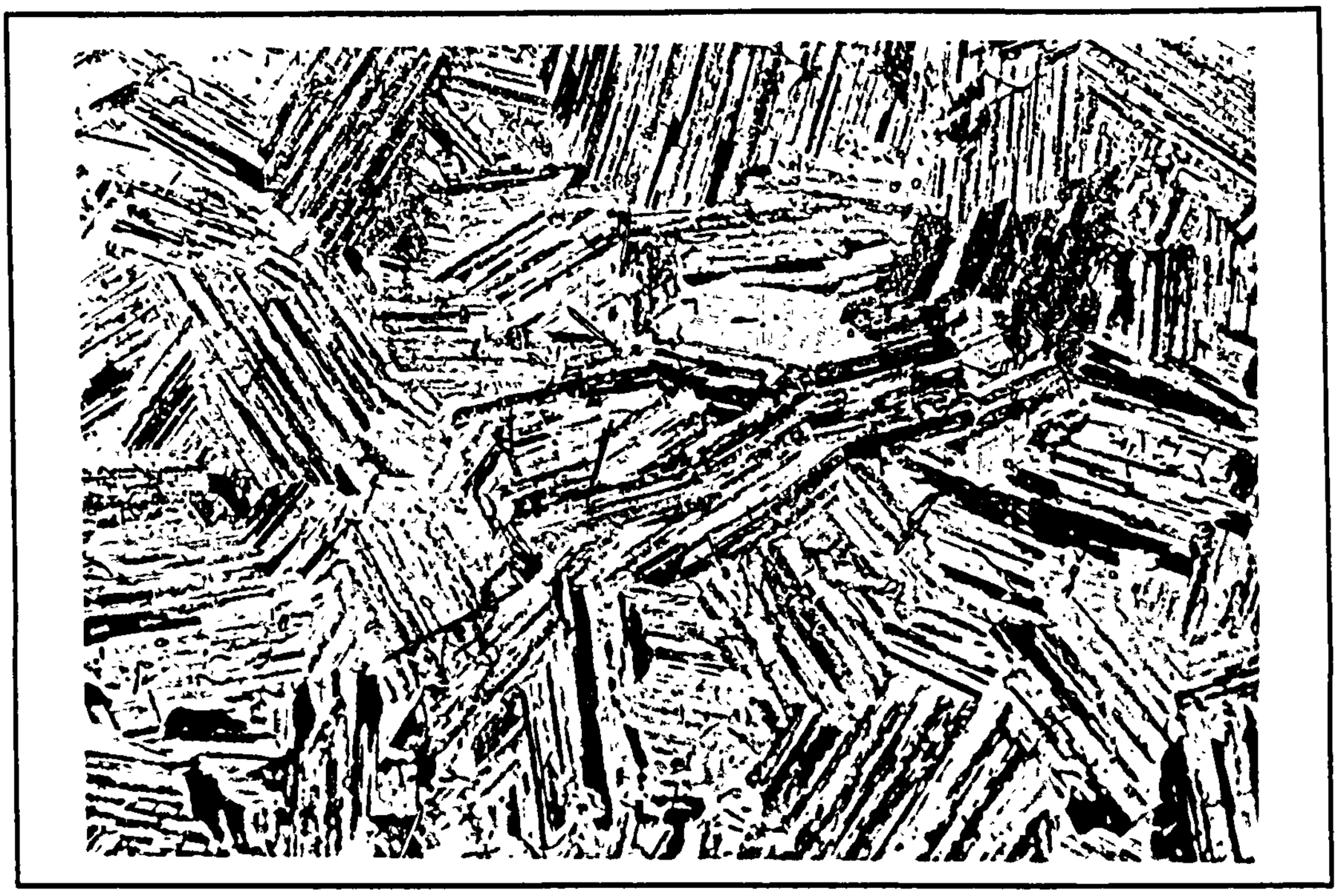

Figure 26: Microstruture of Ti-45Al-2Mn-2Nb + 0.8%TiB_2

7.7 Cleaning Procedure

In order to ensure that the test specimens were free from surface contamination a rigorous cleaning procedure was adopted. This procedure was used before salt coating to optimize the adherence of the salt coating to the specimens surface. Due to the nature of the thermogravimetric and corrosion tests it was essential for the specimens to be contamination free.

1. Initial cleaning with volasil 344 (Analar isopyl alcohol; a high purity grade alcohol)

2. Clean coupon in ultrasonic bath with volasil 344 for 15 minutes.

3. Flush coupon with clean Volasil 344.

4. Flush coupon with isopropanol alcohol (IPA).

5. Clean coupon in ultrasonic bath with IPA for 15 minutes.

6. Flush coupon with IPA.

7. Flush coupon with Analar isopropanol alcohol.

8. Coupons were placed in a reflux condenser containing Analar isopropanol and vapour degreased for approximately 1 hour.

Surgical gloves were worn throughout the cleaning procedure and during all subsequent procedures in order to maintain contaminated free surfaces. The coupons were then stored in a dessiccator to avoid further contact with contaminated surfaces.

7.8 Salting Procedure

7.8.1 Salting

The salt corrosion coupons were salted in a salt fog created in the apparatus shown in figure 27. A typical salt coated Ti-45Al-2Nb-2Mn +0.8%TiB_2 coupon is shown in figure 28.The salt solution was made to a British standard 3900 part F4. The following procedure was used to salt the coupons.

1. Salt solution is initially pumped, using a peristaltic pump, through the pipes to clear any trapped air bubbles.

2. The spraying chamber is lowered and four coupons loaded onto a metal frame attached to a turntable.

3. The furnace is then lowered down over the coupons and switched on. Half an hour is allowed for the furnace to reach 200°C and to allow sufficient time for the coupons to reach this temperature.

Table 10: Composition of salt spraying solution (BS3900)

Composition	**Formula**	**Quantity per litre of Solution (g)**
Sodium Chloride	NaCl	26.5
Magnesium Chloride	$MgCl_2$	4
Magnesium Sulphate	$MgSO_4$	3.3
Potasium Chloride	KCl	0.73
Sodium Bicarbonate	$NaHCO_3$	0.28
Calcium Chloride	$CaCl_2$	1.1

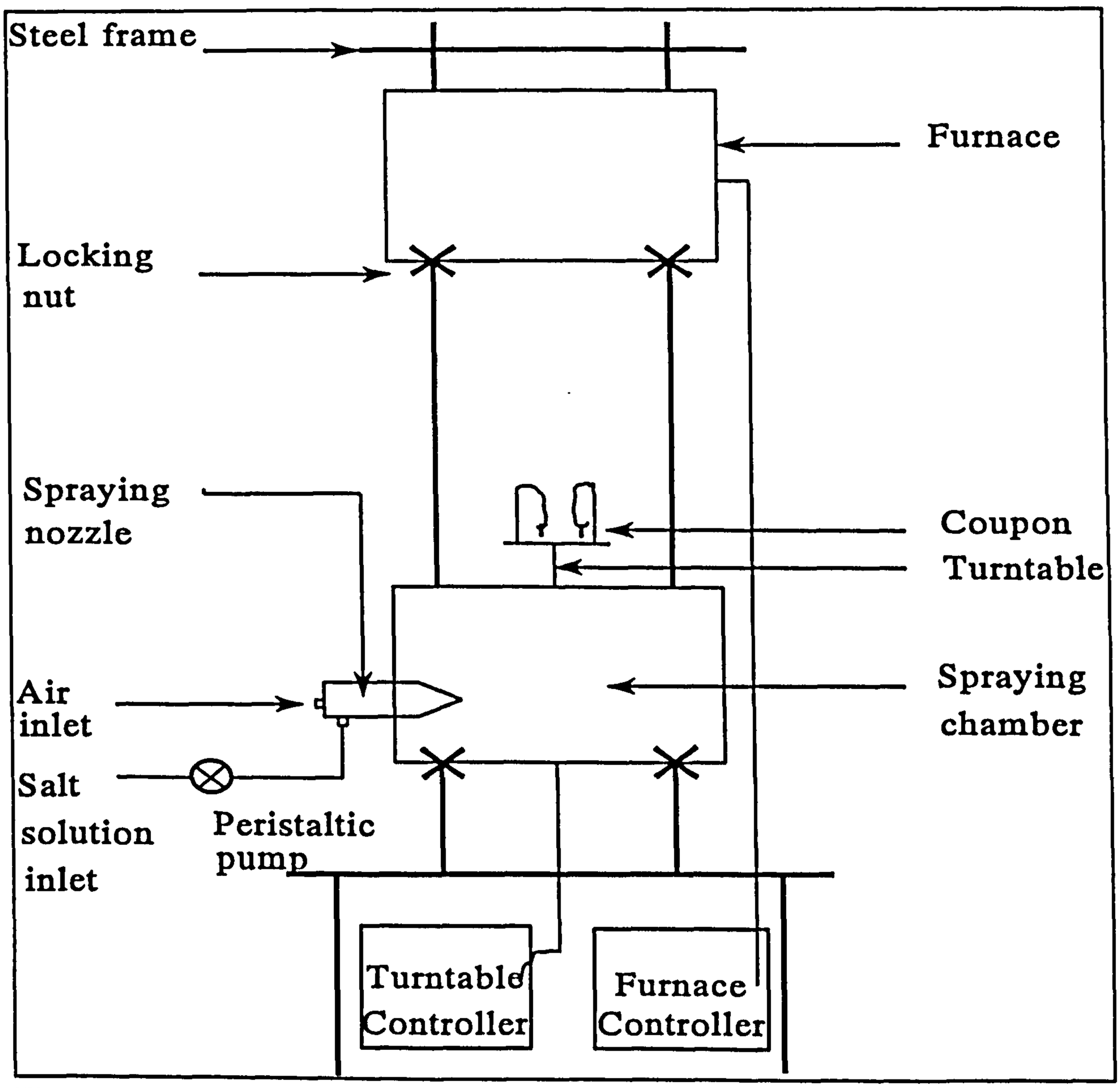

Figure 27: Salt coating rig

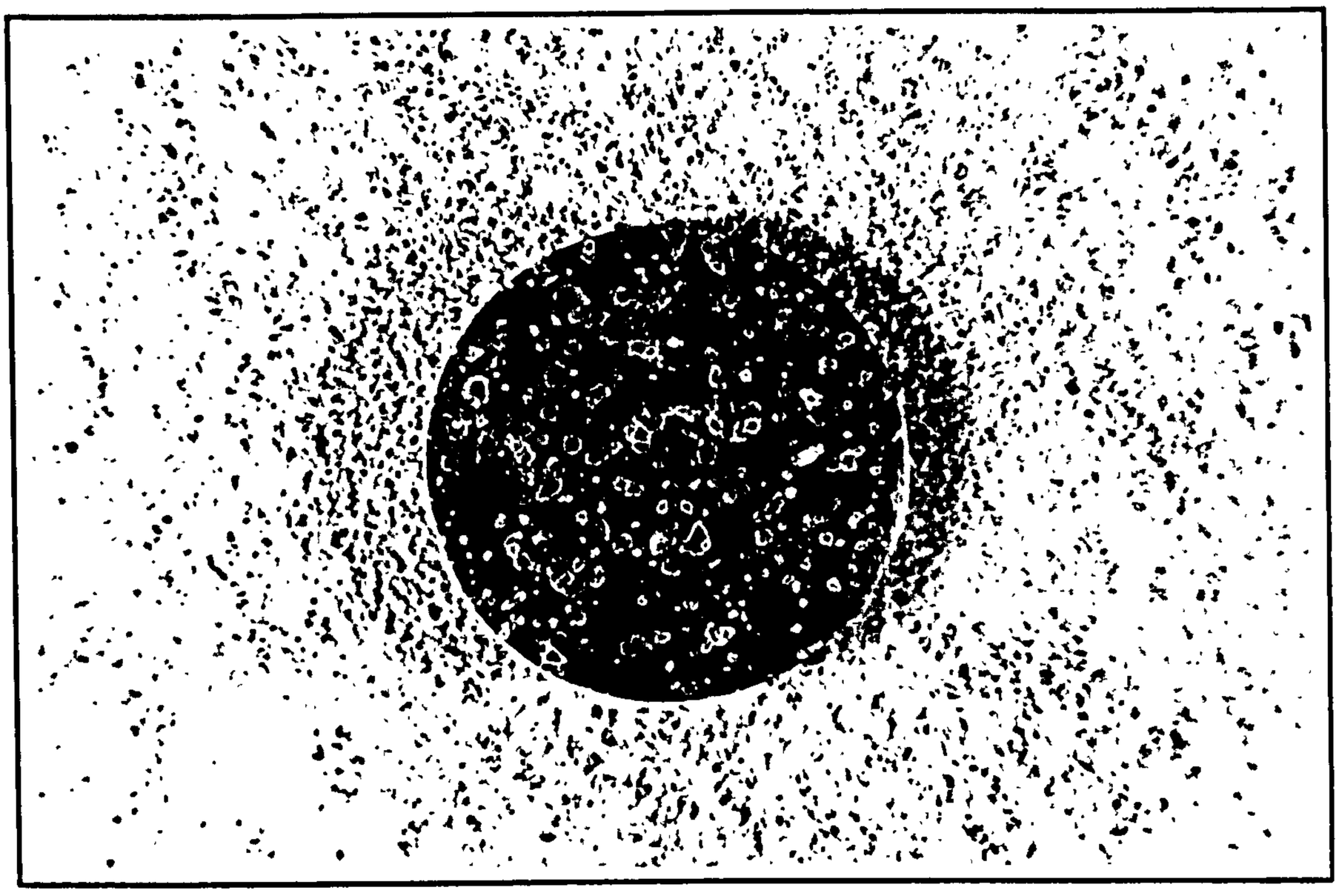

Figure 28: Salt coated Ti-45Al-2Nb-2Mn + 0.8%TiB_2 coupon

4. The furnace is raised and the salting chamber quickly lifted into place.

5. The pump and turntable are then simultaneously switched on.

6. In as fast a time as possible the air flow is turned on at a pressure of 1 bar for a time previously determined (approximately 60 seconds).

7. The pump and turntable are simultaneously 109switched off. As soon as the gas flow has been turned off the spraying chamber can be lowered to allow the coupons to cool.

8. Each coupon is stored in a glass vial and placed in a desicator.

9. One coupon from each batch is placed in de-ionised water for at least eight hours in order for a salt analysis to be made.

7.8.2 Salt analysis

Once salted, one specimen is taken from each batch and placed in de-ionised water. This allows the salt concentration to be determined using titration techniques. An analysis is made using an expandable ion analyser (Orion EA 940) linked to a single junction reference electrode. The procedure followed is detailed below.

1. It is important that the electrodes contain fresh solution and that no residual salt remains from previous analyses.

2. The salt solution obtained from soaking the coupon is poured into a 20 millilitre vial. The coupon container is washed with distilled water and used to make up the 20 millimetre mark.

3. The contents of the vial are then added to a clean Pyrex beaker. One millimetre of low level ionic strength adjuster (Orion 94-011) is also added.

4. The analysis can only work if the titrate is completely mixed in the solution. For this reason the beaker is placed on a magnetic stirrer and set at a level which gives optimum stirring without creating a vortex.

5. The electrodes are then immersed just below the surface of the solution.

6. The analyser is then allowed to stabilise and a reading taken in millivolts.

7. 0.1 Millilitres of silver nitride ($AgNO_3$) 0.005M is then added to the solution.

8. Steps 6 and 7 are repeated until 1.5 millilitres of silver nitride has been added.

9. After cleaning the electrodes with distilled water steps 1 to 8 are repeated on a reference solution containing 20 millilitres of distilled water.

7.8.3 Calculating salt concentration

Salt concentrations are determined by plotting the voltages measured (Y-axis) versus the volume of silver nitride ($AgNO_3$) added (X-axis) on volume corrected plot paper. Two straight lines are thus obtained with the titre of salt concentration being the difference between the intercepts, of the salt solution and reference, on the X-axis.

The following calculations are needed before the salt concentration can be determined.

Mass of Chlorine (Cl^-) deposited

$$m_{Cl^-} = \frac{\text{Titre} \times M_{Cl^-} \times M\ (AgNO_3)}{1000} \text{ in grammes} \qquad (7.8.3a)$$

where M_{cl^-} is the molar weight of chlorine ions in grammes

$M\ (AgNO_3)$ is the molarity of the silver nitride solution used (0.005)

Ratio of Chlorine to salt weights

$$\frac{f_{Cl^-}}{f_{Salt}} = \frac{\left(\frac{m_{NaCl}}{M_{NaCl}} + 2\frac{m_{MgCl_2}}{M_{MgCl_2}} + \frac{m_{KCl}}{M_{KCl}} + 2\frac{m_{CaCl_2}}{M_{CaCl_2}}\right) \times M_{Cl^-}}{m_{NaCl} + m_{MgCl_2} + m_{MgSO_4} + m_{KCl} + m_{NaHCO_3} + m_{NaBr} + m_{CaC} \qquad (7.8.3b)}$$

where m_i is the weight of species i per litre of solution in grammes.

M_i is the molar weight of species in grammes per mole.

Throughout the salt spraying a salt solution with a chlorine to salt weight ratio of 0.55 was used (equation 7.8.3c).

$$\frac{M_{Cl^-}}{M_{Salt}} = 0.55 \qquad (7.8.3c)$$

Mass of salt deposited

Combining equations 7.8.3a and 7.83c allows the mass of salt deposited to be calculated (equation 7.8.3d).

$$m_{salt} = \frac{\text{Titre} \times M_{Cl^-} \times M(AgNO_3)}{550} \quad \text{grammes} \qquad (7.8.3d)$$

The concentration of the salt deposited on the specimens surface can then be calculated

$$[\text{Salt}] = \frac{m_{salt}}{A} \quad \text{grammes/cm}^2 \qquad (7.8.3e)$$

using equation 7.8.3e, were A is the specimens surface area in cm^2.

7.9 Thermogravimetric analysis

During the oxidation and corrosion of titanium aluminides at elevated temperature it is expected that mass gains will occur. It is possible to continuously measure these mass gains in order to evaluate the kinetics of the scales which form. The apparatus used is similar to that used by Birks and Meier[105]. Grabke et al[106,107] discussed standard test procedures for measuring continuous mass gains. An accurate experimental procedure was developed by Chevrot[79] and is explained in the following sections.

7.9.1 Thermogravimetric apparatus

The experimental design is shown in Figure 29. A C.I electronic microbalance, consisting of a MKII vacuum head and a C.I. Robal Control Unit and a cylindrical shaped resistance furnace, was used to measure the weight gains. A 286 IBM-compatible microcomputer

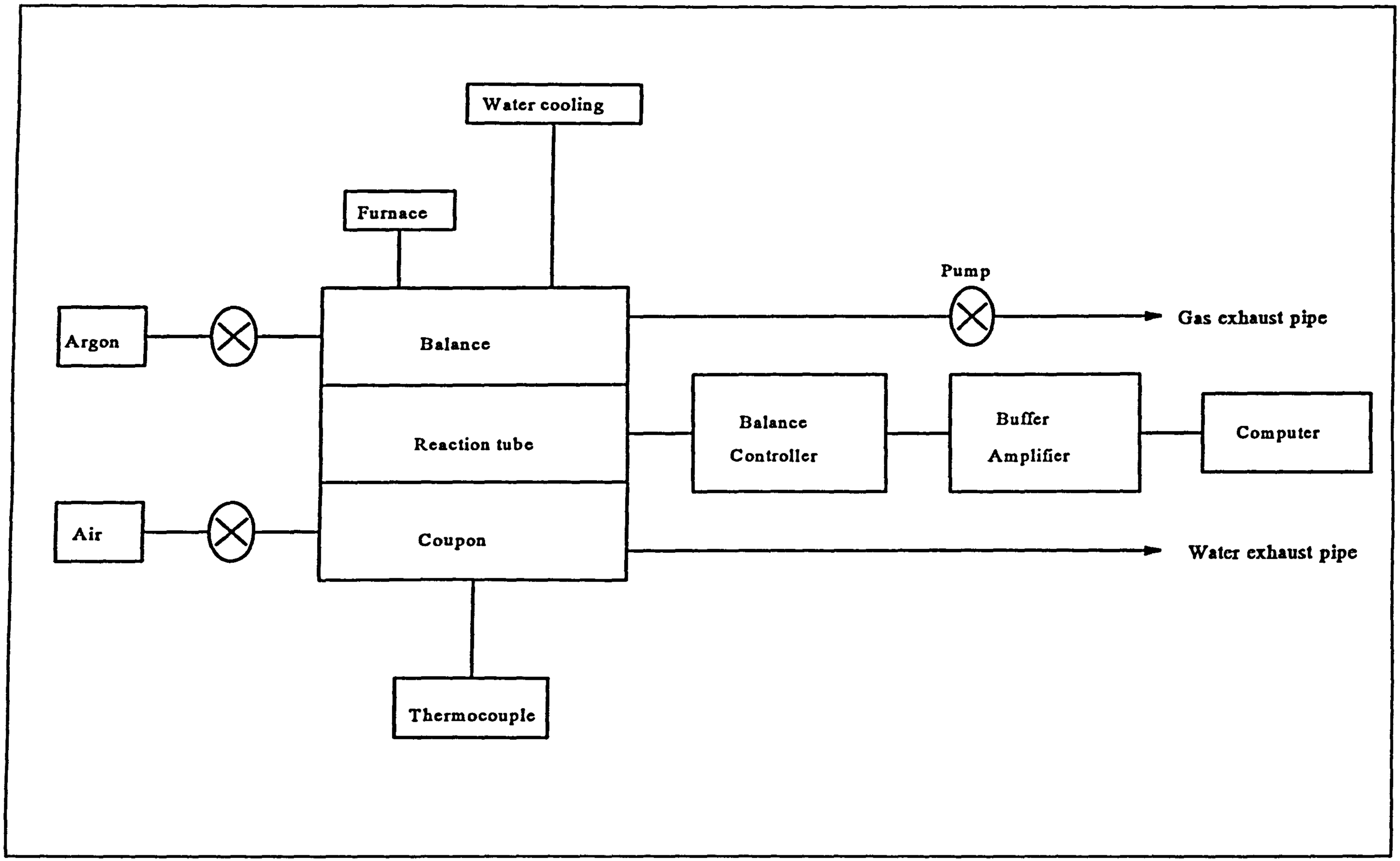

Figure 29: Schematic diagram showing the setup of a thermogravimetric microbalance

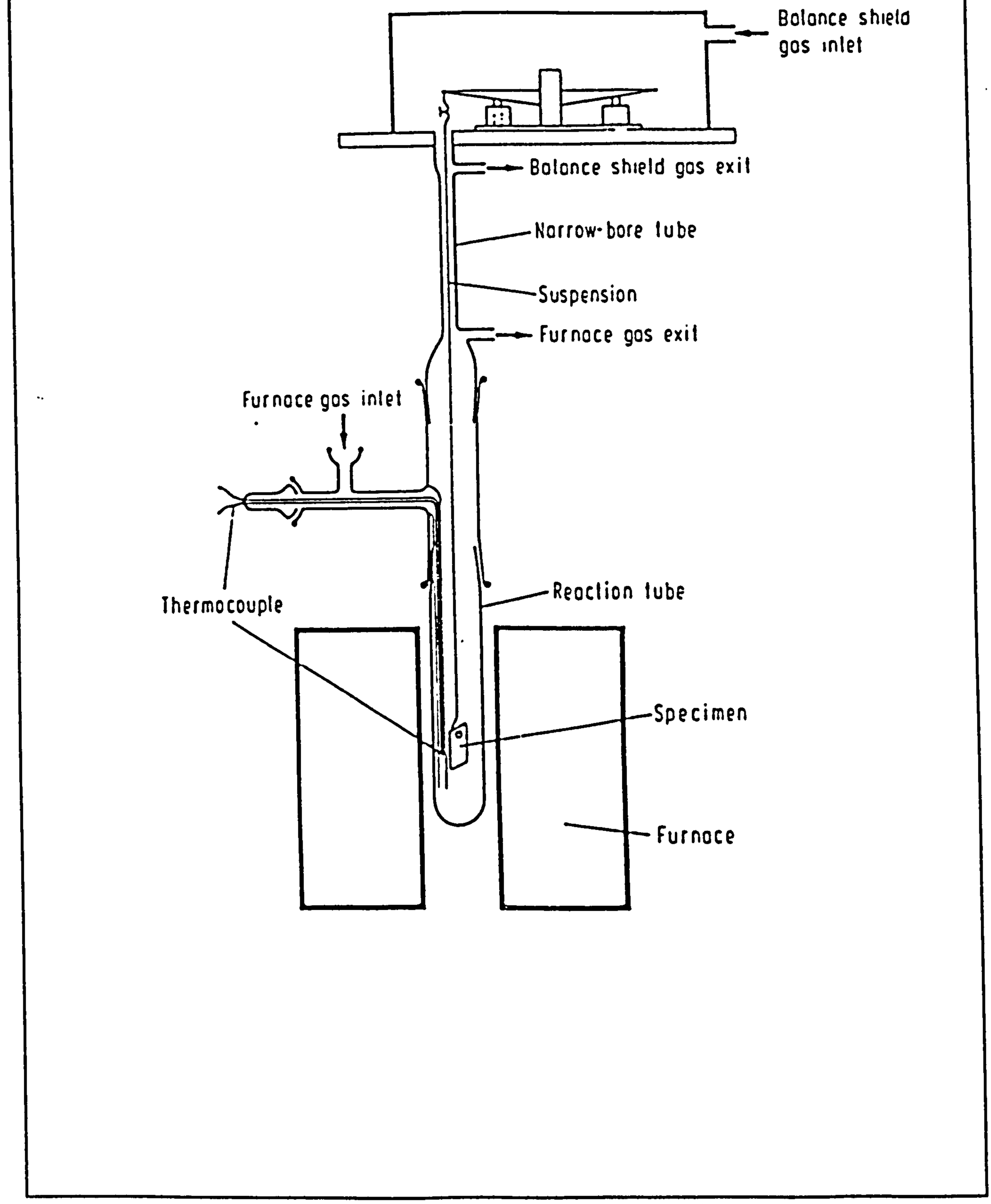

Figure 30: Thermogravimetric microbalance experimental setup[106]

and a Blue Chip ADC-16 data acquisition card stored the data obtained during each test. In order to solve impedance problems between the control unit and the computer a buffer amplifier was used. A Turbo Pascal programme written by Chevrot[79] enabled the frequency of the data points to be taken to be set.

Each data point was an average of 120 readings. The experimental setup incorporating a reaction tube is shown in Figure 30, and is comparable to the experimental arrangement suggested by Grabke et al [106] and is comparable to the arrangement used in this study. The balance head is located within a vacuum head, with argon circulated, at a flow rate of 35-40 cc/min, to prevent the head from being corroded. A small pump was used to draw any reaction gases and argon out of the reaction tube. The water jacket would have otherwise caused these gases to condense. The reaction gases were circulated passed the coupon, at a flow rate of 100 cc/min, fed in from the bottom of the reaction tube. The test coupon is hooked on the end of a length of nonreactive platinum wire and attached to the balance beam, with the counterbalance weights located within the vacuum head.

7.9.2 Thermogravimetric experimental procedure

The procedure used for each test is detailed below and is in agreement with the procedures suggested by Grabke et al[106,107] for mechanistic studies.

1. Before each test the microbalance is calibrated in order to obtain precise results. The platinum wire is initially balanced with counter weights before a 100mg and 10mg weight were each in turn used to tare the microbalance to zero. The resolution being to within +/- 0.02μg on the most sensitive setting using the 10mg weight.

2. Each specimen is then polished to 1200 grit. This removes any large surface defects, eliminating any preferential oxidation sites.

3. The coupons diameters and thicknesses are then measured .

4. The coupon is again cleaned and weighed. From this point onwards the specimens have to be handled with surgical gloves to avoid contamination.

5. The coupons are salted if necessary.

6. The coupon is then loaded in the reaction tube and its weight tared to zero

7. The resistance furnace is raised, and the gas flows set. An air flow of 100cc/cm^2 and an argon flow of 35-40 cc/cm^2 are used. The relevant data are now put into the computer. e.g the length of the test, the interval between data collection and the number of data points used to take an average reading.

8. The computer program used to collect the data is run as soon as the furnace is switched on. The test temperature (±3°C) stabilises within one hour.

7.10 Analytical studies

Analytical studies were needed to support the thermogravimetric curves of mass gain against time, which provided information on the kinetics associated with the corrosion. Optical microscope and Scanning Electron Microscope Studies (S.E.M) were then used to characterise scale growth and enable corrosion mechanisms for the alloy to be made.

Optical microscopy was used to observe cross sections of scales which in general were of the order of 1-20 μm thick. The specimens were thus mounted in non-conductive epoxy resin to preserve the fragile scales. It was therefore often difficult to observe important features using the S.E.M, in which case optical studies had to be used which, although at lower magnifications, were able to identify major features.

S.E.M studies were used to observe the morphologies of scale surfaces to show their development with temperature and time. Electron Probe Micro Analysis' (EPMA) using

the S.E.M were carried out in order to obtain qualitative analyses of the scales surface and cross sections compositions. More comprehensive compositional analysis were made using the S.E.M to analyses a selected area, ie an area through the scale, and evaluate the concentration of a number of elements based on atomic number. The results can then be presented in the form of individual element maps. These Elemental X-ray micrographs provide invaluable information as they enable individual layers and the elements which concentrate within them to be identified. These elemental identification techniques have penetrative depths of approximately 3μm. Certain situations, i.e when the scales or individual layers are less that 3μm, require analysis' to identify surface compositions more accurately without interference from underlying compositions. Auger analysis accomplishes this, by analysing higher energy auger electrons. Auger analysis has penetrative depths of tens of nanometres rather than microns.

Analyses were made of the scale surfaces using X-ray diffraction techniques. X-rays (Cu Kα) were fired at the surface at incremental angles ranging from 30 to 90 degrees (through 2θ). This type of analysis enables the compounds within the surface to be identified. Comparing the peak heights of the identified compounds, from different test pieces, allows comparative concentrations of the individual compounds to be made. The X-rays have a penetrative depth of approximately 3μm, which means that as the scale thickness increases the substrate compound peaks weaken and the scale compound peaks strengthen.

Chapter 8

Results

8.1 Introduction

Titanium Aluminide alloys, as stated in chapter 1, are now being looked at as possible replacement materials in the fourth stage turbine and HP compressor stages in the gas turbine engine. The potential benefits are enormous, not least the substantial weight reductions which would result in higher fuel efficiencies.

These materials have been extensively tested at room and higher temperatures in air. However, due to the new applications being proposed, new environments will be encountered. In order for these materials to successfully operate at high temperatures in these new atmospheres extensive high temperature corrosion work is needed.

As well as being subjected to a continuous flow of air the titanium aluminide alloys will have to operate in the presence of salt and sulphur dioxide. The sea being the source of halide salts, over which the majority of flights operate. Burning of fossil fuels invariably yields sulphur dioxide; even if at low levels in high purity aviation fuels.

No studies have so far been done to characterise the behaviour of titanium aluminides or even titanium alloys in salt and sulphur dioxide atmospheres. This study aims to use continuous and discontinuous thermogravimetric data to compare the oxidation kinetics with that of the hot salt corrosion and sulphidation kinetics of this Ti-45Al-2Mn-2Nb alloy.

Ti-45Al-2Mn-2Nb will be exposed to a combination of bi-oxidants and salt solutions when operating within turbine engines. The possible corrosion mechanisms are difficult to predict as no work has been published explaining the behaviour of this material in a hot corrosion environment. Determining the individual effects of oxygen, sulphur dioxide and salt solutions will enable a more accurate hot corrosion mechanism to be constructed using kinetic and metallographic data over a temperature range of 650-800°C.

8.2 Environmental Studies

8.2.1 Introduction

Oxidation tests were carried out in order to provide a reference to compare with the salt corrosion and sulphidation tests and to compare with published data in the literature. The temperature ranges used were dictated by the mass gains detectable and the potential service temperature range. The oxidation tests (700-900°C) constituted the upper temperature range of the salt corrosion tests, as at lower temperatures no accurate mass gains were measurable. The range of sulphidation temperatures coincided with the oxidation test temperatures as it was postulated that below this temperature range no significant sulphidation would occur.

The benefits of continuous mass gain measurements are two fold. Thermal cycling is avoided, as the specimens do not have to be removed in order for mass measurements to be made, and any spalling which may occur is detected.

The thermogravimetric apparatus could not be used at all exposure temperatures. At the lower temperatures discontinuous mass gain measurements had to be made as these mass gains were outside the resolution of the thermogravimetric apparatus. The specimens will thus have suffered from thermal cycling, but as insufficient scale growth occurred spallation will not have been a problem.

All sulphidation tests were carried out discontinuously as sulphur dioxide can only be used in a closed system, due to it being a potential health hazard if introduced into the atmosphere.

In order to determine the effect of salt on the corrosion of Ti-45-2-2 + 0.8%TiB_2, continuous thermogravimetric weight measurements were made over relatively short periods of time (100 hours). The resulting mass gain against time graphs will allow the kinetics to be determined between 500-800°C.

The hot corrosion behaviour of Ti-45-2Al-2Mn-2Nb was determined discontinuously over short corrosion times (100h). A single salt coat was applied to each specimen before being exposed to an atmosphere containing air and sulphur dioxide. The range of hot corrosion temperatures was determined after the individual salt and sulphur dioxide studies had been completed. No hot corrosion studies were carried out above 800°C as both the sulphur dioxide and salt corrosion studies predicted severe corrosion rates.

8.2.2 Oxidation tests

Tests were carried out in air over the temperature range 700-900°C at intervals of 50°C. Mass gain measurements were recorded every 10 minutes over 100 hours duration. A typical continuous gravimetric curve obtained after 100 hours at 850°C is shown in figure 31 (the curves for the whole temperature range tested are given in Appendix A).

The test conditions and final mass gains for each test are given in Table 11. The parabolic rate constants K_p an important corrosion parameter is also reported. The temperature range over which the alloy behaves in a parabolic manner is an indication of the range of protective behaviour. Furthermore, plotting Log K_p against $10^4/T$, obtained from the Arrhenius equation, allows changes in the oxidation mechanism to be seen if deviations from a linear plot occur, and the activation energy for the oxidation mechanism to be determined.

Arrhenius plots allow direct comparisons to be made with other materials tested under similar conditions. Figure 32 shows the Arrhenius plot obtained over the temperature range 750-900°C. The activation energy for the oxidation of γ-TiAl is -298 KJ/mole. Chevrot[79] calculated an activation energy of -190 KJ/mol in the case of the oxidation of IMI 834 and Schutze[53] -287KJ/mol for Ti35Al5Nb.

Figure 33 shows the parabolic plot obtained using the data from the 100 hour 700°C oxidation test. A straight line cannot be drawn through the points on the graph suggesting that another mechanism is operating, in the early stages of oxidation. Data were obtained

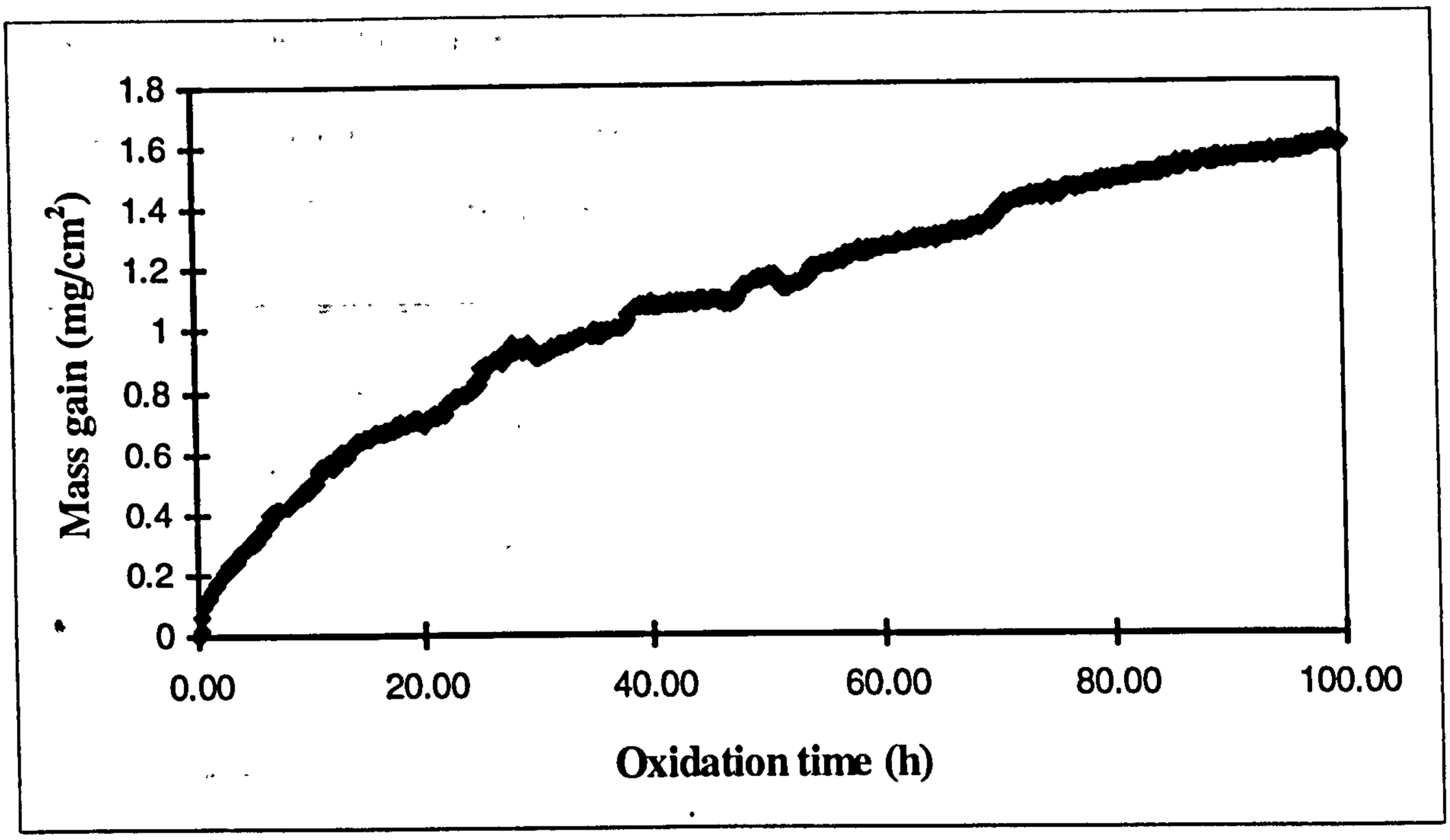

Figure 31: Oxidation behaviour of Ti-45Al-2Mn-2Nb in air at 850°C

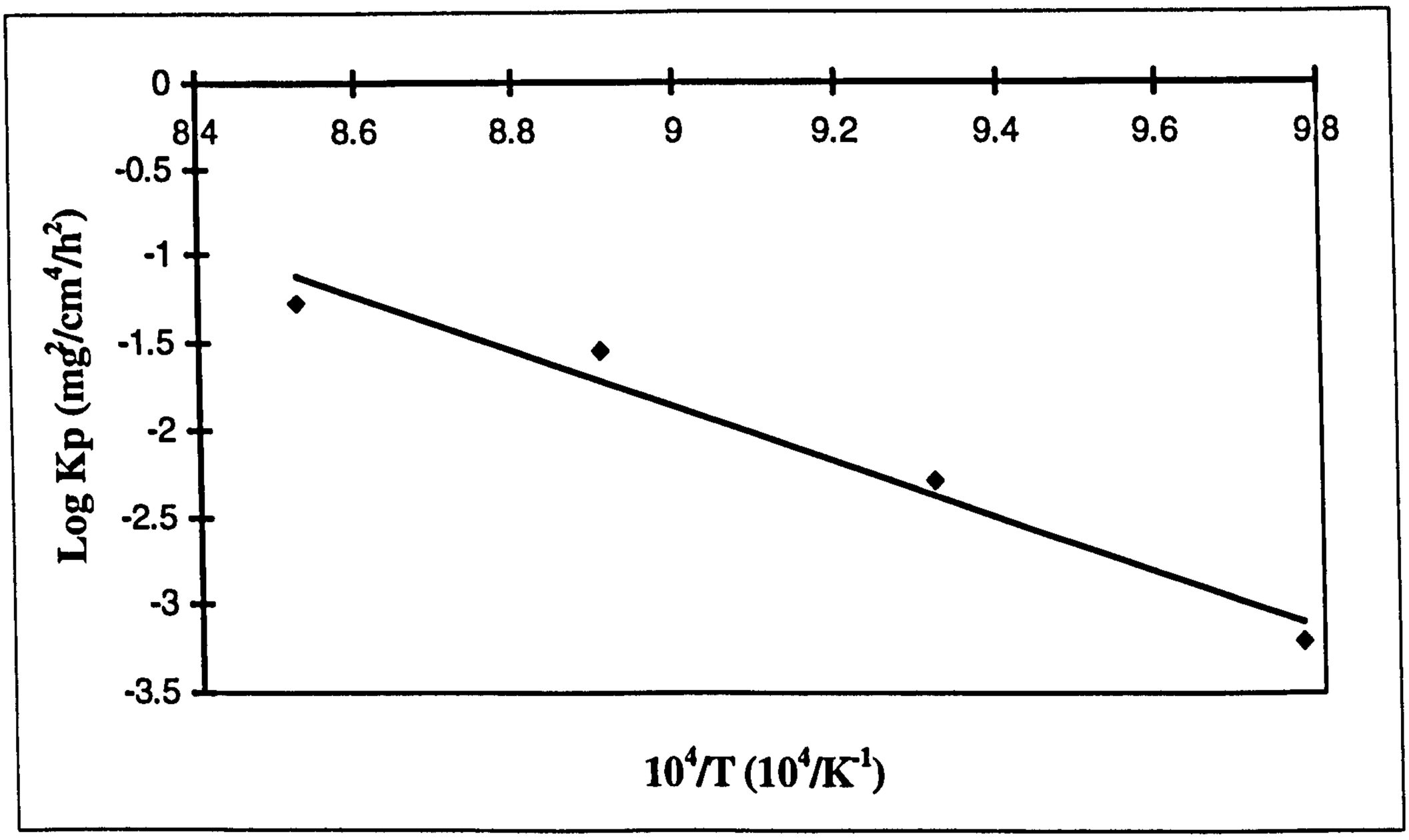

Figure 32: Arrhenius plot of the Oxidation behaviour of Ti-45Al-2Mn-2Nb between 750-900°C

Table 11: Results of Discontinuous and Continuous thermogravimetric Oxidation tests

Test coupon	Temperature (°C)	Exposure time (hrs)	Discontinuous (D) or Continuous (C)	Final mass gain (mg/cm^2)	Log Kp ($mg^2/cm^4/hr$)
Ta 19	700	100	D	0.060	-
Ta 12	700	1000	D	0.230	-
Ta 18	750	100	C	0.260	-3.204
Ta 16	800	100	C	0.720	-2.286
Ta 06	850	100	C	1.600	-1.537
Ta 2i	900	100	C	2.100	-1.269

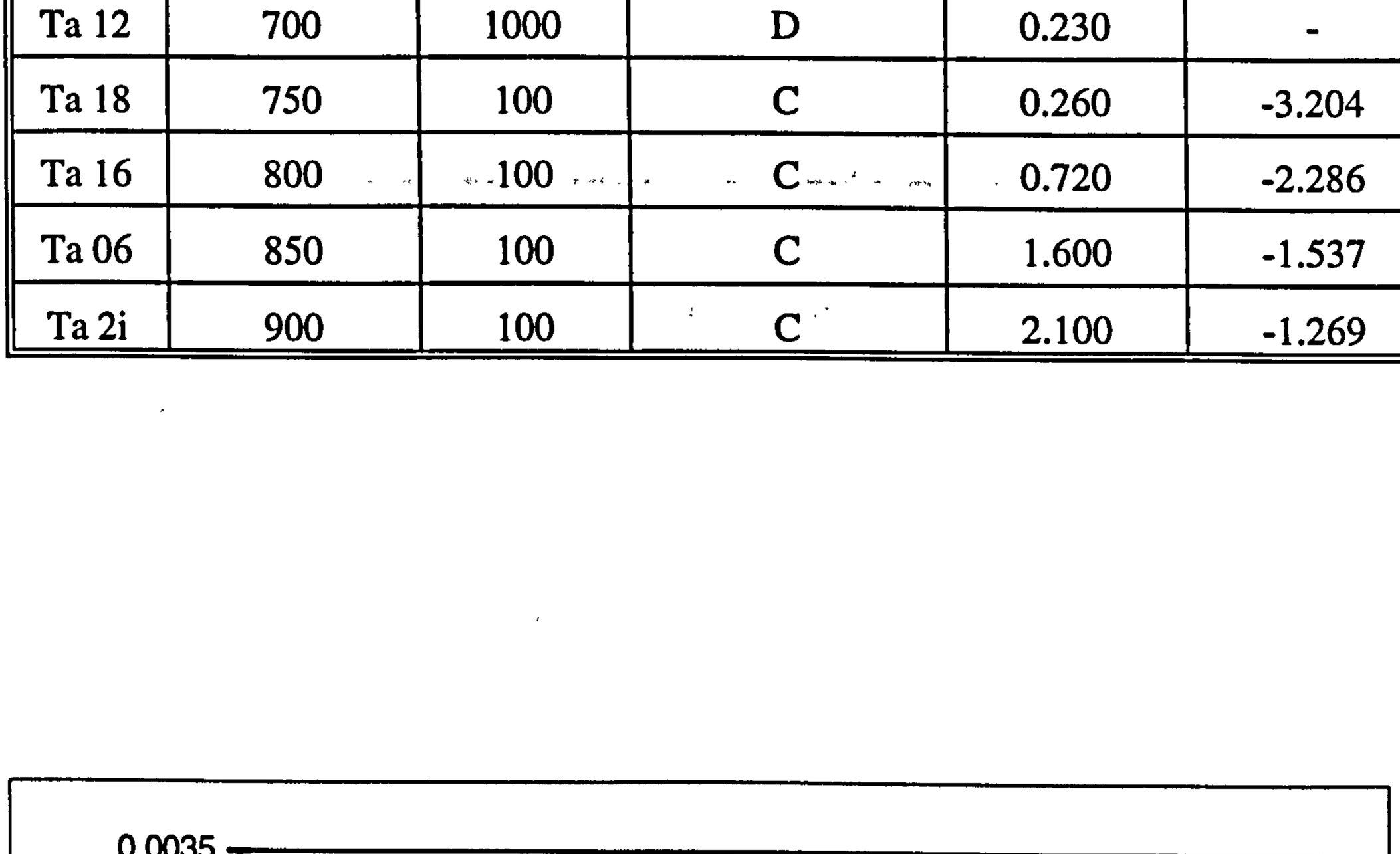

Figure 33: Parabolic plot of the Ti45Al-2Mn-2Nb test after 100h at 700°C in air

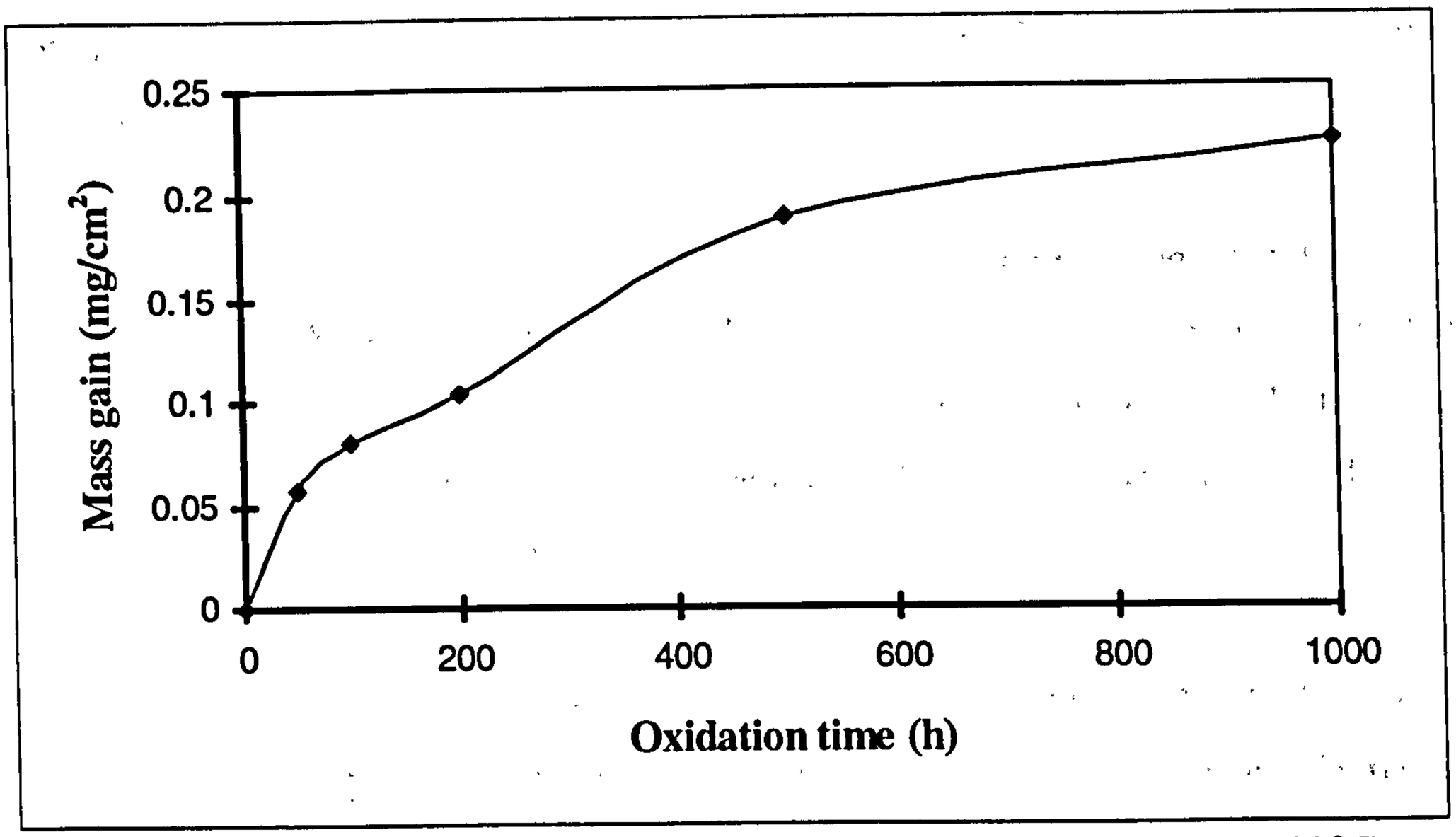

Figure 34: Oxidation behaviour of Ti-45Al-2Mn-2Nb after 1000h in air at 700°C

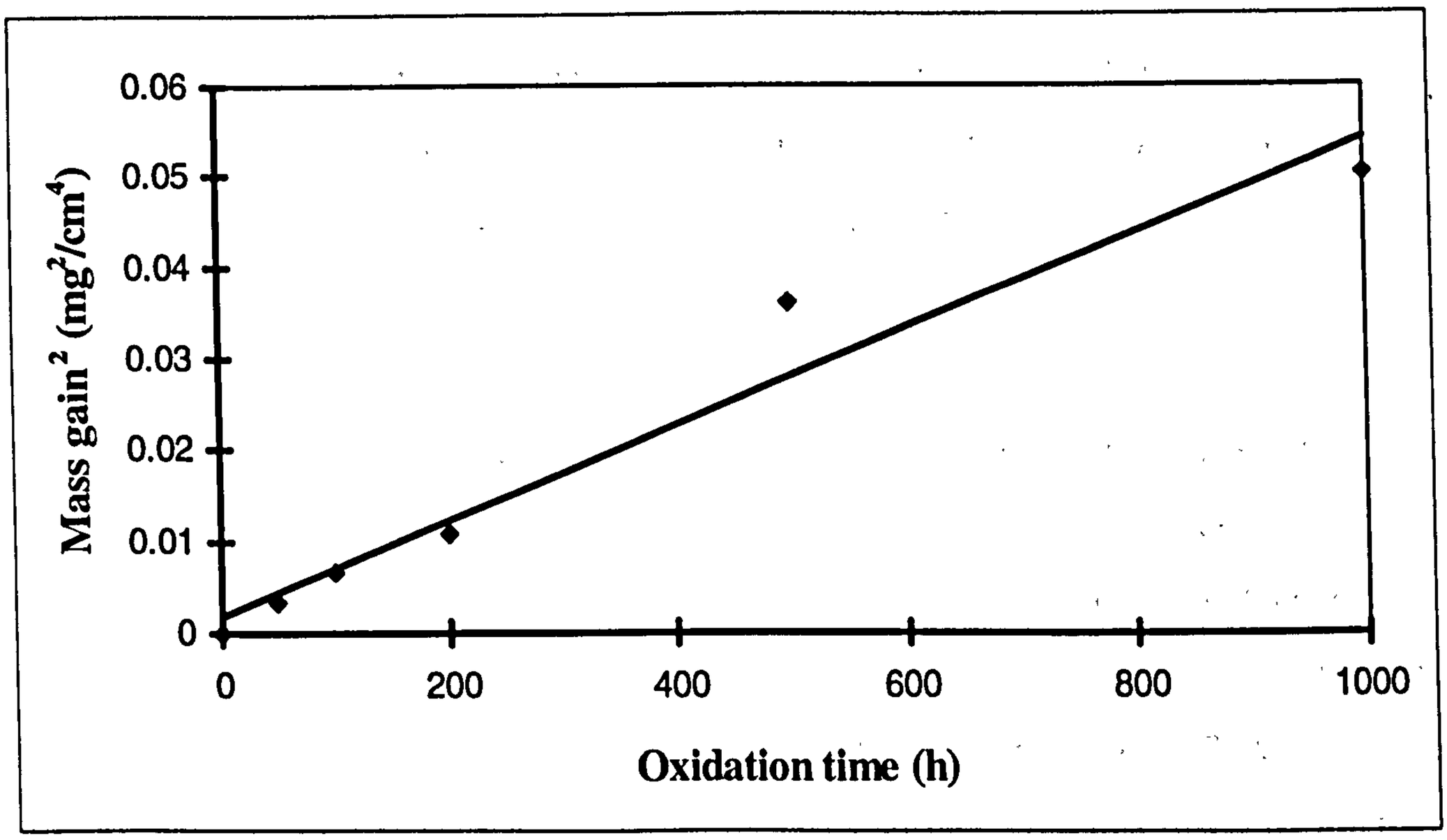

Figure 35: Parabolic plot of the Ti-45Al-2Mn-2Nb test after 1000h at 700°C in air.

out to 1000 hours at 700°C and is shown in figure 34. Figure 35 shows the parabolic plot for these data.

Table 12 shows the development of the surface scale composition with time and temperature using X-ray diffraction analysis. The abbreviations used are defined below the table. The rutile peak strengths increase with both time and temperature whilst the TiAl substrate strengths decrease. This is in agreement with the literature which shows that the outer rutile layer thickens with time and temperature.

Photographs 8.2.2a to 8.2.2g show the development of surface morphology with oxidation time and temperature. The rutile crystals increase in both size and degree of crystallinity with both time and temperature.

Photographs 8.2.2h to 8.2.2k compare the scale cross sections at 750-850°C after 100 hours with that formed after 20 hours at 900°C. After 100h at 850°C or 20h at 900°C, both oxide scales appear to have similar scale thickness' and layer compositions.

To identify the compositions of the layered scales an elemental analysis was made over a typical cross section, photograph 8.2.2l. Photograph 8.2.2m shows the resulting elemental X-ray micrograph obtained highlighting where Al, Ti, Mn and Nb concentrated through the scale.

After 100 hours at 700°C surface whiskers were identified at isolated areas. Due to the thin oxide layer EPMA analyses were inadequate in determining their composition without interference from the substrate. These whiskers were surrounded by a fine dispersion of rutile crystals. Auger analysis was therefore used in an attempt to identify the compositions of the whiskers which were believed to be alumina based. TiAl alloys are non conductive making this technique difficult as surface coatings, used to improve conductance and to thus reduce charging, cannot be used without being detected. Figure 36 shows an Auger scan identifying the presence of titanium and oxygen in the surrounding rutile (red line) and two areas of whiskers (green and purple lines) after 100

hours at 700°C. Strong oxygen peaks support the initial oxidation theories of oxygen adsorption followed by chemisorption. Figure 37 compares the aluminium peaks of the whiskers and surrounding rutile crystals. The three line scans show that approximately equal proportions of aluminium existed in the whiskers and rutile crystals. Rutile growth is thus the more dominant growth mechanism. Figure 38 clearly shows this with stronger titanium peaks being identified when compared with the aluminium peaks in Figure 37.

Table 12: Analysis of surface composition using X-Ray Emission diffraction

Temperature (°C)	Exposure time (h)	TiO_2	Al_2O_3	TiAl
900	20	vs	w	m
900	10	s	w	m/s
900	1	w/m	vw	vs
900	0.2	w/vw	w	vvs
850	100	s	vw	w
800	100	m/s	w	m
750	100	w	w	s
700	100	vw	vw	vs

Table 12 abbreviations: vs / s / m / w = very strong / strong / moderate / weak diffraction peaks.

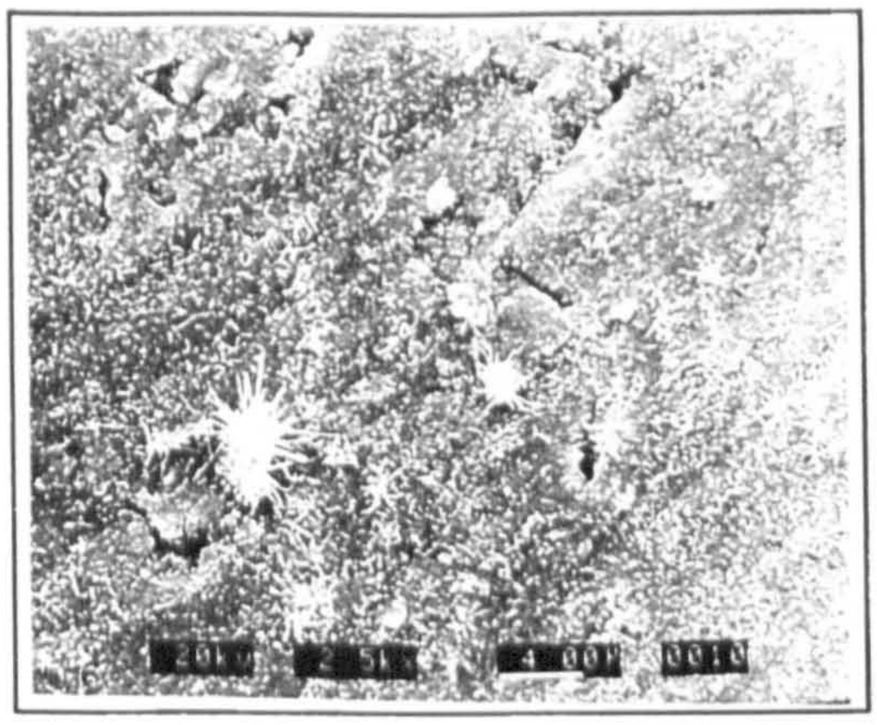

Photograph 8.2.2a: 100h 700°C

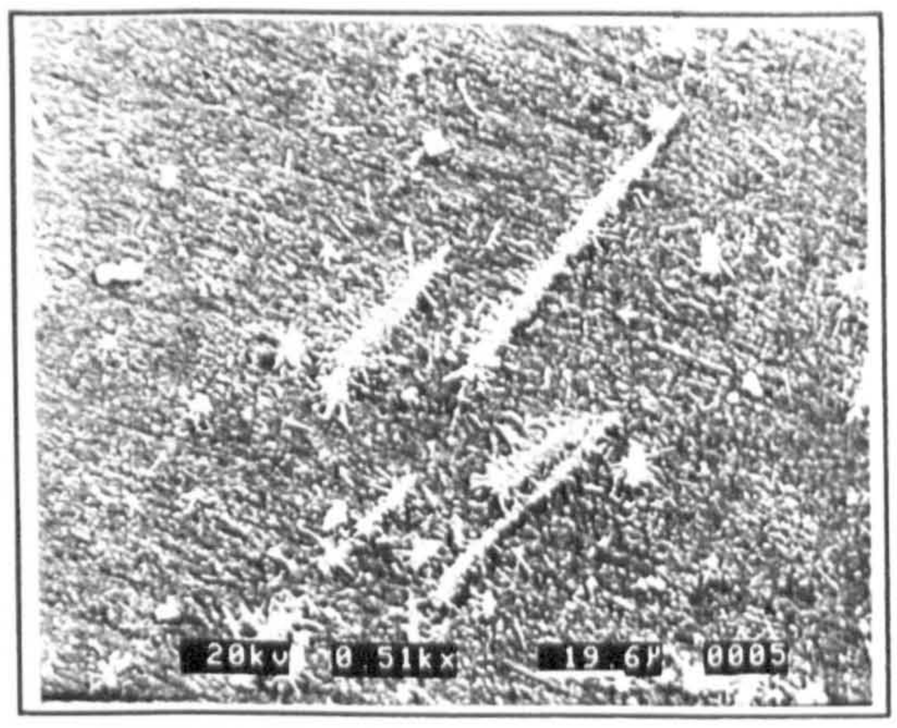

Photograph 8.2.2b:1000h at 700°C

Photographs 8.2.2.a to 8.2.2g:show the development of surface oxide after 100 hours between 700 and 900°C in air.

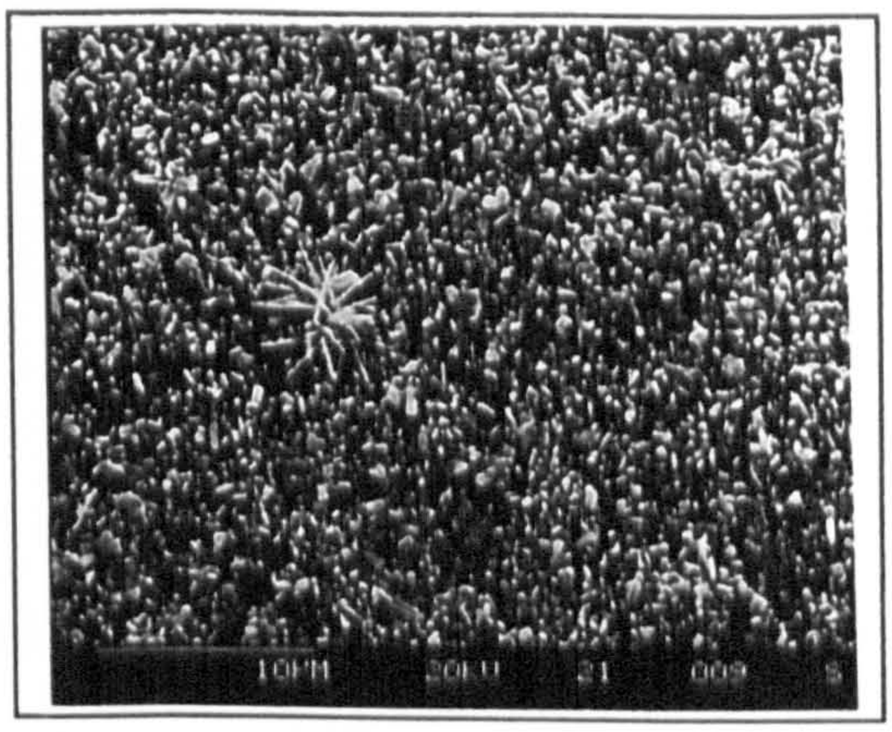

Photograph 8.2.2c: 100 h at 750°C

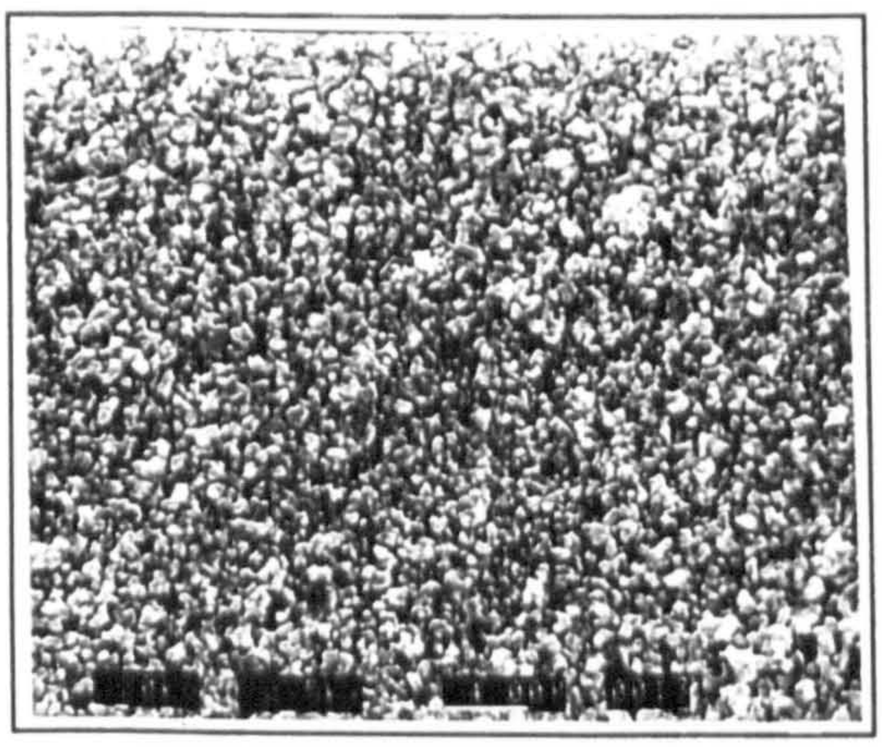

Photograph 8.2.2d: 1h at 900°C

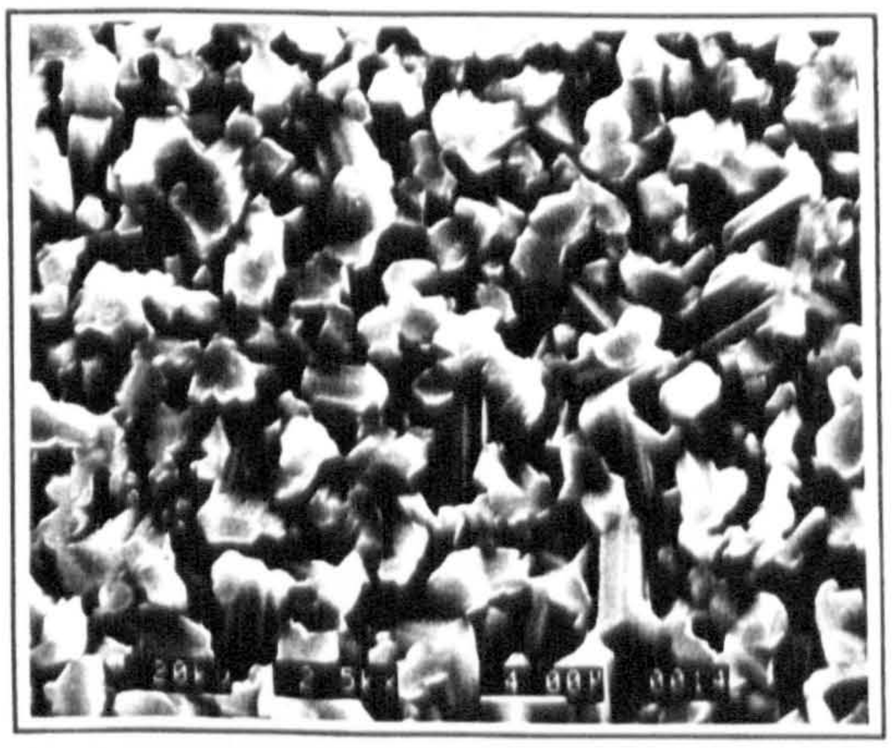

Photograph 8.2.2e : 10h at 900° C

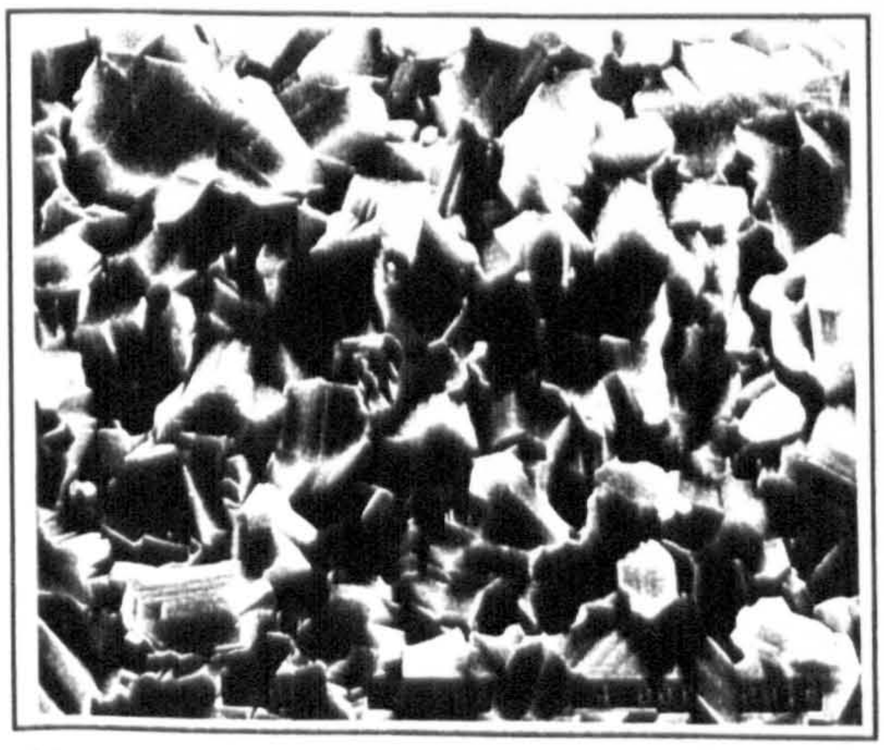

Photograph 8.2.2f: 20 at 900°C

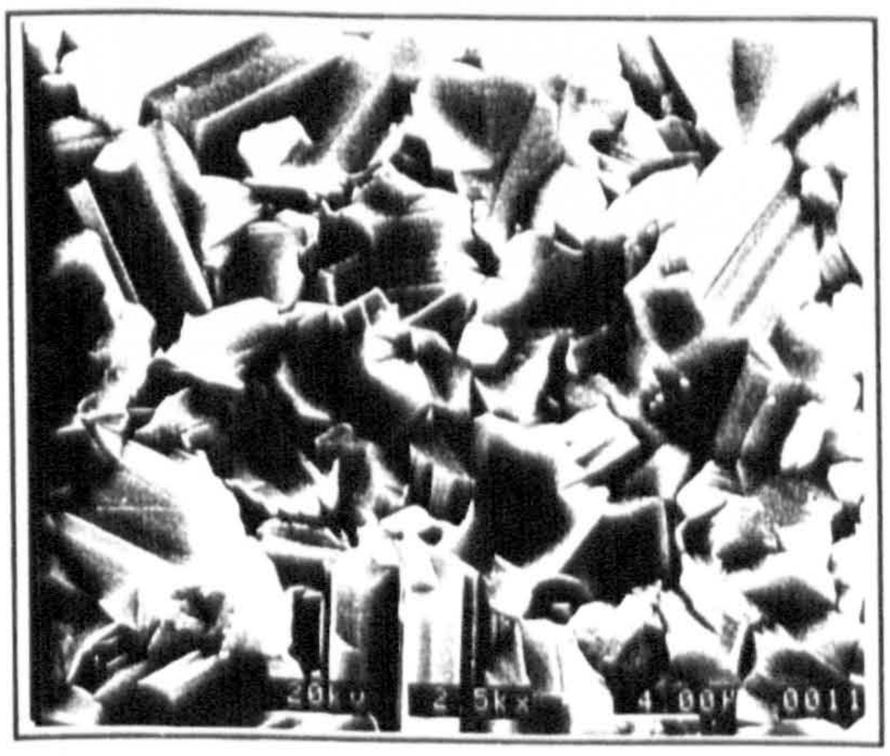

Photograph 8.2.2g: 100h at 900°C

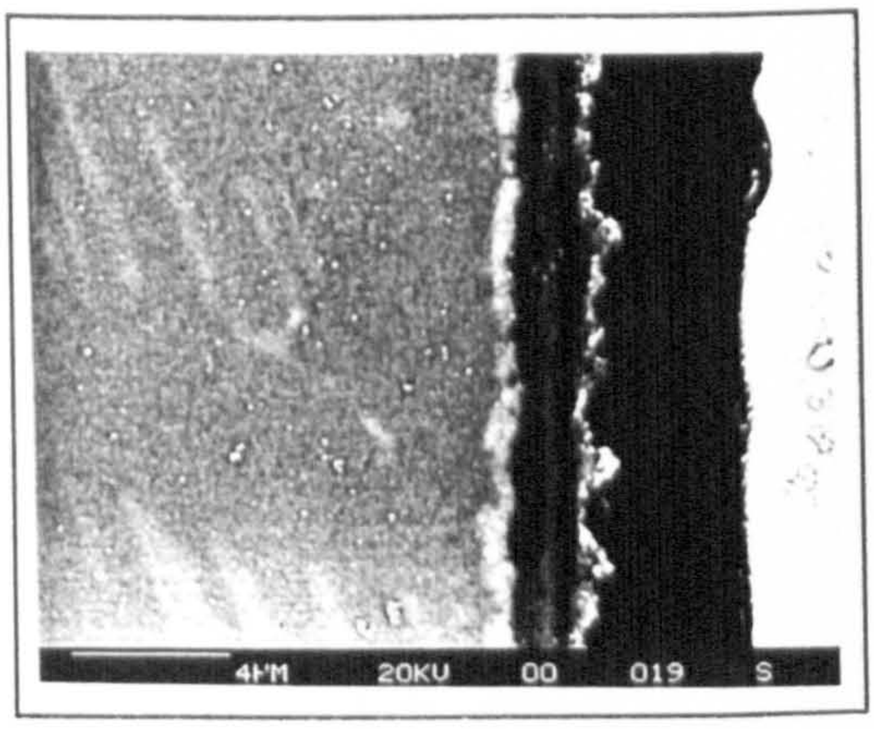

Photograph 8.2.2h: 100 h at 750°C, 5.0kx backscattered image

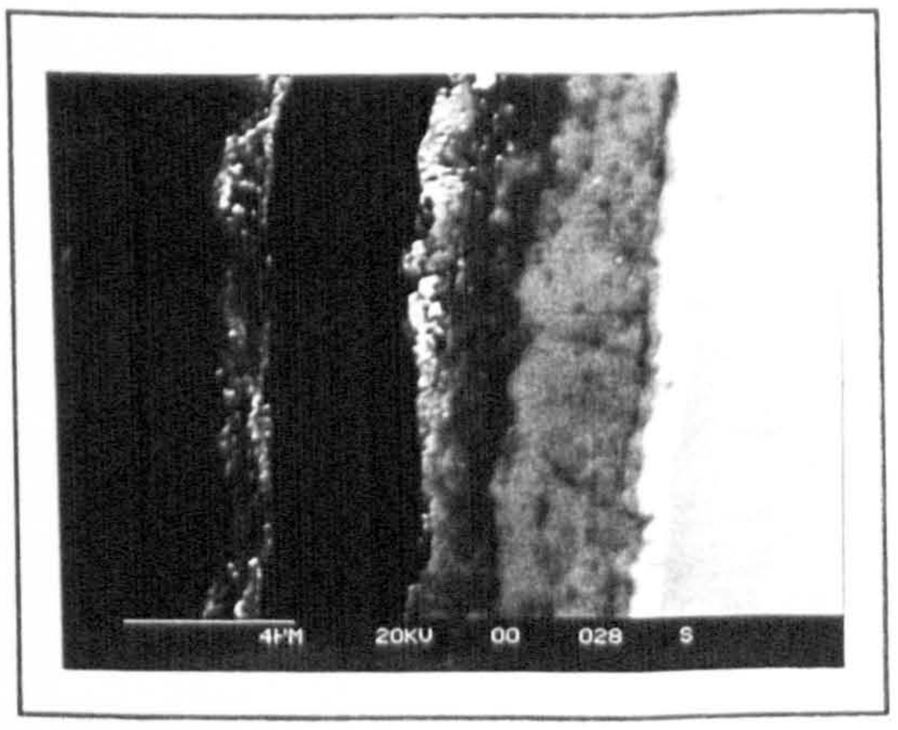

Photograph 8.2.2i: 100 h at 800°C, 6.5kx backscattered image

Photographs 8.2.2h to 8.2.2k: Show the development of oxide scale between 750 and 900°C in air.

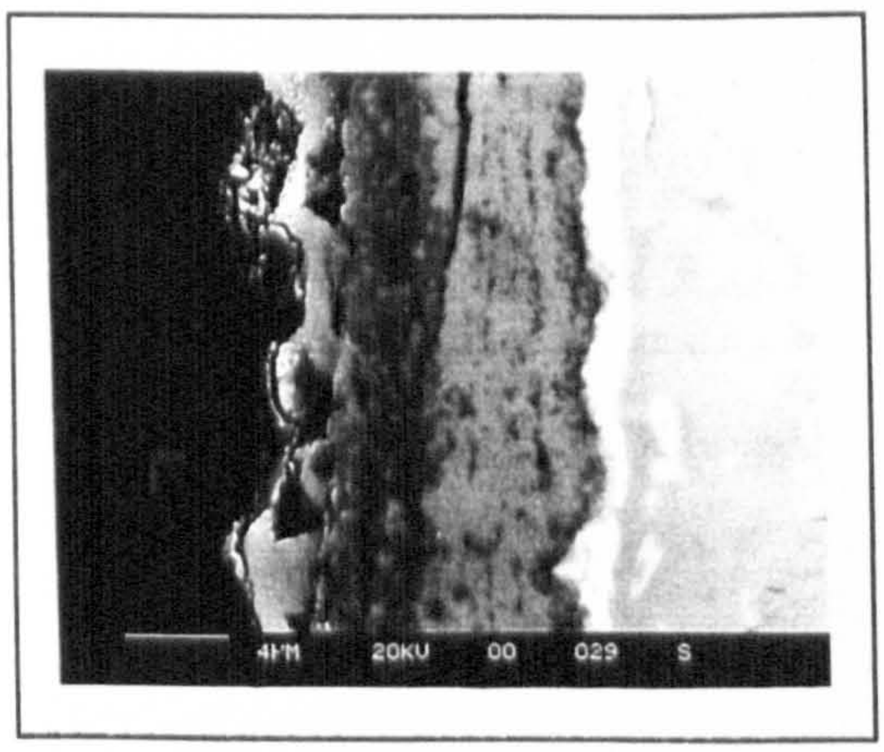

Photograph 8.2.2J: 100h at 850°C, 4.0kx Backscattered image

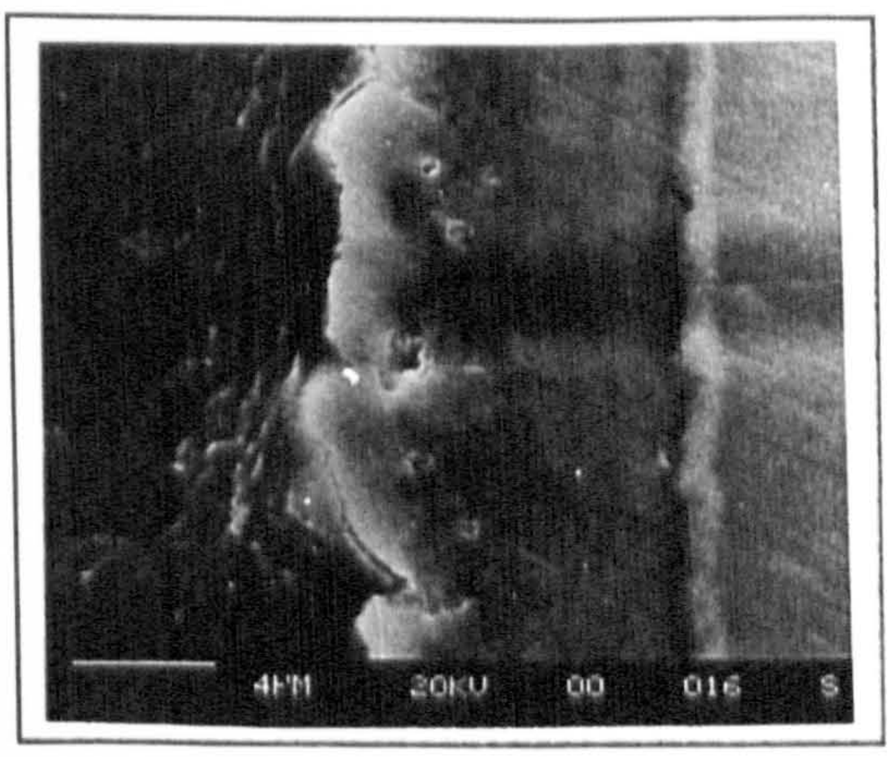

Photograph 8.2.2k: 20h at 900°C, 4.0kx secondary image

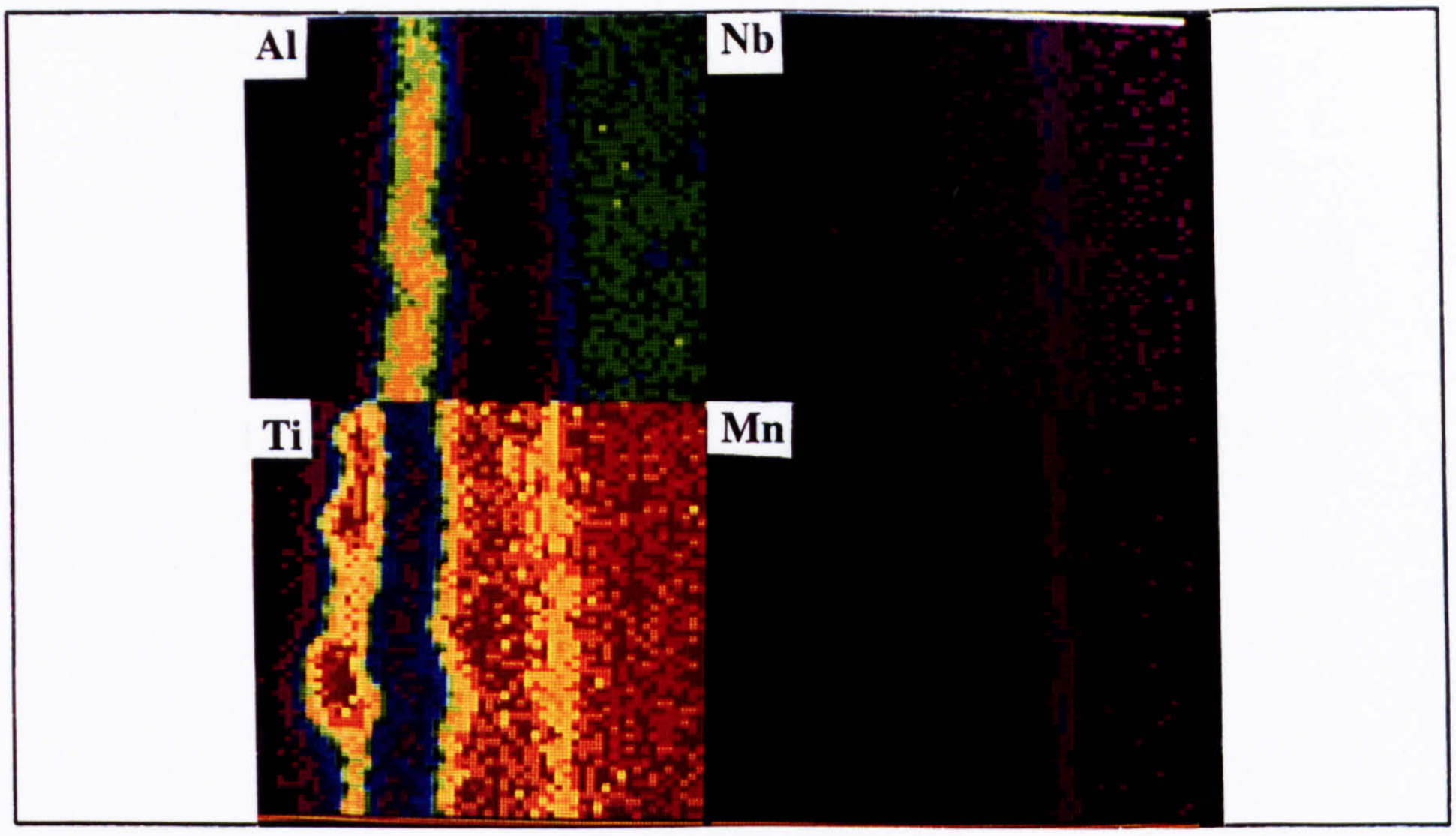

Photograph 8.2.2l: Elemental X-ray micrograph of the elements Al, Nb, Ti and Mn through the cross section of the scale formed after 20 hours at 900°C in air.

The colour scheme associated with above digital map is defined below. The concentra tion at a given point increases from black to white.

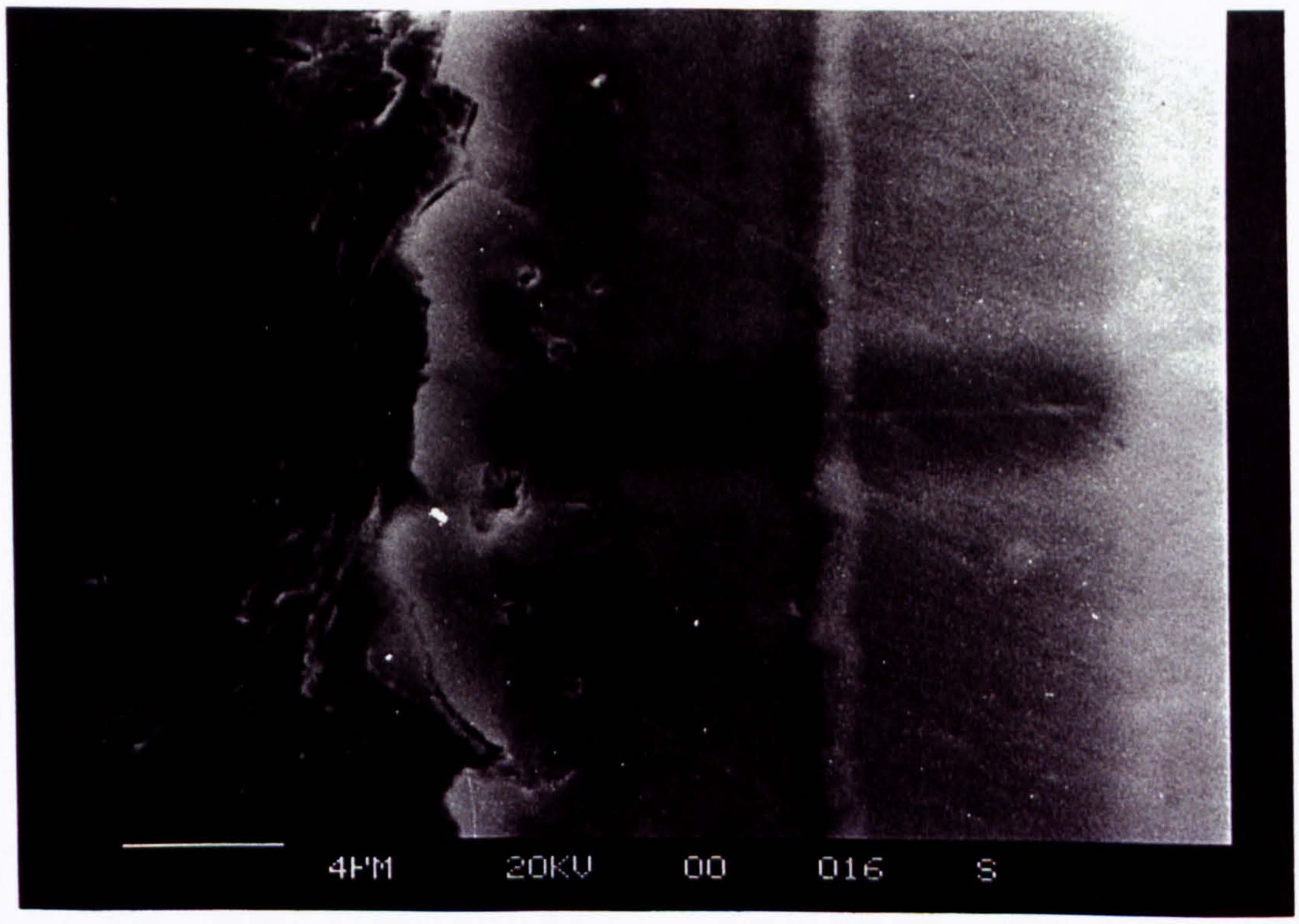

Photograph 8.2.2m: Shows the cross section of the scale developed after 20 hours at 900°C.

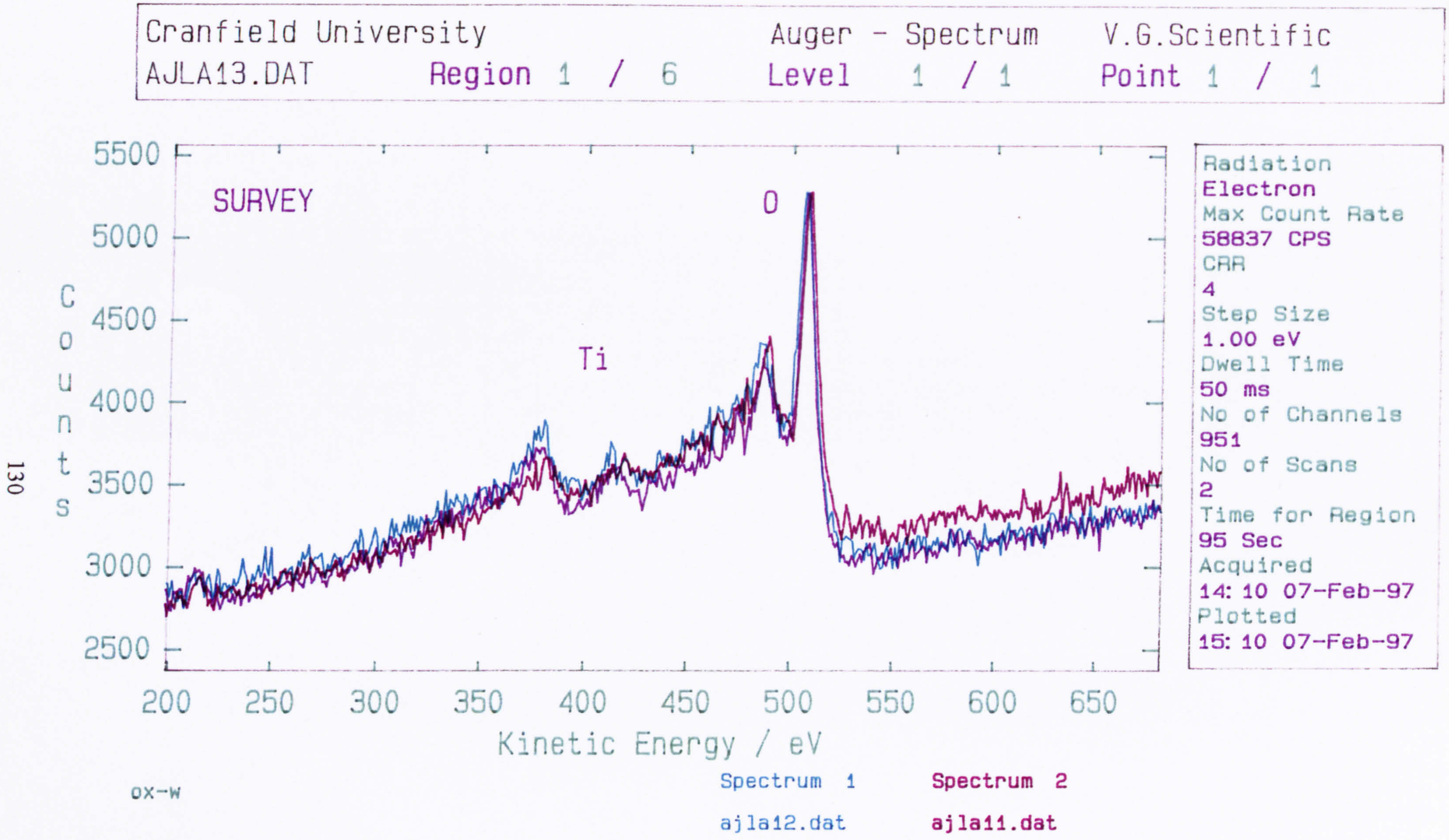

Figure 36: Auger analysis of the surface oxide products formed after 100h at 700°C in air. Line scans compare titanium and oxygen levels.

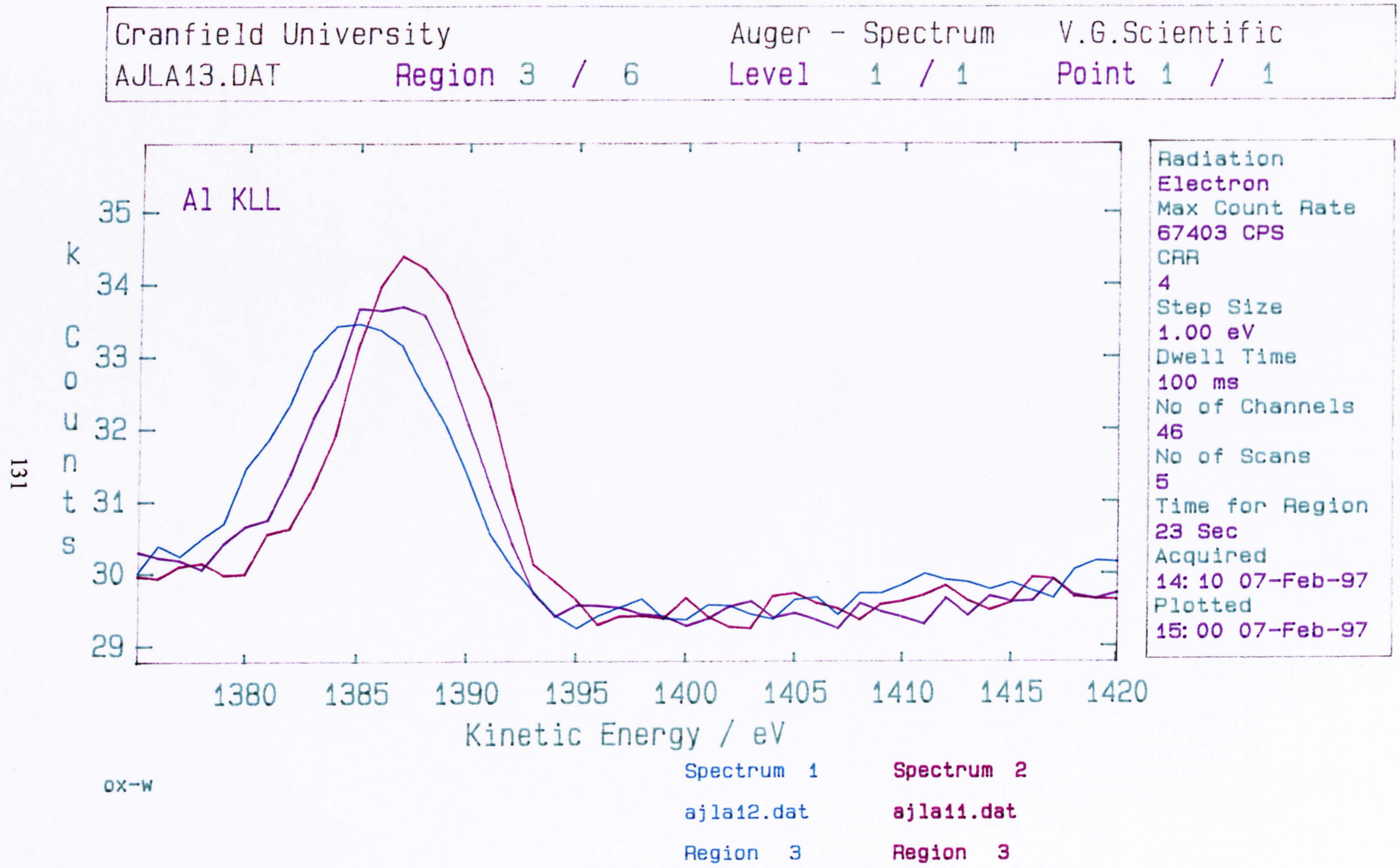

Figure 37: Auger analysis of the surface oxide products formed after 100h at 700°C in air. Line scans compare aluminium levels.

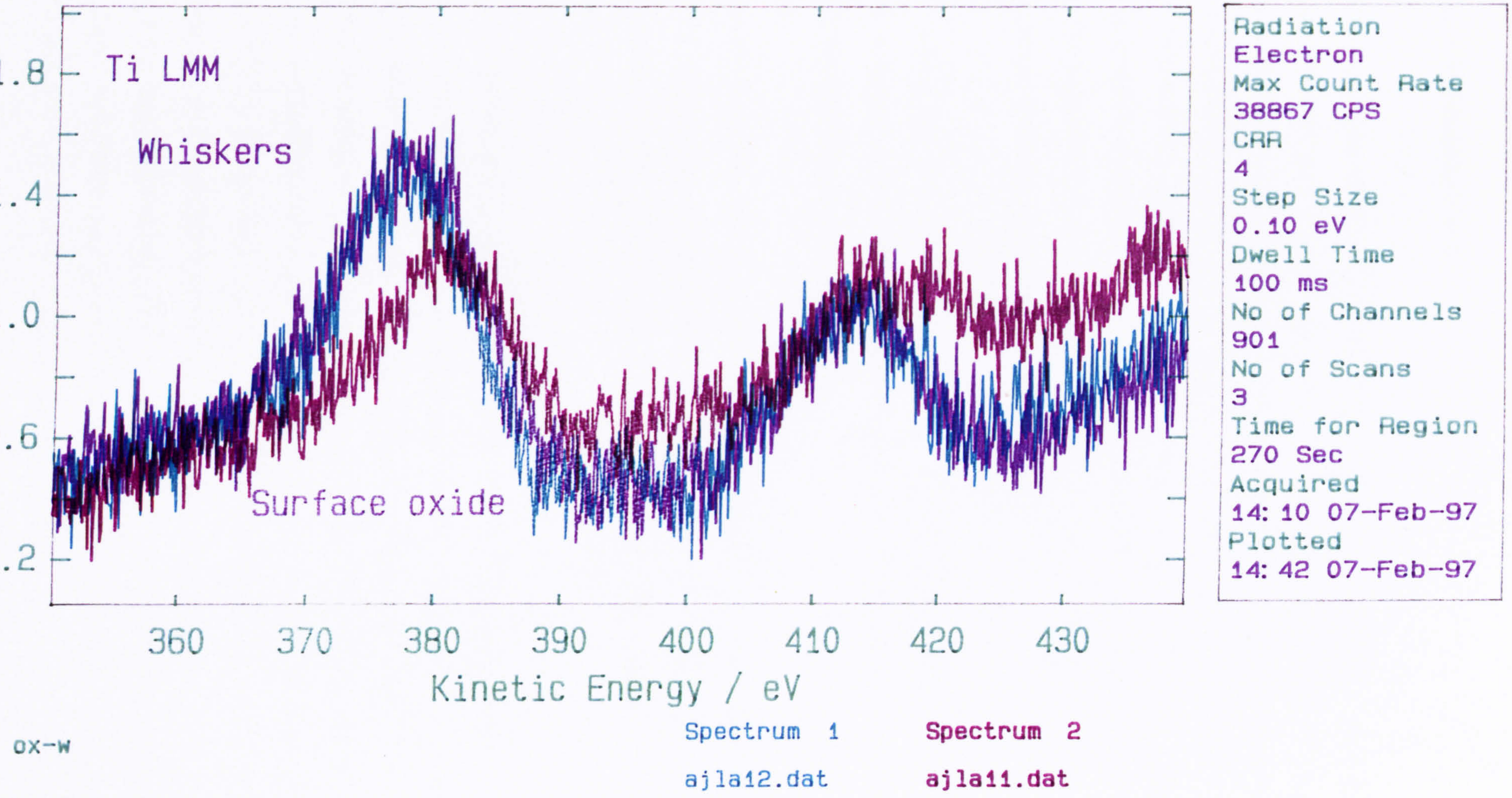

Figure 38: Auger analysis of the surface oxide products formed after 100h at 700°C in air. Line scans compare titanium levels.

8.2.3 Sulphidation tests

Sulphidation tests were carried out between 700 and 900°C. The tests were carried out discontinuously with mass gains being recorded after 5, 10, 20, 50 and 100 hours. Individual specimens were used in each case. Removing the respective specimens from the furnace involved subjecting the specimens to a degree of thermal cycling. At the higher exposure temperatures spalling occurred on cooling. Accurate mass gains were still possible as covers were placed over the crucibles preventing any spalled material from escaping. The respective SO_2 concentrations were subject to the equilibrium reached after allowing the gas to flow through the furnace before each test.

Table 13 shows the test conditions and final mass gains obtained after 100 hour exposures. A typical curve is shown in figure 39 (with the complete range of sulphidation tests being presented in appendix A).

Until recently there were no data on the sulphidation of titanium alloys. The only comparisons possible were with the well established classical sulphidation mechanisms for the nickel alloys used in turbine blades, and these may not apply directly to titanium aluminides.

Spalling occurred during cooling and isothermal corrosion after 20 hours at 800°C. Rapid corrosion rates resulted from the bi-oxidant atmosphere used. The corrosion mechanisms operating involved the formation of rapidly growing, non-protective oxide scales. The elemental micrographs, in photographs 8.2.3a and 8.2.3c, show that a discontinuous alumina layer formed beneath an outer duplex titanium plus manganese oxide layer after 20 hours at 800°C. The elemental micrograph in photograph 8.2.3c shows that niobium was associated with the sulphide layer at the metal/scale interface. However, niobium was also seen in the inner rutile/alumina layer suggesting that niobium diffused outwards and formed oxides in a similar manner as seen in air alone exposures. Photograph 8.2.3b shows the area from which these elemental maps were taken.

Photographs 8.2.3d to 8.2.3m show the morphologies of the scale surfaces after 20 and 100 hours at each temperature. The micrographs show the build up of a predominantly rutile but porous outer oxide layer. Initially discrete particles can be seen sitting proud

Table 13: Sulphidation test conditions and mass gains

Specimen	Temperature(°C)	Exposure time (h)	Mass gain(mg/cm^2)
TC1	700	5	0.05125
TC2	"	10	0.06556
TC3	"	20	0.08841
TC4	"	50	0.16254
TC5	"	88	0.19685
Tai	750	5	0.09244
Taii	"	8.5	0.1188
Taiii	"	21	0.15816
Taiv	"	50	0.4027
Tav	"	100	0.4727
TC 15	800	5	0.3324
TC 14	"	10.5	0.57002
TC13	"	21.6	0.707
TC12	"	50	1.5657
TC11	"	100	2.710
TC6	900	5	0.89632
TC7		11	1.2496
TC8	"	20	1.47943
TC9	"	50	3.9587
TC10	"	100	6.393

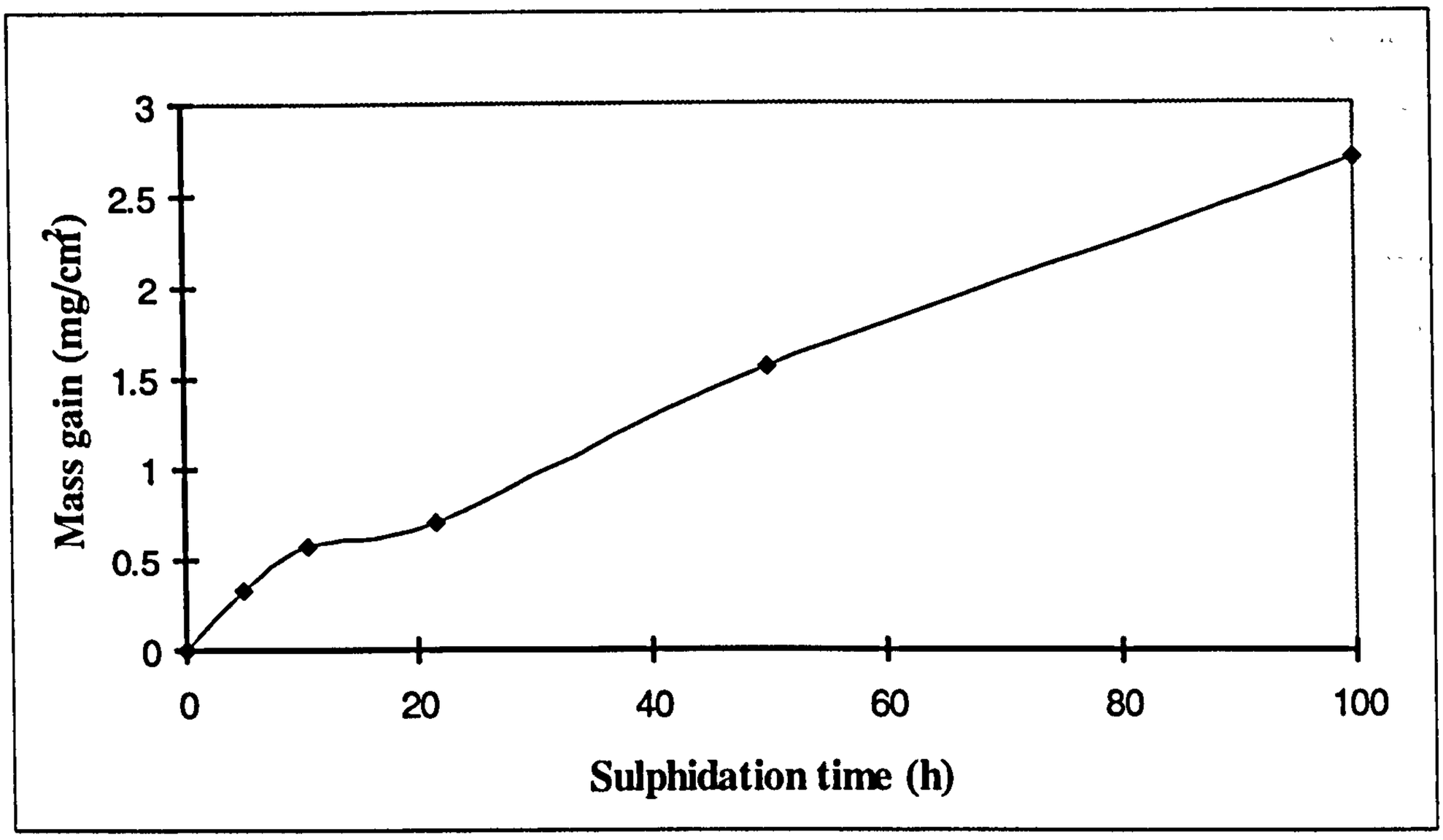

Figure 39: Sulphidation behaviour of Ti-45Al-2Mn-2Nb at 800°C in 650 ppm SO_2

of the underlying rutile and alumina scale. These increased in size and number until the entire surface consisted of large oxide crystals.

EPMA analyses were carried out to determine the surface compositions after 100 hours at 750°C and 100 hours at 900°C to illustrate the development of the surface scale with temperature and time. Photograph 8.2.3n shows a micrograph of the surface morphology observed after 100 hours at 750°C. The accompanying EPMA analyses show that the discrete particles were sulphur rich associated with titanium and/or manganese. The surrounding fine particles were identified as being predominantly titanium rich with a relatively high proportion of aluminium and a low amount of sulphur associated with them.

The discrete particles eventually overgrew the underlying oxides. Photograph 8.2.3o shows the surface morphology developed after 100 hours at 900°C. EPMA analyses of the individual crystals showed the majority to be rutile in nature, although a relatively large proportion were manganese rich oxides.

No direct comparisons, in terms of oxide thickness, were possible between corrosion temperatures and times. This was due to rapid scale growth rates leading to a build up of stress within the scales and hence spallation. Photographs 8.2.3p, 8.2.3q, 8.2.3r show scales of similar thicknesses, typically 50μm. The scale thickness seen in photograph 8.2.3r, obtained after 100 hours at 900°C, does not account for the large mass gain recorded. Comparisons of this micrograph with the micrograph in photograph 8.2.3p, which shows the oxide scale developed after 20 hours at 800°C, suggest that spallation has occurred at the outer rutile/inner rutile and alumina interface.

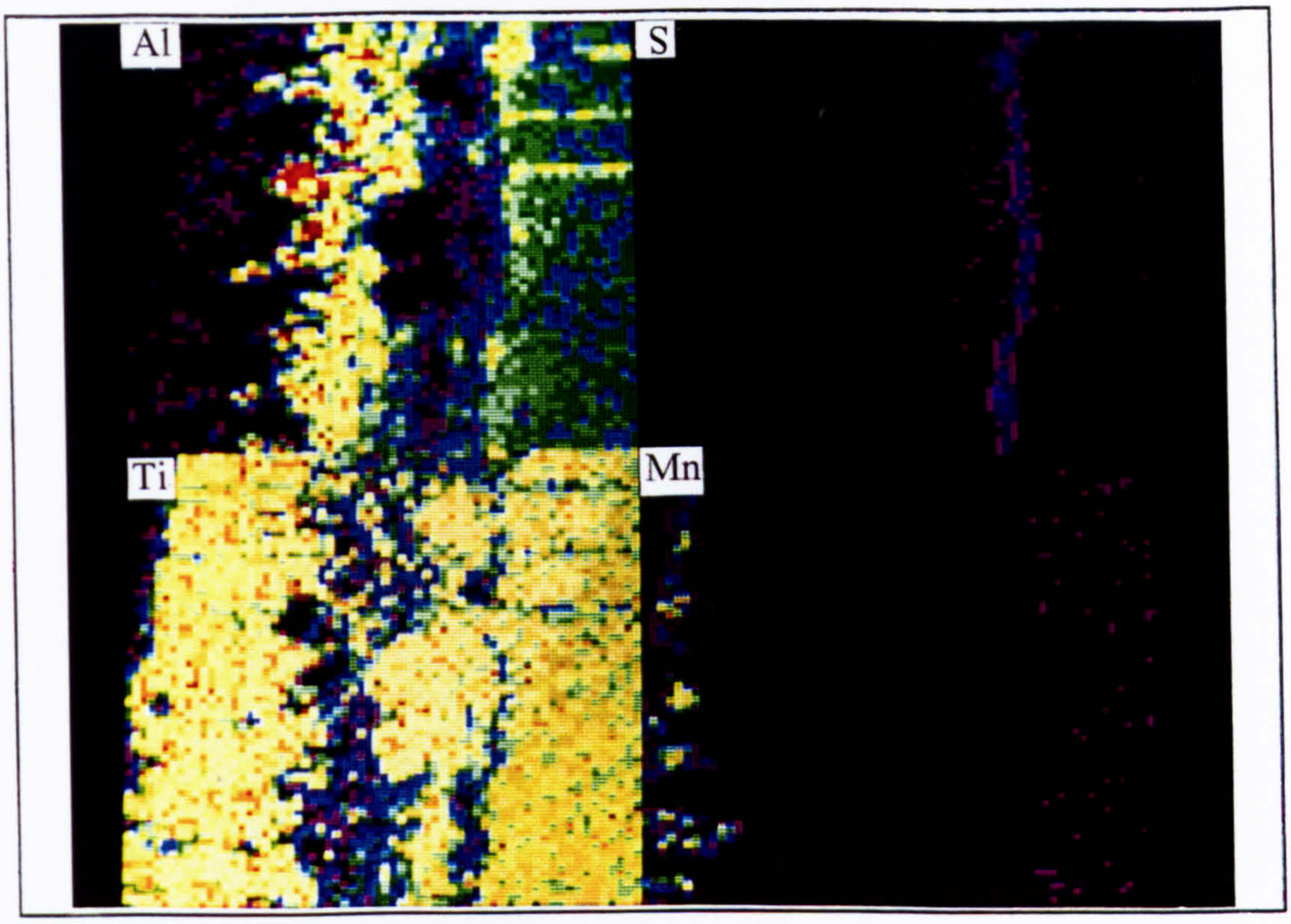

Photograph 8.2.3a: Elemental X-ray map of the scale formed after 20 hours at 800°C in 650ppm SO_2. The concentration at a given point increases from black to white.

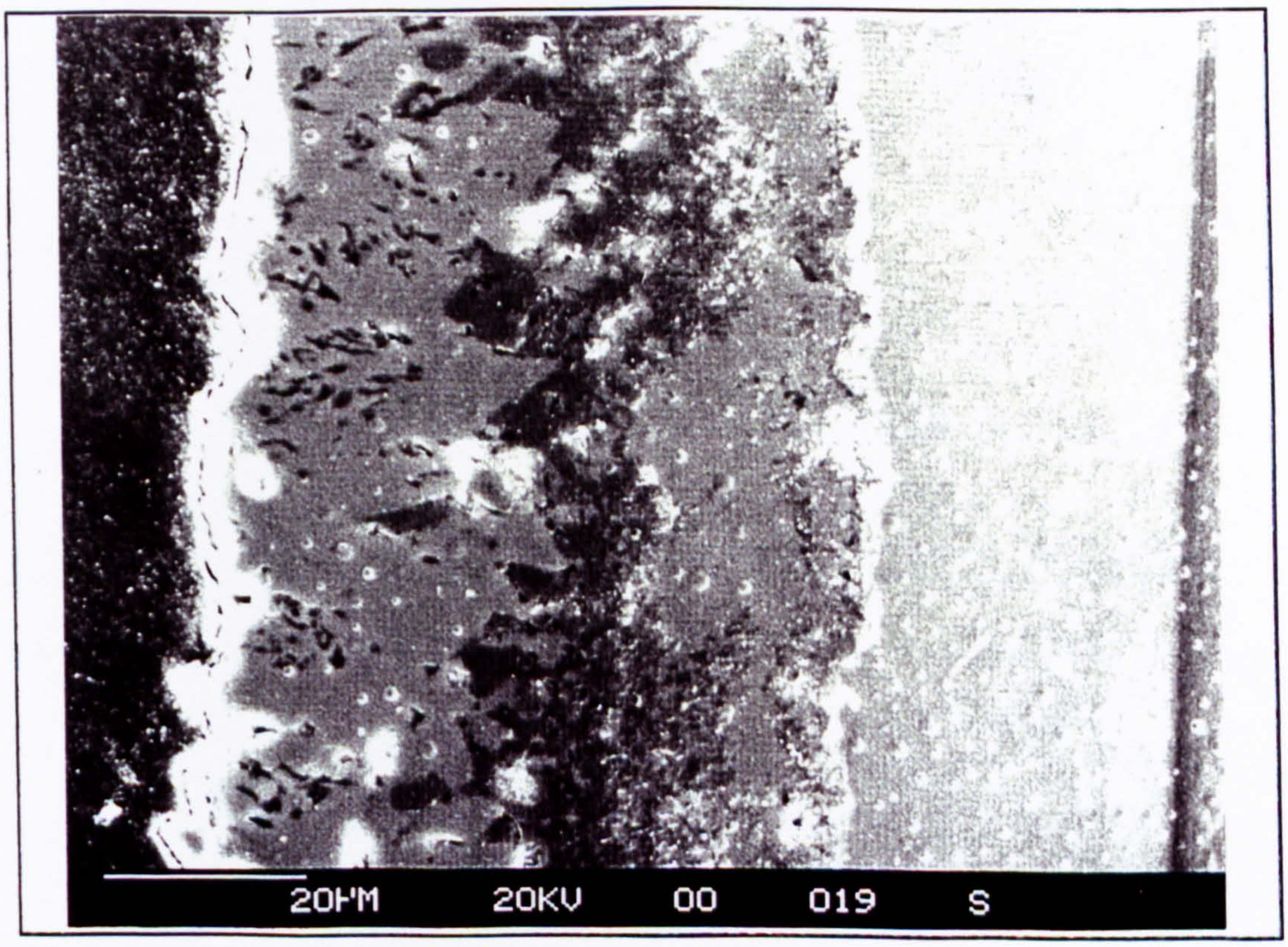

Photograph 8.2.3b: Shows the through thickness of the oxide scale seen after 20 hours at 800°C in air/SO_2 and the area from which the elemental maps in photographs 8.2.3a and 8.2.3c were taken.

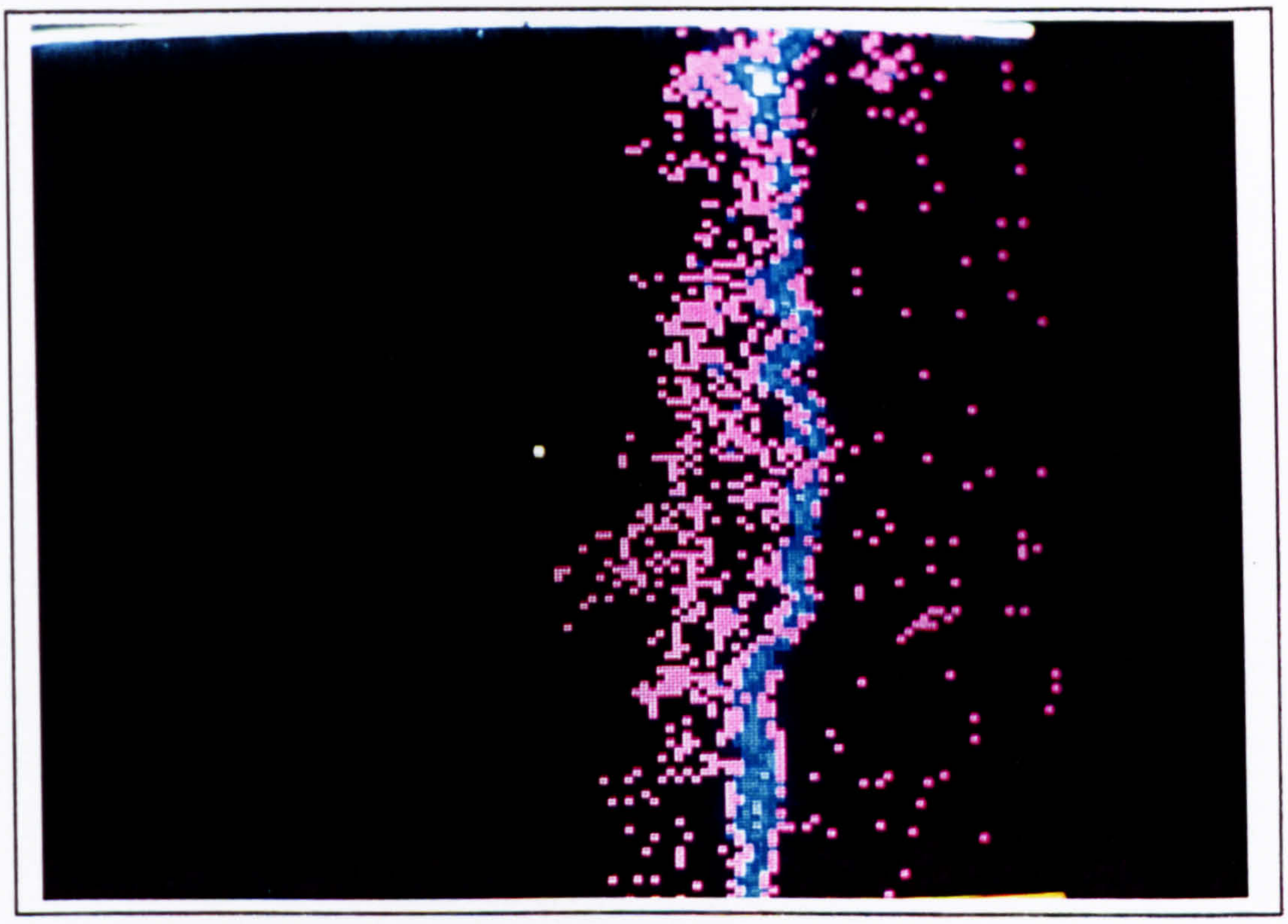

Figure 8.2.3c: Elemental micrograph showing the distibution of niobium in the scale developed after being exposed for 20 hours at 800°C in 650 ppm SO_2.

Photographs 8.2.3d to 8.2.3i: Show the sulphidation scale morphologies after exposures of 20 and 100 hours between 700 and 800°C.

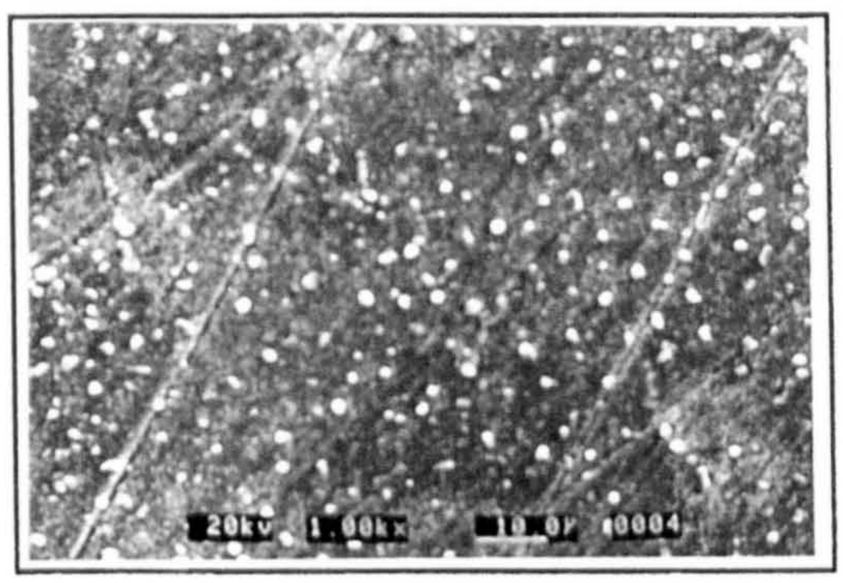

Photograph 8.2.3d: 20h at 700°C

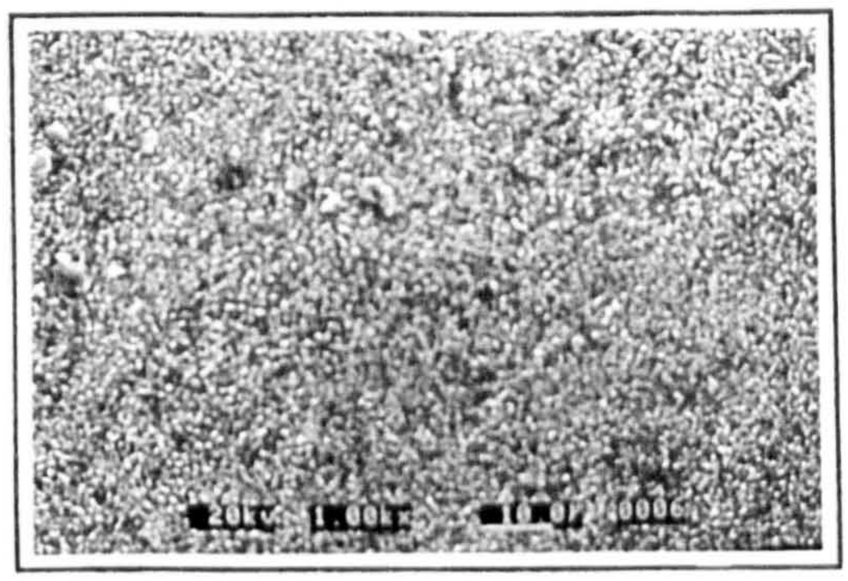

Photograph 8.2.3e: 88h at 700°C

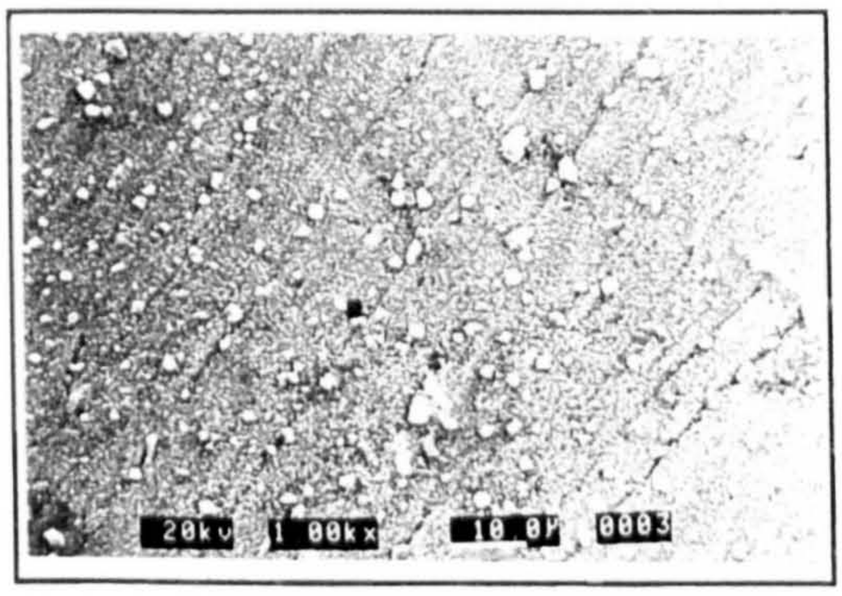

Photograph 8.2.3f: 20h at 750°C

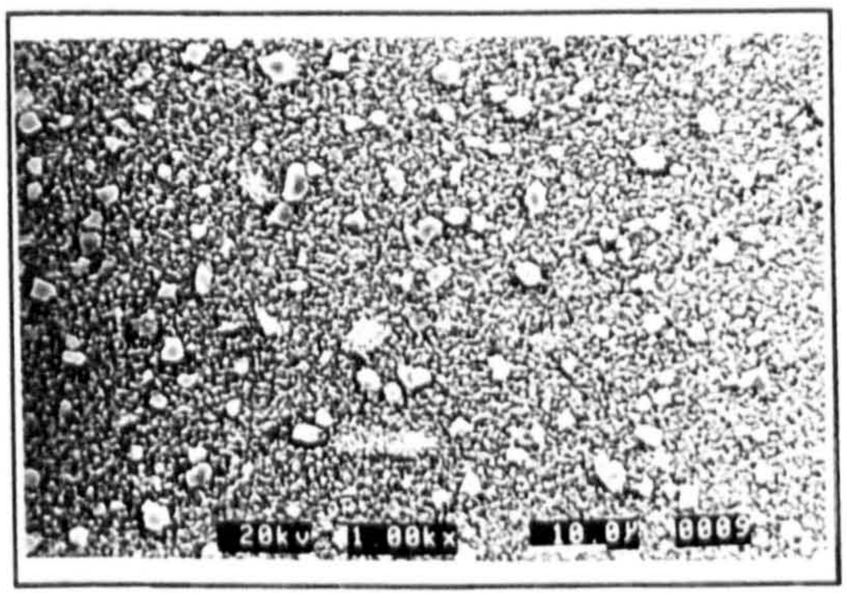

Photograph 8.2.3g: 100 h at 750°C

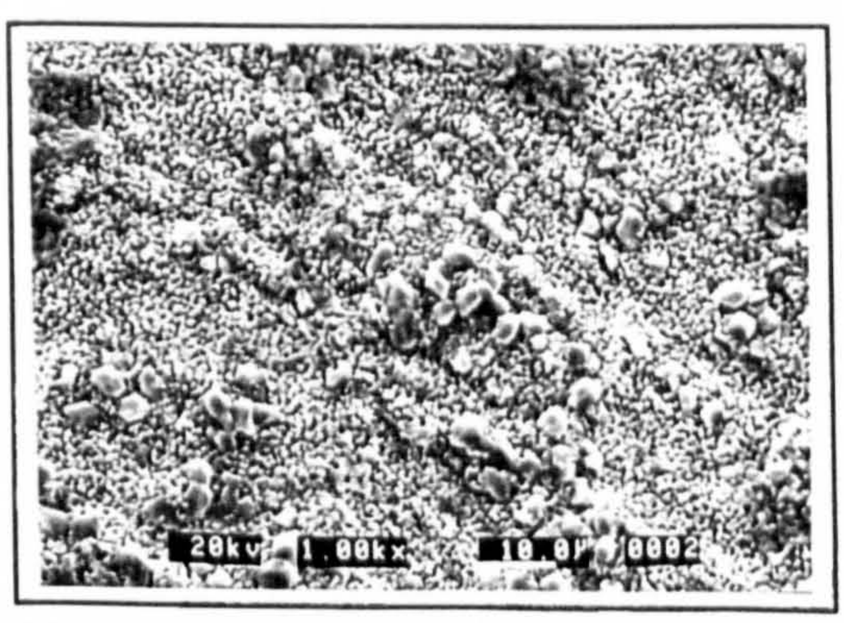

Photograph 8.2.3h: 20 h at 800°C

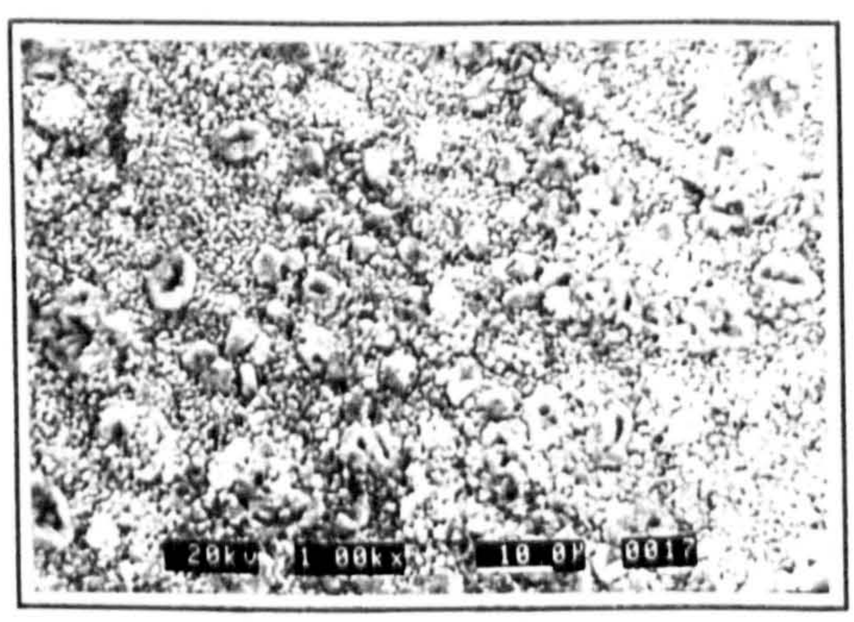

Photograph 8.2.3i: 100h at 800°C

Photographs 8.2.3j to 8.2.3m: Show the sulphidation scale morphologies after exposures of 20 and 100 hours at 850 and 900°C.

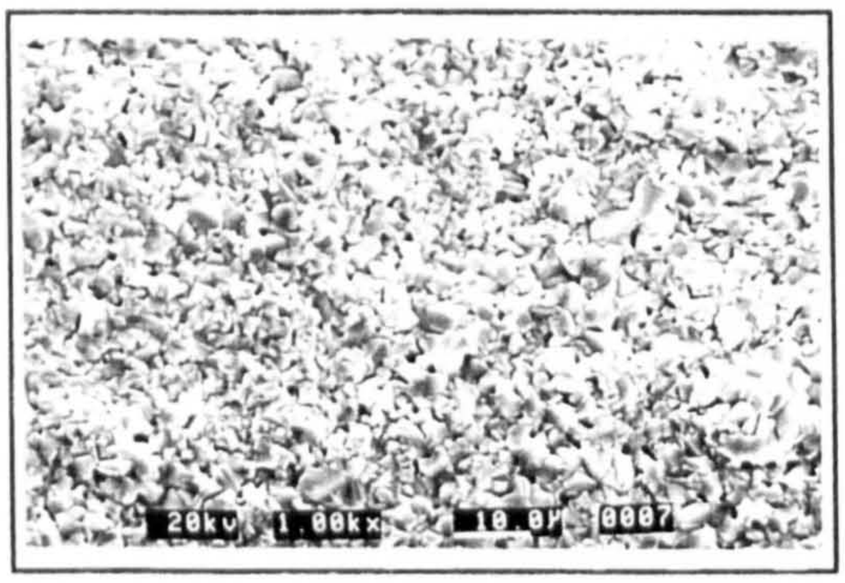

Photograph 8.2.3j: 20h at 850°C

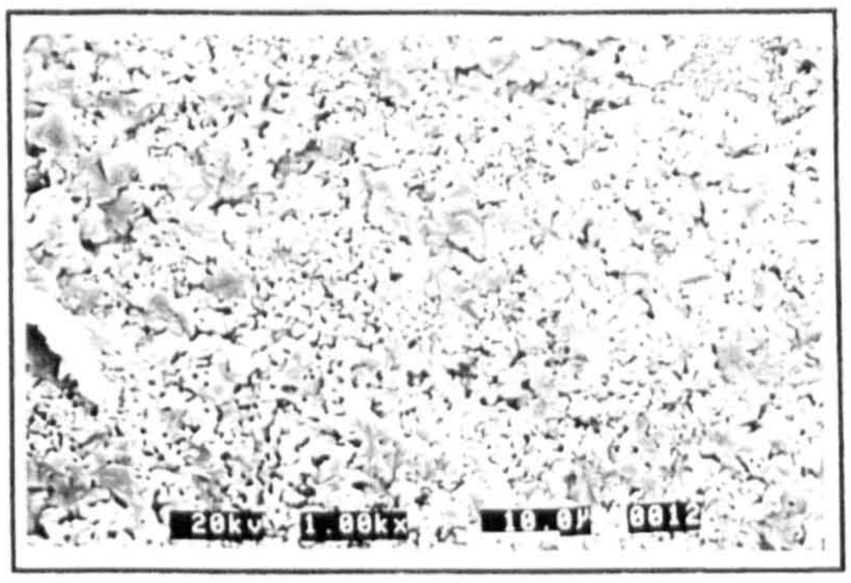

Photograph 8.2.3k: 100h at 850°C

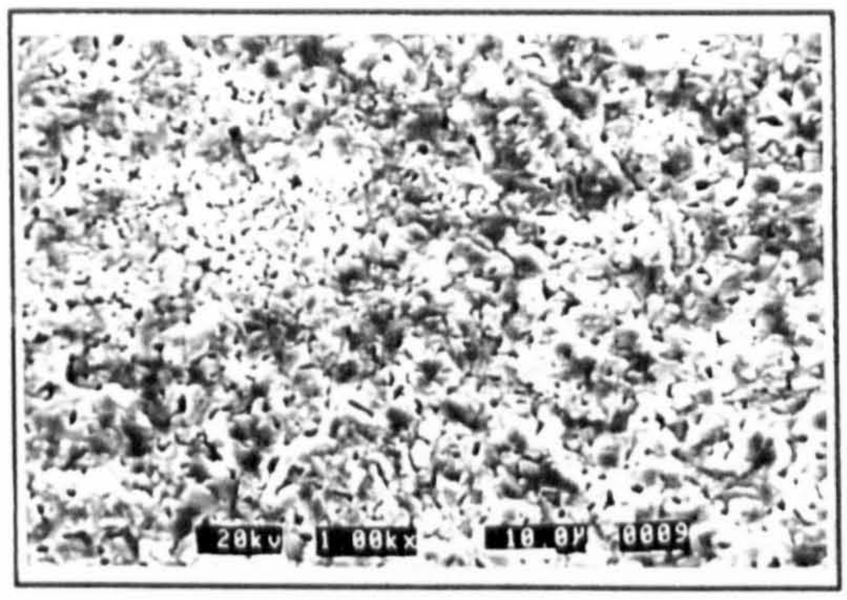

Photograph 8.2.3l: 20h at 900°C

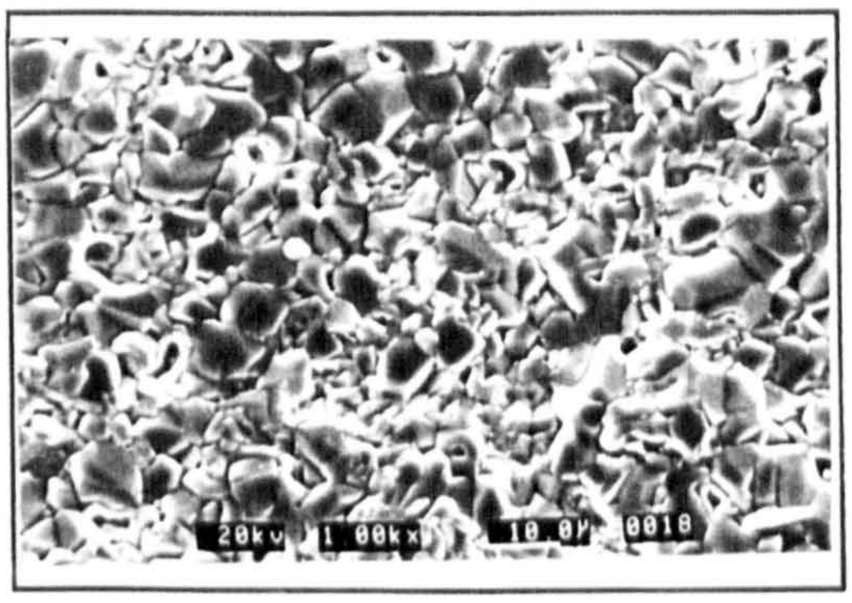

Photograph 8.2.3m: 100h at 900°C

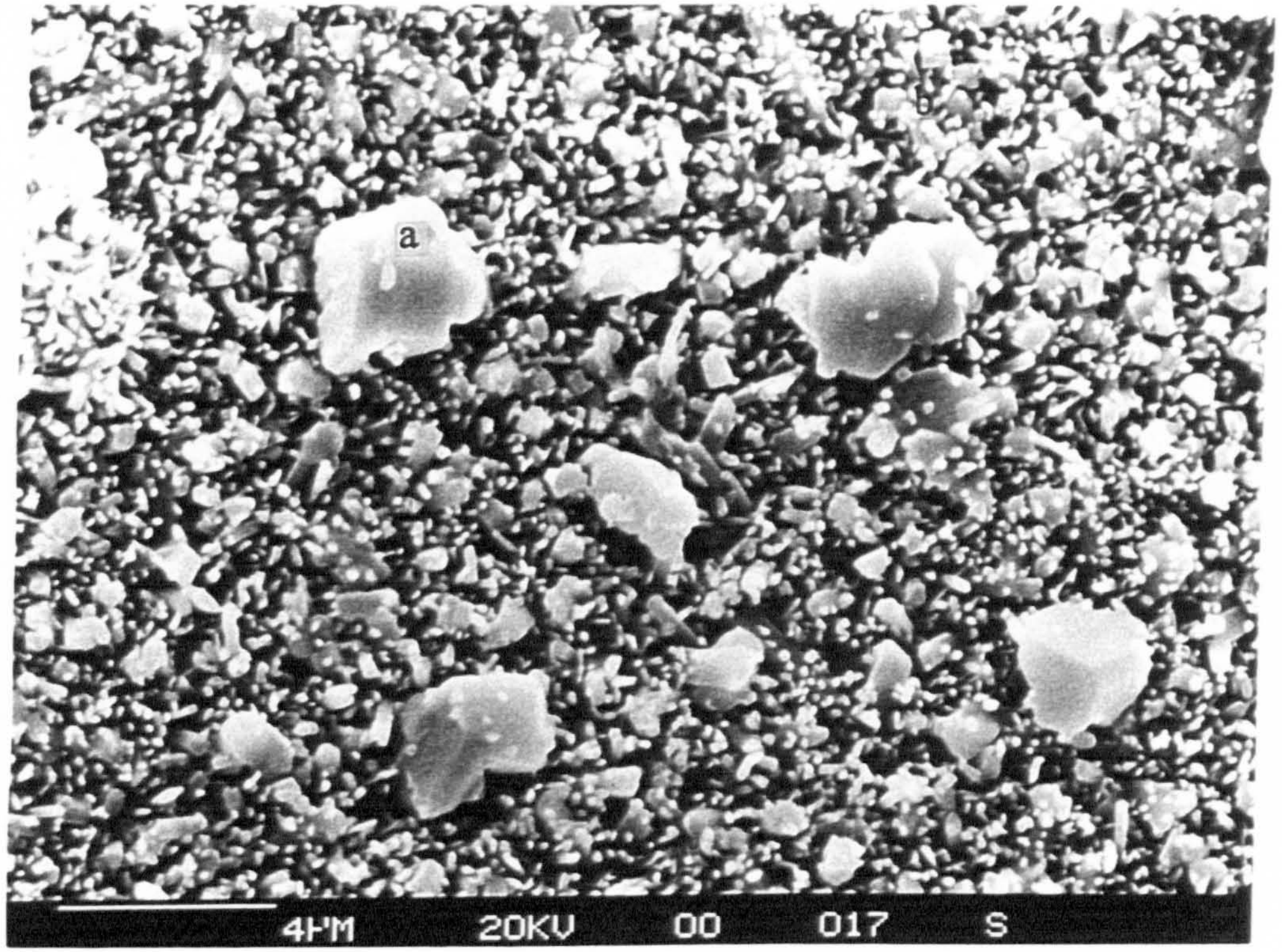

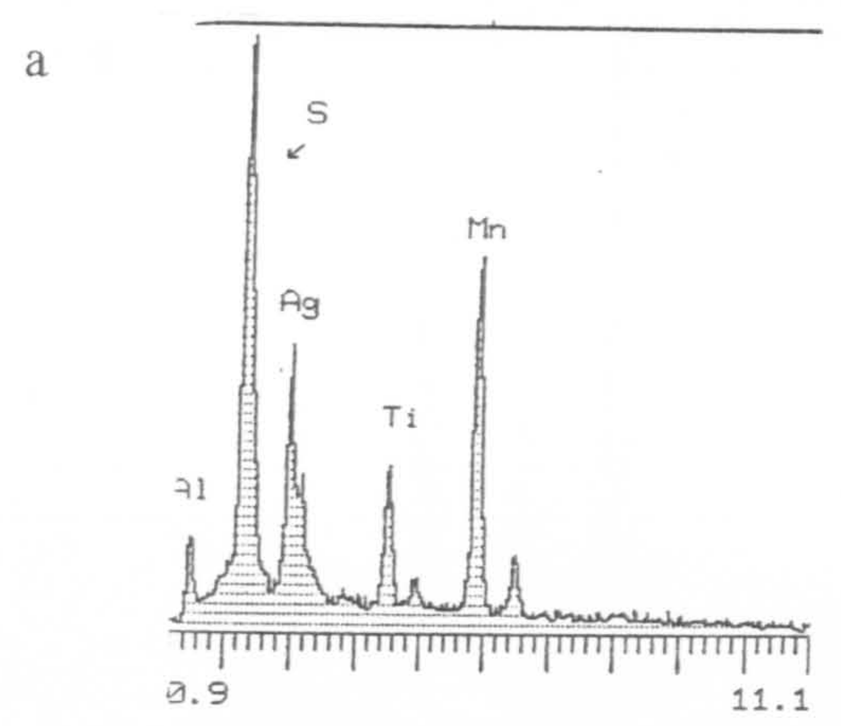

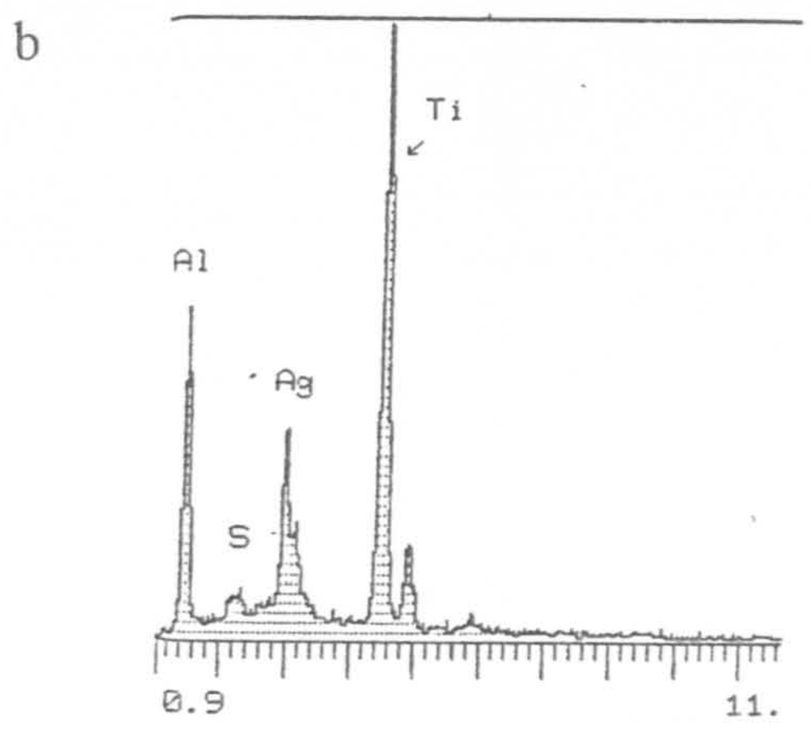

Magnification: 5.0kx

Photograph 8.2.3n: Shows the surface morphology observed after 100 hours at 750°C in 590 ppm SO_2. Two EPMA analysis' identified the relative proportions of Ti, Al, S and Mn found in the large particles overgrowing the much finer rod like crystals.

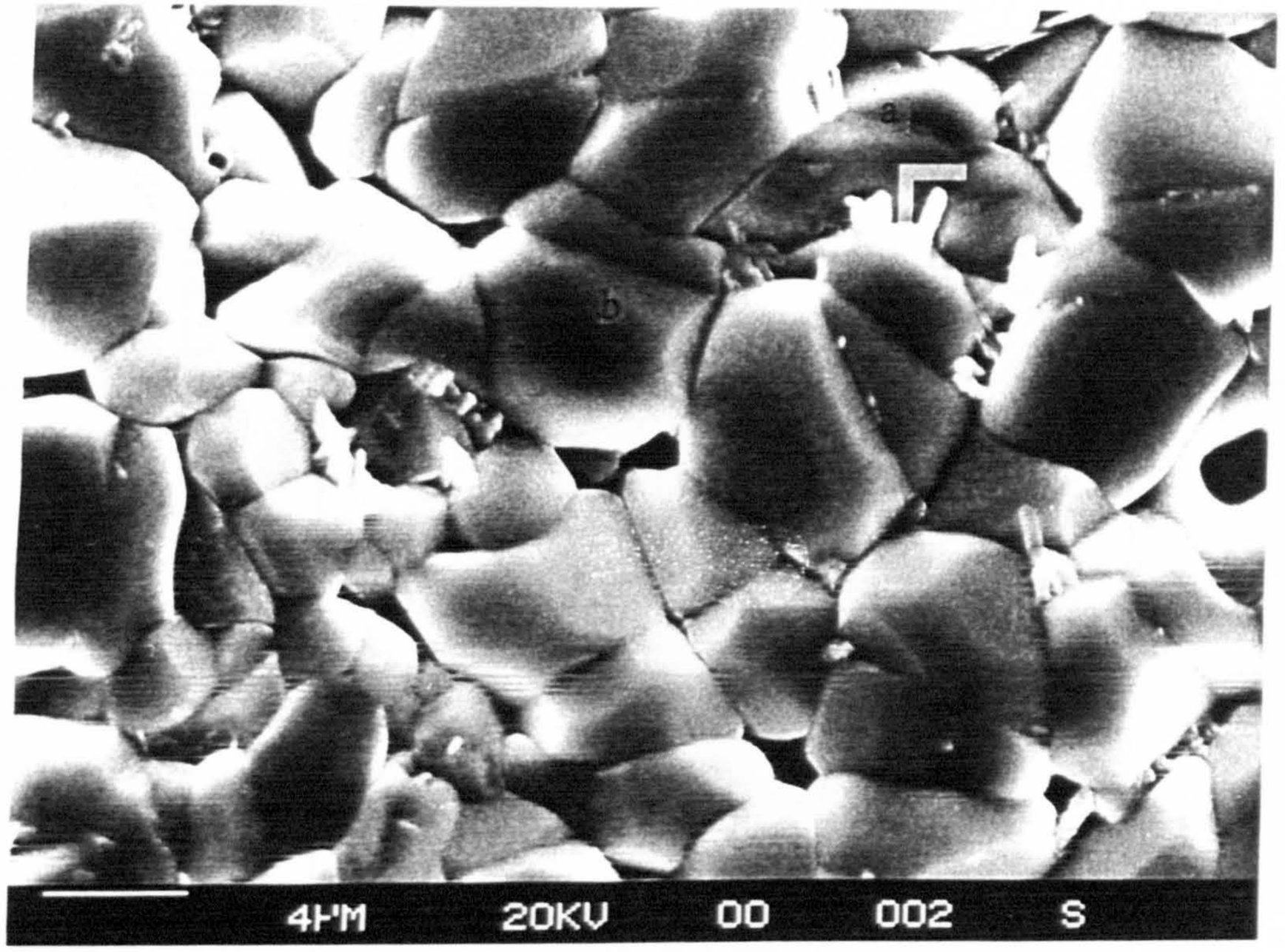

Magnification: 3.0kx

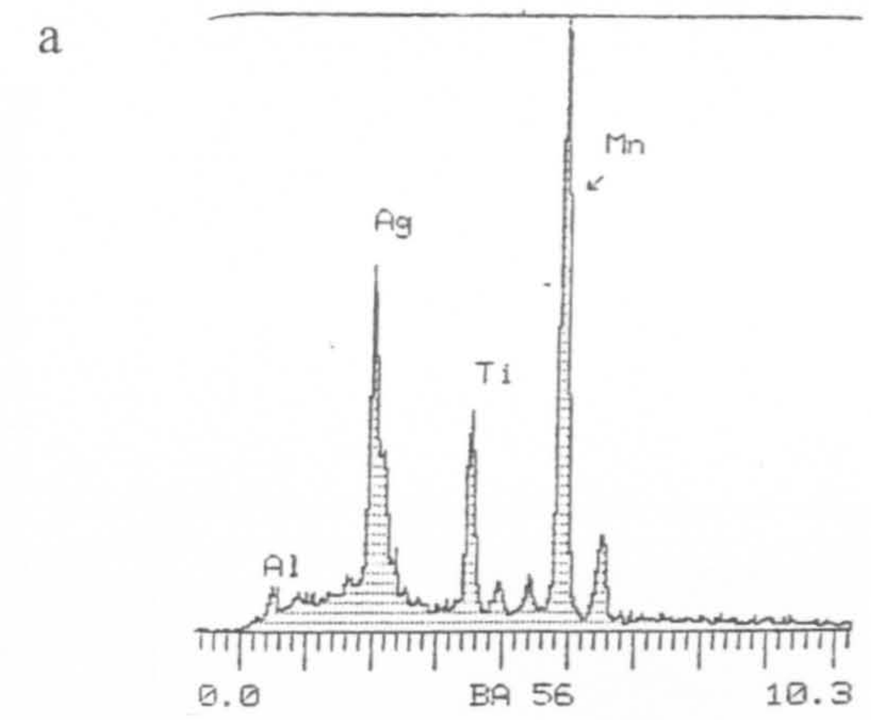

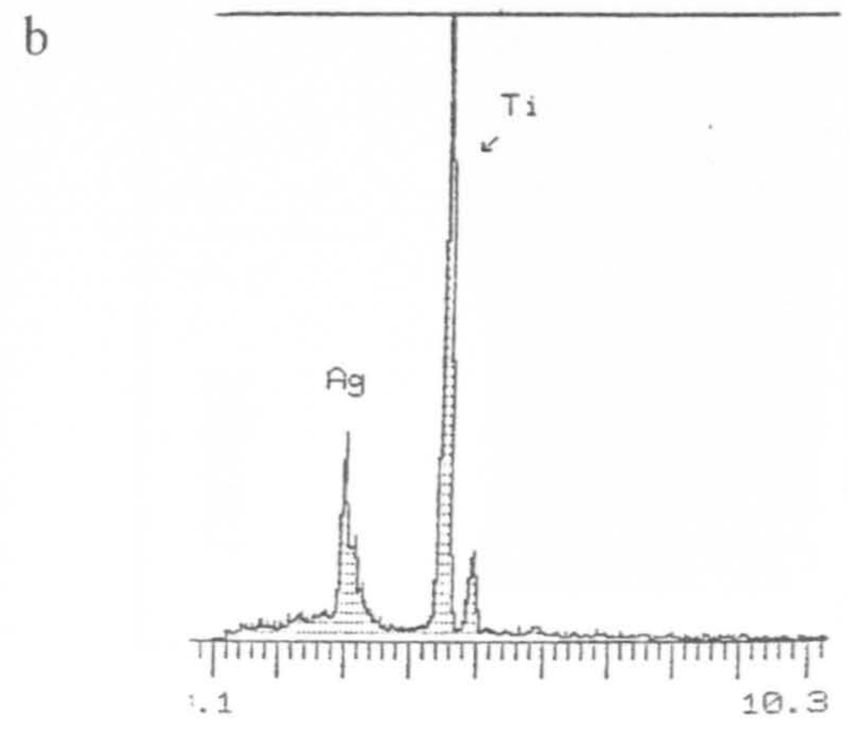

Photograph 8.2.3o: Shows the surface morphology observed after 100 hours at 900°C in 660 ppm SO_2. Two EPMA analysis' identified the two mayor oxides which coexisted.

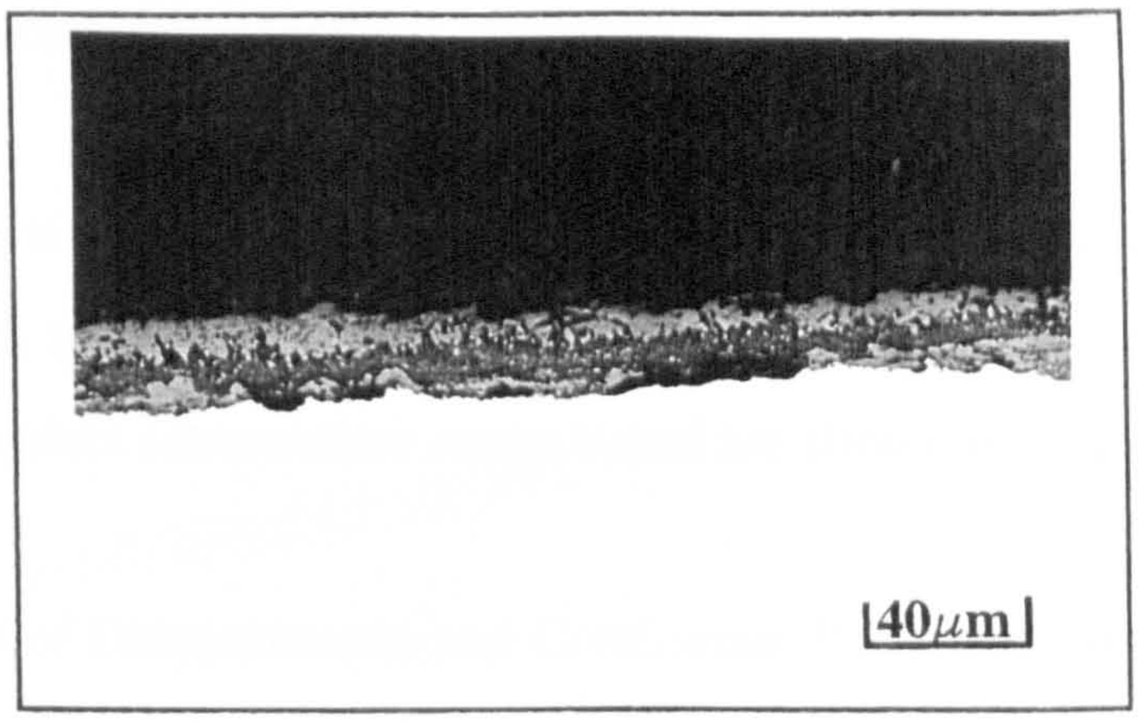

Photograph 8.2.3p: Shows an optical micrograph of the through thickness observed after 20 hours at 800°C in 650ppm SO_2. (Magnification: x100)

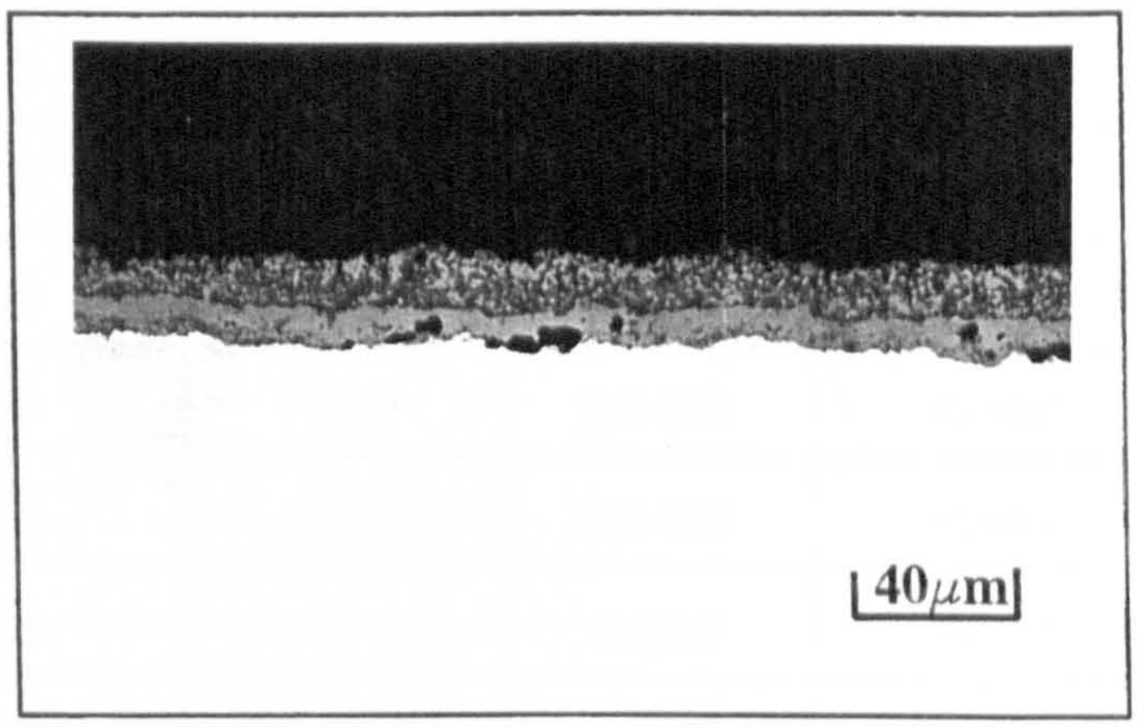

Photograph 8.2.3q: Shows an optical micrograph of the through thickness observed after 100 hours at 850°C in 600ppm SO_2. (Magnification: x100)

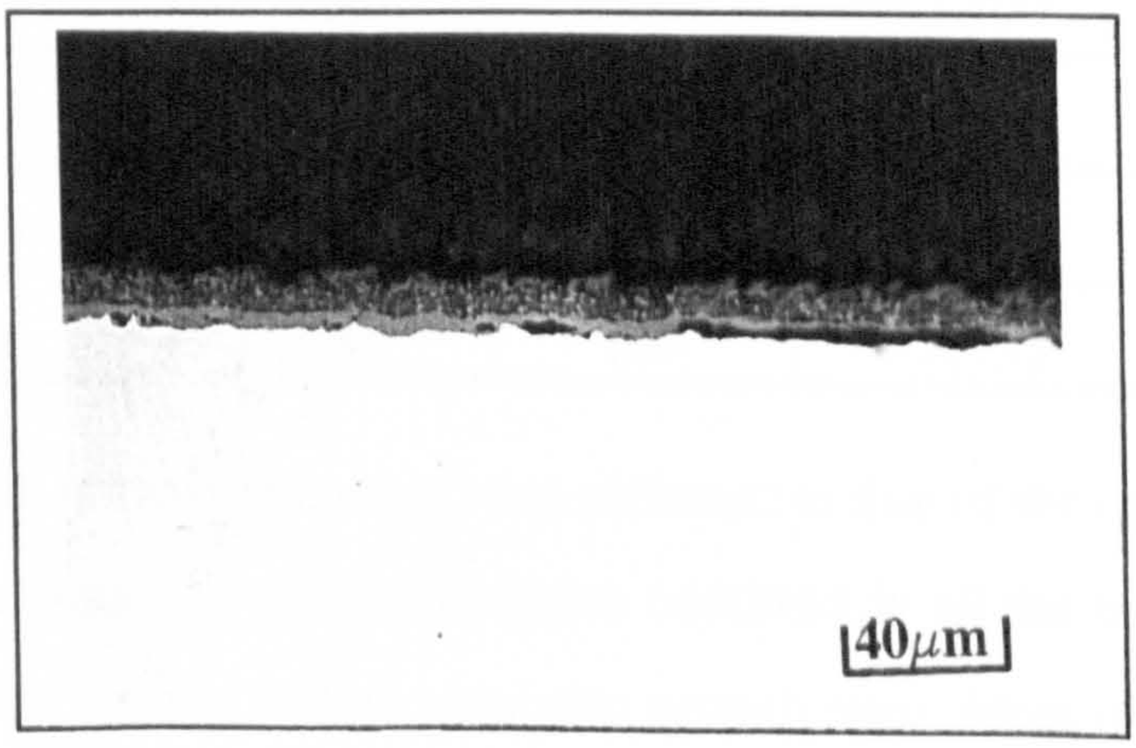

Photograph 8.2.3r : Shows an optical micrograph of the through thickness observed after 100 hours at 900°C in 660ppm SO_2. (Magnification: x100)

8.2.4 Salt corrosion tests

Table 14 shows the test conditions and final mass gains for the tests carried out between 500 and 750°C. A typical continuous gravimetric curve is shown in figure 40.(All the curves for the complete temperature range tested are shown in Appendix A)

Table 14: Results of Discontinuous and Continuous Hot Corrosion thermogravimetric tests

Test coupon	Temperature (°C)	Exposure Time (h)	Salt Level (mg/cm^2)	Final Mass gain (mg/cm^2)	Log Kp ($mg^2/cm^4/hr$)
Ta 27	500	100	0.035	0.062	-4.4152
Ta 28	550	100	0.0406	0.063	-4.409
Ta 39	550	100	0.035	0.065	-4.374173
Ta 33	600	100	0.033	0.345	-2.9243
Ta 23	650	100	0.0423	0.660	-2.3609
Ta 62	675	100	0.0435	0.987	-2.011
Ta 144	700	1	0.036	0.204	-
Ta 145	700	2	0.036	0.361	-
Ta 22	700	100	0.0423	0.700	-2.309
Ta 12	700	100	0.03	0.674	-2.342
Ta 35	700	100	0.033	1.100	-1.957
Ta 52	725	100	0.0509	0.825	-2.167
Ta 34	750	100	0.033	1.050	-1.957
Ta 55	800	100	0.0	0.752	-2.279

The shape of the salt corrosion curves were different to that of the oxidation curves. In the first 5-10 hours much greater mass gains occurred in all the tests than would be expected if the curves were to follow parabolic growth rates. Most of the curves appear to undergo an incubation period of corrosion, or steady state growth rates, after which a period of

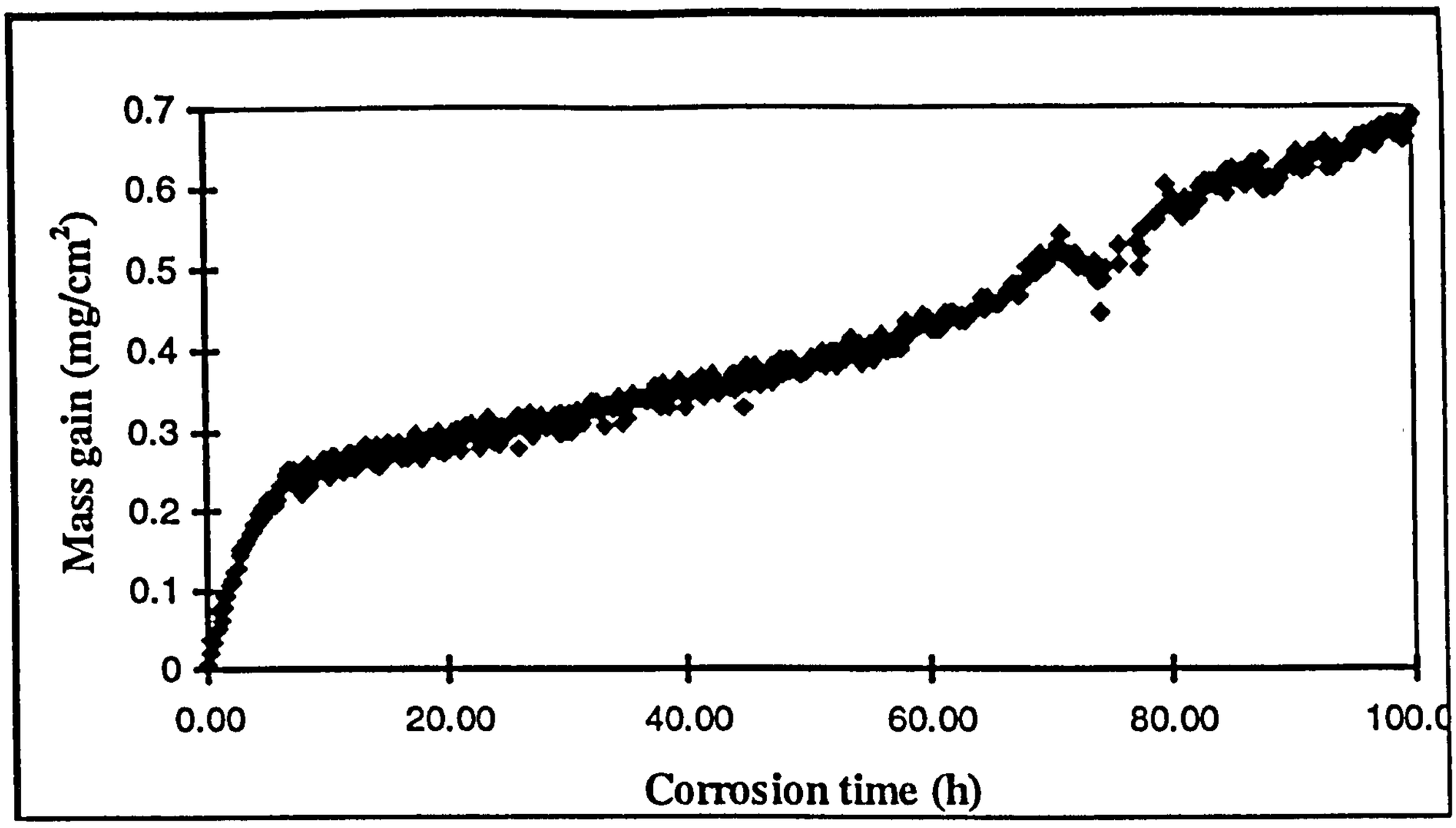

Figure 40: Hot salt corrosion behaviour of Ti-45Al-2Mn-2Nb after 100 h at 700°C in air

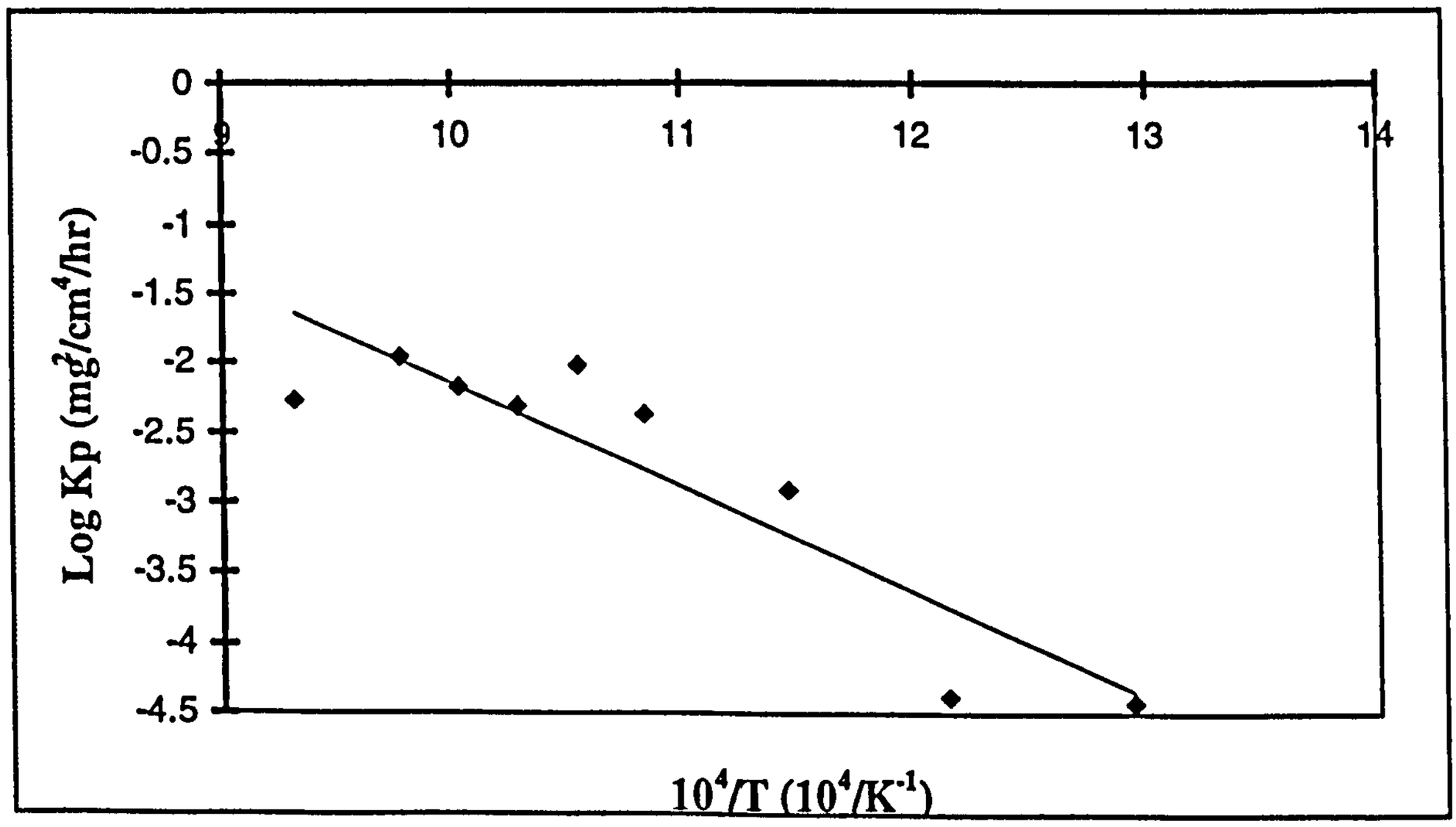

Figure 41: Arrhenius plot of salt corrosion of Ti-45Al-2Mn-2Nb between 500 and 800°C

rapid corrosion occurs. The corrosion rate then follows parabolic growth kinetics.

Even though parabolic kinetics are not followed during the first 5-10 hours it is still possible to estimate parabolic rate constants (Kp) for each test using the later part of the mass gain curve. An Arrhenius plot for the salt corrosion of Ti-45Al-2Mn-2Nb + 0.8% TiB_2 is plotted in figure 41. The scatter observed makes it difficult to state whether or not a single mechanism operates over the tested temperature range without understanding the hot salt corrosion behaviour of this alloy. A more detailed explanation for the Arrhenius plot is therefore made in section 9.3.1 using both the kinetic and metallographic analyses in the following sections.

Detailed metallography was undertaken in order to develop a mechanism for the corrosion behaviour of this titanium aluminide alloy, over the temperature range chosen. Both S.E.M and optical metallographic analyses were used. Table 15 summarises the characteristic kinetic and morphological features at each hot corrosion exposure temperature. Included in the kinetic section are the apparent changes in oxide growth rates. At each test temperature an initial period of logarithmic type oxide growth occurs. Depending on the length of time and temperature a second logarithmic type growth develops. This transition was often accompanied by a rapid or breakaway period of mass gain. The second logarithmic period continued at rapid rates. A second transition, to parabolic growth rates, was observed after shorter exposure times as the test temperature was increased. As the test temperatures increased the proportion of mass gain in the first ten hours with respect to the mass gain after 100 hours also increased. The general surface and transverse morphological trends are summarised in this table, showing the degree of whisker growth and the severity and depth of alpha 2 attack. Whisker coverage was related to the onset of the second period of logarithmic oxide growth. Greater whisker coverage and deeper alpha 2 attack was accompanied by shorter transition times as the test temperatures increased.

Table 15: Summary of the characteristic kinetic and morphological features at each hot salt corrosion temperature.

Temperature (°C)	Kinetics	Surface Morphology	Transverse Morphology
500	Log. out to100h ~62μg/cm^2	Isolated areas of increased corrosion	Initiation of α2 attack at high [salt]
550	Log. out to 100h ~63-65μg/cm^2	Rutile surface oxide No whiskers	" "
600	Log. to 17h, Breakaway, 2nd log. after 31h Para. kinetics>100h 241h = 0.928mg/cm^2	" (Grain boundary rutile growth)	α2 + substrate attack 15-20μm 25-30μm
650	Log. to 3-4h,Breakaway, 2nd log. after 5h Para. from 65h	2h No whiskers 11h Isolated whiskers 100h whiskers over rutile	Initiation of α2 attack (7-8μm) α2 attack (10-15μm) 20-40μm
675	Log. to1h40min Late breakaway 11h 2nd log.17h 46 Para. from 40h	100h Fine whiskers covering majority of surface. Rutile still visible	α2 attack continues at high high salt concentrations
700	30% wt gain in first 10h Log. to 20 min 2nd Log. 40 min Para. from 43h	Whisker growth widespread, obscuring rutile + coarsening	No continuous Al_2O_3 layer severe α2 attack (45-50μm) Some reprecipitation 13-20μm thick oxide
725	60% wt gain after 10h(500μg/cm^2) Log to 20 min, 2nd log. from 40 min, breakaway after 8h, Para. after 13-25h	Dense whisker growth whole surface, areas of coarser whiskers	α2 attack (40μm) Severe substrate attack. Scale cracking Porous outer scale 5-35 μm thick
750	44 % wt gain after 10h log. up to 10-20min, 2nd log. from 20 min, Para. after 17h46min	Coarse whiskers over whole surface	Scale very porous Scale adherence very poor
800	80% wt gain after 10h 2nd log. from 20 min to 1h30min, Para. after 12h30	Coarse whiskers over whole surface	Severe α2 and substrate attack, about 30μm Scale spalled

Table 15 abreviations: Log.=Logarithmic, Para.=Parabolic

The development of the surface structures with temperature and time is shown in photographs 8.2.4a to 8.2.4h. These show that a rutile surface layer forms at low temperatures and after short times at high temperatures. Increasing time and temperature results in whisker growth occurring over the rutile scale. Long term hot salt corrosion studies showed that very fine whiskers initiated at areas of high salt concentrations after 500 hours at 500°C (Photograph 8.2.4j).The density of whiskers increased after 1000 hours at 500°C, but remained extremely fine (Photograph 8.2.4k).

Photographs 8.2.4l to 8.2.4o show the effect of time at 650°C. The scale spreads across the surface initiating from areas of high salt concentrations. Photographs 8.2.4p to 8.2.4s show scale development after 1, 2, 10 and 20 hours at 700°C. No whiskers could be seen after 1 hour. Very fine whiskers developed after 2 hours at discrete areas. The density of whiskers increased after 10 hours, although still fine. After 20 hours much coarser whiskers were observed.

Several surface features were identified as being important in understanding the corrosion mechanism operating. Electron Probe Micro Analyses (EPMA) were completed in an attempt to identify the corrosion products associated with these features. In photograph 8.2.4t cracked glassy phases can be seen to have formed after 193 hours at 500°C. An EPMA of the surrounding area confirmed the presence of NaCl. EPMA' have penetration depths of approximately 3μm. Hence, due to the glassy phases being less than 3μm thick high concentrations of titanium, from the underlying substrate, prevented an accurate compositional analysis of these areas. EPMA' of the area's visible in photographs 8.2.4u to 8.2.4w showed that high levels of titanium, associated with the oxide scale, were observed after 100 hours at 600, 650 and 750°C. Assuming that the scales were thicker than 3μm after 100 hours at these temperatures the EPMA' showed that aluminium is present either within or at the scale's surface. After 100 hours at 750°C the level of aluminium appears to have decreased. Along with the change in surface morphology, which after 100 hours at 750°C shows coarser whiskers, this suggests a change in corrosion mechanism. Low levels of manganese were also identified through EPMA.

Through section analysis of the scales may provide an insight to where manganese, as well as titanium and aluminium, is located within the scale.

Short term salt corrosion tests were carried out at 700°C in an attempt to identify the initial corrosion products. An EPMA at a specific area, identified as 'a' in photograph 8.2.4x, of a salt coated specimen exposed for 15 minutes at 700°C showed the resultant scale to be aluminium rich. High levels of titanium were also present. High levels of chlorine confirmed the surface feature to be an area of high salt concentration. A second EPMA at an area identified as 'b' in this photograph showed high levels of titanium and a decrease in chlorine, manganese and aluminium concentration. The scale or 'shelf', as it appeared to be spreading out from the areas of high salt concentrations, is a complex mixture of corrosion products which results in the formation of liquid phases. Similar features were observed after 30 minutes at 700°C, as shown in photograph 8.2.4y. However an EPMA at an area identified as 'a' shows an increase in the level of titanium, accompanied by a decrease in the level of manganese when compared with the analysis ('a' in photograph 8.2.4v) made after 15 minutes at 700°C.

The degree of attack increased with both temperature and time. Cross section analyses provided visual evidence to support the corrosion mechanisms operating. Photographs 8.2.4z to 8.2.4ee identify areas of severe attack and scale development. Substrate degradation increased with both time and temperature, with preferential attack occurring along alpha 2 laths. The severity of salt attack appears to increase below large salt deposits.

The optical micrographs appear to show the substrate being attacked down $\alpha 2$ laths. This is supported by backscattered images, a S.E.M. technique, of specimens exposed for 100 hours at 600 and 700°C (Photographs 8.2.4ff and 8.2.4gg respectively). Instead of collecting the electrons which are initially targeted at the specimens surface, with the intensity depending on surface morphology, secondary electrons are detected and used to create images based on atomic mass. Secondary electrons are emitted from a specimens surface by the constituent elements. The relative intensities of each element depends on

atomic mass, with the heavier elements such as Ti emitting a greater number of secondary electrons and therefore appearing as light areas in backscattered images. The backscattered images in these photographs show attack down α2 laths, which are differentiated from the surrounding substrate in that they are lighter in appearance. The higher proportion of titanium within these lathes (Ti_3Al) than TiAl accounts for this. At 700°C severe α2 and substrate attack occurred beneath large salt deposits, as shown by the SEM image in photograph 8.2.4hh, up to 20 to 30μm in depth in this case. At 750°C porous scales were developed after 100 hours. This is shown in photograph 8.2.4ii, which also shows that the scales had poor cohesion.

Salt increased the rate of corrosion but it was necessary to identify the composition of any layers that may have existed in the scale. An elemental X-ray micrograph of the scale structure obtained after 100 hours at 700°C is shown in photograph 8.2.4jj (taken from the area identified in Photograph 8.2.4kk), and represents the general scale structure observed. This shows that the majority of the scale developed was rutile and that a continuous alumina layer did not form. However, a thin band of aluminium rich oxide was observed, and due to its low intensity in comparison to that of titanium in the same area can be assumed to be in solution.

Whiskers were observed at the scale/ gas surfaces after 500 hours at 500°C. However, these were extremely fine and could only be seen at high magnifications. The degree of whisker growth increased with temperature, with the most active growth occurring at around 700°C. Elemental X-ray maps gave some evidence suggesting that the whiskers were aluminium based. More accurate analyses were provided through Auger analysis of individual whiskers as well as the rutile nodules over which the whiskers grew. Figure 42 through to figure 47 show whisker and nodule compositions after 20 and 100 hours at 700°C. Figure 42 compares the composition of a whisker (purple line) with that of a rutile nodule(green line) after 20 hours at 700°C. Both lines show the whiskers and nodules to be titanium and oxygen rich, with minor quantities of manganese. Figure 43 compares the aluminium peak strengths of the whisker and nodule formed after 20 hours at 700°C. Similar peak heights clearly identifies the presence of aluminum in both features. The shift

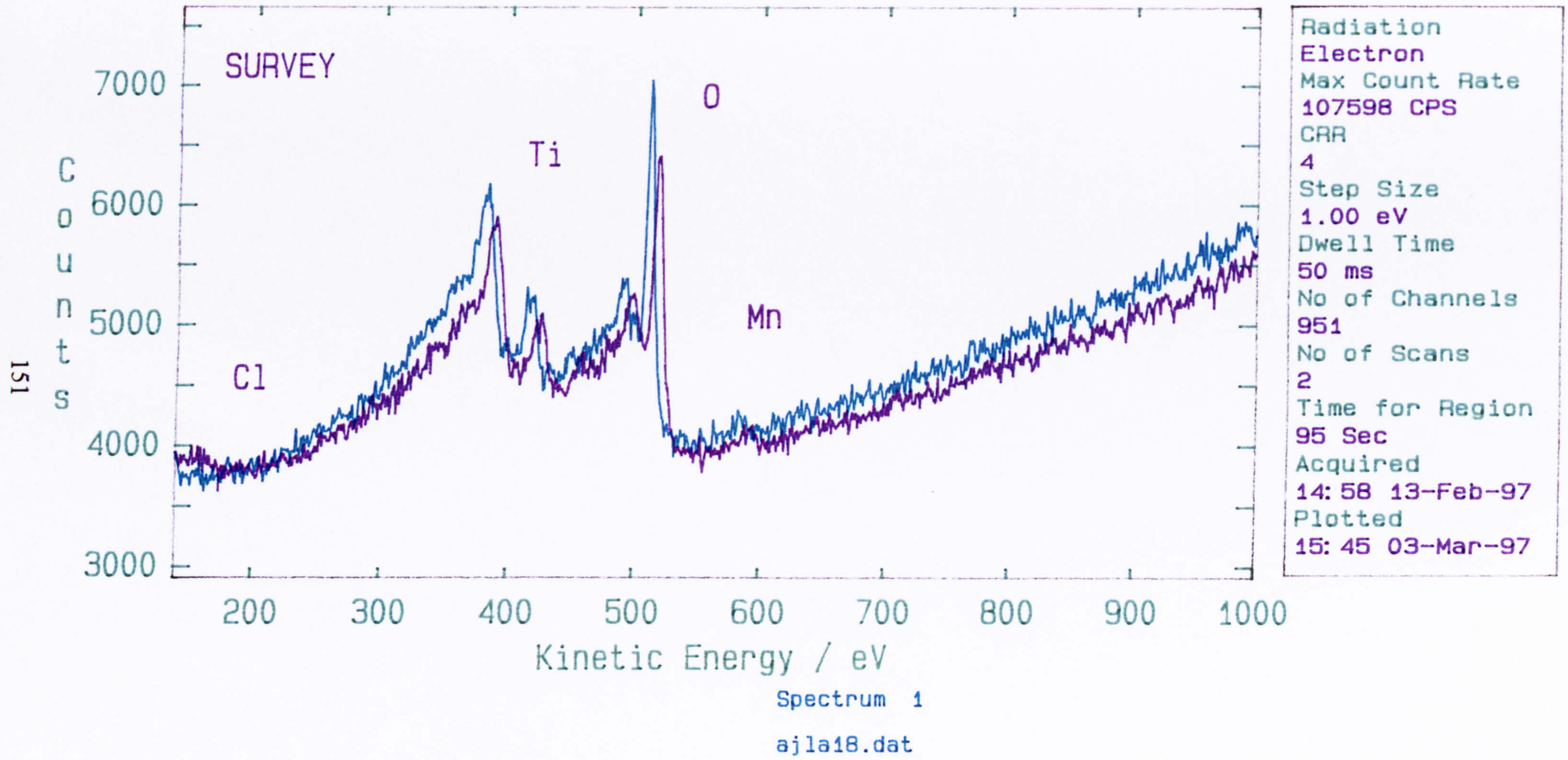

Figure 42: Auger analysis comparing the composition of a whisker (purple line) with that of a rutile nodule(green line) after 20 hours at 700°C in the presence of salt.

Point 1

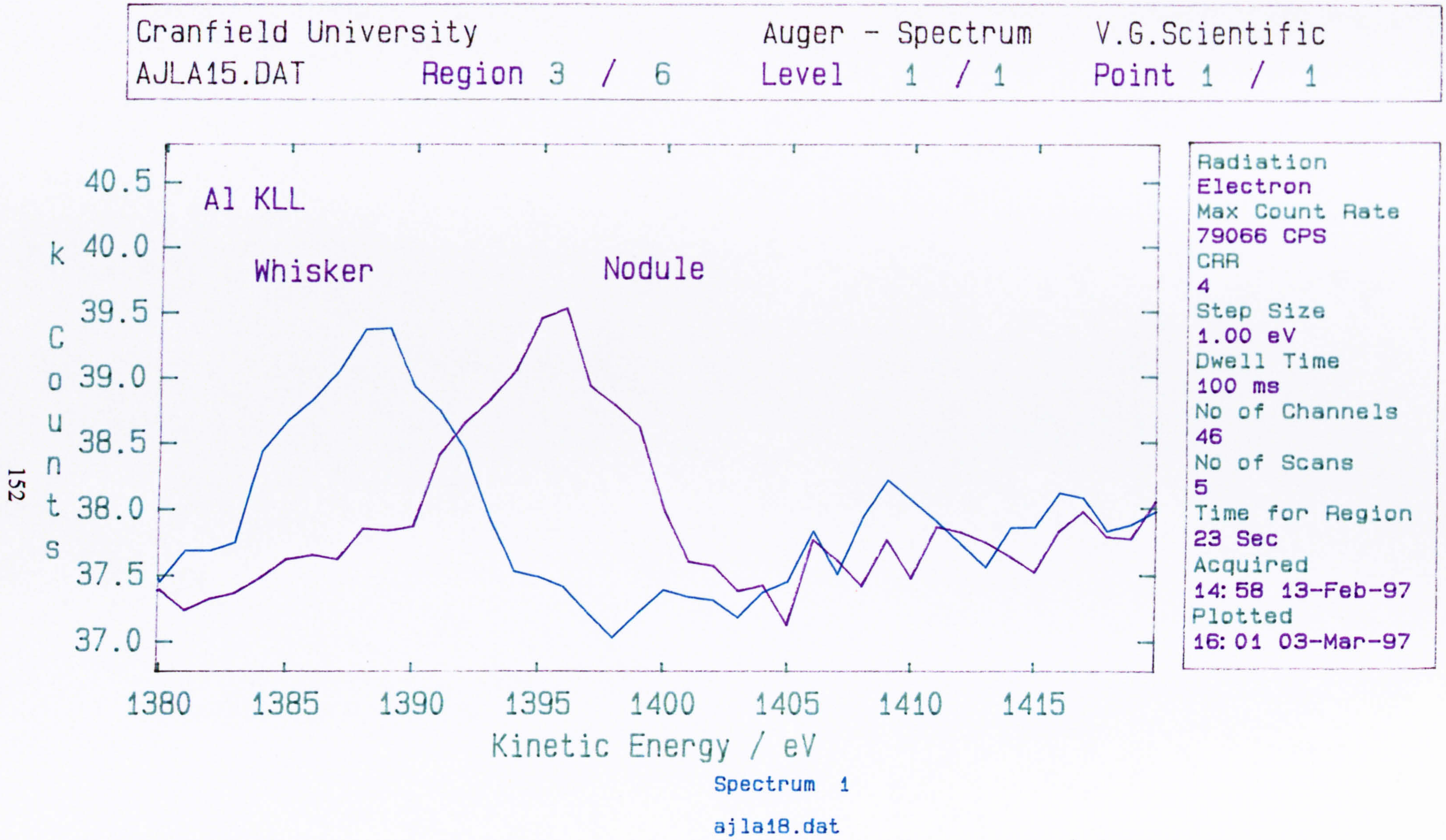

Figure 43: Auger analysis comparing the aluminium levels of a whisker (green line) with that of a rutile nodule(purple line) after 20 hours at 700°C in the presence of salt.

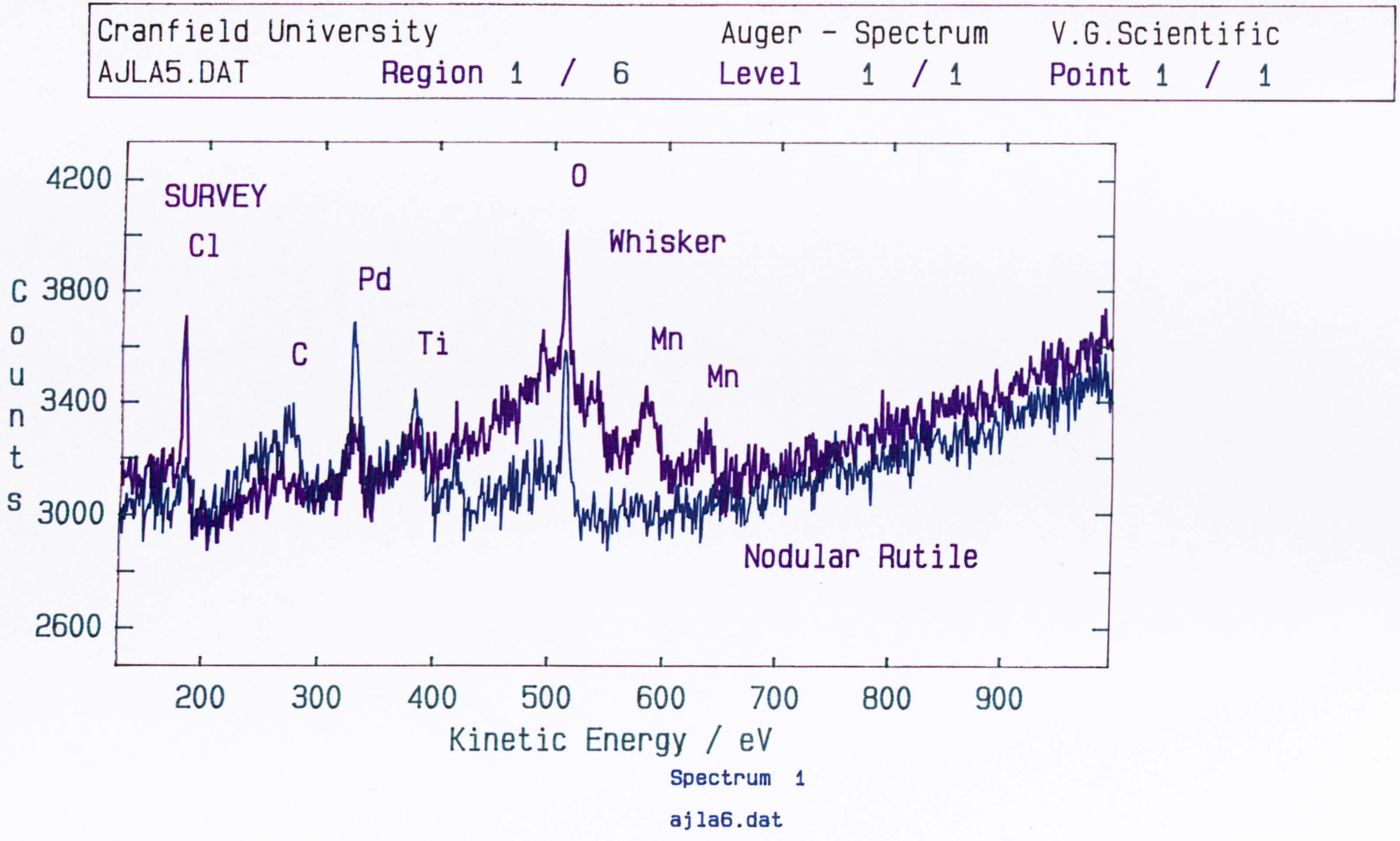

Figure 44: Auger analysis comparing the composition of a whisker (purple line) with that of a rutile nodule(green line) after 100 hours at 700°C in the presence of salt.

Point 1

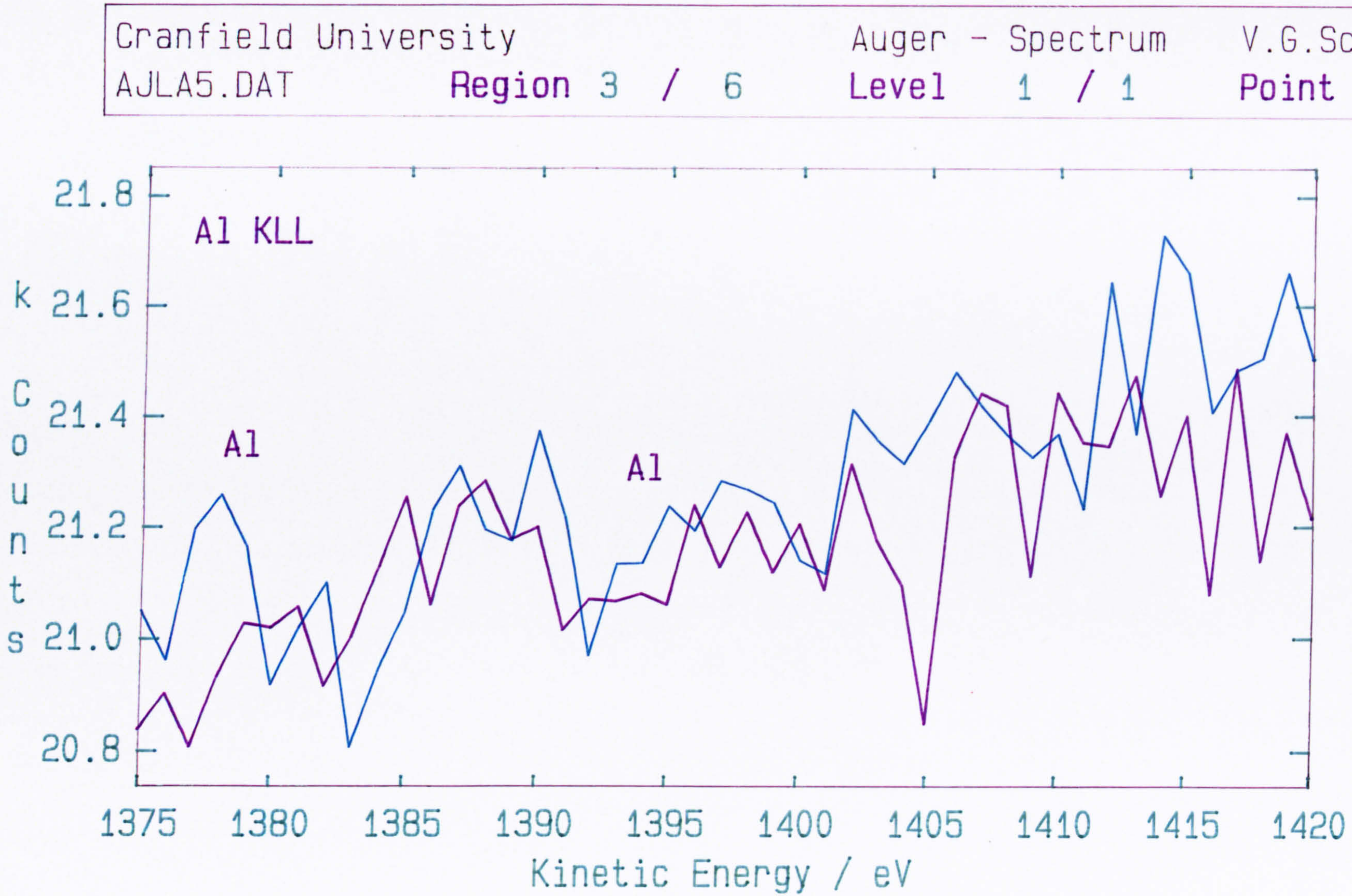

Figure 45: Auger analysis comparing the aluminium level of a whisker (purple line) with that of a rutile nodule(green line) after 100 hours at 700°C in the presence of salt.

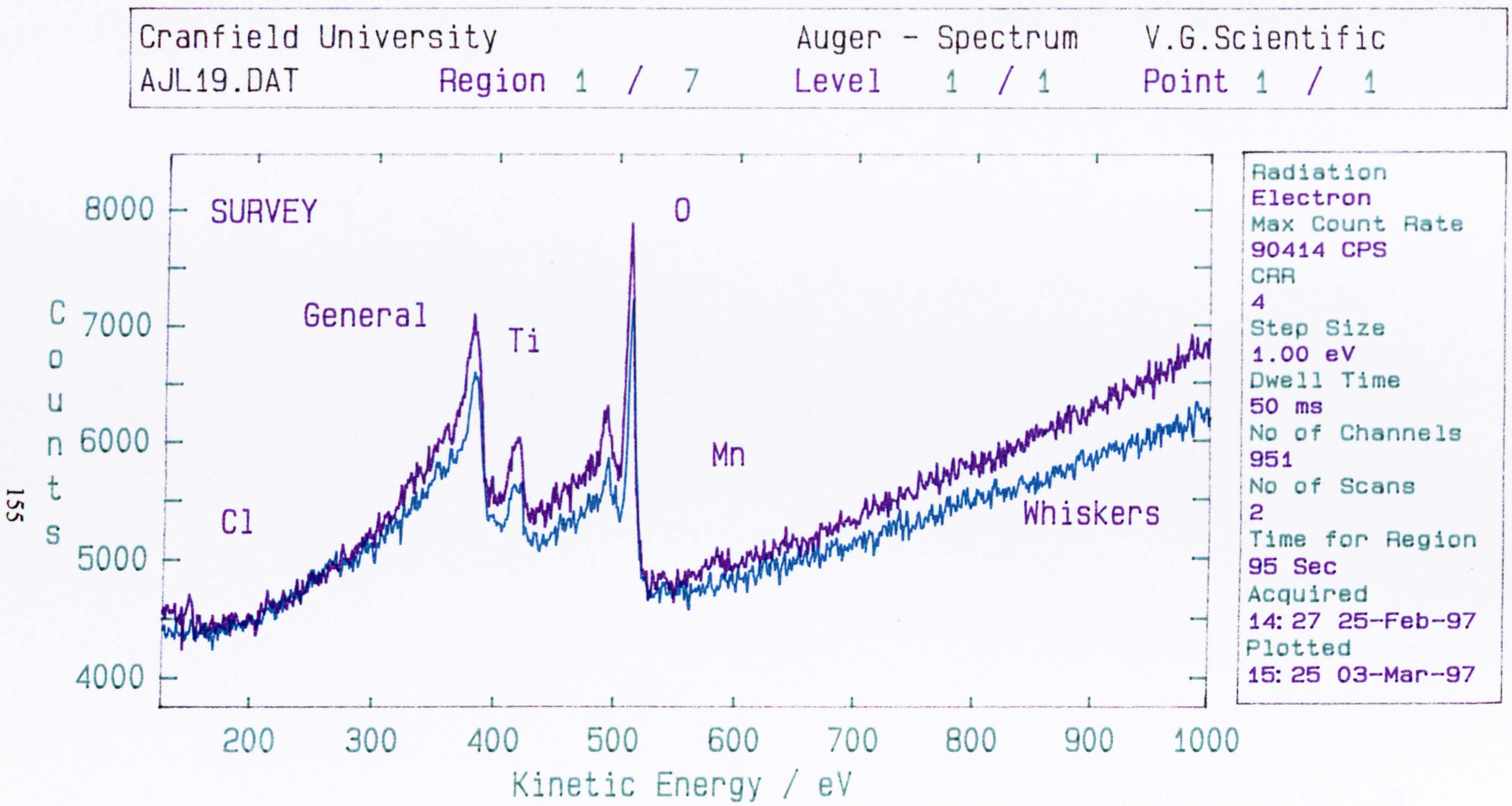

Figure 46: Auger analysis comparing the composition of a whisker (green line) with that of an area of whiskers(purple line) after 100 hours at 700°C in the presence of salt.

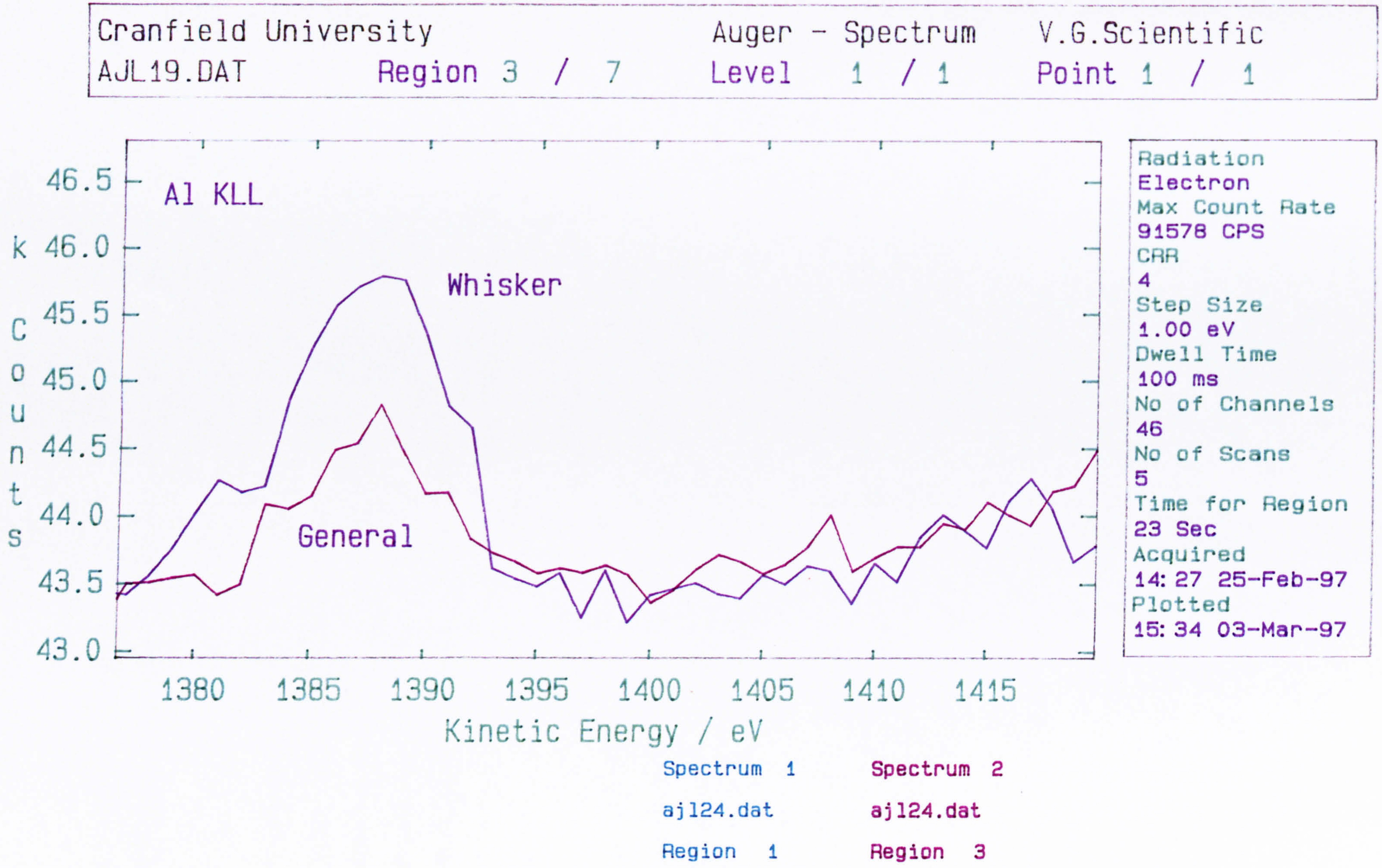

Figure 47: Auger analysis comparing the Al content of a whisker with that of a general area of whiskers after 100 h at 700°C in the presence of salt.

in peak energy may have been due to scale stresses altering atomic structures. The specimen used to obtain the Auger analyses after 20 hours at 700°C was coated with a low level of salt(~0.05mg/cm^2). Further Auger analyses were carried out after coating with higher salt levels(~0.269mg/cm^2) and exposed for 100 hours at 700°C. A comparison of a whisker and rutile nodule under these conditions showed that the differences in composition increased with time. In figure 44, which makes such a comparison under these conditions, the whisker is observed to be chlorine and manganese rich, although a strong titanium peak still exists. A comparison of the aluminium content, figure 45, shows that very little aluminium existed at the surface of the whisker or nodule. A further comparison was made after 100 hours at 700°C at another area of whiskers. In this case a single whisker was compared to an area of whiskers, which will have also included the background rutile nodules. In figure 46 both features were identified as being titanium and oxygen rich. The area of whiskers being shown to be slightly richer in titanium. No chlorine was identified in either case. A weak peak identified manganese over the more general area but it can be seen from the previous analysis of a whisker after 100 hours at 700°C, that manganese is only found in certain whiskers. Figure 47 identifies the single whisker as being richer in aluminium than the area of whiskers, clearly showing that higher levels of aluminium are often found in the whiskers than the background rutile nodules.

8.2.4.1 Effect of salt level

The salt corrosion mechanism proposed was based on salt levels being within the range of 0.02-0.04 mg/cm^2. Increasing or decreasing the salt level deposited should not change this mechanism. However, the mechanism itself predicts that the degree of corrosion should be affected. Several high levels of salt were deposited and exposed at 700°C in air for 100 hours. Table 16 shows the salt levels and degree of corrosion exhibited in each case.

The effect of salt level at 700°C is illustrated graphically in figure 48. The general trend showing an increase in corrosion with level of salt addition, up to a level of salt (~0.12mg/cm^2) above which no further increases in corrosion should occur.

Table 16: Effect of salt level on mass gains at 700°C in air.

Specimen	Exposure time (h)	Salt level (mg/cm^2)	Mass gain (mg/cm^2)
Ta	100	0	0.06
Ta 144	100	0.02247	0.545
Ta 35	100	0.033	1.1
Ta 50	100	0.0316	0.685
Ta 22	100	0.0423	0.7
Ta 63	100	0.056	1.5
Ta 79	100	0.0609	2.1
Ta 82	100	0.0609	1.3215
Ta 116	100	0.1105	2.256
Ta 97	100	0.1605	2.85
Ta 121	100	0.269	2.49

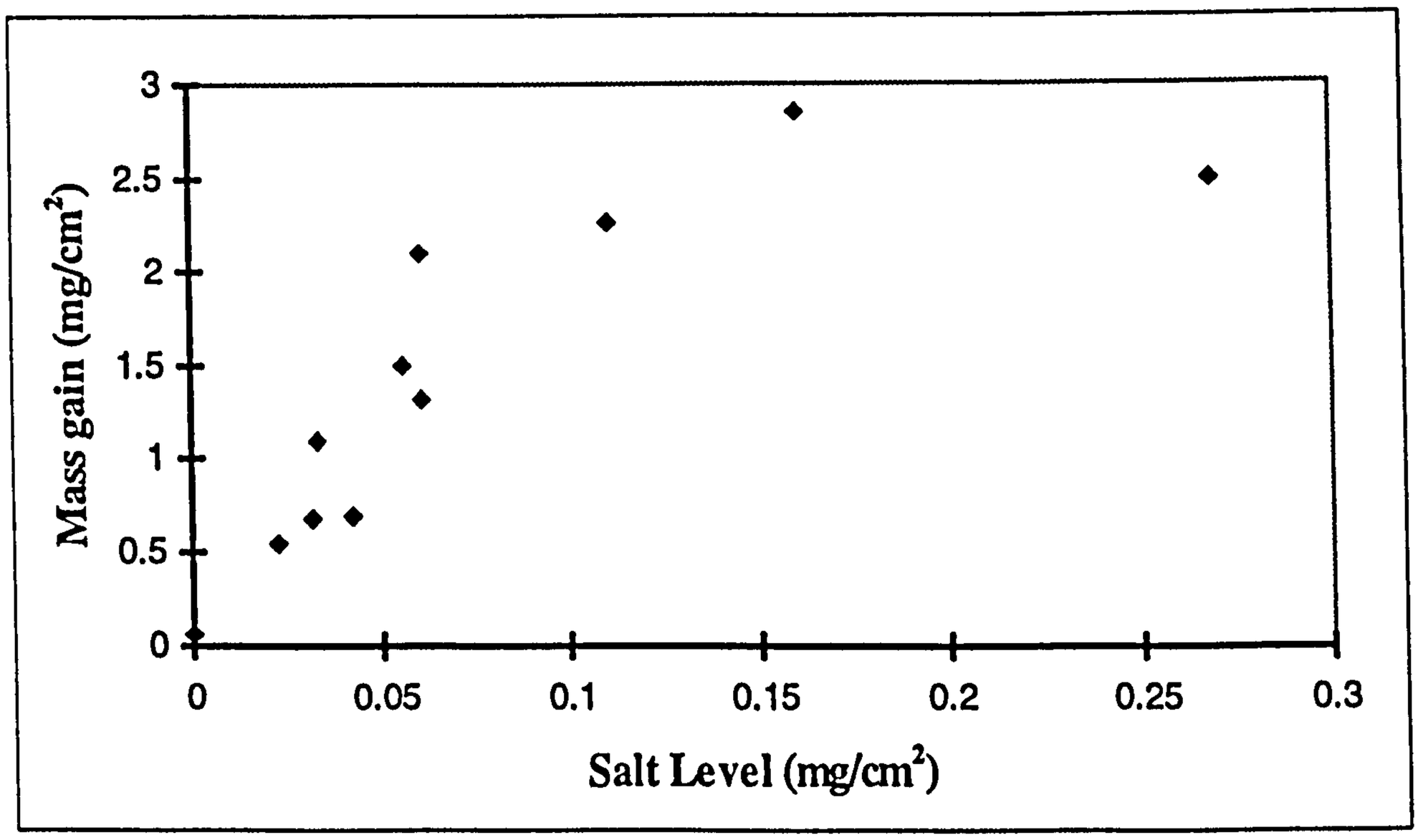

Figure 48: Effect of salt level on the hot salt corrosion behaviour of Ti-45-Al-2Mn-2Nb at 700°C

8.2.4.2 Effect of salt recoating

The work so far has only involved the deposition of a single salt layer. This has allowed the corrosion behaviour of the material to be assessed. However, these results do not take into account the in service conditions of thermal cycling or the deposition of more than one layer of salt.

The effect of salt recoating was studied discontinuously at 700°C. This temperature represents the most likely service temperature for this alloy. Short, intermediate and long term salt recoat experiments were carried out. Recoating involved cooling the specimens from 700°C to room temperature in air, collecting any spallation, weighing the specimen to determine mass gains and recoating the corroded specimen with similar salt levels to the initial level deposited.

The short term recoating experiment involved recoating, within the range of 0.03-0.05 mg/cm^2, after 2, 5, 10, and 15 hours with the final mass gain measurement being recorded after 20 hours. A reference specimen, only coated once before exposure, was weighed under the same conditions enabling the effect of recoating to be established. Figure 49 shows the mass gains obtained for the recoated and single coated specimens.

The intermediate recoat/single coat experiment followed a similar procedure with mass gains obtained after 20, 40, 60, and 80 hours. The final mass gains bing made after 100 hours. Figure 50 shows the effect of salt recoating, with high (>.15mg/cm^2) and low salt levels (<0.05mg/cm^2), after longer periods of time in an attempt to determine if salt recoating thicker corrosion scales effects the corrosion behaviour of this alloy. A higher salt level experiment was run in parallel in order to make comparisons with the lower salt level experiments.

Longer term salt recoating experiments were also carried out in order to observe the effects of recoating during the later corrosion stages during which parabolic kinetics were observed. The question being as to whether or not the vapour phase transport mechanism

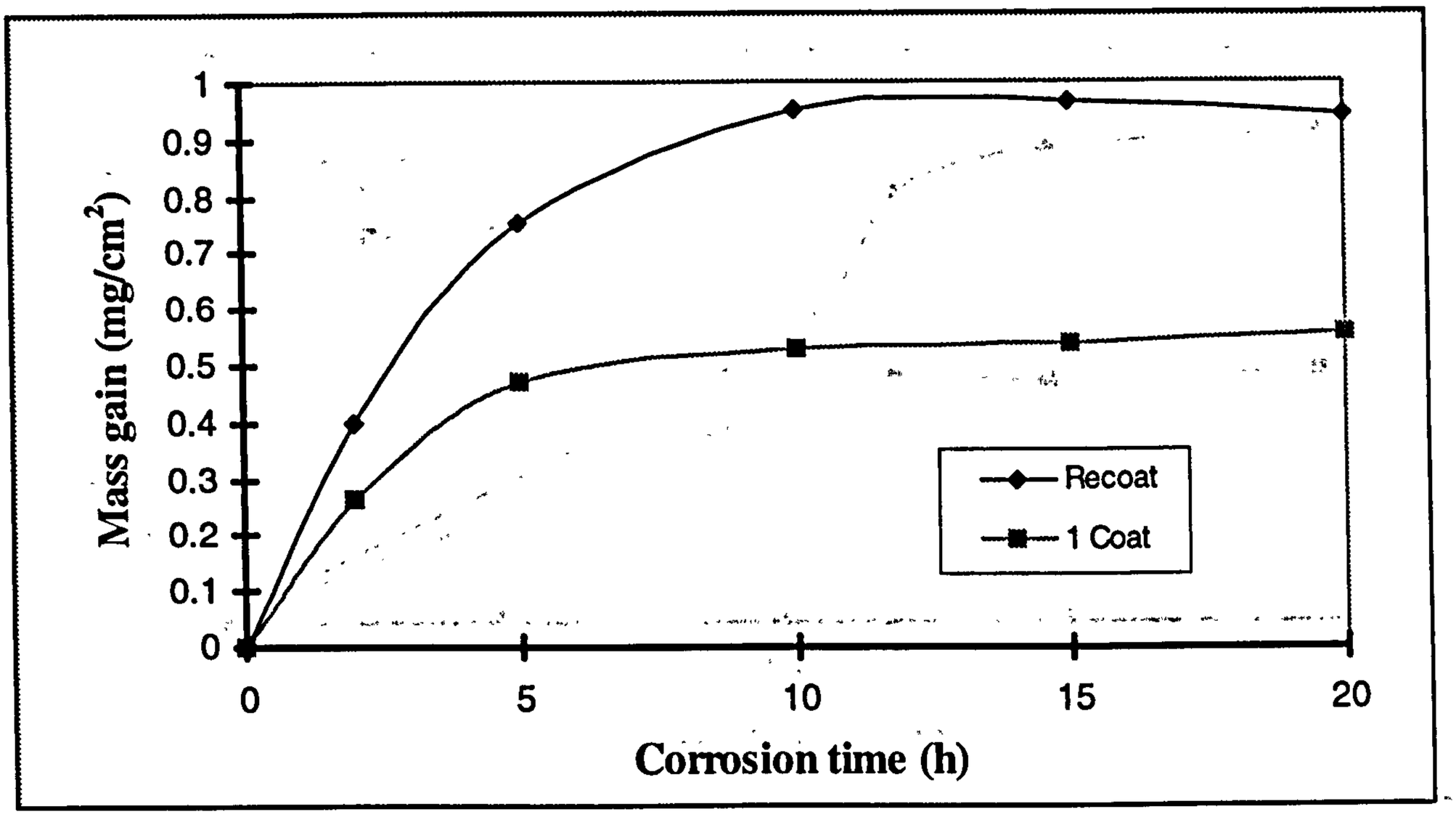

Figure 49: Effect of salt recoating after 0, 2, 5, 10, and 15 hours at 700°C in air

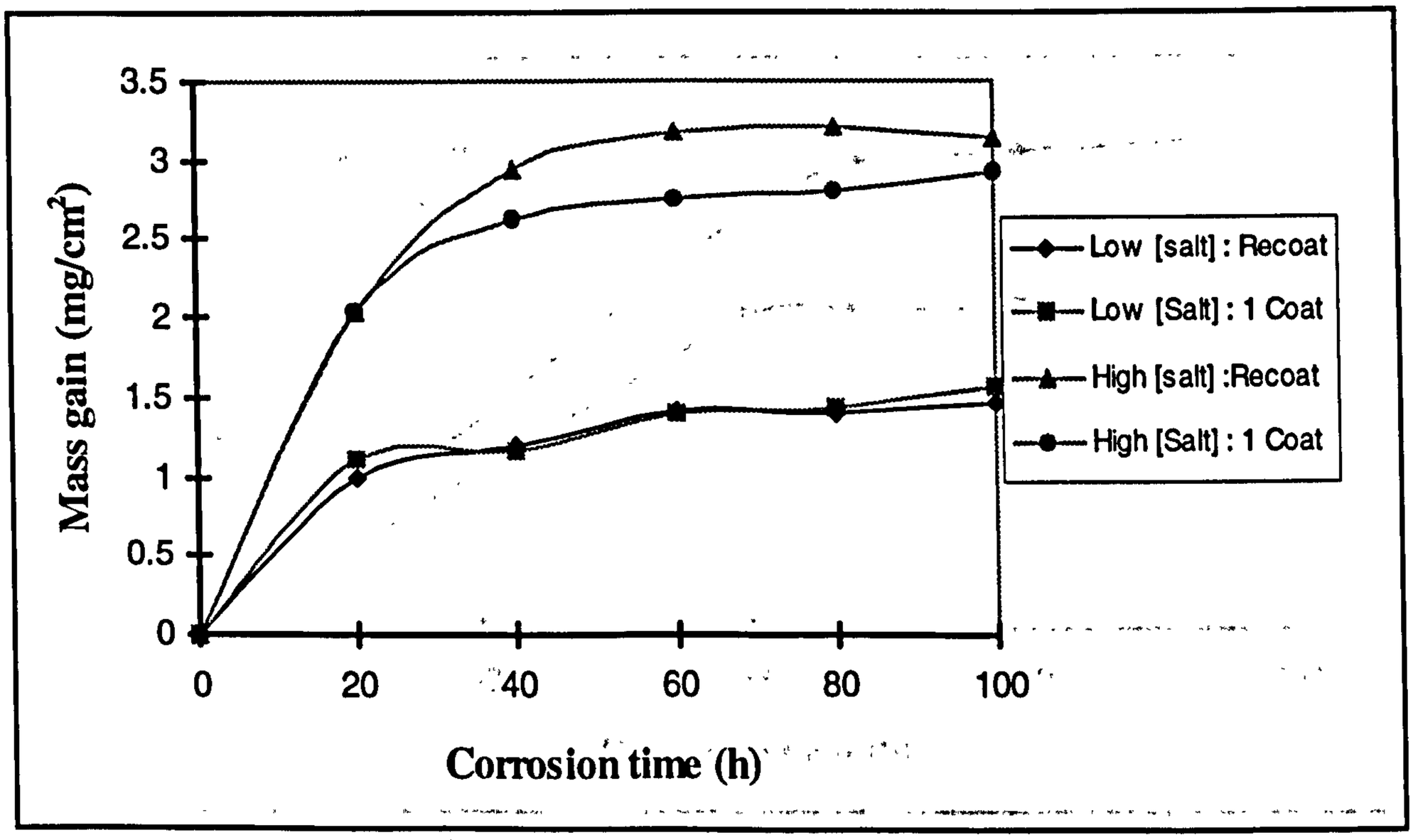

Figure 50: Effect of salt recoating after 0, 20, 40, 60 and 80 hours at 700°C in air

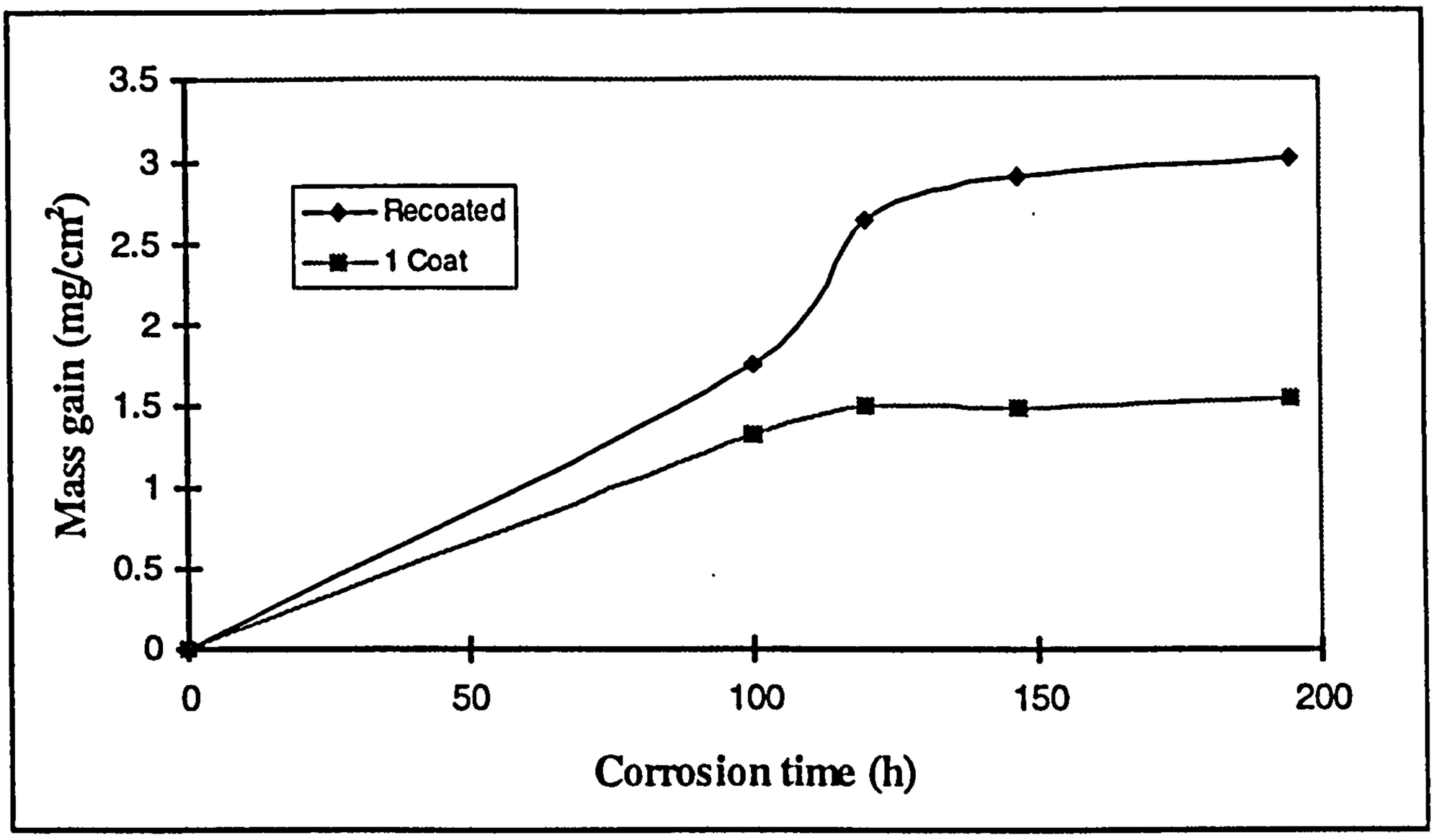

Figure 51: Effect of salt recoating after 0, 100, 120 and 150 hours at 700°C in air. Recoated specimen spalled on cooling

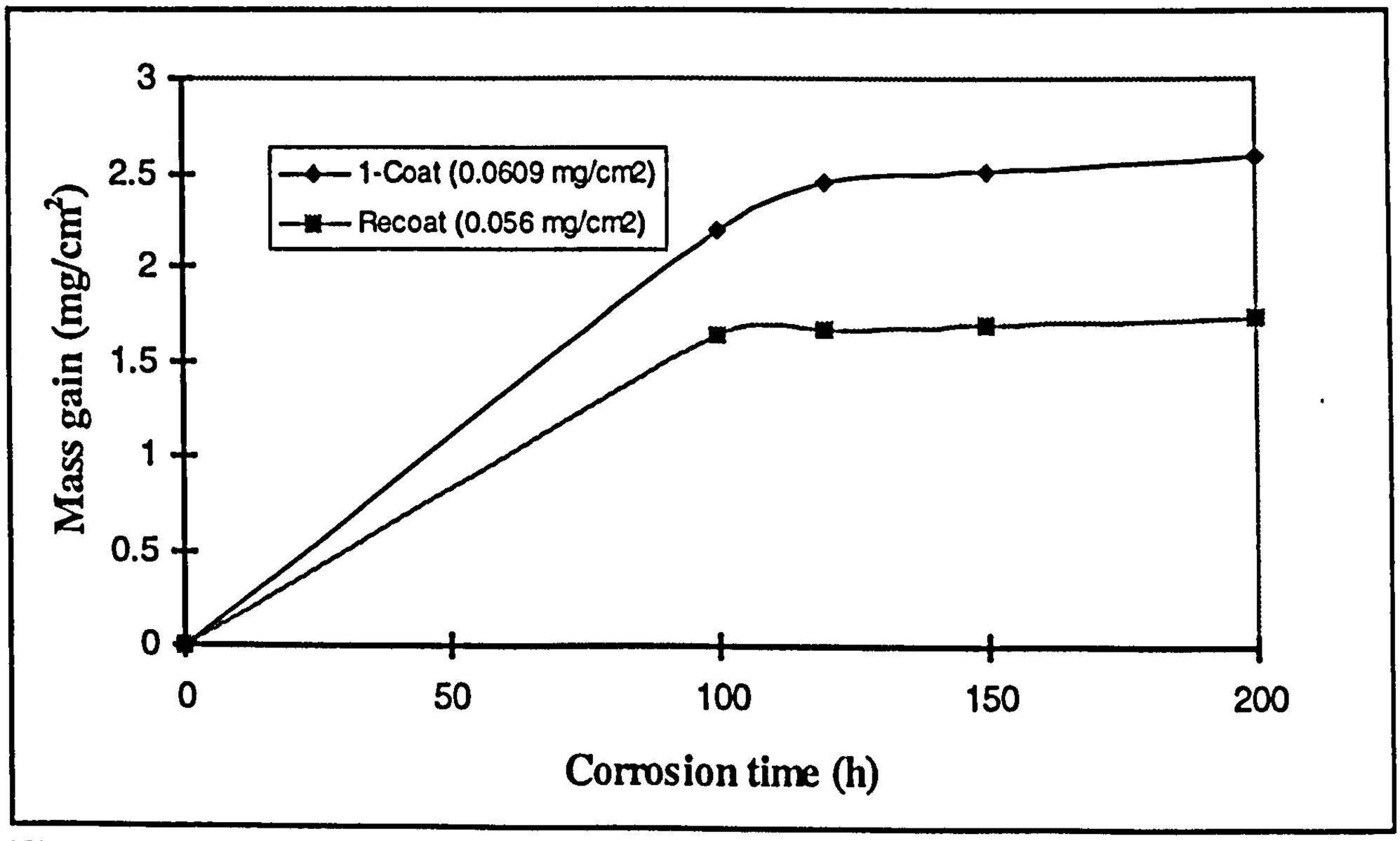

Figure 52: Effect of salt recoating after 0, 100, 120, and 150 hours at 700°C in air. Minimal spallation on cooling

identified during intermediate exposure times reestablishes itself and in so doing increase the corrosion rates again. During two hundred hour exposures the specimen was recoated after 0, 100, 120 and 150 hours. Two identical experiments were carried out as severe spallation occurred during the first experiment. Figures 51 and 52 show that unless spalling occurred the recoat played very little part in increasing the corrosion rate, any changes could almost entirely be accounted for by the level of salt deposit used.

Metallographic examinations of the surface and through sections allowed comparisons to be made between the recoated and one coat specimens. The previous sections, which involved isothermal exposures after one coat of salt, provided the necessary information to determine the effects of salt recoating. Photographs 8.2.4.2a, 8.2.4.2b and 8.2.4.2e to 8.2.4.2l show the surface morphological features at the three separate exposure times.

After short recoating periods out to 20 hours at 700°C distinct morphological differences were seen. Very little whisker growth occurred when only one coat was applied (Photograph 8.2.4.2b). This was surprising as a previous 20 hour exposure, photograph 8.2.4s in section 8.2.4, had shown a high level of whisker growth. The surface of the recoated specimen varied considerably due to spalling effects (Photograph 8.2.4.2a), with areas of sparse whisker growth (photograph 8.2.4.2u) and other areas similar to that seen when only an initial salt deposition had been made. This suggests that thermal cycling may modify the vapour phase transport mechanism attributed to whisker growth. The combination of thermal cycling and recoating lead to spallation and hence allowed salt to redeposit directly upon the substrates surface.

At the intermediate exposure temperature of 100 hours at 700°C, where salt concentrations within the range if 0.03-0.045mg/cm^2 were deposited every 20 hours introducing thermal cycling on cooling, differences between salt recoating and a single salt coat were evident. Photograph 8.2.4.2e of a specimen recoated every 20 hours at 700°C, shows an area of dense but short whisker growth. A specimen was removed from the furnace with the recoated specimen and returned to the furnace without being recoated. Photograph 8.2.4.2f shows the resulting surface morphology after 100 hours. Very little

whisker growth was evident with the majority of the surface having a wrinkled nodular like morphology. A similar set of experiments were carried out using higher concentrations of salt deposited (0.16-0.25mg/cm^2). Similar differences were observed when comparing the recoated and single coated specimens. Recoating resulted in a higher proportion of the surface being covered by whiskers (Photograph 8.2.4.2g). The whisker morphologies differed from those seen after the low salt concentration recoating experiment in that a high proportion were longer and thinner. Again a wrinkled nodular morphology, with very few whiskers, was observed when a specimen with a single salt coat was exposed every 20 hours out to 100 hours at 700°C (Photograph 8.2.4.2h).

Longer term salt recoating, after 100, 120, and 150 hours at 700°C, resulted in two possible kinetic routes. If spalling occurs as in the first instance the corrosion mechanism is initiated again at these areas, accompanied by accelerated corrosion rates. However, after the first recoating, the scale rehealed itself and returned to slower growth rates. Fine, short but dense whiskers were observed after recoating out to 200 hours (Photograph 8.2.4.2i) whilst no whiskers were observed after the single salt coat experiment (Photograph 8.2.4.2j). After 200 hours without salt recoating the surface morphology began to change. The initiation of fine almost crystallographic protrusions, identified during the early stages of oxidation in section 8.2.2 as being TiO_2, were observed. The effects of recoating after longer periods of time were altered by the fact that the scales spalled during cooling and so were repeated. The recoated specimen did not spall in this experiment. Photographs 8.2.4.2k and 8.2.4.2l show the resultant scale morphologies seen after salt recoating and single coating out to 200 hours at 700°C, respectfully. In both cases short, coarse whiskers developed, again beginning to resemble the initial morphology of rutile crystals.

Recoating increased the degree of corrosion resulting in thicker scales and increased substrate attack if spalling occurred. This is evident from photographs 8.2.4.2c, 8.2.4.2d and 8.2.4.2m to 8.2.4.2t which show the through section features seen as a result of the three salt recoat exposure conditions.

Salt recoating after 0, 2, 5, 10 and 15 hours virtually doubled the mass gains when compared to the specimen salt coated once. This is reflected in the optical micrographs of the degree of substrate attack. Photograph 8.2.4.2c shows the scales developed after recoating. Scale growth can be seen to be in an advanced stage of development with the substrate having been severely attacked. Photograph 8.2.4.2d shows the degree of substrate attack exhibited by a specimen with a single salt coat. The oxide scales were damaged and removed from the substrate during polishing. However, the substrate can be seen to have been degraded up to depths of approximately 5μm down α2 lathes or grain boundaries.

Salt recoating every 20 hours at 700°C resulted in severe substrate attack. This is illustrated in Photograph 8.2.4.2m. Porous scales developed up to 30μm thick. Recoating and a single salt coat resulted in similar mass gains after 100 hours. Recoating degraded the substrate over a wider front with the scale advancing into the bulk of the specimen. The single coated specimen was attacked down α2 lathes in the same manner as seen during continuous hot salt corrosion with penetration depths of approximately 40μm (Photograph 8.2.4.2n). Low levels, within the range of 0.03-0.045mg/cm^2, of salt were deposited during each recoat.

Increasing the level of salt deposited, within the range of 0.16-0.25mg/cm^2, resulted in greater mass gains. Again recoating did not result in a continuation of the initial rapid corrosion rates.

Salt recoating has been shown to alter the corrosion front. The depth of attack down α2 lathes appears shorter, when in fact salt attack is as great if not more severe than single coat degradation. Recoating after longer periods of time (100,120 and 150 hours) at 700°C modified the degree of substrate attack. Difficulty existed when attempting to compare differences between recoating and single salt coating as spallation played an important role and in the first set of experiments greater substrate degradation was apparent. Recoating, as shown in photograph 8.2.4.2q, attacked both the substrate and the α2 lathes up to depths of 40-50μm producing scales 20-30μm thick. Photograph

8.2.4.2r shows the scale developed after a single salt coat was initially deposited. Much greater variation in scale thicknesses were observed (between 3-20μm), with α2 lathes being attacked up to depths of 10-20μm. The 200 hour recoat/single coat exposures were repeated due to the initial recoated specimen having spalled during cooling between recoats. Again substrate degradation was severe but the scale morphologies were consistent with previous scale morphologies developed when no spallation occurred. Similar substrate attack was observed in both cases although thicker scales, up to 30μm, were developed by the single salt coated specimen (photograph 8.2.4.2t).

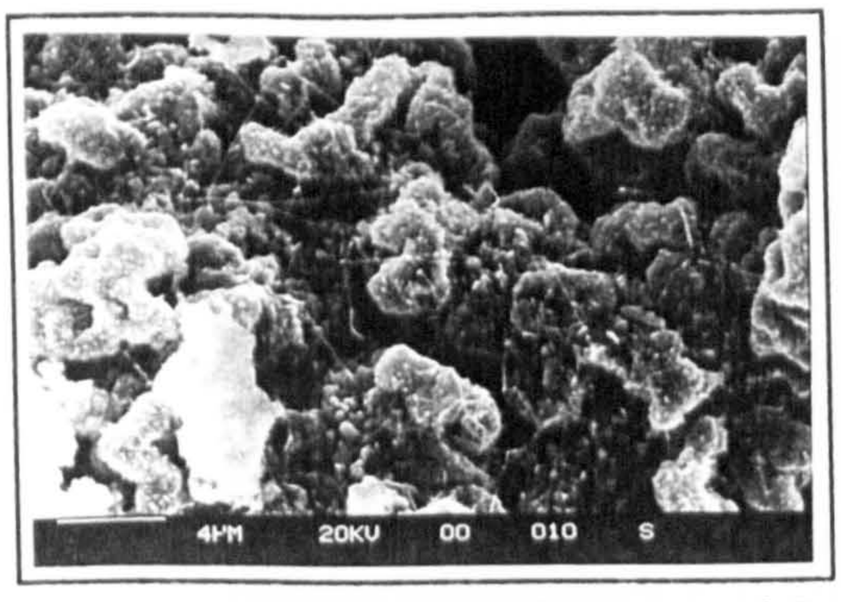

Photograph 8.2.4a: 100h at 550°C

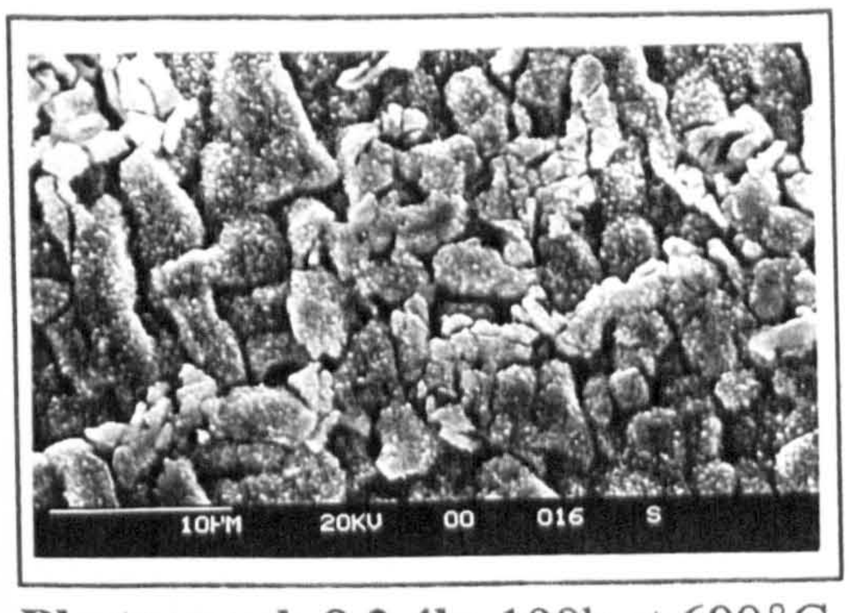

Photograph 8.2.4b: 100h at 600°C

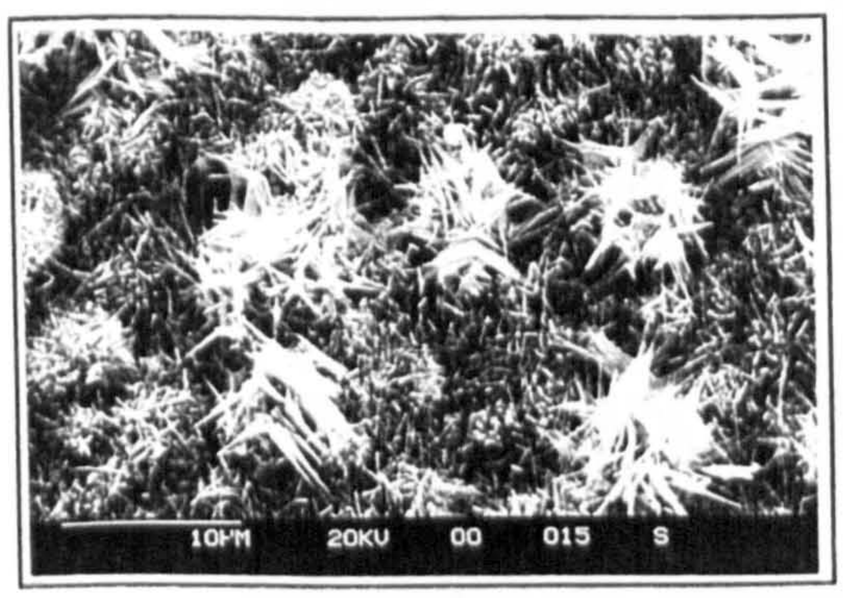

Photograph 8.2.4c: 100h at 650°C

Photograph 8.2.4d: 100h at 675°C

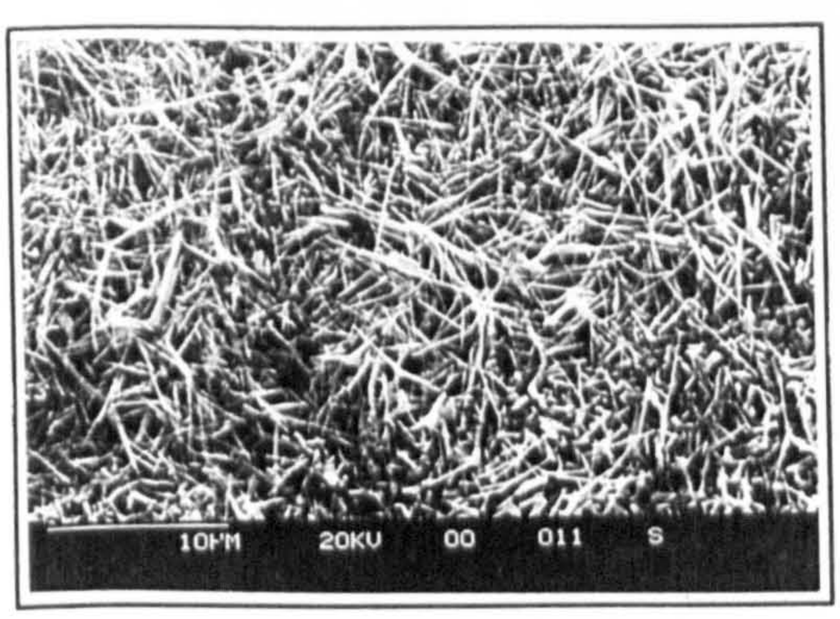

Photograph 8.2.4e: 100h at 700°C

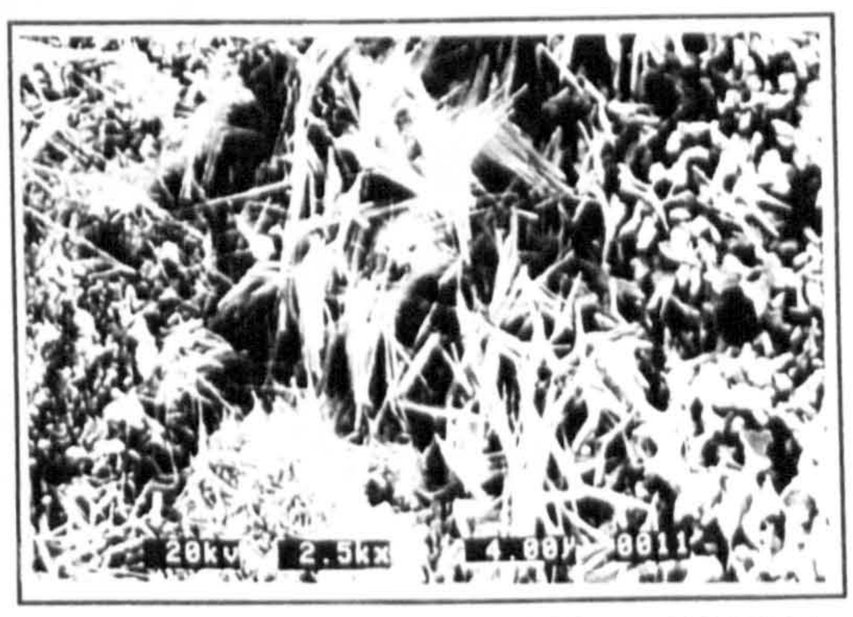

Photograph 8.2.4f: 100h at 725°C

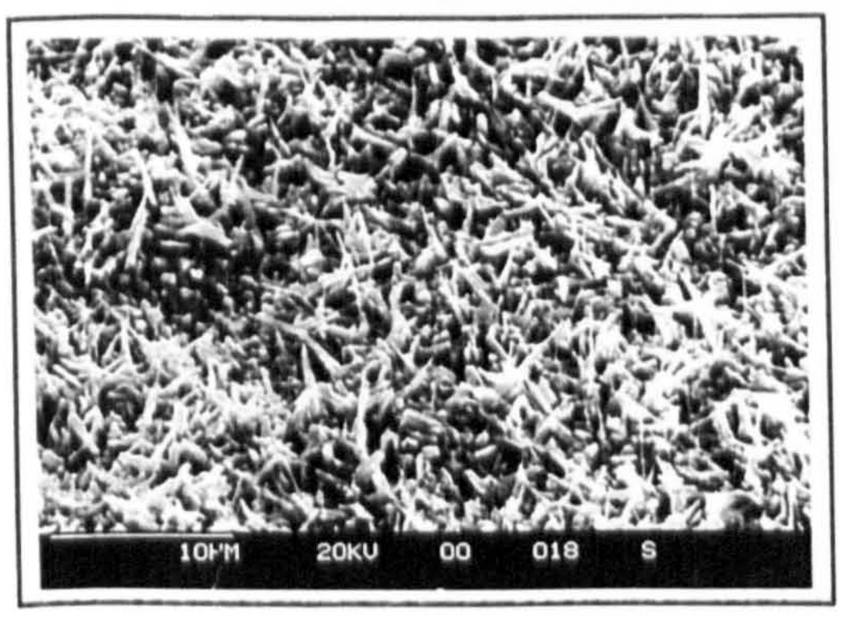

Photograph 8.2.4g: 100h at 750°C

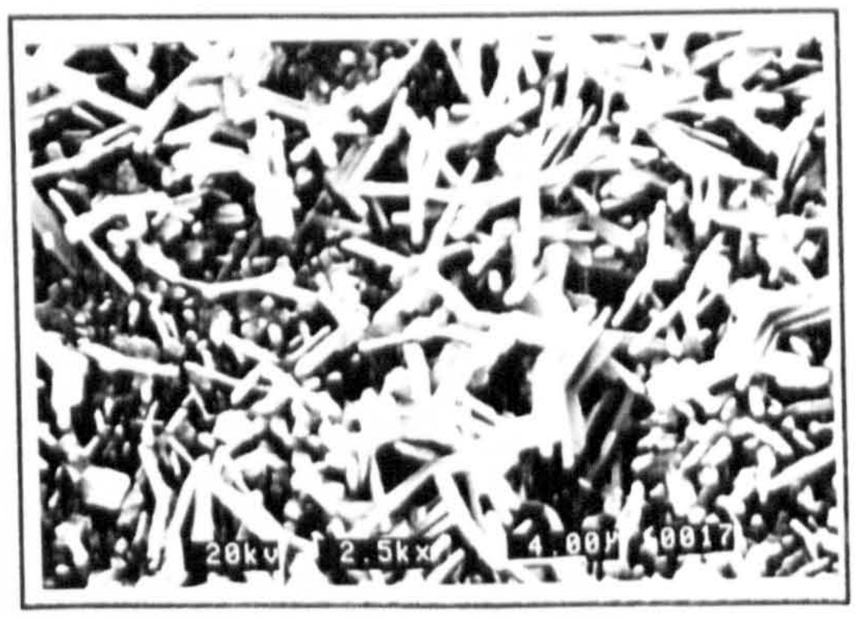

Photograph 8.2.4h: 100h at 800°C

Photographs 8.2.4a to 8.2.4h show the development of surface scale with temperature and time in air and in the prescence of salt.

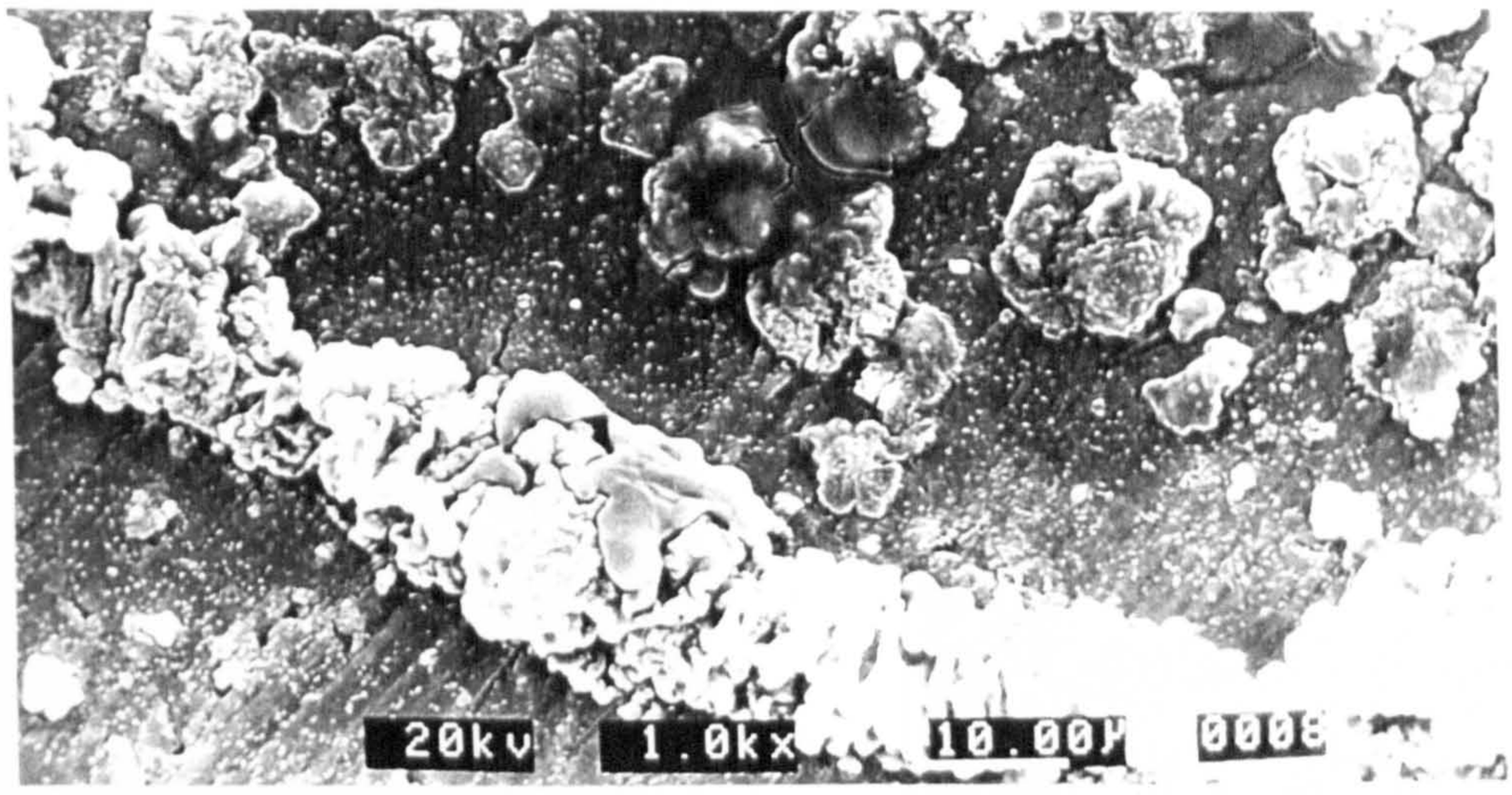

Photograph 8.2.4i: Salt corrosion morphology after 193 hours at 500°C in air

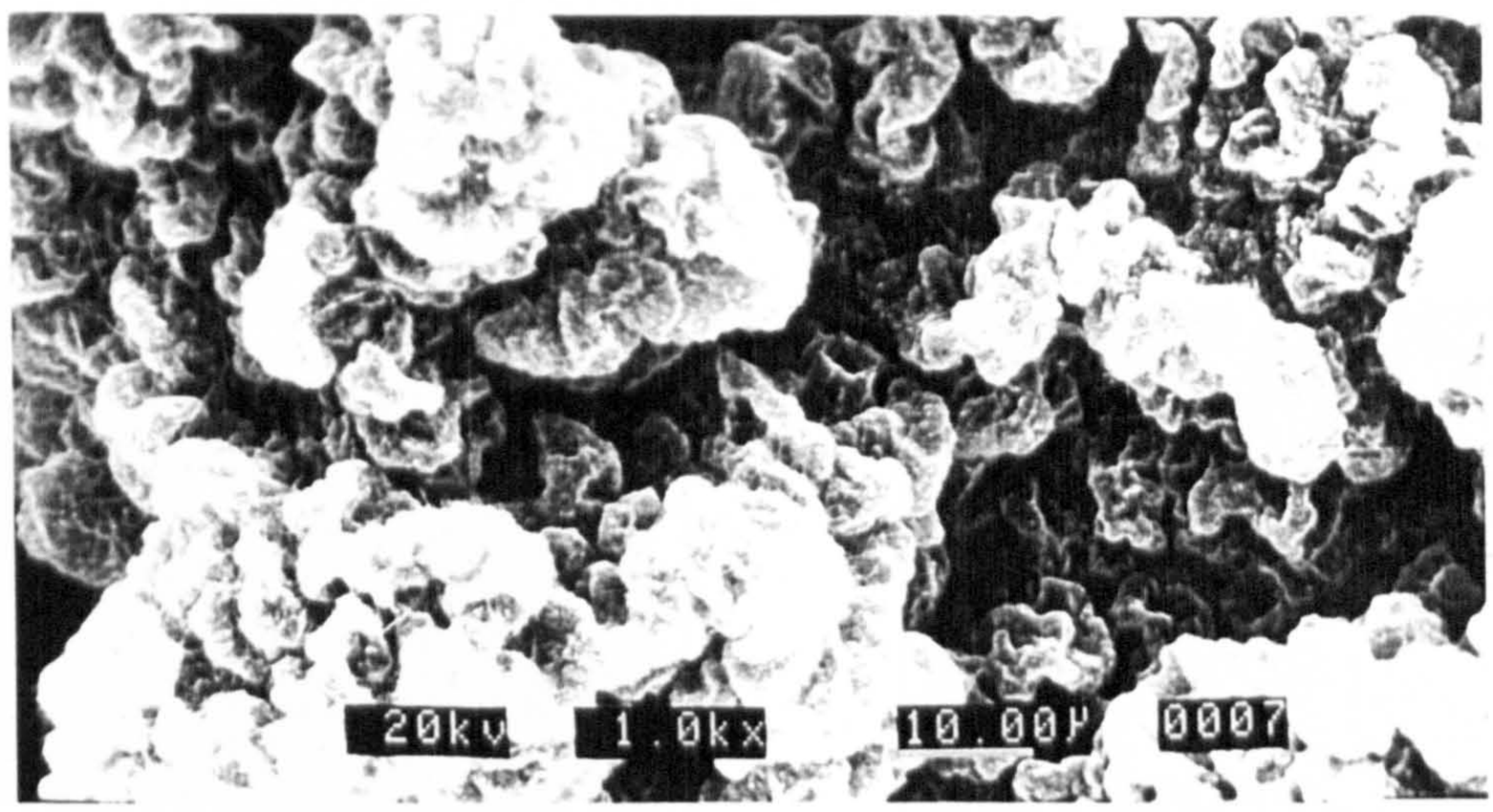

Photogragh 8.2.4j: Salt corrosion morphology after 500 hours at 500°C in air

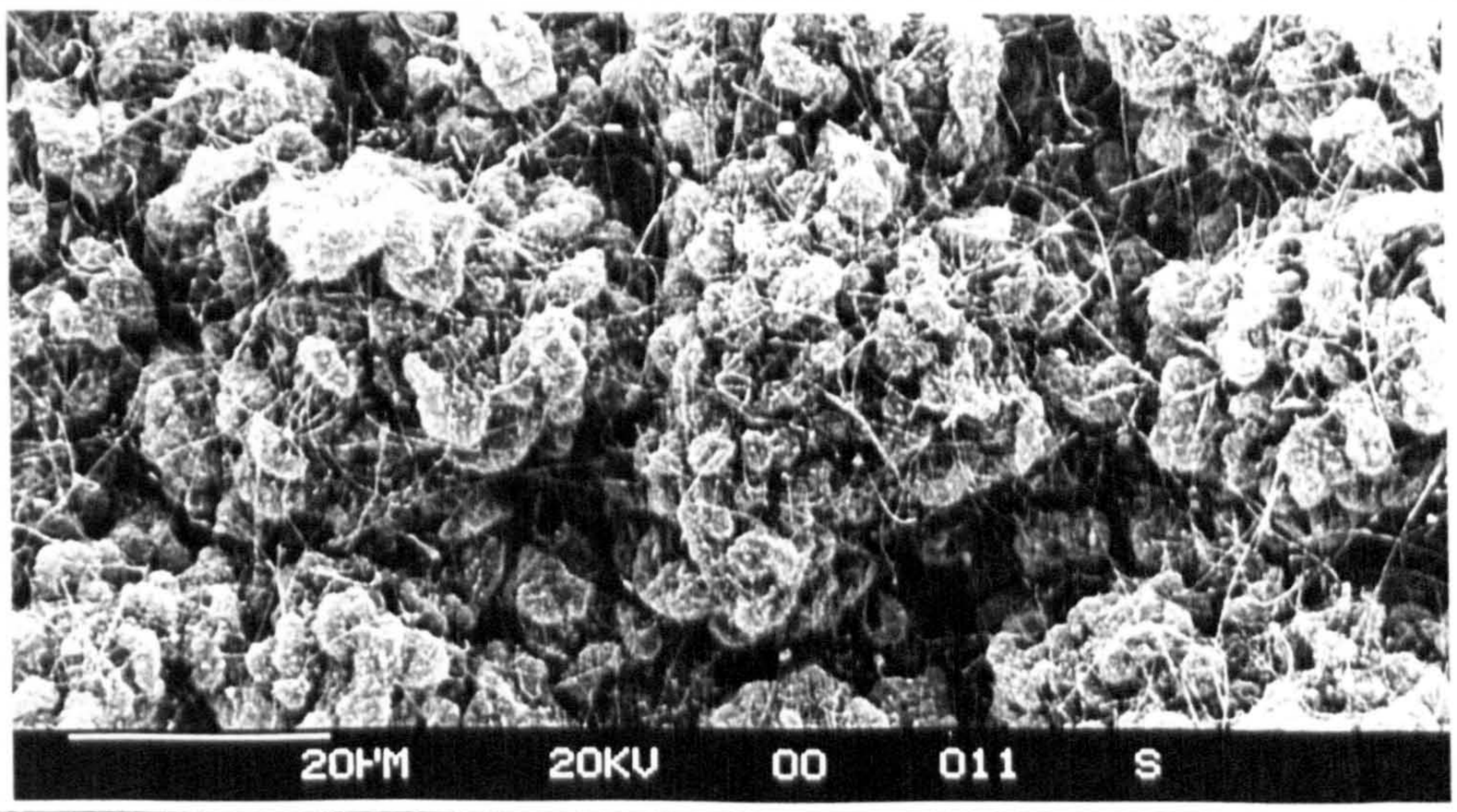

Photogragh 8.2.4k: Salt corrosion morphology after 1000 hours at 500°C

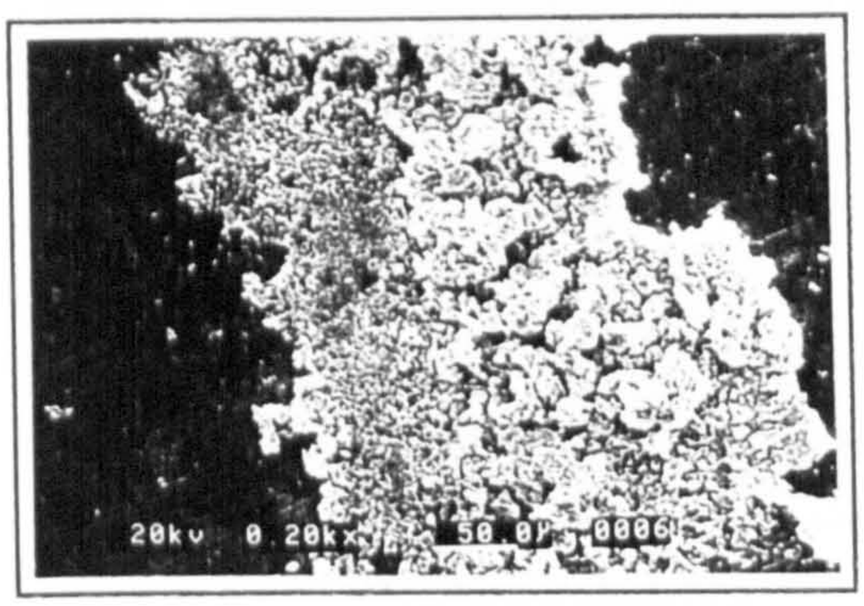

Photograph 8.2.4l:2h at 650°C

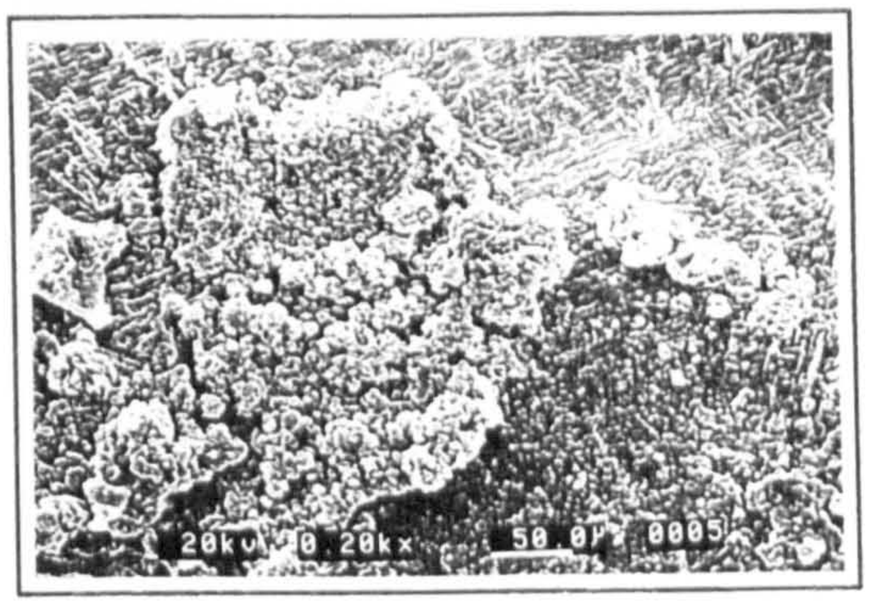

Photograph 8.2.4m: 2h at 650°C

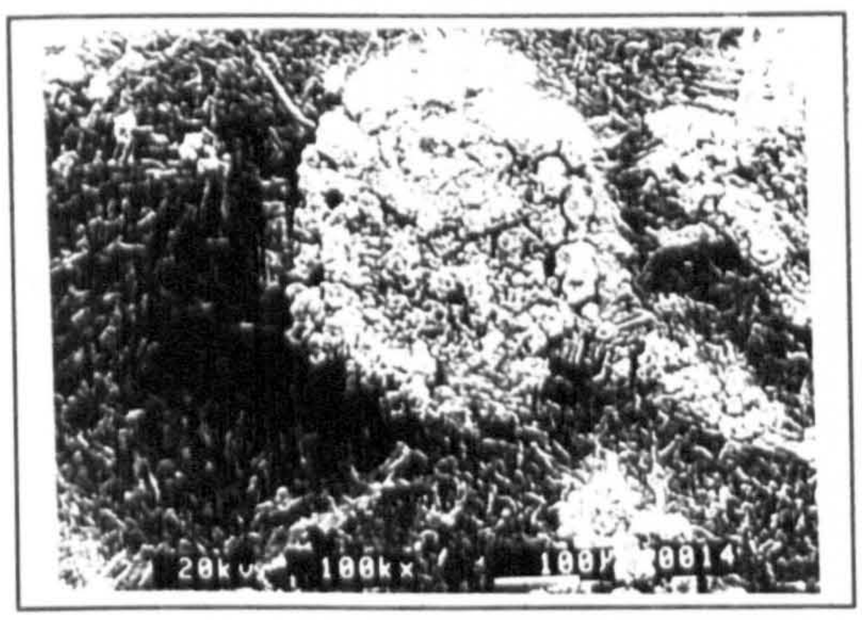

Photograph 8.2.4n: 11h at 650°C

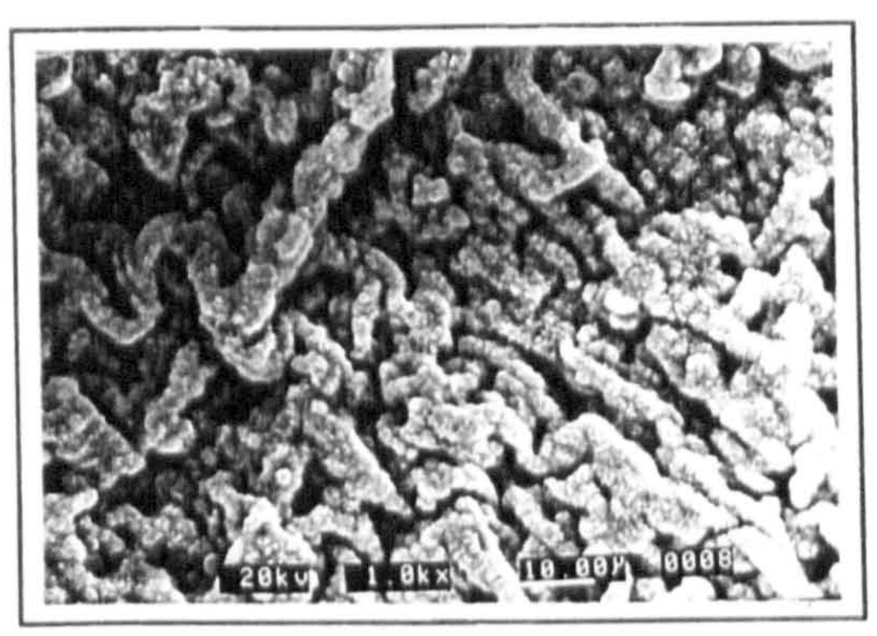

Photograph 8.2.4o: 11h at 650°C

Photographs 8.2.4l to 8.2.4o: Show the development of surface scale after 2 and 11 hours at 650°C in the prescence of salt.

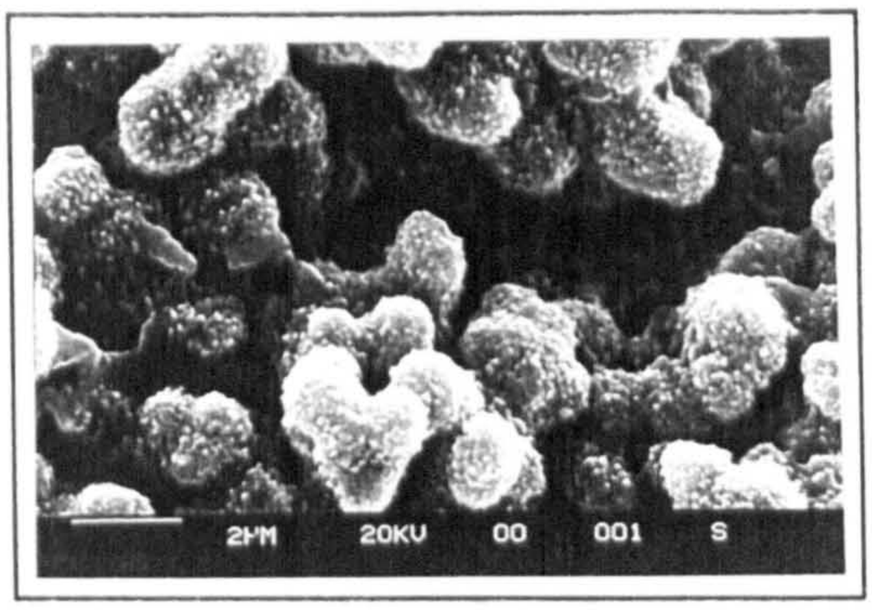

Photograph 8.2.4p: 1h at 700°C
7.0kx

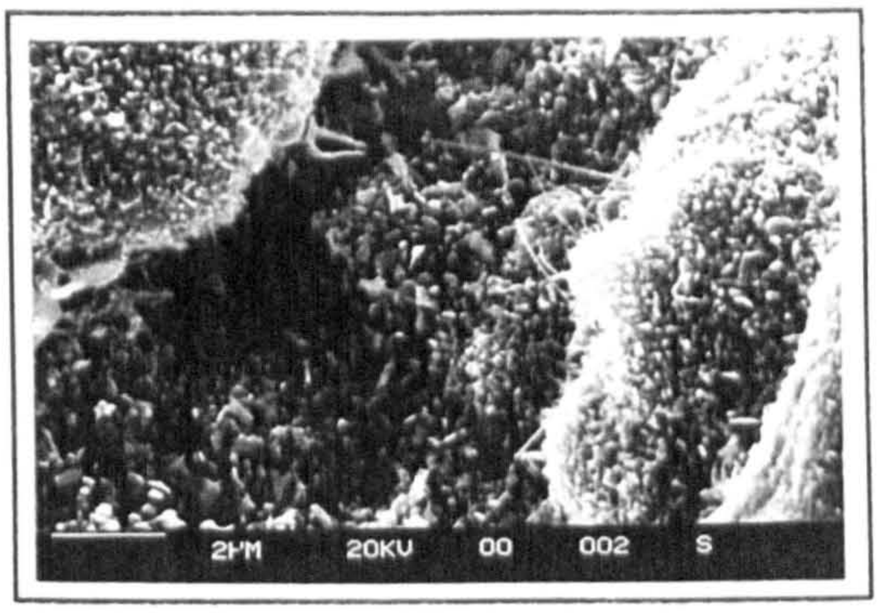

Photograph 8.2.4q: 2h at 700°C
7.0kx

Photographs 8.2.4p to 8.2.4s: S.E.M micrographs showing the development of whiskers at 700°C with time.

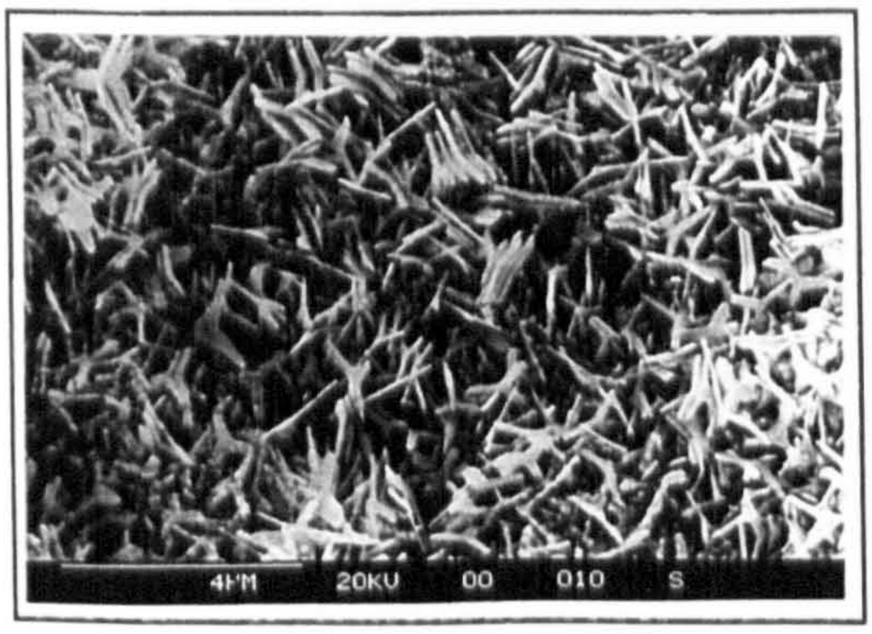

Photograph 8.2.4r: 10h at 700°C
8.0kx

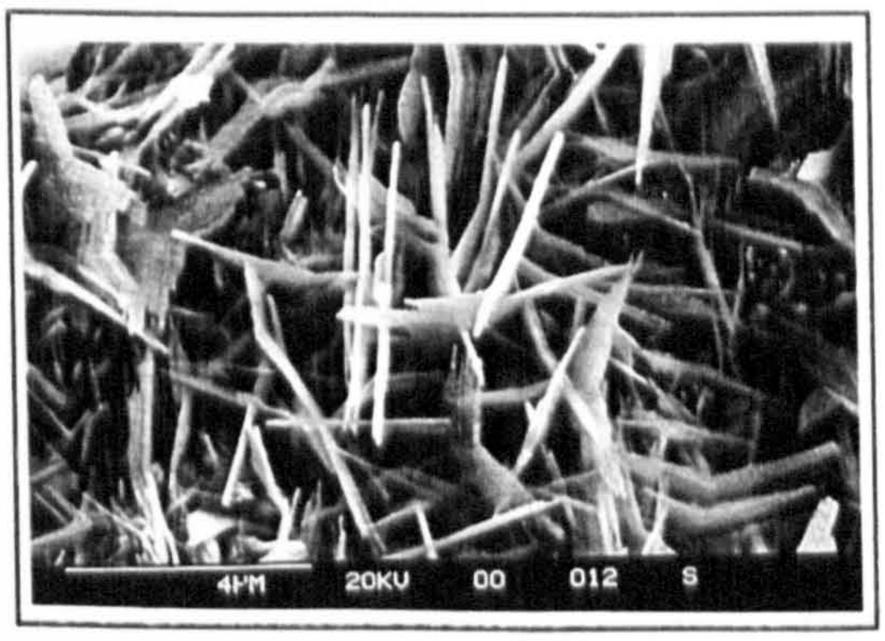

Photograph 8.2.4s: 20h at 700°C
8.0kx

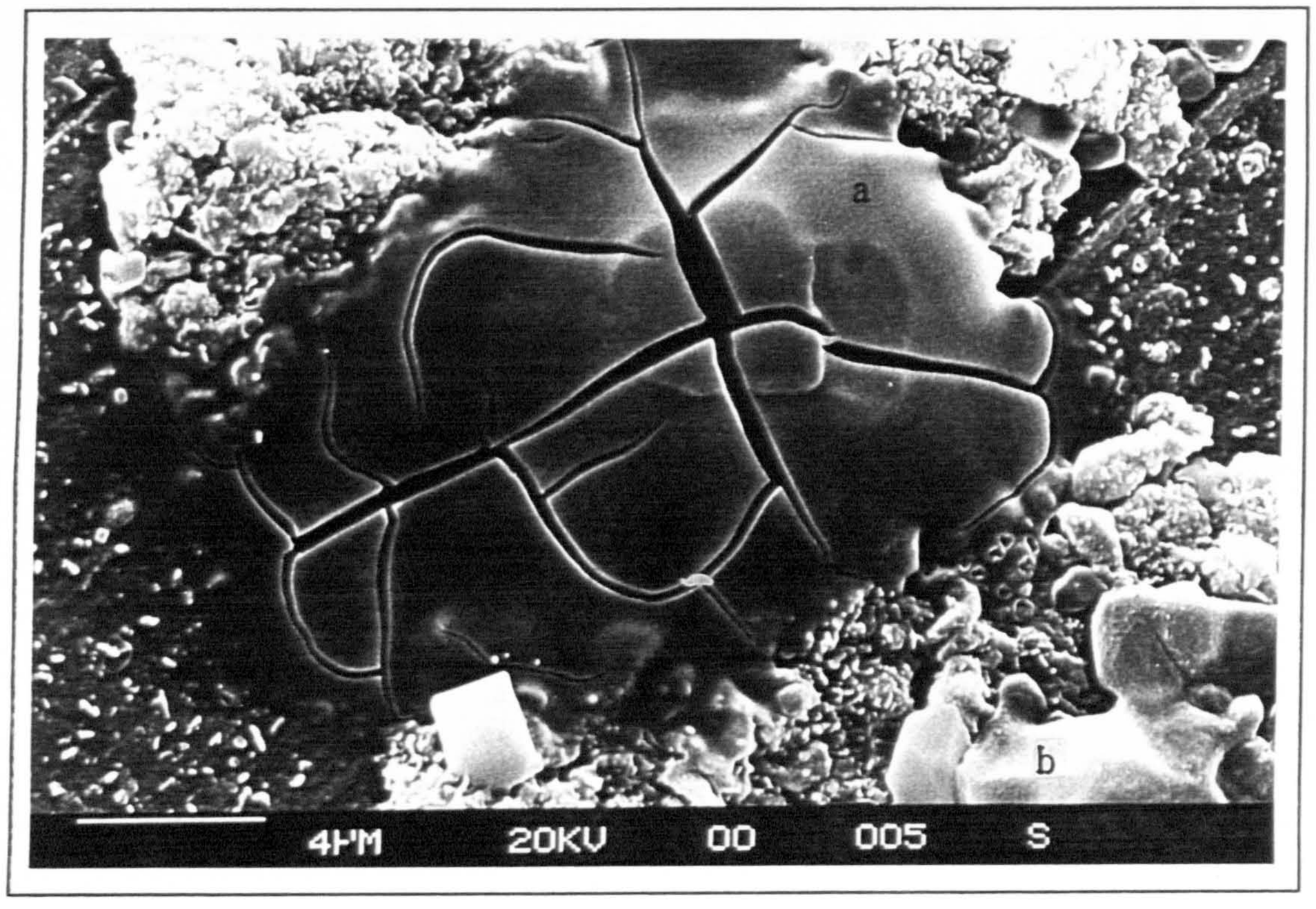

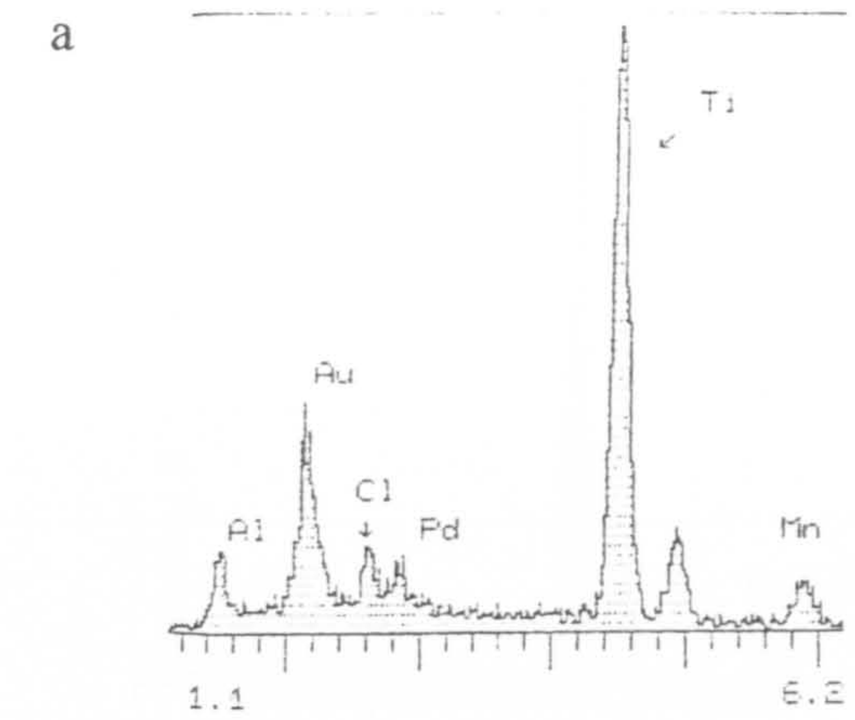

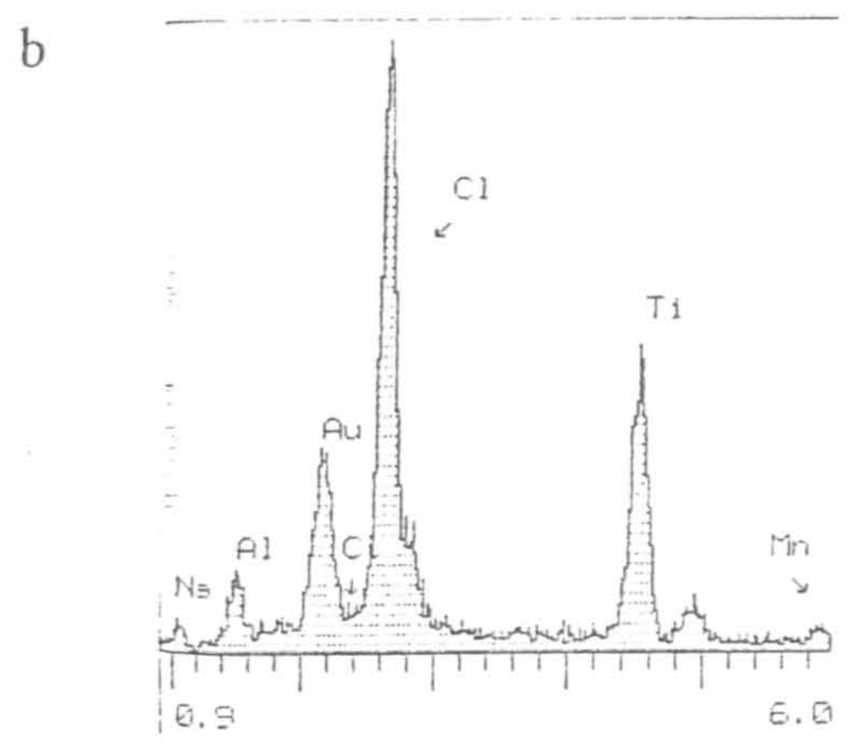

Photograph 8.2.4t: S.E.M micrograph of a salt coated specimen exposed for 193 hours at 500°C. The mudflat cracks provide evidence of the existence of low melting point eutectics having existed. EPMA's identify the liquid phase to have been titanium rich with equal levels of aluminium, manganese and chlorine. The area surrounding these cracks are identified as being NaCl rich.

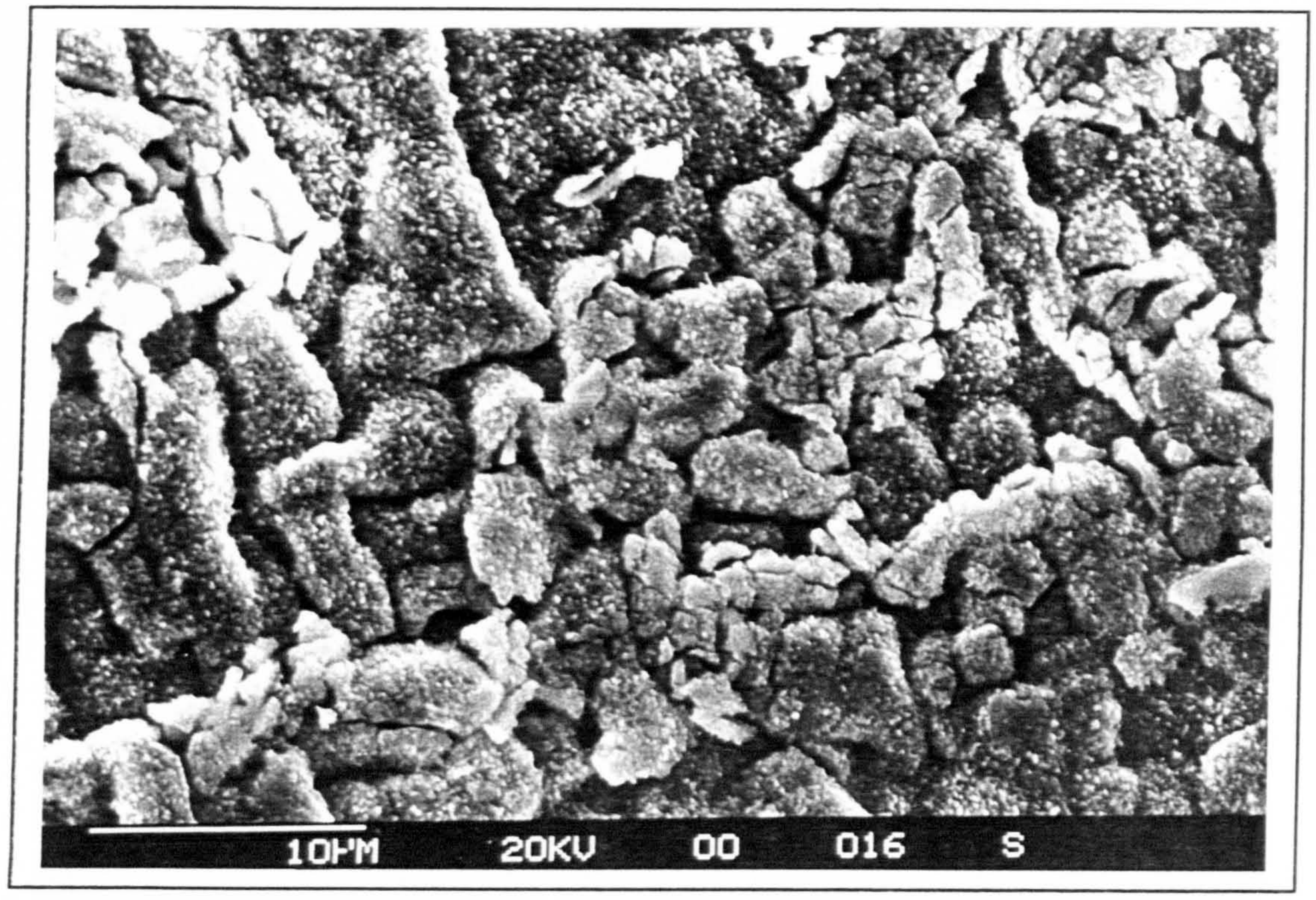

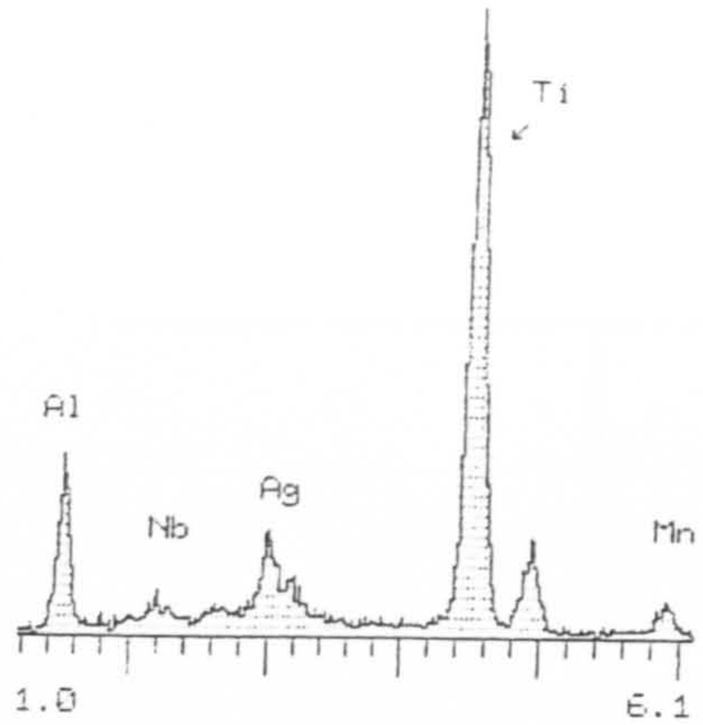

General

Photograph 8.2.4u: S.E.M micrograph of a salt coated specimen exposed for 100 hours at 600°C. The accompanying EPMA analysis' were taken from two areas encompassing the above features.

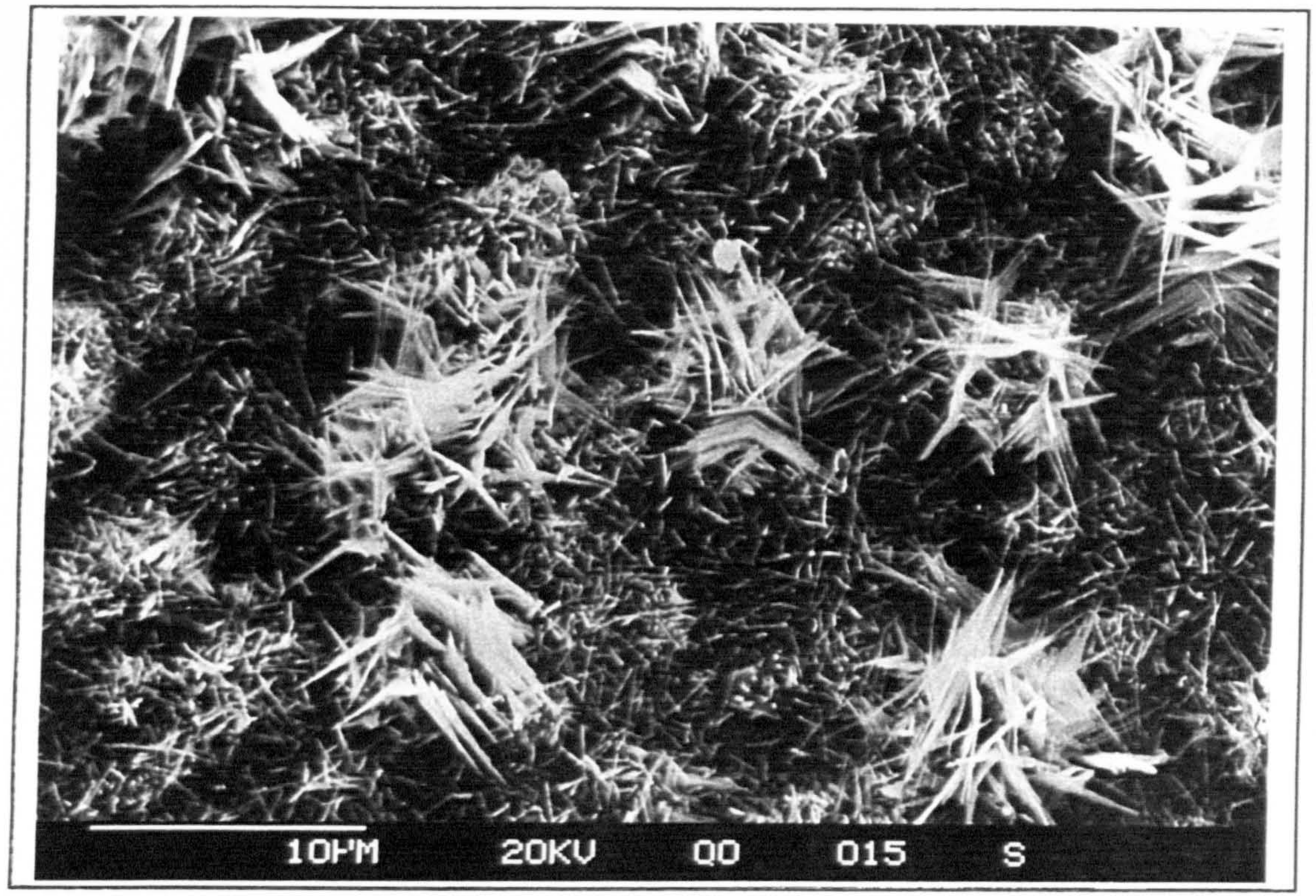

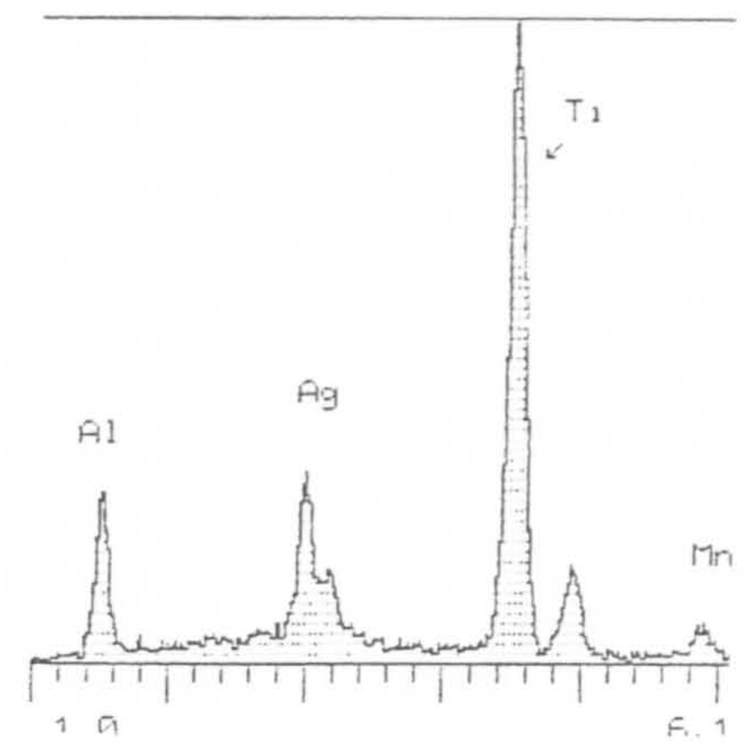

General

Photograph 8.2.4v: S.E.M micrograph of a salt coated specimen exposed for 100 hours at 650°C. The accompanying EPMA analysis shows the high level of background titanium.

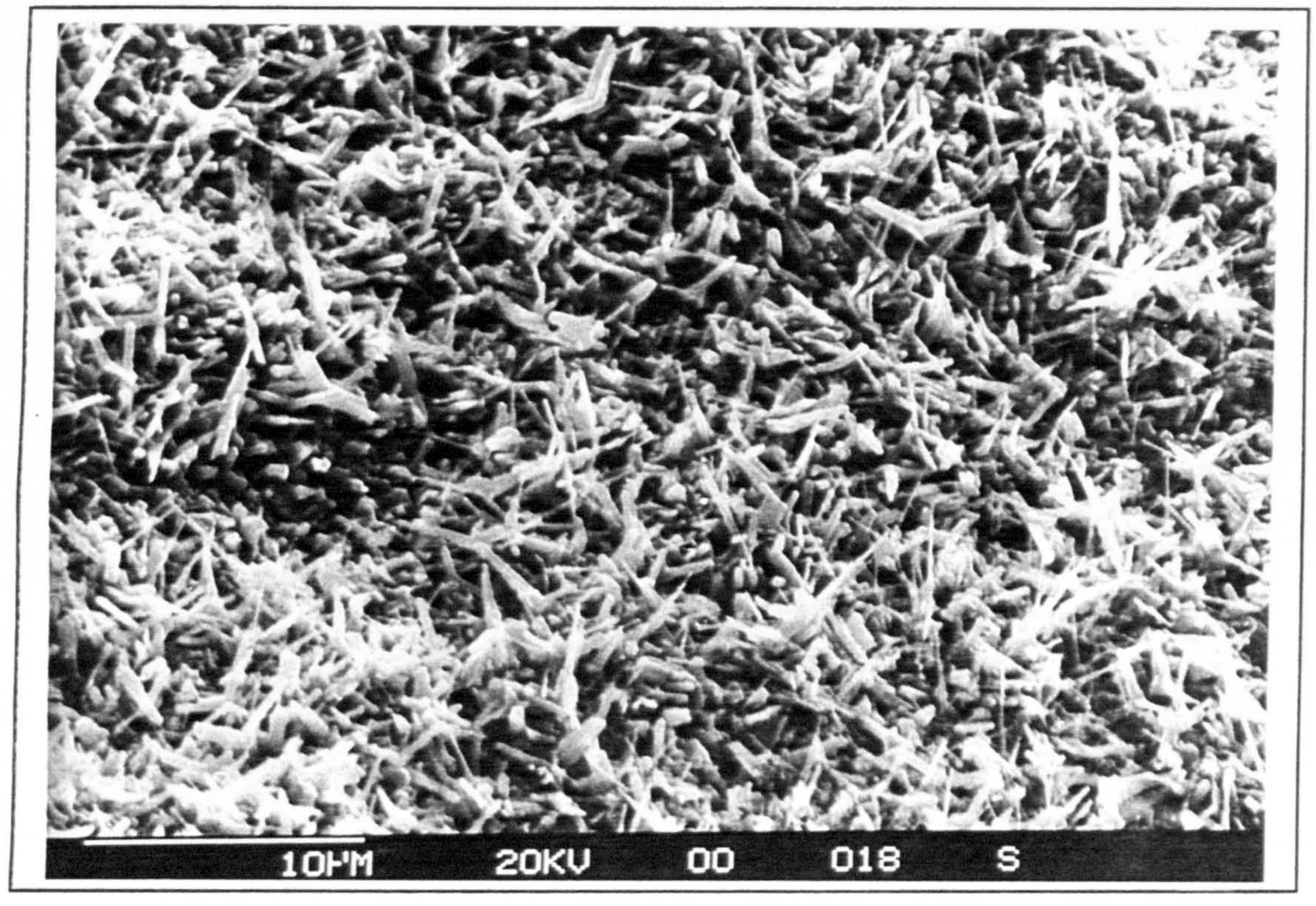

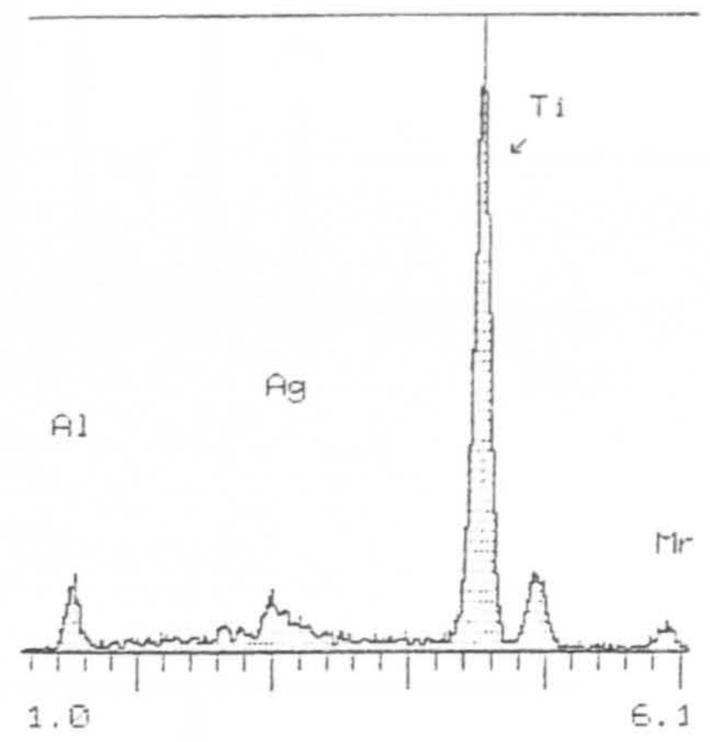

General

Photograph 8.2.4w: S.E.M micrograph of a salt coated specimen exposed for 100 hours at 750°C. The accompanying EPMA analysis shows the high level of background titanium, but aluminium and manganese still present.

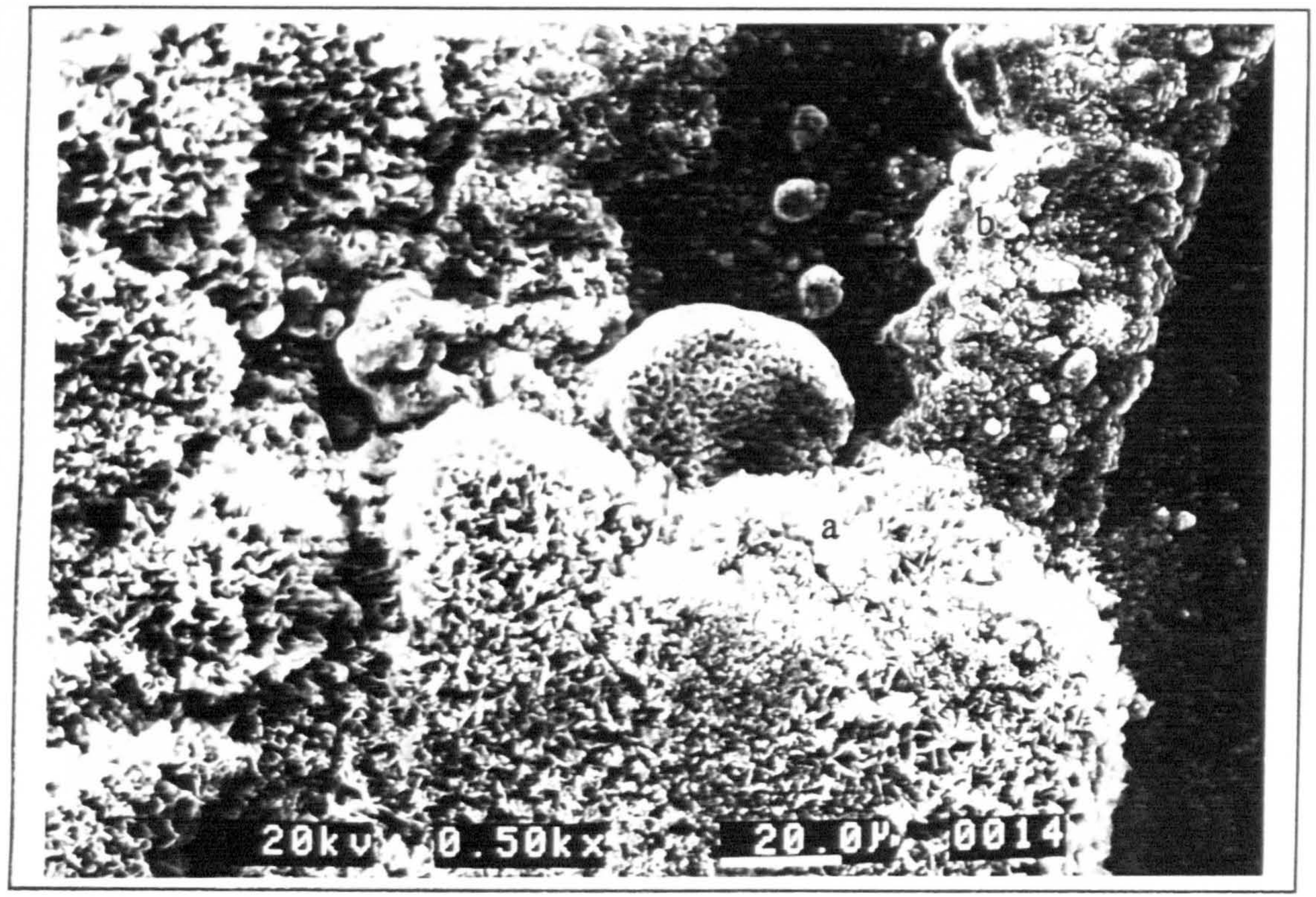

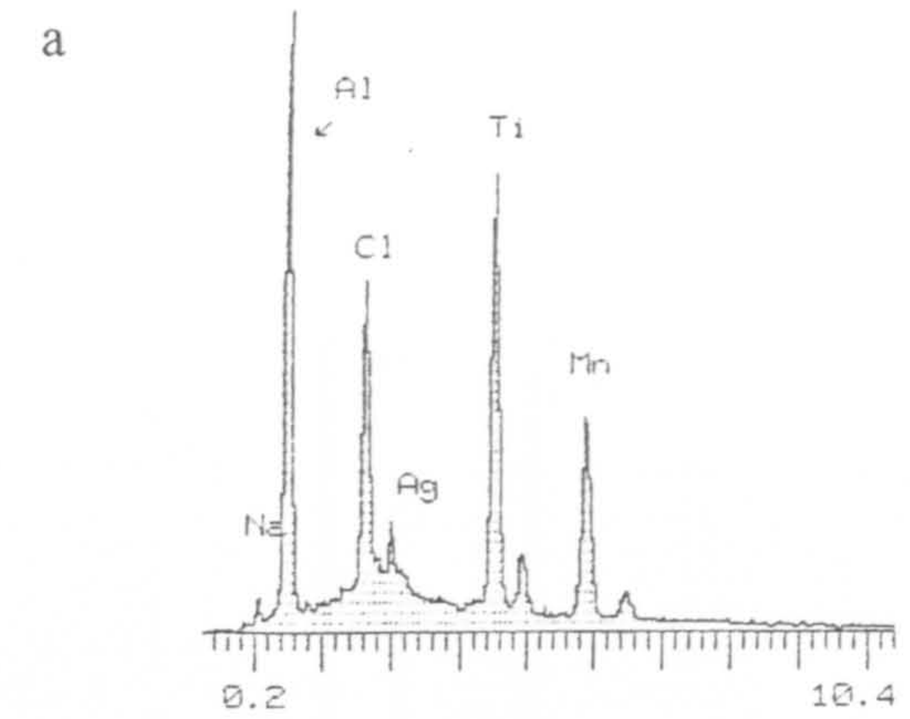

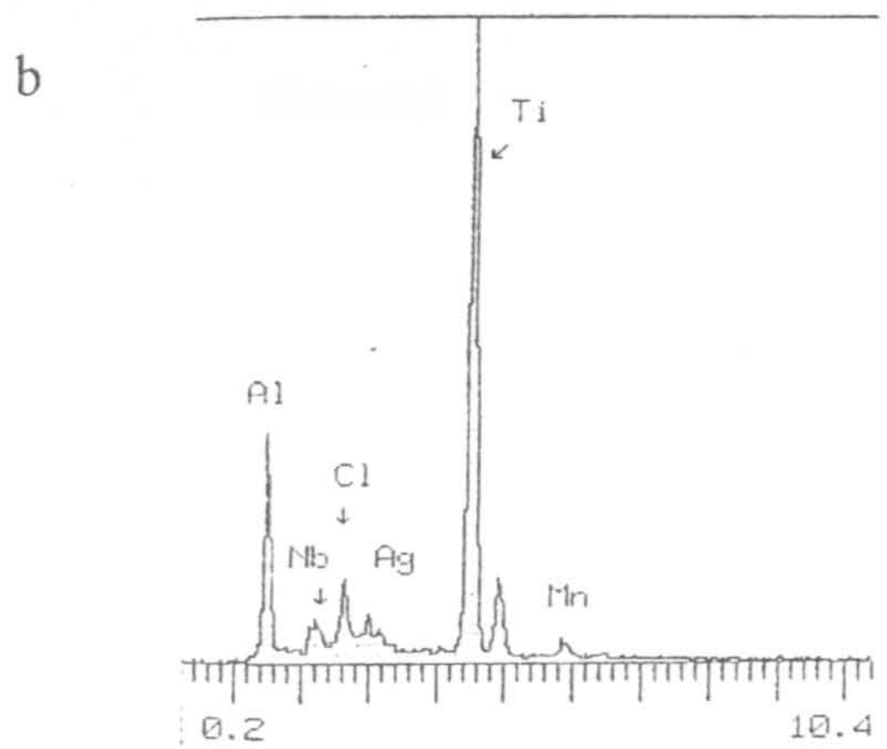

Photograph 8.2.4x: S.E.M micrograph of a salt coated specimen exposed for 15 minutes at 700°C. The accompanying EPMA analysis' show the initial salt deposits to quickly become saturaated in high levels of aluminium, titanium, and manganese. The salt can be seen to be forming "shelves" around these salt deposits. The EPMA showed that lower aluminium, chlorine and manganesse levels were detected.

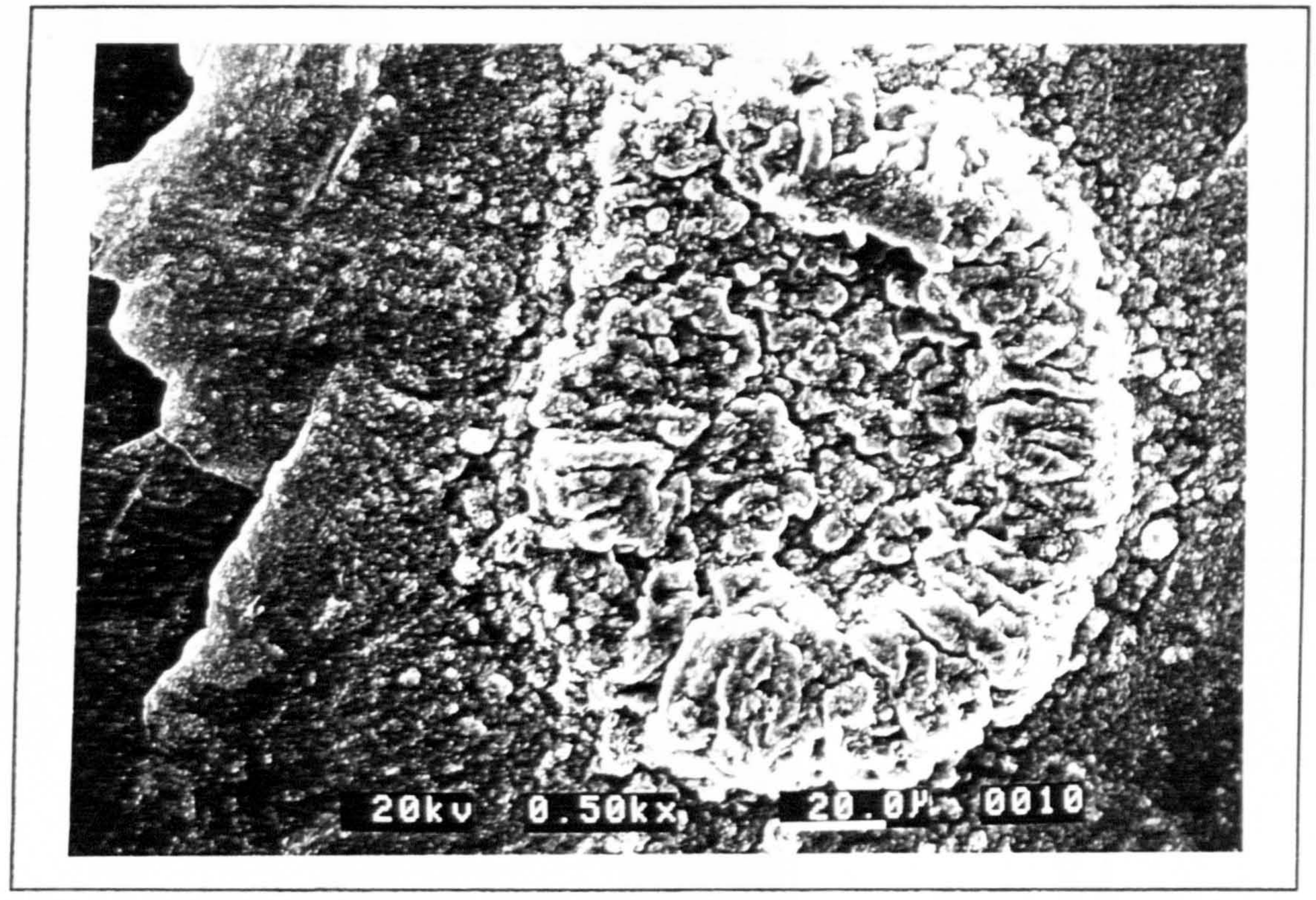

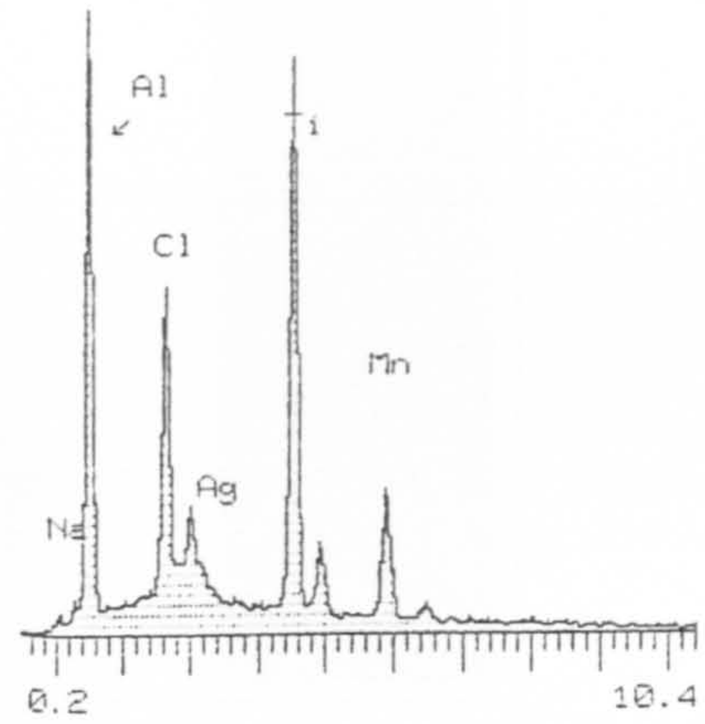

General

Photograph 8.2.4y: S.E.M micrograph of a salt coated specimen exposed for 30 minutes at 700°C. The accompanying EPMA analysis shows the high levels of aluminium and titanium. However, a comparison with the 15 minute exposure at this temperature shows an increase in the amount of titanium to similar aluminium levels. There also appears to be a decrease in the level of manganese

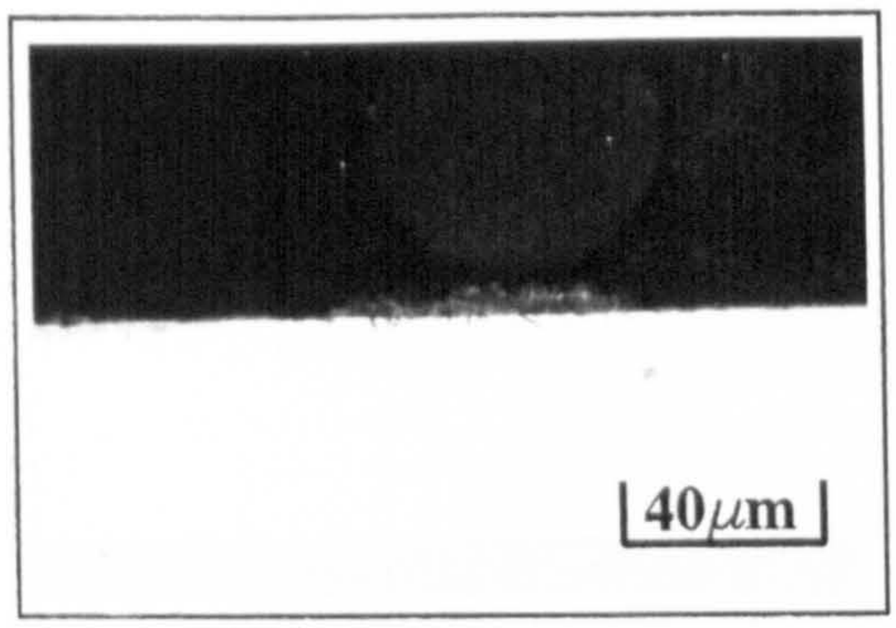

Photograph 8.2.4z: 100h at 550°C, 150x Optical

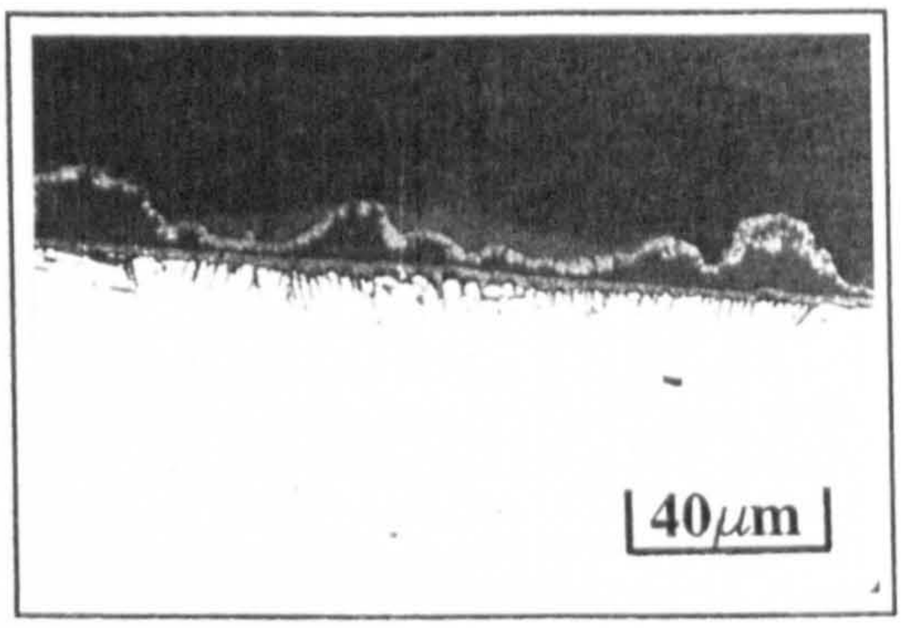

Photograph 8.2.4aa: 100h at 600°C, 150x Optical

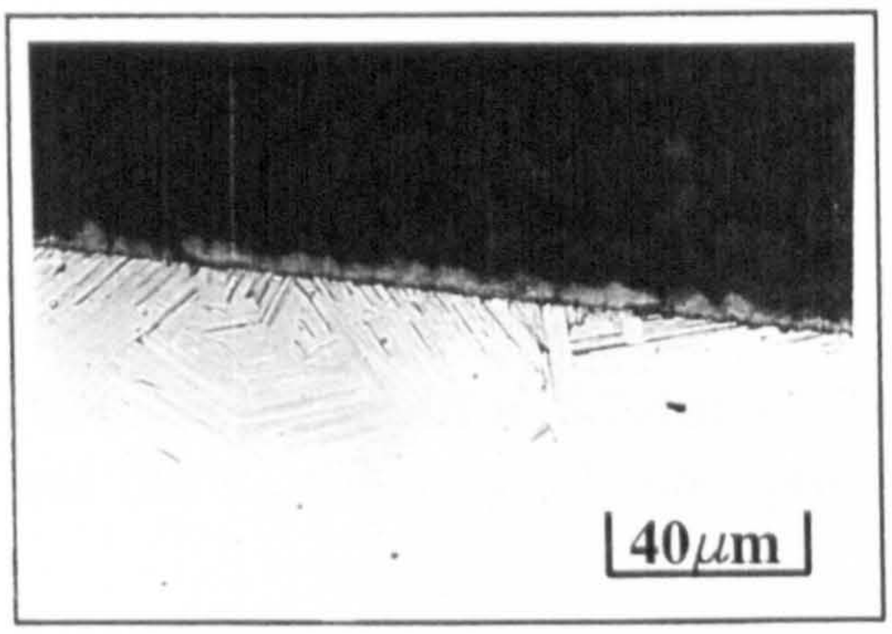

Photograph 8.2.4bb: 100h at 650°C, 150x Optical

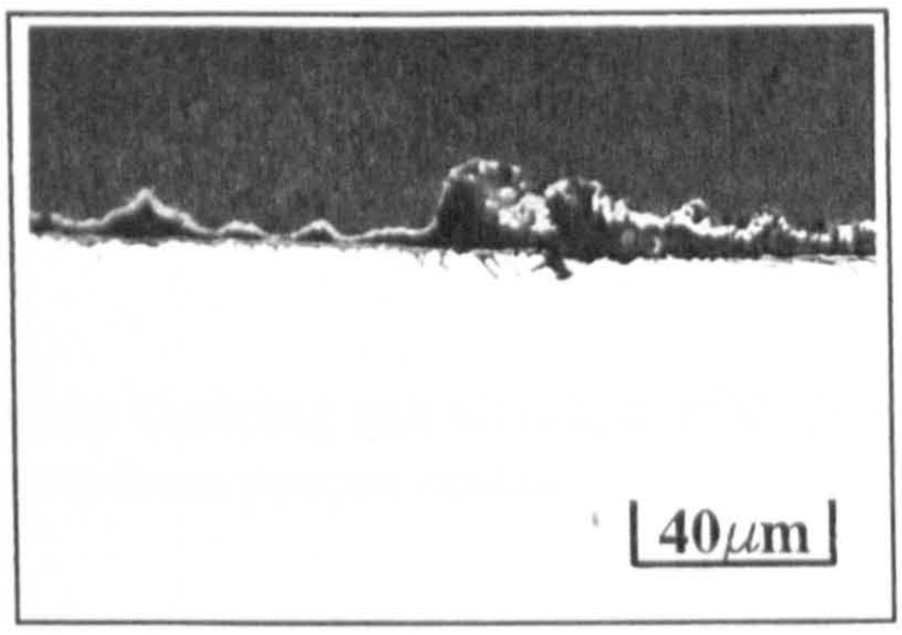

Photograph 8.2.4cc: 100h at 675°C, 150x Optical

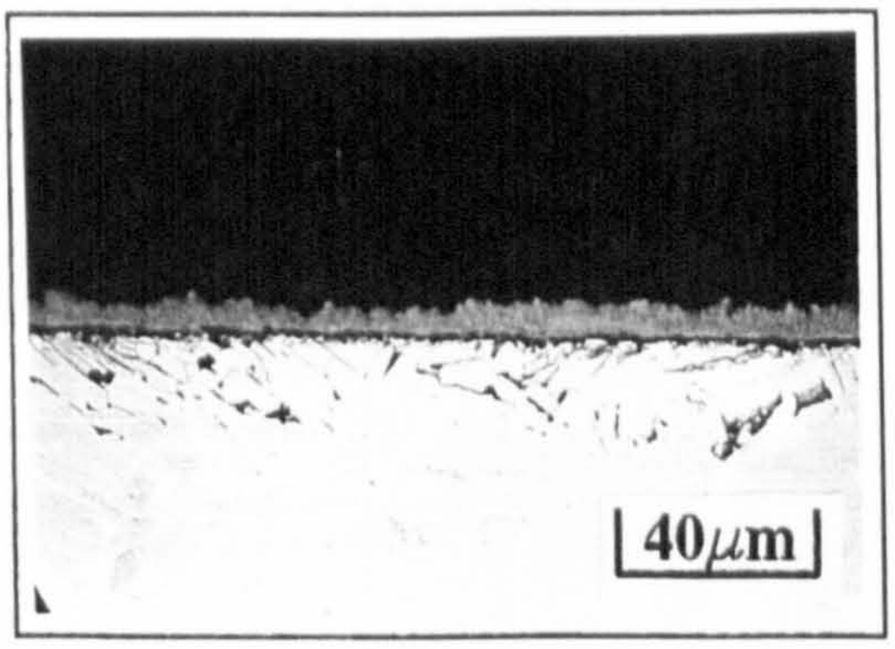

Photograph 8.2.4dd: 100h at 700°C 150x Optical

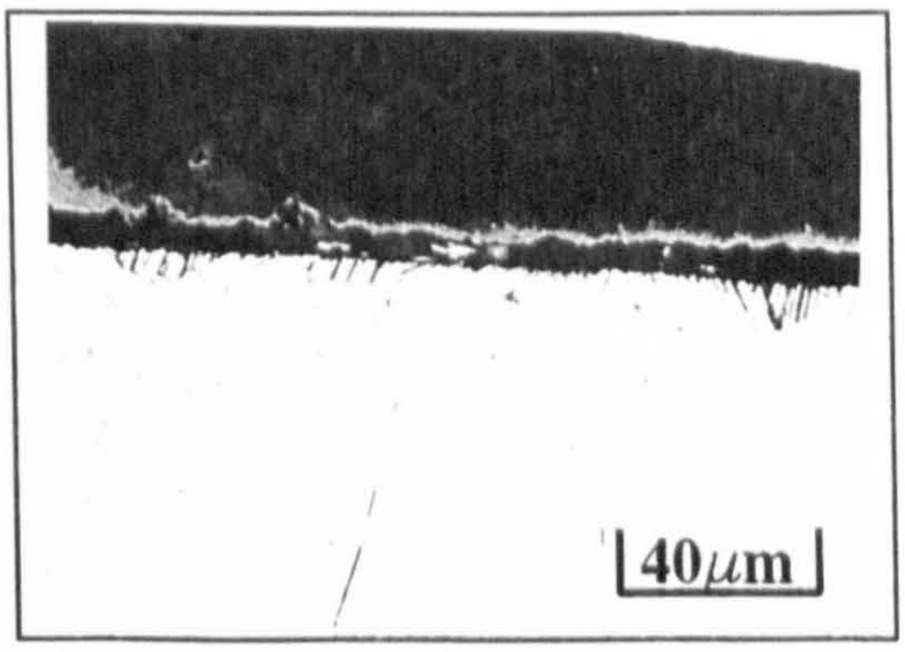

Photograph 8.2.4ee: 100h at 725°C 150x Optical

Photographs 8.2.4z to 8.2.4ee: Show the severity of substrate attack after 100 hours between 550 and 725°C, in the presence of salt.

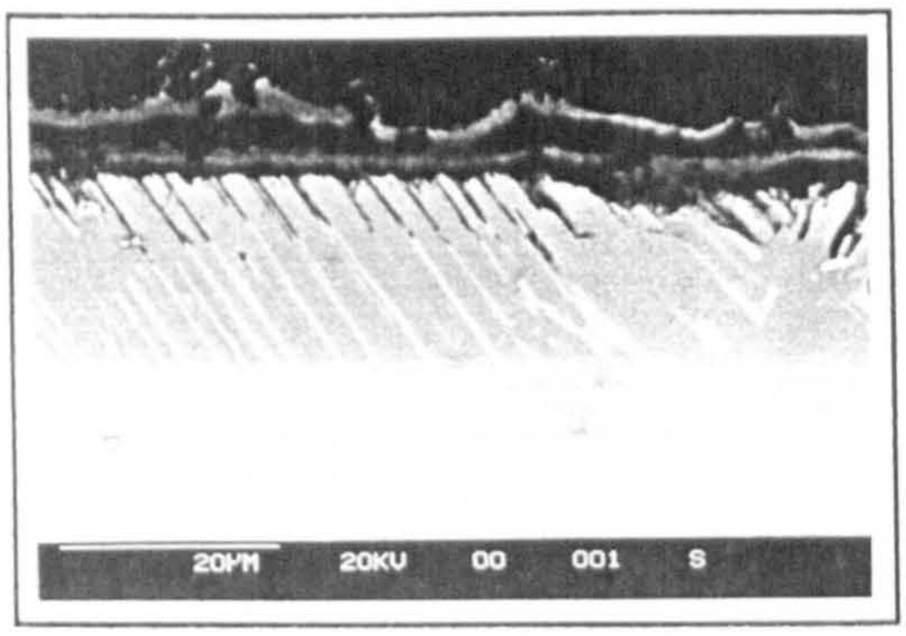

Photograph 8.2.4ff: 100h at 600°C
1.5kx

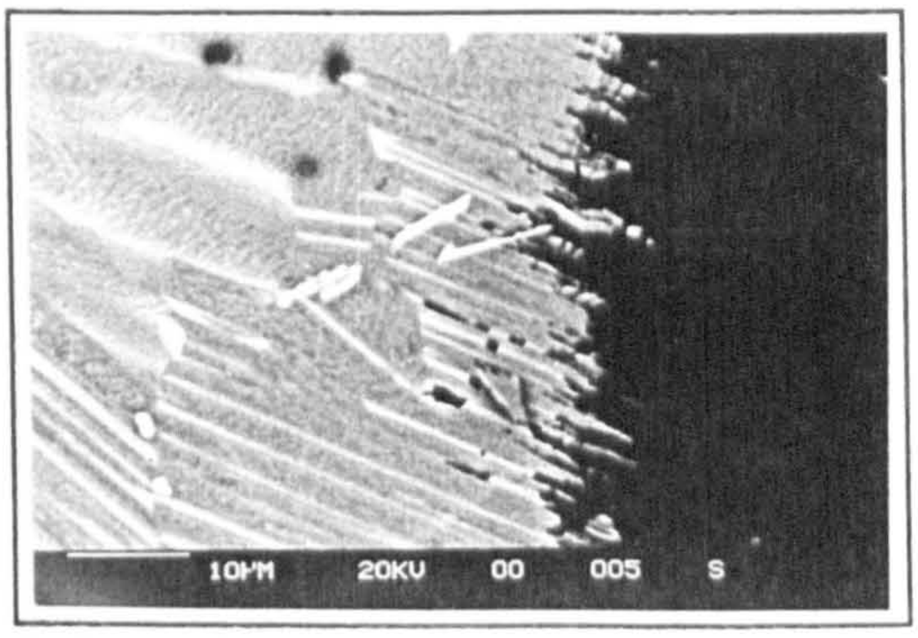

Photograph 8.2.4gg: 100h at 700°C
1.5kx

Photographs 8.2.4ff to 8.2.4ii: S.E.M micrographs showing salt attack, at 600, 700 and 750°C, down the α2 lathes producing non-uniform porous scales.

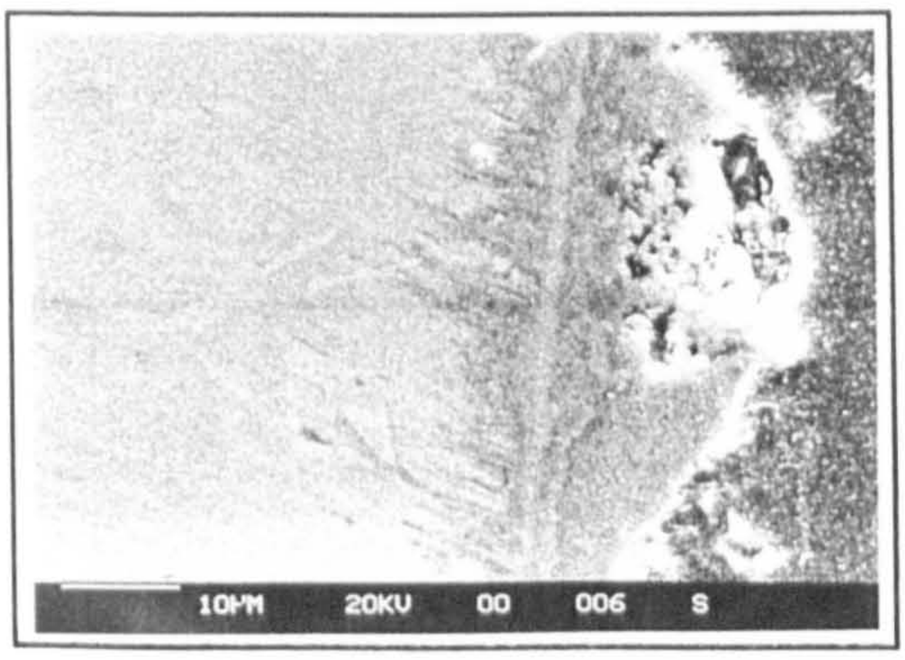

Photograph 8.2.4hh: 100h at 700°C
1.5kx

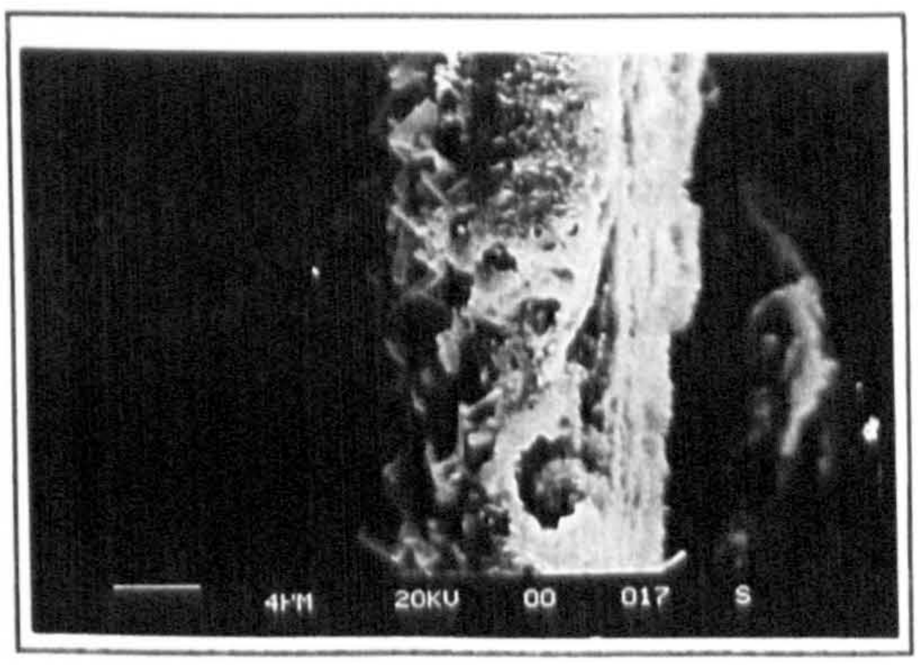

Photograph 8.2.4ii: 100h at 750°C
3.0kx

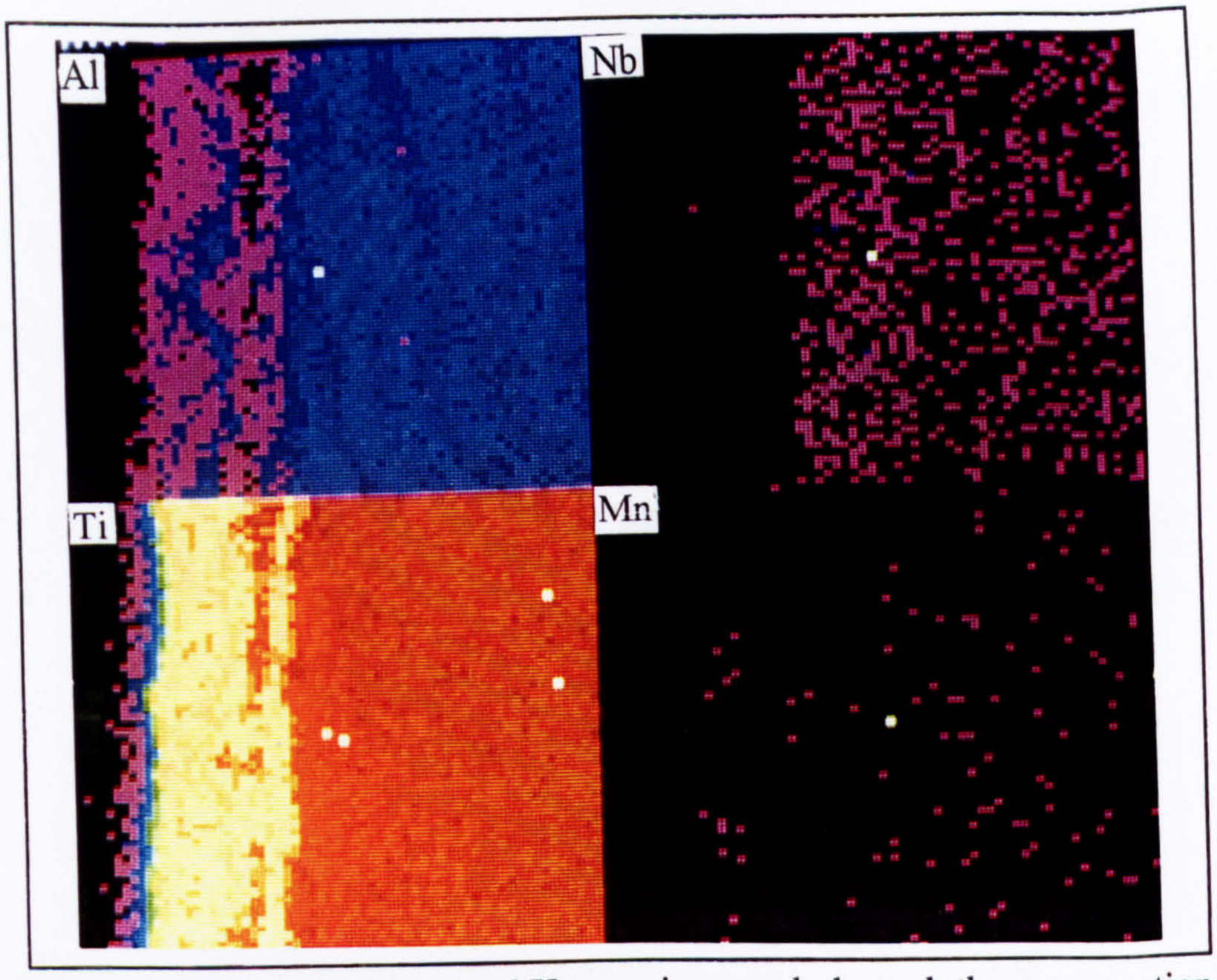

Photograph 8.2.4jj: Elemental X-ray micrograph through the cross section of the scale formed after 100 hours at 700°C in air, in the presence of salt. The concentration at a given point increases from black to white.

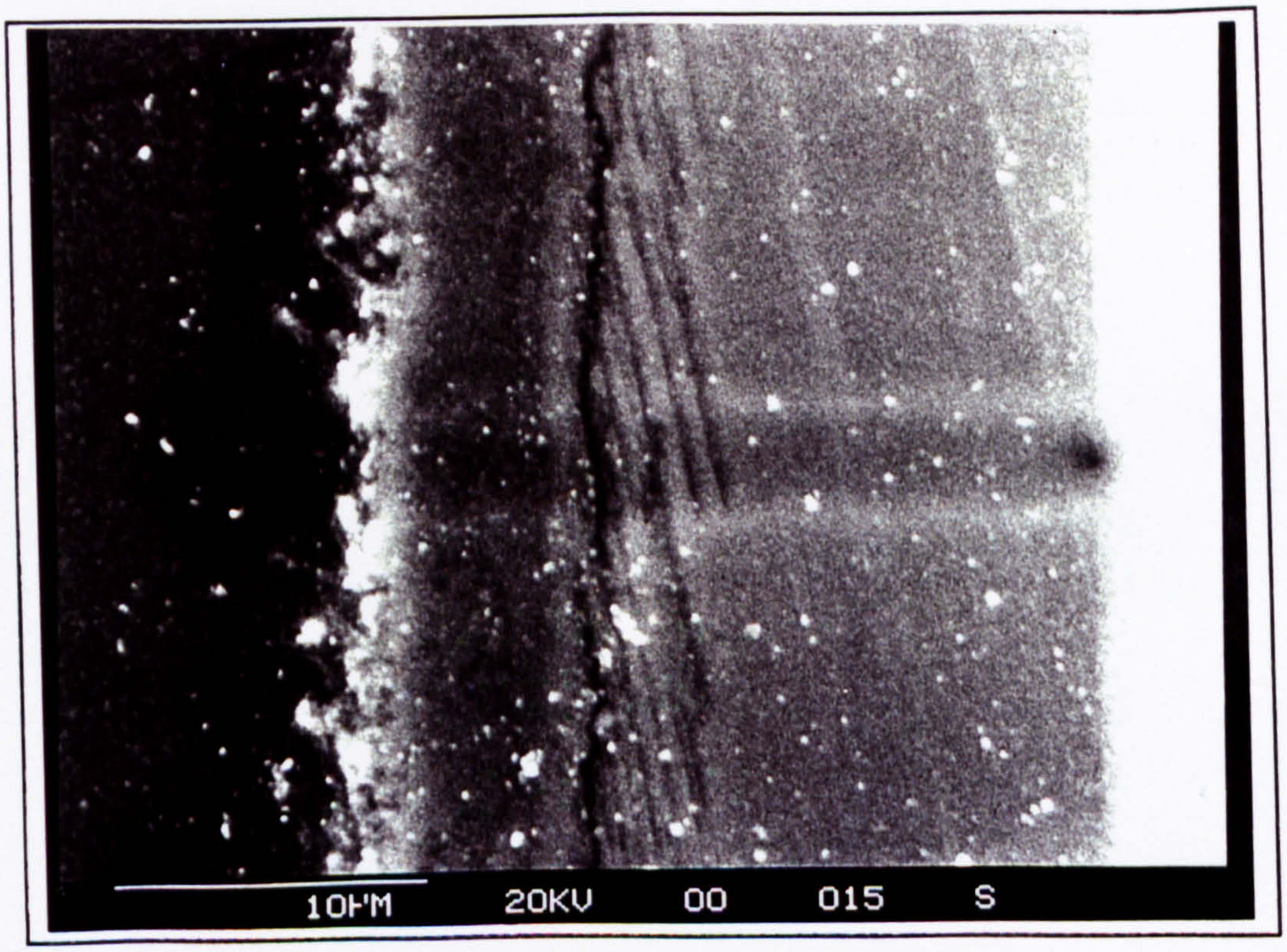

Photograph 8.2.4kk: Shows the cross section of the scale which was used to obtain the Elemental X-ray map in photograph 8.2.4jj (100 hours at 700°C, in the presence of salt)

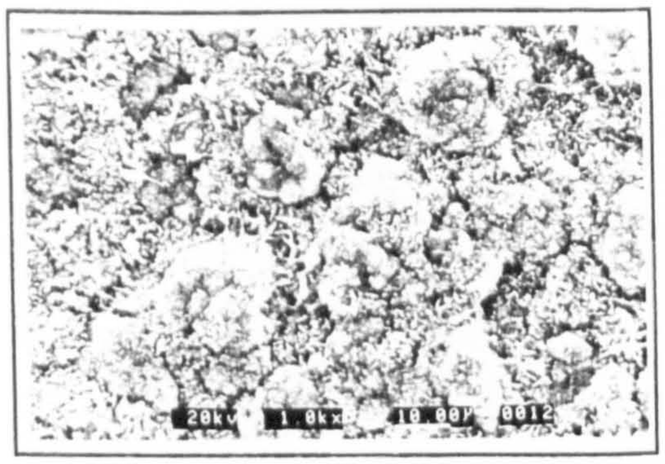

Photograph 8.2.4.2a: 20h at 700°C
Salt recoated after 0, 2, 5, 10, 15 h

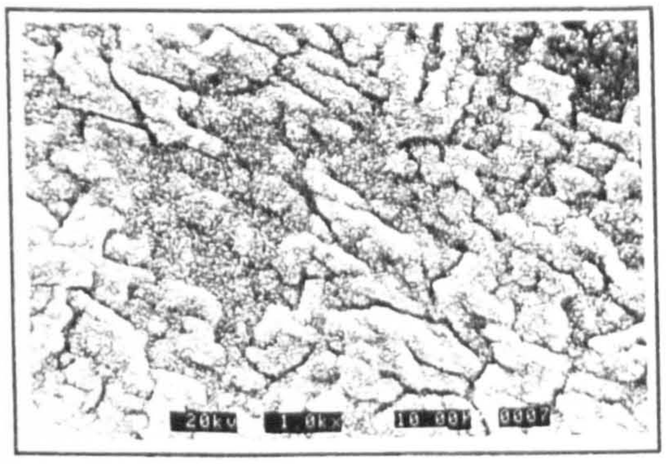

Photograph 8.2.4.2b: 20h at 700°C
Single salt coat

Photographs 8.2.4.2a and 8.2.4.2b: S.E.M micrographs showing the effect of short term salt recoating at 700°C in air.

Photographs 8.2.4.2c and 8.2.4.2d: Optical micrographs showing the effect of short term salt recoating on substrate degradation at 700°C in air.

-

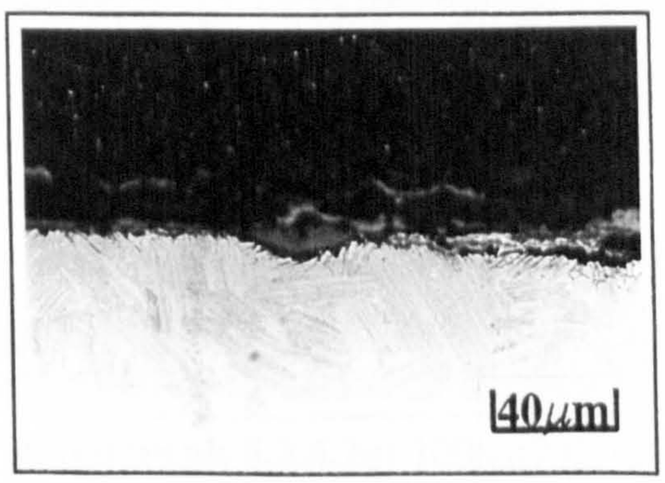

Photograph 8.2.4.2c: 20h at 700°C
salt recoated after 0, 2, 5, 10, 15h
Mag : 100x

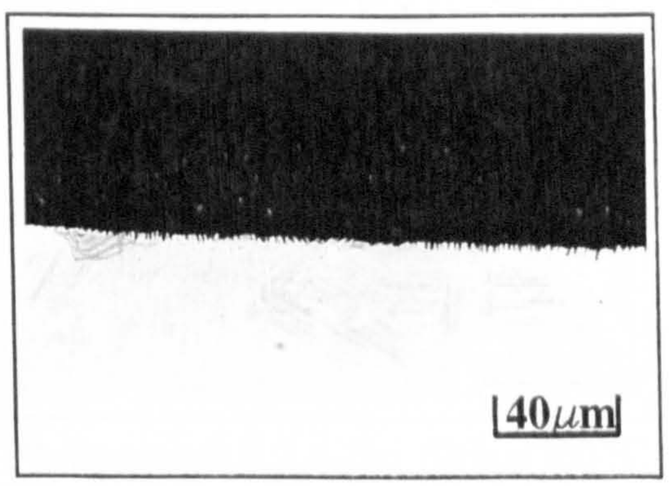

Photograph 8.2.4.2d: 20h at 700°C
Single salt coat
Mag : 100x

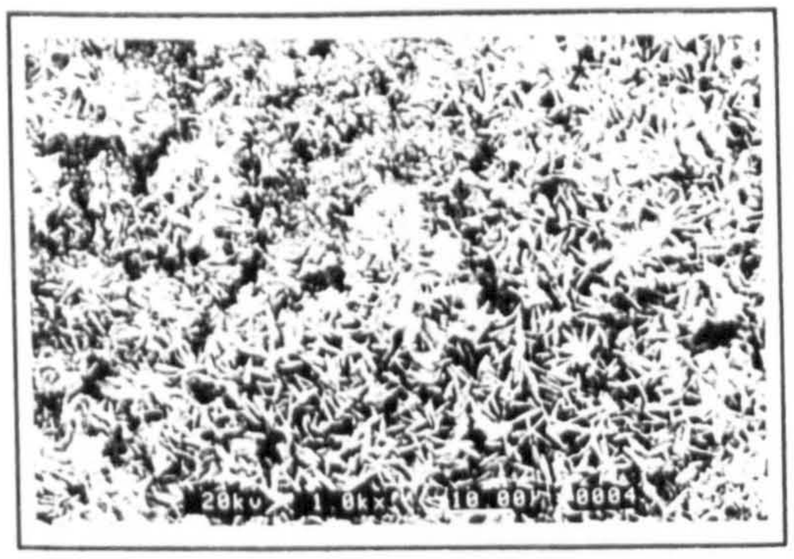

Photograph 8.2.4.2e: 100h
at700°C
Salt recoated afte 0, 20, 40, 60, 80h

Photograph 8.2.4.2f: 100hat 700°C
Single salt coat

Photographs 8.2.4.2e and 8.2.4.2f: SEM micrographs showing the effect of salt recoating every 20 hours at 700°C. Low salt concentrations [0.03-0.045mg/cm^2]

Photographs 8.2.4.2g and 8.2.4.2h: S.E.M micrographs showing the effect of salt recoating every 20 hours at 700°C. High salt concentrations [0.16-0.25mg/cm^2]

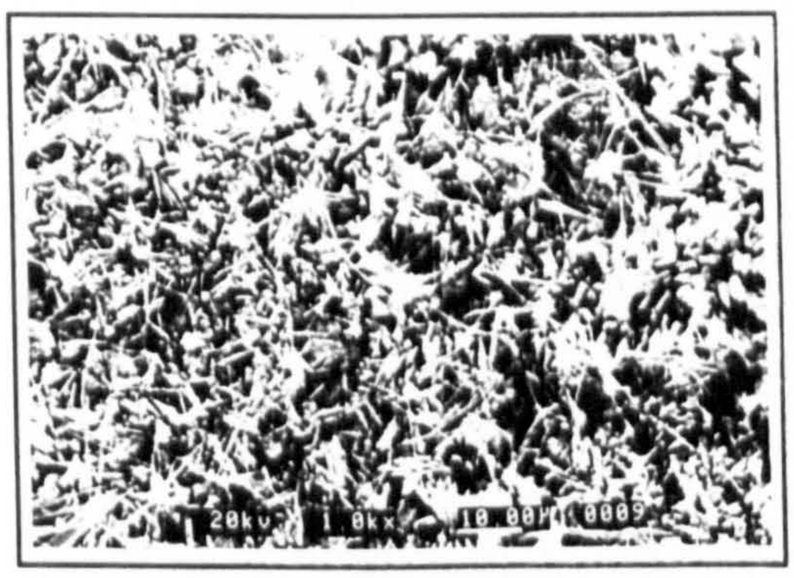

Photograph 8.2.4.2g: 100hat700°C
Salt recoated after 0, 20, 40, 60 ,80h
Mag : 100x

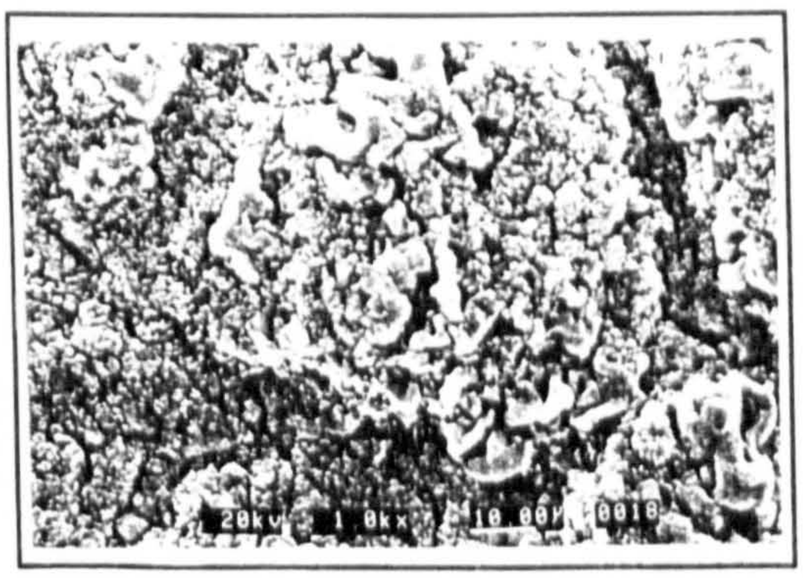

Photograph 8.2.4.2h: 100hat700°C
Single salt coat
Mag : 100x

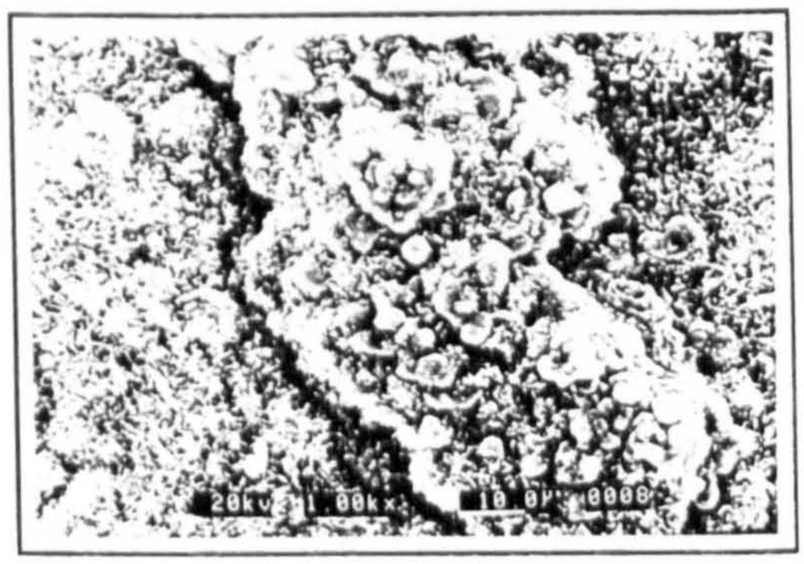

Photograph 8.2.4.2i: 200h at700°C
Salt recoated after 0,100,120,150 h

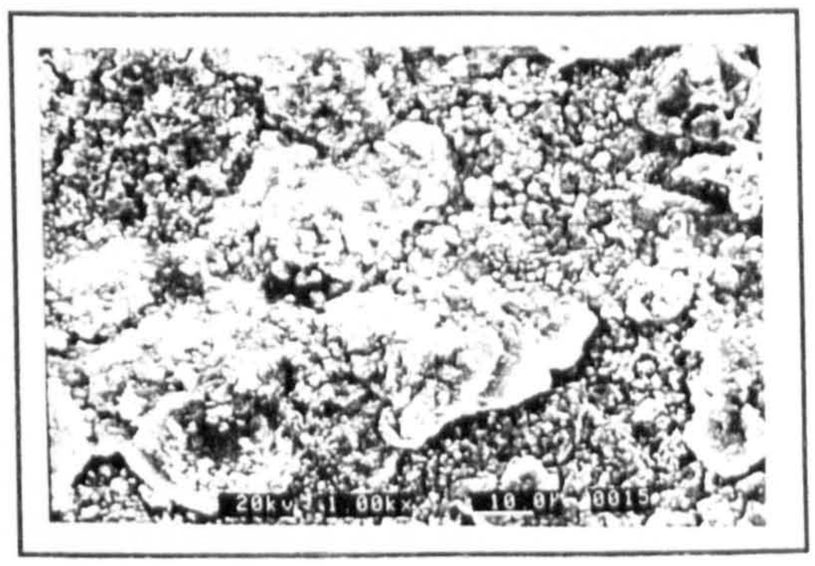

Photograph 8.2.4.2j: 200h at700°C
Single salt coat

Photographs 8.2.4.2i and 8.2.4.2j: S.E.M micrographs showing the effect of long term salt recoating at 700°C in air. Spallation occurred during recoating cycles.

Photograhs 8.2.4.2k and 8.2.4.2l: S.E.M micrographs showing the effect of long term salt recoating at 700°C in air. Minimal spallation during recoating cycles.

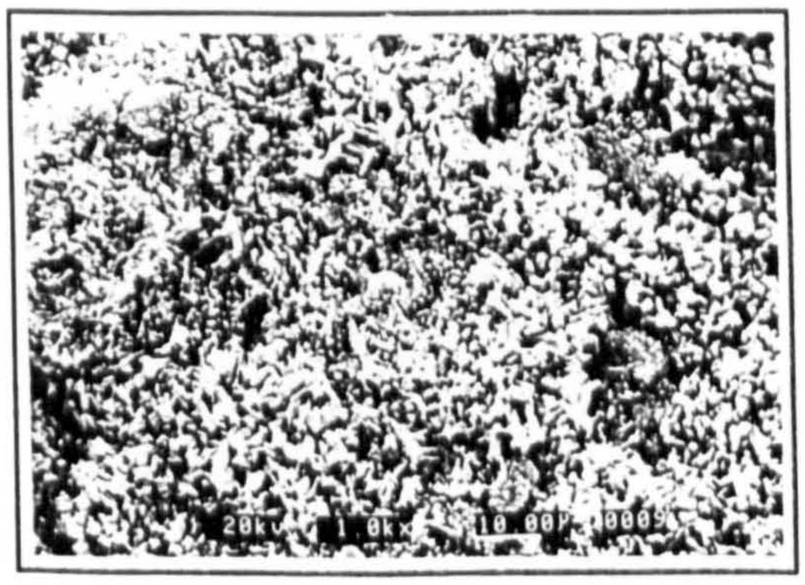

Photograph 8.2.4.2k:200h at700°C
Salt recoated after 0,100,120,150h

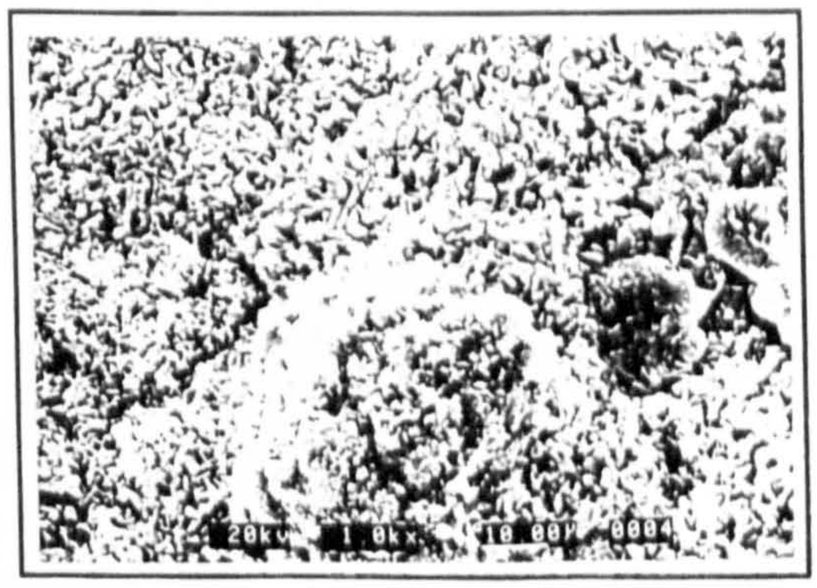

Photograph 8.2.4.2l:200h at700°C
Single salt coat

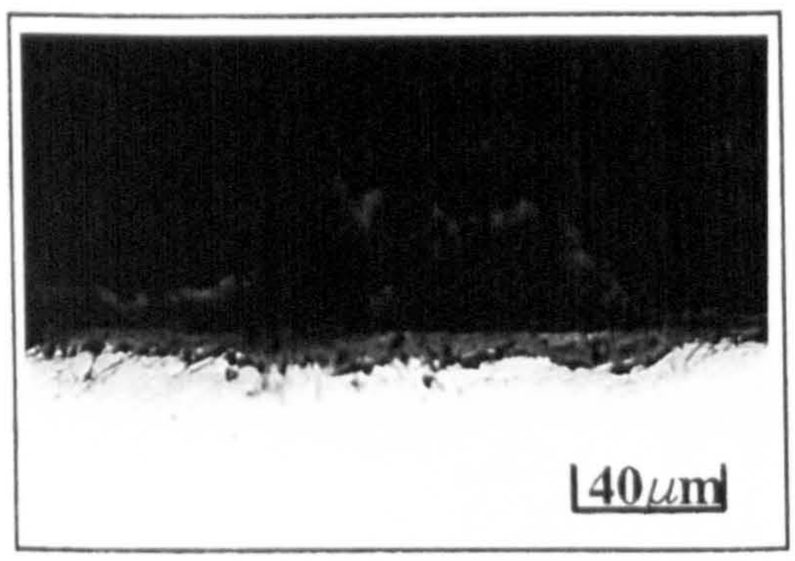

Photograph 8.2.4.2m: 100hat700°C
Salt recoated after 0,20,40,60,80h
Mag : 100x

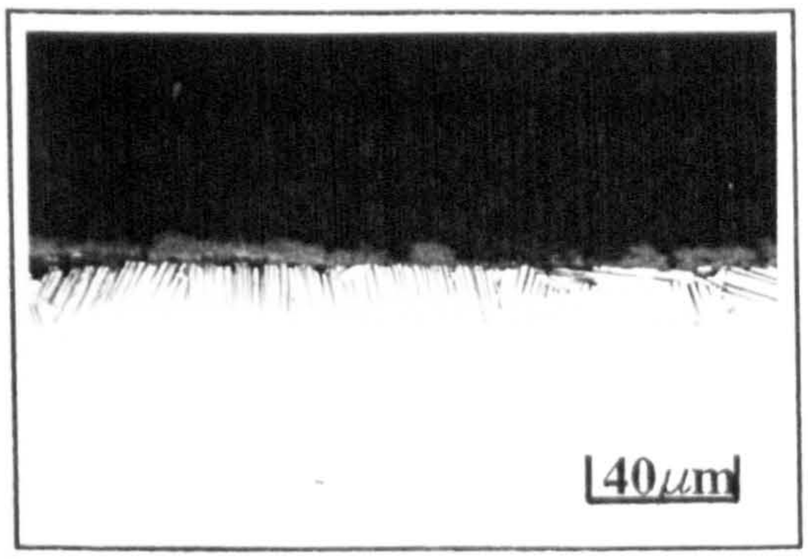

Photograph 8.2.4.2n: 100h at700°C
Single salt coat
Mag : 100x

Photographs 8.2.4.2m and 8.2.4.2n: Optical micrographs showing the effect of salt recoating every 20 hours on substrate attack at 700°C in air. Low salt concentrations [0.03-0.045mg/cm^2].

Photograhs 8.2.4.2o and 8.2.4.2p: Optical micrographs showing the effect of salt recoating every 20 hours on substrate attack at 700°C in air. High salt concentrations [0.16-0.25mg/cm^2].

-

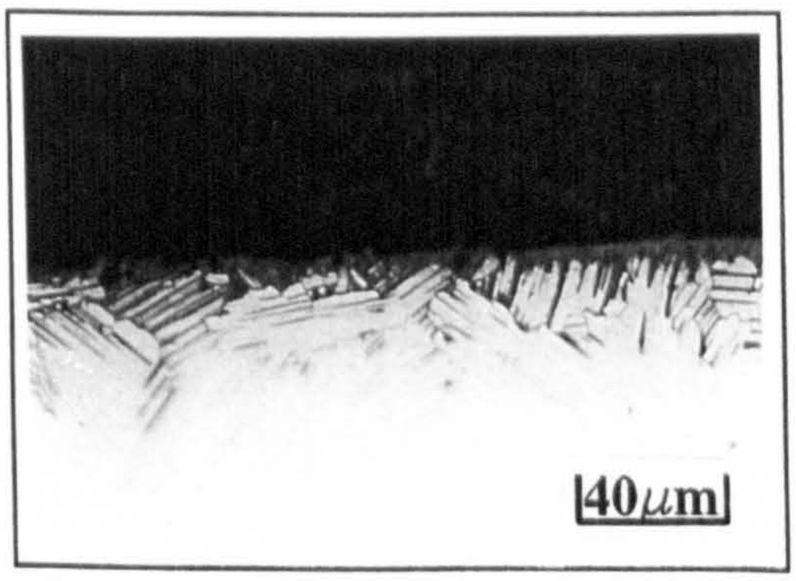

Photograph 8.2.4.2o: 100h at700°C
Salt recoated after 0,20,40,60,80h
Mag : 100x

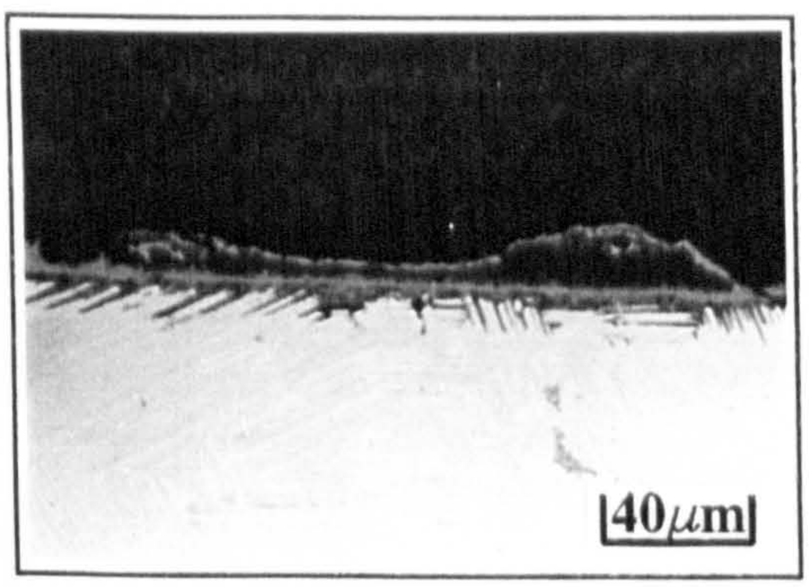

Photograph 8.2.4.2p: 100h at700°C
Single salt coat
Mag : 100x

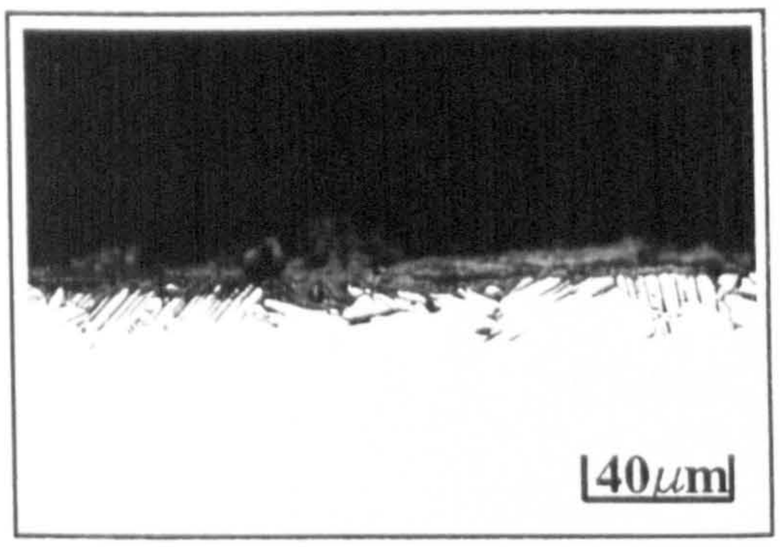

Photograph 8.2.4.2q: 200hat700°C
Salt recoated after 0,100,120,150 h
Mag : 100x

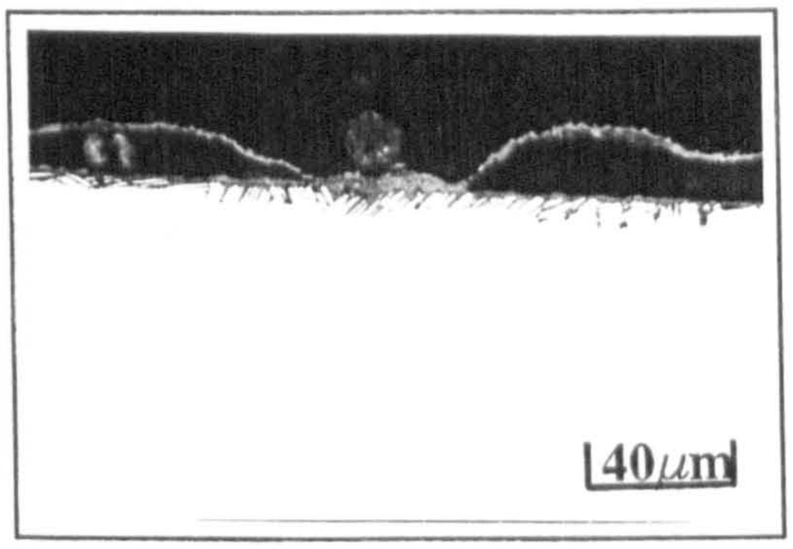

Photograph 8.2.4.2r: 200hat700°C
Single salt coat
Mag : 100x

Photographs 8.2.4.2q and 8.2.4.2r: Optical micrographs showing the effect of long term salt recoating on substrate degradation at 700°C in air. Spallation occurred during recoating cycles.

Photograhs 8.2.4.2s and 8.2.4.2t: Optical micrographs showing the effect of long term salt recoating on substrate degradation at 700°C in air. Minimal spallation during recoating cycles.

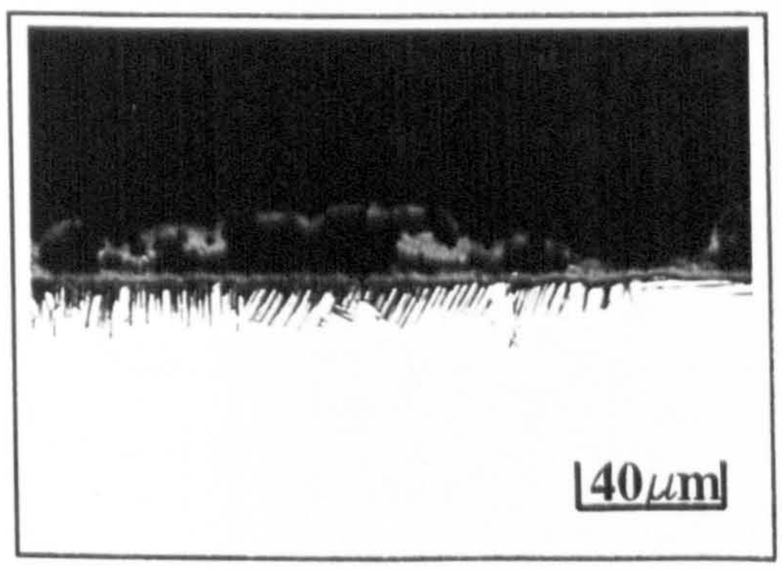

Photograph 8.2.4.2s: 200hat700°C
Salt recoated after 0, 100, 120, 150h
Mag :100x

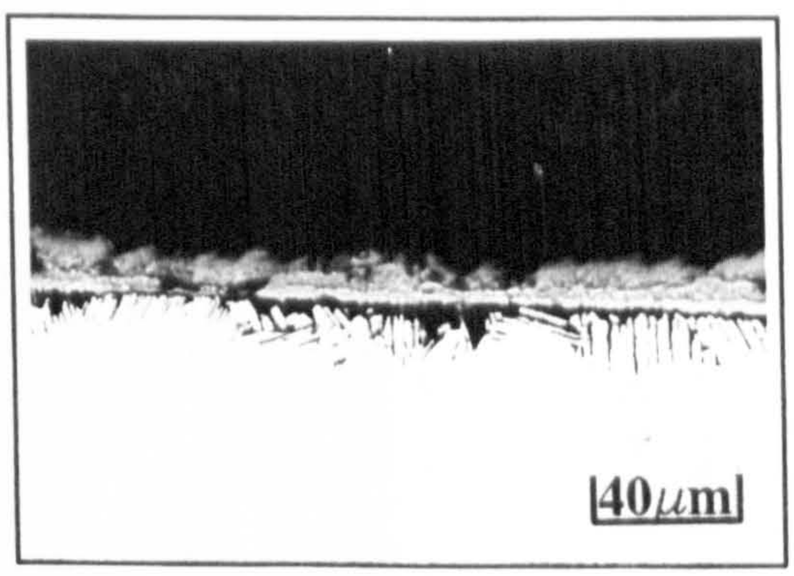

Photograph 8.2.4.2t: 200hat700°C
Single salt coat
Mag : 100x

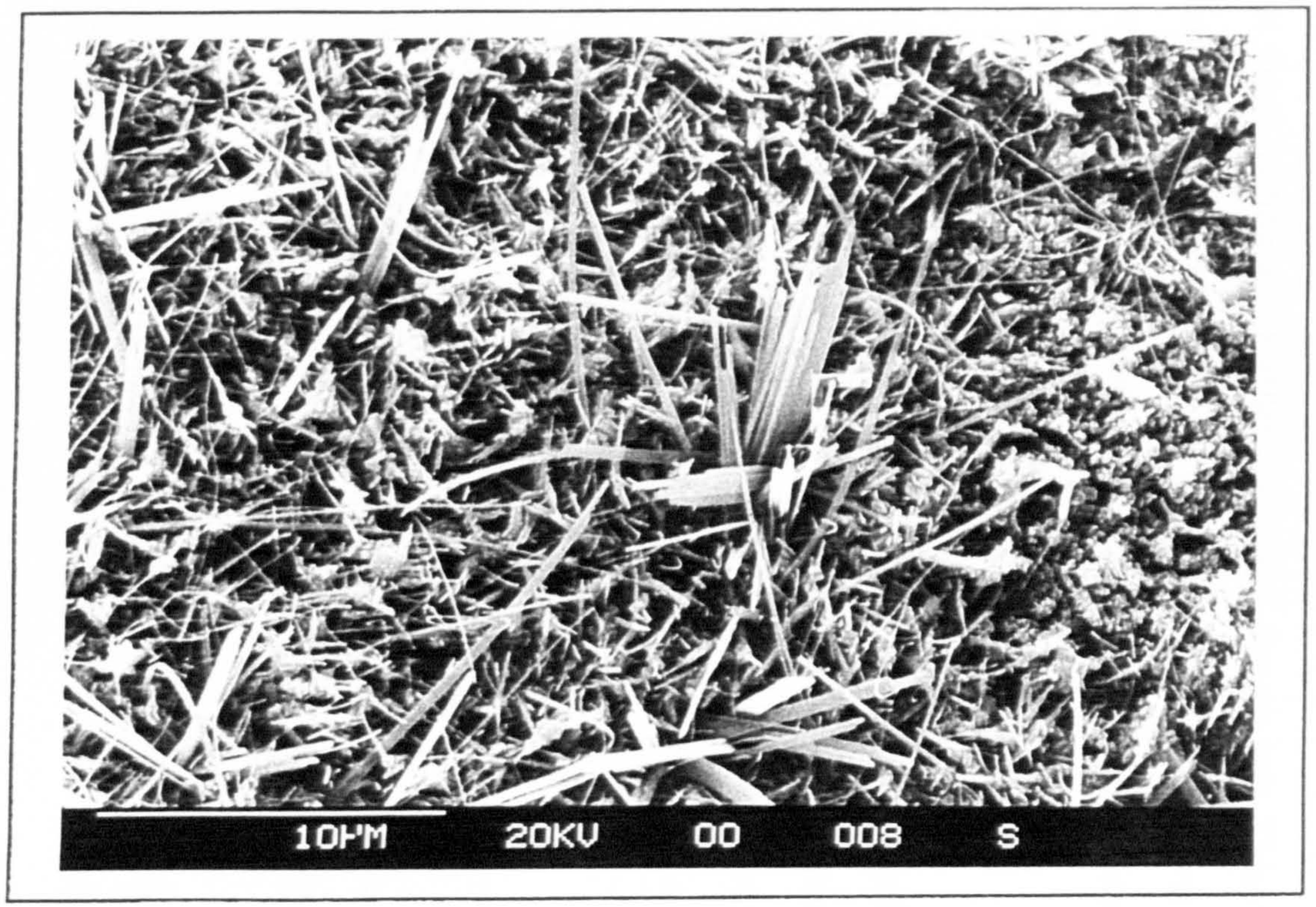

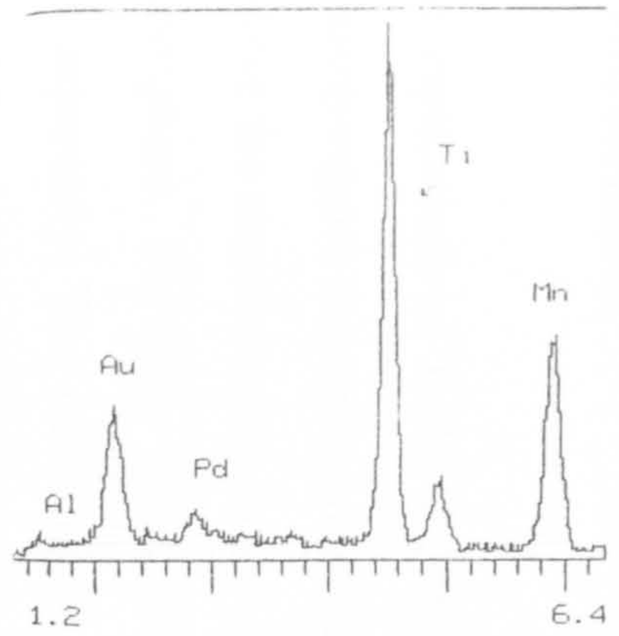

General

Photograph 8.2.4.2u: S.E.M micrograph of a specimen salt recoated after 0, 2, 5, 10 and 15 hours at 700°C. The accompanying EPMA analysis was taken from an area of whiskers.

8.2.5 Hot corrosion

The potential applications of Ti-45Al-2Mn-2Nb, in the low pressure turbine (LPT) for example, ultimately expose the components to hot corrosion environments. By definition this could involve the simultaneous exposure to sulphur bearing gases and salt ingested from the atmosphere. Previous work has enabled the understanding of the two environments separately. The culmination of this work was therefore to acquire an understanding of the corrosion processes operating in the respective environments and to then use this in the selection of a temperature range which would provide the basis for a thorough mechanistic investigation of the synergistic behaviour of sulphur and salt containing environments, under hot corrosion conditions.

A temperature range of 650°C - 800°C was chosen. The salt corrosion studies showed that NaCl caused accelerated corrosion but at 800°C was lost to the atmosphere after relatively short times halting any further corrosion due to salt. This defined the upper temperature range. The lower temperature range was chosen knowing that Na_2SO_4 was expected to form. In which case low melting point eutectic mixtures could also form with the possibility of causing increased corrosion at lower temperatures.

The hot corrosion results are presented in tables 17 to 20. The results were obtained discontinuously with each exposure time constituting a separate specimen. In general the exposure times were after 5, 10, 20, 50 and 100 hours, although some variation did occur. Figure 53 shows the kinetic behaviour of this alloy over the temperature range investigated.

Due to the complexity and large number of reactions that were possible in depth analytical studies had to be carried out. These included S.E.M, EPMA, Optical microscopy, and Elemental mapping techniques after 5, 20 and 100 hours at each temperature.

In depth topological S.E.M studies of each specimen enabled the development of the outer scale layers to be determined with time and temperature. Photographs 8.2.5a to 8.2.5l

show the general surface features at each temperature. At 650°C the surface of Ti-45Al-2Mn-2Nb

Table 17: Hot corrosion results for specimens exposed to SO_2 concentrations of 400ppm at 650°C

Specimen	Time (h)	Salt concentration (mg/cm^2)	Mass gain (mg/cm^2)
Ta 128	5.333	0.0507	0.3847
Ta 129	10.08	0.0507	0.4972
Ta 130	24h.50 min	0.0507	0.494
Ta 111	50	0.053	0.44
Ta 108	100	0.053	0.52

Table 18: Hot corrosion results for specimens exposed to SO_2 concentrations of 520 ppm at 700°C

Specimen	Time (h)	Salt concentration (mg/cm^2)	Mass gain (mg/cm^2)
Ta 132	0.5	0.045	0.167
Ta 135	1	0.045	0.171
Ta 71	5	0.0395	0.43119
Ta 21	10	0.0469	0.513
Ta 64	24	0.0501	0.635
Ta 70	50	0.0394	0.8785
Ta 68	100	0.0501	1.028

Table 19: Hot corrosion results for specimens exposed to SO_2 concentrations of 470 ppm at 750°C

Specimen	Time (h)	Salt concentration (mg/cm^2)	Mass gain (mg/cm^2)
Ta 87	5	0.0488	1.0195
Ta 98	10	0.056	1.076
Ta 85	23	0.051	1.1
Ta 91	50	0.05097	2.028
Ta 99	75	0.0629	2.039
Ta 90	125	0.0629	3.459
Ta 86	150	0.0629	5.317

Table 20: Hot corrosion results for specimens exposed to SO_2 concentrations of 470 ppm at 800°C

Specimen	Time (h)	Salt concentration (mg/cm^2)	Mass gain (mg/cm^2)
Ta 76	5	0.0555	1.5104
Ta 78	24	0.0555	1.924
Ta 74	52	0.0561	2.865
Ta 75	100	0.0561	3.898

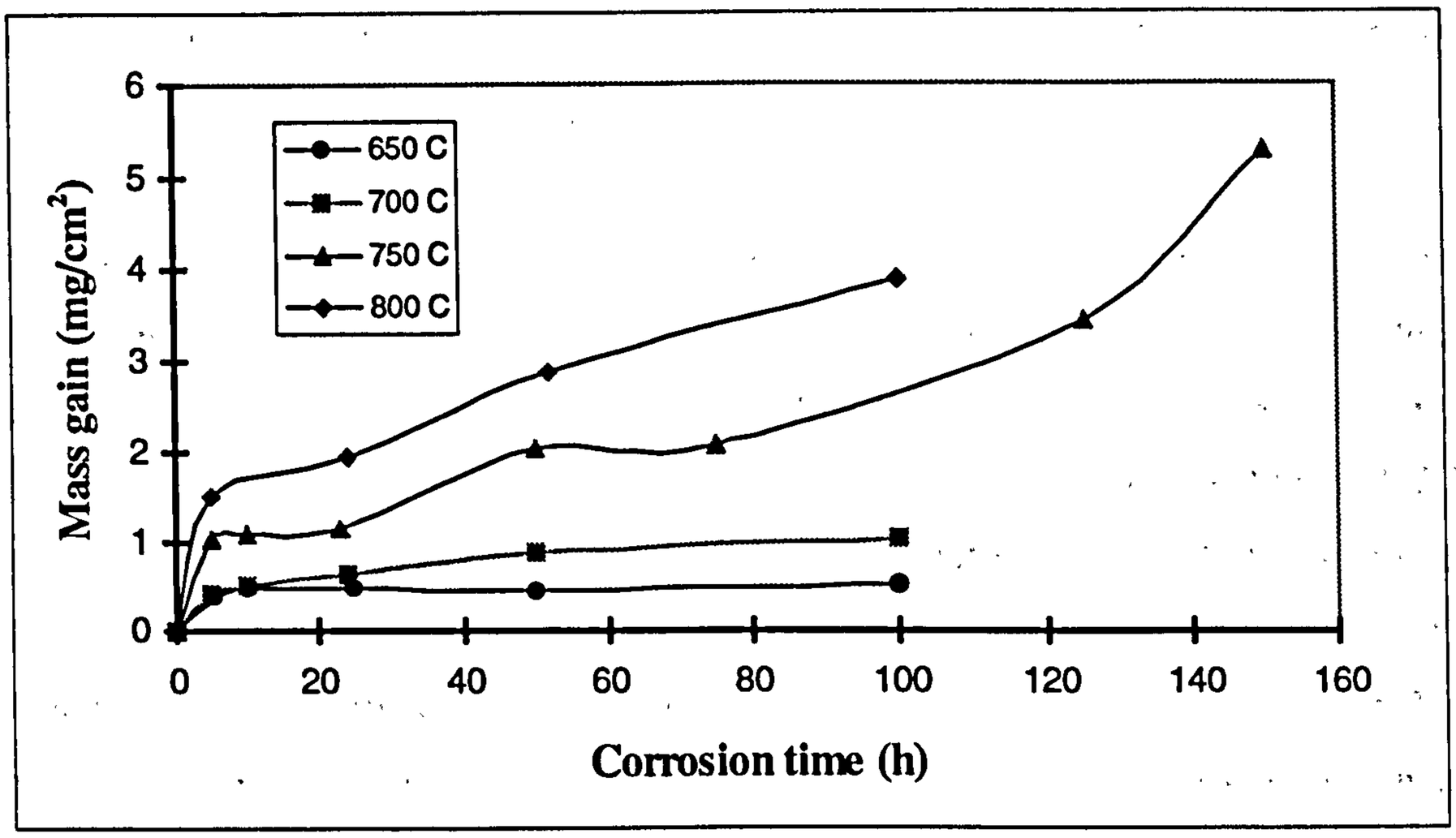

Figure 53: Hot corrosion behaviour of Ti-45Al-2Mn-2Nb over the temperature range of 650°C to 800°C

remained relatively flat out to 100 hours. However, an increase in both the porosity of the scale and number of surface particles is evident.(photographs 8.2.5a to 8.2.5c). At 700°C these surface particles appear to have formed at a much faster rate, increasing in size and initially giving the surface a rough and porous appearance. After 100 hours a decrease in the surface roughness is evident with the initial particles having been overgrown. An increase in surface porosity is evident (photographs 8.2.5d to 8.2.5f). At 750°C a marked increase in the corrosion rate was observed (Figure 53). Similar surface morphologies were observed after 5 hours at 750°C, (photograph 8.2.5g) and 100 hours at 700°C (photograph 8.2.5f). A change in surface appearance was also evident with darker "glassy" areas now appearing. The nature of surface particles is seen to change with time at 750°C (photographs 8.2.5g to 8.2.5i). More crystallographic protrusions developed after 24 hours, with lighter and more continuous regions developing after 100 hours (photograph 8.2.5i). The degree of spallation increased with temperature due to the thicker scales formed as a result of the increased corrosion rates. After 5 hours at 800°C contrasting rough and smooth areas existed (photograph 8.2.5j). The corrosion rate remained fairly uniform out to 20 hours at 800°C (photograph 8.2.5k) with similar surface features developing to those observed after 100 hours at 750°C (photograph 8.2.5i). The

corrosion rate then increased more rapidly and a very undulating and porous surface was developed after 100 hours (photograph 8.2.5l).

The previous surface photographs compared the general surface features over the whole temperature range investigated. However, the low magnifications needed to characterise the general corrosion morphologies of Ti-45Al-2Mn-2Nb were inadequate in showing the more specific features unique to each time and temperature. Photographs 8.2.5m to 8.2.5y were taken at higher magnifications accompanied with EPMA's. The EPMA's of general areas, at 650°C, show an increase in the level of manganese and sulphur with time. The density of surface particles or protrusions also increased with time (photographs 8.2.5m to 8.2.5o show this), with some of the particles showing higher levels of aluminium, manganese and sulphur than at a general area after 20 hours. After 100 hours dark areas up to 20-30μm wide, containing high levels of sulphur and manganese, were identified (photograph 8.2.5o). Short term S.E.M analyses were carried out at 700°C (photographs 8.2.5p and 8.2.5q) in an attempt to identify the initial corrosion reactions taking place. After 30 minutes at 700°C areas rich in sulphur were observed. This is shown in photograph 8.2.5p with some areas taking on a glassy appearance. Compared to the general EPMA's at 650°C higher levels of aluminium are already evident. The majority of the particles/protrusions were aluminium and sulphur rich, some containing sodium but no chlorine. After an hour at 700°C the dark areas increased in size (photograph 8.2.5q), with an EPMA showing very high levels of sulphur associated with manganese and titanium. The level of aluminium over a general area had also increased suggesting a change occurring in the surface composition. This trend continued with higher levels of aluminium and sulphur being detected in general and at protrusions with increasing time at 700°C. Photographs 8.2.5r to 8.2.5t show this. After 100 hours at 700°C the protrusions had been overgrown with the surface having similar high levels of aluminium and titanium. Discrete NaCl rich areas were also detected. Manganese rich glassy areas were detected after 5 hours at 750°C, photograph 8.2.5u illustrates this. Comparison of EDX traces of the general micrograph over the temperature range 650-800°C would show that at 750°C and above lower levels of sulphur exist, suggesting that sulphur had been freed at the surface and either diffused into the scale or escaped back into the

atmosphere at the more elevated temperatures studied. One feature which became more prominent with time at 750°C was the development of these manganese and aluminium rich areas. Aluminium dominated in the areas around the manganese rich sites. After 100 hours at 750°C (photograph 8.2.5w) a large proportion of the surface consisted of these manganese rich areas. However, an EPMA, incorporating a general area, showed the surface to still be aluminium rich. EPMA's of a selection of protrusions after 100 hours at 750°C (photograph 8.2.5w) revealed another change occurring with some of the previously aluminium rich protrusions now being titanium rich. At 800°C the hot corroded surface continued this trend in that higher titanium levels were detected after 5 hours (photograph 8.2.5x) with very low levels of aluminium and sulphur. This continued out to 24 hours, although a high proportion of the particles/protrusions were aluminium rich. This is shown in photograph 8.2.5y. After 100 hours at 800°C (photograph 8.2.5z) mass gains of approximately 4mg/cm^2 were observed. Severe spallation also occurred giving a variable scale thickness. Rutile surface layers dominated with aluminium rich areas and particles over the surface.

Ti-45Al-2Mn-2Nb hot corrosion mechanisms have as yet not been formulated. Many previous investigations have looked at the hot corrosion of Ni and Co based alloys. The surface analysis' above suggest that aluminium and manganese played important roles in the hot corrosion of γ-TiAl alloys. Glassy phases were observed below the melting point of NaCl. Luthra[102] suggested that localised pitting was an indication of preferential attack resulting in the formation of low melting point eutectics. Photographs 8.2.5aa and 8.2.5bb show the degree of pitting seen after 5 and 100 hours at 750°C, respectively. These regions of spallation provide further evidence supporting the mechanisms that were in operation. After 5 hours very little substrate attack occurred, although pits appear to be in the early stages of development. After 100 hours pitting appears to be in a much more advanced stage, with preferential attack seemingly occurring along what may have been α2 lathes and grain boundaries.

Understanding the early stages of hot corrosion is important and allows the later stages of corrosion to be better described in detail as the early stages establish the chemistry for

propagation of the hot corrosion attack. Knowing the initial corrosion products that form allows the reactions that take place to be deduced. EPMA's enable general conclusions to be made concerning the composition at specific sites and over a general area. They do not however show the concentration of an element over a relatively large area. Elemental X-ray maps were used to clarify the uncertainty still existing over the composition of the initial corrosion products. Photographs 8.2.5cc and 8.2.5ee show the concentration of O, Al, S, Ti and Mn at a glassy area, exposed for 100 hours at 650°C (photograph 8.2.5dd shows the area analysed).The glassy area is confirmed as being Mn, S and O rich, implying the existence of $MnSO_4$. Additional Elemental X-ray maps are presented in photographs 8.2.5ff and 8.2.5hh, showing the concentration of O, Al, S, and Ti at a typical area observed after 5 hours at 750°C. Photograph 8.2.5gg shows the microstructural features from which this map was constructed. Similar features were observed after 100 hours at 700°C. The map identifies similar concentrations of aluminium and titanium associated with sulphur.

A hot corrosion problem has been shown to exist when a salt coated Ti-45Al-2Mn-2Nb alloy is exposed to air + SO_2 atmospheres. In the absence of SO_2 preferential substrate attack was observed, with the $\alpha 2$ lathes being attacked up to a depth of 50μm after 100 hours at 700°C. The optical micrographs in photographs 8.2.5ii and 8.2.5jj show the through sections seen after 100 hours at 700 and 750°C respectively. At 700°C the scale thickness varied between about 4-8μm and at 750°C between 13-18μm. The differences in kinetics may explain the increases in scale thickness and porosity. Breakaway corrosion begins to dominate at 750°C (figure 53), which may also explain the decrease in scale adherence, seen in figure 8.2.5kk.

Elemental X-ray maps taken from through sections of specimens exposed for 100 hours at 650, 700, 750 and 800°C enabled the corrosion mechanisms operating to be elucidated. The elemental maps shown in photographs 8.2.5ll and 8.2.5nn show that a sulphur and titanium rich layer was being developed near the scale/substrate interface after 100 hours at 650°C. An aluminium rich layer can be seen to be forming. After 100 hours at 700°C pits began to form. Photograph 8.2.5pp shows a typical pit morphology. The elemental

maps in photograph 8.2.5oo show that a sulphur, manganese and aluminium rich layer was being developed at the surface of the pit. The scale beneath this layer was titanium rich, with a depletion in aluminium and sulphur. A section adjacent to this pit was shown to be developing a sulphur rich layer at the scale/substrate interface. Similar levels of aluminium and titanium were identified within a layer near the scale/gas interface. Below this layer the scale was predominantly titanium rich. After 100 hours at 750°C a similar scale structure developed (photographs 8.2.5qq and 8.2.5ss). However, the layer compositions became more pronounced with a very aluminium rich layer being developed at the surface and a similarly very sulphur rich layer at the scale/substrate interface. The area from which the elemental maps were taken is shown in photograph 8.2.5rr. The scale thickness is also shown to be more uniform at 750°C. Severe spallation occurred at 800°C suggesting that the scale thickness' observed in photograph 8.2.5uu, which shows the area from which the elemental maps in photograph 8.2.5tt was taken, corresponds to an area for which little spallation had occurred. A sulphur rich layer can be seen at the scale/substrate interface. Aluminium is seen throughout the scale, but is lower in the sulphur rich region. Titanium is predominant throughout the scales.

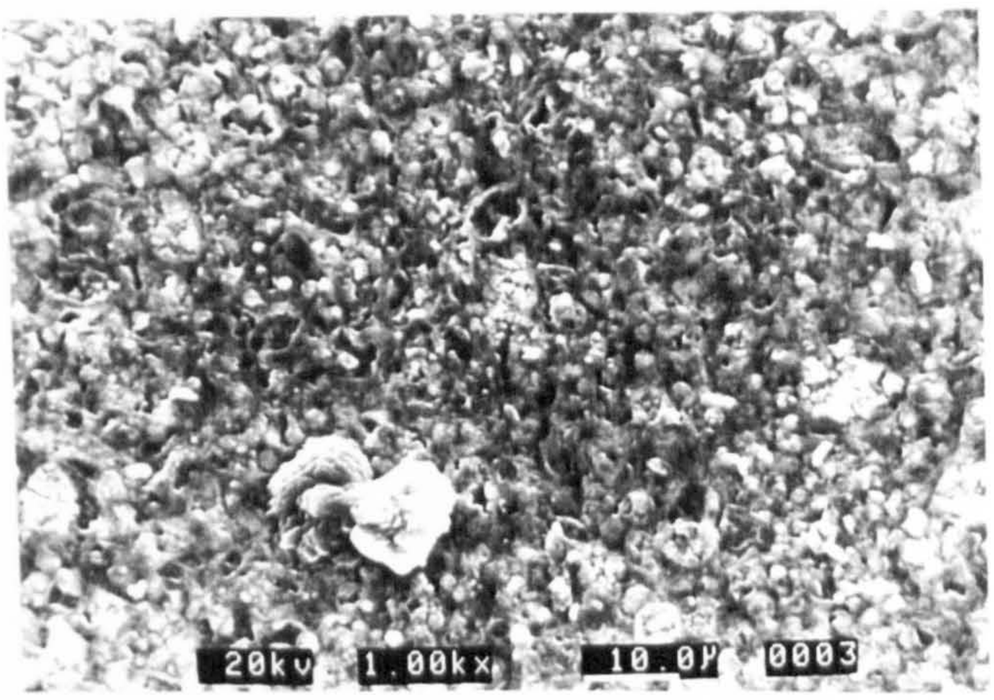

Photograph 8.2.5a: Hot corrosion morphology after 5h at 650°C

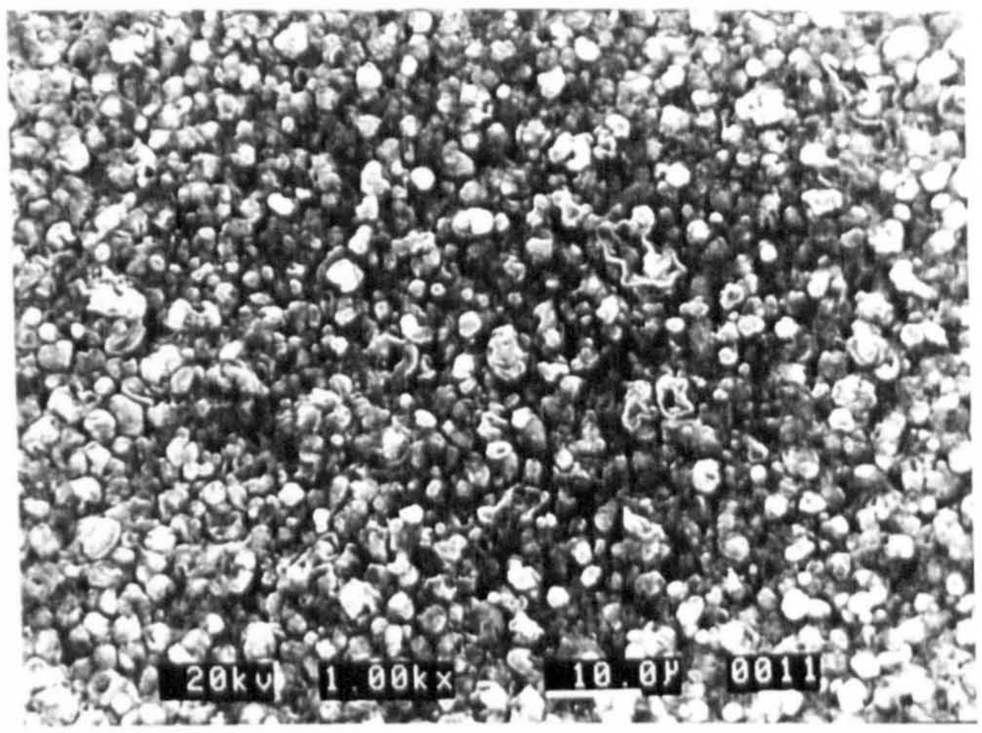

Photograph 8.2.5b: Hot corrosion morphology after 20h at 650°C

Photograph 8.2.5c: Hot corrosion morphology after 100h at 650°C

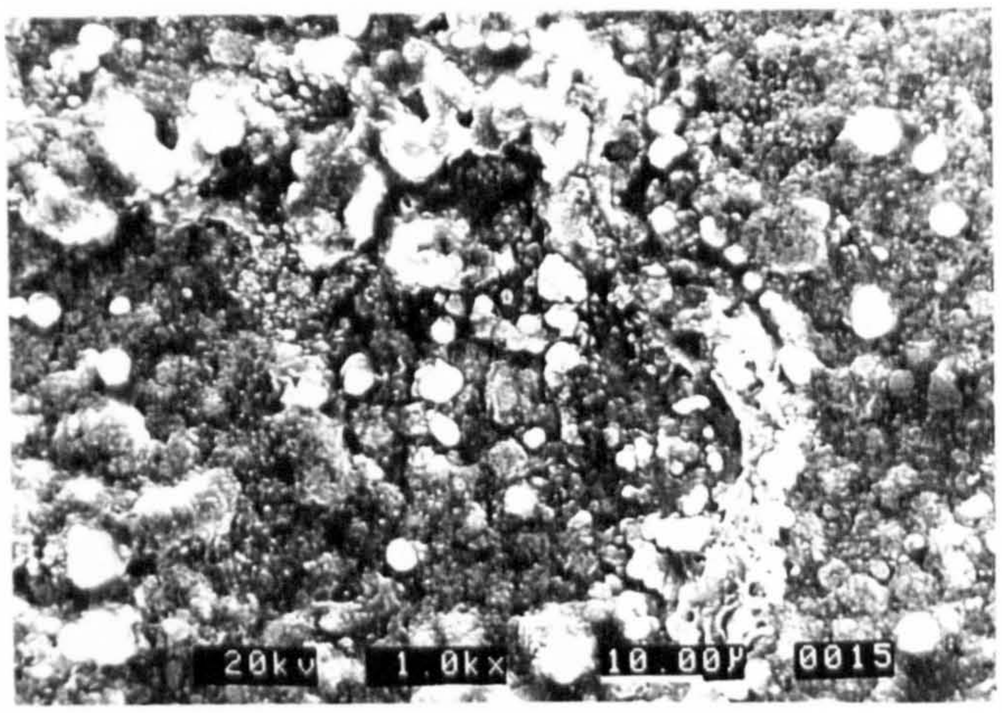

Photograph 8.2.5d: Hot corrosion morphology after 5h at 700°C

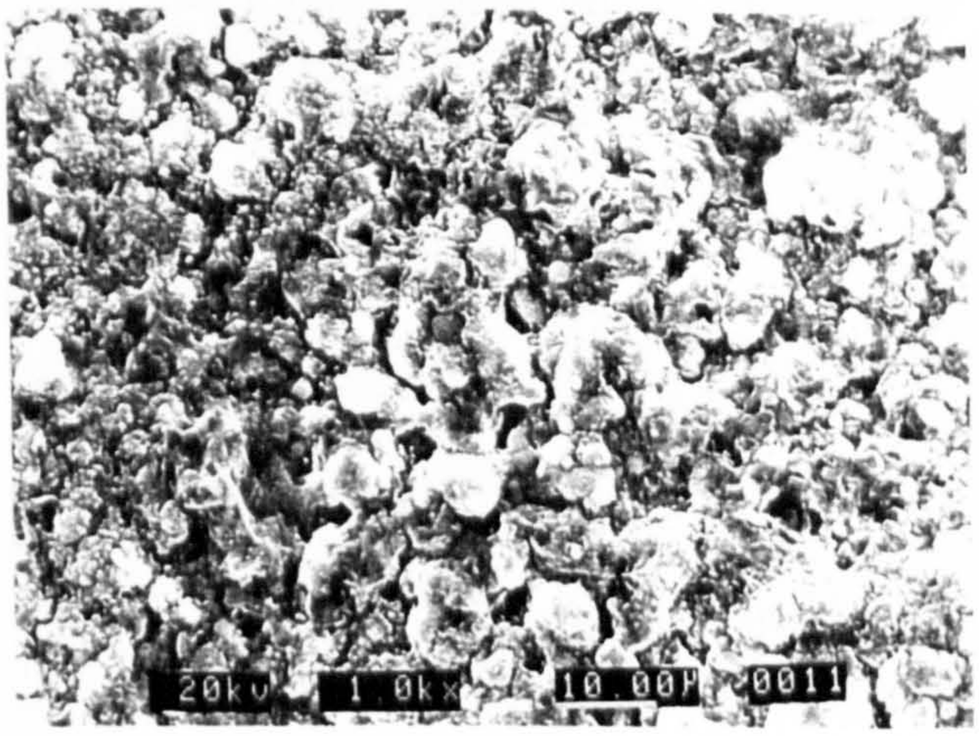

Photograph 8.2.5e: Hot corrosion morphology after 24 h at 700°C

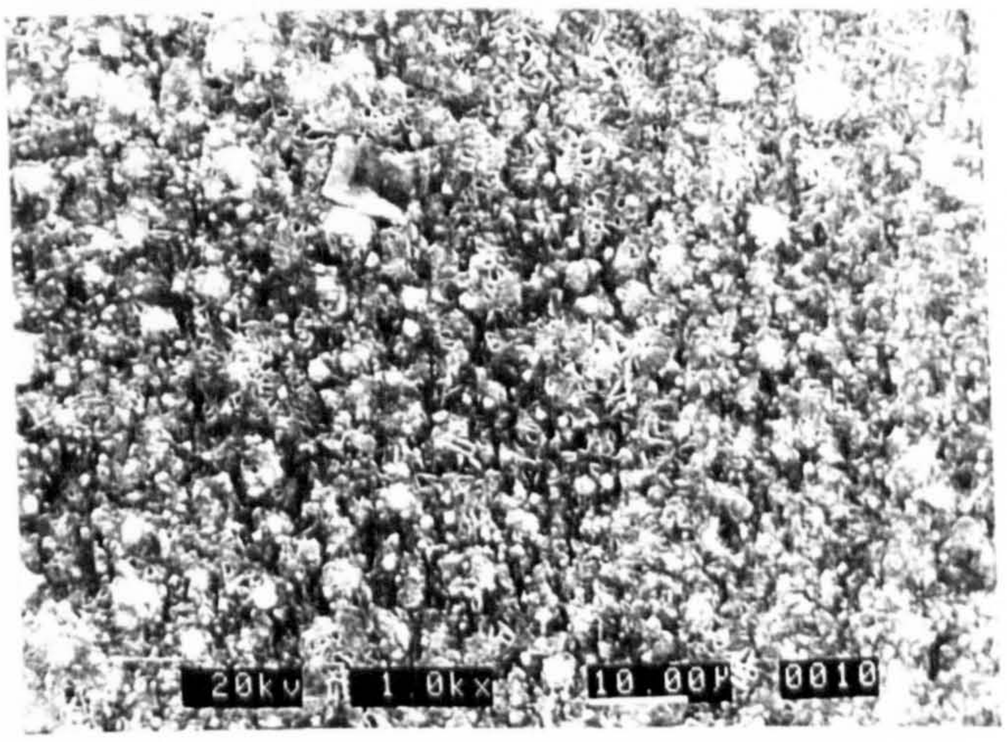

Photograph 8.2.5f: Hot corrosion morphology after 100h at 700°C

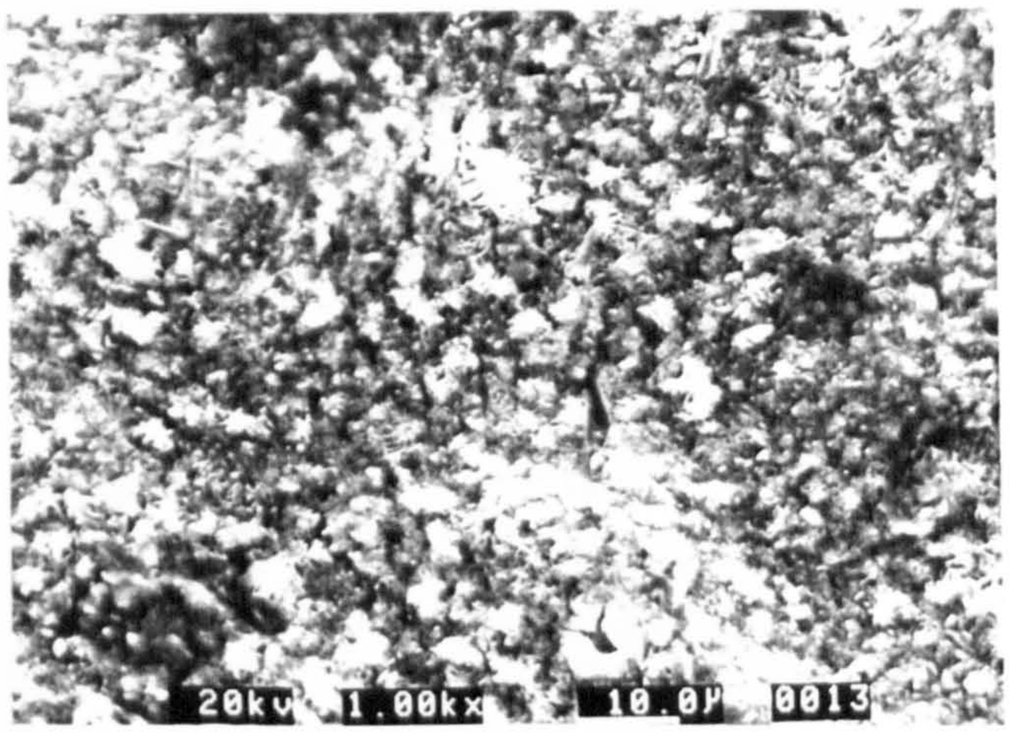

Photograph 8.2.5g: Hot corrosion morphology after 5h at 750°C

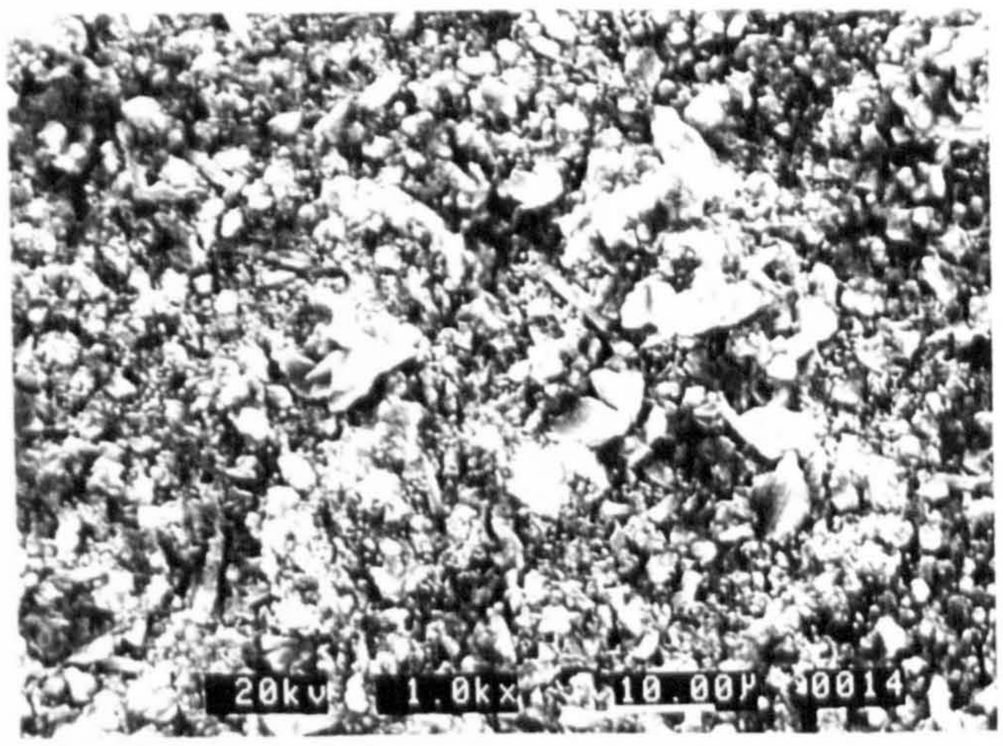

Photograph 8.2.5h: Hot corrosion morphology after 24h at 750°C

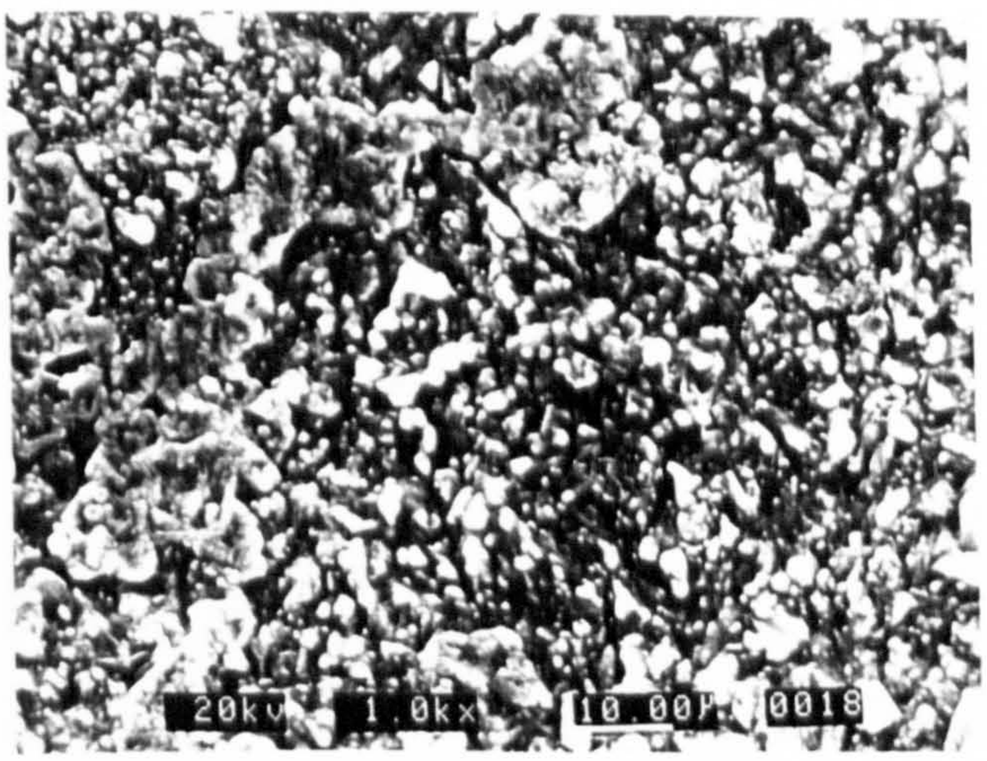

Photograph 8.2.5i: Hot corrosion morphology after 100h at 750°C

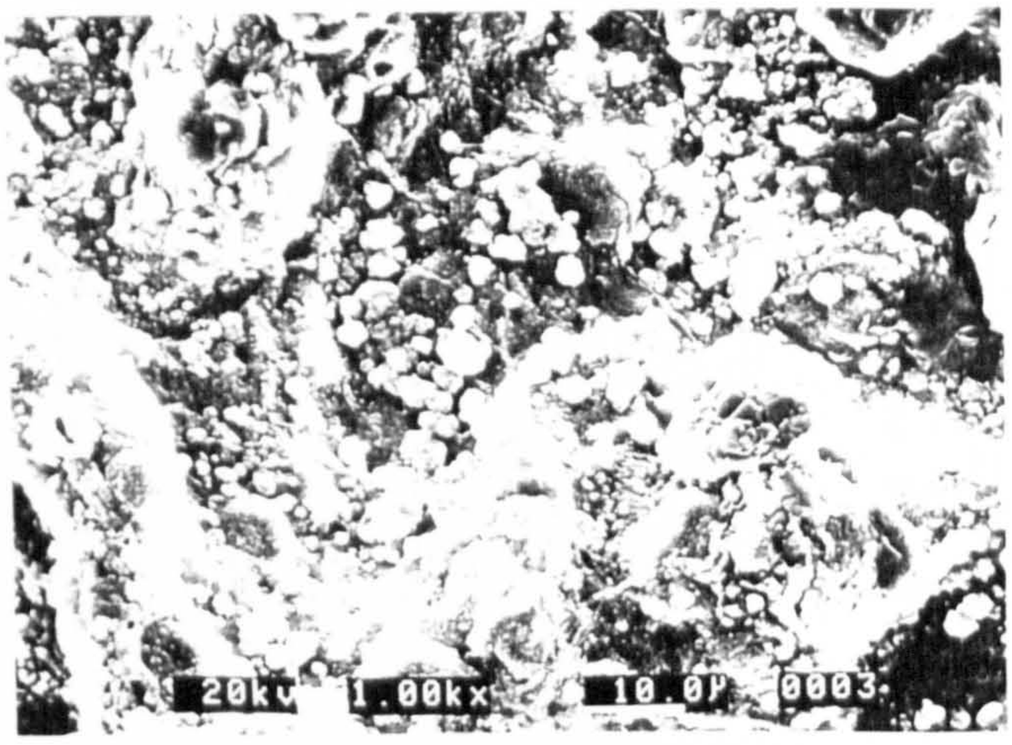

Photograph 8.2.5j: Hot corrosion morphology after 5h at 800°C

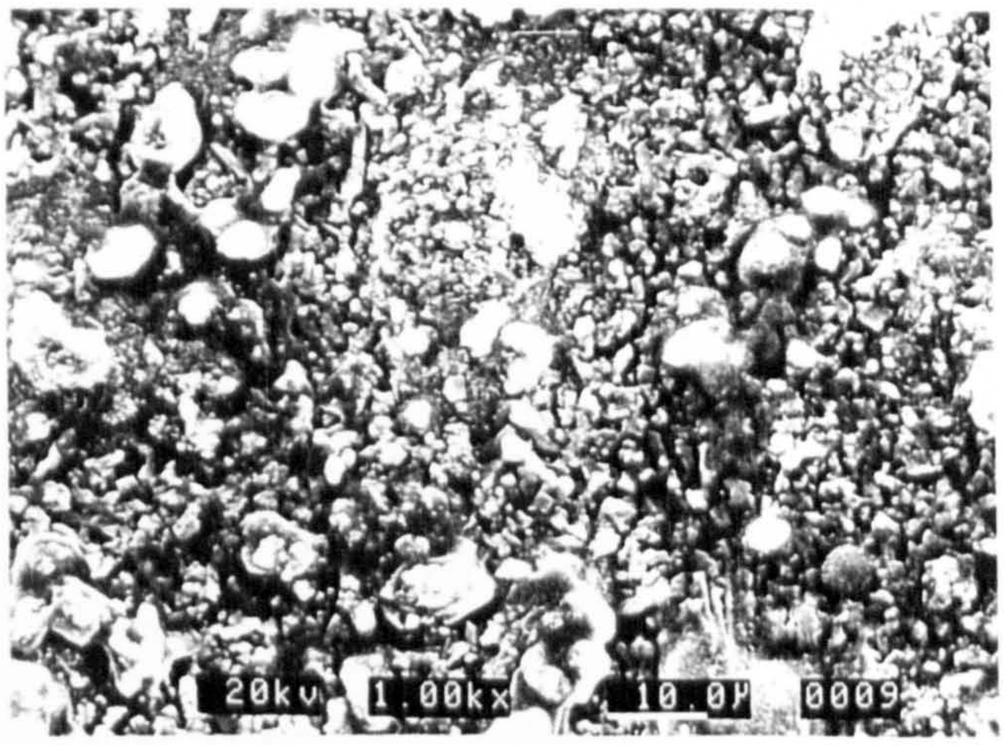

Photograph 8.2.5k: Hot corrosion morphology after 20h at 800°C

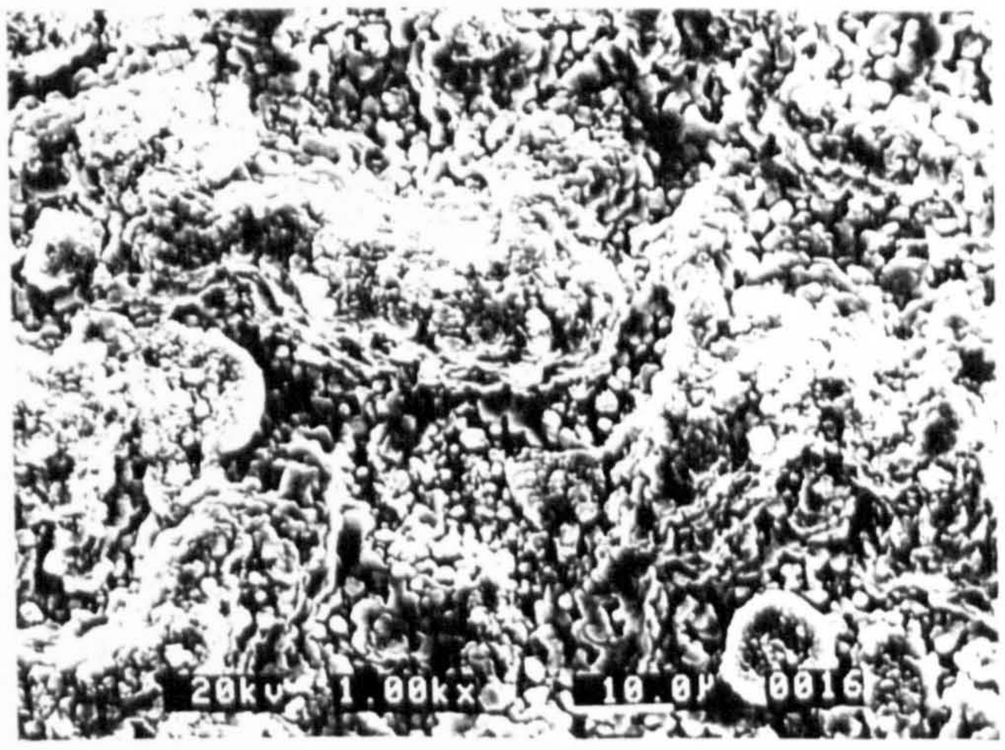

Photograph 8.2.5l: Hot corrosion morphology after 100h at 800°C

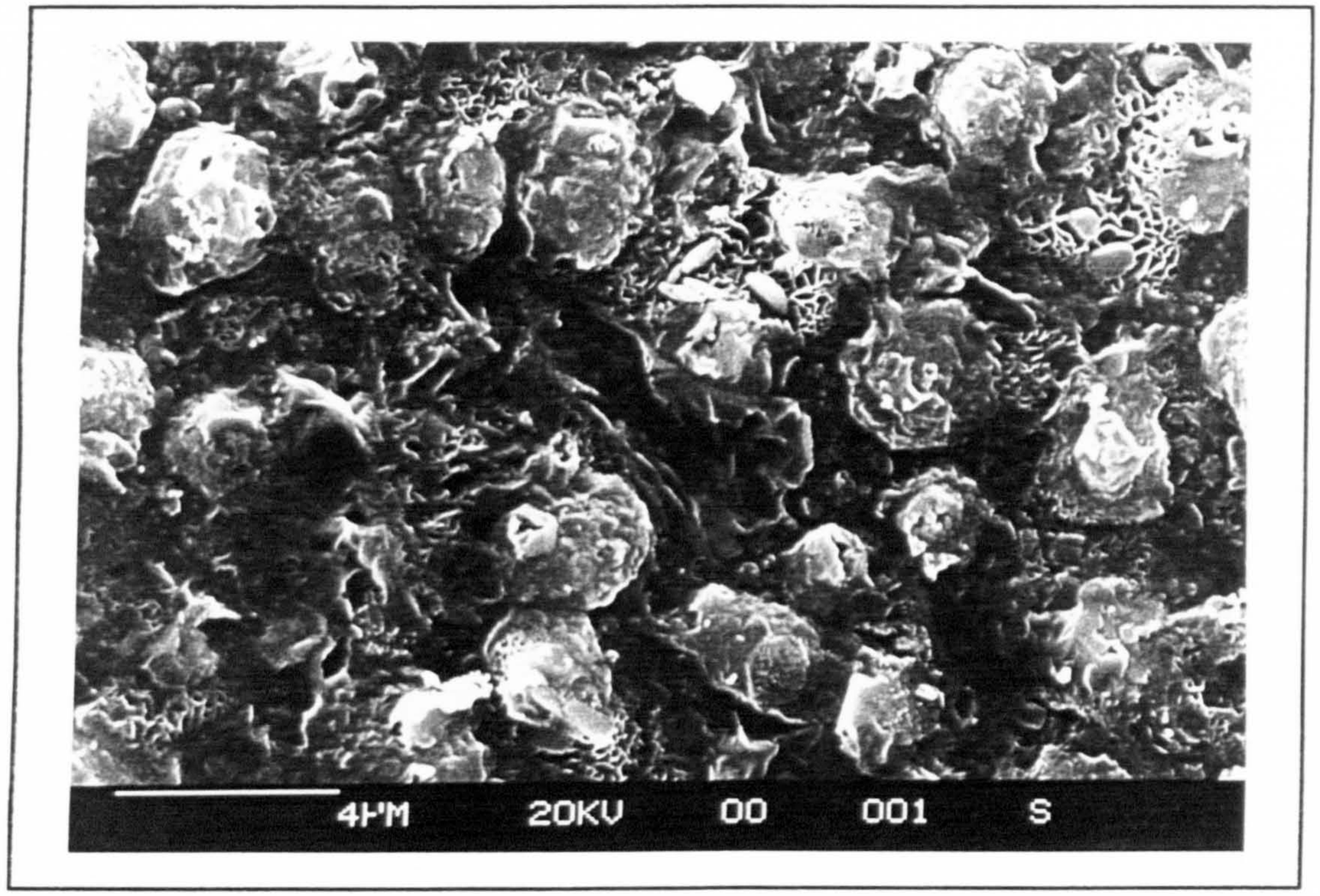

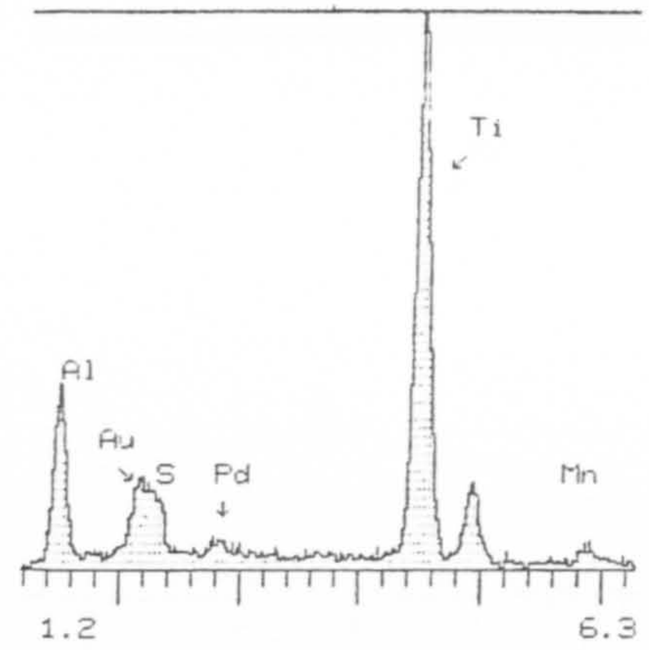

General

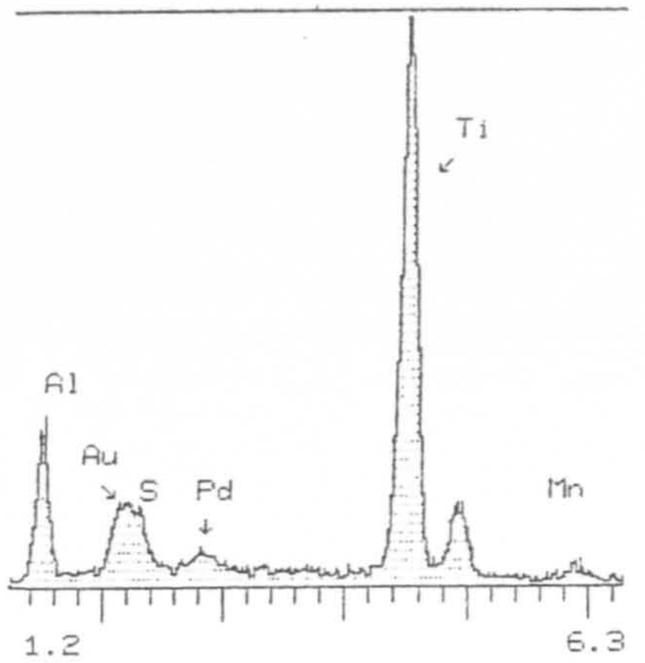

General

Photograph 8.2.5m: S.E.M micrograph of a salt coated specimen exposed for 5 hours at 650°C in an atmosphere of air + 400 ppm SO_2. The accompanying EPMA analysis'identify key features.(Magnification:5.0kx)

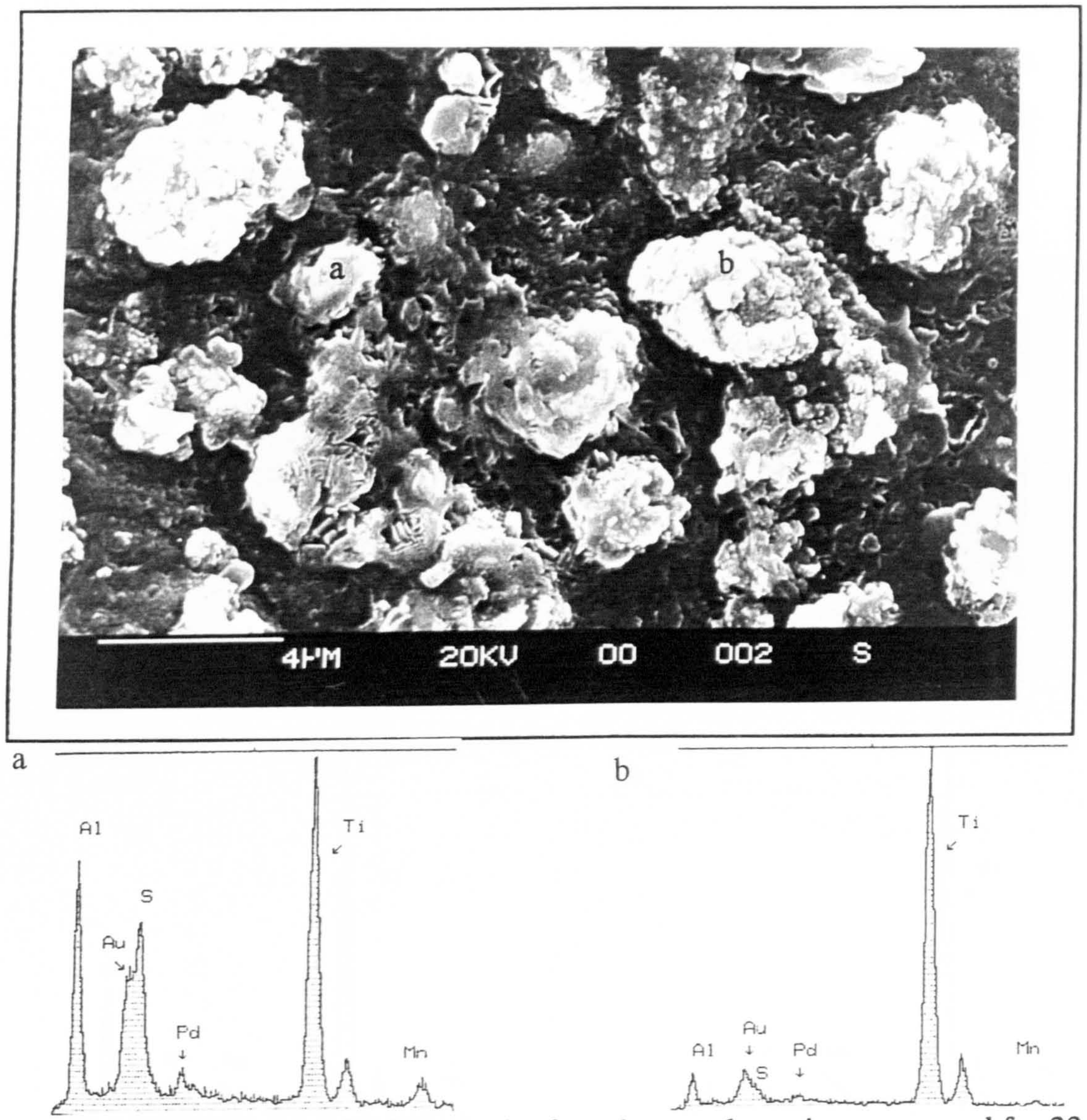

Photograph 8.2.5n: S.E.M micrograph of a salt coated specimen exposed for 23 hours at 650°C in an atmosphere of air + 400 ppm SO_2. The accompanying EPMA analysis'identify key features.(Magnification:5.0kx)

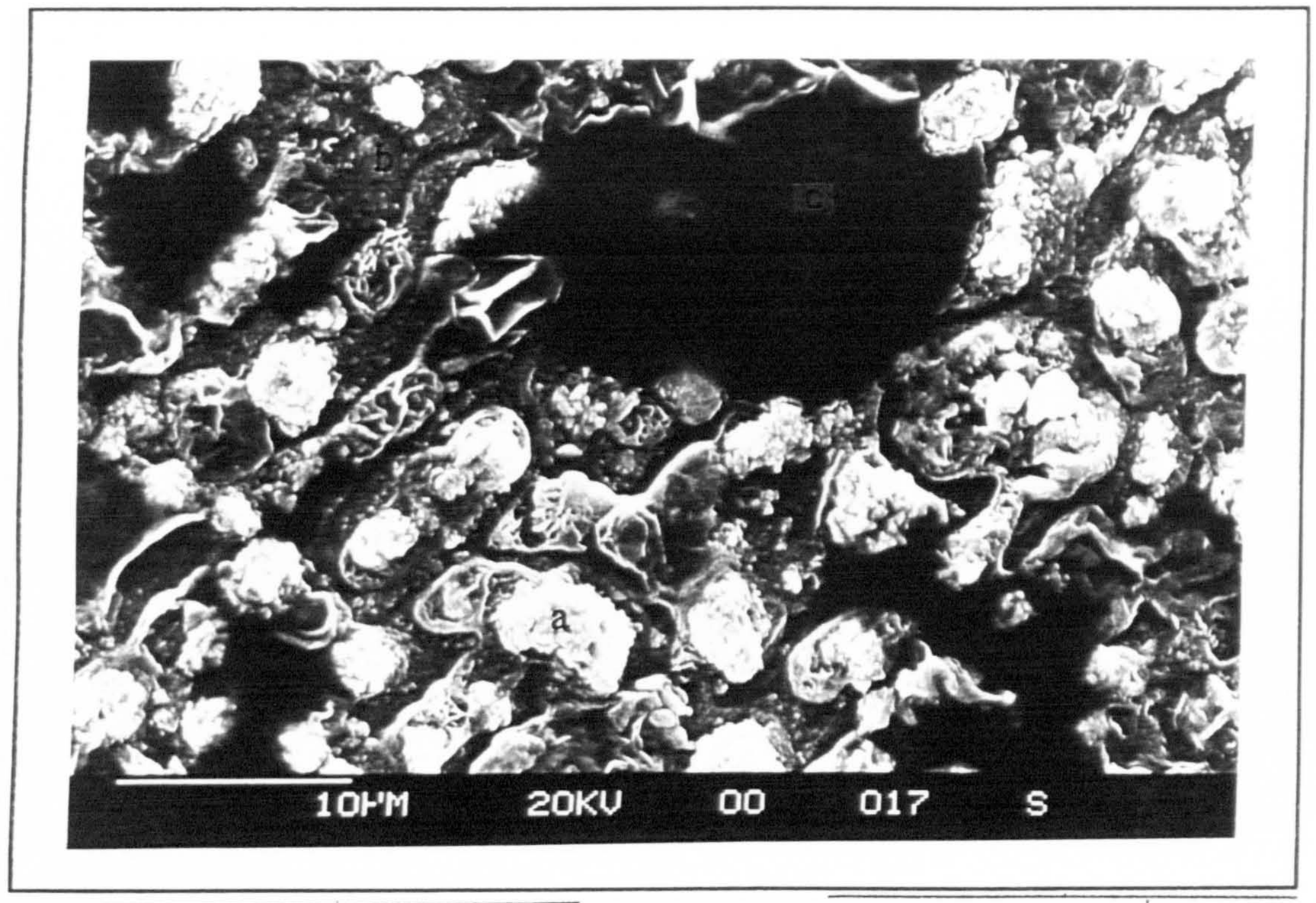

Photograph 8.2.5o: S.E.M micrograph of a salt coated specimen exposed for 100 hours at 650°C in an atmosphere of air + 400 ppm SO_2. The accompanying EPMA analysis'identify key features.(Magnification:1.0kx)

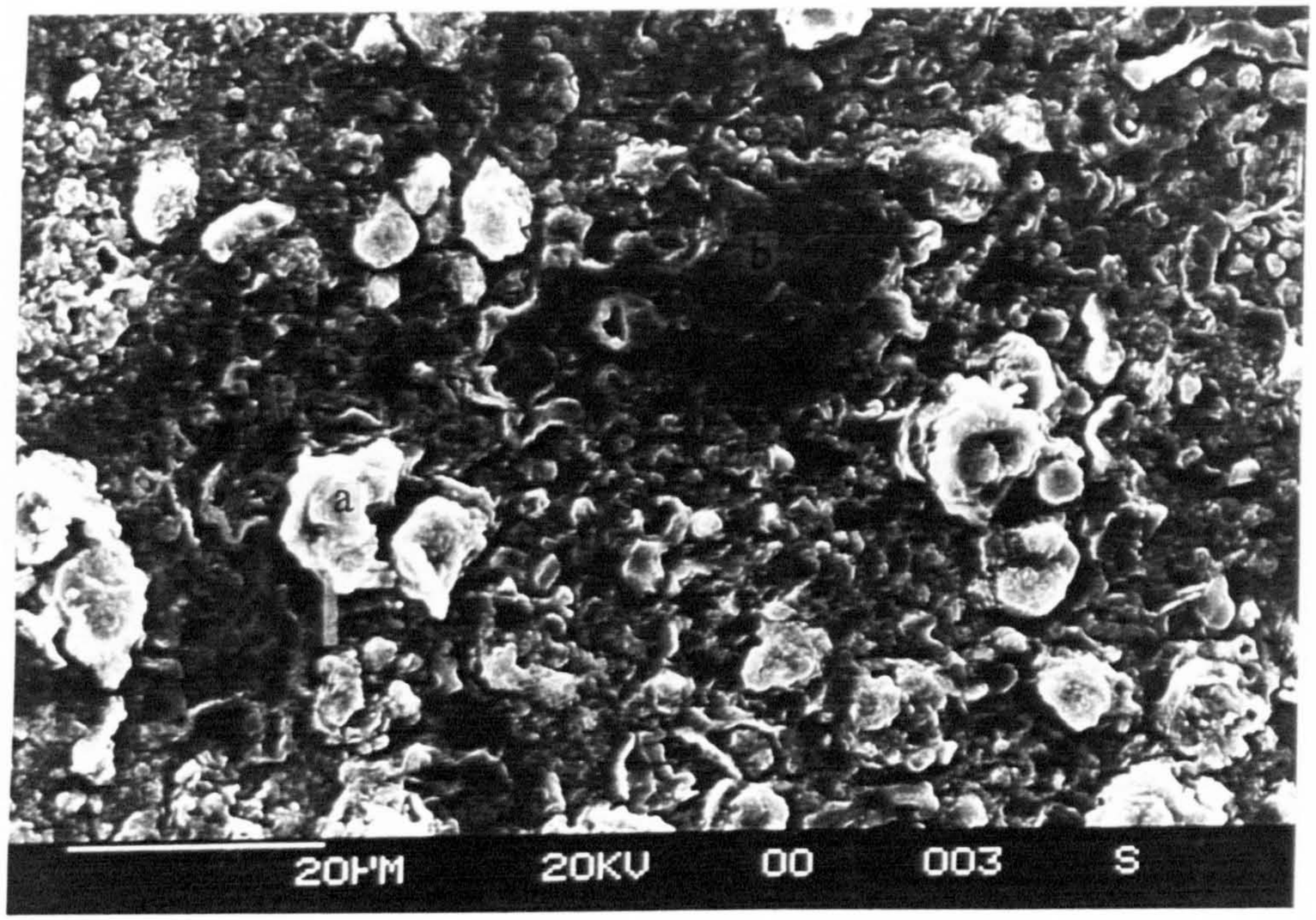

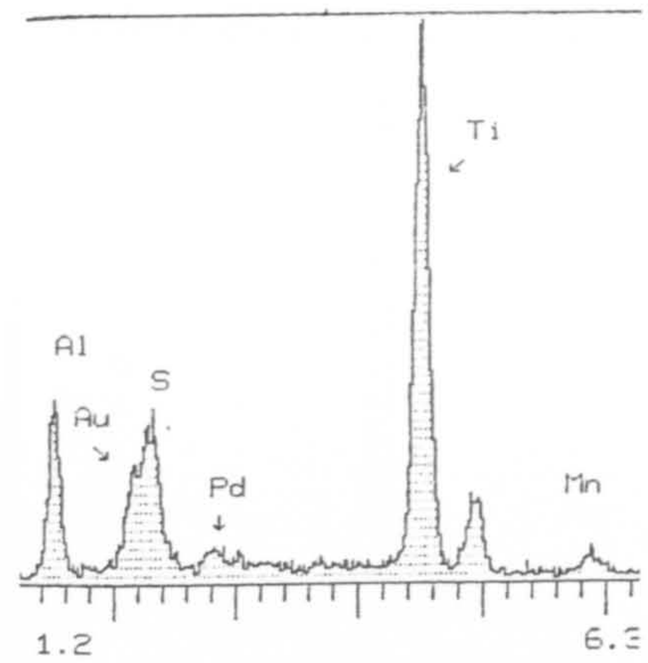

General

a

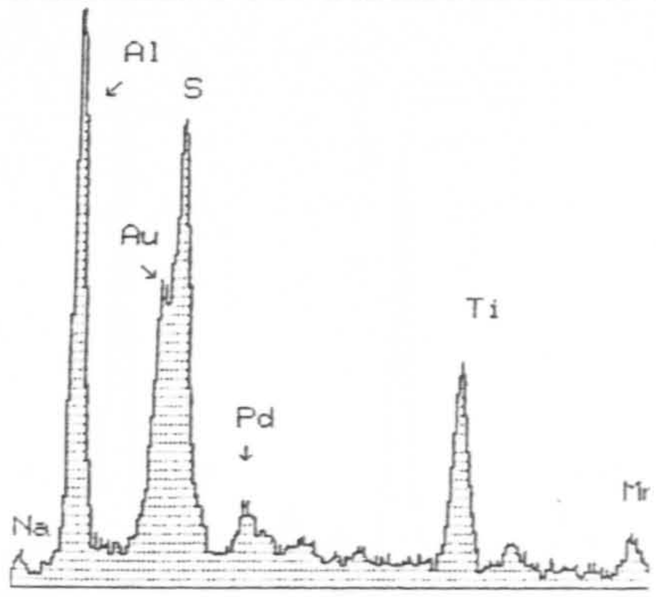

b

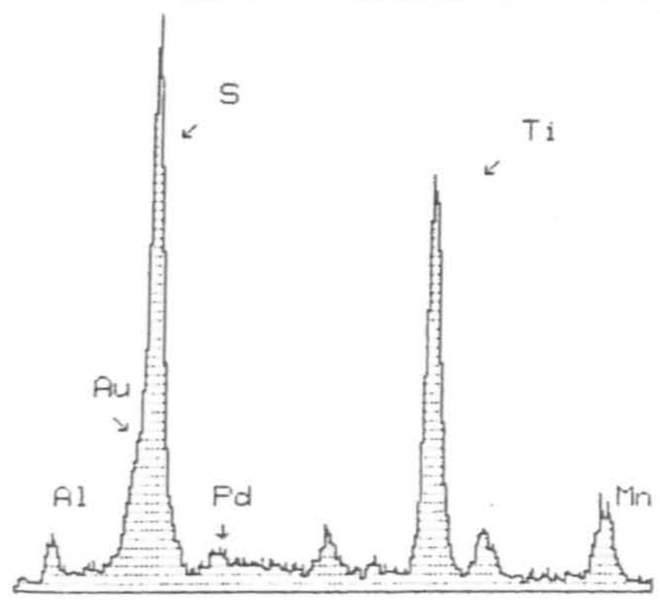

Photograph 8.2.5p: S.E.M micrograph of a salt coated specimen exposed for 30 minutes at 700°C in an atmosphere of air + 520ppm SO_2. The accompanying EPMA analysis' identify key features.

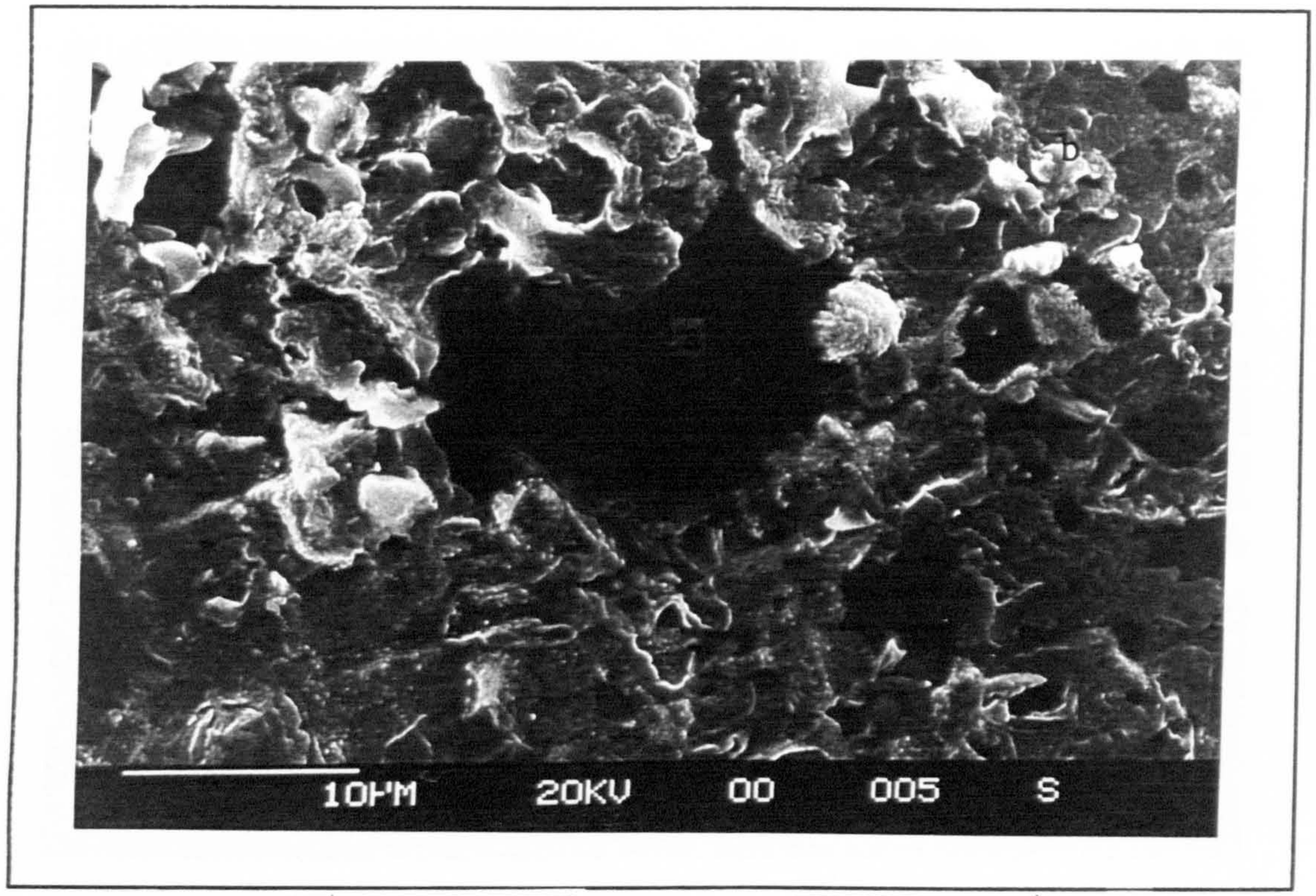

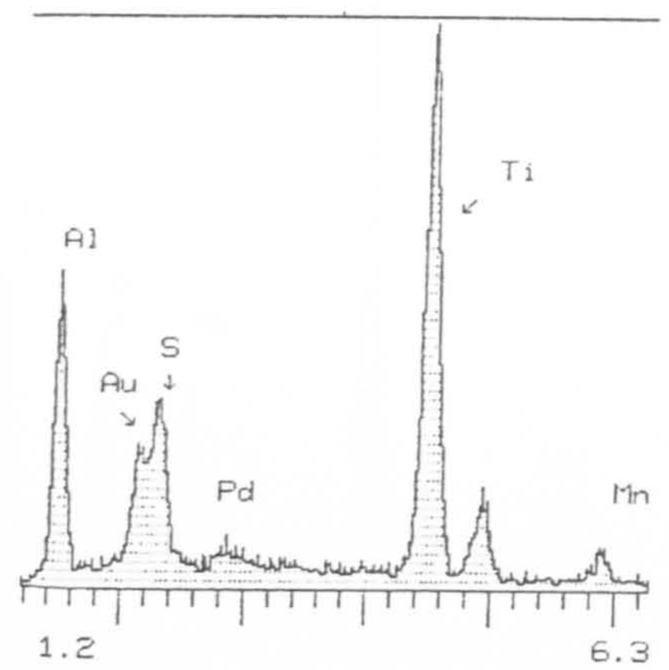

General

a

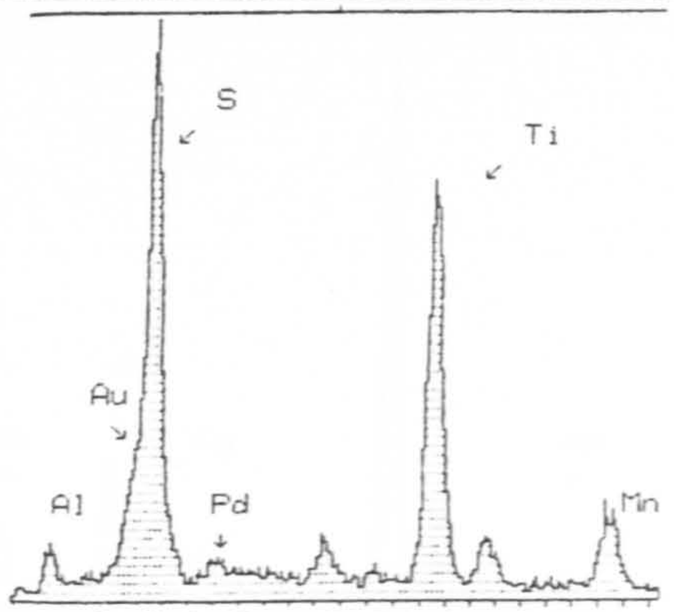

b

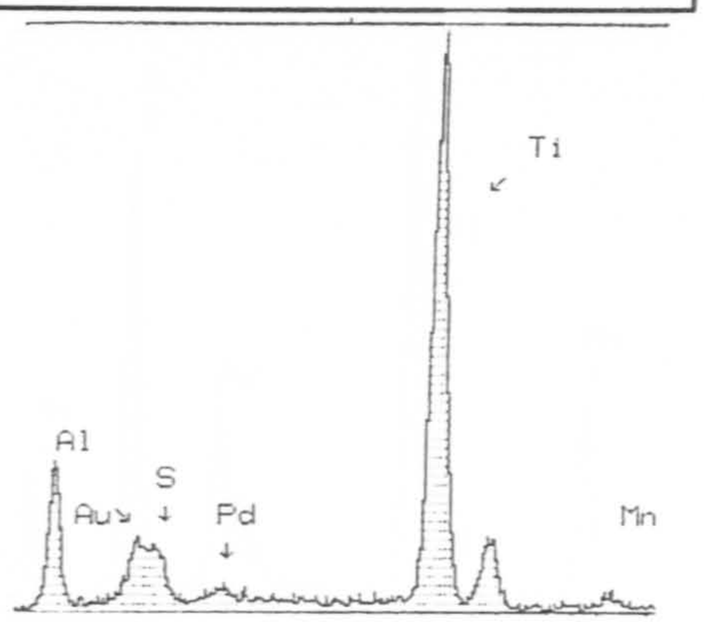

Photograph 8.2.5q: S.E.M micrograph of a salt coated specimen exposed for one hour at 700°C in an atmosphere of air + 520 ppm SO_2. The accompanying EPMA analysis'identify key features.

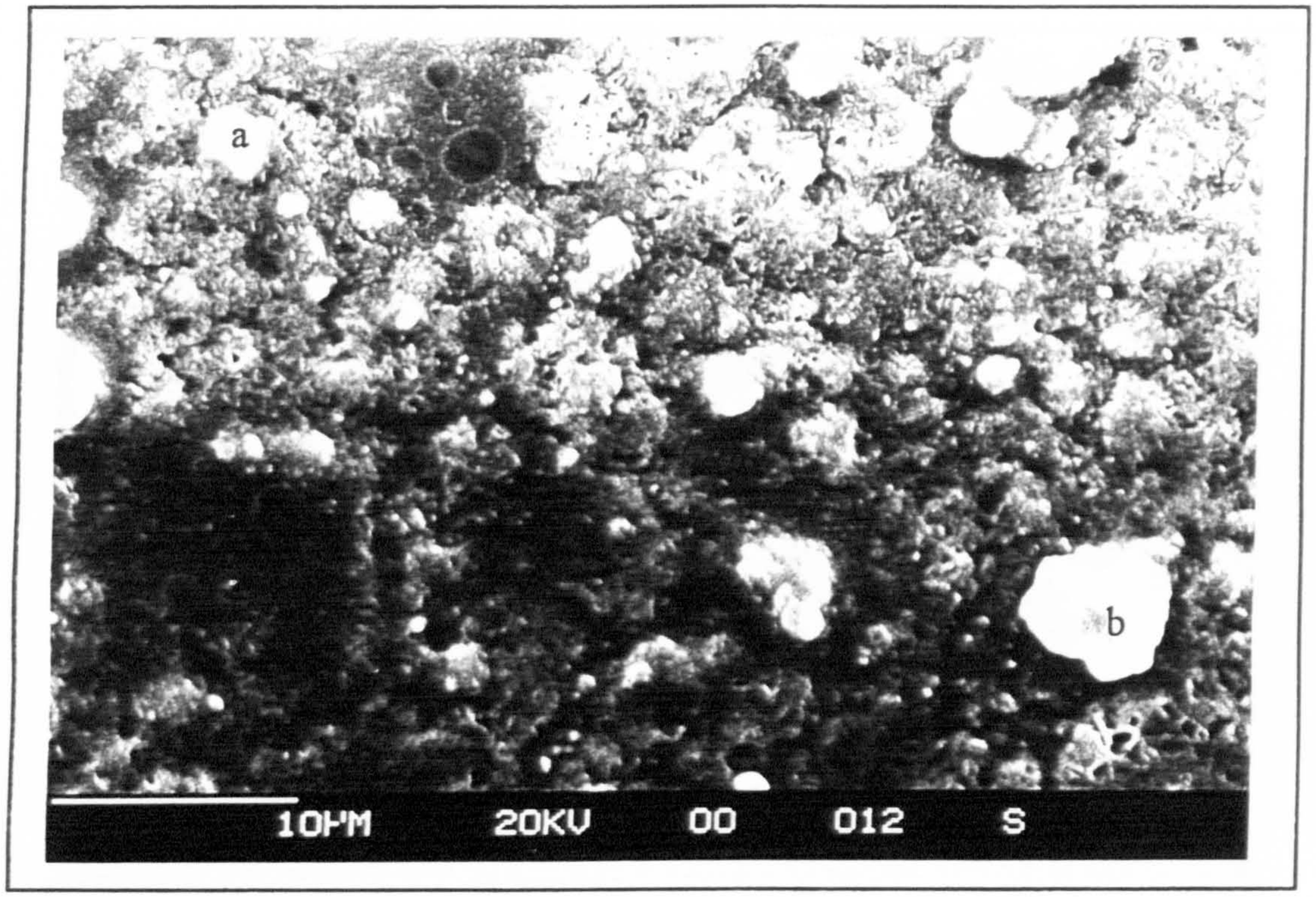

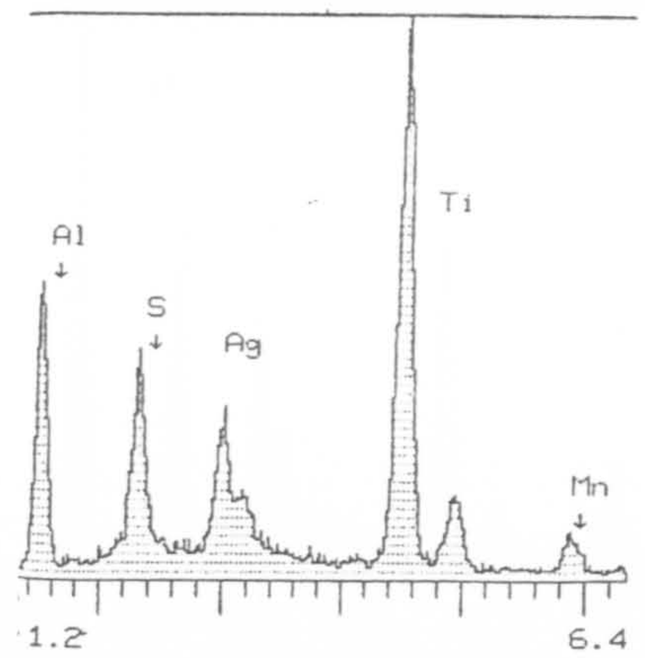

General

a

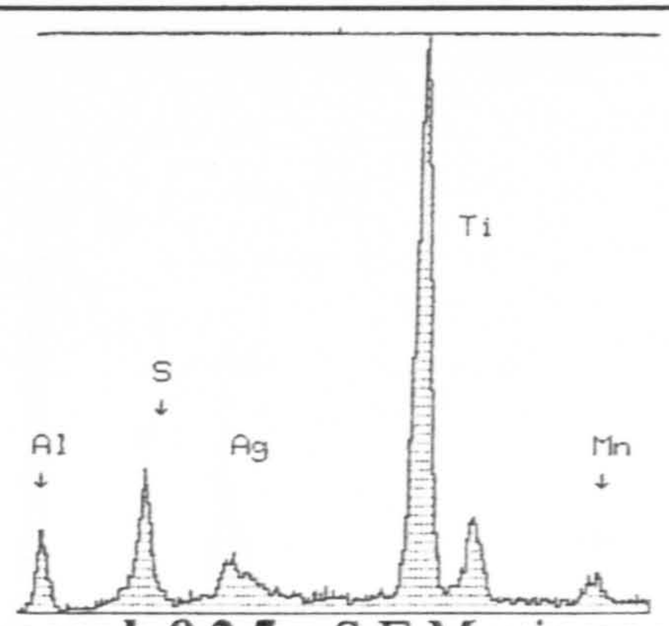

b

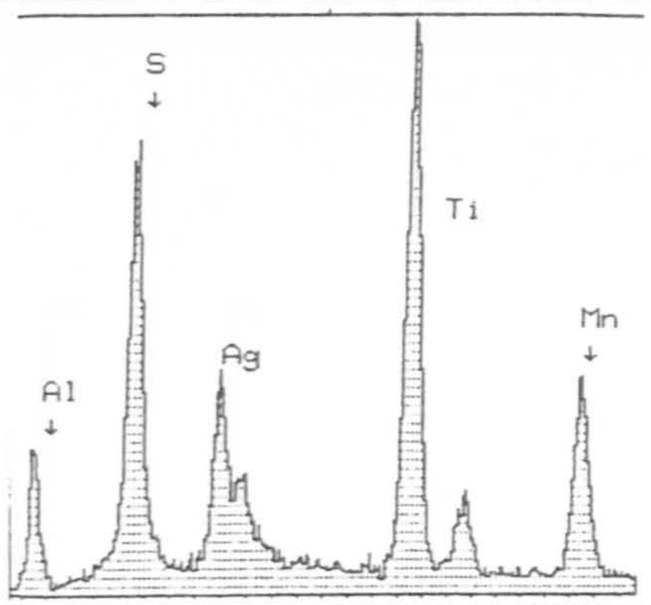

Photograph 8.2.5r: S.E.M micrograph of a salt coated specimen exposed for 5 hours at 700°C in an atmosphere of air +520 ppm SO_2. The accompanying EPMA analysis'identify key features. (Magnification: 2.0kx)

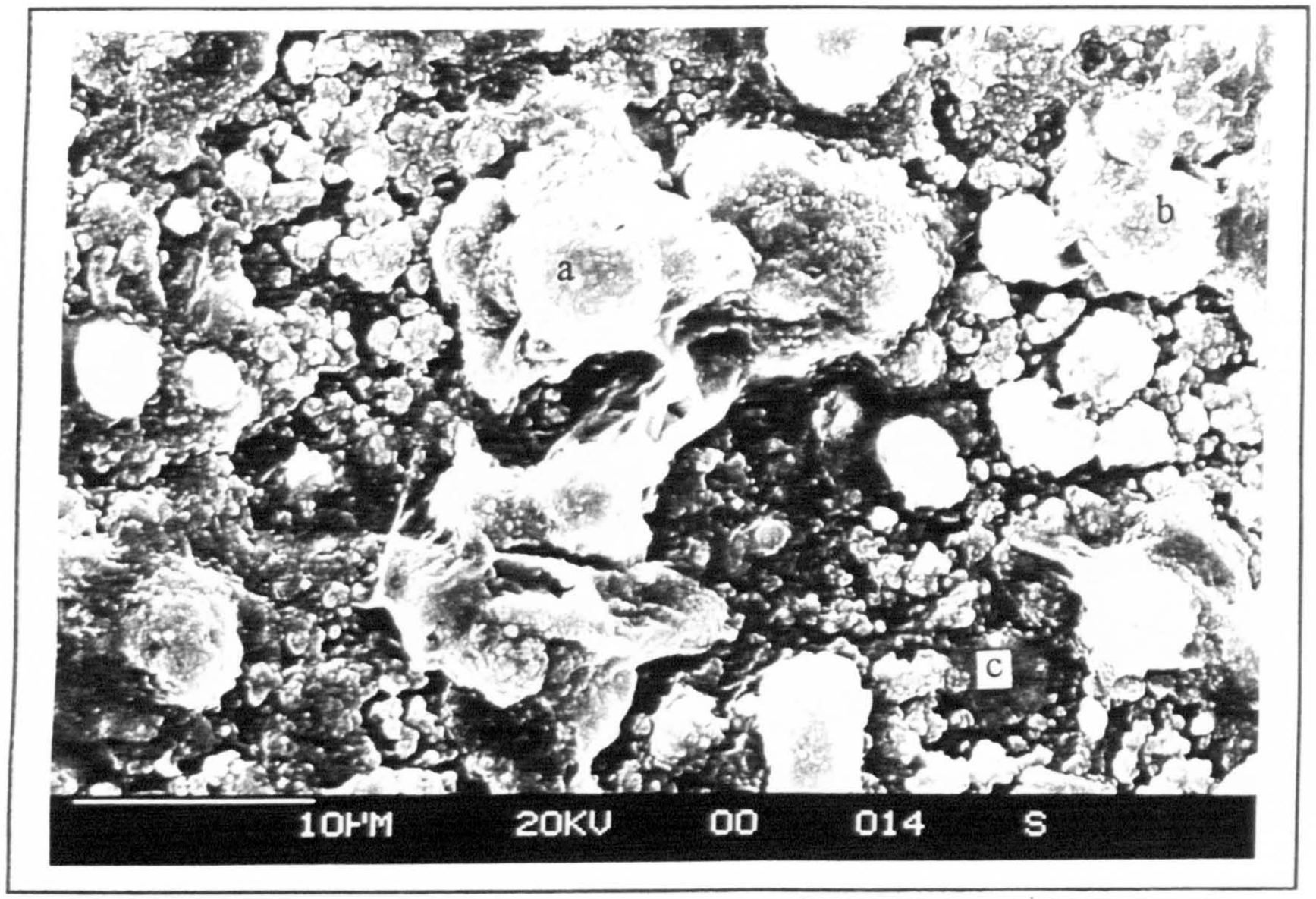

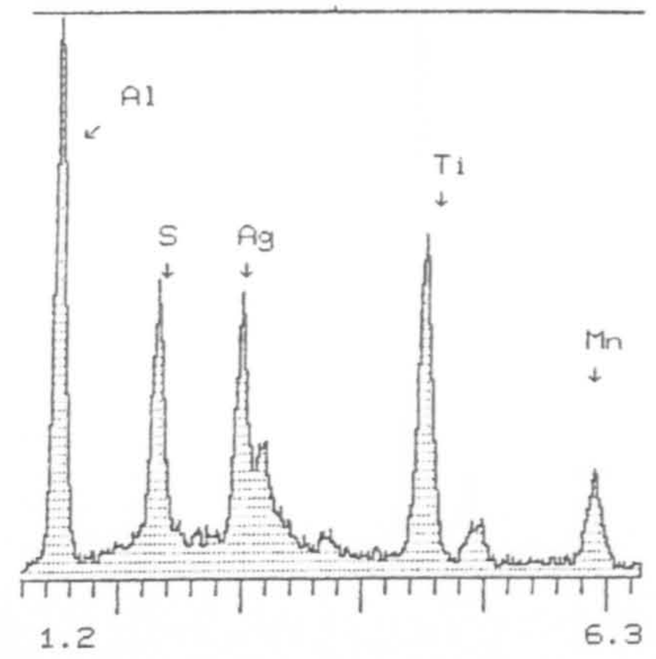

General

a

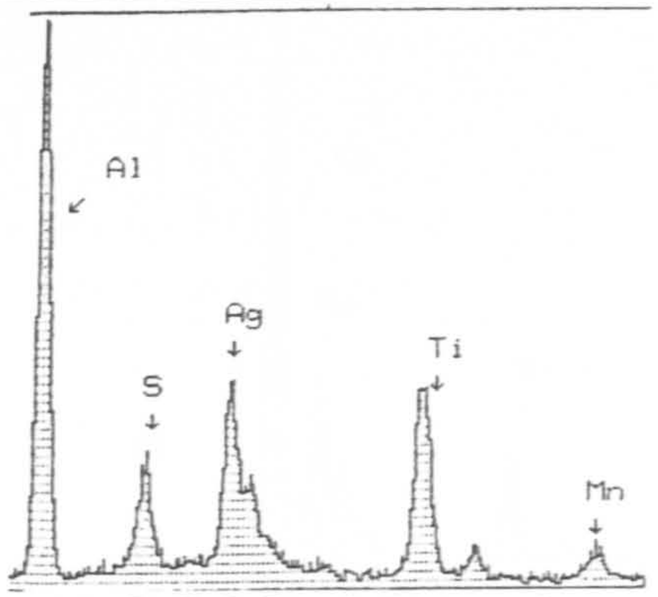

b

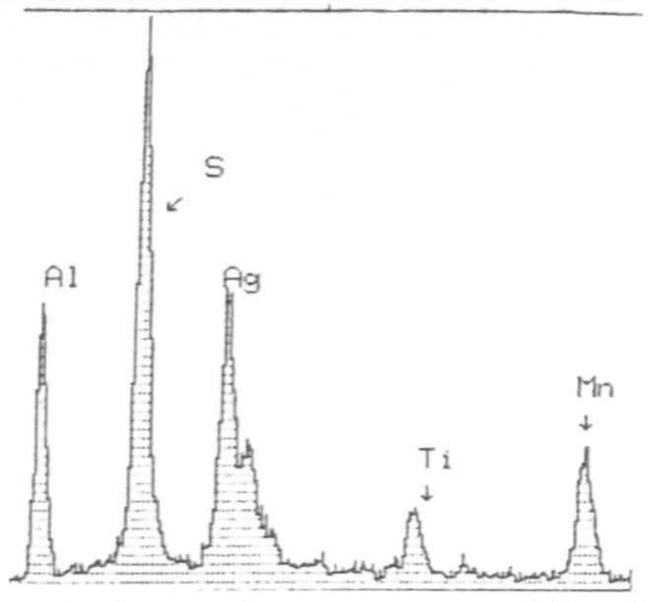

c

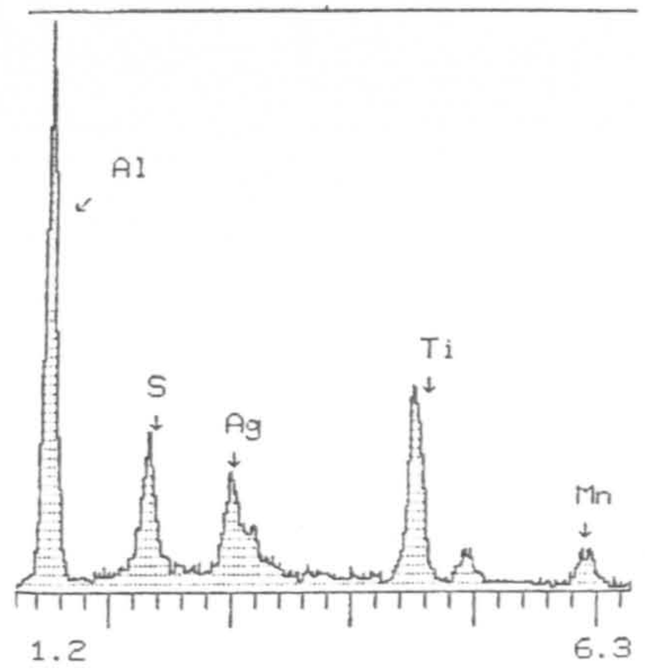

Photograph 8.2.5s: S.E.M micrograph of a salt coated specimen exposed for 20 hours at 700°C in an atmosphere of air + 520 ppm SO_2. The accompanying EPMA analysis'identify key features.(Magnification: 2.0kx)

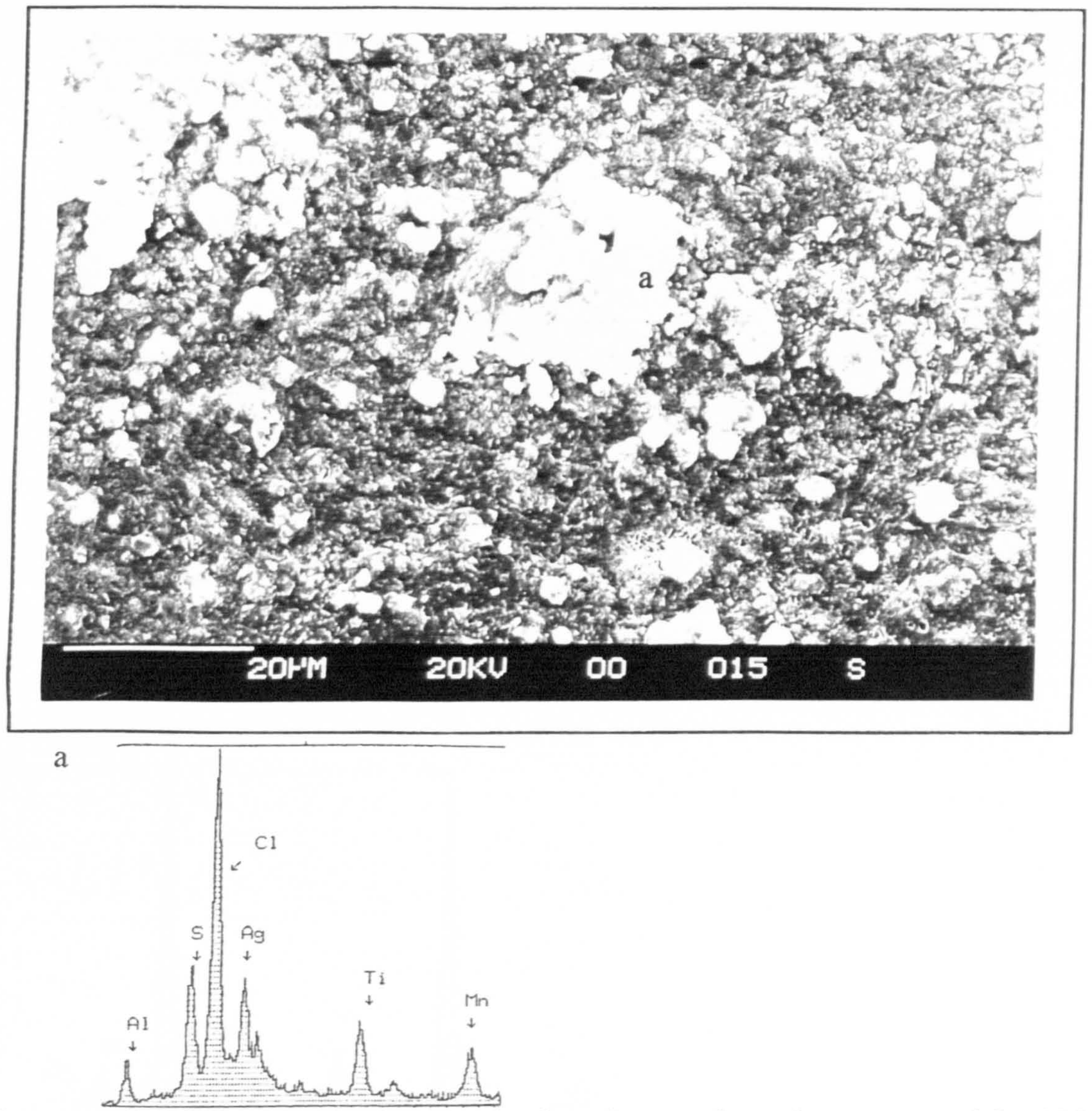

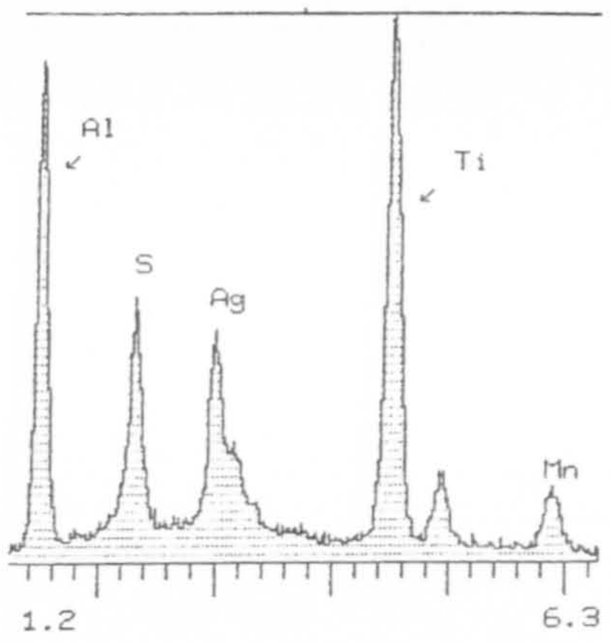

General

Photograph 8.2.5t: S.E.M micrograph of a salt coated specimen exposed for 100 hours at 700°C in an atmosphere of air + 520 ppm SO_2. The accompanying EPMA analysis'identify key features.(Magnification: 1.0kx)

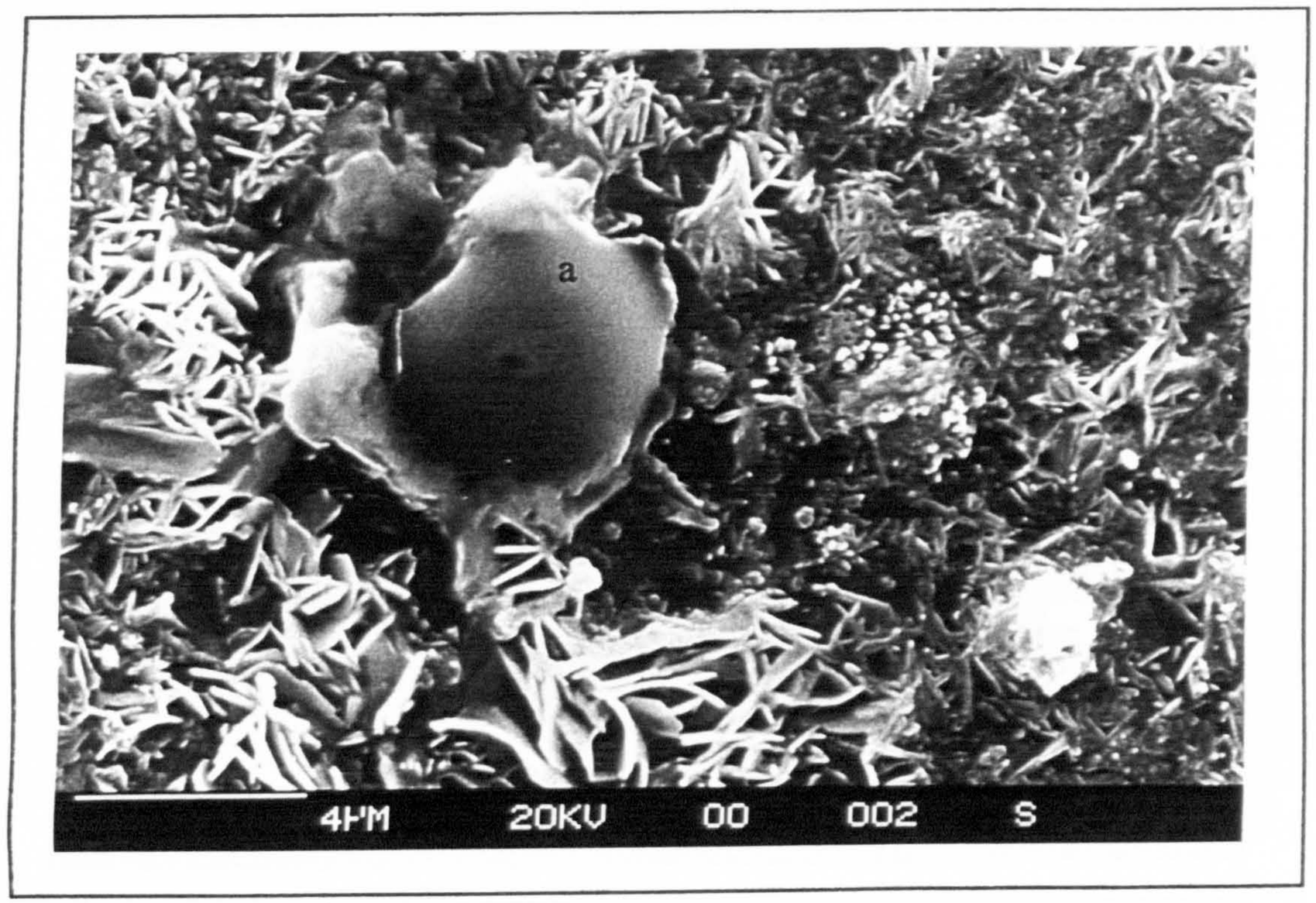

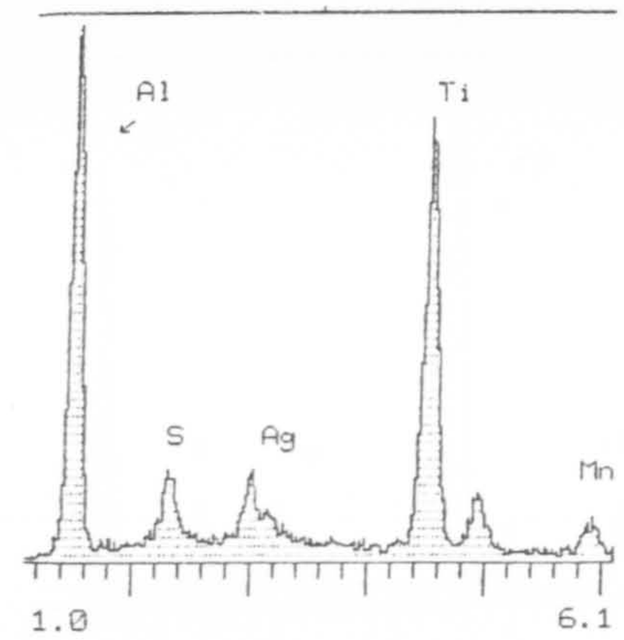

General

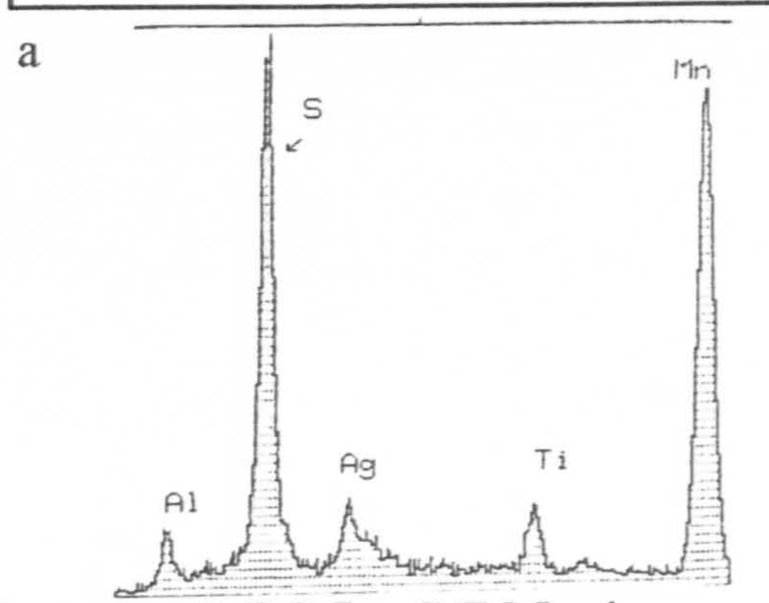

Photograph 8.2.5u: S.E.M micrograph of a salt coated specimen exposed for 5 hours at 750°C in an atmosphere of air + 470 ppm SO_2. The accompanying EPMA analysis' identify key features.(Magnification: 5.0kx)

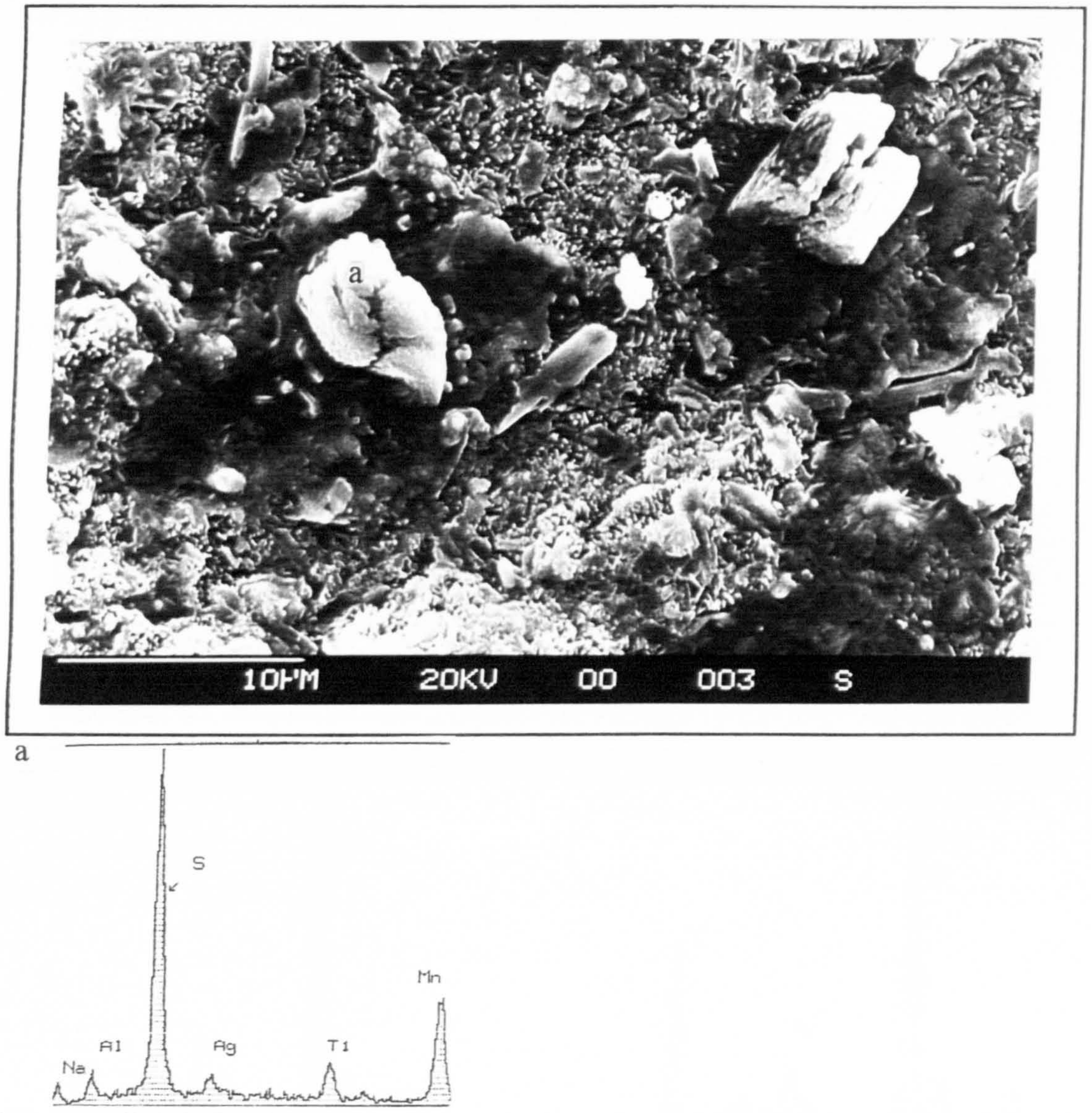

General

Photograph 8.2.5v: S.E.M micrograph of a salt coated specimen exposed for 23 hours at 750°C in an atmosphere of air + 470 ppm SO_2. The accompanying EPMA analysis'identify key features.(Magnification: 2.5kx)

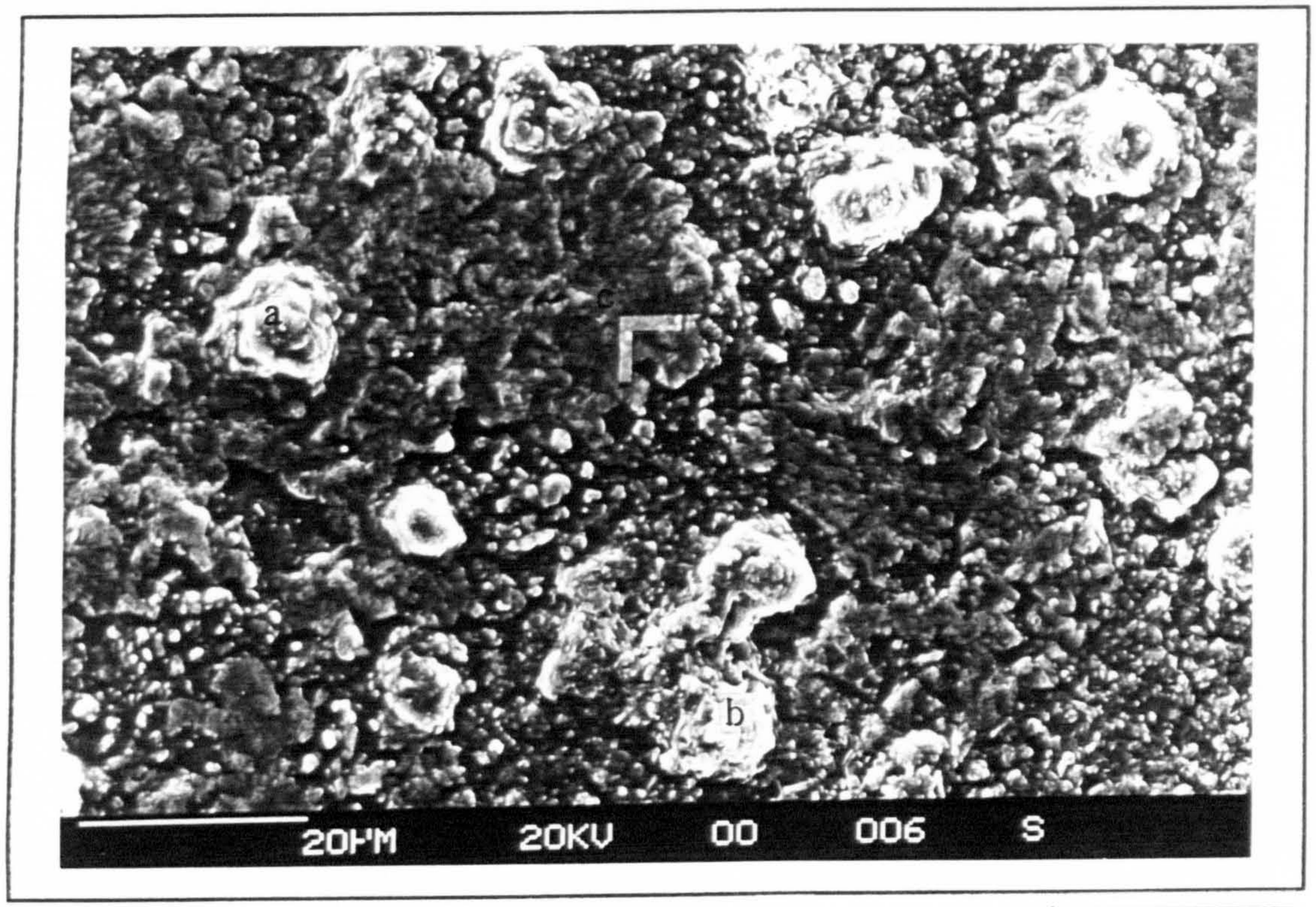

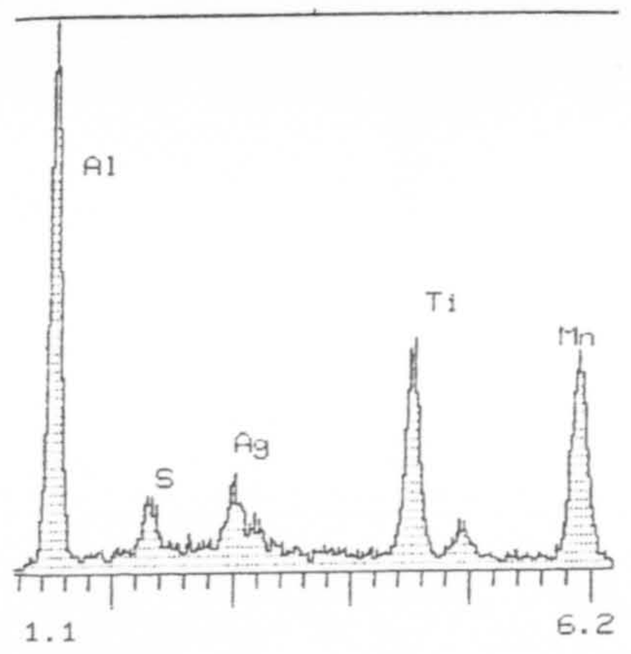

General

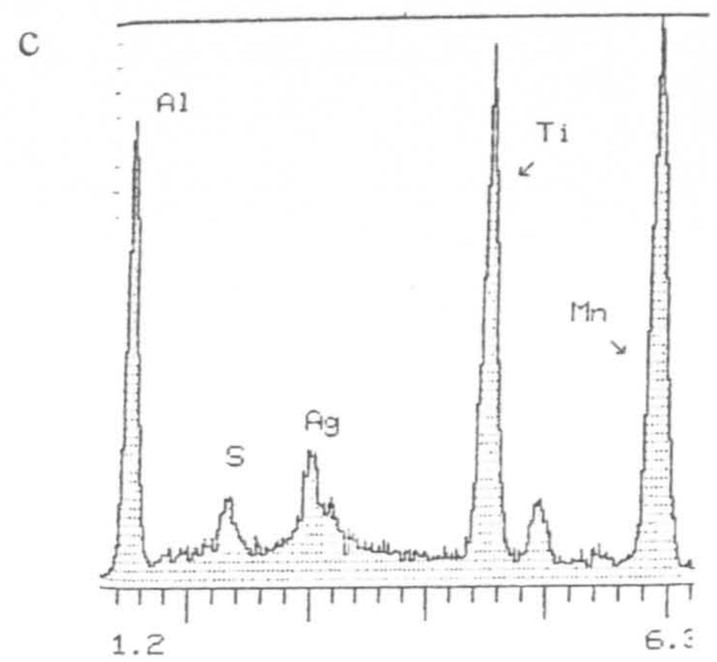

a

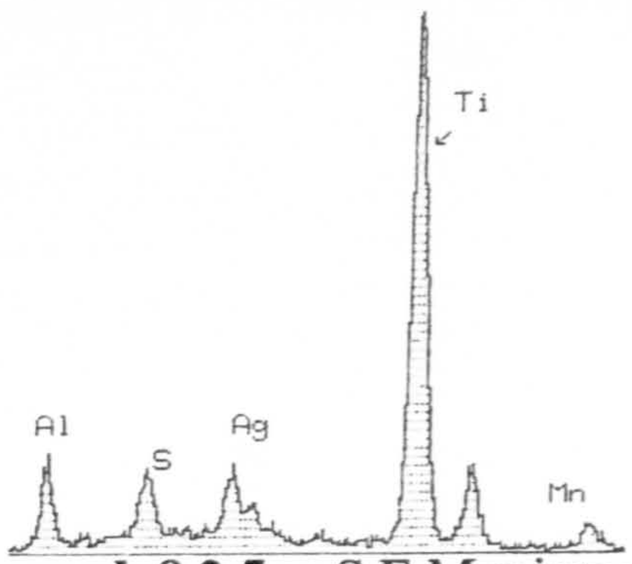

b

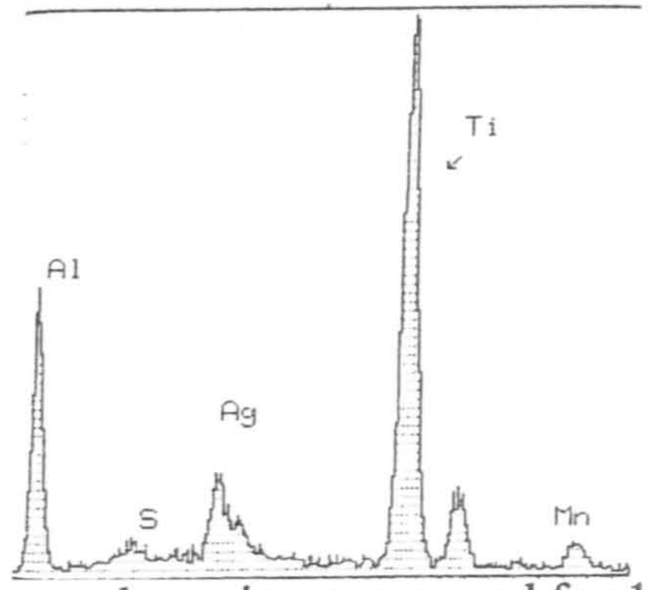

Photograph 8.2.5w: S.E.M micrograph of a salt coated specimen exposed for 100 hours at 750°C in an atmosphere of air + 470 ppm SO_2. The accompanying EPMA analysis' identify key features.(Magnification:1.0kx)

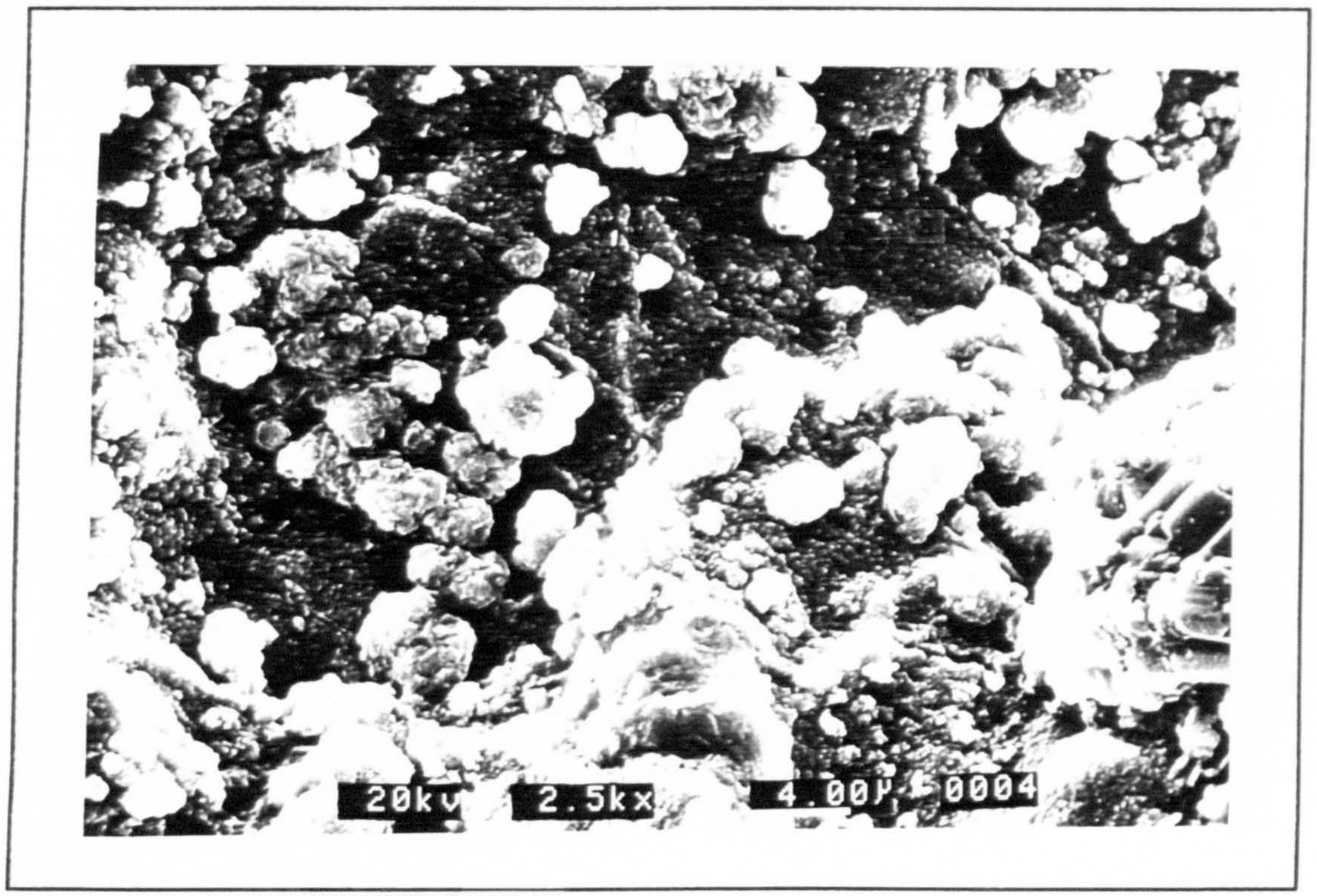

a

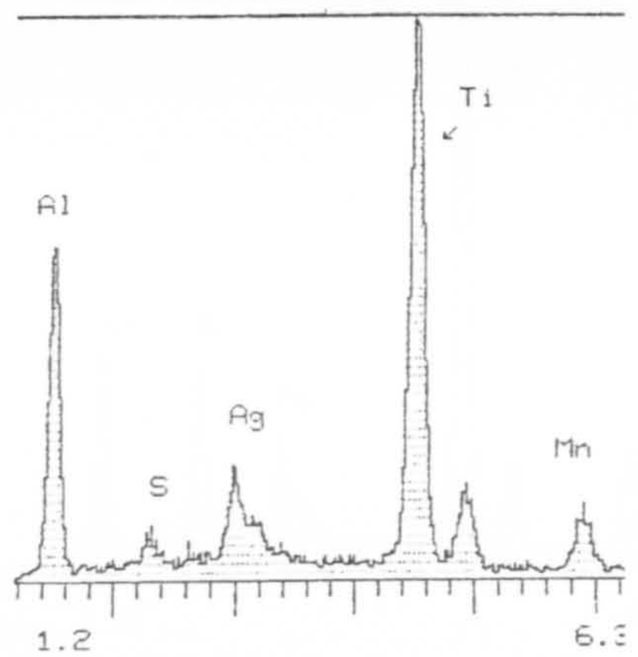

General

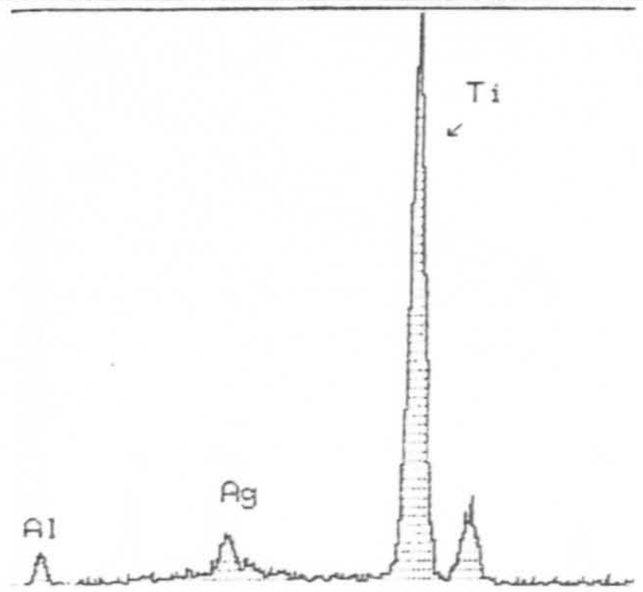

Photograph 8.2.5x: S.E.M micrograph of a salt coated specimen exposed for 5 hours at 800°C in an atmosphere of air + 470 ppmSO_2. The accompanying EPMA analysis'identify key features.(Magnification:2.5kx)

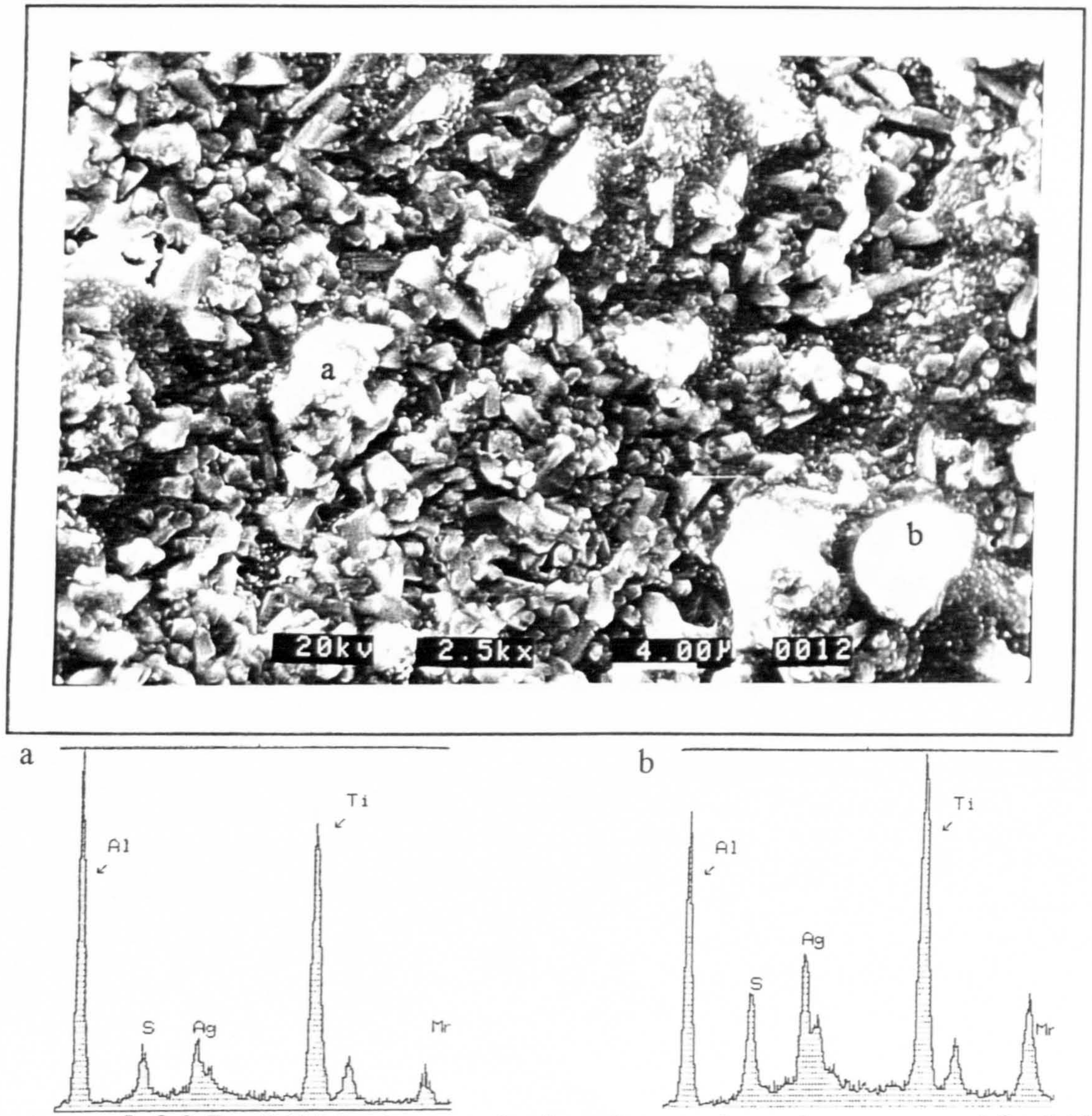

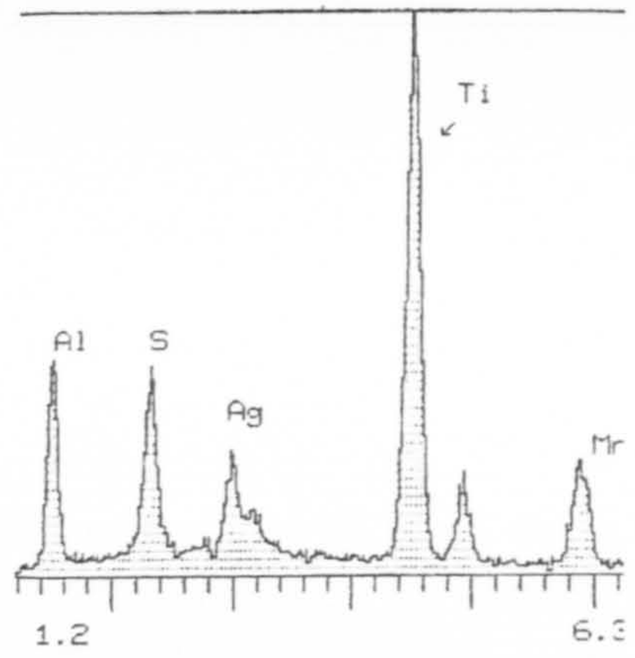

General

Photograph 8.2.5y: S.E.M micrograph of a salt coated specimen exposed for 24 hours at 800°C in an atmosphere of air + 470 ppm SO_2. The accompanying EPMA analysis'identify key features.(Magnification:2.5kx)

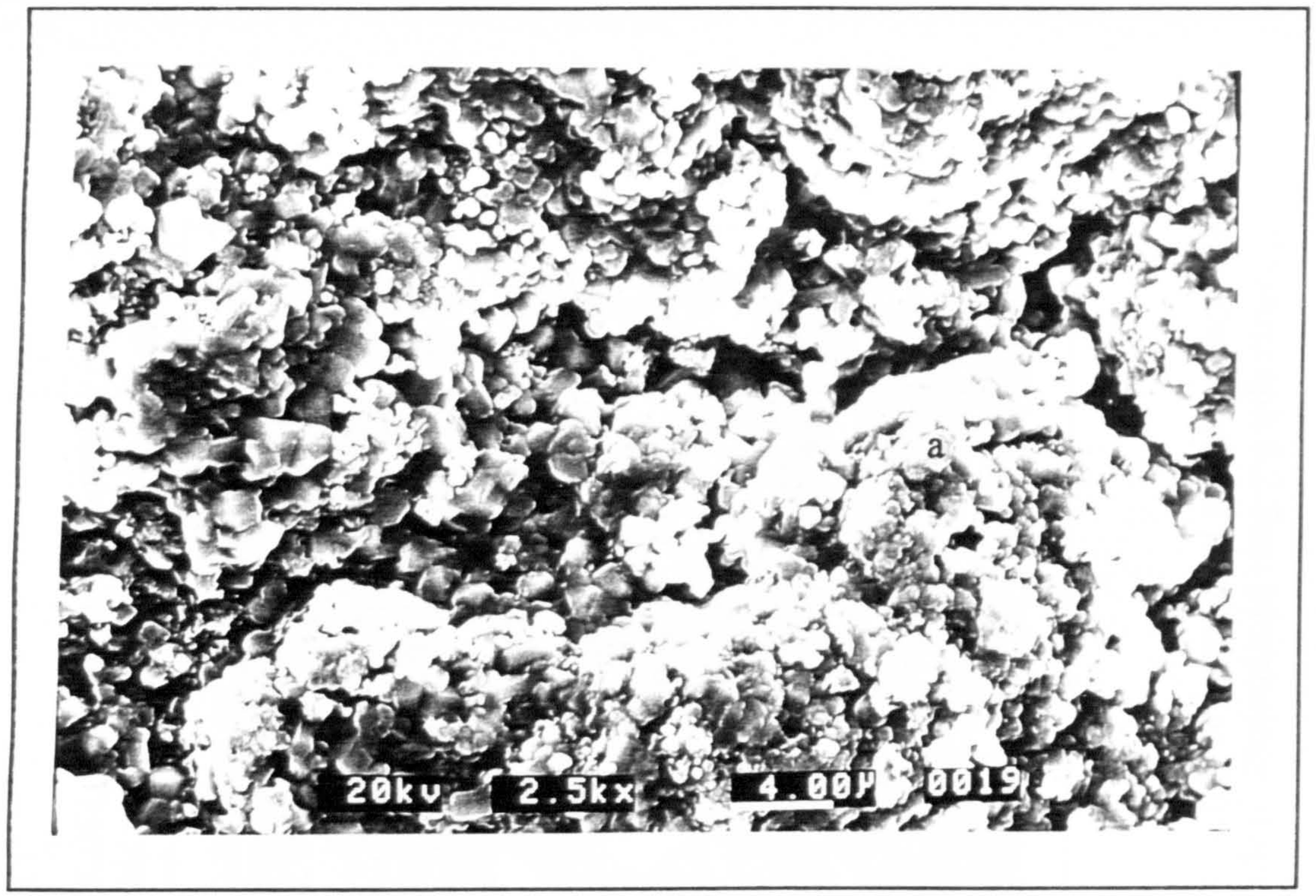

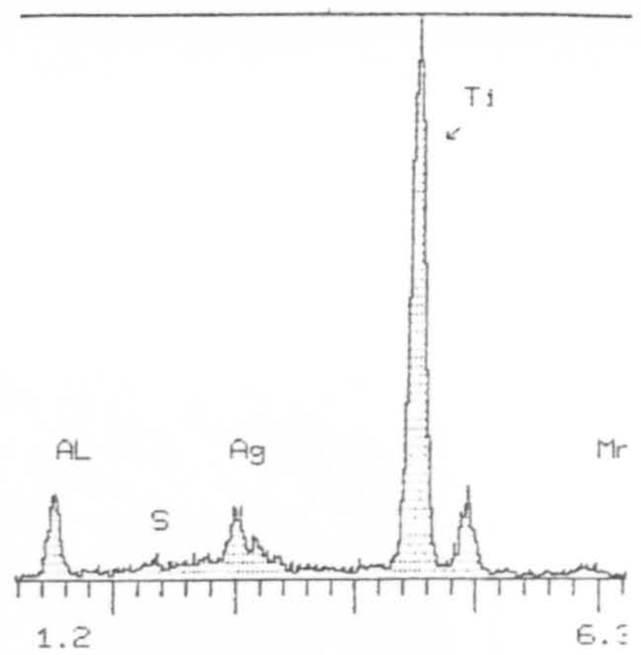

General

a

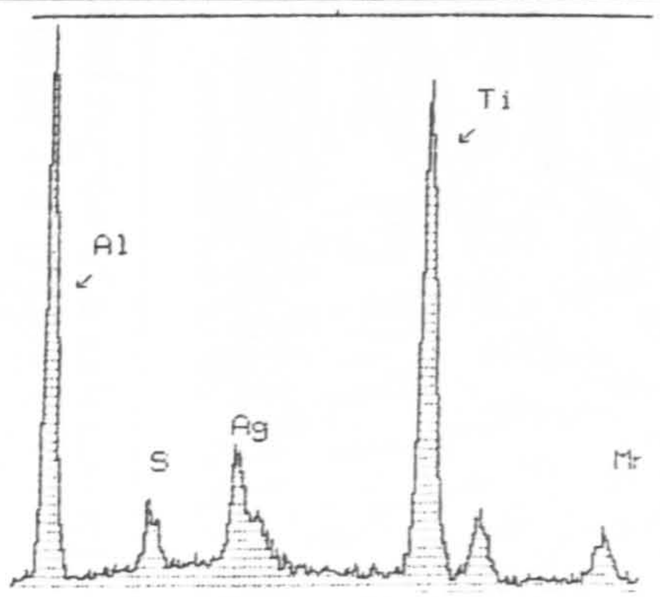

Photograph 8.2.5z: S.E.M micrograph of a salt coated specimen exposed for 100 hours at 800°C in an atmosphere of air + 470 ppm SO_2. The accompanying EPMA analysis'identify key features.(Magnification:2.5kx)

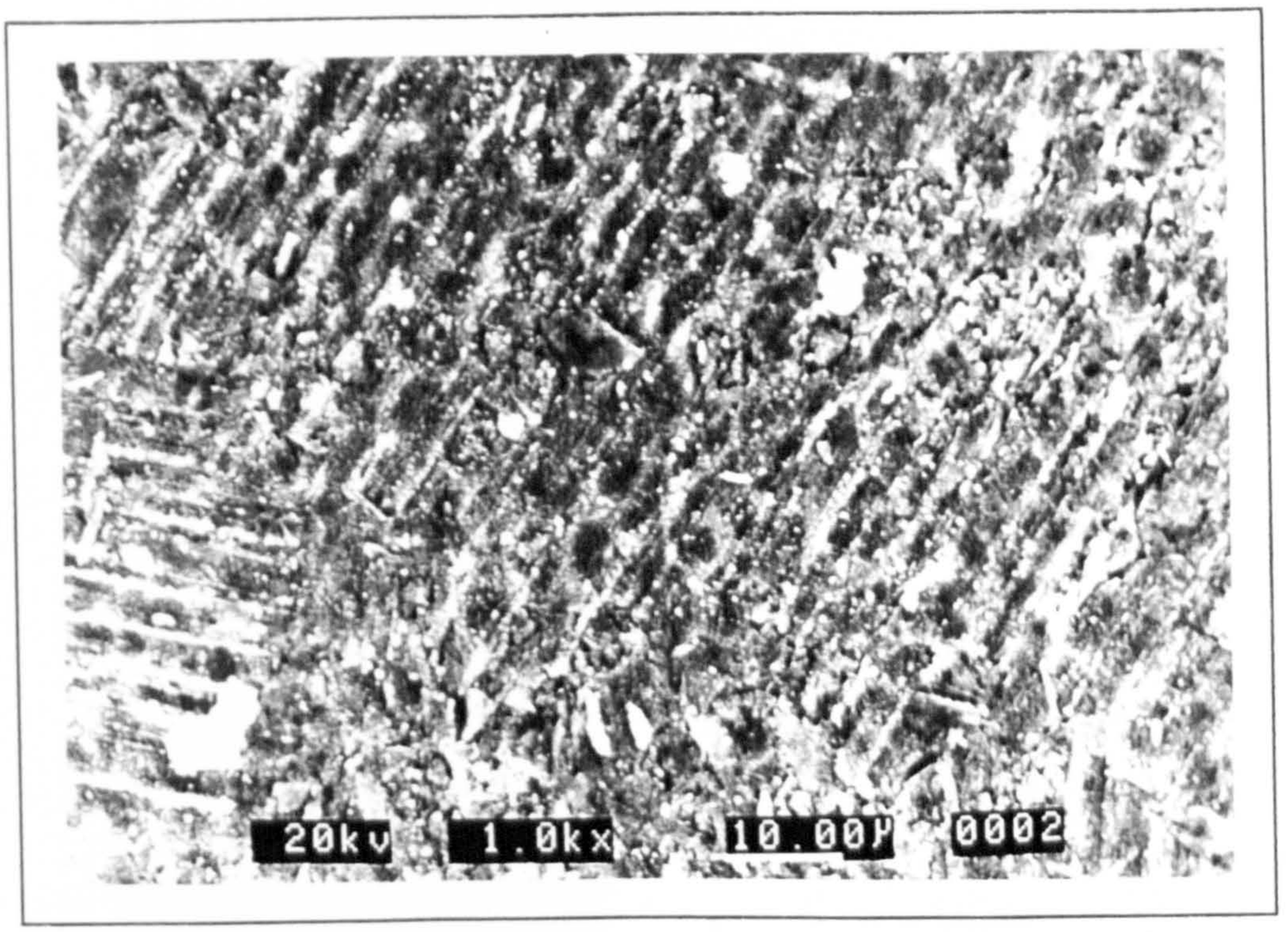

Photograph 8.2.5aa: Morphology of spalled region af a salt coated specimen exposed for 5 hours at 750°C in air + 470 ppm SO_2.

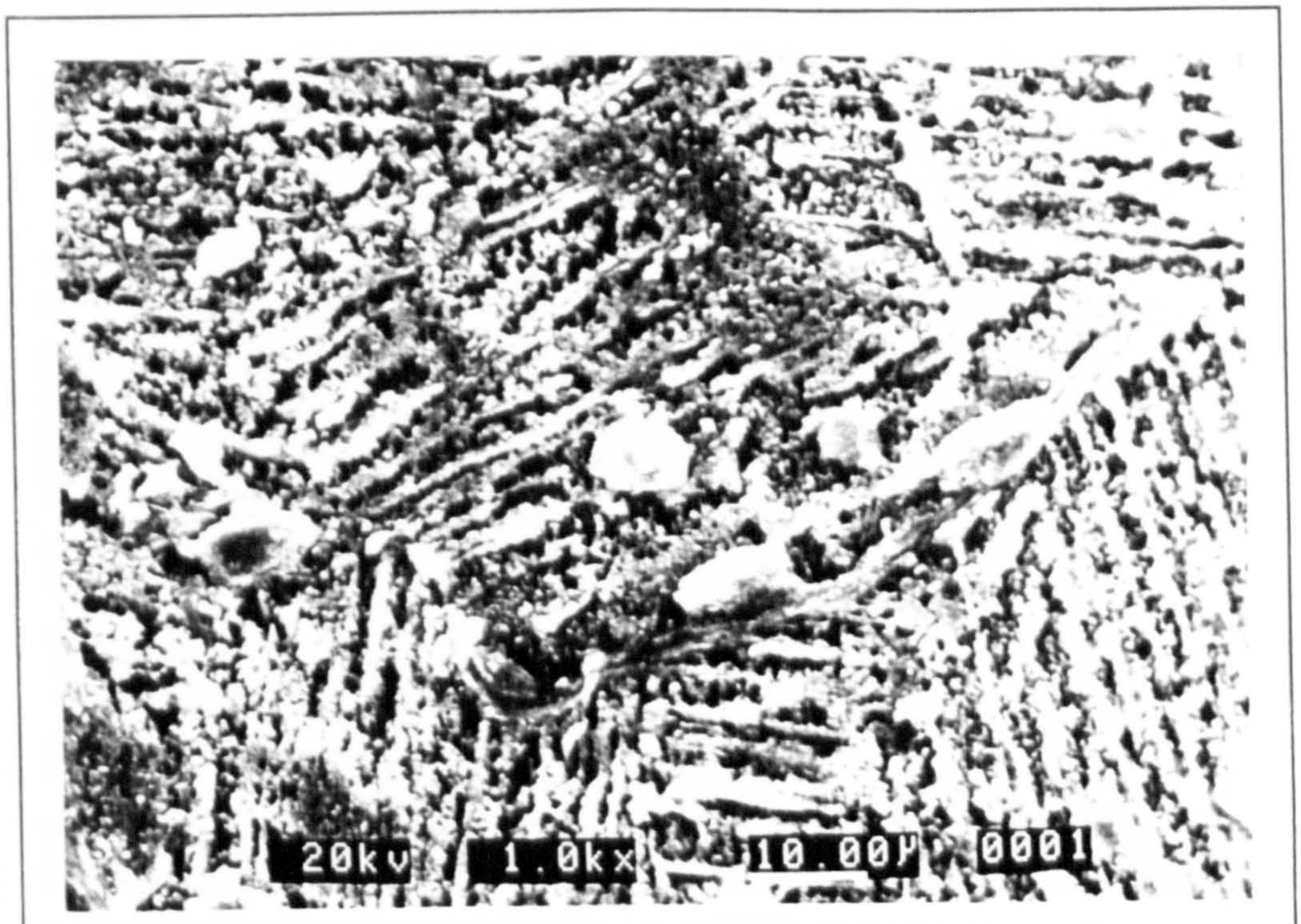

Photograph 8.2.5bb: Morphology of spalled region af a salt coated specimen exposed for 100 hours at 750°C in air + 470 ppm SO_2.

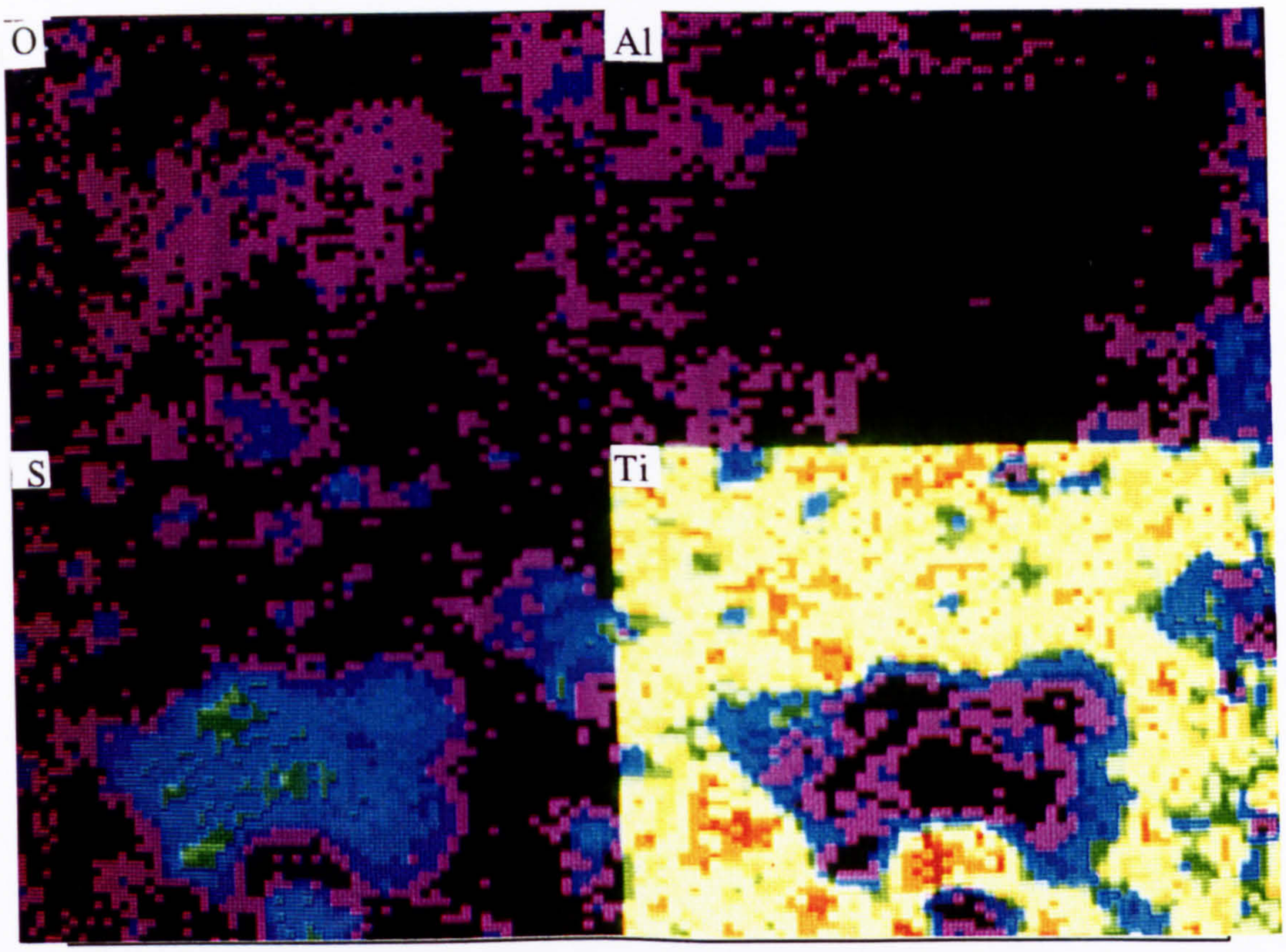

Photograph 8.2.5cc: Elemental X-ray map of the surface morphology formed after 100 hours at 650°C in air + 400 ppm SO_2, in the presence of salt.

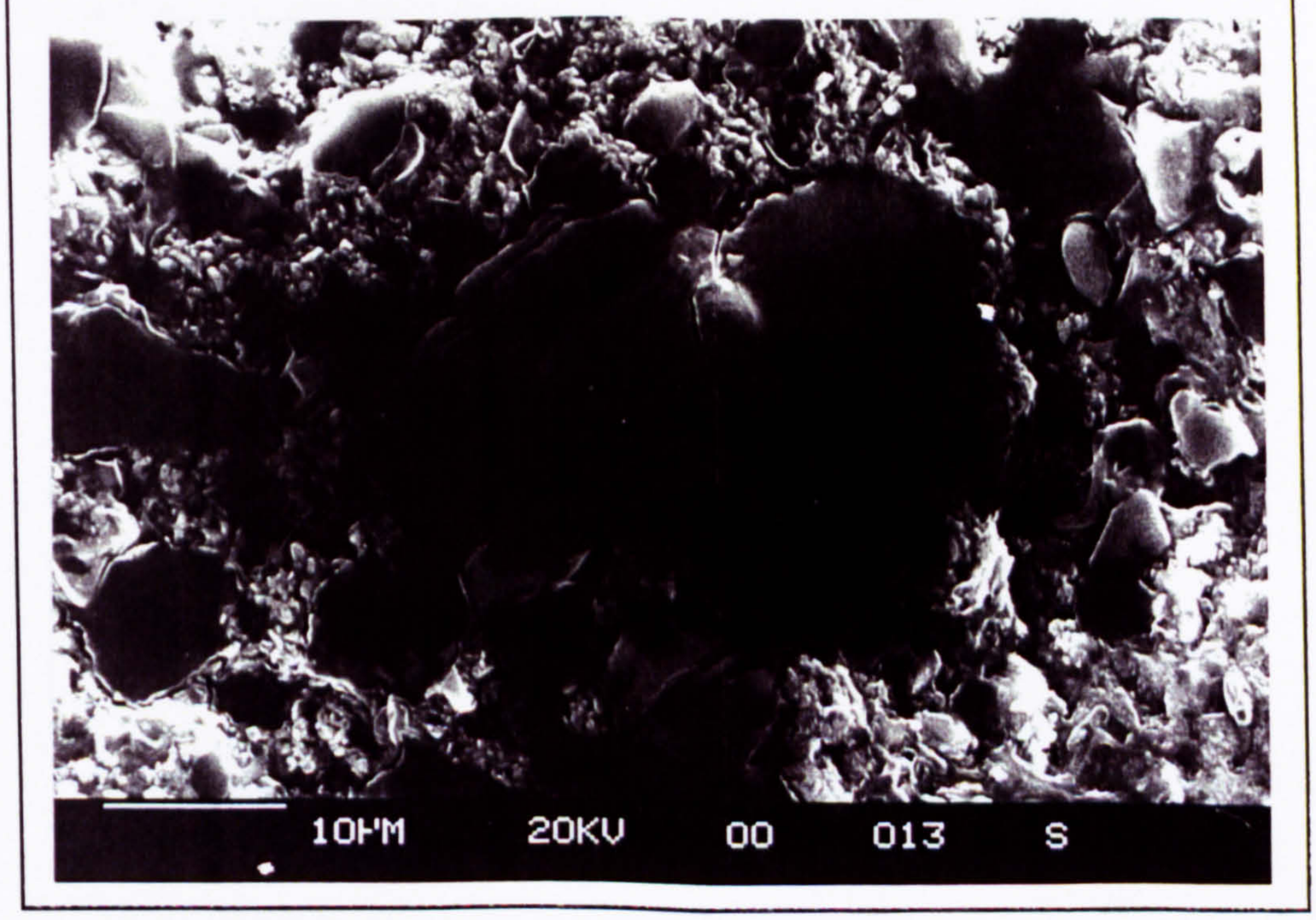

Photograph 8.2.5dd: Shows the surface morphology of the scale which was used to obtain the above Element map (100 hours at 650°C, in the presence of salt +SO_2)

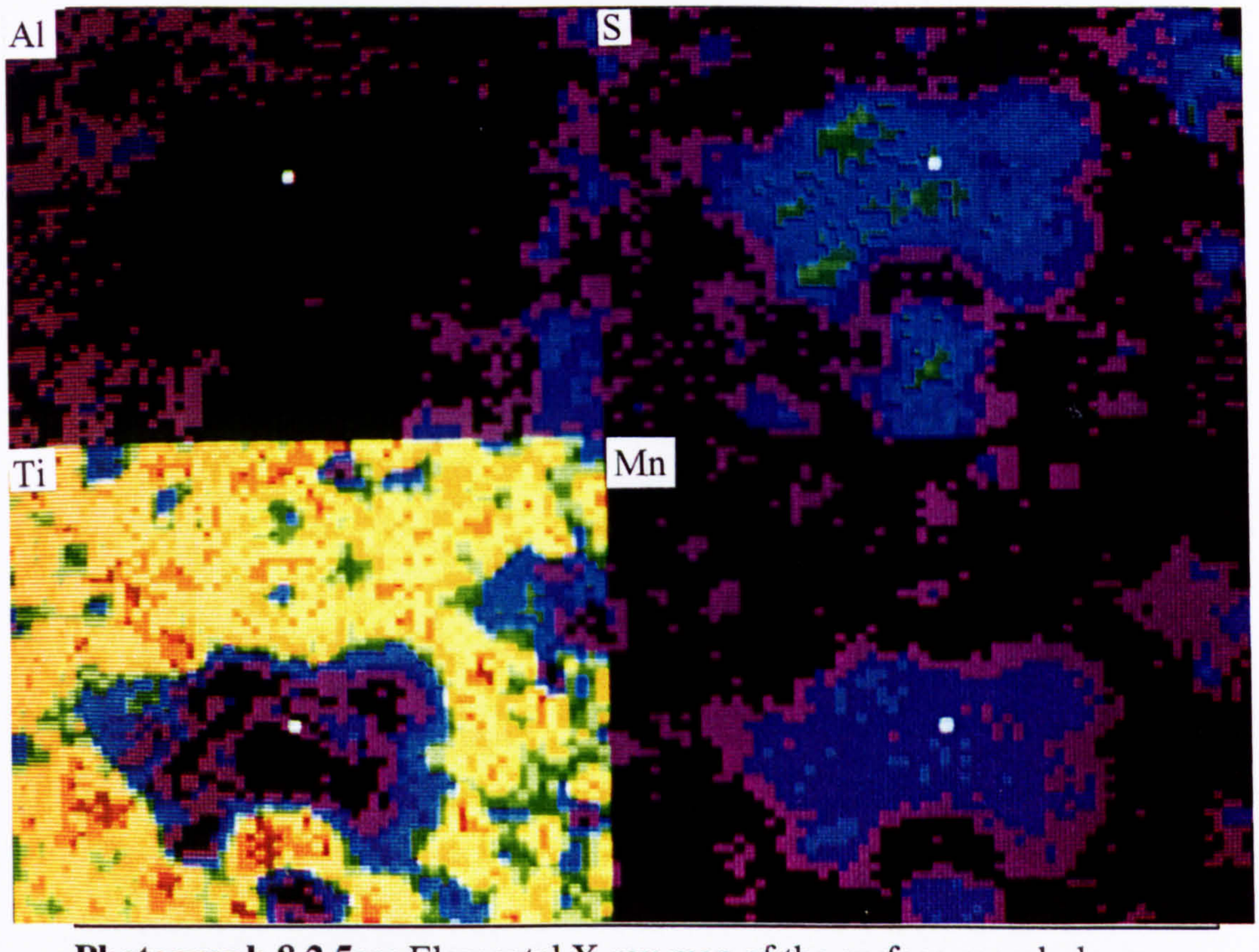

Photograph 8.2.5ee: Elemental X-ray map of the surface morphology formed after 100 hours at 650°C in air + 400 ppm $SO_{2,}$ in the presence of salt.

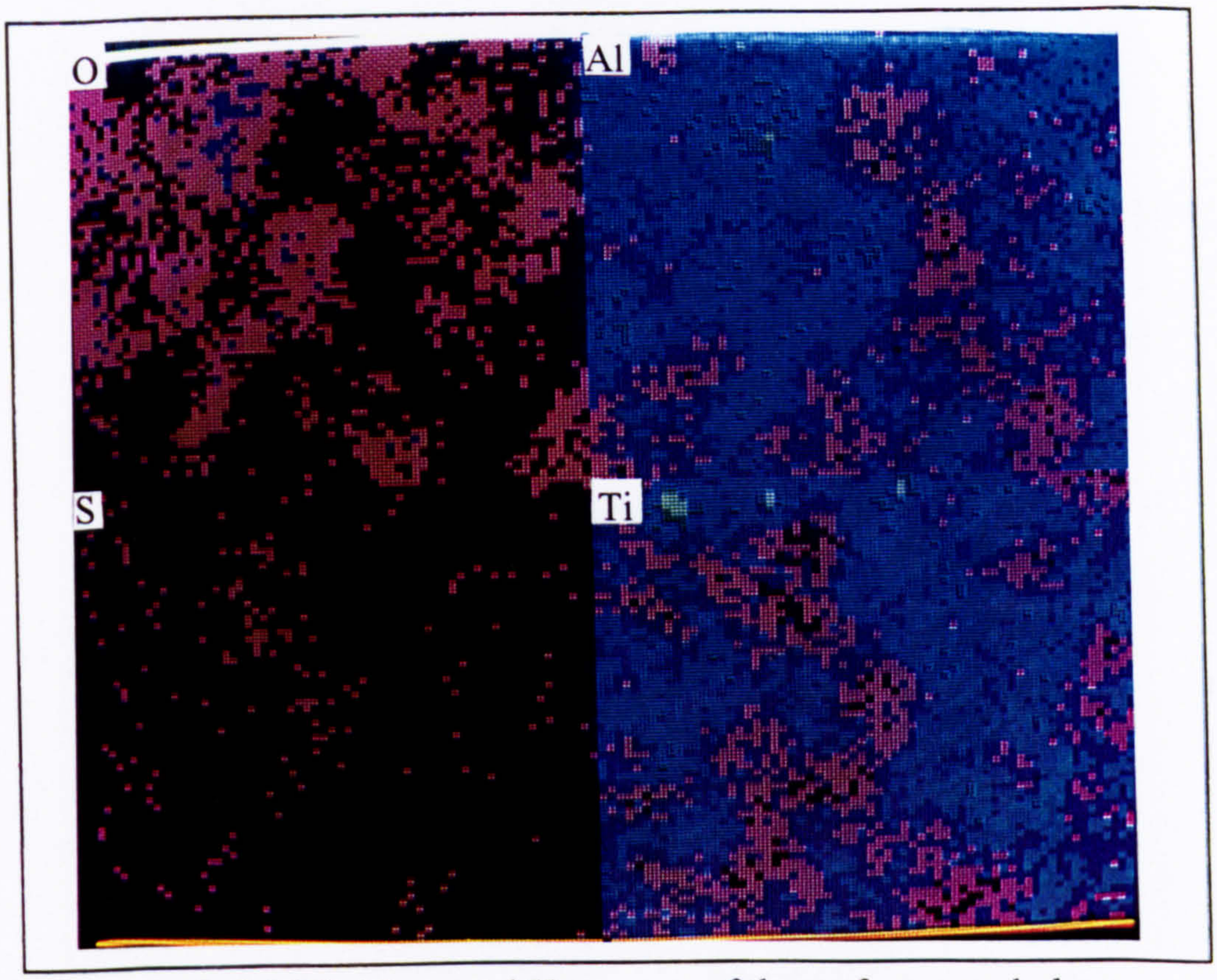

Photograph 8.2.5ff: Elemental X-ray map of the surface morphology formed after 5 hours at 750°C in air + 470 ppm SO_2 in the presence of salt.

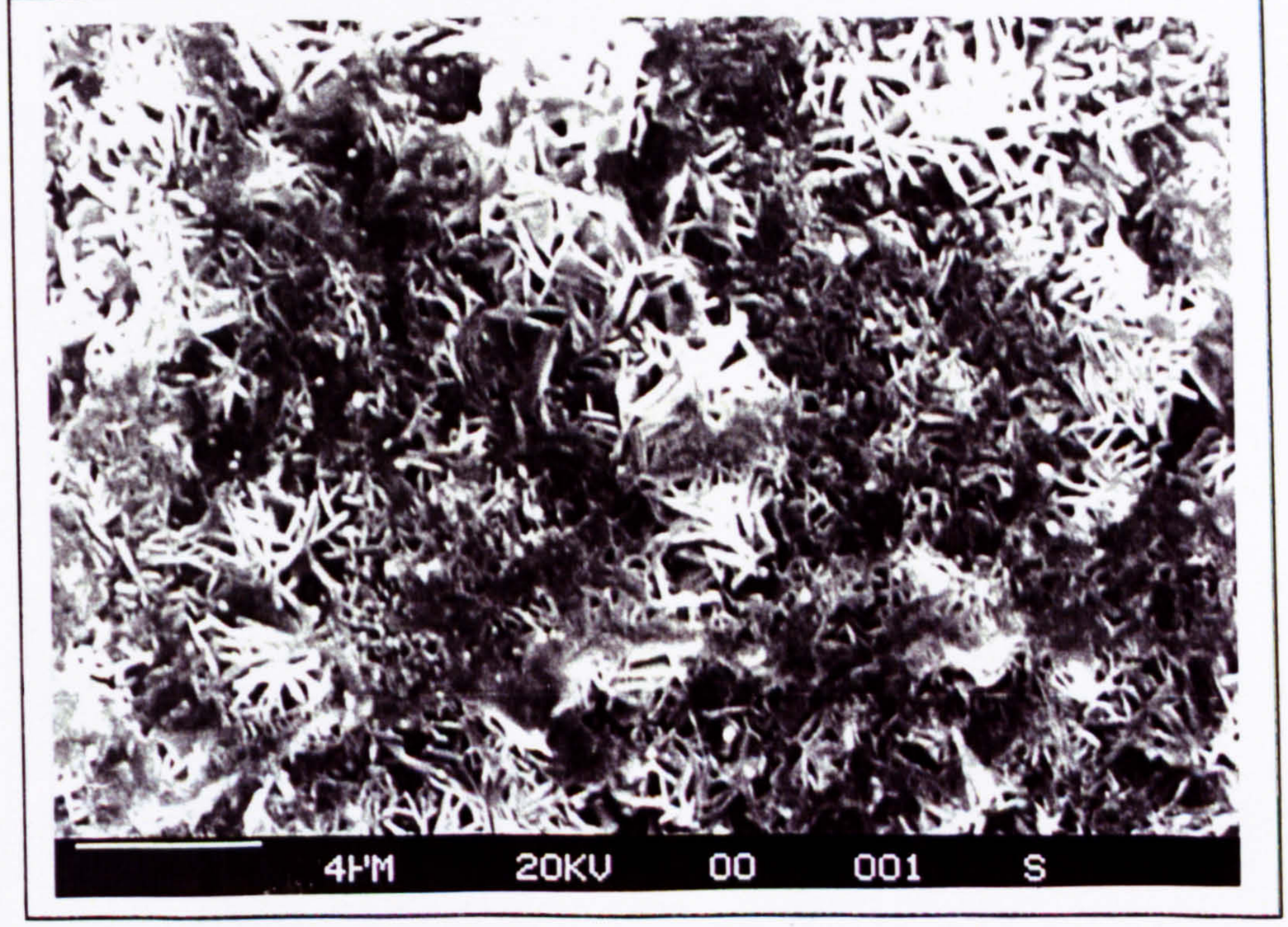

Photograph 8.2.5gg: Shows the surface morphology of the scale which was used to obtain the above Element map (5 hours at 750°C, in the presence of salt +SO_2)

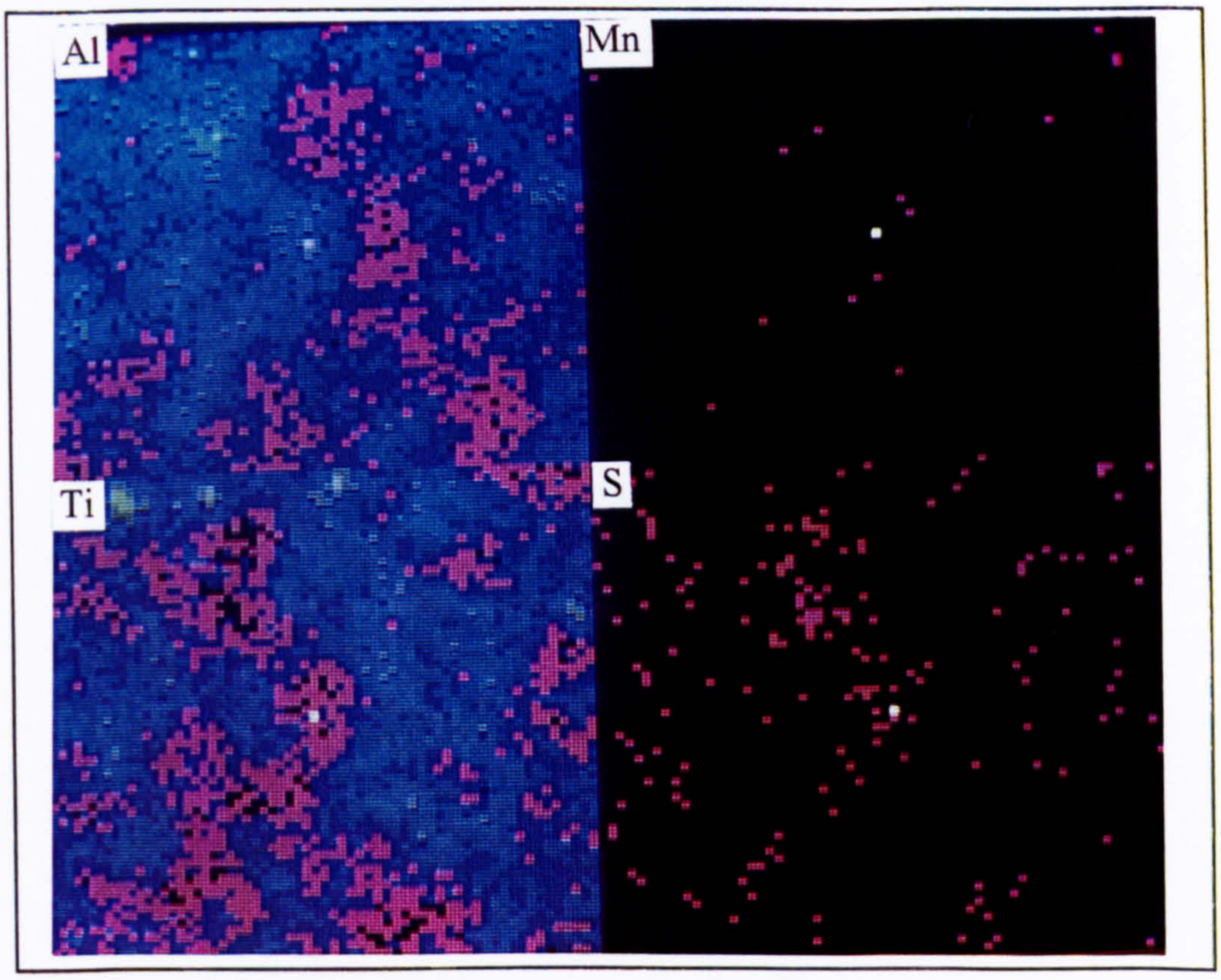

Photograph 8.2.5hh: Elemental X-ray map of the surface morphology formed after 5 hours at 750°C in air + 470 ppm SO_2, in the presence of salt.

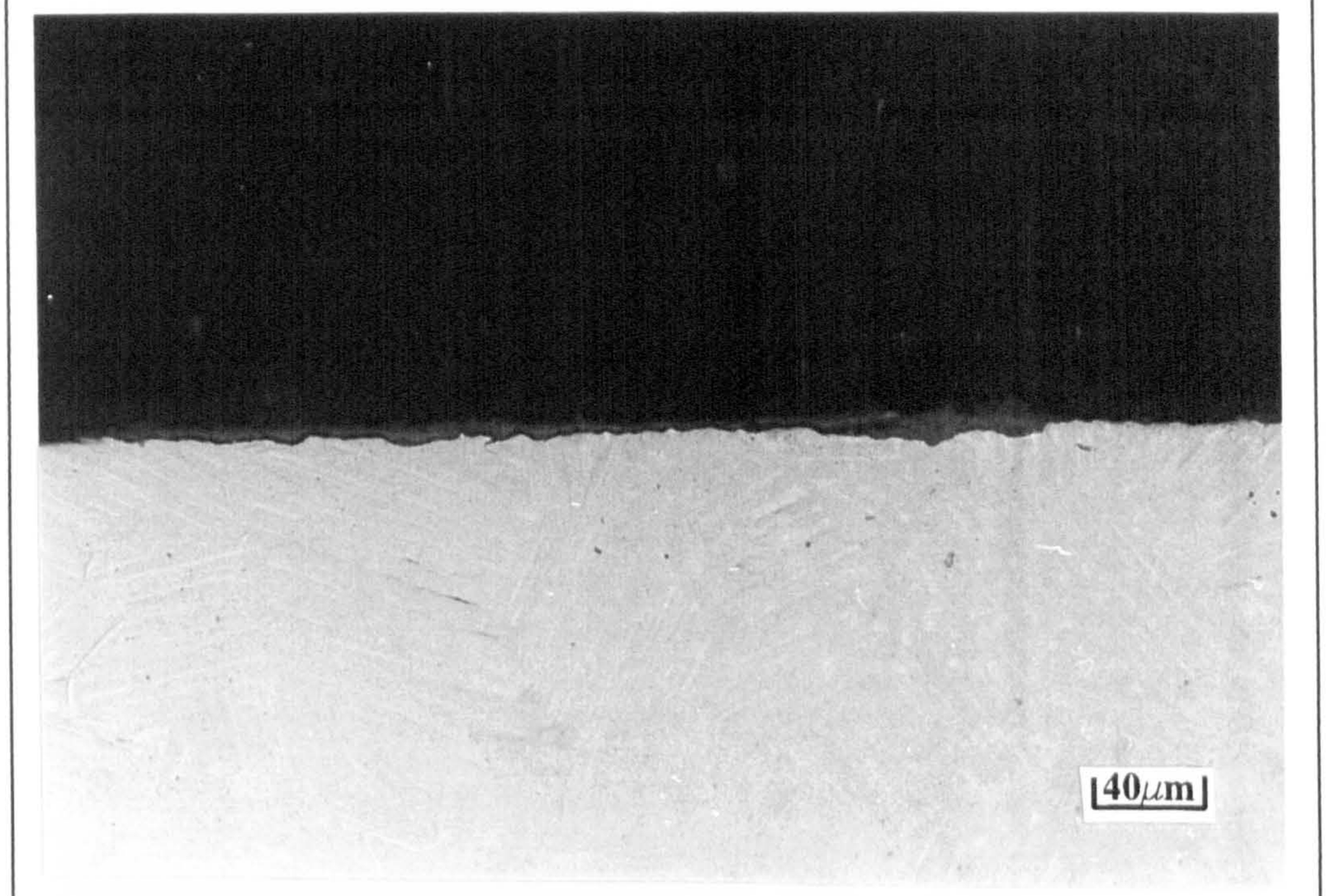

Photograph 8.2.5ii: Optical micrograph of the through section of a salt coated specimen exposed for 100 hours at 700°C in air + 520 ppm SO_2. (Magnification =100x)

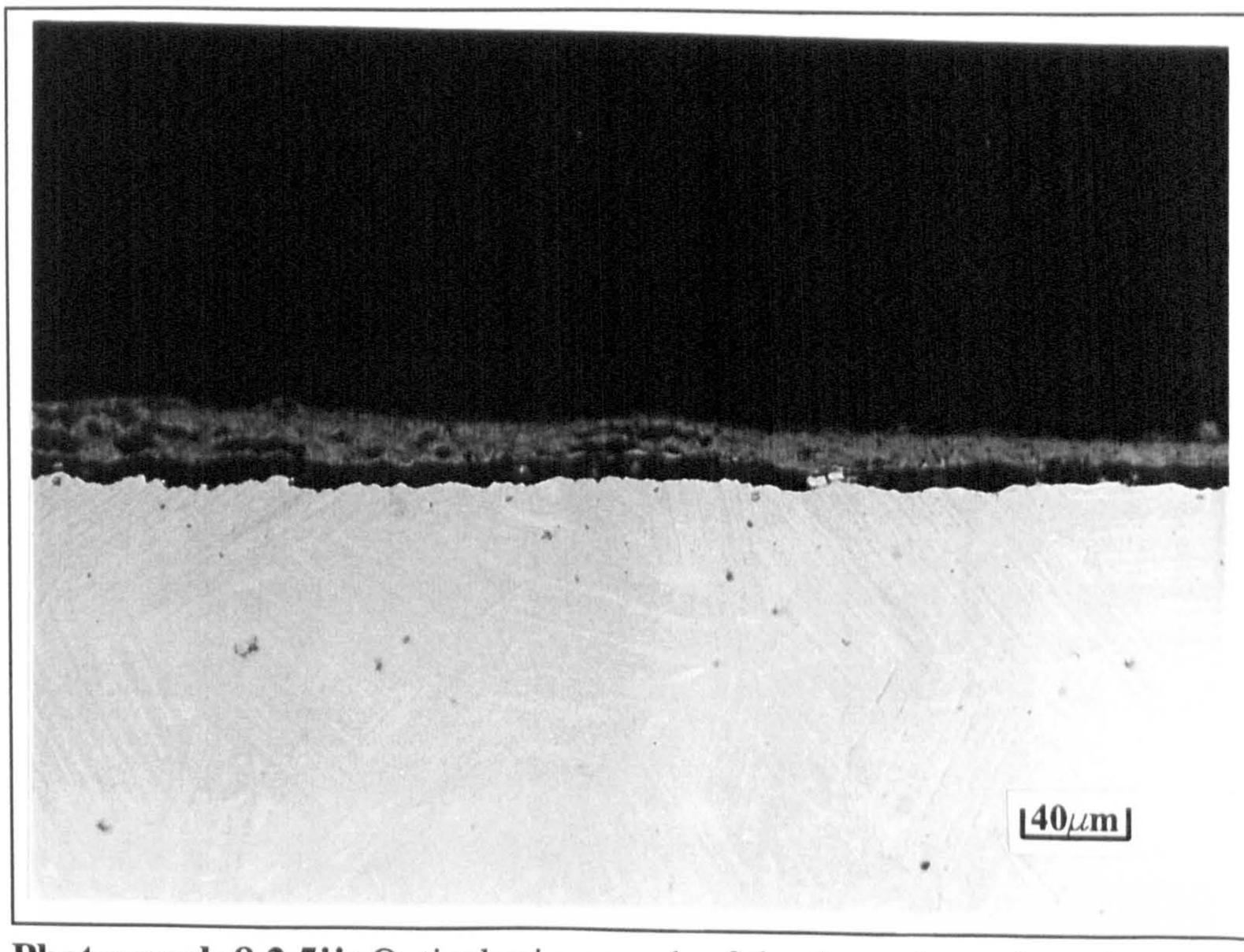

Photograph 8.2.5jj: Optical micrograph of the through section of a salt coated specimen exposed for 100 hours at 750°C in air + 470 ppm SO_2. (Magnification =100x)

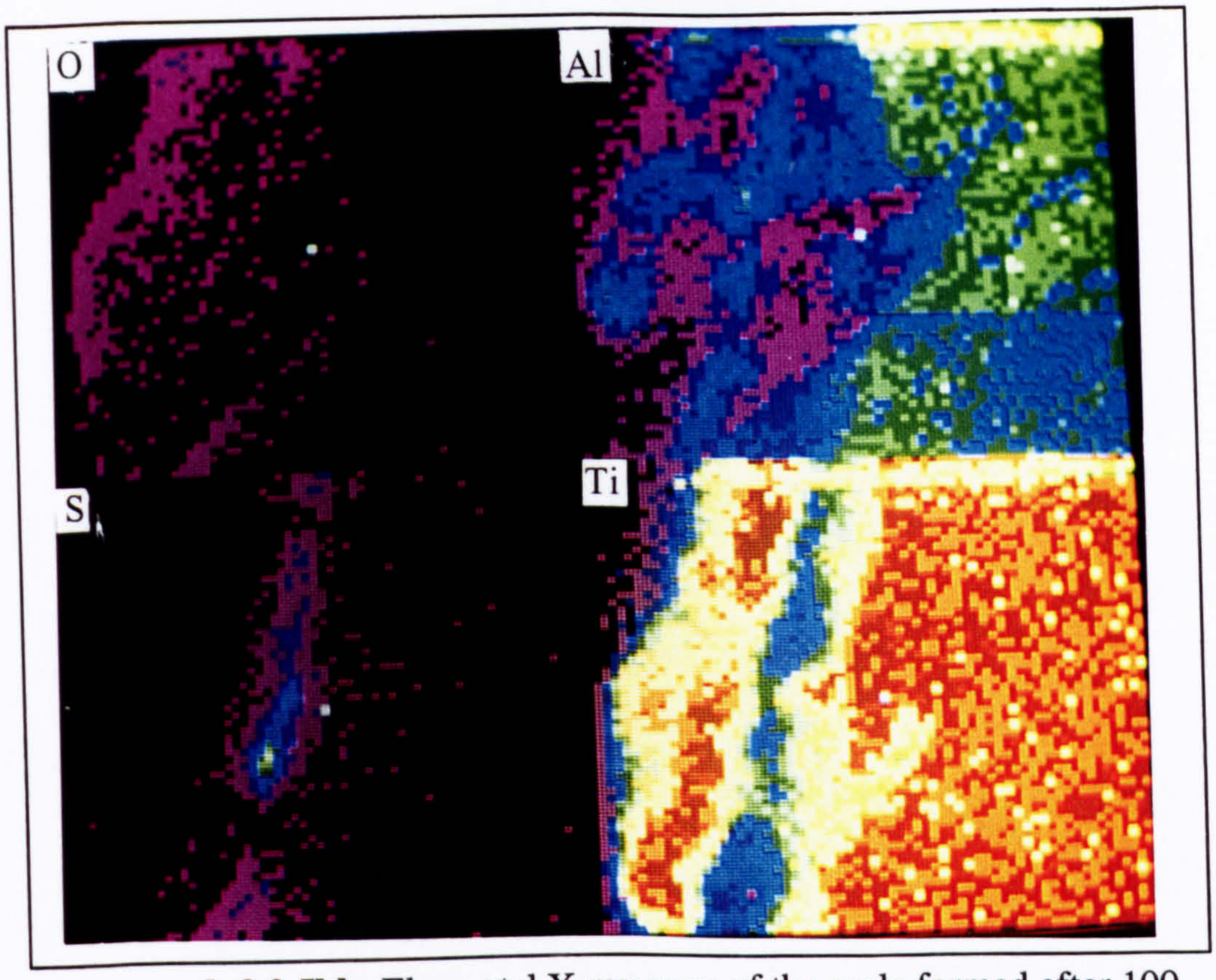

Photograph 8.2.5kk: Elemental X-ray map of the scale formed after 100 hours at 650°C in air + 400 ppm SO_2, in the presence of salt.

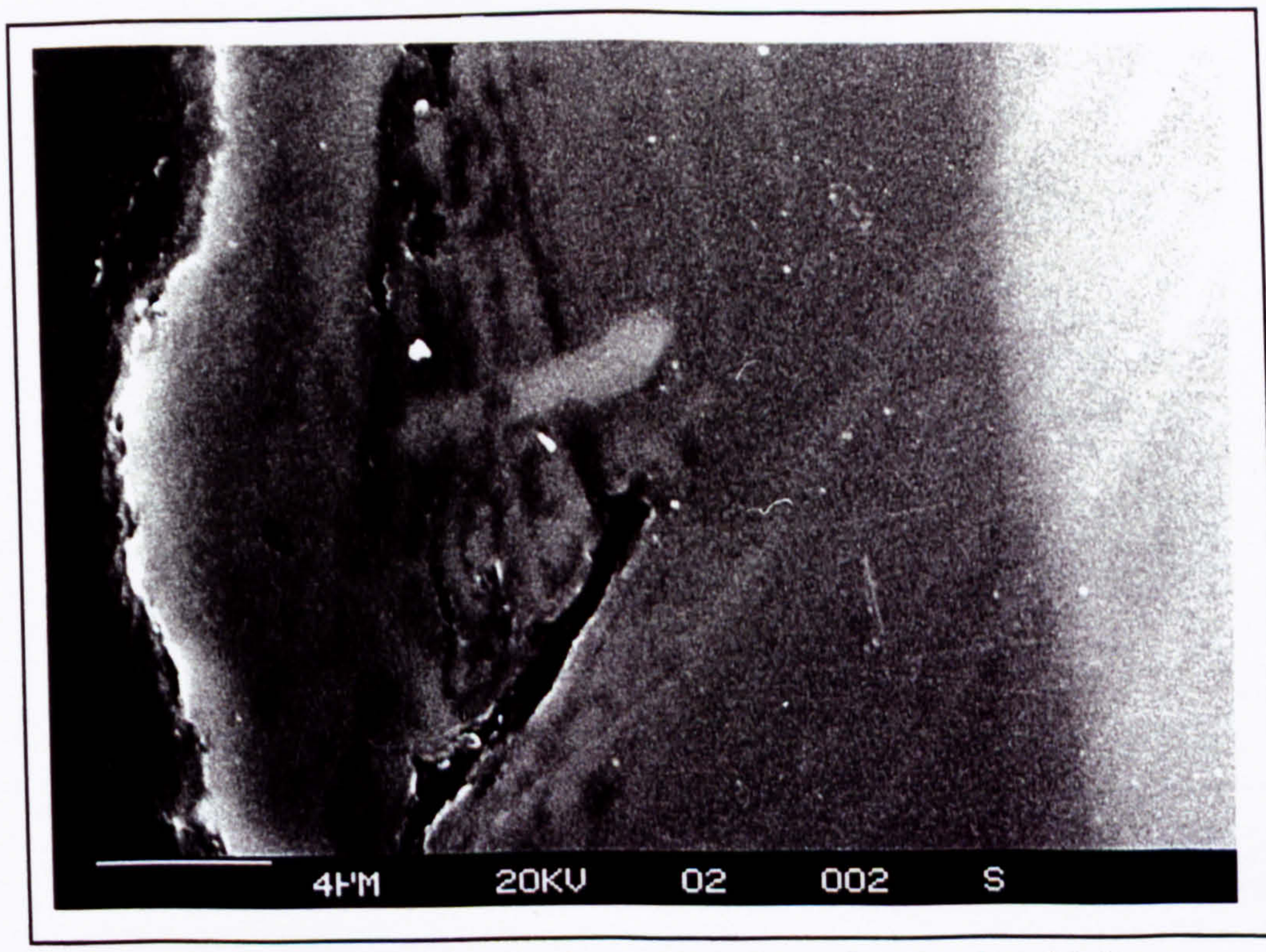

Photograph 8.2.5ll: Shows thethrough section of the scale which was used to obtain the above Element map (100 hours at 650°C, in the presence of salt +SO_2)

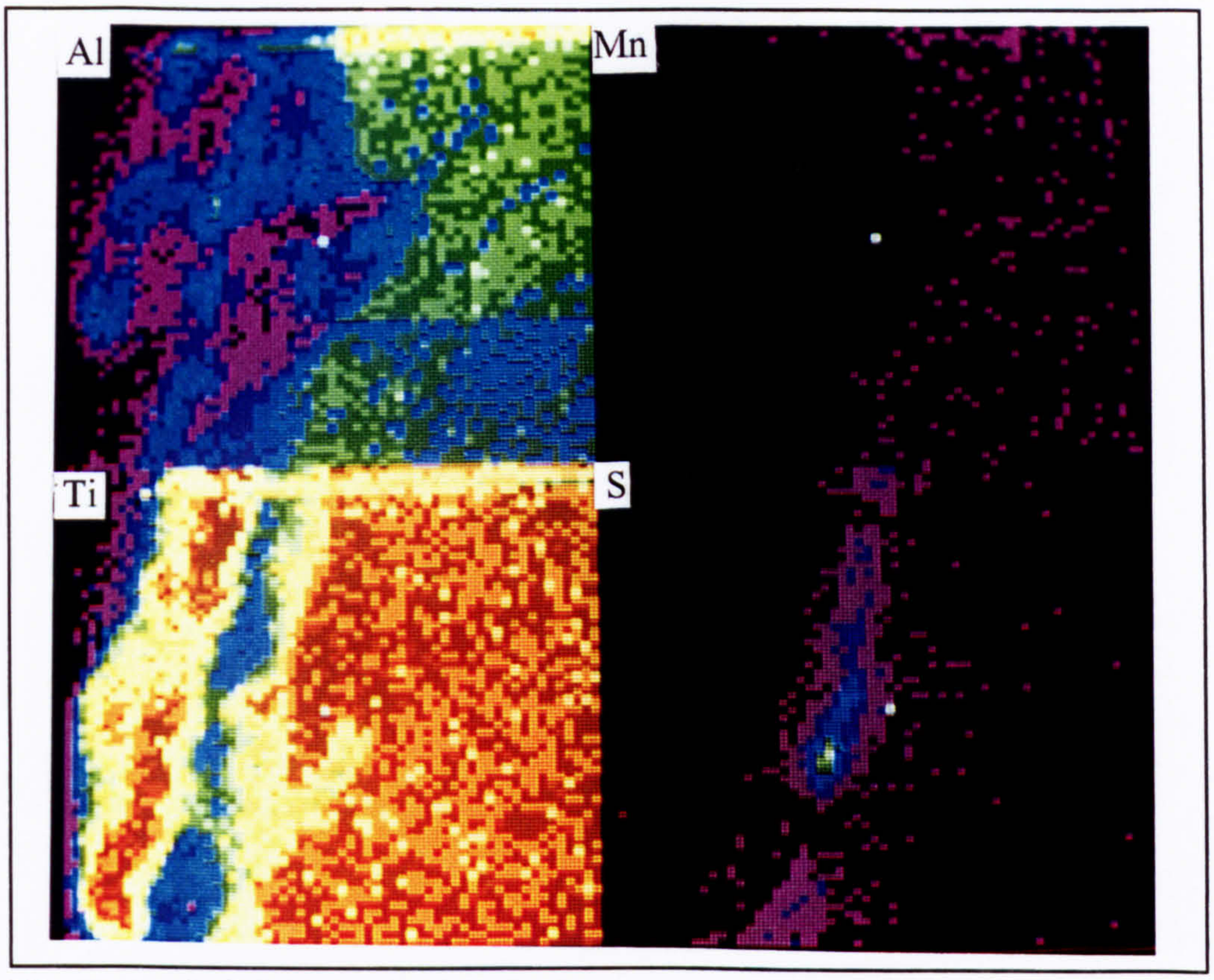

Photograph 8.2.5mm: Elemental X-ray map of the scale formed after 100 hours at 650°C in air + 400 ppm SO_2, in the presence of salt.

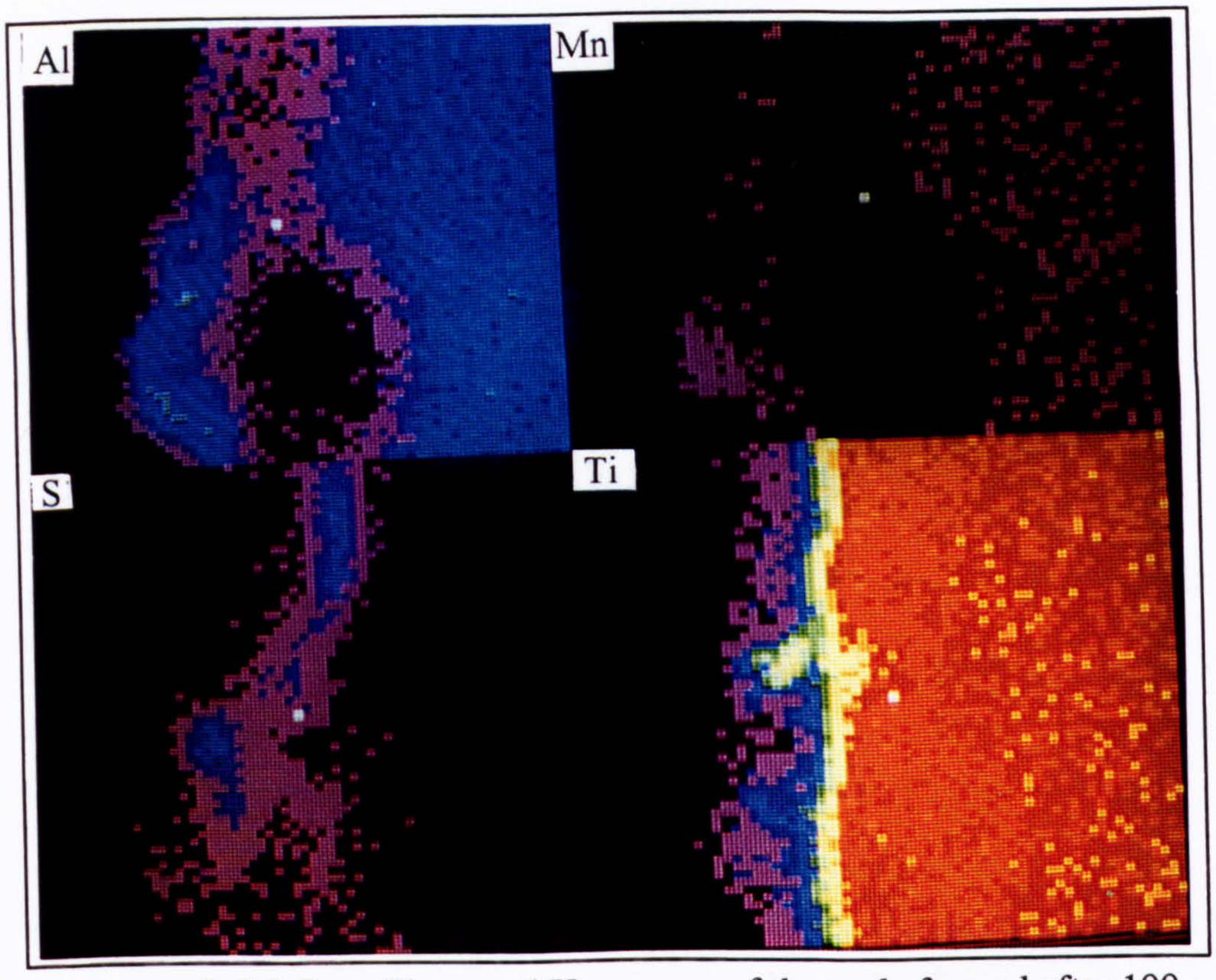

Photograph 8.2.5nn: Elemental X-ray map of the scale formed after 100 hours at 700°C in air + 520 ppm SO_2, in the presence of salt.

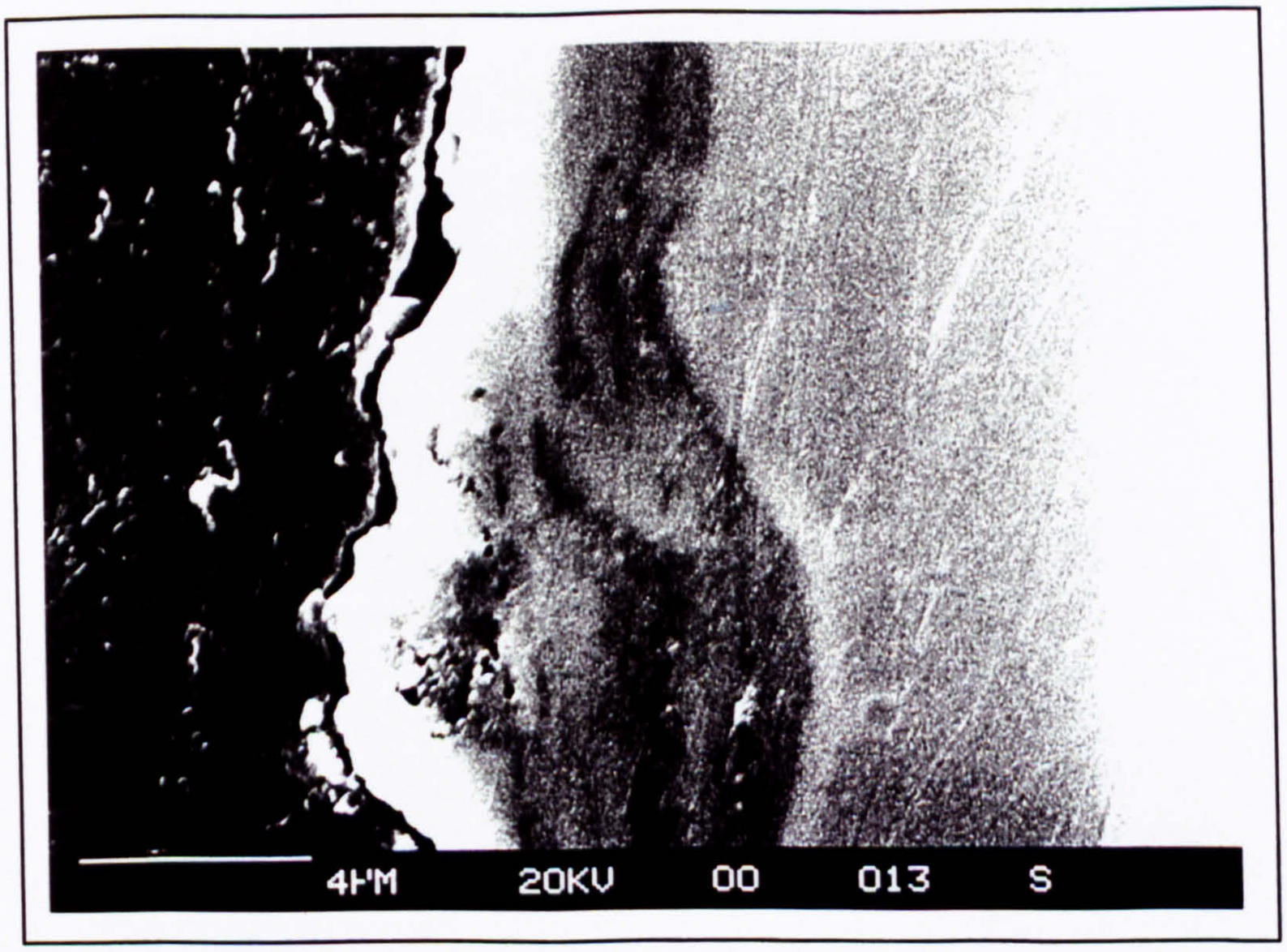

Photograph 8.2.5oo: Shows the cross section of the scale which was used to obtain the Elemental X-ray map in photograph 8.2.5nn (100 hours at 700°C, in the presence of salt +SO_2)

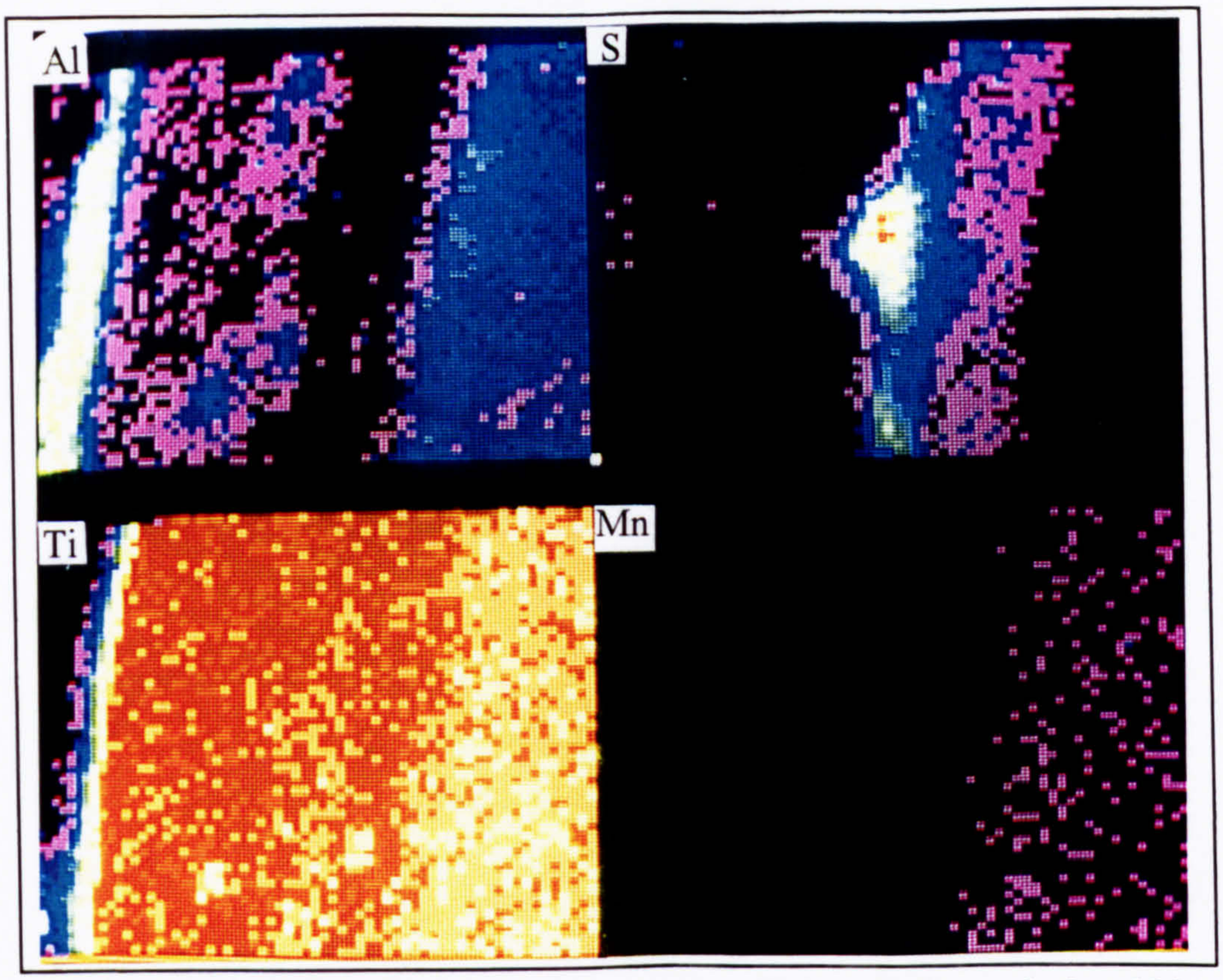

Photograph 8.2.5pp: Elemental X-ray map of the scale formed after 100 hours at 750°C in air + 470 ppm SO_2, in the presence of salt.

Photograph 8.2.5qq: Shows the cross section of the scale which was used to obtain the Elemental X-ray map in photograph 8.2.5pp (100 hours at 750°C, in the presence of salt +SO_2)

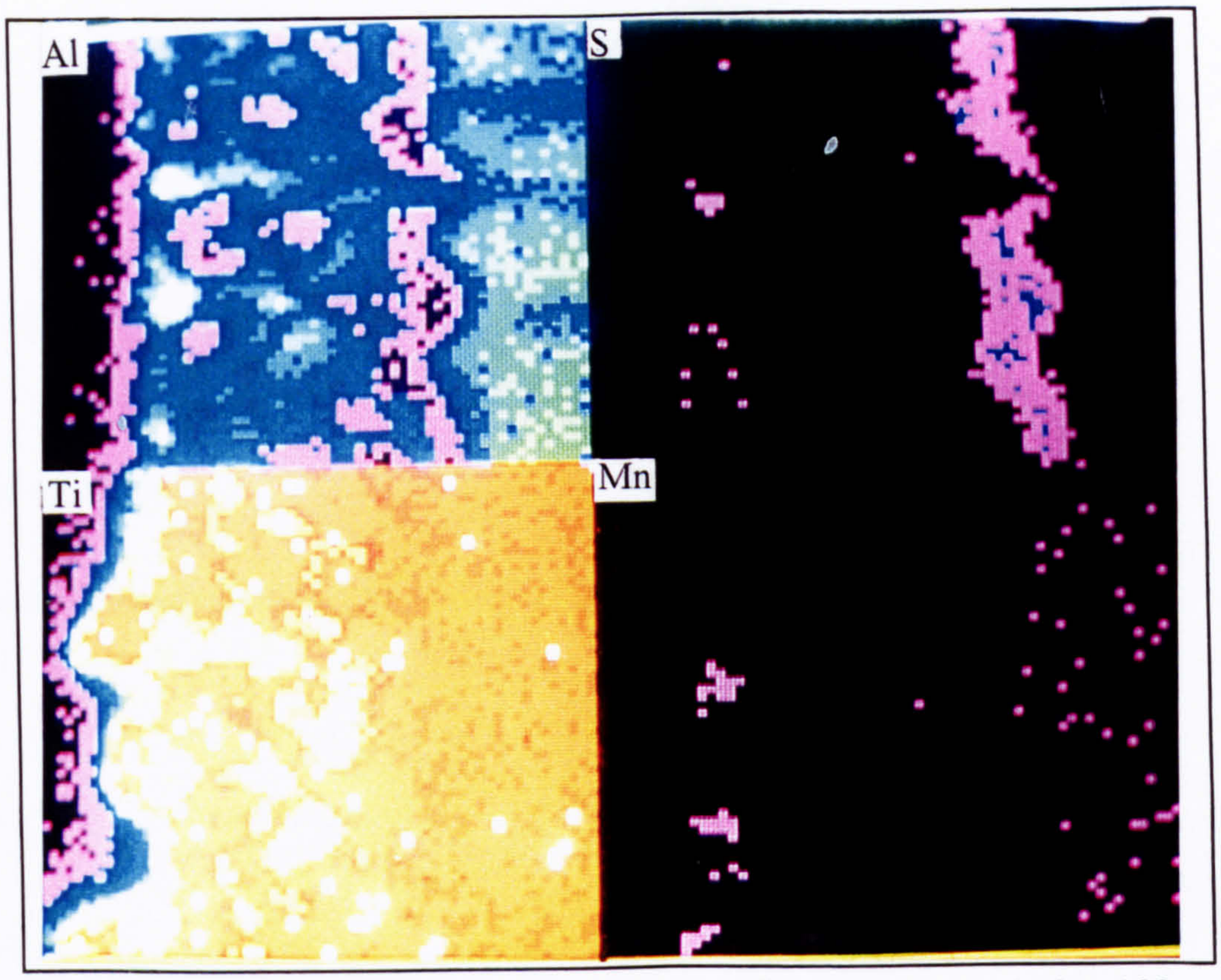

Photograph 8.2.5rr: Elemental X-ray map of the scale formed after 100 hours at 800°C in air + 470 ppm $SO_{2,}$ in the presence of salt.

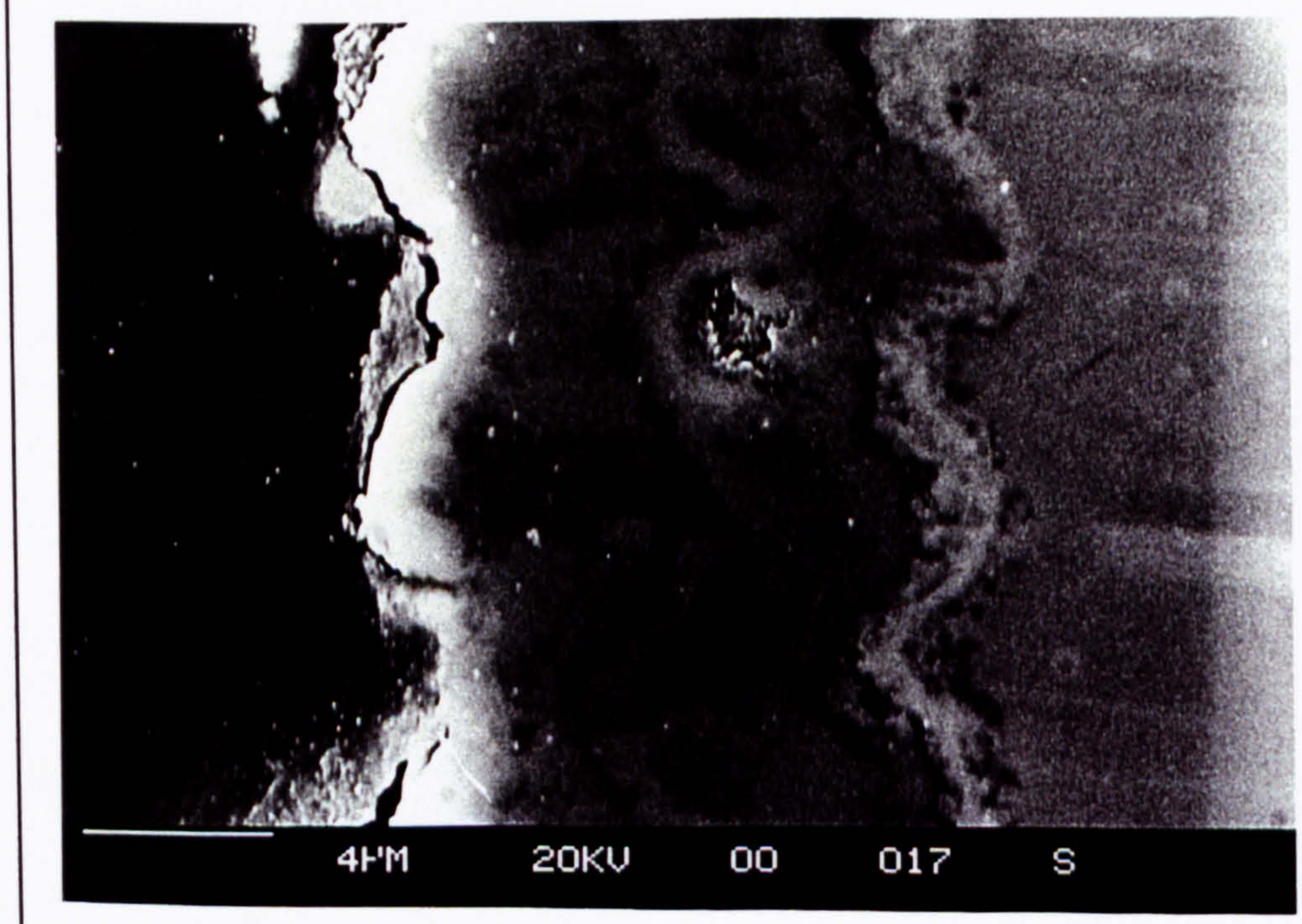

Photograph 8.2.5ss: Shows the cross section of the scale which was used to obtain the Elemental X-ray map in photograph 8.2.5rr (100 hours at 800°C, in the presence of salt +SO_2)

Chapter 9

Discussion

9.1 Oxidation of Ti-45-2-2

The oxidation behaviour of Ti45Al2Nb2Mn has been studied to enable a clearer understanding of the influence of hot salt corrosion and sulphidation on corrosion rates to be made. Knowing the oxidation mechanism that operates over a selected temperature range will also allow direct comparisons with observed corrosion mechanisms to be made.

Current literature on the oxidation of this alloy [see chapter 2] has reported the formation of multilayered scales at high temperatures. These were observed to follow parabolic growth rates. Figure 54 shows an Arrhenius plot of the parabolic rate constants, comparing the oxidation behaviour of Ti-45Al-2Nb-2Mn with other Ti-Al alloys. The oxidation behaviour observed for this alloy is in agreement with other alloys with similar compositions. Alloys containing greater amounts of Nb tend towards alumina forming kinetics, whilst the binary TiAl alloys in general tend towards rutile forming kinetics with greater growth rates. The majority of work in the literature has been at 800 to 900°C with very few authors reporting data on low temperature oxidation of this alloy. It was thus important to characterise this alloy at both low and high temperatures.

Figure 55 shows the oxidation behaviour of Ti-45-2-2 between 700 and 900°C. Mass gains ranged from 0.06mg/cm^2 at 700°C to 2.1 mg/cm^2 at 900°C after 100 hours exposure. Between 750-900°C the oxidation of Ti-45-2-2 followed parabolic growth rates (figure 56). Over this temperature range layered scales developed the thickness of which was dependent on temperature and time. An elemental X-ray micrograph, photograph 8.2.2l, of the oxide scale formed after 20 hours at 900°C clearly identifies three distinct layers, as well as several less defined layers. The secondary electron image in photograph 8.2.2m shows the area from which the digimap was taken. Similar scale structures and thickness's were identified at 850°C after 100 hours, photograph 8.2.2i, as those seen after 20 hours at 900°C, Photograph 8.2.2k. The layered structure obtained is shown in figure 61, stage 5.

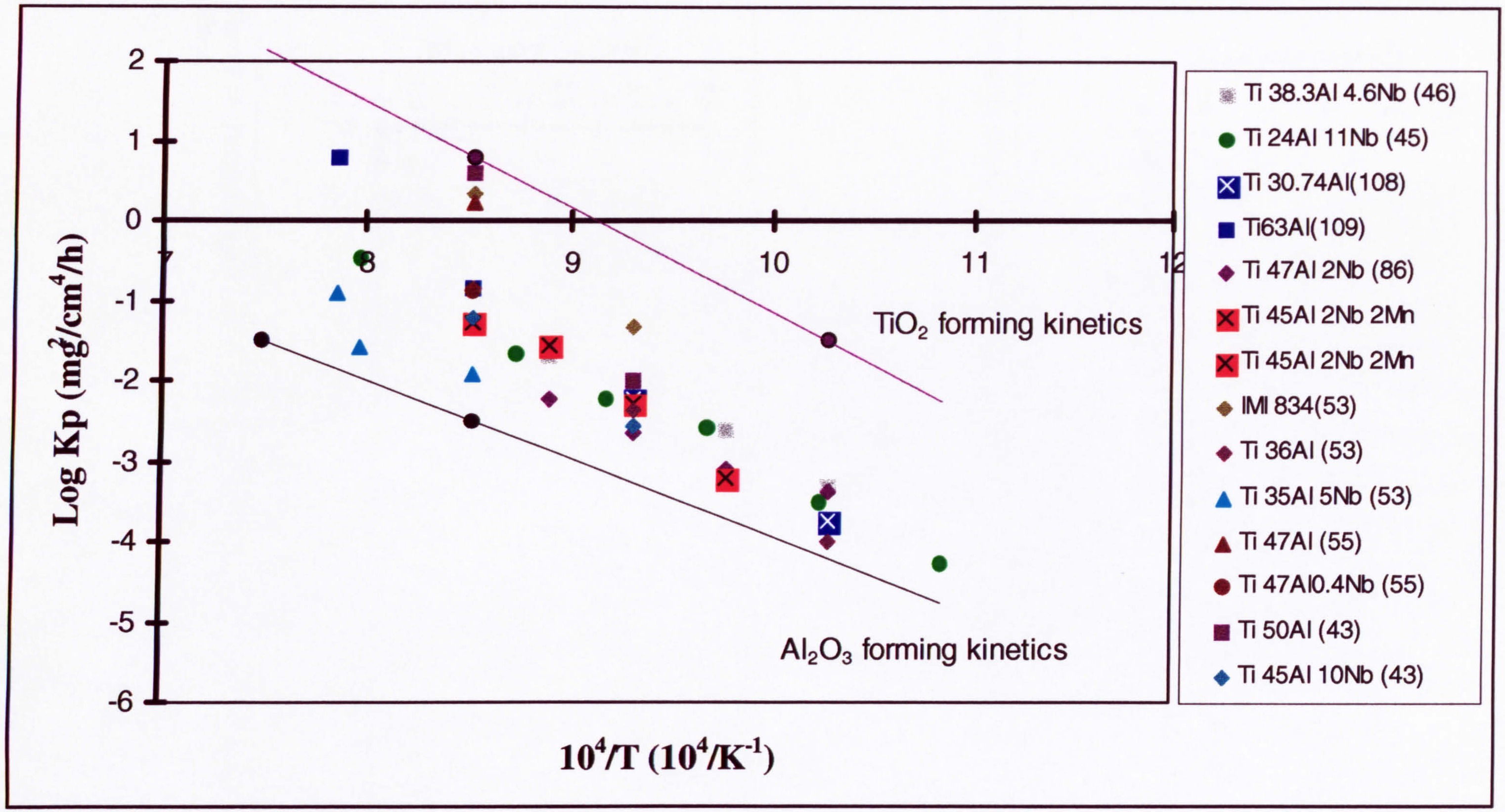

Figure 54: Arrhenius plot comparing the oxidation behaviour of various TiAl alloys

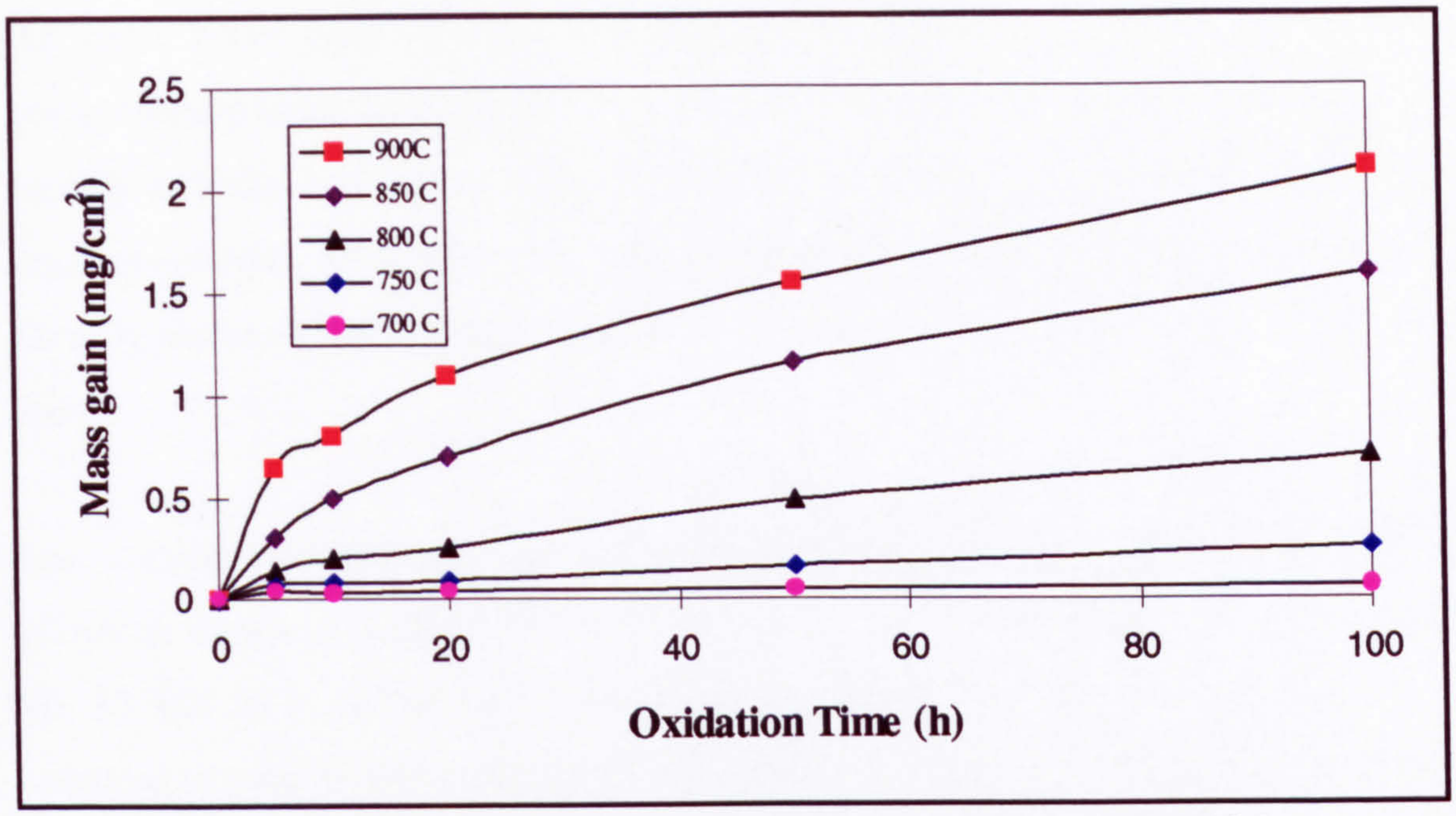

Figure 55: Oxidation behaviour of Ti-45Al-2Mn-2Nb between 700-900°C

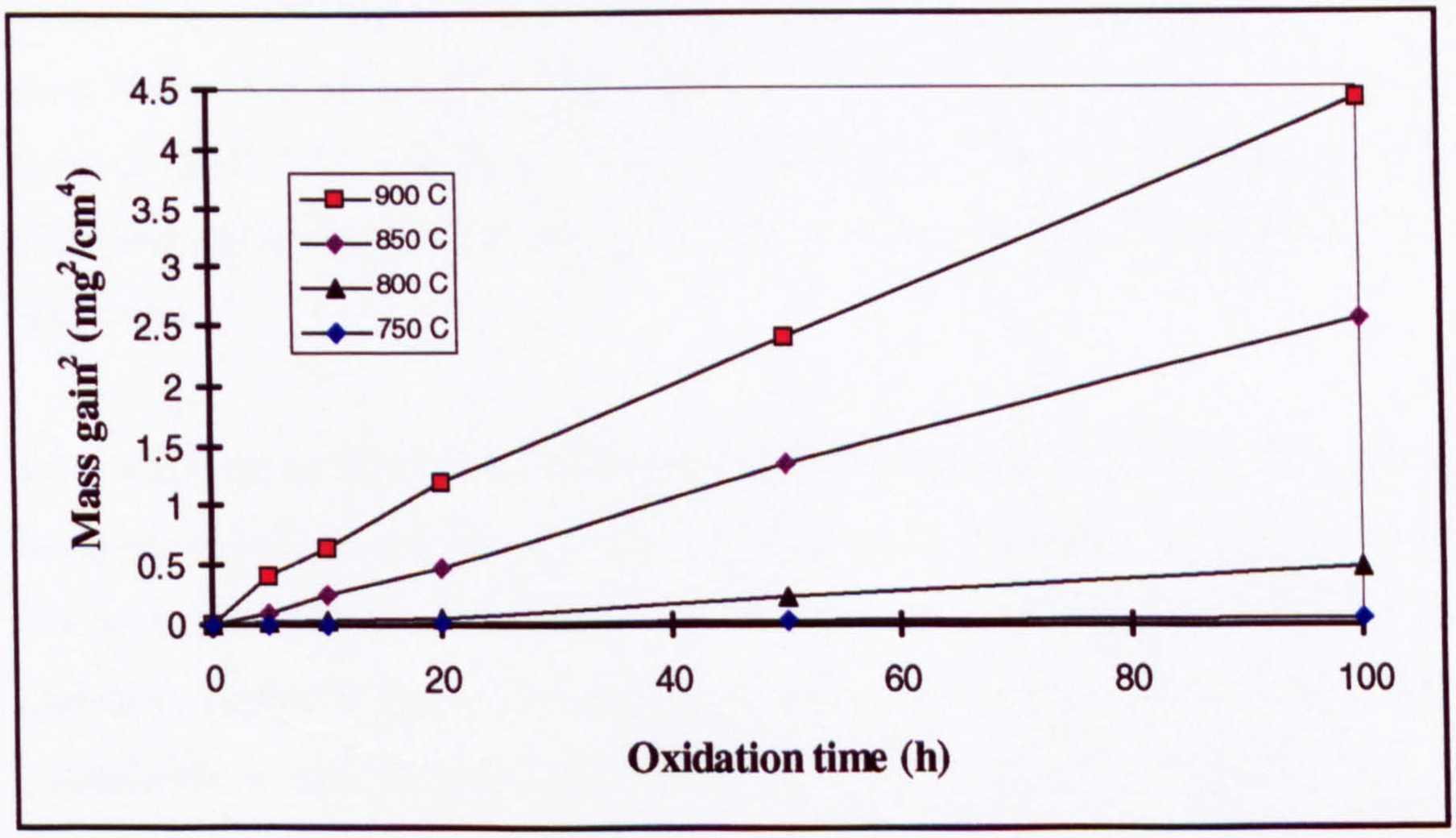

Figure 56: Parabolic behaviour of Ti-45Al-2Mn-2Nb oxidised in air between 750and 900°C

An outer rutile layer overlays a predominately alumina rich layer. Below this a predominately rutile layer can be seen. The Elemental X-ray maps in photograph 8.2.2l identify a further two layers, with one either side of the metal oxide/metal interface. A titanium rich layer, associated with aluminium, and niobium exists at the substrate surface. Directly above a slightly depleted titanium rich layer associated with manganese can be seen.

Few authors have reported alumina whisker growth at 700°C on titanium aluminide alloys, as shown in photograph 8.2.2a, and identified through Auger analysis in Figures 36, 37 and 38 in section 8.2.2. Their random distribution suggests that their growth occurred at areas on the surface where fast diffusion paths existed. These could include grain boundaries or screw dislocations which intersect the surface. Long term (1000 hours) oxidation at 700°C temperature showed that the oxidation rate began to increase after approximately 200 hours, figure 57. A change in oxidation mechanism has thus occurred. The oxidation reaction in this case has changed from being described as logarithmic oxidation, to diffusion controlled. Figure 58 would suggest that a parabolic relationship is followed over the whole range within measurement accuracy, or at least from 100 hours. A comparison of the surface micrographs after short and long exposure times at 700°C (photographs 8.2.2a and 8.2.2b) shows that the alumina crystals coarsened and increased in number. This appears to be the only major difference seen on the surface.

After 100 hours at 700°C very small mass gains were observed, with the scale thickness's being measured at less than 0.1μm. The growth of the scale followed logarithmic kinetics during this early stage of oxidation compared to parabolic kinetics at longer times, as shown in Figure 59 below. A thin rutile layer was observed to have formed almost immediately, along with discrete regions of alumina whisker growth. Logarithmic kinetics is consistent with the thin uniform scale growing as a result of a strong electric field across the film drawing atoms through the scale. This mechanism was first proposed by Mott[14] As figure A1 shows, in appendix A, the oxidation rate decreased as the scale thickness increased and the electric field strength is weakened. A similar change in oxidation

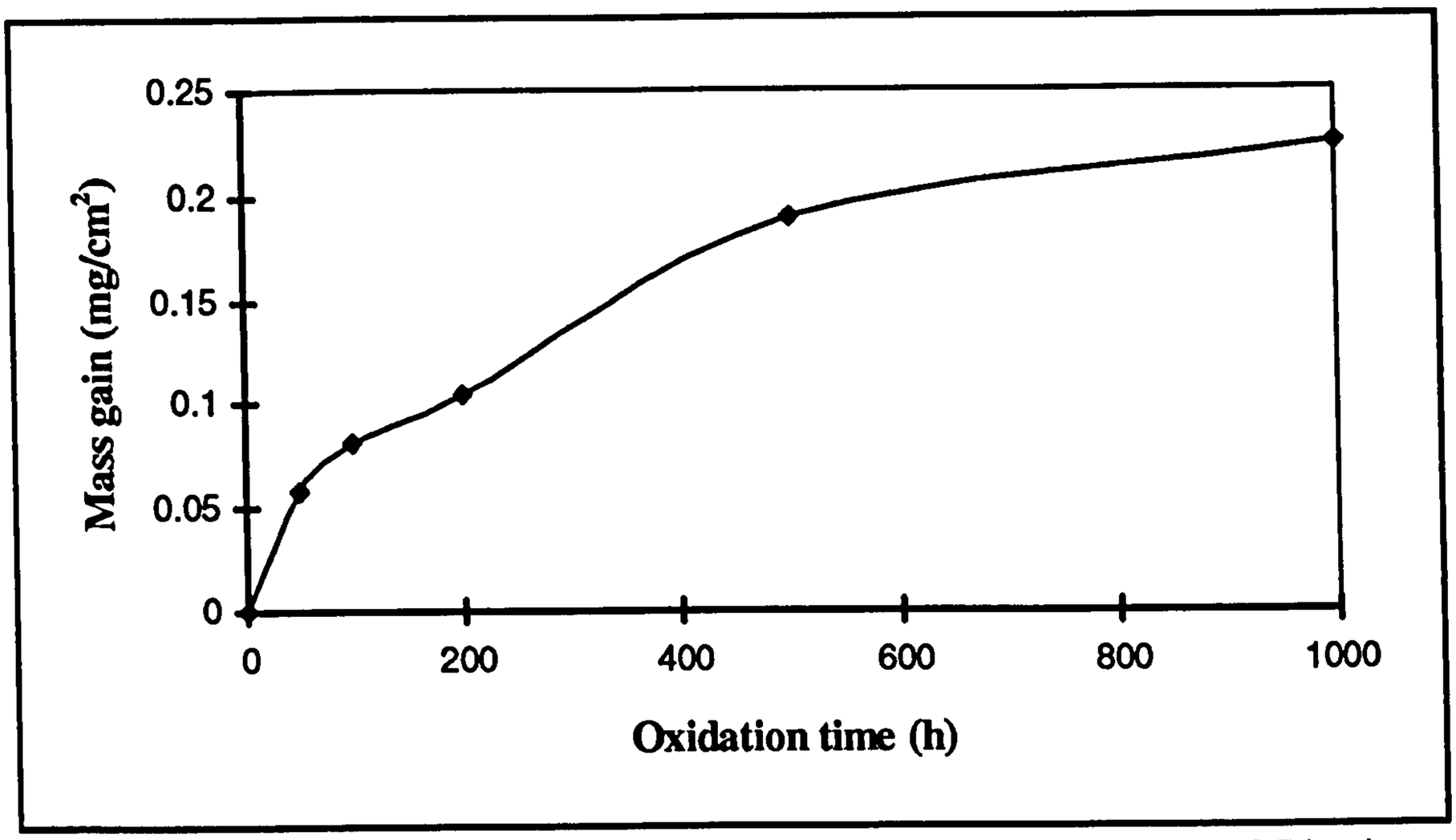

Figure 57: Oxidation behaviour of Ti-45Al-2Mn-2Nb after 1000 h at 700°C in air

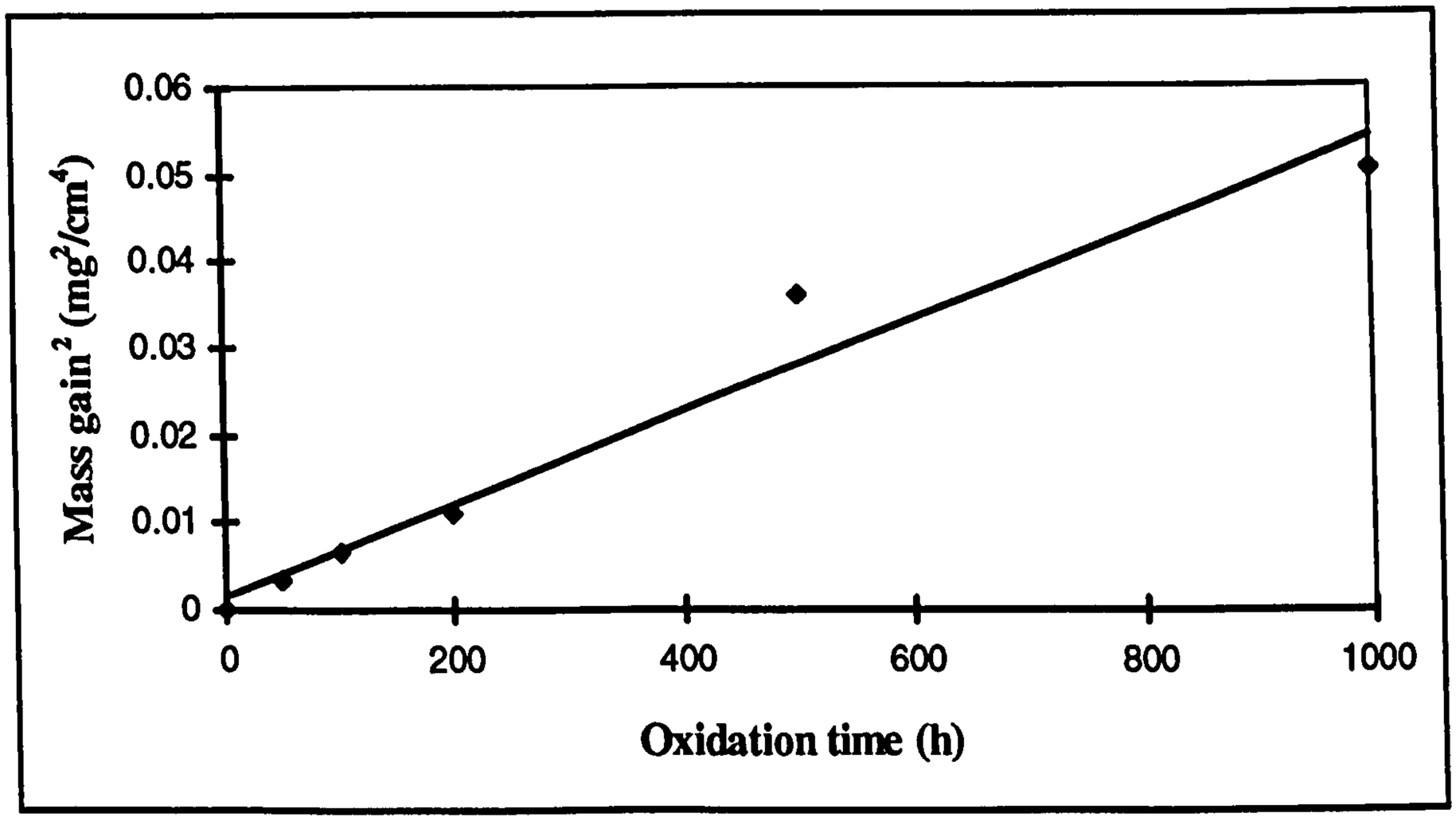

Figure 58: Parabolic behaviour of Ti-45Al-2Mn-2Nb after 1000h at 700°C in air

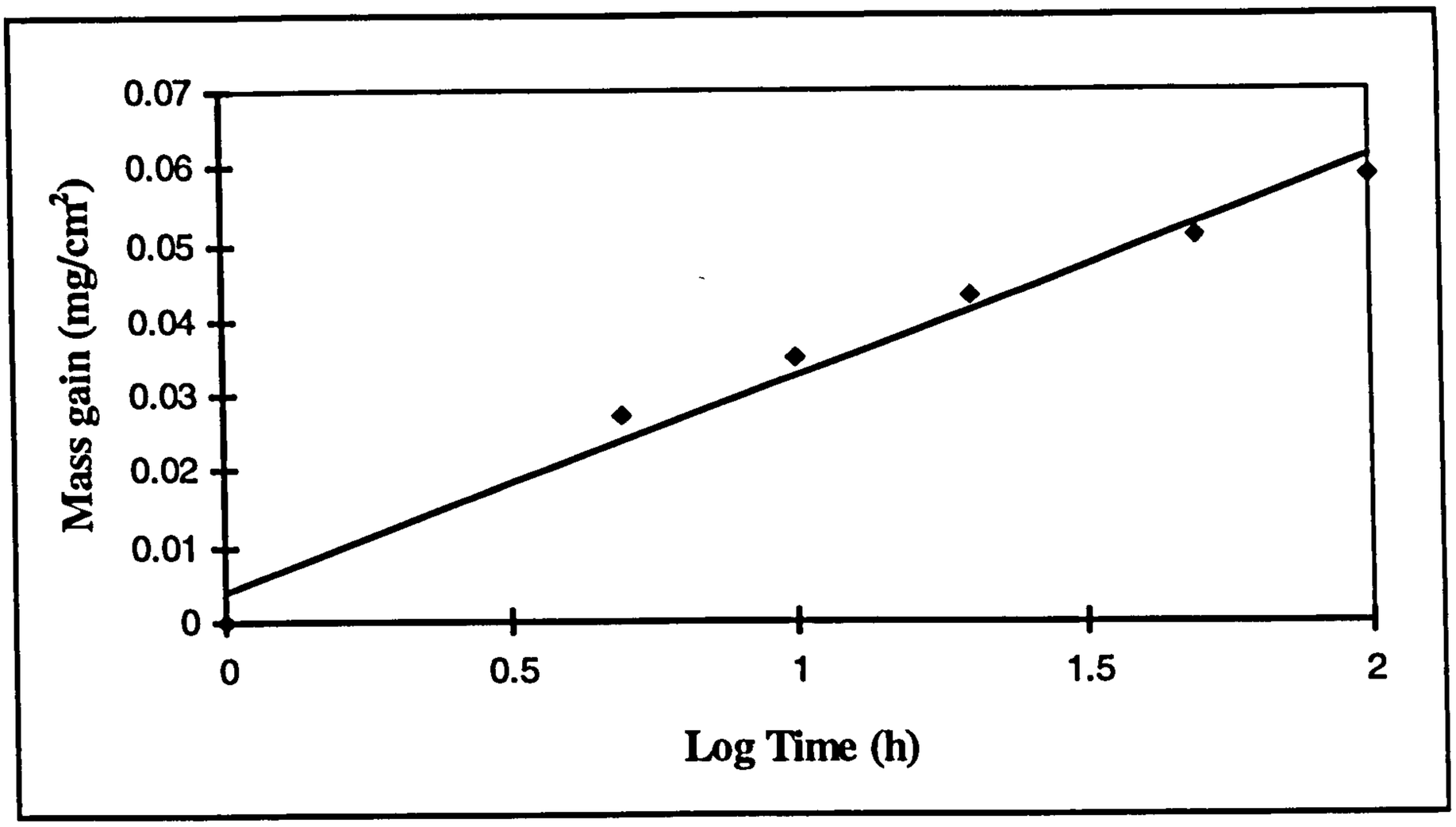

Figure 59: Logarithmic behaviour of Ti-45Al-2Mn-2Nb oxidised in air for 100 h at 700°C

mechanism was seen after only 10- 13 hours at 750°C. The scale thickness at this point had increased but was still only about 1μm. The specimens surface morphology, Photograph 8.2.2c showed that a coarsening of the rutile crystals occurred and that the alumina whiskers, although coarsening, were being overgrown by the rutile crystals.

Parabolic kinetics resulted in the formation of relatively thin oxide scales (up 12 to 20 μm at 900°C), which only lost substrate adherence above 850°C (100 h) and after 20 hours at 900°C. The protective alumina layer acted as a diffusion barrier, with no internal oxidation occurring. Nb was seen to concentrate, as shown by the Elemental X-ray maps in photograph 8.2.2l, at the scale/metal interface which according to Shida et al[41] reduces the oxygen solubility in the substrate by occupying cation vacancy sites. A random distribution of Nb was observed in the mixed alumina/rutile layer. Nb grain boundary segregation in this layer would, according to Bennett et al[48] , reduce internal oxidation by blocking fast oxygen ion transport routes. As a result of the continuous alumina layer being maintained and the potential effects of Nb, relatively slow growing scales develop on Ti-45Al-2Mn-2Nb. Slowing or blocking the diffusion routes of both cations and anions resulted in the development of compact and relatively pore free scales. Photographs 8.2.2d to 8.2.2g show the developement of the external rutile layer at 900°C. The rutile crystals

increase in size with oxidation time but remain closely packed as a consequence of titanium arriving at the oxide/gas interface at a slower rate.

9.1.1 Thermodynamic considerations

Titanium aluminide alloys, in particular the alloy Ti-45Al-2Mn-2Nb form mixed oxide scales when exposed to air at high temperatures. The Ellingham diagram shown in figure 60 shows the stabilities of the four major oxides. Al_2O_3 is the most stable oxide over the whole temperature range, whilst both TiO_2 and Al_2O_3 are more stable than MnO and Nb_2O_5.

Mixed Ti, Al, Nb oxide layers were observed near the scale/metal interface. These are most likely to have formed as a consequence of increased Nb activity at the scale/metal interface due to the outward diffusion of both Al and Ti.

9.1.2 Oxidation mechanism

A schematic of the oxidation mechanism for the Ti-45-2-2 alloy is shown in figure 61. In the initial period of exposure the alloy surface chemisorbs oxygen. During this stage both titania and alumina crystals form on the surface.

At the low temperatures of exposure a thin film develops, which is predominantly rutile. In localized regions alumina whiskers form on top of the rutile layer or from the alumina crystals, within the scale.

As the temperature is raised or after longer exposure times the alumina whiskers are progressively overgrown by an outwardly growing rutile layer. At this stage the alumina crystals begin to grow laterally. Whilst a discontinuous alumina layer exists more rapid oxidation rates are observed. This is due to the higher diffusion rates of titanium in rutile, than aluminium in alumina.

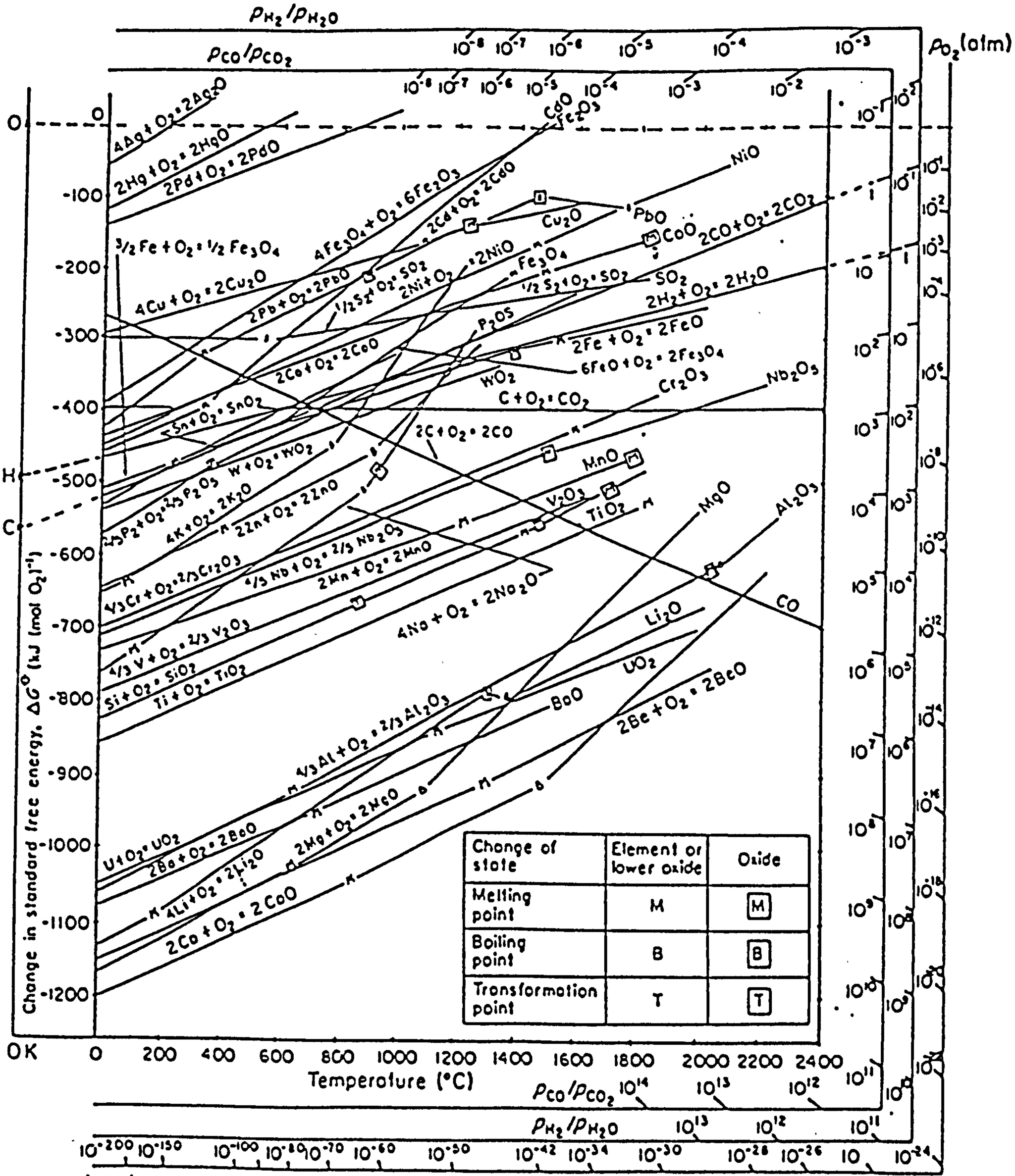

Change of state	Element or lower oxide	Oxide
Melting point	M	[M]
Boiling point	B	[B]
Transformation point	T	[T]

Figure 60: Ellingham diagram for various metal oxides[26]

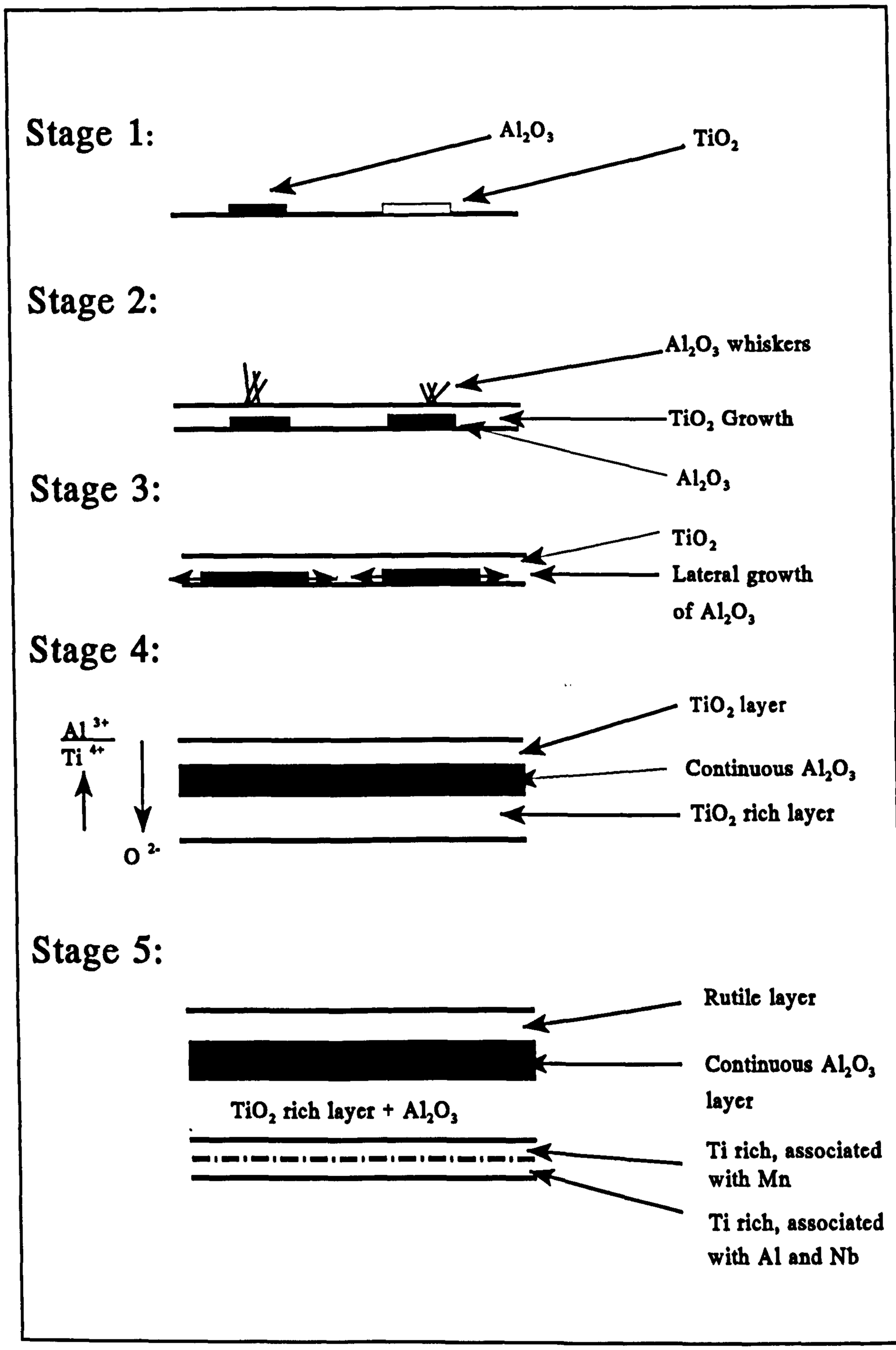

Figure 61: Oxidation mechanism for Ti-45Al-2Mn-2Nb between 700-900°C in air.

Once a continuous alumina layer has formed the oxidation rate decreases and a steady state develops. The outward diffusion of aluminium and titanium ions continues, with a depletion of aluminium occurring near the metal oxide/metal interface. Once below a critical level of aluminium a predominantly rutile layer begins to form below the alumina layer. The continuous alumina layer acts as a diffusion barrier to both oxygen and titanium transport slowing the growth of this inwardly growing rutile layer.

A further factor affecting the growth of the oxide scale is the distribution of niobium and manganese in and near the scale/substrate interface. Niobium was shown to diffuse into the inner rutile layer, but more importantly it is concentrated in an aluminium rich layer at the scale/substrate interface. This indicates that a second protective alumina layer may form, as a result of the addition of niobium, the activity of which increases at the substrate/scale interface due to the outward diffusion of aluminium and titanium. Niobium may bind alumina and titania in the titania rich layer reducing porosity and promote the formation of a second continuous alumina rich layer.

Manganese is concentrated in a titanium rich layer above the alumina/niobium rich layer at the scale/substrate interface. It's effect is unknown but could be a source for scale decohesion as it may embrittle an already brittle scale. Cracks may form if the scale reaches a critical scale thickness at which point the stresses are high enough to initiate oxide fracture.

In this study the oxidation behaviour of Ti-45Al-2Mn-2Nb was determined over the temperature range of 700 to 900°C. The mechanisms proposed are in agreement with those proposed by Schutze et al[53], although more emphasis was placed on the oxidation behaviour between 700 and 800°C, the most likely upper service temperatures. At these temperatures the oxidation rates were slow, with the low mass gains after 100 hours making it difficult to determine the growth rate laws operating. The early stages of oxidation are important to the development of compact, pore free, protective scales. These develop after longer times at 700 to 800°C but unlike the scales developed by Schutze [53] after 1000 hours above 900°C, they do not form nitride layers beneath the

outer rutile/alumina layers. The formation of nitride layers was shown by Schutze to be detrimental, reducing the scales by embrittling the scale/substrate interface. Accelerating the oxidation rate, by increasing the temperature, results in the formation of more porous and therefore less protective oxide scales.

Schutze [53] developed a mechanism for the formation of a continuous alumina layer by predicting the manner in which the outer and inner scales developed, resulting in oxygen vacancy gradients across the scale. Alumina was believed to reprecipitate at the outer rutile/inner alumina plus rutile interface due to a sharp decrease in the solubility of alumina in rutile. The following section shows how the kinetic transitions, identified at each temperature, were identified using both kinetic and metallographic data.

9.1.3 Predicting oxidation transitions

An investigation was carried out to determine the duration of an initial period of parabolic oxidation, corresponding to relatively rapid oxidation rates, and the time to when a continuous slow growing alumina layer has formed. In effect there were 2 kinetic transitions which occurred over the first 100 hours of oxidation. The first occurred after an initial period in which both alumina and rutile crystals formed on the surface at logarithmic growth rates. During this period the oxidation rate continued at decelerating rates. Once the scale had exceeded a critical thickness oxidation became diffusion controlled. The faster corrosion rates corresponded to a change in kinetics, from logarithmic to parabolic. This period was controlled by temperature. As this period involved the lateral growth of alumina, it is not surprising that at the higher temperatures a continuous alumina layer is formed after shorter times. At this point there is a change in kinetics, corresponding to the second transition. The continuous alumina layer acts as a diffusion barrier slowing the oxidation rate. However, parabolic kinetics still operate and this second transition goes from one form of parabolic kinetics to another.

The oxidation data obtained after 100 hours at 900°C is used in figure 62 to illustrate the methodology used to determine the kinetic transitions at each temperature. The first

transition was determined from a plot of mass gain against log time, Figure 62b. The logarithmic period corresponded to a linear relationship. The second transition was determined from this graph and a plot of mass gain squared against time, Figure 62c. The first parabolic region followed a linear relationship on this plot. The second region also followed parabolic kinetics but corresponded to a change in slope. Figure 63 shows these transitions over the temperature range of 700 to 900°C.

At 900°C the rate of oxidation is such that the transitions occur after short periods of time. The second transition, which occurs after less than 10 hours, shows that a continuous layer is developed early in the test at this temperature. Figure 63 suggests that parabolic kinetics will always be developed no matter the temperature over the range of temperatures examined in this study. However, the time to this transition at low temperatures will occur after much longer periods of time. Figure 57 shows the mass gains at 700°C out to 1000 hours. A change in mechanism corresponding to the second transition to parabolic kinetics occurs after approximately 200 hours, which was predicted by the plot of transition time against temperature.

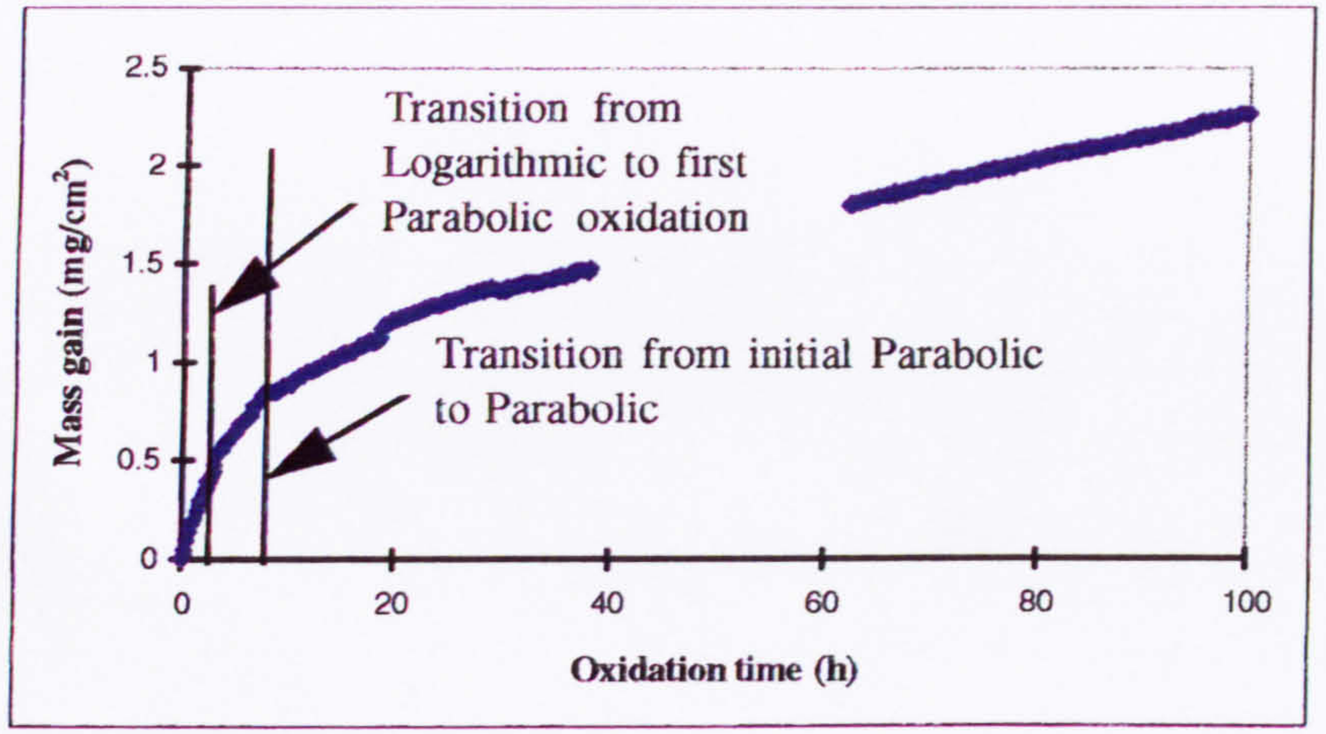

Figure 62a

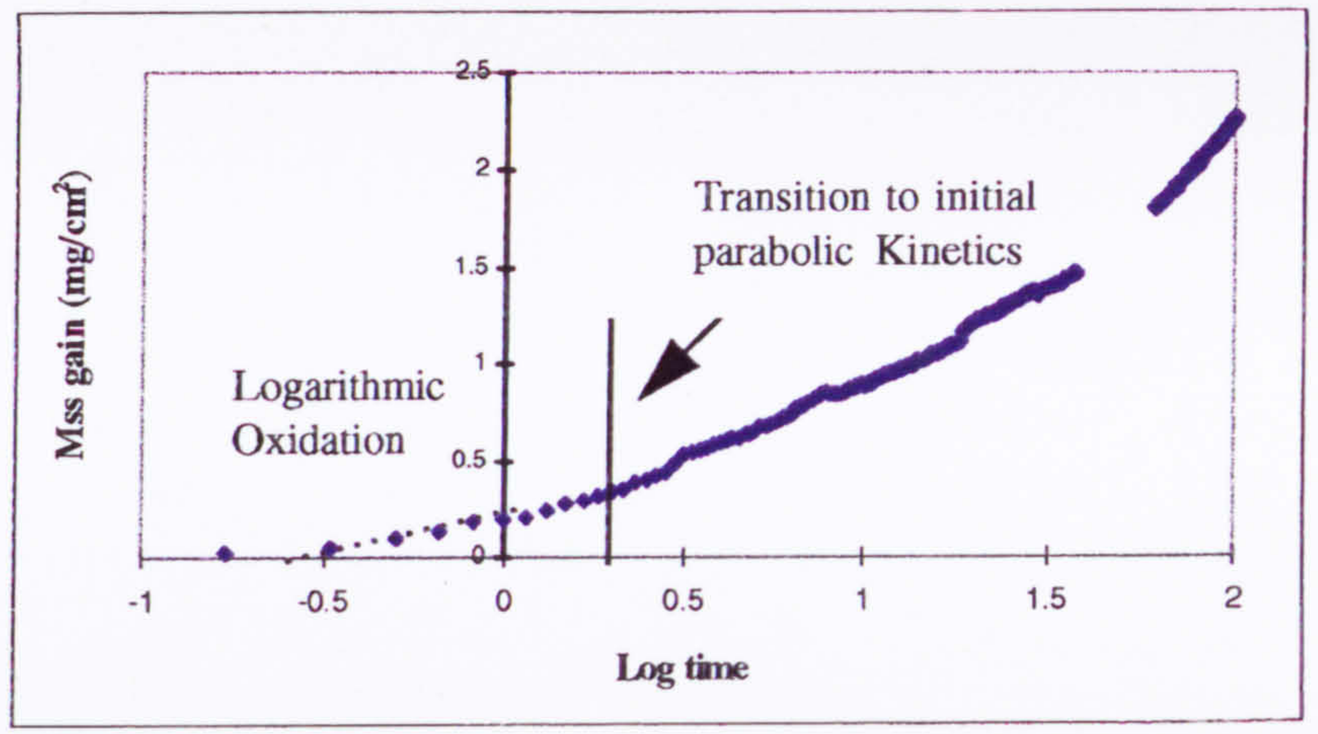

Figure 62b

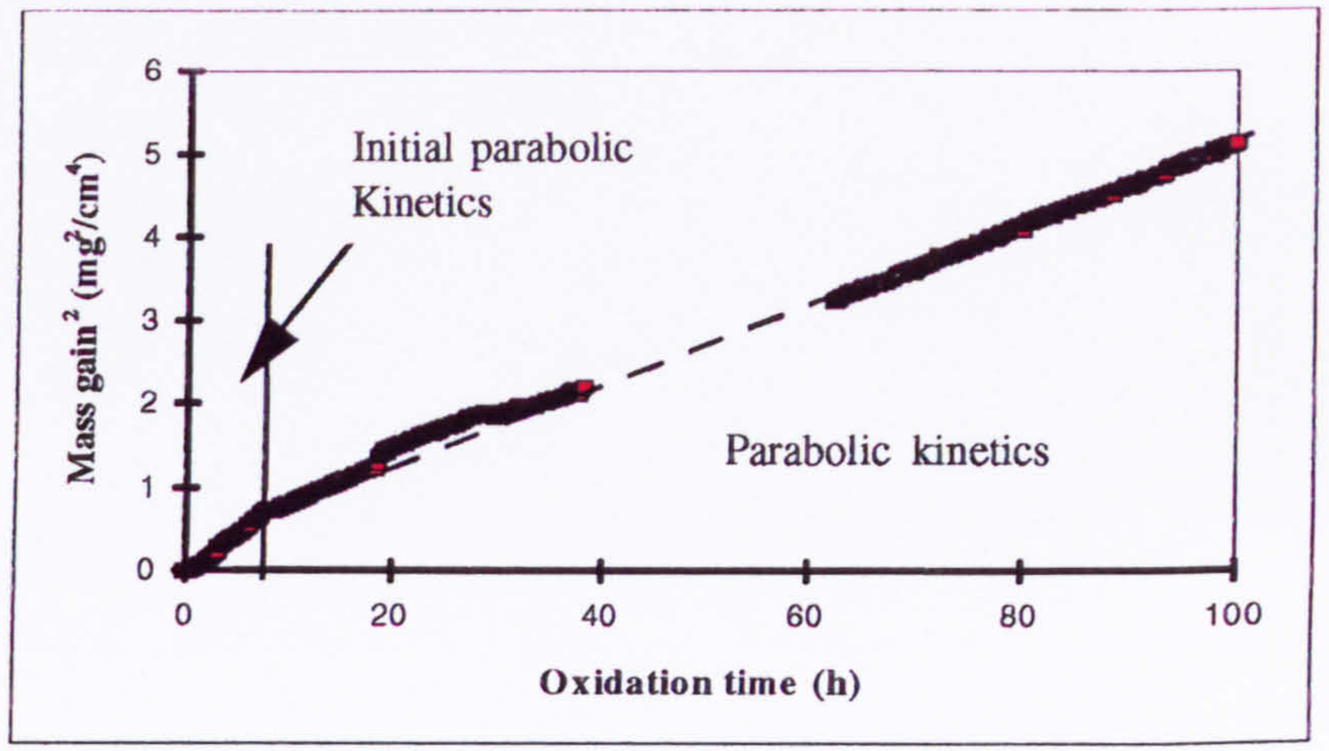

Figure 62c

Figure 62: Example of the method used to determine the oxidation transitions. Figure 62a shows the mass gain verse temperature data at 900°C in air. Figure 62b shows the logarithmic plot of this data and Figure 62c shows the corresponding parabolic plot.

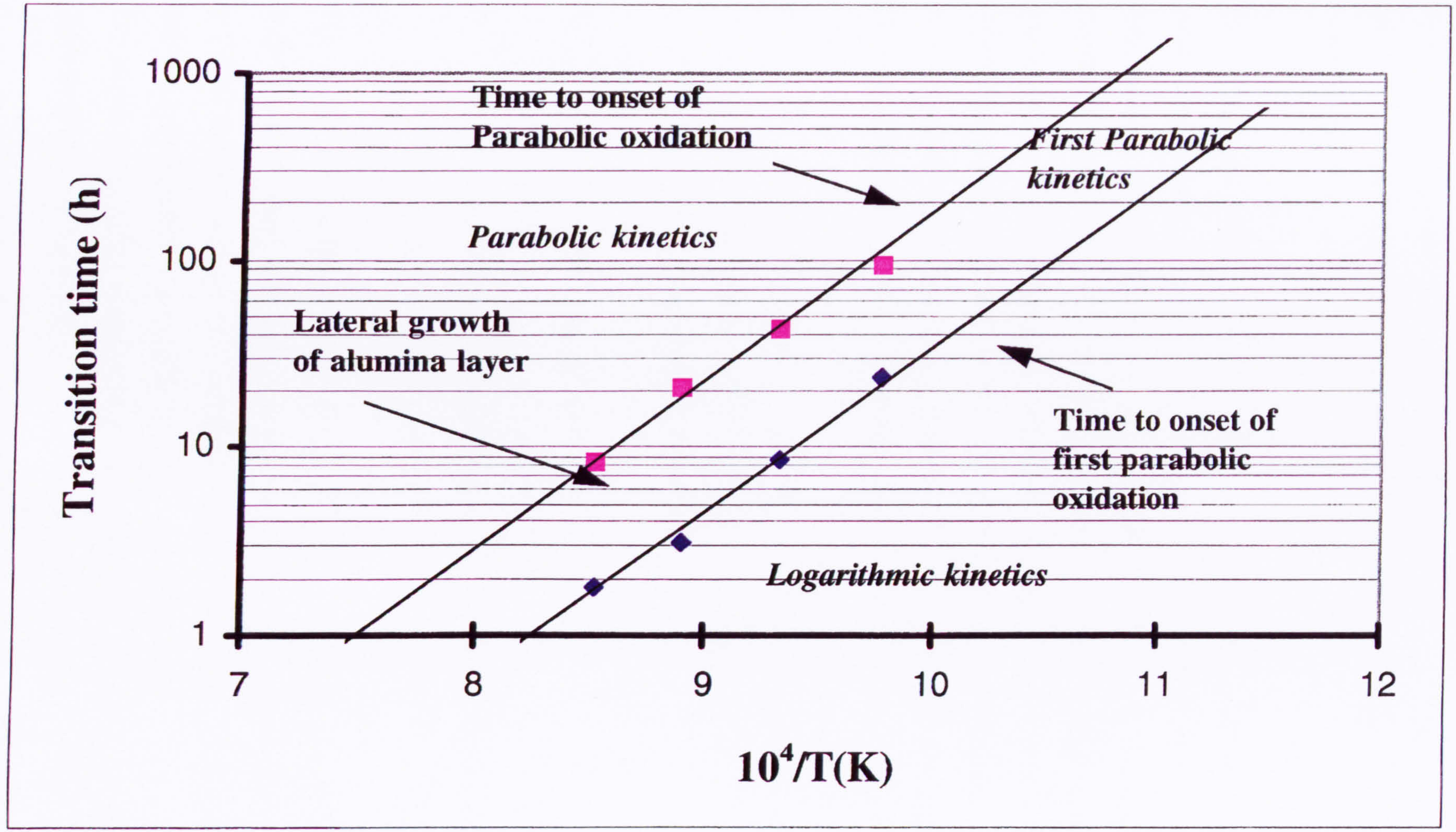

Figure 63: Arrhenius plot showing the kinetic Oxidation transitions observed over the temperature range 700 to 900°C in air.

9.2 High Temperature Sulphidation

The sulphidation behaviour of Ti-45Al-2Mn-2Nb is important if this material is to be used in the applications being suggested. However, sulphidation on its own is only relevant if the reactions can be determined to enable the combined effects of sulphur and salt to be understood.

The sulphidation results, in section 8.2.3 (page 133), show that a bi-oxidant atmosphere, containing sulphur dioxide and air, has a more detrimental effect on the corrosion behaviour of Ti-45Al-2Mn-2Nb than air alone. The mass gain verse time graphs show that the reaction kinetics differ from the oxidation graphs. Initially the tests follow logarithmic kinetics after which the mechanism operating changes and continues at either logarithmic or parabolic rates. This would indicate that substantial alloy degradation would occur if exposed to high concentrations of sulphur dioxide. The general features characteristic of the sulphidation of this alloy were that;

1. The sulphidation kinetics, over the temperature range studied, followed logarithmic rates during the first 20 hours. Logarithmic or parabolic kinetics were again followed after a period of breakaway kinetics.

2. Severe spallation occurred above 800°C and

3. No internal sulphidation was observed even at the high temperature exposures

The graphs in appendix A show the mass gain curves over the temperature range 700-900°C, with the final mass gains ranging from 300μg/cm^2 to 6.4mg/cm^2 after 88 hours at 700°C and 100 hours at 900°C respectively. Closer examination shows that a critical sulphidation temperature occurs above 800°C. Although similar rate curves are seen over the whole temperature range a major difference exists below 800°C. In all cases logarithmic kinetics operate followed by a steep rise in the corrosion rate, characteristic

of breakaway corrosion. Figure 64 compares the sulphidation behaviour with the oxidation behaviour of Ti-45Al-2Mn-2Nb at 750°C. After an initial rapid rise in the corrosion rate, irrespective of whether oxidation or oxidation/sulphidation operates, the rate decreases substantially, with a greater decrease observed under oxidising conditions, than under oxidising-sulphidising conditions. Figure 65 shows a similar comparison at 800°C. In this instance the corrosion rate continued to increase at a parabolic rate right up to 100 hours of exposure.

The sulphidation curves seen at 750 and 800°C are plotted on mass gain squared against corrosion time graphs in figures 66 and 67. These curves illustrate the kinetic behaviour of this material above and below 800°C. As mentioned above logarithmic kinetics operate during the first 20 hours at both temperatures. After the rise in corrosion rate the rate returns to parabolic rates, at 750°C, suggesting that a change in mechanism had occurred which above 800°C resulted in a continuation of accelerated or breakaway kinetics. Below 800°C it can be surmised, and studied in more depth at a later stage, that breakaway kinetics are not seen as diffusion controlled kinetics again dominate.

Metallographic studies were carried out for 20 and 100 hours at each exposure temperature to characterise Ti-45Al-2Mn-2Nb. Similar through section features were observed over the whole temperature range. The characteristic features are;

1. The development of outer Mn_2O_3 and TiO_2 layers,

2. The development of a discontinuous Alumina layer between outer and inner rutile layers, and

3. The development of a continuous sulphide layer at the scale/substrate interface

The oxidation/sulphidation tests followed similar kinetics over the first 20 hours to the respective oxidation tests, with the mass gains during these period typically only 1.5 to 2 times greater. The mass gains after 100 hours increased to being approximately 3 times

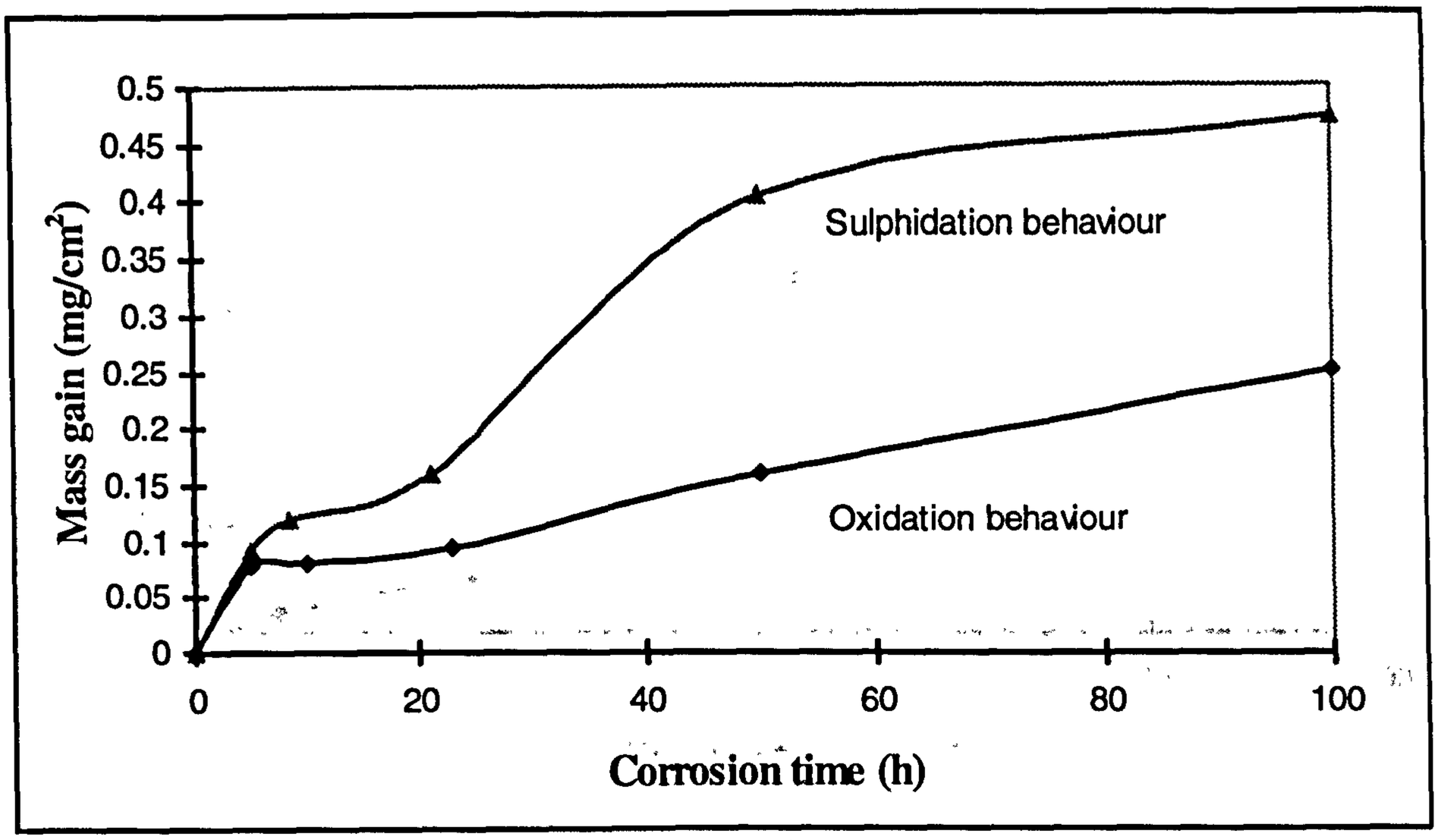

Figure 64: Oxidation and sulphidation behaviour of Ti-45Al-2Mn-2Nb at 750°C

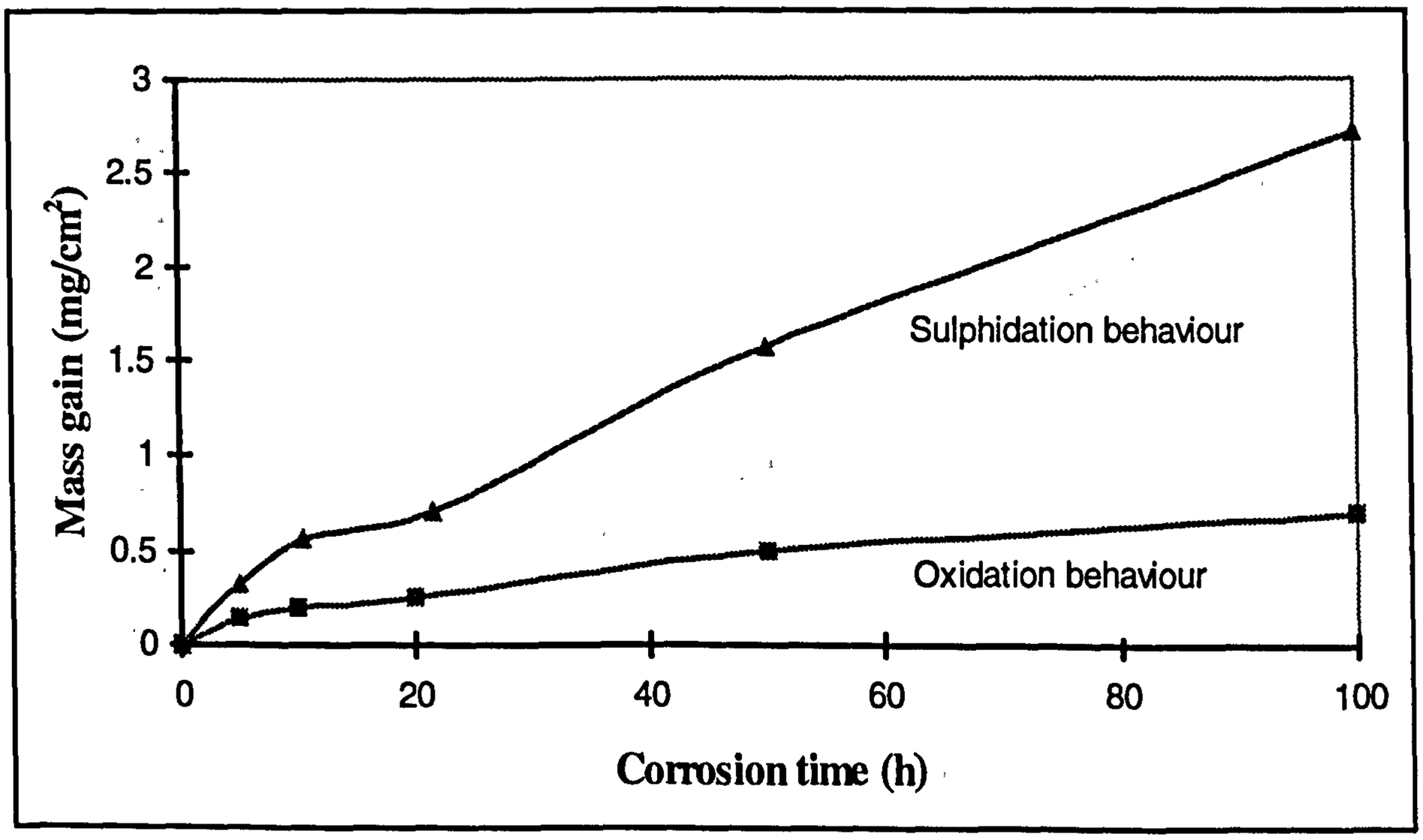

Figure 65: Oxidation and Sulphidation behaviour of Ti-45-2Mn-2Nb at 800°C

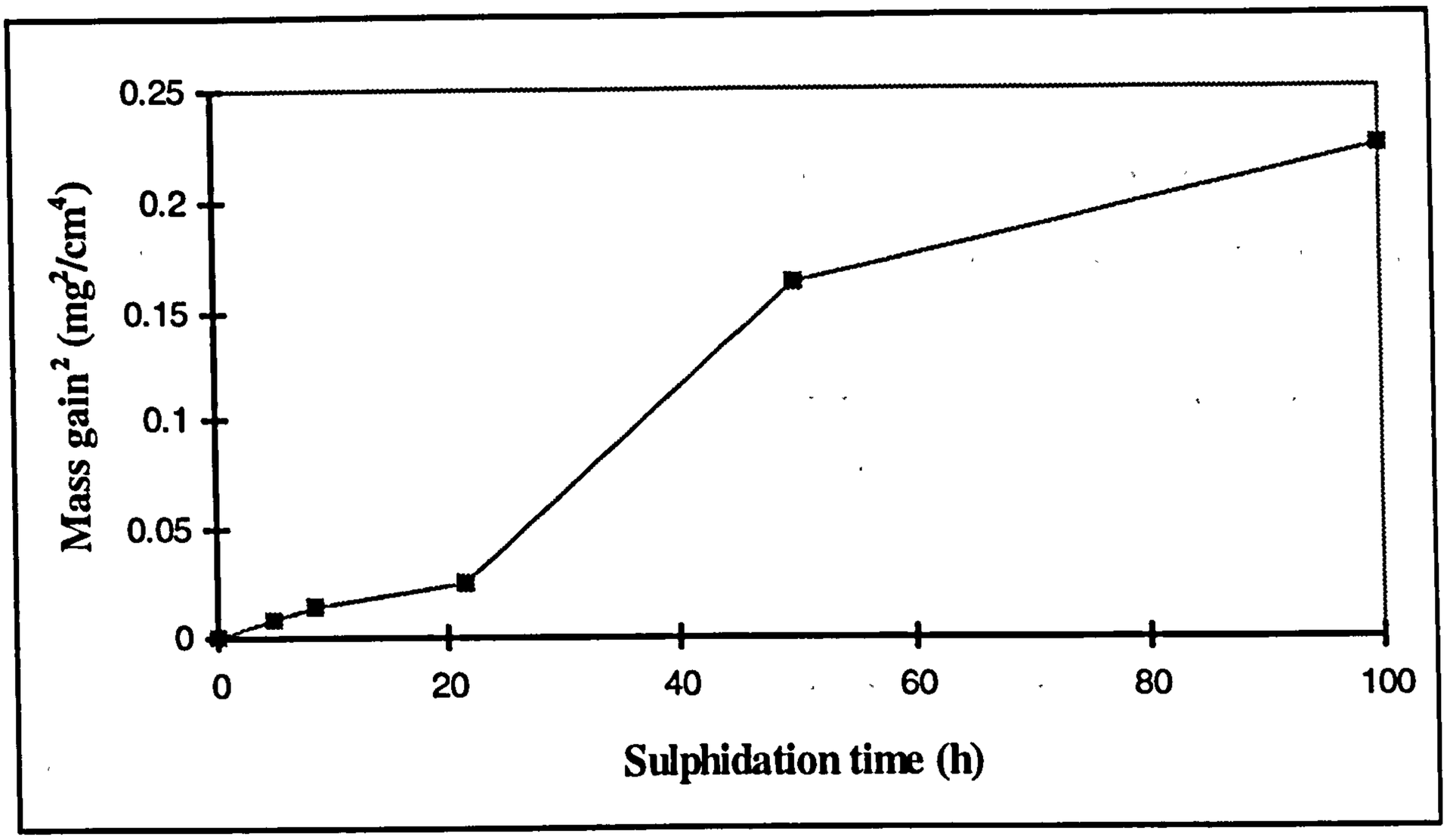

Figure 66: Plot of mass gain squared versus sulphidation time after 100 hours exposure at 750°C

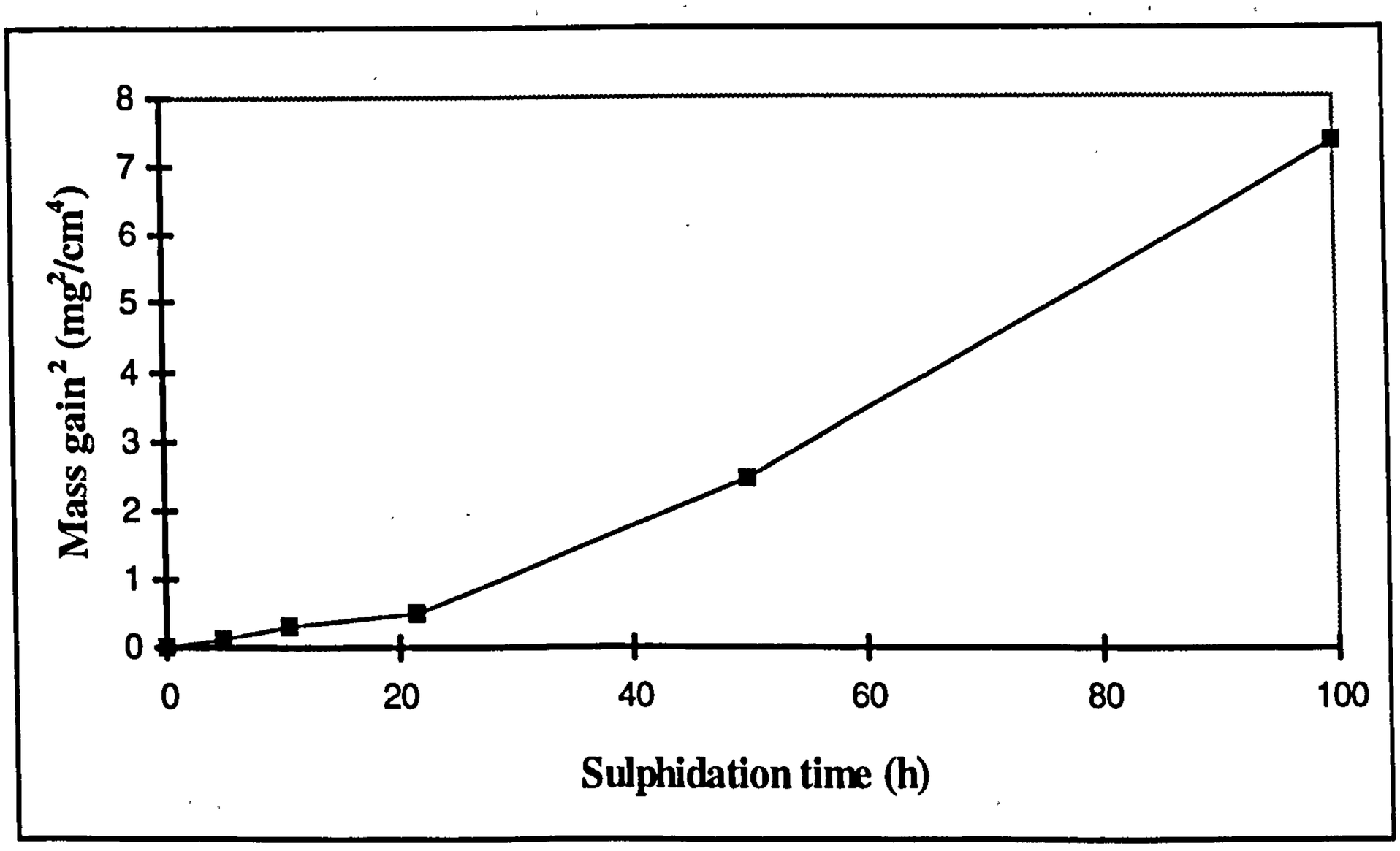

Figure 67: Plot of mass gain squared versus sulphidation time after 100 hours exposure at 800°C

greater again suggesting a change in corrosion mechanism.

To understand the change in kinetic behaviour that occurs above 800°C comparisons need to be made of the surface chemistry above and below this temperature. Photographs 8.2.3n and 8.2.3o show the development of the surface scale at 750 and 900°C after 100 hours and are accompanied by EPMA analyses identifying the surface compositions. At 750°C manganese/sulphur rich particles are identified on a porous alumina and rutile surface layer. At 900°C, a porous rutile and Mn/O surface layer was identified at regions where no recent spallation had occurred. When making these comparisons it is important to note that spalling occurred each time the specimen holder was removed from the furnace and cooled resulting in moderate thermal cycling. This has proved useful, as thermal cycling is expected in service. In some cases, several oxide layers built up confirming that cracking had occurred at each thermal cycle. The development of a continuous rutile and Mn/O surface layer is observed at each of the exposure temperatures as illustrated in photographs 8.2.3d to 8.2.3m.

The change in surface composition, from the formation of surface sulphates to surface oxides must be driven by thermodynamic factors and differences in the gas component partial pressures. These effects are discussed in the next section. For this system through section analysis was unable to separate changes in corrosion kinetics, they only showed that the scales developed at very rapid rates and then spalled at a given thickness. Photographs 8.2.3p and 8.2.3q show that similar scale thicknesses of ~ 50 μm, occurred prior to scale spallation. Where the scale had not spalled thicker scales were observed, 40 to 60μm with a large degree of porosity close to the scale/substrate interface.

9.2.1 Thermodynamic analysis of the Ti-O-S, Al-O-S, Mn-O-S PSD's

Phase stability diagrams were calculated using MTData, a thermodynamic phase stability program[110], for the three main elements involved in the sulphidation/oxidation reactions at 750 and 800°C. The diagrams were calculated using unit activities, under equilibrium conditions. Table 21 shows the ranges of pSO_2 and pO_2 above which the sulphides are

thermodynamically stable.

Table 21: pSO_2 above which and pO_2 below which the sulphide phases are stable at the scale/substrate interface; at 750 and 800°C

Alloy system	Temperature (°C)	pSO_2 Stability range of sulphide (atm)	pO_2 Stability range of sulphide (atm)
Ti-O_2-SO_2	750	5.48×10^{-43} - 5.48×10^{-59}	5.14×10^{-46} - 1×10^{-60}
Ti-O_2-SO_2	800	1.3×10^{-41} - 6.3×10^{-60}	1.6×10^{-43} - 1×10^{-60}
Al-O_2-SO_2	750	1.35×10^{-41} - 3.16×10^{-51}	7.01×10^{-47} - 1×10^{-60}
Al-O_2-SO_2	800	3.3×10^{-39} - 6.06×10^{-56}	3.09×10^{-44} - 1×10^{-60}
Mn-O_2-SO_2	750	9×10^{-29} - 6.7×10^{-57}	1.66×10^{-32} - 1×10^{-60}
Mn-O_2-SO_2	800	4.9×10^{-27} - 3.0×10^{-57}	1.0×10^{-30} - 1×10^{-60}

<u>Ti-O_2-SO_2 system</u>

Figures 68 and 71 show the PSD's obtained for the system Ti-O_2-SO_2 at 750 and 800°C respectively. These diagrams show that in environments containing both oxygen and sulphur a range of stable solid titanium oxides and sulphides can form. At the surface of the material, where Log $p(O_2) = 0$, a stable TiO_2 layer would be expected to form. As the $p(O_2)$ is reduced a series of diagonal lines determine the Sulphur pressures above which TiS or TiS_2 are thermodynamically stable. The sulphides are thus unstable at the scale/gas interface and therefore unlikely to form at this surface where high partial pressures of oxygen exist.

This situation changes as the scale is traversed with the oxygen activity expected to decrease significantly as the scale/substrate interface is approached. The sulphur activity is expected to remain unchanged. Hence TiS and TiS_2 become more thermodynamically

stable. According to the PSD in figure 68 and listed in table 21, solid TiS forms if the oxygen activity is below approximately 10^{-46} atmospheres and the sulphur activity greater than approximately 10^{-43} atmospheres, at 750°C. As the oxygen activity is reduced further the sulphur activity above which the sulphides are stable also decreases. The gas used in this study contained sulphur activities of the order of 10^{-4} atmospheres. Thus TiS_2 would be expected to form as a stable layer at the scale/substrate interface.

Increasing the temperature from 750 to 800°C had very little effect on the stabilities of the titanium sulphides. Higher partial pressures of sulphur are required at the scale/substrate interface if a continuous sulphide layer is expected. A slight shift occurred in the oxide stabilities with the pressures above which the oxides were stable increasing from 3.16×10^{-28} to 1×10^{-25} atmospheres. No changes in scale structure are therefore expected at 800°C.

<u>Al-O_2-SO_2 system</u>

Figures 69 and 72 show the PSD's for the system Al-O_2-SO_2 at 750 and 800°C respectfully. These diagrams show that Al_2O_3 would be expected to form at the scale/gas interface. The partial pressure of oxygen decreases through the scale resulting in Al_2S_3 becoming the more thermodynamically stable compound. Solid Al_2S_3 is predicted to begin forming at the scale/substrate interface if the partial pressure of oxygen is less than 7.01×10^{-47} atm and the sulphur activity greater than 1.35×10^{41}, at 750°C. The stability of Al_2S_3 decreases as one moves back through the scale towards the scale/gas interface, with greater sulphur activities being needed for Al_2O_3 and Al_2S_3 to remain in equilibrium with each other. At the surface the oxygen activity is known to be equivalent to 1 atmosphere, and the sulphur activity was calculated to be in the region of 10^{-4} atmospheres. The phase stability diagrams show that $Al_2(SO_4)_3$ may form and remain in equilibrium with Al_2O_3, if the oxygen activity is slightly greater than one atmosphere.

Increasing the temperature from 750 to 800°C results in very little change in the stabilities of Al_2O_3 or Al_2S_3. The partial pressure of oxygen above which the oxide forms increases

slightly, whilst the partial pressure above which the sulphide forms decreases slightly. The changes in stabilities are not substantial, although they show that Al_2S_3 becomes more favourable at the scale/substrate interface as the temperature is increased.

Mn-O_2-SO_2 system

Figures 70 and 73 show the PSD's for the system Mn-O_2-SO_2 at 750 and 800°C respectfully. Again these diagrams show that the oxides are more thermodynamically stable in high pO_2 atmospheres and will form in preference to the sulphides at the scale/gas interface.

The stability of manganese sulphides increases with decreasing oxygen partial pressure, with MnS being stable at the scale/substrate interface below oxygen partial pressures of 1.66×10^{-32} atmospheres at 750°C. Traversing back out to the scale/gas interface results in an increase in oxygen partial pressure and a change in oxide stability. MnO is the only oxide stable in contact with manganese. Above a pO_2 of approximately 10^{-11} atmospheres Mn_3O_4 is the more stable oxide. At the scale/gas interface Mn_2O_3 is the most stable oxide, with MnO_2 only becoming stable at oxygen partial pressures greater than atmospheric pressures. $MnSO_4$ is stable at the scale/gas interface, in contact with Mn_2O_3, if the partial pressure of sulphur is greater than approximately 2.46×10^{-3} atmospheres at 750°C.

Increasing the temperature to 800°C had very little effect on the stabilities of the sulphides and oxides. The most important change being that the stability of $MnSO_4$ decreases with greater sulphur partial pressures, approximately 0.018 atmospheres at 800°C, needed for this phase to exist at the scale/gas interface.

Comparing the three PSD systems: Ti-O_2-SO_2, Al-O_2-SO_2, and Mn-O_2-SO_2

In more complex systems, where all three elements are present in an alloy, the stabilities of the corrosion products can only be predicted by superimposing the individual PSD's. In this manner it becomes possible to state the corrosion products which are most likely

to form first under given partial pressures. This enables a picture to be created as to what reactions are most likely to occur as the scale is traversed. Superimposing the PSD's for the three systems analysed at 750 and 800°C allowed the following conclusions to be made.

1. At the scale/substrate interface TiS and MnS would be expected to form before Al_2S_3. MnS remains stable over a wider pSO_2 range than TiS, with TiS_2 becoming the stable titanium sulphide.

2. The presence of a Ti/S rich layer at the scale/substrate interface indicates the thermodynamically stable sulphide phase to be TiS and thus gives a possible pSO_2 range.

3. If a path is followed from the scale/substrate interface to the scale/gas interface, knowing that the pSO_2 lies within the stable TiS phase field at the substrate surface, the possible corrosion products can be predicted as the pO_2 increases. At the scale/gas interface the following conditions exist; Log pO_2=O and Log pSO_2 = ~ 10^{-4}. Thus a straight line can be drawn if one assumes a linear gradient in pO_2 and SO_2. This allows predictions to be made as to the most thermodynamically stable phase that can form as cations diffuse from the scale/substrate interface to the scale/gas interface. A black line indicates a possible pO_2/pSO_2 gradient. At the substrates surface, under the most likely partial pressures, TiS and MnS are the most stable sulphides. MnS exists over a wider range of SO_2 partial pressures, with TiS_2 becoming the stable titanium sulphide phase. The stability of Al_2S_3 decreases rapidly as the pO_2 is increased with much greater pSO_2 needed for this phase to exist. As the pO_2 is increased further TiO and Al_2O_3 can coexist with MnS. Above oxygen partial pressures of ~ 1×10^{-30} atm only the oxides are stable. As the route is followed towards the scale/gas interface TiO_2 becomes the most stable phase in contact with MnO and Al_2O_3. As the pO_2 increases further as the scale/gas interface is approached various manganese oxide phases are stable in contact with Al_2O_3 and TiO_2. At the scale/gas interface $MnSO_4$ can be seen to

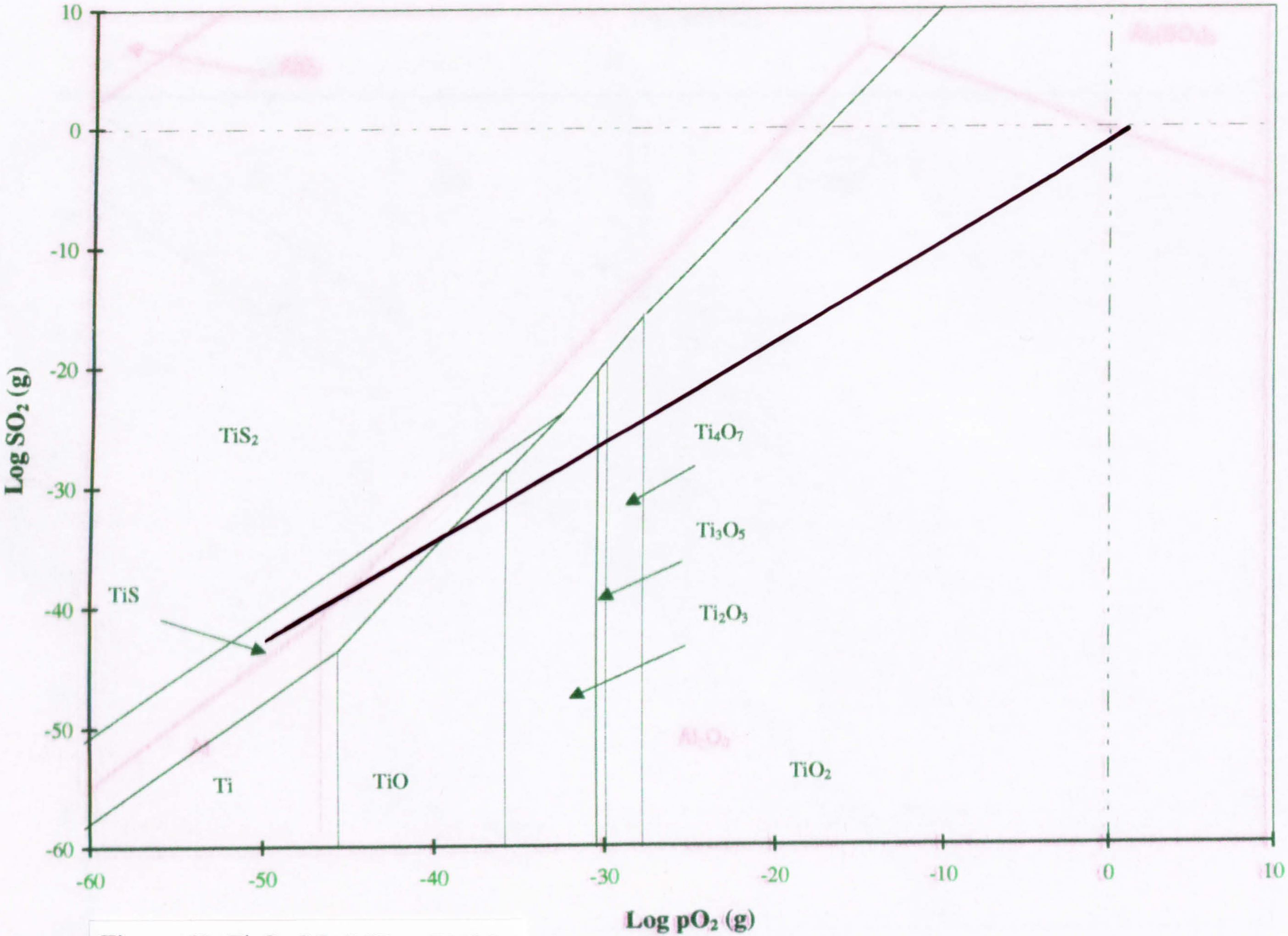

Figure 68: Ti-O_2-SO_2 PSD at 750°C

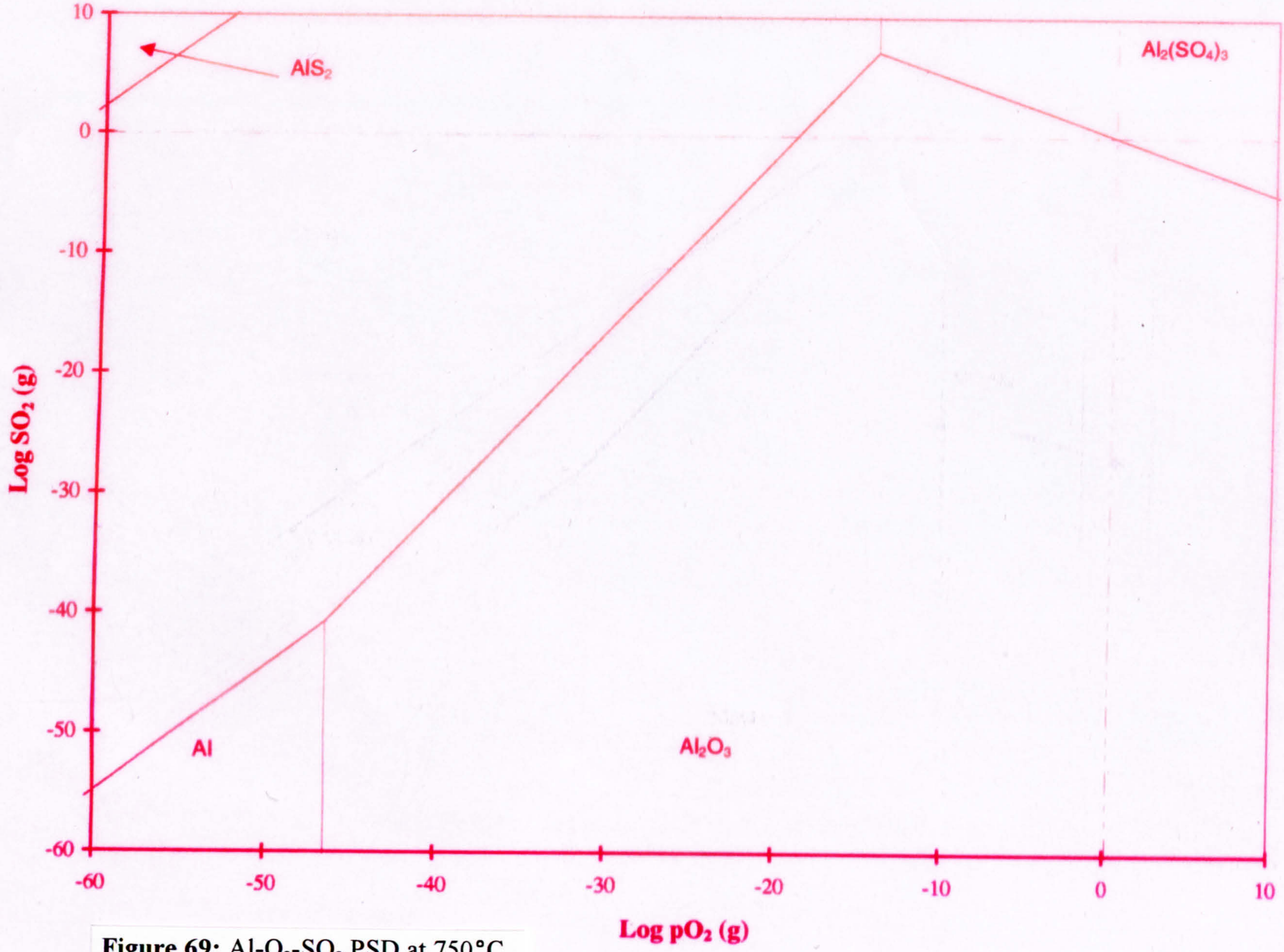

Figure 69: Al-O_2-SO_2 PSD at 750°C

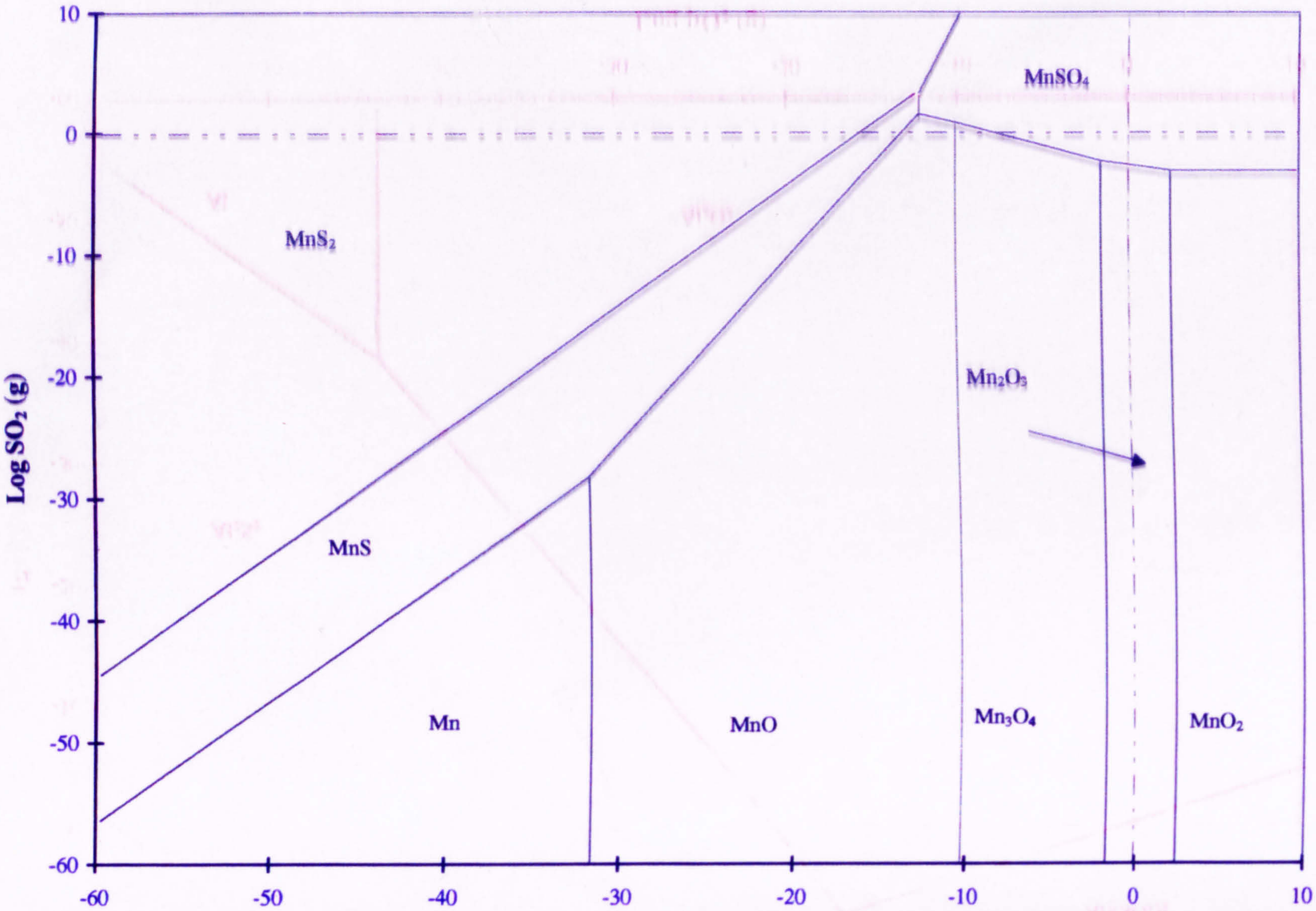

Figure 70: Mn-O_2-SO_2 PSD at 750°C

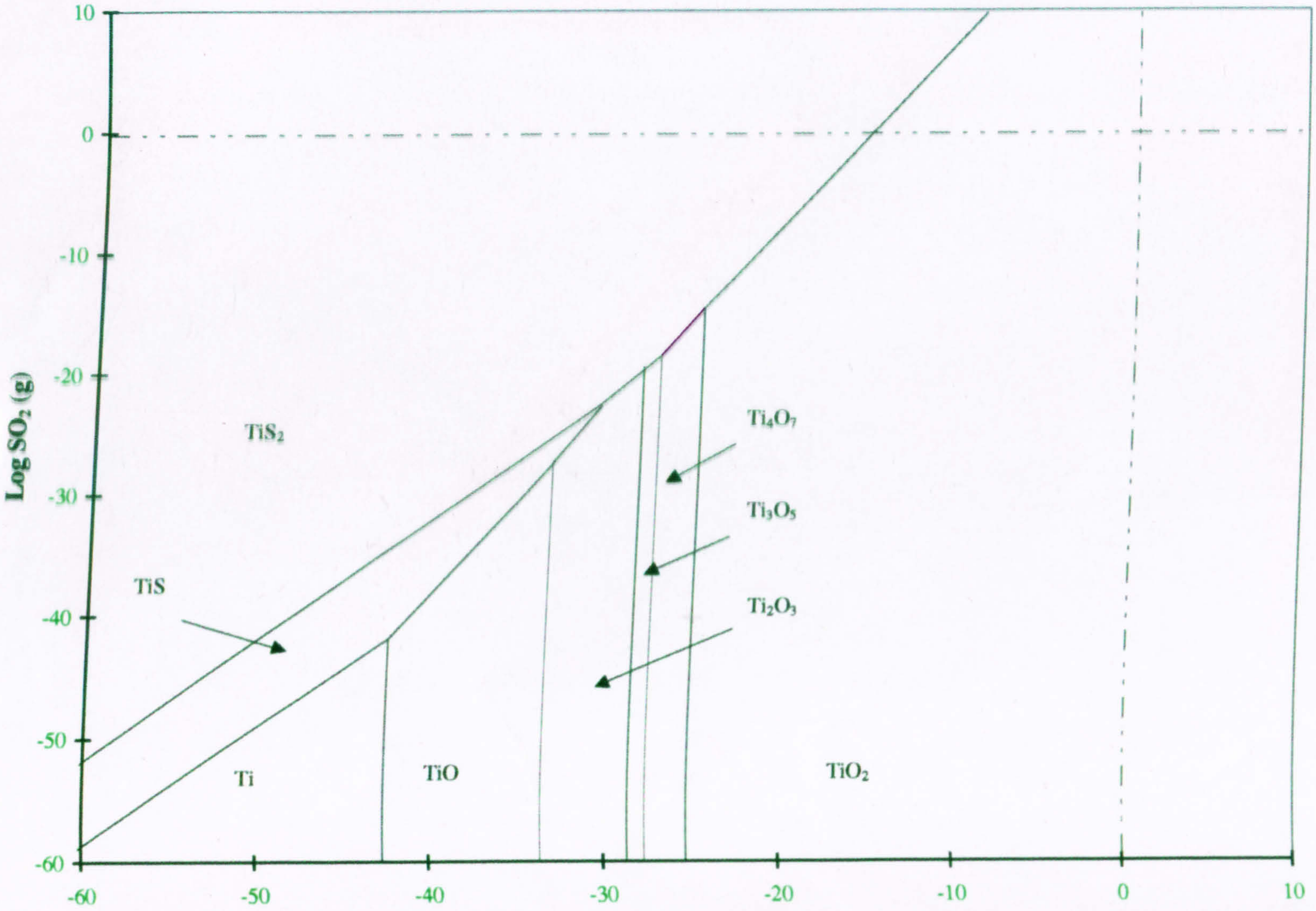

Figure 71: Ti-O_2-SO_2 PSD at 800°C

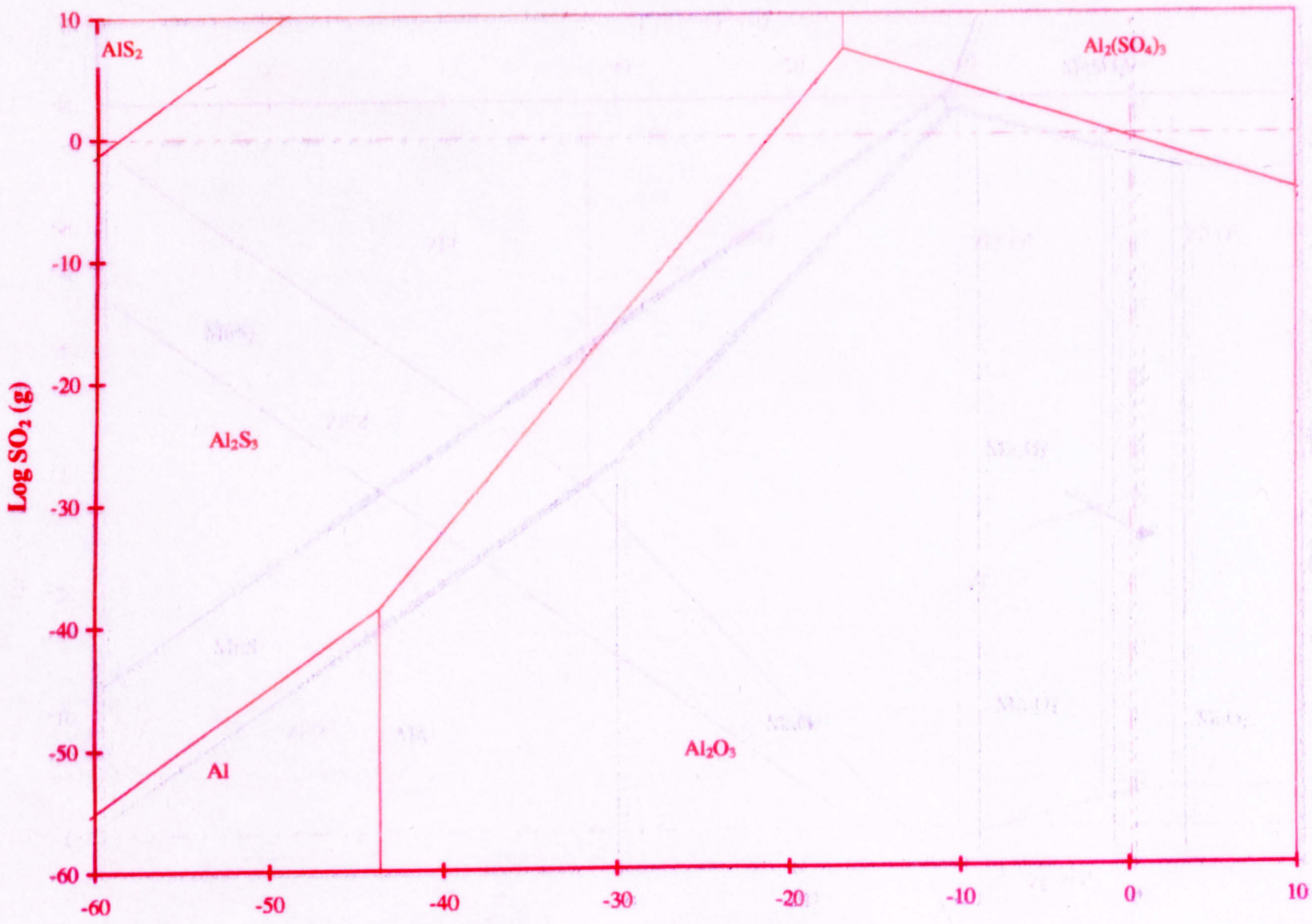

Figure 72: Al-O_2-SO_2 PSD at 800°C

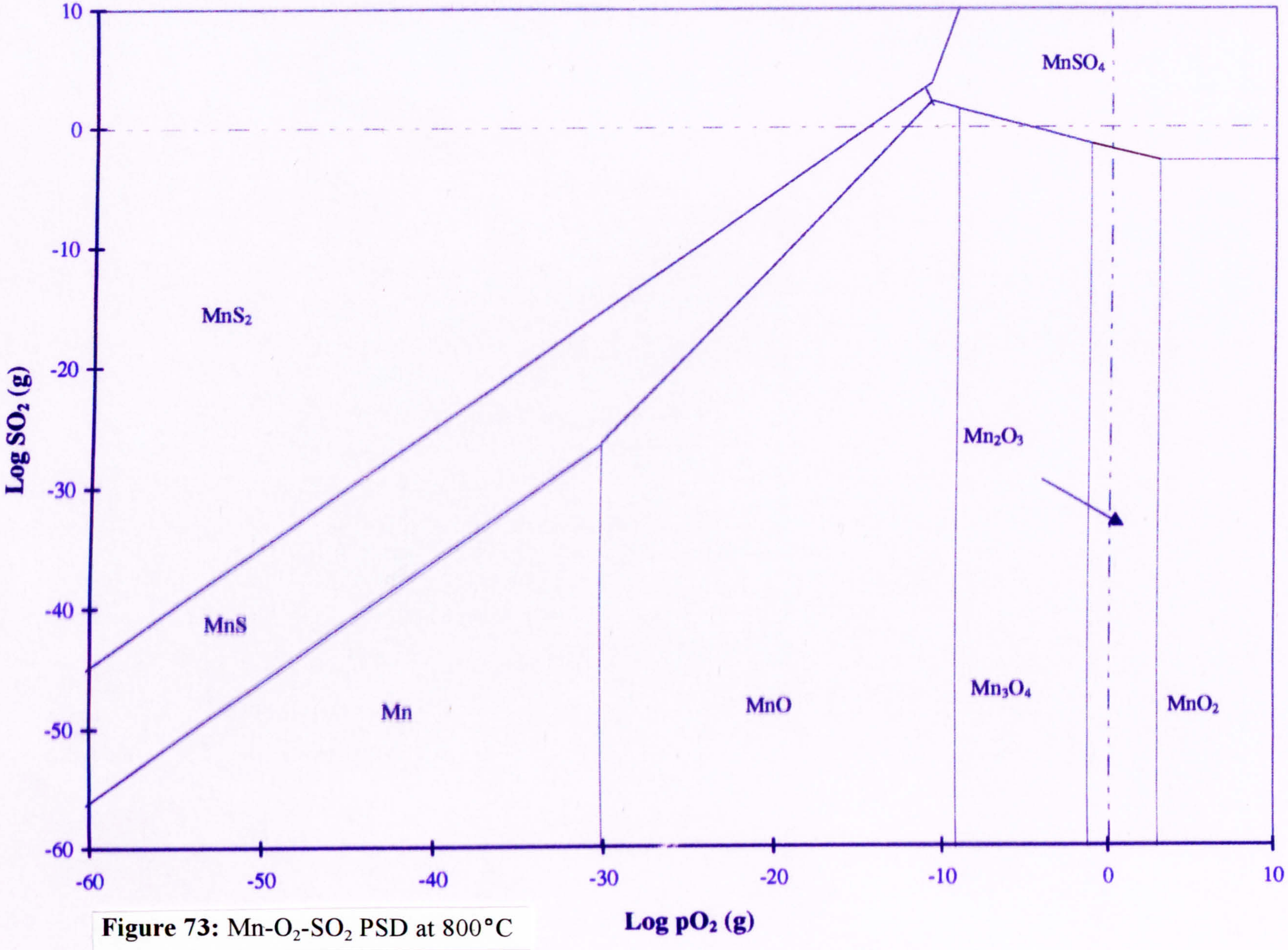

Figure 73: Mn-O_2-SO_2 PSD at 800°C

be the most thermodynamically stable phase in contact with TiO_2, Al_2O_3 and MnO. Atmospheric pressures greater than unity are needed for $Al_2(SO_4)_3$ to exist at the scale/gas interface.

The predictions made through superimposing PSD's are useful in providing comparisons as to the phases which are stable and able to exist adjacent to each other. The individual diagrams can be expected to alter if the relative activities were taken into account. This becomes important if, as in this case, a phase such as $Al_2(SO_4)_3$ is predicted to be unstable at the scale/gas interface. Calculations to determine new stability lines, were unnecessary as the diagrams, assuming unit activities, predicted the phases which were seen in this investigation. Other considerations must accompany the predictions made by PSD's. The rate of a reaction may result in selective oxidation/sulphidation. This may also depend on the diffusivity of the cations through the corrosion products at the substrate interface.

9.2.2 Modeling the sulphidation behaviour of Ti-45Al-2Mn-2Nb

In this section the kinetic, metallographic and thermodynamic data will be used to propose a model for the sulphidation of Ti-45Al-2Mn-2Nb in low $p(SO_2)$, high $p(O_2)$ environments.

The mechanisms which describe the sulphidation of this high aluminium content intermetallic alloy are similar to those used by Du et al[69] to explain the sulphidation of pure titanium and Ti-6Al-4V. Figures 74 and 75 show SEM micrographs of the scales formed on these alloys in $H_2/H_2O/H_2S$ environments ($pO_2 = 10^{-18}$ atm, $pS_2 = 10^{-1}$ atm). Du et al[69] observed that an inner and outer rutile layer developed in both cases simultaneously as shown by a platinum marker study, with alumina precipitating in the outer layer in the case of the aluminium containing alloy. In both cases a sulphide layer formed at the scale/substrate interfaces, TiS_2 in the case of pure titanium and Al_2S_3 and TiS_2 in the case of Ti-6Al-4V. In this investigation a much higher aluminium containing titanium alloy was used along with different oxygen and sulphur pressures, however similar reaction kinetics were observed. A major difference existed in the mass gains and

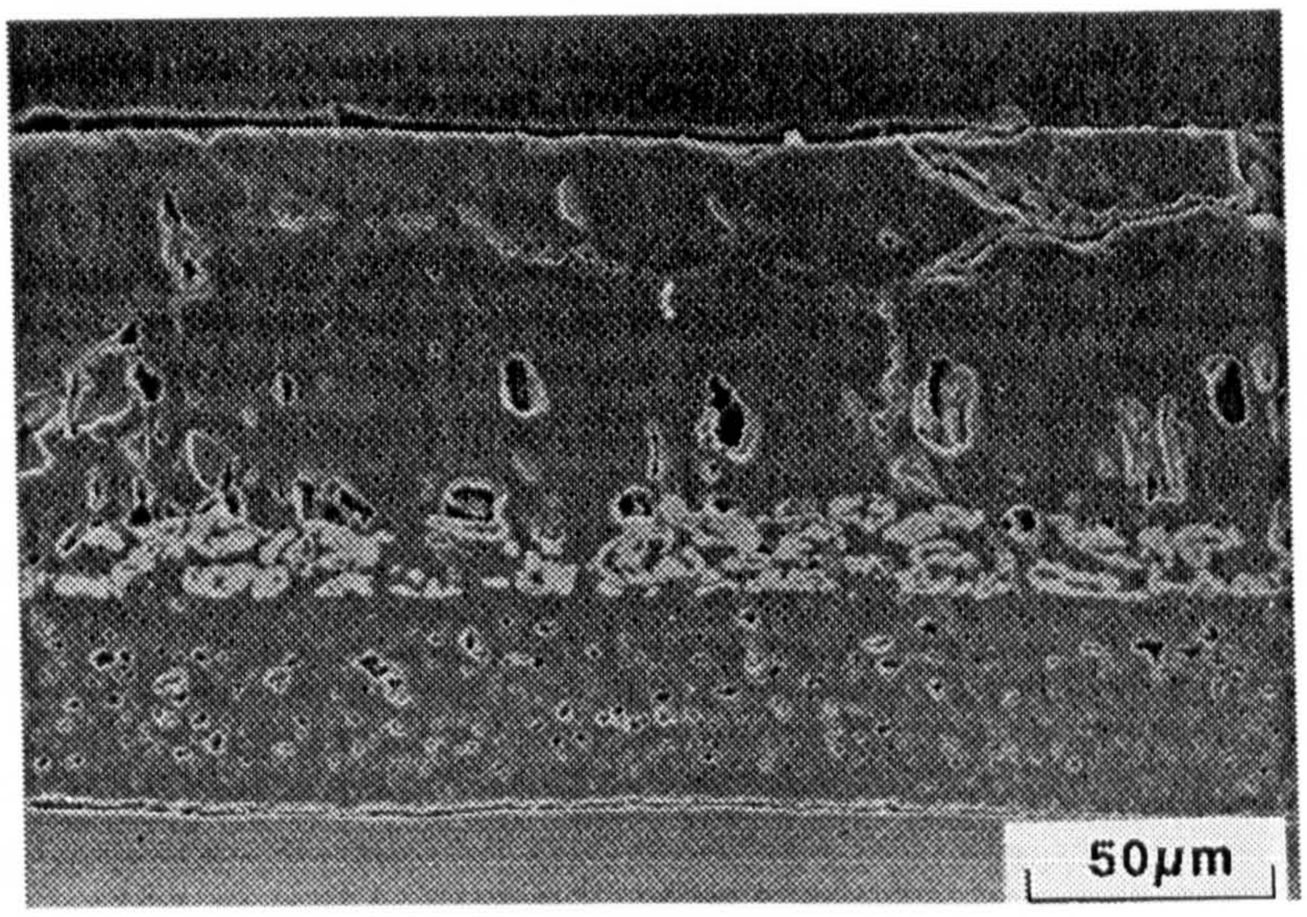

Figure 74: SEM micrograh showing the through thickness morphology of Ti after exposure for 168 hours at 750°C in an $H_2/H_2O/H_2S$ environment[69]. Light phase (Pt marker) has segregated to the rutile/rutile interface.

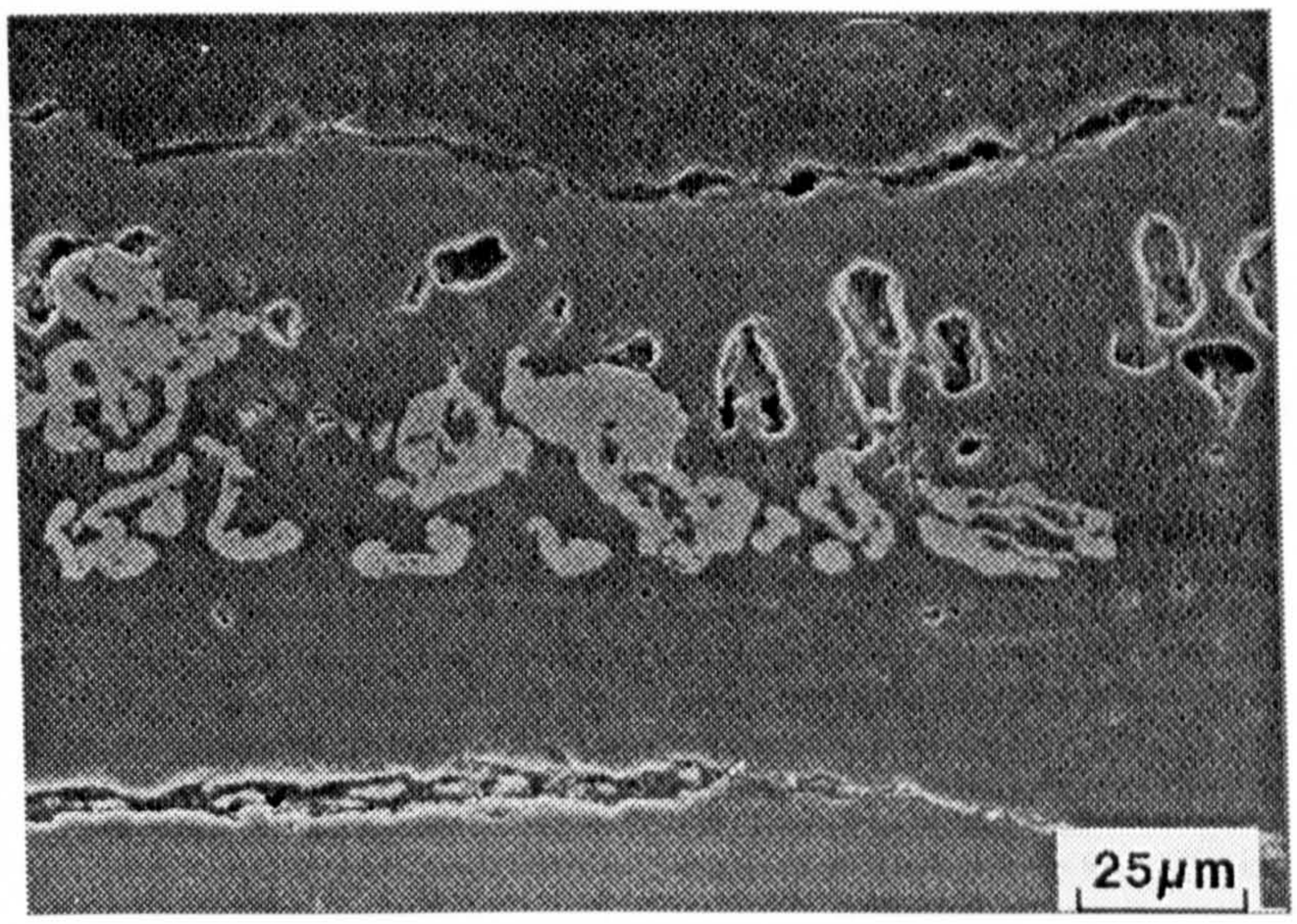

Figure 75: SEM micrograh showing the through thickness morphology of Ti-6Al-4V after exposure for 168 hours at 750°C in an $H_2/H_2O/H_2S$ environment[69]. Light phase (Pt marker) has segregated to the rutile/rutile interface.

scale thicknesses obtained at 750°C. Mass gains of approximately 19 and 11 mg/cm^2 resulted after exposure to high sulphur containing atmospheres for pure Titanium and Ti-6Al-4V after 100 hours, while Ti-45Al-2Mn-Nb resulted in a mass gain of 0.5 mg/cm^2 after 100 hours for a lower sulphur (pS_2 = ~10^{-4} atm), high oxygen containing environment. The addition of six atomic percent aluminium to pure titanium reduced the scale thickness from 150 to 100μm after 168 hours exposure, which was again reduced to less than 15μm with an aluminium content of 45 atomic percent.

The sulphidation model shown in figure 76 categorises the corrosion behaviour of Ti-45Al-2Mn-2Nb over the temperature range of 700 to 900°C. Three mechanistic stages have been proposed based on the metallographic and thermodynamic evidence gathered over this temperature range. Each stage is treated individually with the possible reactions discussed with reference to the preceding sections.

Stage 1

Initially a porous rutile and alumina layer forms at the substrate interface due to the higher pO_2 compared to pSO_2. As the scale quickly thickens manganese sulphate particles form over this initial mixed oxide layer. Manganese sulphate was shown in section 9.2.1, which compared the sulphur/oxygen PSD's, to be the most stable sulphur bearing phase able to exist in contact with TiO_2 and Al_2O_3 at the scale/gas interface. This reaction is shown below;

$$\mathbf{Mn\ (s) + SO_2\ (g) + O_2\ (g) = MnSO_4\ (s)}$$

Manganese appears to play an important role in the oxidation/sulphidation of this alloy and is therefore expected to play an important part in the hot corrosion behaviour of this alloy as well. The hot corrosion behaviour is investigated in section 9.4 with the significance of manganese explained in more depth.

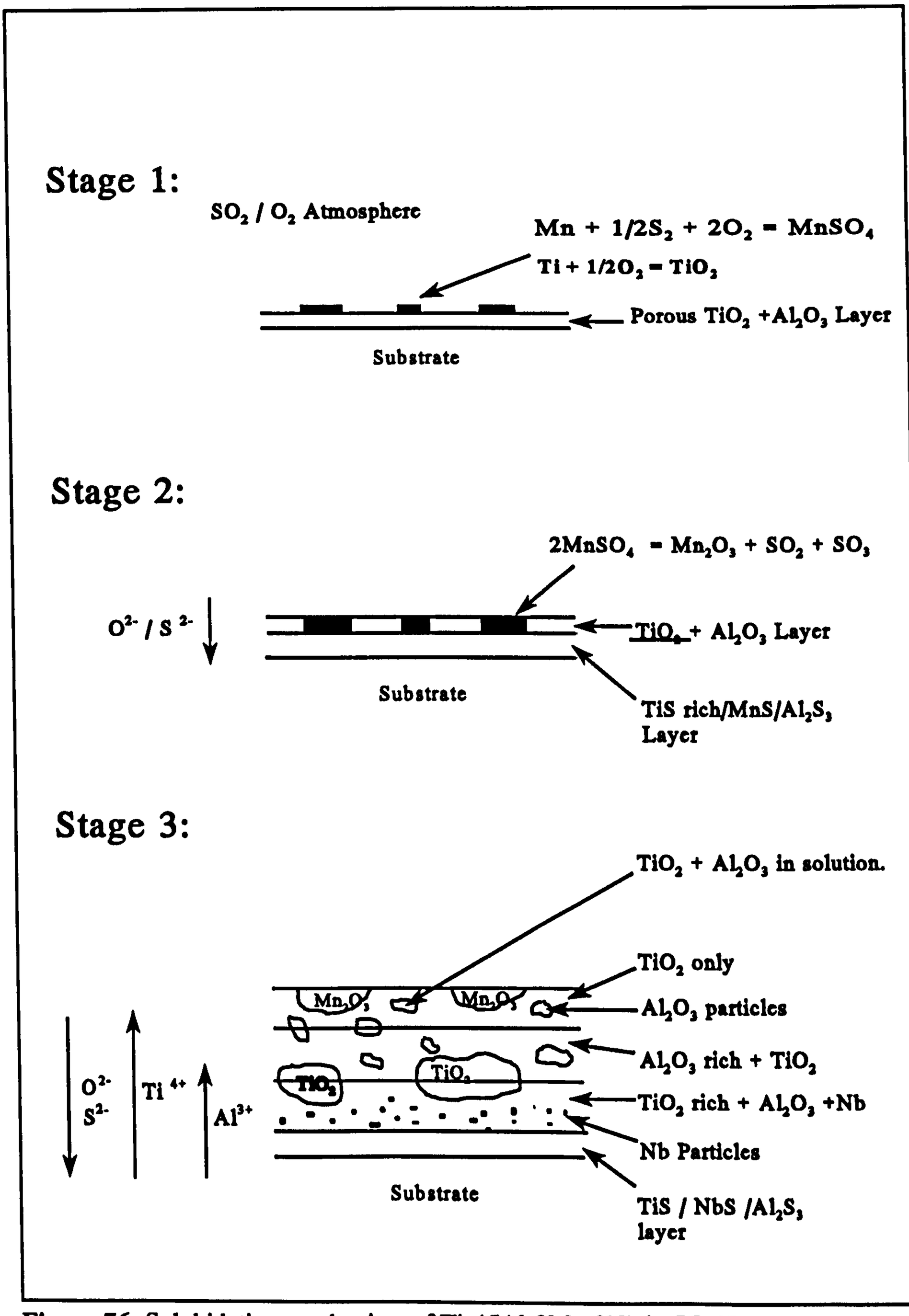

Figure 76: Sulphidation mechanism of Ti-45Al-2Mn-2Nb in SO_2/O_2

Stage 2

After longer exposure times or at higher temperatures a titanium and manganese oxide surface layer develops. The absence of sulphur suggests that the manganese sulphate particles are no longer stable and decompose shortly after forming;

$$2MnSO_4\,(s) = Mn_2O_3\,(s) + SO_2(g) + SO_3(g)$$

Thus sulphur is released and is able to diffuse inwards where it reacts with the substrate. Sulphur dioxide is thought to penetrate through the porous oxide layer. Thus a titanium sulphide rich, plus aluminium sulphide layer forms at the scale/substrate interface.

Stage 3

During this stage a discontinuous alumina layer forms between the outer and inner rutile layers. There is thus an outward diffusion of aluminium. Both titanium and aluminium must diffuse outwards through the sulphide layer formed at the scale/substrate interface. If the inward flux of sulphur remained high further sulphides would be expected to form increasing the sulphide layer thickness, and limiting the outward flux of cations when a non-protective outer oxide scale is formed. This does not however account for the discontinuous alumina layer. The more likely explanation, in agreement with the mechanism proposed by Du et al [69], is for a reduction in the inward flux of sulphur to occur as the scale thickens resulting in the sulphides decomposing. This would allow both aluminium and titanium to diffuse outwards. These cations reprecipitate as the pO_2 increases near the scale/gas interface. The free sulphur diffuses inwards to react with the substrate and therefore maintain the sulphide layer. The decomposition reactions are shown below.

$$TiS_2\,(s) = Ti\,(s) + S_2\,(g)$$

$$Al_2S_3\,(s) = 2Al\,(s) + (3/2)\,S_2\,(g)$$

The precipitation of a more continuous alumina layer, due to the higher aluminium content of this alloy, may account for the much lower mass gains observed at 750°C in comparison with those seen by Du et al. This layer may act as a partial diffusion barrier to the inward diffusion of anions and the outward diffusion of cations. At the lower temperatures and after short exposure times at high temperatures the kinetics remain within a diffusion controlled regime. The faster diffusion routes, i.e grain boundaries, usually determine the corrosion rates during this period. If these are blocked cation and anion diffusion may occur either through the scale lattice or pores/fissures in the scale. The elemental X-ray micrograph in photograph 8.2.3c, showing the distribution of niobium in the scale, identifies niobium as having diffused outwards and precipitated within the inner rutile layer. This may have contributed to the relatively small growth rates whilst in this diffusion controlled regime. Rapid near linear scale growth occurs above 20 hours at 800°C indicating that the discontinuous alumina layer no longer provides partial protection. Severe spalling occurred during this period suggesting that sulphur penetrated through cracks which developed as a critical scale thickness was exceeded. In this manner a porous scale, through which both anion and cations can diffuse rapidly, is created.

Manganese was only identified in the outer rutile scale. A thermodynamic review of the standard free energies of formation of the oxides, shown in table 22, may help explain why manganese is not observed in the intermediate scale layers. The oxides of Ti and Al are more stable than the Mn oxides. During the early stages, before an inner sulphide layer has had time to form, it is thermodynamically more favourable for Al and Ti to form oxides at the scale surface. The formation of $MnSO_4$ was shown in section 9.2.1 to be thermodynamically more favourable than $TiSO_4$ or $Al_2(SO_4)_3$ providing the driving force for Mn to diffuse outwards via vacancies in the scale to react with sulphur in the gas. Once the outer oxide had exceeded a critical thickness and a continuous sulphide layer had formed at the scale/substrate interface the outward diffusion of Mn stops. There is no longer a driving force for the outward diffusion of Mn as the sulphur activity increases at the scale/substrate interface.

Table 22: Standard free energies of formation of some oxides. ($kJmol^{-1}$)

Corrosion product	600°C	700°C	800°C
$2Mn+O_2 = 2MnO$	-710	-690	-670
$4/5Nb + O_2 = 2/5Nb_2O_5$	-610	-595	-580
$4/3Al + O_2 = 2/3\ Al_2O_3$	-940	-915	-890
$Ti + O_2 = TiO_2$	-750	-730	-715

9.3 Hot salt corrosion

Sodium chloride (NaCl) is known to accelerate the corrosion rate of titanium alloys. Chevrot[79] showed that an IMI 834 titanium alloy substrate was severely attacked, which led to a loss in mechanical properties of the alloy. No data were available in the open literature to indicate to what extent Ti-45Al-2Mn-2Nb would be corroded in the presence of salt. The immediate question was whether or not niobium would still promote the formation of a protective alumina layer in the scale. Yao,[86] in his study of hot salt corrosion, did not provide enough evidence to clearly identify the corrosion mechanisms operating between 500 and 800°C.

NaCl has been shown to affect the corrosion rate to a greater extent in the early stages of exposure. Every corrosion test, when salt coated, suffered an initial high rate of mass gain, figure 77, after which the rate decreased to levels slightly higher than that corresponding to oxidation. A comparison of the salt corrosion, sulphidation and oxidation behaviour of this alloy at 700°C, figure 78, shows NaCl to be the more aggressive environment.

Three kinetic stages are identifiable in each of the salt corrosion tests. Each being controlled by different rate controlling factors. During the first stage a form of logarithmic kinetics operated. In the majority of cases the onset of stage 2 was accompanied by breakaway kinetics after which the rate of corrosion continued to increase at logarithmic growth rates. Table 15, in section 8.2.4, identifies the onset of breakaway kinetics and the times after which logarithmic kinetics were again followed. This second stage transition corresponded with the development of whiskers on the component surface. The length of this second stage depended on both temperature and time. The third stage was characterised by the onset of parabolic kinetics. The change in corrosion mechanism from logarithmic to parabolic indicates that the rate of corrosion has changed from being whisker controlled, which is indicative of vapour phase transport, to being diffusion controlled. Figure 79a to 79c give an example of how the transitions were identified. Figure 79a shows the stage transitions on a mass gain curve. Each transition is clearly identified from logarithmic and parabolic plots given in figures 79b and 79c.

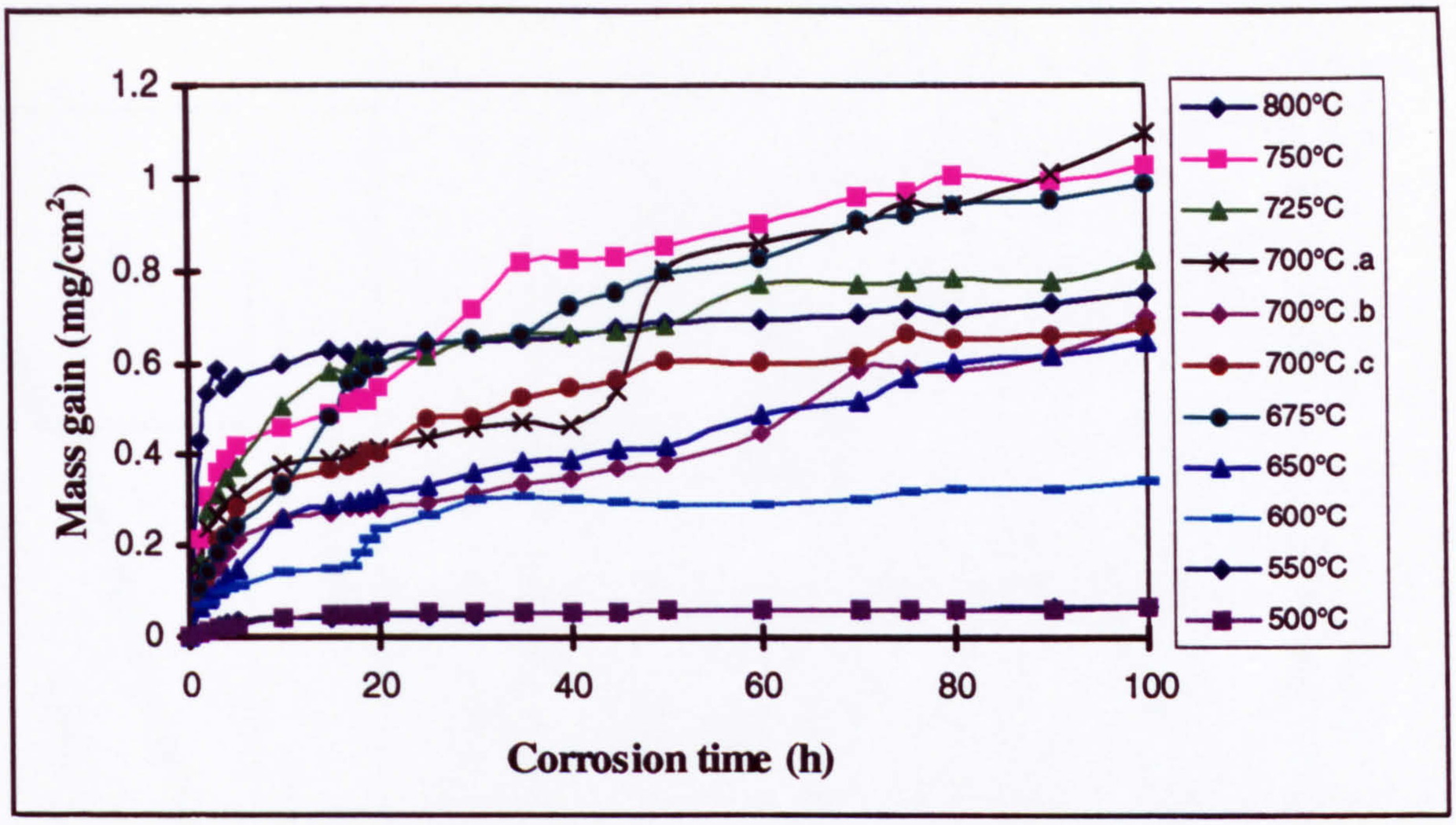

Figure 77: Hot salt corrosion behaviour of Ti-45Al-2Mn-2Nb after 100h exposures between 500 and 800°C

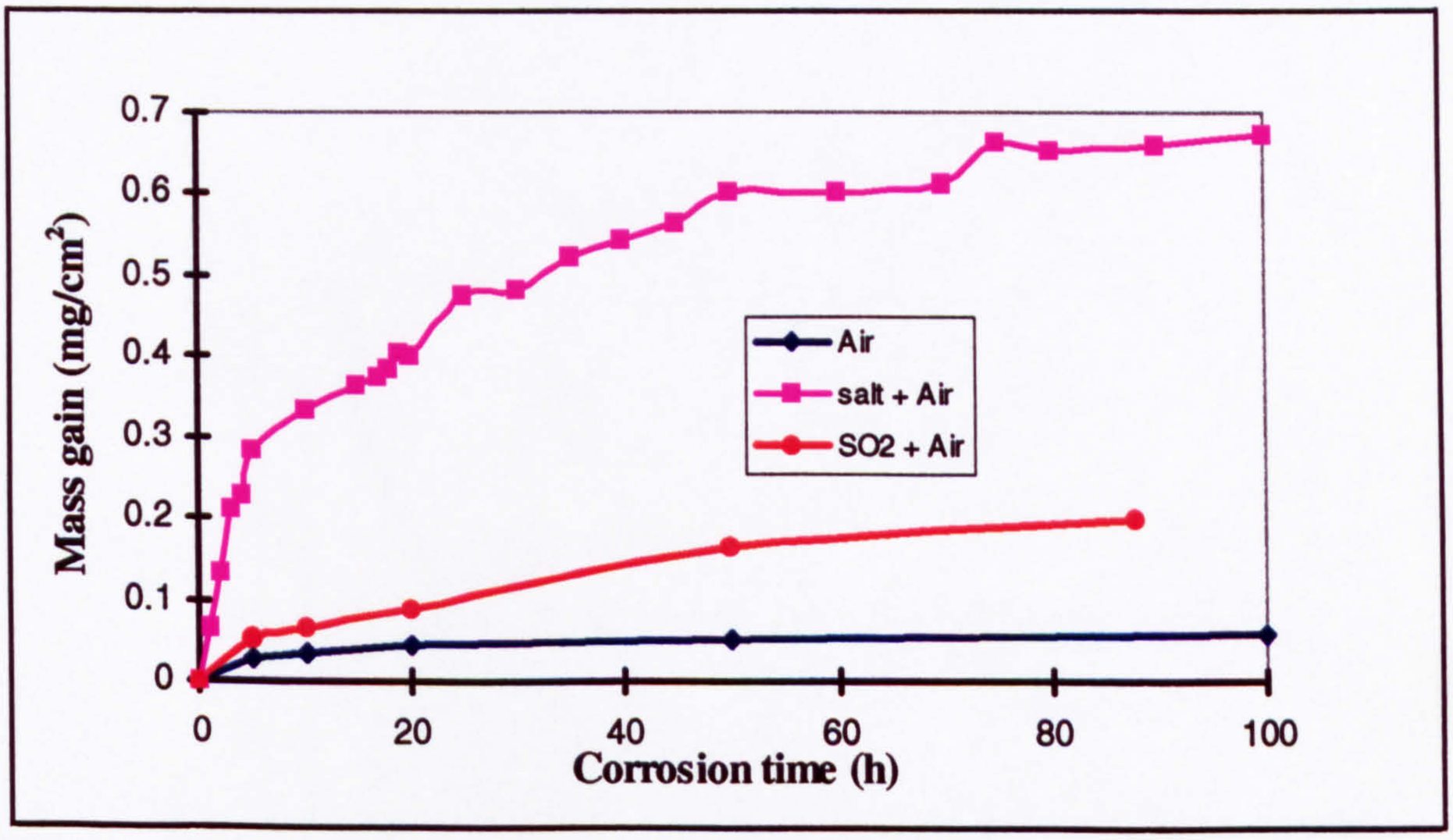

Figure 78: Mass gain versus tiime plot comparing the hot salt corrosion, oxidation and sulphidation behaviour of Ti-45Al-2Mn-2Nb after 100 h at 700°C

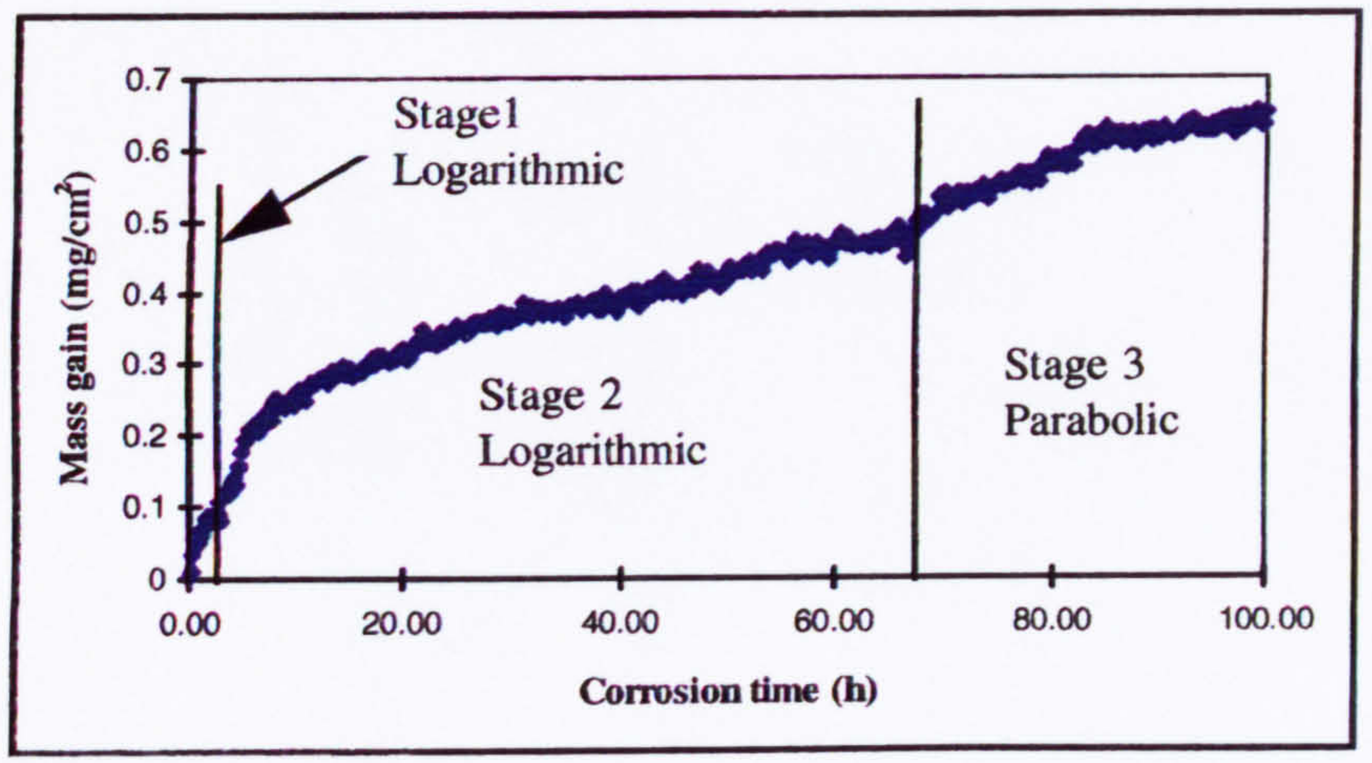

Figure 79a

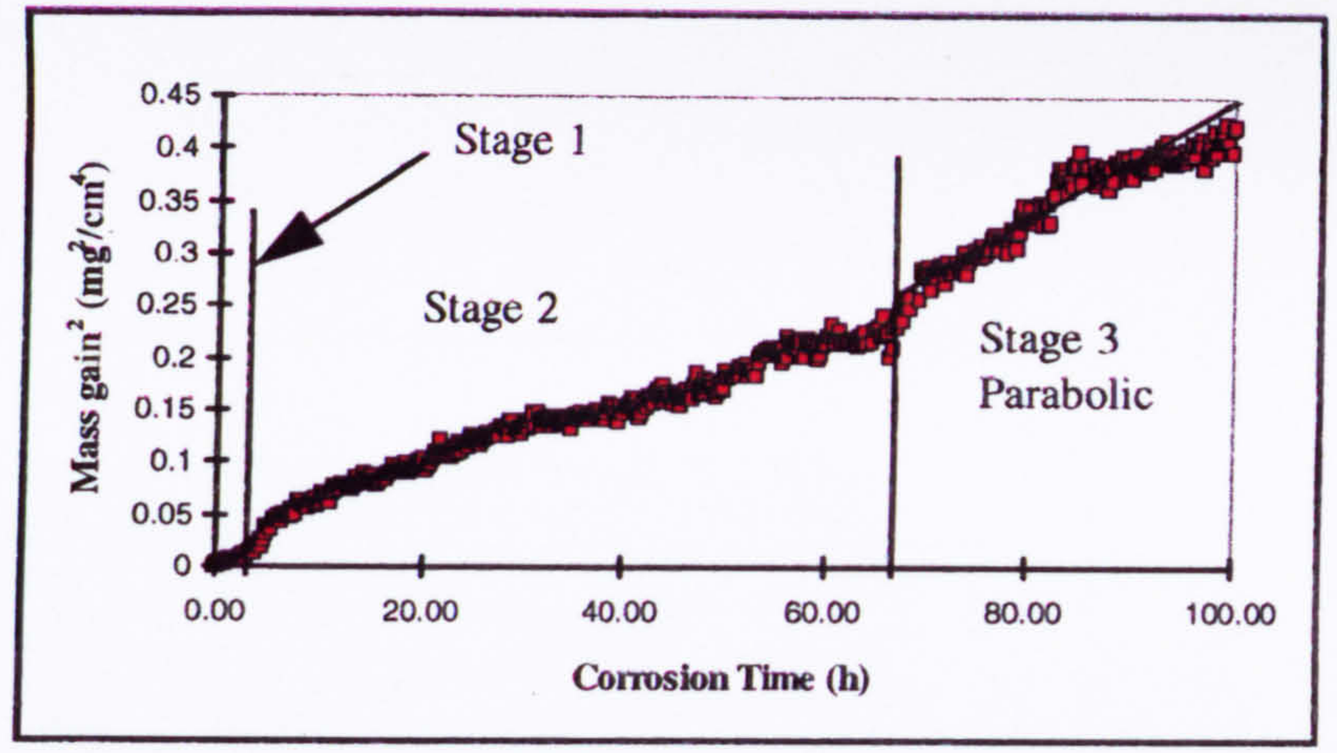

Figure 79b

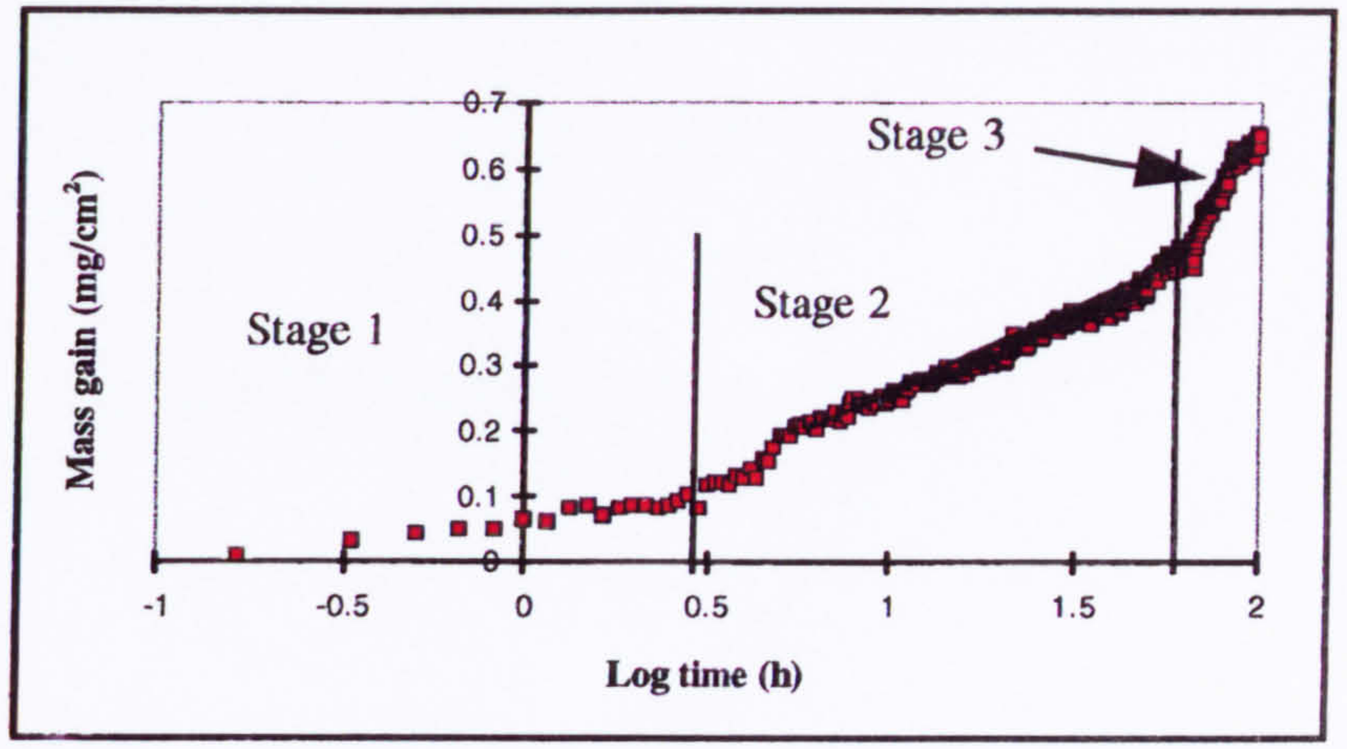

Figure 79c

Figure 79: Example of the method used to determine the hot salt corrosion transitions. Figure 79a shows the mass gain verse temperature data at 650°C. Figure 79b shows the parabolic plot of this data. Figure 79c shows the corresponding logarithmic plot.

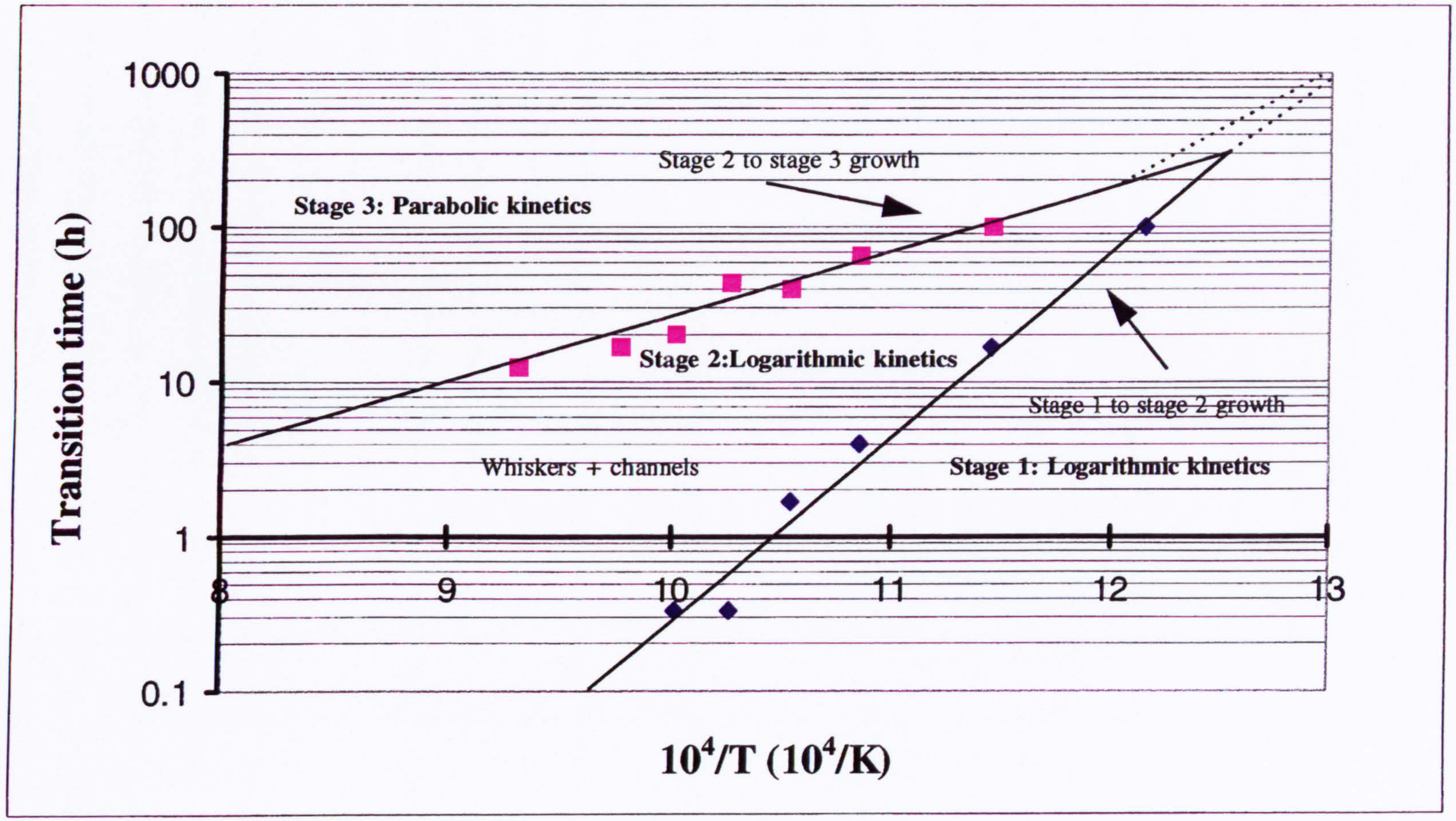

Figure 80: Arrhenius plot showing the kinetic hot salt corrosion transitions observed over the temperature range of 500 to 800°C.

The transition times at each temperature are plotted on an arrhenius plot in figure 80. The two transitions all occurred within 100 hours over the temperature range of 600 to 800°C. However, logarithmic kinetics continued to operate beyond 100 hours at 550 and 500°C. To monitor these transitions beyond 100 hours at these temperatures discontinuous mass gain measurements were used, reducing the accuracy with which the transition times could be determined. The transitions at these low temperatures could not therefore be determined from changes in kinetics. The transition to stage 2 was thus identified by the appearance of whiskers. At 550°C these occurred after approximately 100 hours, photograph 8.2.4a. Photograph 8.2.4j shows the appearance of whiskers after 500 hours at 500°C. Figures A11 and A12 in appendix A show plots of the mass gains obtained after 1000 hours at 500 and 450°C, respectively. The corrosion rates remained low with localised corrosion being observed. These kinetic graphs do not show a transition to parabolic kinetics. At these low temperatures the rate controlling factor may remain one of whisker growth out to much longer times, until scale thicknesses are such that the whiskers through which the corrosion products are transported are closed off and the scale growth is controlled by diffusion processes.

The three stages of salt corrosion were supported by metallographic analyses of both the surface and through sections of specimens corroded at each temperature. Various intermediate exposure times were also examined to validate the transition times determined kinetically. Similar characteristic features were observed during each stage over the whole temperature range studied. Table 15 in section 8.2.4, summarises the surface and through section observations made after 100 hours at each exposure temperature.

The first stage of hot salt corrosion, where a form of logarithmic kinetics operates, is characterised by accelerated oxidation rates. This mechanism of corrosion continued for 100 hours at 550°C. As the exposure temperature increased the transition to stage two occurred after shorter periods of time. At 700°C the first change in corrosion mechanism occurred after approximately 20 minutes. At temperatures above 700°C the transition from stage 1 to stage 2 was unidentifiable from kinetic data, occurring within the first 10

minutes of exposure in a hot salt environment. For comparison logarithmic kinetics were observed out to 100 hours at 700°C in air alone with final mass gains of approximately 60 $\mu g/cm^2$. Similar mass gains were observed after 100 hours at 500 and 550°C in the presence of salt. Comparisons of the mass gains developed after 20 minutes at 700°C in the presence of salt, SO_2, and air; 37, 3 and 1.8 $\mu g/cm^2$ respectfully, show that initially salt deposits accelerated the early stages of high temperature corrosion. Salt depositions within the range of 0.02-0.04mg/cm^2 increased the oxidation rates by a factor of 20. Low partial pressures of SO_2 increased the mass gains by a factor of ~1.5. Thus salt depositions, in the presence of air, resulted in mass gains 12 times greater than in SO_2 + air.

The presence of salt is found to affect the oxidation rates almost immediately with no apparent incubation period. Predominantly rutile scales develop during this initial stage. This is seen in photograph 8.2.4 of a specimen exposed for 100 hours at 500°C. Areas of high salt concentrations are evident with little corrosion occurring between these areas. This is supported by photograph 8.2.4z which shows substrate attack only occurring below these areas of high salt concentrations. As a result "ledges" begin to form around these areas of salt deposits. Photograph 8.2.4l, of the surface morphology seen after 2 hours at 650°C, illustrates this. These features suggest that as the salt reacts with the substrate the corrosion products become incorporated with the salt forming semi-solid (solid-liquid) salt mixtures. The liquid content of the salt increases with time as further corrosion occurs. This is thought to be due to the formation of low temperature eutectic phases. The NaCl-$TiCl_2$, NaCl-$MnCl_2$, and NaCl-$AlCl_3$ phase diagrams shown in figure 81, show that eutectic points are reached at approximately 602, 425 and 110°C respectively. The NaCl-$AlCl_3$ phase diagram has low melting point liquid phases with a melting temperature of 160°C or below from NaCl.10 mole % $AlCl_3$ to $AlCl_3$ .20 mole % NaCl, a substantial dynamic range. Further evidence of the existence of a liquid phase developing at 500°C is provided in photograph 8.2.4t, which shows an area of mudflat cracks after being exposed for 193 hours. The accompanying EPMA's show the mudflat area to be titanium rich, with similar levels of manganese, aluminium and chlorine. The titanium levels, may well result from the underlying oxide, suggesting a $MnCl_2$, $AlCl_3$

NaCl-$AlCl_3$

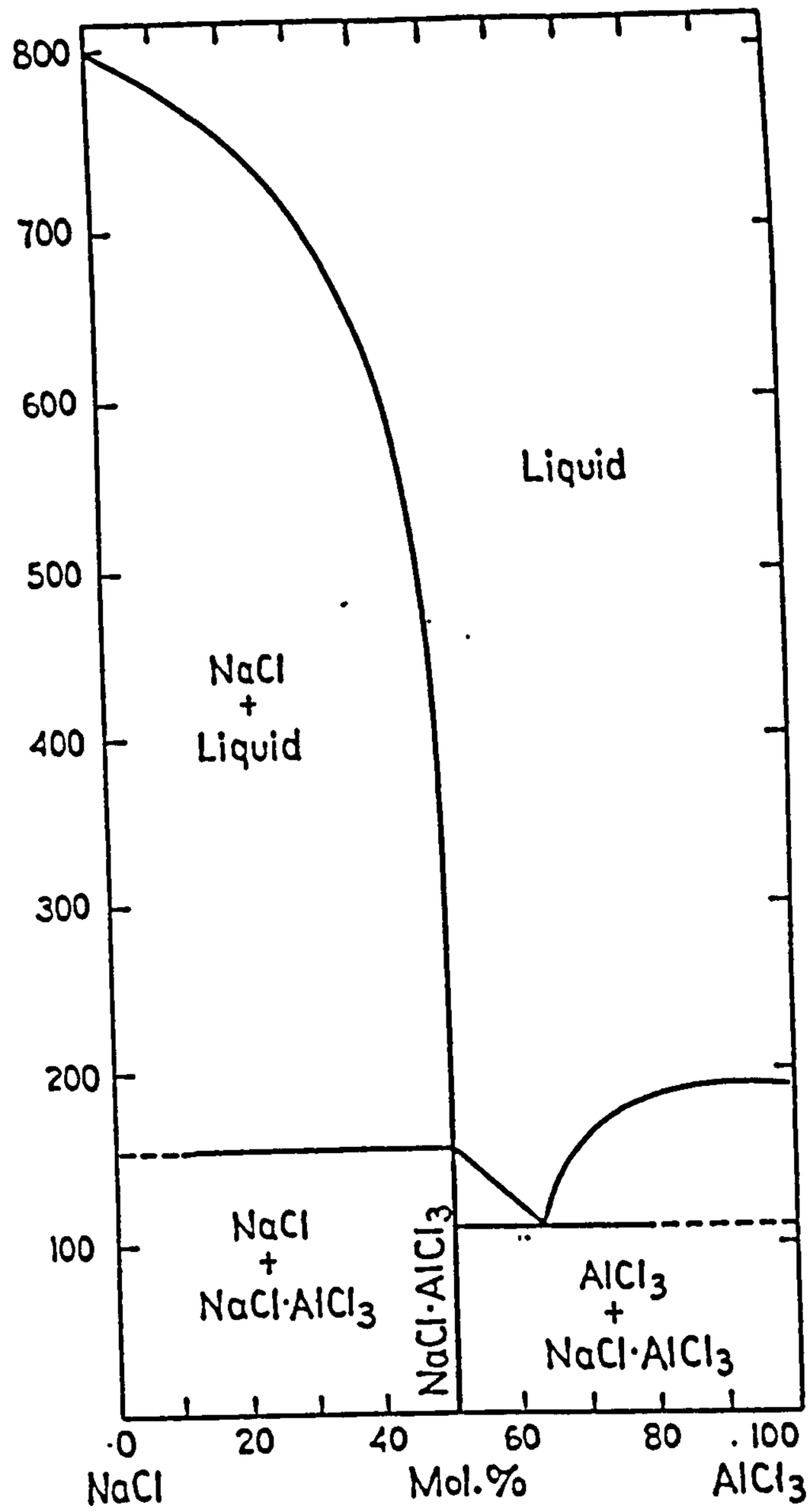

Figure 81a:

NaCl-$TiCl_2$

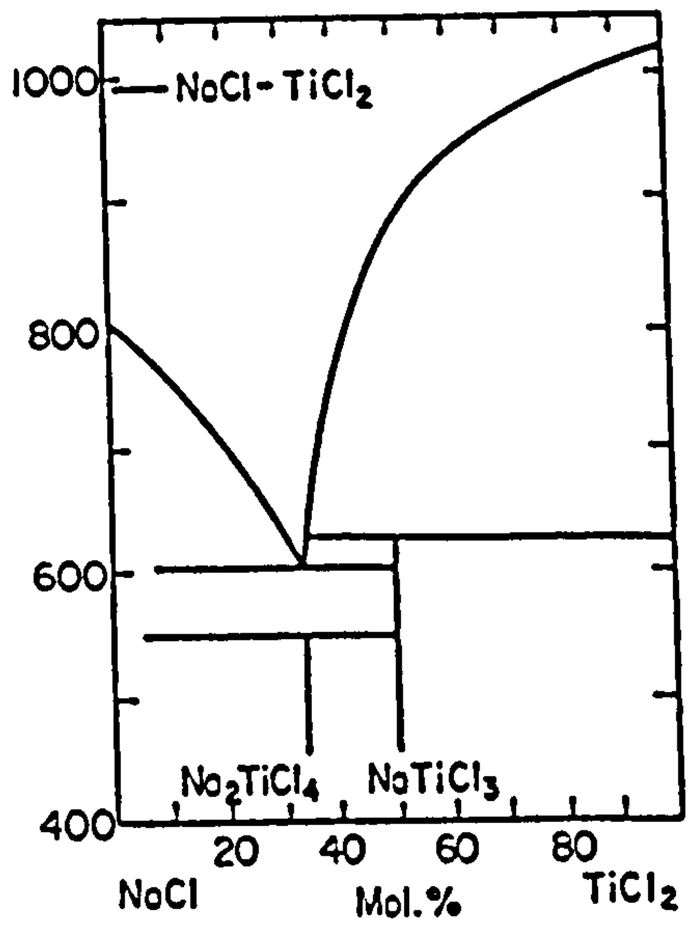

Figure 81b:

NaCl-$MnCl_2$

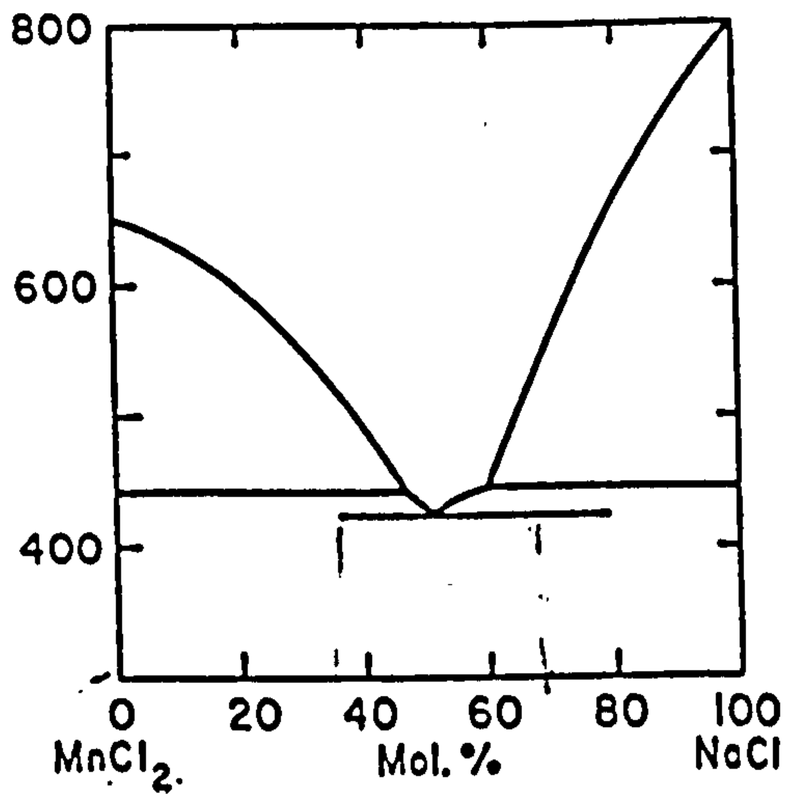

Figure 81c

Figure 81: NaCl Phase diagrams, a) NaCl-$AlCl_3$ b) NaCl-$TiCl_2$ c)NaCl-$MnCl_2$

eutectic which may have a lower melting point than 110°C. An area adjacent to the cracks was identified as being predominantly NaCl. Mudflat cracks are indicative of liquid phases having existed, as they suggest that on cooling the high strains, caused by the differences in thermal expansion coefficients, result in cracking. At 700°C similar corrosion behaviour develops after much shorter times. Short exposure times of 15 and 30 minutes confirmed that the above mechanism operates at higher temperatures. High levels of aluminium and chlorine were identified after both exposure times. Relatively high levels of manganese were identified in both cases although a decrease appears to have occurred after 30 minutes. The accompanying ledges which developed were titanium rich, with lower levels of aluminium and chlorine. The higher levels of titanium may have been due to interference from the substrate if the shelf was thinner than the penetrative depth of the EPMA, which was ~3μm. Photographs 8.2.4z and 8.2.4y show the accompanying EPMA's used to come to these conclusions.

The change in kinetics, signifying the transition to the second stage, was evident by the onset of whisker formation and thought to be due to a short circuit diffusion or vapour transport mechanism. This was often accompanied by a short period of rapid corrosion. In some instances, as was the case for a specimen exposed for 100 hours at 700°C, this occurred after the transition to the second stage. The first form of accelerated kinetics is directly related to a change in corrosion mechanism whilst the second may have been caused by severe scale cracking creating rapid transport routes for the corrosion products. It was during this stage, where variations in mass gain were observed between samples. Three specimens were exposed for 100 hours at 700°C in air, figures A18 to A20 in appendix A. The salt concentrations were each different but all were within the specified range of 0.02-0.04mg/cm^2 . Three different mass gain curves were generated, with final mass gains of 0.8, 0.7 and 1.1 mg/cm^2. Two out of the three curves behaved as expected with no major breakaway regions. The third specimen showed a period of approximately 10 hours over which rapid scale growth occurred and resulted in the largest mass gains. These experiments illustrate the variations that can exist in both the kinetics and mass gains, the most likely explanation being that the salt coating technique used deposited an uneven coverage of salt, mirroring service conditions more closely.

During stage two the salt continued to react with the initial rutile layer and spread laterally across the specimen's surface resulting in complete coverage. Whisker growth initiated at regions of high salt levels. This is illustrated in photograph 8.2.4n, which shows the surface morphology after 11 hours at 650°C. Very fine whisker growth developed at the low temperatures due to lower partial pressures of the vapour phase gases being generated. At the higher temperatures a profusion of whiskers developed quickly over the majority of the underlying rutile scale. The sequence of four photographs (8.2.4p to 8.2.4s) show this development at 700°C. After 2 hours very fine isolated whiskers were observed. These then developed into thicker bundles of whiskers after 10 hours. Near the predicted transition to stage 3, in this case 20 hours, whisker coverage continued to increase.

The increased corrosion rates developed during stage 2 resulted in much greater substrate attack. For this to occur the initial rutile layer is breached allowing NaCl direct access to the substrate where preferential attack occurs at sites of more rapid diffusion, short circuit diffusion paths such as grain boundaries or along $\alpha 2$ lathes. An outward vapour phase transport mechanism is thought to operate during stage 2 and results in outer and inner wrinkled rutile layers being developed with whiskers growing over these, photographs 8.2.4b to 8.2.4h show this development with temperature. Wrinkled scale morphologies are thought to form as a consequence of compressive stresses causing buckling. The presence of salt may also reduce scale adhesion, reducing the compressive stresses required for buckling. Porous scales are formed due to the rapid transport of halide and chloride species through short circuit diffusion paths, the net result being a loss of scale adhesion.

The second transition to parabolic kinetics resulted in similar corrosion rates to that observed during isothermal oxidation. Table 23 compares the percentage mass gains at the start of stage 3 compared with that after 100 hours at each test temperature, for temperatures above 600°C. At every temperature, except 750°C and one case at 700°C, the percentage mass gains were greater than 74%. NaCl thus substantially affects the oxidation behaviour during the first two stages. The transition time to stage 3 decreased

as temperature increased. The corrosion mechanism in stage 3 was now diffusion controlled. Salt effects are minimised with the scale becoming more protective.

Figures A18 to A20 show that the presence of very small amounts of salt increased the final mass gains by 11 to 20 times at 700°C. At 700°C the presence of salt has a greater effect than an atmosphere of SO_2/O_2, which only increases the final mass gains by up to 5 times.

The third stage of salt corrosion was characterised by the formation of porous rutile scales between 5-35μm thick. Optical microscopy was sufficient to show the extent of substrate attack at each exposure temperature (photographs 8.2.4z to 8.2.4ee). Photograph 8.2.4ff shows a backscattered image of the internal attack which occurred after 100 hours at 600°C. The alpha 2 lathes are distinguished from the gamma phase by being lighter in contrast. In this photograph and photograph 8.2.4gg, of an area beneath a large salt deposit, the alpha 2 lathes

Table 23: Percentage mass gains after stages 1 and 2 during hot salt corrosion above 650°C.

Temperature (°C)	3rd stage transition time (h)	Mass gain after 100 h (mg/cm²)	Mass gain after stage 1&2 (mg/cm²)	% mass gain after stages 1&2
650	65	0.650	0.480	74
675	40	0.98	0.724	74
700.a	43	1.08	0.491	46
700.b	43	0.691	0.353	70
700.c	43	0.674	0.544	80
725	20	0.824	0.606	74
750	17.73	1.01	0.511	51
800	12.5	0.7521	0.610	81

are shown to have been attacked to depths of up to 50μm. An elemental map, in photograph 8.2.4jj, of the scale developed after 100 hours at 700°C shows that a discrete discontinuous alumina phase existed throughout predominantly rutile scales. The low levels of aluminum infer that it is either in solution or distributed as micro particles below the resolution of the SEM. Small concentrations of alumina were also detected through Auger analysis of the surface whiskers (figures 42 to 47) developed after 20 and 100 hours at 700°C. The whiskers, previously thought to be alumina rich, were shown to contain Mn and high levels of Ti. High levels of manganese were also detected in the outer rutile rich scale suggesting that manganese was also transported through the scale as gaseous $MnCl_2$, which was then oxidised to form MnO rich regions.

Small amounts of salt result in a change in corrosion mechanism. During the first two stages the corrosion products are rapidly transported outwards. The Arrhenius plot in Figure 82 compares the salt corrosion behaviour with that of pure oxidation. This shows that as the melting point of salt (~804°C) is approached oxidation type kinetics begin to dominate. The faster corrosion rates associated with hot salt corrosion at the low temperatures reach a peak in terms of the final mass gains, observed after 100 hours, at around 725-750°C. Above these temperatures a proportion of the gaseous halide reaction products are not reoxidised but escape into the surrounding atmosphere reducing the available salt to continue the hot salt corrosion processes.

The slope of a Log Kp versus $10^4/T$ plot, derived from the general equation for the rate of a reaction (Equation 9.3a), determines the activation energy of a corrosion process.

$$\mathbf{Kp = Aexp(-Q/RT)} \qquad \mathbf{(9.3a)}$$

Where Q = Activation energy in KJ mole $^{-1}$, R = Universal gas constant (8.134J/mole/K) and T = Temperature in K.

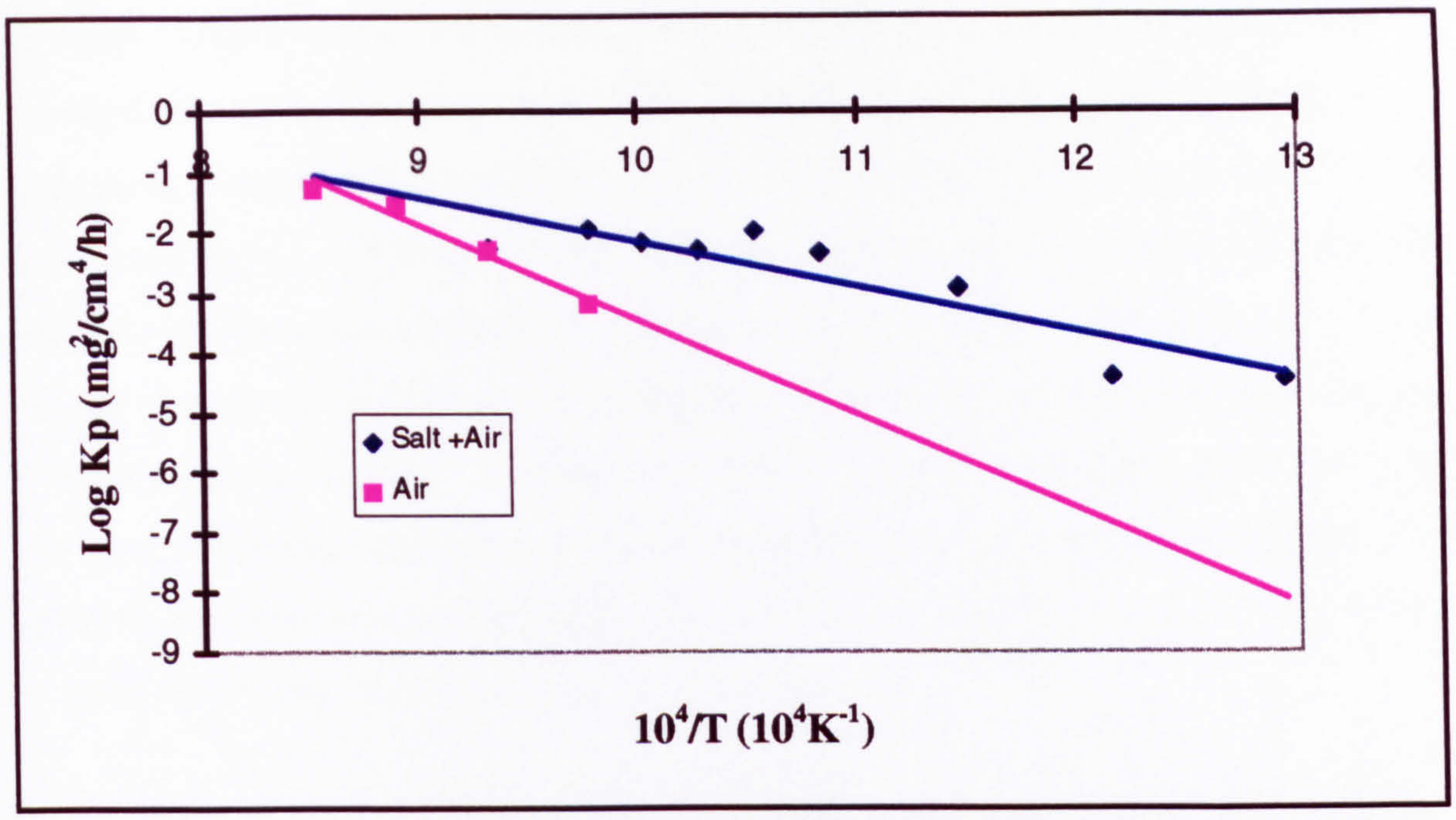

Figure 82: Arrhenius plot comparing the behaviour of Ti-45Al-2Mn-2Nb after 100 h under oxidising and salt corrosion conditions.

This is the energy needed for a proccess or reaction to occur. The higher this energy the more stable the reaction product. Activation energies of -298 KJ mol^{-1} were calculated for the oxidation of Ti-45Al-2Mn-2Nb, the alloy used in this study, -287 KJ mol^{-1} for the oxidation of Ti-35Al-5Nb, determined by Schutze[53], and -190 KJ mol^{-1} for the oxidation IMI 834; determined by Chevrot[79]. Similar activation energies were obtained for the oxidation of the alloy used in this study and the alloy used by Schutze. Both had similar compositions and were observed to form continuous alumina layers, which reduced the oxidation rates in both cases. The activation energies thus show whether or not alumina or rutile are the more dominant oxide former. Alumina forming kinetics dominated in the cases where there was sufficient aluminium present. Where there was insufficient aluminium present, as in the case of IMI834, rutile kinetics dominated.

If the activation energy, for a particular system, changes with temperature the general conclusion can be that a change in corrosion mechanism has occured or is in the proccess of occuring. Figure 82, compares the kinetic behaviour of Ti-45Al-2Mn-2Nb under oxidising and salt corrosion conditions.The activation energies are comparable, although different temperature ranges were used in each case. The oxidation rate constants for each

exposure temperature lie on a straight line suggesting that a single corrosion mechanism operated over this temperature range. Greater scatter existed in the case of the salt coated specimens. A change in kinetics appears to be occurring above 725°C in figure 82. This is illustrated in figure 83, which shows that stable rutile kinetics were favoured up to this temperature. Above this temperature a change in gradient and therefore activation energy occurs with almost no increase in rate constant. This could be due to the loss of halides to the atmosphere resulting in a change in corrosion mechanism. Extrapolating a line from 725°C shows that the kinetic behaviour, and therefore corrosion mechanism, changes and could be predicted to continue in an oxidation manner with a continuous intermediate alumina layer being developed.

A detailed thermogravimetric study has been made of the salt corrosion behaviour of Ti-45Al-2Mn-2Nb. The subsequent kinetic and metallographic analyses have enabled the processes controlling the salt corrosion of this alloy to be characterised. A mechanism, for the hot salt corrosion of Ti-45Al-2Mn-2Nb, is proposed in section 9.3.2. Metallographic studies supported the predicted kinetic transitions. The observed features showed the importance of stages 1 and 2 during which the initial oxide was breached resulting in the formation of surface whiskers. Severe substrate degradation down grain boundaries and $\alpha 2$ lathes provided rapid transport routes for the inward transport of vapour chlorides and the outward transport of vapour metal chlorides. The most likely corrosion products and in particular the vapour species are determined through a thermodynamic analysis in section 9.3.1. The severity of attack is of considerable importance when the potential areas of application for this material are considered.

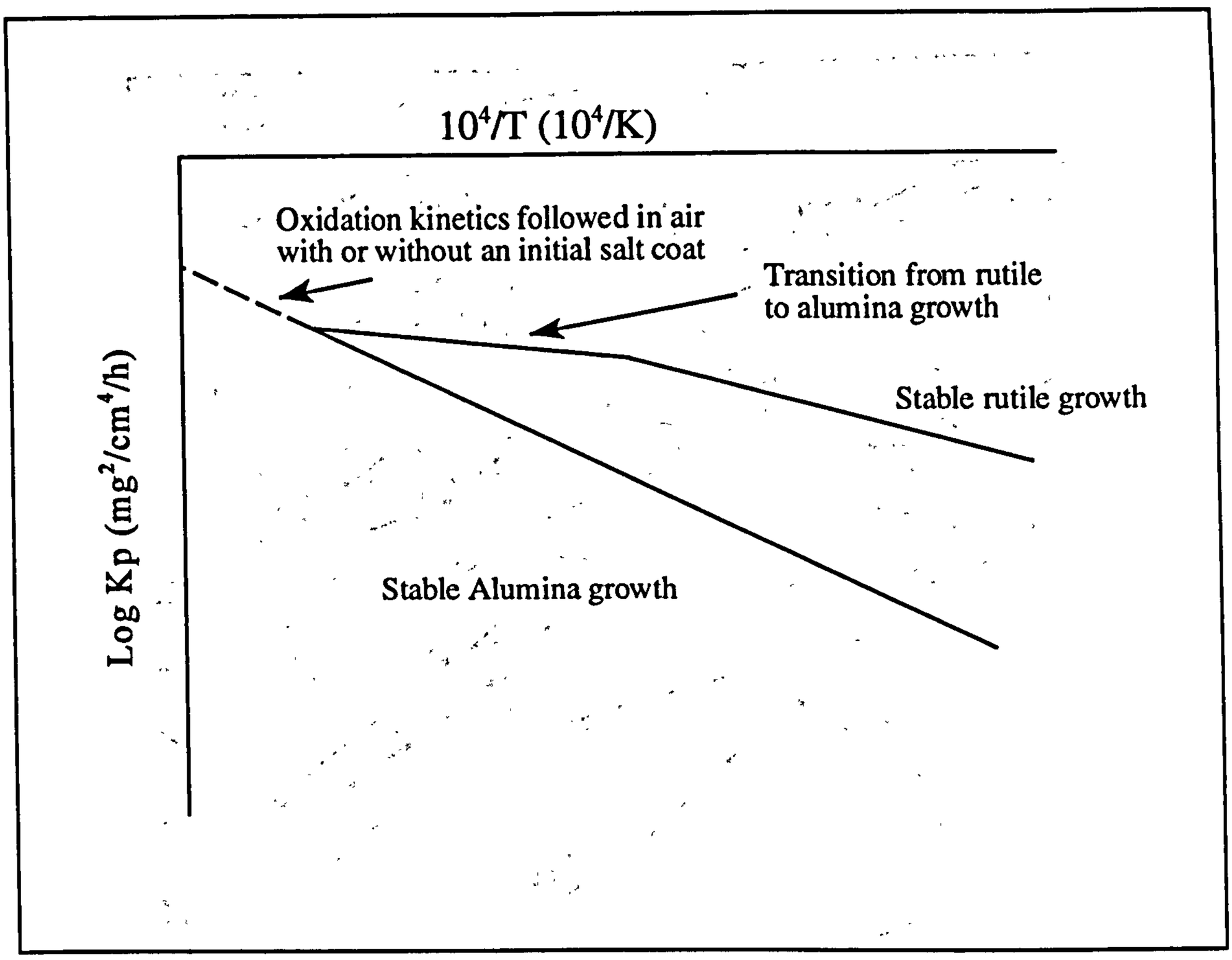

Figure 83: Schematic diagram of the Arrhenius plot in figure 82. Both the oxidation and salt corrosion kinetic behaviour are extrapolated to higher temperatures

9.3.1 Thermodynamic studies

The preceding section has shown the hot salt corrosion behaviour of Ti-45Al-2Mn-2Nb to be more complex than its oxidation or sulphidation behaviour. During the hot salt corrosion of this alloy various intermediate reactions are predicted to occur, the majority of which are undetectable in isolation. The hot salt corrosion behaviour centres around vapour phase transport mechanisms resulting in whisker growth over a predominantly rutile scale. The unstable nature of the corrosion products which are transported through the whiskers makes it difficult to predict the reactions which occur. However, it is possible to determine whether or not a reaction product is thermodynamically favourable. The Ellingham diagram in Figure 84 reviews the free energies of formation of some of the major metal chlorides, the corrosion species expected to be transported through the

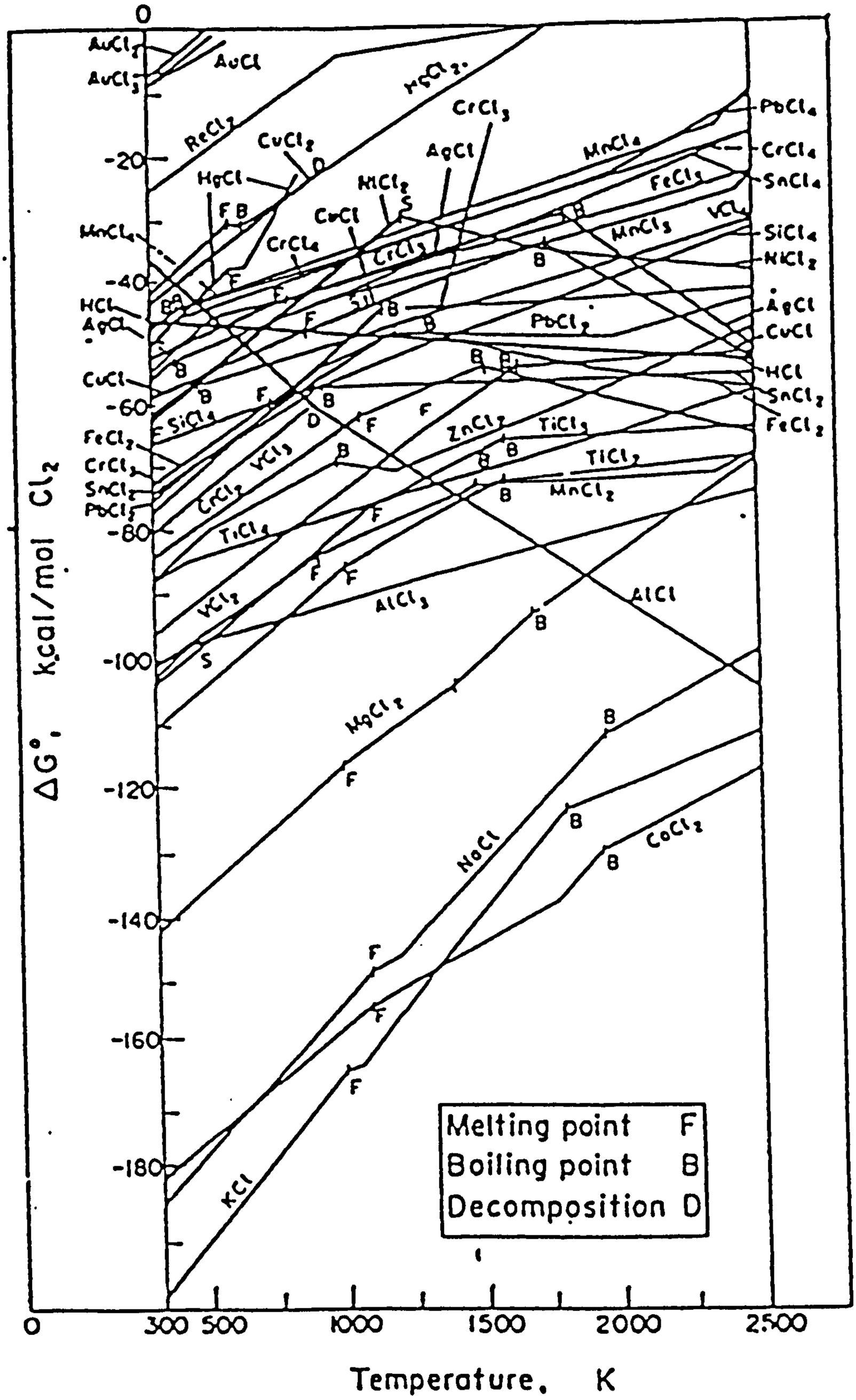

Figure 84: Ellingham diagram of the free energies of formation of the major metal chlorides.

whiskers. Up to approximately 527°C $MnCl_2$ is the most stable halide species, in this Ti/Al/Mn/Nb system, and therefore the most likely to form from a thermodynamic point of view. Above 527°C $AlCl_3$ is the more thermodynamically stable halide species, with the free energies of formation of $TiCl_2$ showing this phase to be thermodynamically less favourable. However, the differences between the free energies of formation of the halide species are not large. Ellingham diagrams assume unit activities under atmospheric pressures. More informative diagrams can be constructed if the partial pressures of chlorine and oxygen are taken into account. This enables predictions to be made as to the reactions occurring throughout the scale. The phase stability diagrams for the systems Ti-O_2-Cl_2, Al-O_2-Cl_2, and Mn-O_2-Cl_2 are described below;

Ti-O_2-Cl_2 system

Figures 85 and 88 show phase stability diagrams for the Ti-O_2-Cl_2 system at 500 and 700°C respectively. At the scale/gas interface, where Log $p(O_2)$=0, TiQ is thermodynamically the most stable phase. As the partial pressure of oxygen is reduced the stability of various titanium chlorides increases.

The PSD's thus show that titanium chlorides are unable to form at the scale/gas interface. However, the partial pressure of oxygen decreases beneath this interface, with the $p(Cl_2)$ remaining unchanged. $TiCl_2$ is expected to form at the scale/metal interface if the $p(Cl_2)$ is greater than approximately 1×10^{-25} atmospheres at 500°C and 1×10^{-19} atmospheres at 700°C. Increasing the temperature thus makes the formation of titanium chlorides less thermodynamically favourable as greater partial pressures of Cl_2 are required to form a stable species. The activity of chlorine through the scale is difficult to calculate as it is generated from the NaCl deposits. However, knowing the reaction between the oxide, salt and water to produce a titanate and HCL allows an approximation to be made, although the partial pressure of water has to be estimated.

The presence of low concentrations of salt resulted in accelerated oxidation rates with attack occurring down α2 lathes during the hot salt corrosion of the Ti-45Al-2Mn-2Nb.

Within the channels which develop the chlorine activity is expected to increase, increasing the likelihood of $TiCl_4$ forming. However, as the temperature is increased the oxides become more stable, with the range of partial pressures over which $TiCl_4$ is stable in contact with TiO_2 decreasing dramatically. The formation of titanium chloride species is thus unlikely when compared to the formation of $AlCl_3$ and $MnCl_2$, with limited vapour phase transport ensuing.

Al-O_2-Cl_2 system

Figures 86 and 89 show the phase stability diagrams for the system Al-O_2-Cl_2 at 500 and 700°C. At the scale/gas interface Al_2O_3 is the most stable phase, with the stability of $AlCl_3$ increasing through the scale towards the scale/substrate interface as the partial pressure of oxygen decreases.

Although $AlCl_3$ is only stable in relatively high activities of chlorine its stability does not decrease appreciably with increasing temperature. The activity of chlorine above which $AlCl_3$ is stable at the scale/substrate interface increases from less than 3×10^{-23} atm at 500°C to 3×10^{-20} atm at 700°C. $AlCl_3$ remains stable in contact with Al_2O_3 throughout the scale, with the possibility of vapour phase $AlCl_3$ forming within the channels which develop down α2 lathes.

Mn-O_2-Cl_2 system

Figures 87 and 90 show the phase stability diagrams for the system Mn-O_2-Cl_2 at 500 and 700°C. At 500°C MnO_2 is the most stable species, and therefore expected to form at the scale/gas interface. At 700°C Mn_2O_3 becomes the more stable oxide. The stability of $MnCl_2$, the only stable chloride species, increases as the partial pressure of oxygen decreases through the scale towards the scale/substrate interface.

At the scale/substrate interface $MnCl_2$ forms if the activity of chlorine is greater than 1.3×10^{-26} atm at 500°C and 3×10^{20} atm at 700°C. Increasing temperature decreases the

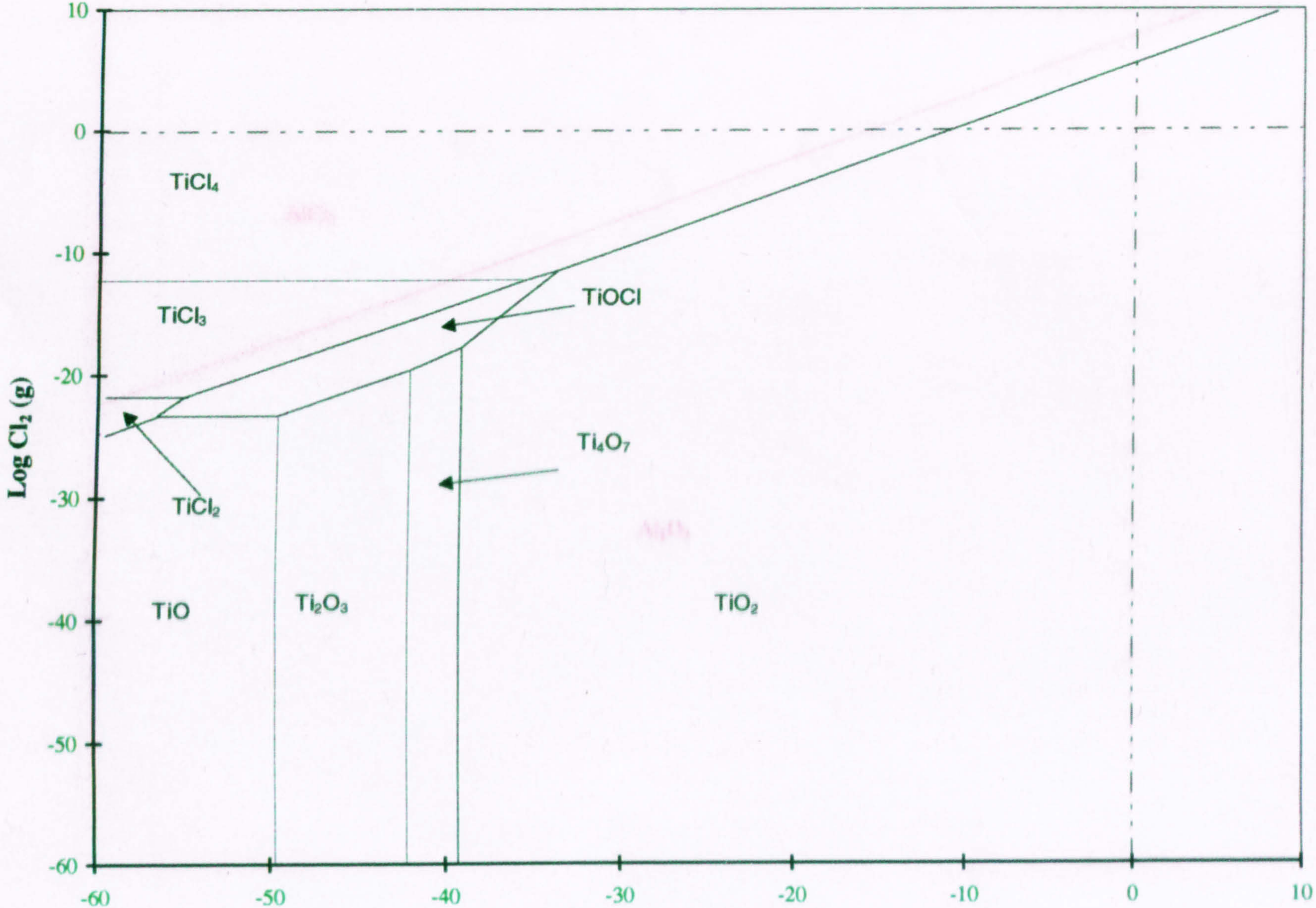

Figure 85: Ti-O_2Cl_2 PSD at 500 °C

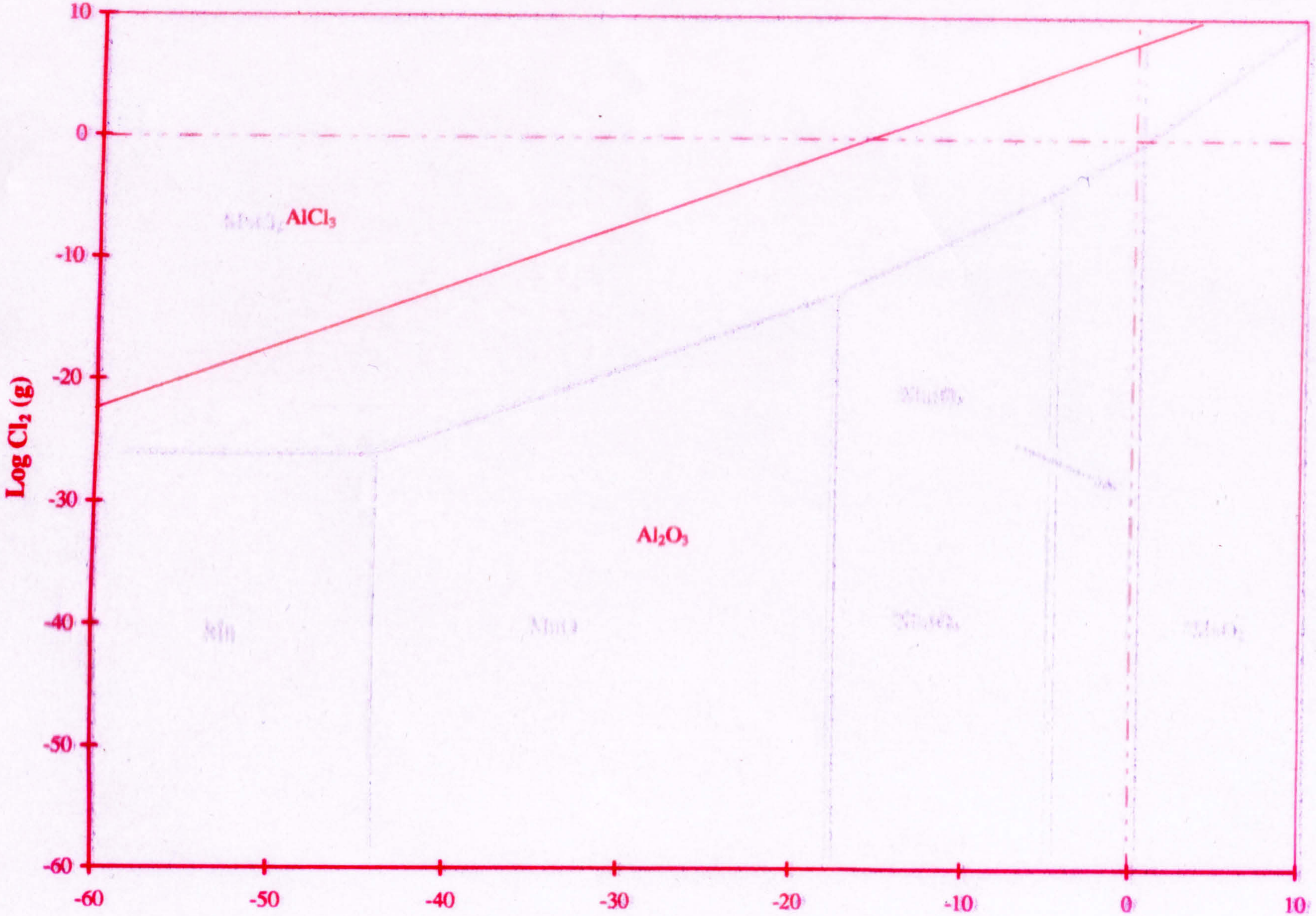

Figure 86: Al-O_2-Cl_2 PSD at 500°C

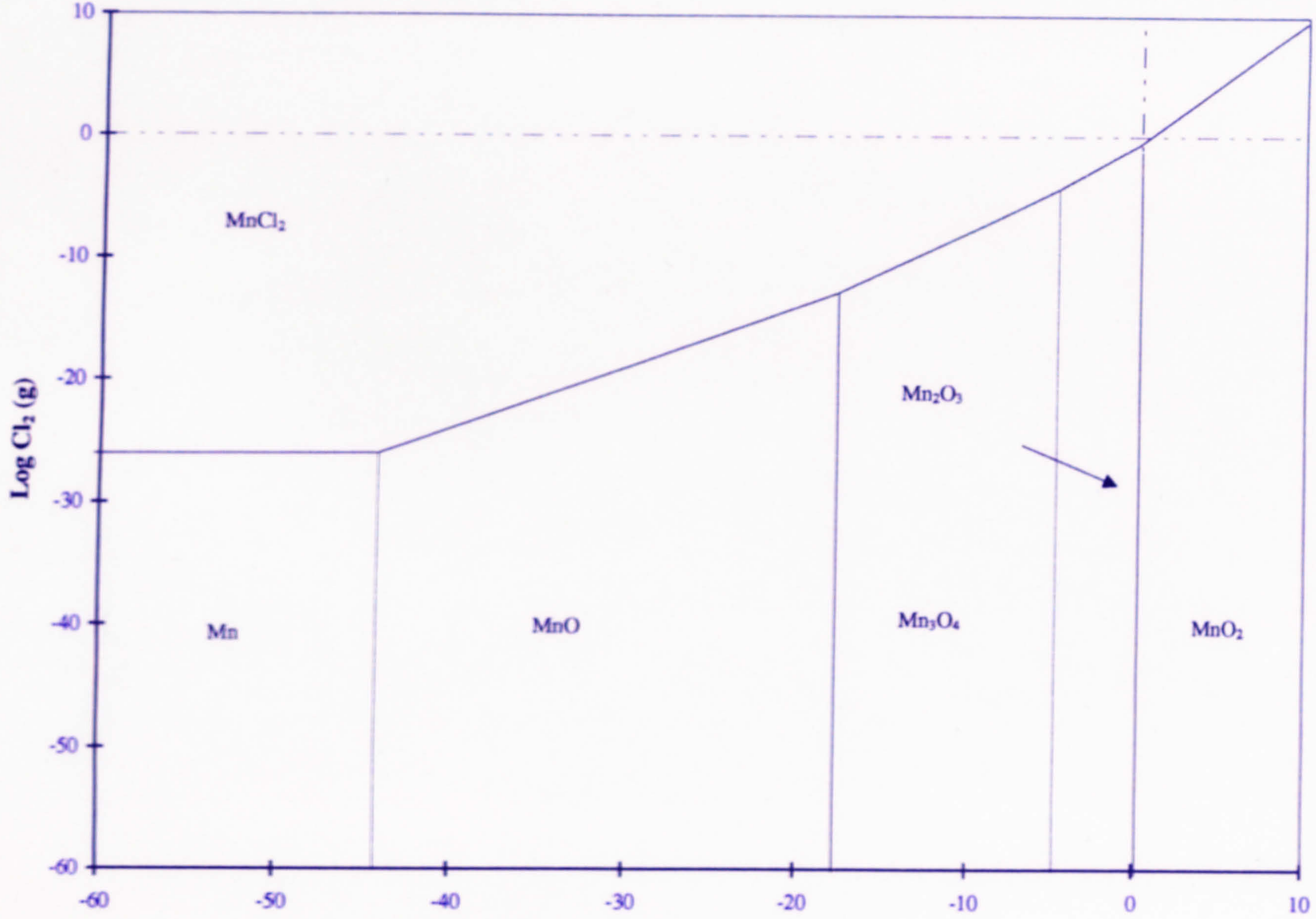

Figure 87: Mn-O_2-Cl_2 PSD at 500°C

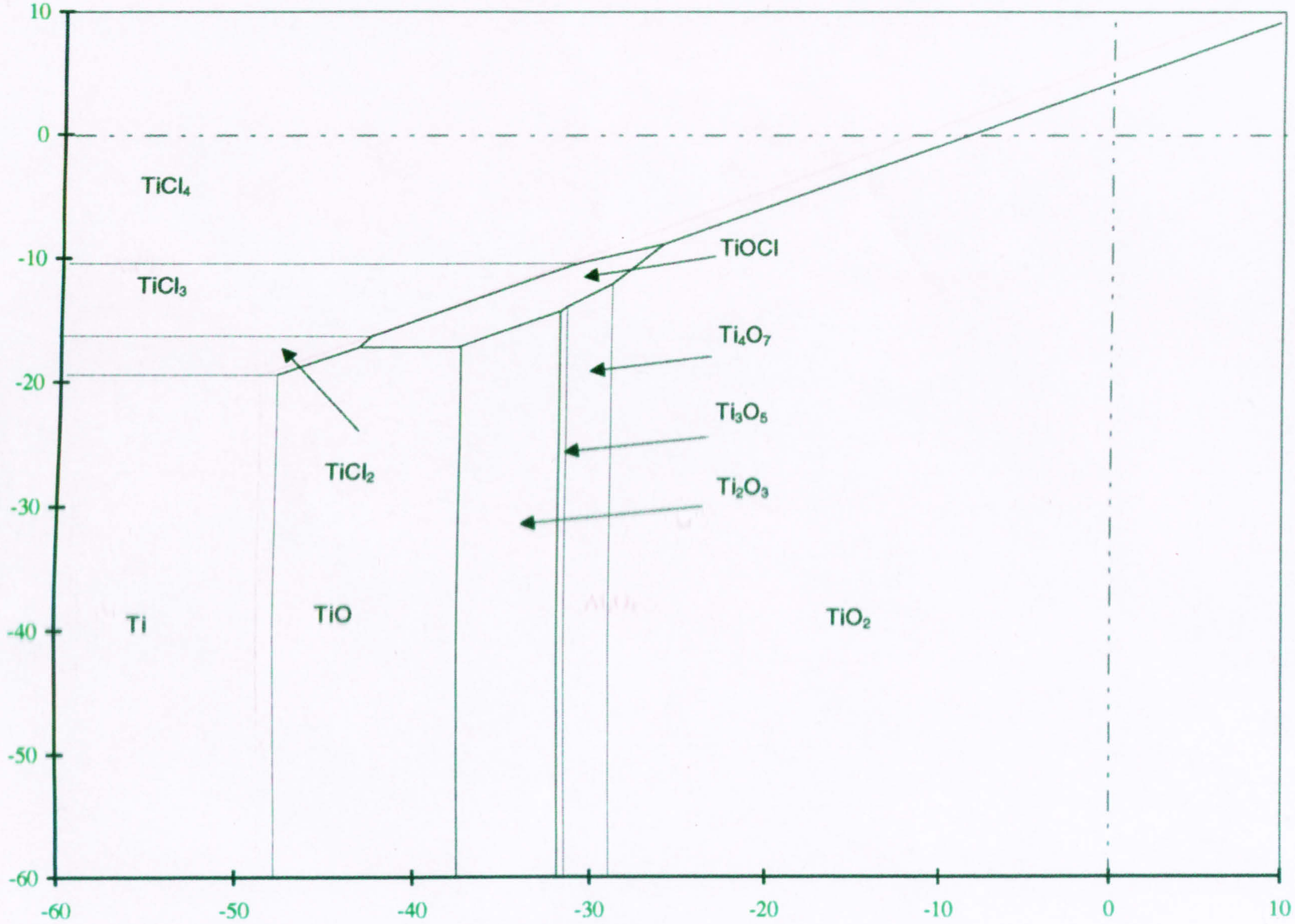

Figure 88: Ti-O_2-Cl_2 PSD at 700°C

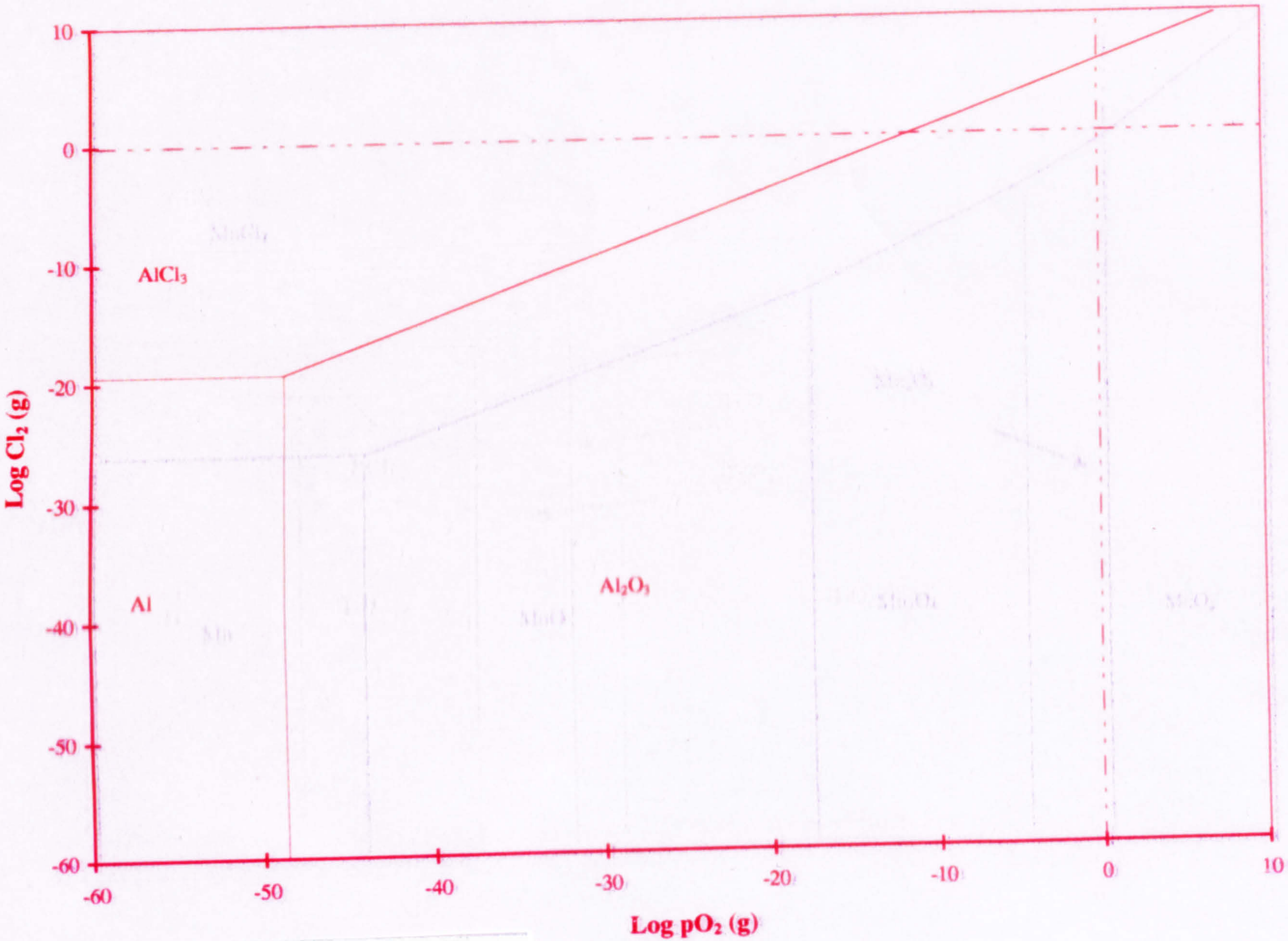

Figure 89: Al-O_2-Cl_2 PSD at 700°C

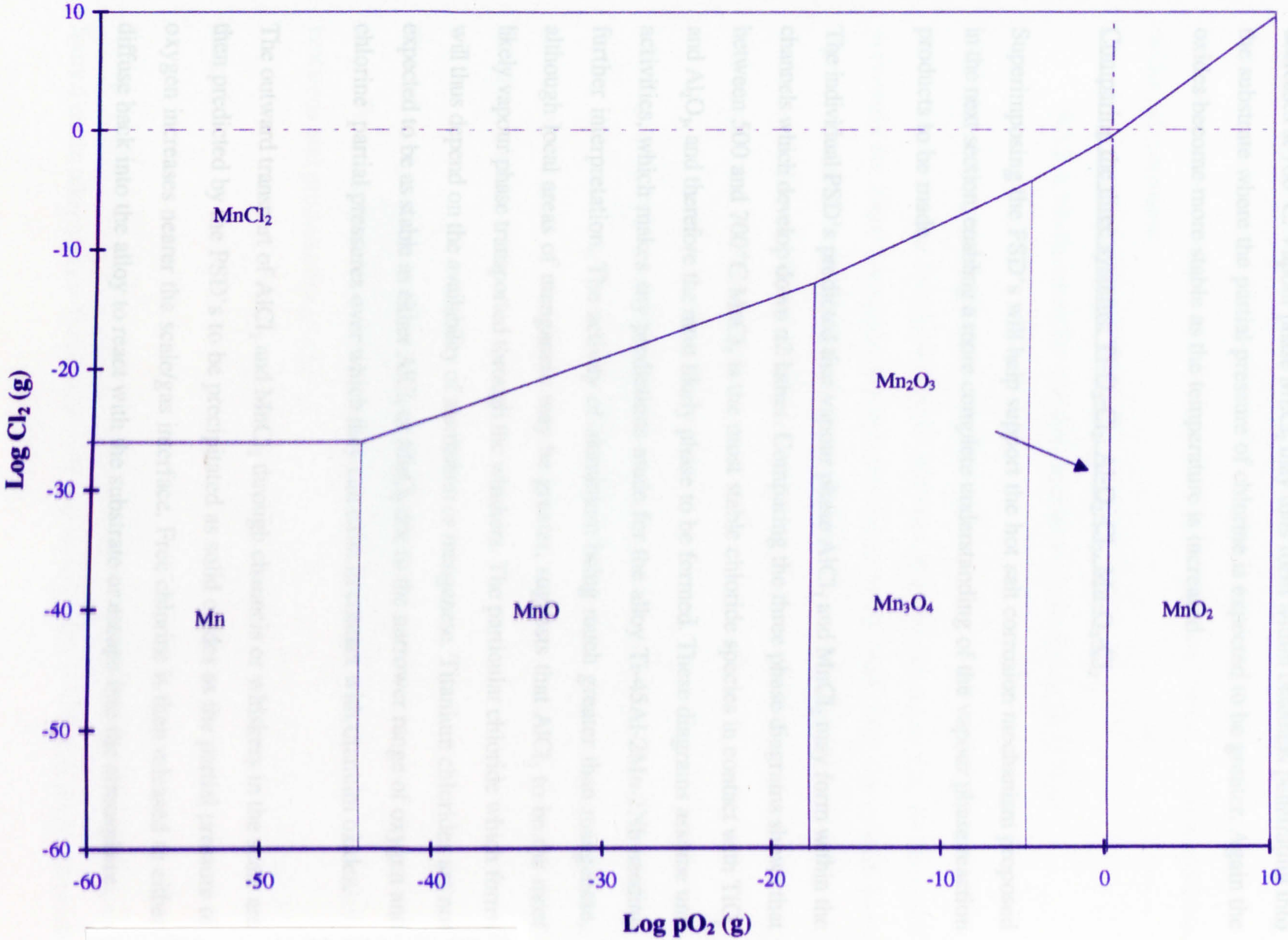

Figure 90: Mn-O_2-Cl_2 PSD at 700°C

chloride stability, with greater chlorine activities needed for this phase to form. At both temperatures the chloride is stable in contact with manganese oxides throughout the scale, however the range of oxygen and chlorine partial pressures over which this is true decreases at 700°C. Vapour phase $MnCl_2$ may thus form within channels penetrating into the substrate where the partial pressure of chlorine is expected to be greater. Again the oxides become more stable as the temperature is increased.

Comparing the three systems; Ti-O_2-Cl_2, Al-O_2-Cl_2, Mn-O_2-Cl_2

Superimposing the PSD's will help support the hot salt corrosion mechanism proposed in the next section, enabling a more complete understanding of the vapour phase reaction products to be made.

The individual PSD's predicted that vapour phase $AlCl_3$ and $MnCl_2$ may form within the channels which develop down α2 lathes. Comparing the three phase diagrams shows that between 500 and 700°C $MnCl_2$ is the most stable chloride species in contact with TiO_2 and Al_2O_3, and therefore the most likely phase to be formed. These diagrams assume unit activities, which makes any predictions made for the alloy Ti-45Al-2Mn-2Nb needing further interpretation. The activity of aluminium being much greater than manganese, although local areas of manganese may be greater, suggests that $AlCl_3$ to be the most likely vapour phase transported through the whiskers. The particular chloride which forms will thus depend on the availability of aluminium or manganese. Titanium chlorides are not expected to be as stable as either $AlCl_3$ or $MnCl_2$ due to the narrower range of oxygen and chlorine partial pressures over which they can exist in contact with titanium oxides.

The outward transport of $AlCl_3$ and $MnCl_2$ through channels or whiskers in the scale are then predicted by the PSD's to be precipitated as solid oxides as the partial pressure of oxygen increases nearer the scale/gas interface. Free chlorine is then released to either diffuse back into the alloy to react with the substrate or escape into the atmosphere.

Phase stability diagrams cannot be used on there own to predict the corrosion behaviour of this TiAl alloy accurately. Other factors such as the individual metal activities, and rates of particular reactions which again may alter the corrosion processes. The phase stability diagrams have however provided a range of possible chemical reactions resulting in the outward transport of metallic chlorides and precipitation of oxides. These diagrams have also provided insights into the susceptibility, to different extents, of alloy additions to hot salt corrosion.

9.3.2 A Mechanism for the Salt accelerated oxidation of γ-TiAl

NaCl has been shown to cause an acceleration in the initial oxidation rates. This acceleration occurred during the first 5- 10 hours of every corrosion test. As discussed previously the initial mass gains are increases by up to 20 times. This was evident from figure 78 which shows the high corrosion rates observed at 700°C. Discontinuous salt corrosion studies at 500 and 550°C had similar mass gains to those observed at 700°C under isothermal oxidation studies.

Metallographic analyses at 500 and 550°C enabled the corrosion mechanism 's operating during the initial stages of salt accelerated corrosion to be deduced. Figure 91 is a schematic diagram of the three stages of scale growth identified kinetically and metallographically.

The following sections will review the possible reactions that could occur during each stage. From the kinetic, metallographic and thermodynamic analyses, the most likely reactions and products are proposed.

<u>Stage 1</u>

During this first stage of growth the localised salt deposits react with the thin rutile scale formed on the alloy surface. Previous hot salt corrosion studies of titanium alloys showed

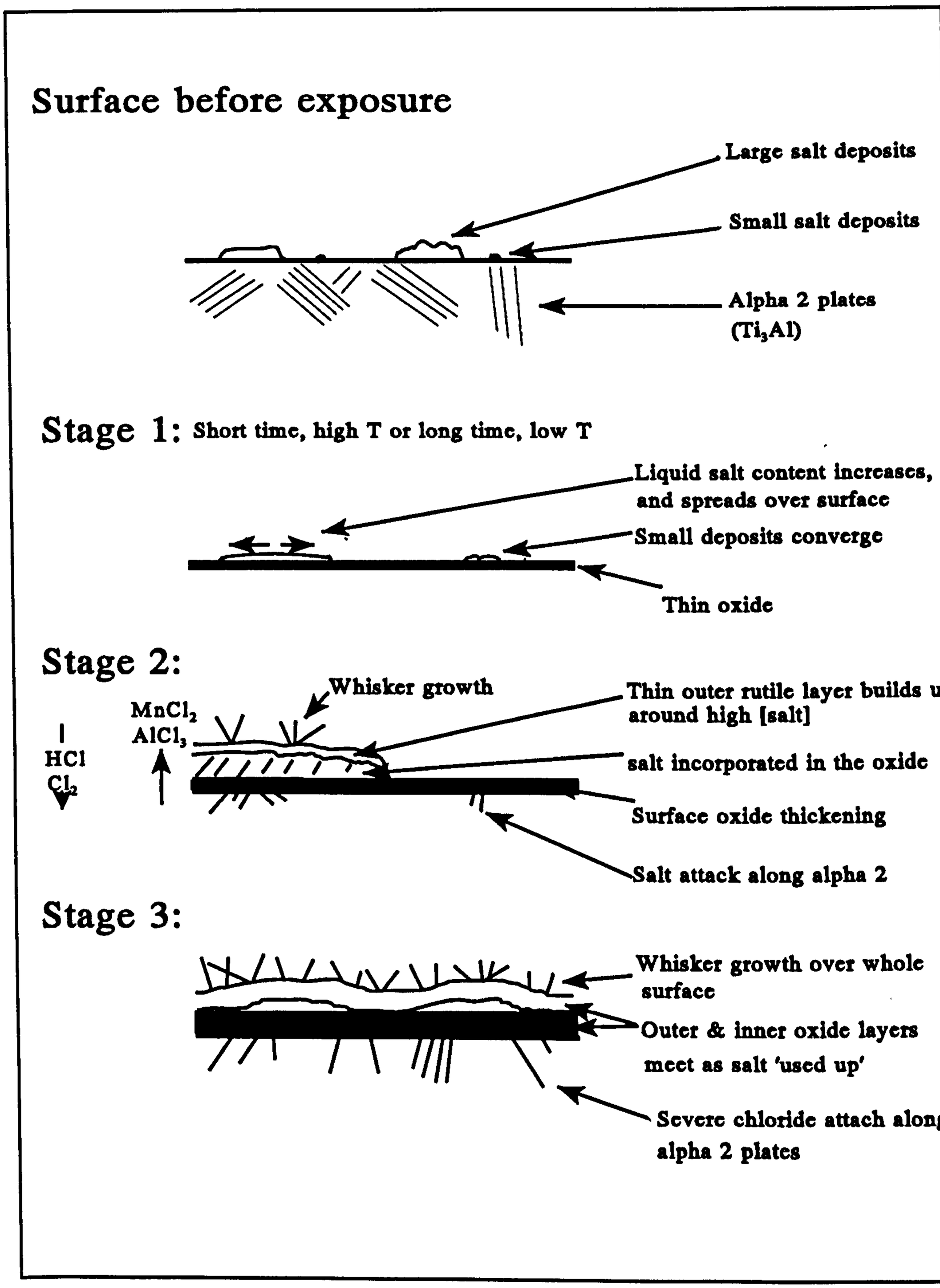

Figure 91: Hot salt corrosion mechanism for Ti-45Al-2Mn-2Nb between 500-800°C in air.

that sodium titanate[111], and sodium hydroxide[112] could be expected to form. Some of the possible reactions are given below;

$$NaCl(s) + H_2O(g) \rightleftharpoons HCl(g) + NaOH(s) \quad (9.3.2a)$$

$$2NaOH(s) + TiO_2(s) \rightleftharpoons Na_2TiO_3(s) + H_2O(g) \quad (9.3.2b)$$

$$Ti(s) + 2HCl(g) \rightleftharpoons TiCl_2(s) + 2H(Ti) \quad (9.3.2c)$$

$$Ti(s) + 2NaCl(s) + 2H_2O(g) \rightleftharpoons TiCl_2(s) + 2NaOH(s) + 2H(Ti)(s) \quad (9.3.2d)$$

$$TiCl_2(s) + O_2(g) \rightleftharpoons TiO_2(s) + Cl_2(g) \quad (9.3.2e)$$

This list is by no means exhaustive with aluminium, manganese, and niobium possible substitutes for titanium in these reactions. A thermodynamic analysis by Travkin[113] confirms that complex oxide scales are formed when titanium and its alloys react with NaCl. The formation of volatile chlorides were shown, by Travkin (reported in section 9.3.1), to be thermodynamically favourable, especially for the alloying additions Zr, Mo and Al. The subsequent pyrohydrolysis of these metal chlorides can lead to the formation of HCl gas. Previous work suggested that the major pyrohydrolysis reaction would involve $AlCl_3$, with the presence of alumina within the scales acting as a catalyst[114]. EPMA and Auger analyses of stage 1 reaction products showed that $MnCl_2$ played an equal if not greater role in these reactions.

Thus during stage 1 growth, local salt deposits react with the rutile scale and the alloy surface resulting in the production of sodium hydroxide, and sodium titanate. Al_2O_3 and MnO_2 can also be formed within the scale through the pyrohydrolysis of $AlCl_3$ and $MnCl_2$. The pyrohydrolysis of $TiCl_2$, producing TiO_2, is unlikely but may occur at areas where the concentration of aluminium and manganese are very low.

$$Ti(s) + NaCl(s) + H_2O(g) + 1/2O_2(g) \rightleftharpoons TiCl_2(s) + 2NaOH(s) \quad (9.3.2f)$$

$$TiCl_2(s) + H_2O(g) + 1/2O_2(g) \rightleftharpoons TiO_2(s) + 2HCl(g) \quad (9.3.2g)$$

$$TiO_2(s) + 2NaCl(s) + H_2O(g) \rightleftharpoons Na_2TiO_3(s) + 2HCl(g) \quad (9.3.2h)$$

and

$$2Al(s) + 6NaCl(s) + 3H_2O(g) + 3/2O_2(g) \rightleftharpoons 2AlCl_3(s) + 6NaOH(s) \quad (9.3.2i)$$

$$2AlCl_3(s) + 3H_2O(g) \rightleftharpoons Al_2O_3(s) + 6HCl(g) \quad (9.3.2j)$$

$$Al_2O_3(s) + 2NaCl(s) + H_2O(g) \rightleftharpoons Na_2Al_2O_4(s) + 2HCl(g) \quad (9.3.2k)$$

and

$$Mn(s) + 2NaCl(s) + H_2O + 1/2O_2 \rightleftharpoons MnCl_2(s) + 2NaOH(s) \quad (9.3.2l)$$

$$MnCl_2(s) + H_2O(g) + 1/2O_2(g) \rightleftharpoons MnO_2(s) + 2HCl(g) \quad (9.3.2m)$$

$$MnO_2 + 2NaCl(s) + H_2O(g) \rightleftharpoons Na_2MnO_3(s) + 2HCl \quad (9.3.2n)$$

The HCl and Cl_2 gases then diffuse through the scale and react further with the substrate. These reaction products are important as they control the rate of corrosion. The melting point of the salt is lowered through the formation of mixed chlorides. The NaCl-$AlCl_3$, NaCl-$TiCl_2$ and NaCl-$MnCl_2$ phase diagrams, in figure 81, show that low melting point eutectics are produced in each case. As the liquid content of the salt increases it spreads across the surface, increasing the area open to salt accelerated attack.

Thermogravimetric studies showed this to be a rapid process disrupting the initial oxide, with no internal oxidation occurring suggesting rapid consumption of the alloy from the surface. The corrosion rate initially increases as a result of these series of complex reactions, until the surface is completely covered in salt; where upon the corrosion rate is controlled by transport through a thickening scale.

Stage 2

Stage 2 growth is characterised by the appearance of whiskers on the oxide surface, the onset of chloride attack of the α2 lathes and the formation of a porous rutile scale at areas of high salt concentration. This stage is reached after 100 hours at 550°C, 17 hours at 600°C, and 20 minutes at 700°C.

The inward transport of HCl and Cl_2 gases, initially evolved during stage 1, is believed to occur through pores and channels in the rutile scale down to the metal/oxide interface. The halide gases are then able to react with the metal forming volatile chlorides. The three most likely reactions are shown below.

$$Ti(s) + 2HCl(g) \rightleftharpoons TiCl_2(g) + 2H(Ti) \qquad (9.3.2o)$$

$$Al(s) + 3HCl(g) \rightleftharpoons AlCl_3(g) + 3H(Ti) \qquad (9.3.2p)$$

$$Mn(s) + 2HCl(g) \rightleftharpoons MnCl_2(g) + 2H(Ti) \qquad (9.3.2q)$$

The initiation of these reactions may have resulted in a short period of breakaway kinetics as seen in the majority of cases. This may have depended on the distribution of salt and the integrity of the rutile scale. If an even distribution of salt had been deposited the rutile and substrate will have been attacked on a broad front. The result being that the halide gases will have diffused back into the alloy at roughly the same time increasing the corrosion rate at several areas over the substrate simultaneously. Stage 1 is a rapid process which leads to the formation of porous non adherent scales providing the pores and channels for these gases to diffuse down to the metal/scale interface.

The formation of $MnCl_2$ and $AlCl_3$ were shown , in section 9.3.1, to be thermodynamically more favourable. The $AlCl_3$, $TiCl_2$ and $MnCl_2$ gases formed diffuse outward through the same pores and channels, where they react within the outer part of the scale, or at the scales surface. The hydrogen byproduct diffuses away into the TiAl alloy. The preferential attack of the $\alpha 2$ phase had previously been identified in other high aluminium containing titanium alloys.[111]

Examples of the reoxidation reactions of the metal halides at or near the scale/gas interface are shown below.

$$TiCl_2(g) + O_2(g) \rightleftharpoons TiO_2(s) + Cl_2(g) \qquad (9.3.2r)$$

$$AlCl_3(g) + 3H_2O(g) \rightleftharpoons Al_2O_3(s) + 6HCl(g) \qquad (9.3.2s)$$

Halide gases are thus regenerated and are able to diffuse back down the existing pores and channels where they react again with the substrate. A counter flux is created with the HCl and Cl_2 gases diffusing inwards and the volatile $AlCl_3$, $TiCl_2$ and $MnCl_2$ diffusing outwards through these pores and channels. A self sustaining system is set up requiring only small quantities of chloride phases to be present.

The vapour phase transport mechanism described above explains the growth of whiskers at the scales surface. The volatile $TiCl_2$, $AlCl_3$ and $MnCl_2$ species, formed within the scale or at the metal/oxide interface, diffuse through the available short circuit diffusion paths. They are then rapidly reoxidised at the top of these channels forming hollow whiskers, producing further HCl.

Aluminium can also be transported through the porous oxide scales that are formed, resulting in a fine dispersion of alumina throughout the rutile. The discontinuous alumina layer means that no alumina barrier is able to form giving rise to the fast corrosion rates observed. Manganese rich areas were established near the scale/gas interface and within the whiskers suggesting manganese has also been attacked by the halide gases and transported out through a combination of pores and channels in the rutile scale. Preferential attack of the $\alpha 2$ lathes was evident, photograph 8.2.4dd and resulted in channels penetrating for example 40-50μm into the substrate at 700°C.

The near logarithmic kinetics operating during stage 2 highlight the competition between parabolic oxide growth and short circuit diffusion down preferred channels. The short circuit diffusion paths account for the early rapid corrosion rates. A transition to parabolic kinetics occurs at a later stage believed to be due to the closure of these short circuit channels and marking the onset of the third stage of scale growth.

Stage 3

Stage 3 is characterised by a profusion of surface whiskers, severe internal substrate attack and thick two layered scales. Photographs 8.2.4aa and 8.2.4cc show this form of

attack. Parabolic growth rates suggest the corrosion mechanism to be dominated by diffusion through the scale. The surface whiskers were shown to coarsen during this stage (photographs 8.2.4d to 8.2.4h) providing evidence to suggest the short circuit diffusion paths had closed. The increased path length ($\alpha 2$ lathe depth of attack + scale thickness + whisker length) may also account for the corrosion behaviour now being diffusion controlled as the short circuit flux may now match that transported through the scale.

The transition to Stage 3 may also be the result of a breakdown in the self sustaining vapour phase transport mechanism. Very little salt remained between the inner and outer rutile layers that formed (photograph 8.2.4cc) which suggests that the vapour halide species which contributed to stage 2 growth were lost to the environment. A continuous supply of salt is more likely in the applications proposed for this alloy and would be expected to extend the duration of stage 2.

The next section discusses the effect of initial salt level knowing the mechanisms by which salt accelerates the oxidation rate of Ti-45Al-2Mn-2Nb. Several unanswered questions provided the need for a study into this area.

1. What effect would increasing the initial salt concentration have on the final mass gains?

2. Is there a level of salt concentration above which the final mass gains are no longer affected by change in salt concentration?

The final section addresses the problem of salt recoating. At the same time thermal cycling was introduced (a necessity for the salt recoat procedure). Careful consideration was given to the recoat times, with the stage of salt corrosion in mind. The answers to the questions here will give an indication to the potential problems that small amounts of salt will have on the integrity of this material once in service.

1. Will stage 2 continue indefinitely if salt is continuously redeposited?

2. Knowing that poor adhesion exists at the scale/metal interface for salt coated samples, will spallation occur during the cooling down period that is necessary before recoating?

3. Will increasing the salt level during recoating change the salt recoating behaviour in any way?

4. What differences exist kinetically and metallographically between the recoated and single coated specimens? Attention must also be given to any differences that might exist between the specimens thermally cycled but not recoated to those which were previously isothermally hot salt corroded.

9.3.3 Effect of salt concentration

A mechanism for the hot salt accelerated oxidation of Ti-45Al-2Mn-2Nb was proposed in the last section. The thermogravimetric study was based on salt levels within the range of 0.02-0.05mg/cm^2. Hancock[115] calculated that for salt levels of 0.6ppm, ingested into marinised gas turbines, the contaminant flux is expected to be 350μg/cm^2/h. If only 10% of the ingested salt deposited and the atmospheric aerosol through which the aircraft flies is 0.006ppm[116], then salt deposition rates of 0.35μg/cm^2/h could be expected. Hence, the deposition rates of approximately 30-40μg/cm^2 per 100 hours used in the previous mechanistic study are not unrealistic.

Titanium alloys are known to be susceptible to hot salt corrosion. This was identified as early as 1950. Bauer[117] attributed a reduction in creep life to severe surface cracking originating from salt found in fingerprints on the materials surface. These observations lead to a lot of research into the hot salt corrosion behaviour of titanium alloys. Ashbrook [118] carried out field tests to determine the actual salt deposited onto compressor components, during engine overhaul. Assuming that engine overhauls occur every 500

hours then the average salt concentration of 155μg/cm^2 deposited is consistent with the above salt deposition calculations.

Thus, the salt levels used in the previous mechanistic study are consistent with the salt deposition rates observed in civil aircraft flying along coastal routes. The general conclusion from the mechanistic study being that at the perceived service temperature of 700°C Ti-45Al-2Mn-2Nb would suffer severe substrate attack, with preferential corrosion, of up to 50μm, down α2 lathes.

Figure 48 in section 8.2.4.1 shows that an asymptotic relationship exists between the level of salt deposited and mass gain at 700°C. The scatter observed can be attributed to the inconsistent deposition method used to salt the specimens. Initially small increases in the amount deposited resulted in appreciable increases in mass gain after 100 hours. Above a level of approximately 0.125mg/cm^2 the mass gains plateau with no further increases in mass gain occurring. This plateau represents an increase of approximately 2.5 to 3.5 times the mass gains observed when salt levels within the range 0.02-0.05mg/cm^2 were deposited.

The increase in mass gain with salt level can be explained from the hot salt corrosion mechanism of Ti-45Al-2Mn-2Nb. Severe corrosion occurs beneath individual salt beads which then spread across the substrate. As greater salt concentrations are deposited it can be assumed that a greater number of these salt beads exist. Hence, the substrate will be attacked at a greater number of initial sites. The transition to stage 2 and the development of whiskers should not be effected as no matter the salt level the breakdown of the surface oxide and substrate attack occur after a finite time. However, a consequence of higher initial salt levels is the greater amount of chloride that is available. The transition to stage 3 was effected by the loss of chloride species to the atmosphere. If more chlorine is present the vapour phase transport mechanism may continue to dominate for longer periods of time. Hence greater mass gains would be expected during this stage before the transition to slower parabolic kinetics.

Hot salt corrosion proceeds preferentially at sites of high salt concentrations spreading across the surface until they meet. This sets one constraint in that when no more sites are available for chloride attack a limit is put on the corrosion rate. Over 100 hours halides are gradually lost to the atmosphere as Cl_2 or HCL gas. Time is therefore another constraint with an upper limit on the corrosion rate existing. Hence, mass gain is dependent on available surface area for attack and corrosion time.

9.3.4 Effect of salt recoating

This section attempts to provide some insight into the corrosion behaviour of Ti-45Al-2Mn-2Nb when successive salt coats are deposited. This will also introduce a degree of thermal cycling. The mechanistic study looked into the behaviour of Ti-45Al-2Mn-2Nb in the presence of a single salt deposition before each exposure. Salt recoating studies were inappropriate whilst investigating the mechanistic aspects of salt corrosion as they would have provided conflicting observations which may have resulted in incorrect interpretations being made.

The most likely service temperature, at which Ti-45Al-2Mn-2Nb components will operate, appears to be at around 700°C. The greatest corrosion rates were observed at this temperature making a salt recoat investigation at 700°C even more relevant.

The understanding gained during the mechanistic studies was used to plan the salt recoat experiments. In depth recoat experiments over the whole temperature range were deemed unnecessary as the corrosion mechanism was shown to be controlled by salt coverage and corrosion time. Which means that salt recoating, below 700°C, will increase the overall mass gains but not the rate of substrate attack at localised areas. The individual recoat experiments are outlined below with the reasons for the recoat times explained.

- A specimen was salt coated after 0, 2, 5, 10 and 15 hours and removed after 20 hours. These recoat times lie within stage 2 whisker growth. This study evaluated whether or not initial whisker growth was effected.

- A specimen was coated after 0, 20, 40, 60, and 80 hours and removed after 100 hours. These recoat times constitute the upper limits of stage 2 whisker growth. The point of interest being whether or not stage ½ growth kinetics carried on.

- A specimen was salt coated after 0, 100, 120 and 150 hours and removed after 200 hours. This experiment was repeated due to severe scale spallation during the first 200 hour experiment. The salt recoats were deposited knowing that after 100 hours the rate of corrosion would have been diffusion controlled. In this case it was important to determine whether or not resupplying the surface with salt increased the corrosion rates.

Figure 49 in section 8.2.4.2 shows the effect of salt recoating after 0, 2, 5, 10, and 15 hours at 700°C in air. Recoating after 2 and 5 hours increased the accelerated oxidation rates usually observed during the early stages of hot salt corrosion. The corrosion rates remained unaffected after the 10 and 15 hour recoats.

Detailed metallographic analyses compared the characteristic features of the singly salt coated specimen with the salt recoated specimen after 20 hours at 700°C. The following critical points were noted.

- Very little spallation occurred during or between exposure of the salt recoated specimen. The integrity of the salt recoated oxide scale appeared better than the singly coated specimen.

- Salt recoating affected the surface features characteristic of isothermal salt corrosion. Photograph 8.2.4.2u shows the coexistence of short and long whiskers. The second and third salt recoats caused an increase in accelerated corrosion rates, with salt having been deposited at areas with very little or no salt. Hence, the substrate was attacked over a wider area during a much shorter period of time. The accompanying EPMA shows that higher than usual manganese levels were

identified within the whiskers. One possibility for this could be that the formation of $MnCl_2$ is favoured at higher salt concentrations as it appears to form alongside $AlCl_3$ as a solid-liquid salt mixture at low temperatures. The MCl-NaCl phase diagrams in figure 81 show this. At higher temperatures these corrosion products would be expected to volatilise and as discussed previously in section 9.3.2, sustain a flux of MCl out and chlorides inwards through pores and channels leading to the formation of whiskers.

Thermal cycling of the specimen coated only once resulted in a decrease in whisker coverage. The interlocking rutile nodules in photograph 9.2.4.2b resemble those seen after 100 hours at 600°C (photograph 9.2.4b).

- Recoating accelerated the development of a two layered oxide scale. Photograph 8.2.4.2c shows the scale formed after recoating at 700°C. In comparison photograph 8.2.4.2d, for the specimen coated once, shows much thinner rutile scales which were often removed during metallographic preparation. Recoating increased the degree of substrate attack, with preferential attack down the $\alpha 2$ lathes to a depth of ~20μm.

Increasing the time interval between successive recoats changed the salt corrosion behaviour in an unexpected way. Continuously supplying salt to the surface was expected to maintain accelerated oxidation rates with stage 2 whisker growth continuing indefinitely. However, when salt levels within the range of [0.03-0.06mg/cm^2] were applied every 20 hours at 700°C no substantial increases in mass gain were seen. In figure 50 in section 8.2.4.2 the recoated specimen behaved in almost an identical manner to the specimen coated only once. Thus the majority of corrosion occurred within the first 20 hours. The corrosion rates then continued at near parabolic growth rates.

Applying higher salt levels, within the range of [0.16-0.26mg/cm^2] at 700°C, resulted in similar growth kinetics. Higher initial mass gains were observed as predicted from the salt

level studies in section 8.2.4.1. Again the recoat and single coat salted specimens behaved in a similar kinetic manner. The resalted specimen continued at a slightly higher corrosion rate after the first 20 hour recoat but then followed identical growth kinetics to the singly coated specimen. Increasing the salt level deposited did not increase the mass gain beyond the plateau level, determined in section 8.2.4.1, of between 3 and 3.5 mg/cm^2 even after recoating. An explanation for this will be given after the metallographic studies have been discussed.

The critical points made from metallographic studies of the intermediate salt recoat investigations are again outlined and discussed below.

- In both sets of experiments involving high and low salt recoating very little spallation was observed during cooling and reheating. The scales remained brittle and often buckled during cooling. This may explain the slightly increased corrosion rates which occurred after the first recoat during the high salt concentration experiment. Cracks may have opened up allowing salt access to the substrate.

- Whiskers were observed after 100 hour isothermal exposure at 700°C. Removing the specimen every 20 hours changed the surface morphology. Photographs 8.2.4.2f and 8.2.4.2h, of the specimens initially coated by low and high salt concentrations respectively, show whisker growth to have been drastically reduced when compared with the recoated specimens. Rutile nodules dominate with very fine whisker coverage. Recoating maintained whisker growth with photographs 8.2.4.2e and 8.2.4.2g, after low and high salt recoating, showing areas where whiskers obscured the rutile beneath. Distinct differences existed between the high and low salt recoat whisker morphologies. High salt recoating resulted in a wider range of whisker sizes and distribution suggesting the vapour phase transport mechanism, described in section 9.3.1, to be more active. This could also be accounted for through salt depositions reactivating this mechanism at sites of no

previous salt deposits, resulting in the initiation of hot salt corrosion at different start times.

- Severe substrate degradation occurred in all cases after 100 hours at 700°C. However, photograph 8.2.4.2m, of a specimen recoated with low salt concentrations, shows that the substrate was corroded over a wider front with less preferential α2 attack. The resulting scale was thicker than the singly coated specimen, photograph 8.2.4.2n, with a much higher degree of porosity at the scale/substrate interface.

The final salt recoat investigation looked at the effect of recoating during the third salt corrosion stage. Salt was redeposited after 100, 120, and 150 hours. Figure 51 in section 8.2.4.2 shows the discontinuous mass gains obtained out to 200 hours. In this case severe spallation resulted in salt depositing upon unprotected substrate. However, the increased corrosion rate was not maintained suggesting that the scale rehealed itself by forming a continuous rutile layer. Again though the maximum mass gains obtained during salt corrosion of approximately 3-3.5 mg/cm^2 were not exceeded. The investigation was repeated to determine if spalling was an inherent problem during cooling beyond 100 hour exposures. Figure 52 in section 8.2.4.2 shows the resulting mass gain curve. In this instance the recoated specimen did not spall on cooling and no marked increases in corrosion occurred. The specimen coated only once showed greater mass gains which were related to the higher salt level deposited.

The critical points made from the metallographic investigations are detailed below.

- Spallation directly affected the degree of corrosion, although the scale eventually reheals and acts as a barrier between the salt and substrate.

- Whisker growth was maintained after 200 hours at 700°C in the cases where salt was redeposited. However, as seen in photograph 8.2.4.2k of the unspalled specimen, coarser whiskers existed similar to those seen after 100 hours at 750°C (photograph 8.2.4g). The singly coated specimen behaved differently in that the

specimen removed with the recoated specimen which spalled was virtually whisker free (photograph 8.2.4.2j). While coarse whiskers were identified on the specimen removed alongside the unspalled recoat specimen (photograph 8.2.4.2l). The distribution of salt developed during the initial salt deposition determines the vapour phase transport behaviour during the subsequent thermal cycles. Even distributions of salt are more likely to result in prolonged whisker growth due to thinner scales being developed and lower scale stresses. The build up of thick scales due to spallation and uneven salt depositions effectively stops the vapour phase transport mechanism.

- The depth of substrate attack after 200 hours at 700°C was similar to that after 100 hours at 700°, although scale thicknesses had increased. In the salt recoat instances, after 200 hours, marked differences existed between the spalled and unspalled specimens. The 200 hour spalled recoat specimen suffered from attack over a broader front, photograph 8.2.4.2q, with seemingly less preferential $\alpha 2$ attack. Photograph 8.2.4.2s of the recoated specimen which did not spall shows the classic $\alpha 2$ attack below a two layered rutile scale seen after isothermal hot salt corrosion of this alloy.

The preceding sections have shown that very small concentrations of salt result in severe substrate attack, especially down $\alpha 2$ lathes. The majority of attack was shown to occur within the first 10-20 hours with a self sustaining vapour phase transport mechanism operating. Salt recoating showed that the rate of corrosion was only increased if spallation occurred allowing salt contact with the substrate. Thermal cycling caused the pores and channels, through which the vapour metal chlorides and chlorides maintained a flux, to close. The initial distribution of salt was important as it determined the likelihood of spallation during thermal cycling. Uneven distributions result in non uniform scale thicknesses and therefore higher scale stresses.

9.4 Hot Corrosion

No in depth studies have as yet been made characterising the hot corrosion behaviour of Ti-45Al-2Mn-2Nb or in fact any titanium alloys, coated with low concentrations of salt and exposed to atmospheres composed of air plus low partial pressures of SO_2. All previous hot corrosion studies have centered around Ni and Co based superalloys. These alloys have been extensively studied by previous authors. However, these studies showed a high degree of variation in kinetic and mechanistic behaviour. General hot corrosion mechanisms for these alloys depended on alloy composition, temperature range, salt and gaseous composition.

Not knowing the hot corrosion mechanism most likely to operate influenced the nature of the experimental study. The hot corrosion mechanisms were determined over the most likely service temperature range of 650-800°C. Similar salt levels were deposited as in the case of the hot salt corrosion investigations. The same range of SO_2 partial pressures, used in the sulphidation tests, were also incorporated into the hot corrosion studies. Getting to the stage of being able to interpret the hot corrosion results required a thorough understanding of the individual effects of salt and SO_2. It was important to avoid introducing new variables into the experiments not considered in the previous investigations.

The hot corrosion behaviour of Ti-45Al-2Mn-2Nb, between 650-800°C, in an atmosphere containing air plus low partial pressures of SO_2 (within the range of ~10^{-4} atmospheres) is shown in figure 53, in section 8.2.5. The combination of solid NaCl deposits and SO_2 containing atmospheres resulted in severe alloy degradation, with a substantial degree of spallation occurring during cooling to room temperature especially for the thicker scales. Porous oxide scales were developed at rapid growth rates. The individual effects of NaCl and SO_2 were also evident. The hot corrosion behaviour of Ni and Co based alloys coated with Na_2SO_4 salts is characterised by an incubation period during which very slow initial corrosion rates were observed. Ti-45Al-2Mn-2Nb behaved differently in that no such initial period existed over the whole temperature range tested. This is thought to be due

to the presence of NaCl in the deposits. Instead rapid rates of attack occurred almost immediately. The effects of SO_2 became more obvious with exposure time and temperature . Sulphide layers developed at the scale/substrate interface, eventually leading to breakaway type kinetics.

The kinetic behaviour of Ti-45Al-2Mn-2Nb is related to time and temperature with logarithmic type kinetics initially dominating, similar to that observed for NaCl alone. After extended corrosion or at higher temperatures parabolic kinetics operated for brief periods of time before linear or breakaway kinetics dominated. Once breakaway kinetics developed large mass gains resulted.

Figures 92 to 95 compare the high temperature corrosion behaviour of Ti-45Al-2Mn-2Nb between 650 and 800°C in the four environments studied. Such comparisons provide insights into the kinetic behaviour of Ti-45Al-2Mn-2Nb in hot corrosion environments.

At 650°C the high initial hot corrosion rates resulted in the majority of the mass gain being developed after the first 10 hours (figure 92). In the absence of SO_2 high initial corrosion rates were also observed, however the specimen then continued to corrode at parabolic growth rates. Thus salt appears to accelerate the oxidation behaviour of Ti-45Al-2Mn-2Nb. The combination of salt and SO_2 resulted in ~ a 50% increase in mass gain after 10 hours when compared with the specimen exposed to salt just in air. The mass gain plot exhibits a plateau and little further corrosion after 10 hours, out to 100 hours. This implies that the mechanism of corrosion during the first 10 hours caused the ensuing scale to become more protective against further attack, when compared to the behaviour in air plus NaCl alone.

The kinetic behaviour of a material gives an indication of the nature of the scale being developed. Figure 93 compares the corrosion behaviour of Ti-45Al-2Mn-Nb in four different environments after 100 hours at 700°C. This appears, at present, to represent the most likely service temperature for this material. Good oxidation and sulphidation resistance were accompanied by low corrosion rates. However, low levels of salt

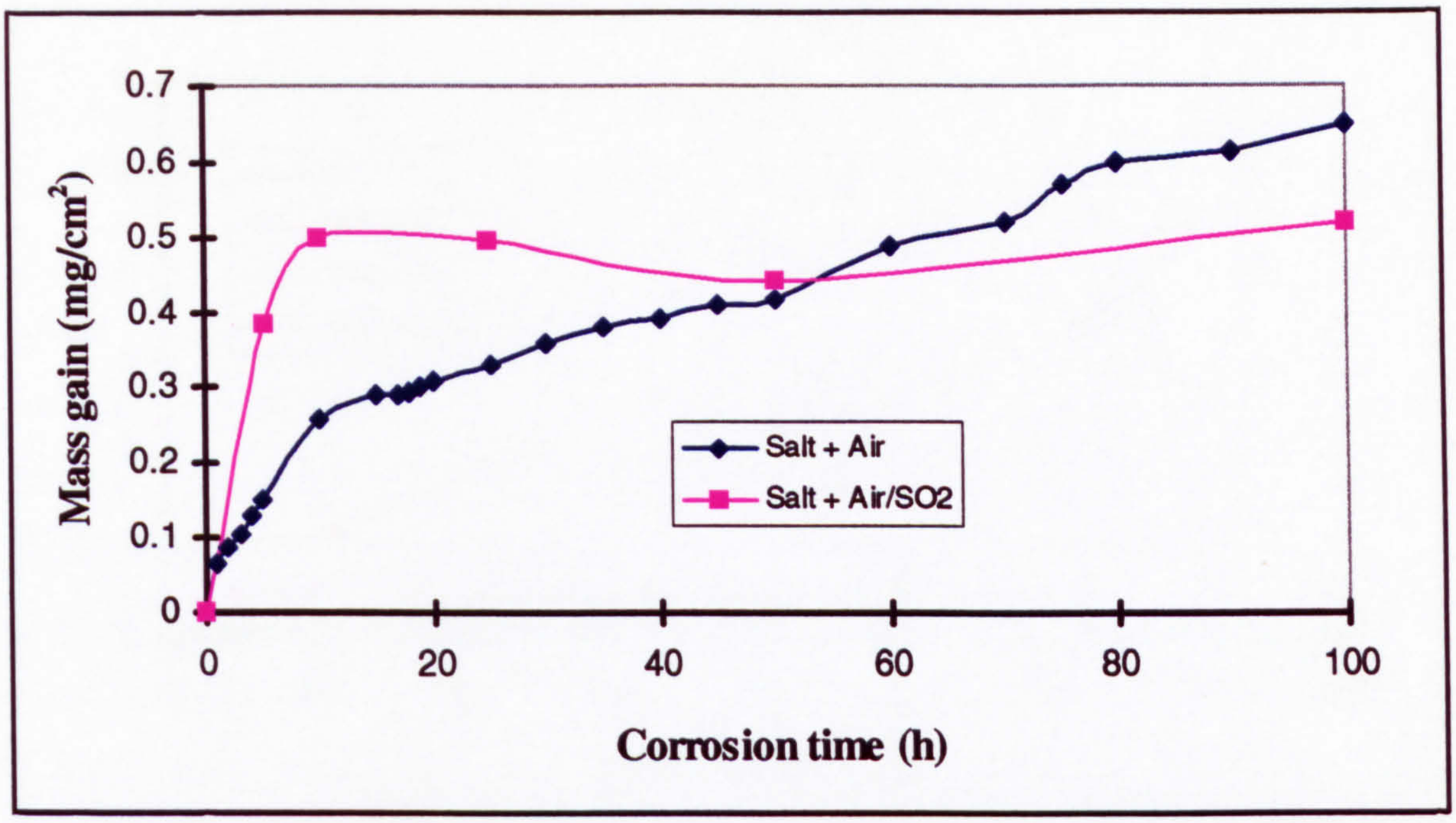

Figure 92: Environmental behaviour of Ti-45Al-2Mn-2Nb after 100h at 650°C

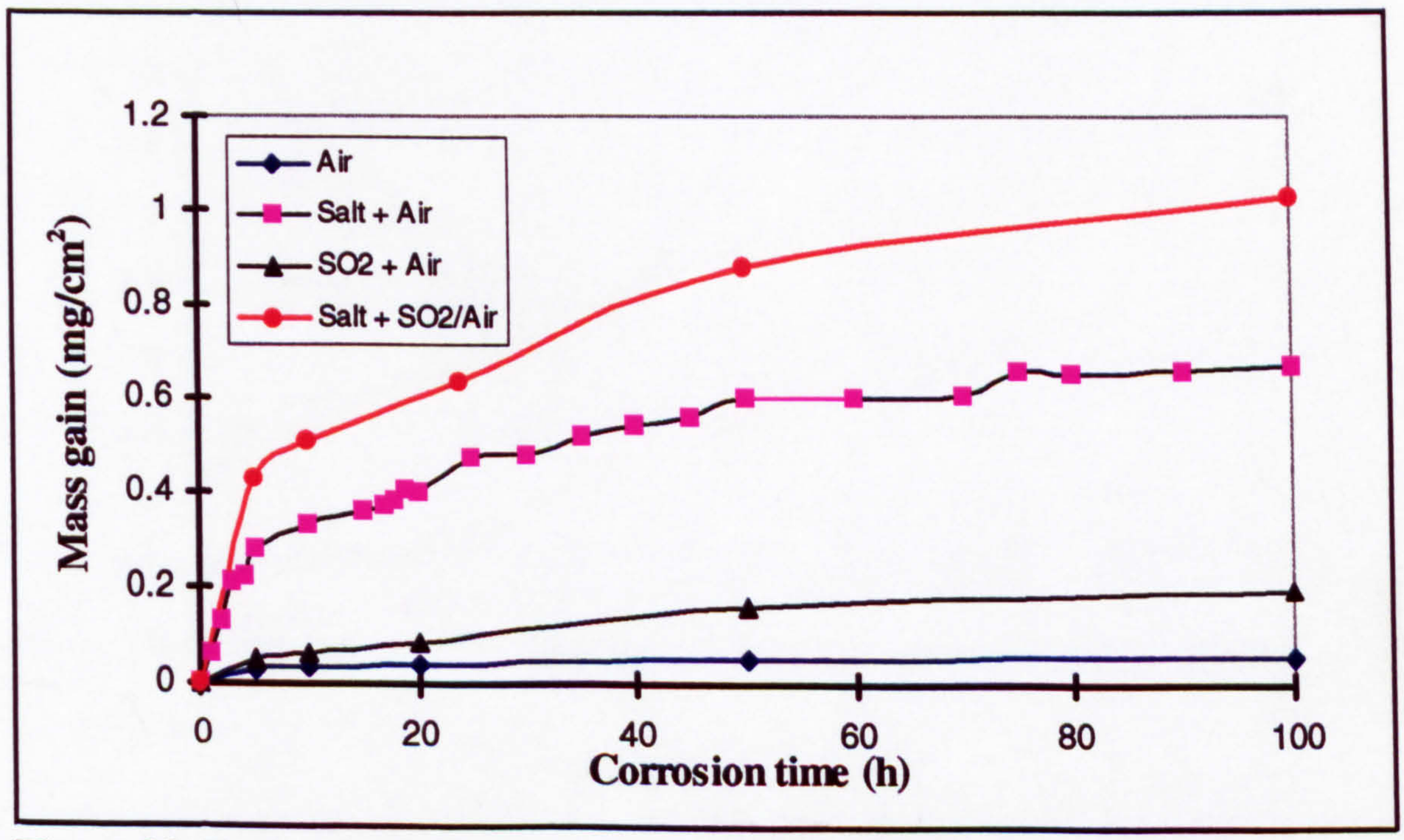

Figure 93: Environmental behaviour of Ti45Al-2Mn-2Nb after 100h at 700°C

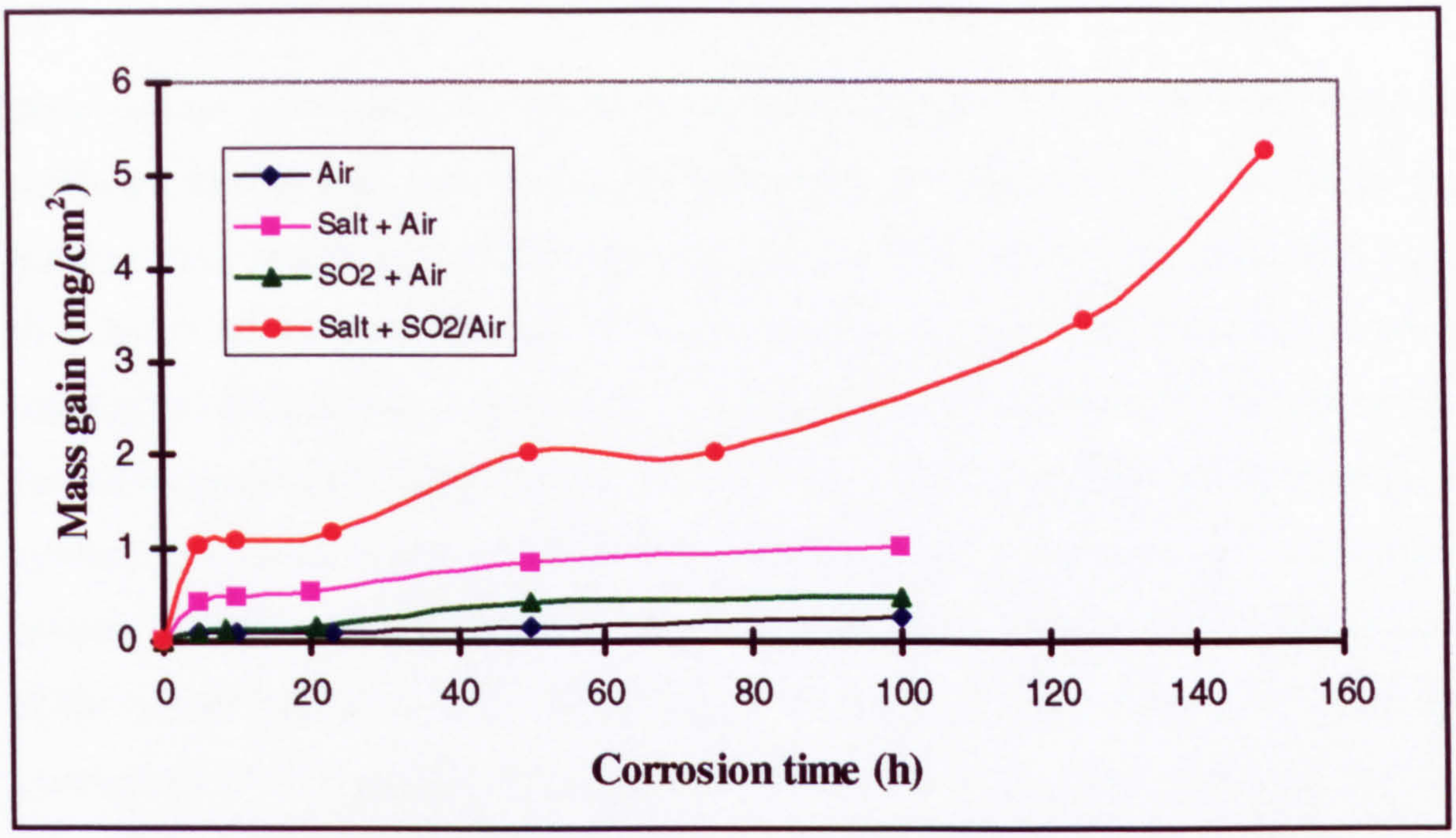

Figure 94: Environmental behaviour of Ti-45Al-2Mn-2Nb after 100h at 750°C

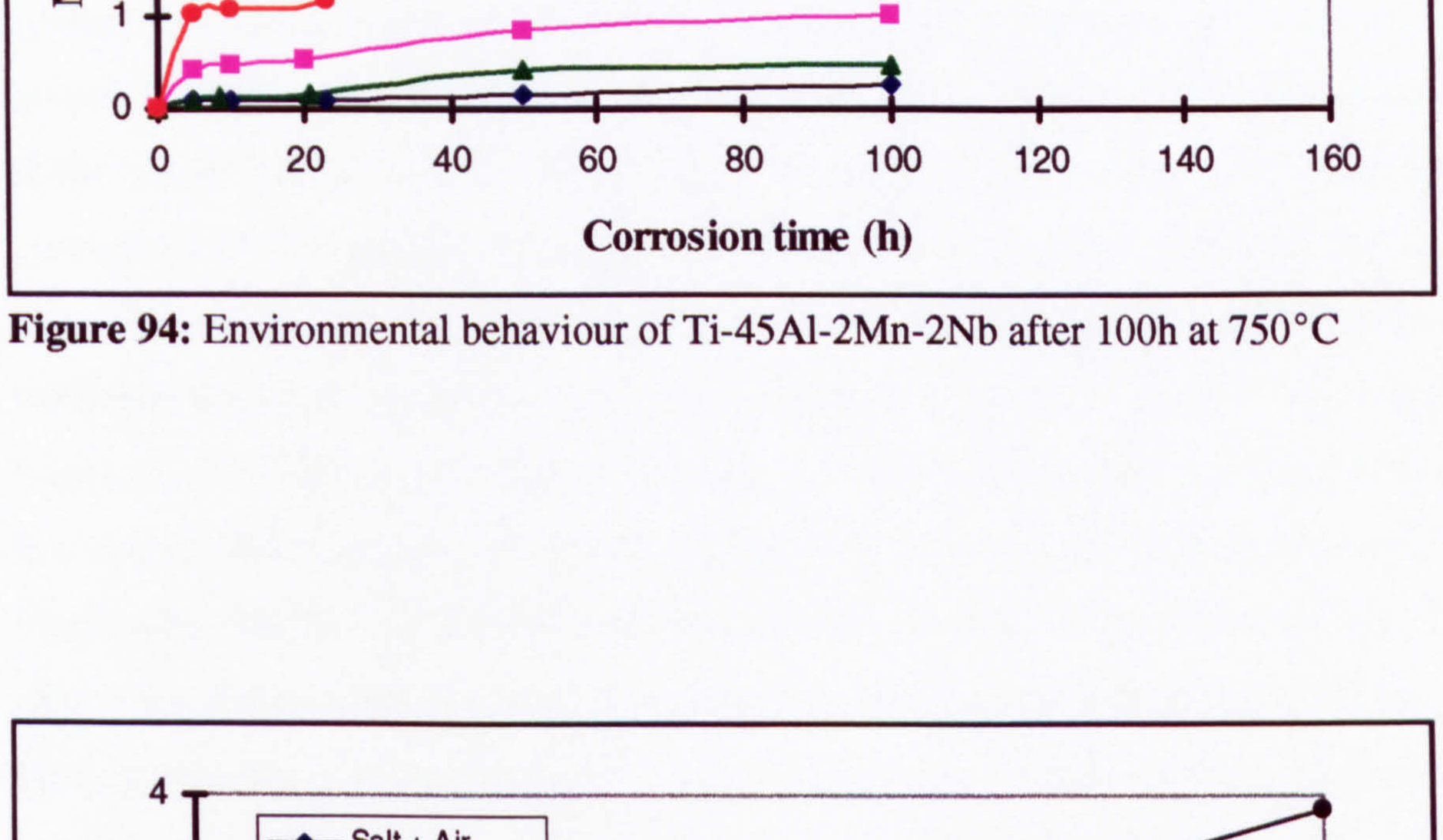

Figure 95: Environmental behaviour of Ti-45Al-2Mn-2Nb after 100h at 800°C

deposited on the specimen's surfaces increased the corrosion rates by up to a factor of ~10 times, after 20 hours, when compared to corrosion in air alone. The combination of salt and an atmosphere of air plus low levels of SO_2 increased the corrosion rates by up to a factor of 14 over the same time period. This implies that non protective scales develop in environments containing low levels of salt. SO_2 increases the corrosion rates further suggesting that different or additional corrosion mechanisms are operating, and implies that NaCl reacts with SO_2 in the atmosphere, as suggested by a number of authers[94,96], accelerating oxidation and sulphidation reactions. Metallographic analyses of the reaction products were carried out to determine the hot corrosion mechanisms operating and are discussed later in this section. Hot salt corrosion studies of Ti-45Al-2Mn-2Nb have shown the first 10 to 20 hours to be the most important, as it was during this period that rapid vapour phase transport mechanisms operated, at 700°C. The kinetic behaviour of Ti-45Al-2Mn-2Nb after the first 20 hours was altered in an SO_2 containing atmosphere. The corrosion rate increased suggesting a change in or additional corrosion mechanism. The rate of corrosion initially followed logarithmic type kinetics with the corrosion rates decreasing and following parabolic kinetics after approximately 50 hours. From the oxidation studies this implies that semi protective oxide scales are formed.

Previous studies have shown that increasing the exposure temperature accelerates the operating corrosion mechanisms by reducing the protective nature of the scale. At 750°C rapid corrosion rates were observed during the first 5 hours of exposure (figure 94) under hot corrosion conditions. Logarithmic type kinetics then operated out to approximately 23 hours. This was followed by a rapid increase in the corrosion rate. Again this was followed by a plateau, whereby virtually no further increase in corrosion was observed. Ti-45Al-2Mn-2Nb specimens were then taken beyond the usual exposure times of 100 hours to show that breakaway kinetics eventually dominate. During this breakaway period severe spallation made surface and through section analyses difficult. The corrosion behaviour of Ti-45Al-2Mn-2Nb in SO_2 alone shows a rapid increase in corrosion rate after approximately 20 hours corresponding to the rapid increase seen under hot corrosion conditions. Sulphidation studies suggested this was due to a change in corrosion

mechanism with continuous sulphide layers at the scale/substrate interface providing rapid transport routes for the outward diffusion of cations. SO_2 appears in the gas phase to cause breakaway type kinetics after 20 hours whilst salt in air alone results in parabolic kinetics dominating after 20 hours.

Although 800°C may be above the likely service temperatures, under hot corrosion conditions, for Ti-45Al-2Mn-2Nb the kinetic stages are exaggerated making any transitions easier to identify. Figure 95 compares the kinetic behaviour of Ti-45Al-2Mn-2Nb at 800°C in the four environments tested. The contributions of SO_2 and salt to the high corrosion rates observed are evident. The high corrosion rates seen during the first five hours, under hot corrosion conditions, lead to mass gains of approximately 1.5 mg/cm^2, equivalent to a ten fold increase in the oxidation rate. Logarithmic type kinetics were followed for approximately 24 hours. This behaviour is dominated by the presence of salt (NaCl). The effect of salt, in air, at this temperature was to disrupt the oxide scale thereby enabling high corrosion rates to continue. However, the melting point of NaCl occurs at ~804°C, which has been shown to be above the melting point of the eutectic mixtures which form, resulting in the loss of chlorine to the atmosphere and virtually no further corrosion. Breakaway kinetics occurred after approximately 20 hours under hot corrosion conditions and during corrosion in air/SO_2 alone. Similar high rates of attack were then followed. Severe spallation resulted in both cases. Metallographic analyses of the through sections in each case were carried out to determine if similar scale structures developed, after 100 hours, suggesting that above a certain temperature and length of exposure time similar corrosion mechanisms operated, in air-SO_2 or air-SO_2-salt.

The hot corrosion of Ti-45Al-2Mn-2Nb is characterised by four kinetic stages summarised below and shown schematically in figure 96. Stage 2 is reached after 100 hours at 650°C. At 700°C stage 2 and 3 are not clearly defined, suggesting that the mechanisms operating in each stage are competing with each other. All four kinetic stages developed after 150 hours at 750°C. At 800°C stages 1 and 2 are well defined, with stages 3 and 4 merging, again suggesting a competition between corrosion mechanisms with neither dominating.

Stage 1: This stage is characterised by rapid corrosion kinetics similar to the initial rapid hot salt corrosion kinetics previously observed.

Stage 2: Steady state scale growth rates follow on from stage 1 according to logarithmic type kinetics.

Stage 3: During this stage parabolic kinetics are followed.

Stage 4: The final stage is characterised by breakaway kinetics, accompanied by severe spallation.

The hot corrosion scales developed by Ti-45Al-2Mn-2Nb were different from those developed in air alone, in air plus low partial pressures of SO_2 or when coated with NaCl

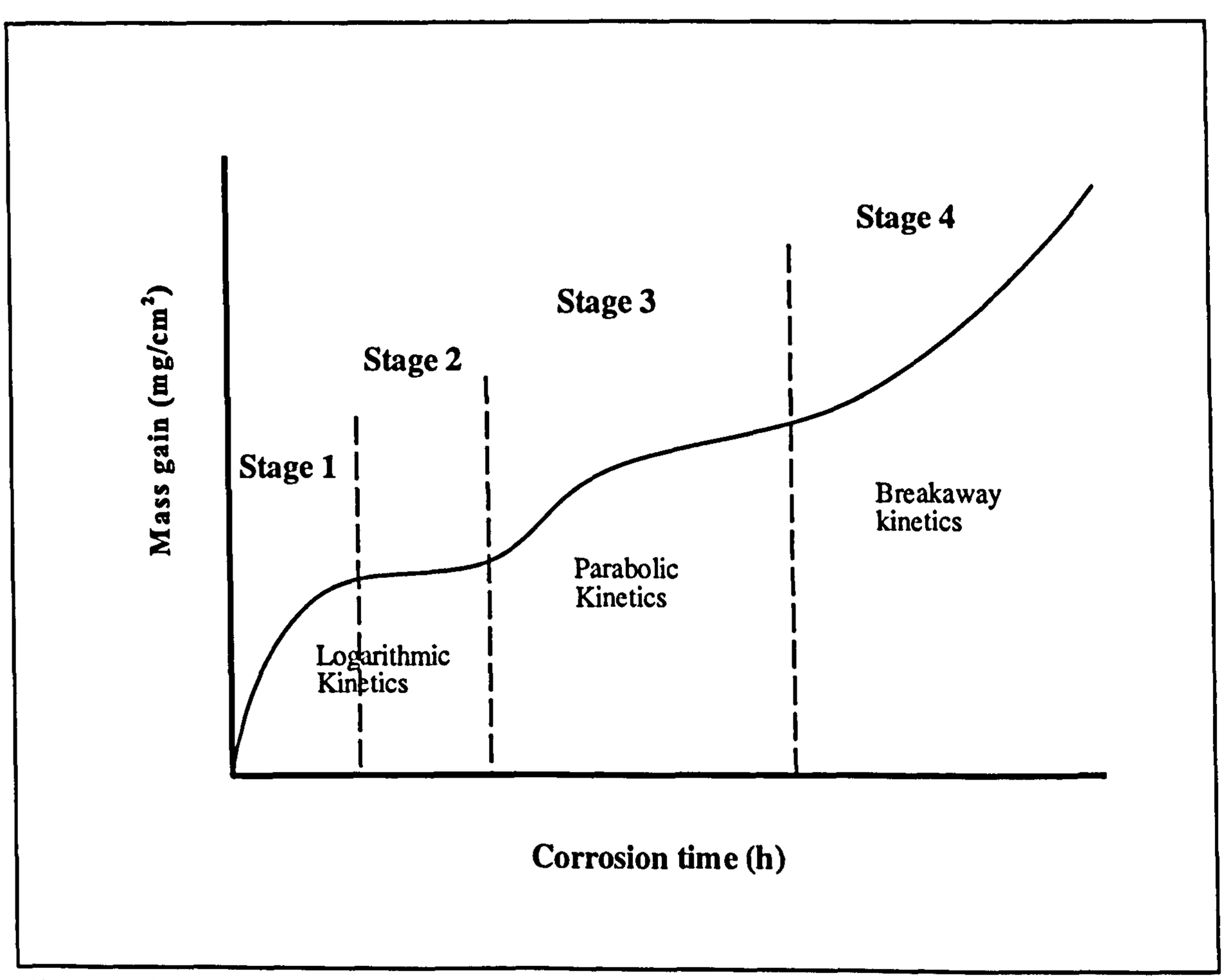

Figure 96: Kinetic behaviour of Ti-45Al-2Mn-2Nb, coated with low concentrations of NaCl, between 650-800°C in air + SO_2 (~ 10^{-4} atm)

in air. Photographs 8.2.5a to 8.2.5l show the development of hot corrosion scales with time at each exposure temperature. The following comparisons compare the general surface features developed under hot corrosion conditions with the individual environments previously discussed.

1. In air alone crystallographic rutile crystals formed at the oxide/gas interface. These increased in size with exposure time and temperature. Under hot corrosion conditions porous oxide and sulphate surface scales developed.

2. Although the oxide scales formed when Ti-45Al-2Mn-2Nb was exposed to air plus SO_2, were porous they bore very little resemblance to those observed after hot corrosion. In air/SO_2 relatively flat rutile and MnO_2 surface scales formed. The surface roughness after hot corrosion depended on the corrosion stage. More complex corrosion products form during hot corrosion.

3. Hot salt corrosion was characterised by the development of oxide whiskers over rutile scales. SO_2 modifies the effect of salt as no whiskers were observed. During the initial stage of hot salt corrosion localised corrosion occurred at areas of high salt levels. The protrusions developed at the surface of hot corroded specimens imply that this was a result of localised corrosion or higher corrosion rates occurring as a consequence of preferential corrosion, possibly the position of previous salt deposits.

The surface features shown in photographs 8.2.5a to 8.2.5l also show that similar scale structures develop at each temperature but after different exposure times. The scales developed after 100 hours at 650°C, photograph 8.2.5c, resemble the scales developed after 5 hours at 700°C, photograph 8.2.5d, in that the surfaces were relatively flat, with random particle coverage and light and dark areas. This stage of scale development corresponded to stage 2 of the hot corrosion mechanism. The scales developed after 100 hours at 700°C (photograph 8.2.5f) resemble those seen after 5 hours at 750°C (photograph 8.2.5g), being flat and porous in nature. It is at this point that it becomes

difficult to say when there is a clear transition to a the third stage without comparing the through section scales. After 24 hours at 750°C (photograph 8.2.5h) the surface has changed little although there are more protrusions. The surface remains comparitivly flat even after 100 hours at 750°C (photograph 8.2.5i). From initial observations two areas now appear to exist. The first being comparable to the earlier dark areas with a coverage of particles or protrusions. The second area appears lighter in appearance with virtually no particle/protrusion coverage. This stage of scale development appears to have been entered after 20 hours at 800°C (photograph 8.2.5k). The scales developed after 100 hours at 800°C (photograph 8.2.5l) are again different in that they are more porous and show much more variation in scale thickness.

The preceding section discussed the kinetic behaviour of Ti-45Al-2Mn-2Nb and identified four stages of scale growth. The subsequent morphological analysis of the development of the surface hot corrosion scales identified the major features of interest and allowed comparisons to be made with salt, SO_2 and purely oxidised specimens from previous sections. The next section uses the EPMA and Elemental X-ray analyses of the major features to explain how the outer scale composition changes through these four kinetic stages. A full understanding of the scale development can only be gained through an in depth study of the through sections developed with time and temperature.

Photographs 8.2.5m to 8.2.5o and the accompanying EPMA'S, at 650°C, show that initially predominantly rutile oxide scales develop under hot corrosion conditions. The level of sulphur increased over the whole surface, although higher levels were identified at specific sites. An elemental X-ray micrograph, photograph 8.2.5cc, identified these areas as being Mn, O and S rich. The glassy appearance of these areas, typically up to 15μm in diameter, implies that these regions were in a liquid state at high temperatures. At the same time many of the surface particles/protrusions contained higher proportions of aluminium. The first stage sees the formation of a mainly rutile surface at rapid corrosion rates. During the second stage, particles/protrusions develop richer in aluminium although still titanium rich. Liquid manganese sulphate areas develop at the same time but do not appear to have resulted in rapid corrosion rates yet (100 hours at 650°C). Similar

scale development occurred at 700°C. The liquid phases appear to begin forming after half an hour (photograph 8.2.5p) and are developed after 1 hour (photograph 8.2.5q). However, the EPMA' only show slight increases in manganese levels at these areas. The dominant elements being sulphur and titanium. After 5 hours at 700°C the dark glassy areas begin to disappear (photograph 8.2.5r). General EPMA' of the surface showed the aluminium, sulphur and manganese contents to be increasing with time at 700°C (photographs 8.2.5r to 8.2.5t) and the titanium levels to be decreasing, this may imply that the surface is progressively being covered with $MnSO_4$ and Al_2O_3 (or $Al_2(SO_4)_3$).

Some overlap exists between the stages of oxide growth. No clear boundaries appear to exist. Glassy phases, rich in manganese and sulphur were identified after 5 hours at 750°C (photograph 8.2.5u) However, these were not as widespread as at lower temperatures. An elemental X-ray map of the surface morphology after 5 hours at 750°C, shown in photograph 8.2.5ff, shows similar levels of aluminium and titanium across the surface. The surface became richer in aluminium with time at 750°C, as seen in photographs 8.2.5u to 8.2.5w. With respect to surface development the third stage, defined by accelerated corrosion kinetics and occurring after 20 hours at 750°C (figure 53 in section 8.2.5), is characterised by the continued development of an aluminium rich porous surface, with manganese/aluminium rich areas.

After 24 hours at 800°C (photograph 8.2.5x) the titanium content at the surface began to increase again, becoming titanium rich after 100 hours (photograph 8.2.5z). The corrosion kinetics are supported by metallographic evidence and show a change in corrosion kinetics occurring. However, due to the limited number of data points a clear transition time to the onset of breakaway kinetics, and thus stage 4, cannot be stated.

Under hot corrosion conditions Ti-45Al-2Mn-2Nb forms non protective oxide scales. The combination of salt and SO_2 causes rapid corrosion rates leading to the development of porous rutile and alumina layers with a subscale sulphide rich region. The elemental X-ray micrographs shown in photographs 8.2.5kk and 8.2.5mm show the scale structure developed after 100 hours at 650°C. The scale is predominantly rutile although aluminium

is present throughout, possibly in solution. Although no manganese rich areas can be seen it was shown through surface analysis that they exist; not as continuous layers but at discrete points on the surface. As the exposure time and temperature was increased pits were developed, photographs 8.2.5aa and 8.2.5bb of hot corrosion after 5 and 100 hours at 750°C show this with pitting at what appear to be $\alpha 2$ laths, below salt deposits resulting in the development of low melting point sulphate rich zones. The depth of pitting does not appear to increase with exposure temperature (phototgraphs 8.2.5ii and 8.2.5jj show the scale thicknesses after 100 hours at 700 and 750°C) indicating that the mechanism which initiated the pits is no longer operating or is no longer the dominant corrosion mechanism. The Elemental X-ray micrographs shown in photographs 8.2.5kk to 8.2.5ss show the development of an external alumina rich layer with discrete manganese and sulphur rich regions. The intermediate layer beneath this external layer remains predominantly rutile although as the scale thickens the concentration of alumina increases to levels approaching those seen within the base alloy. A titanium sulphide rich layer is developed at the scale/substrate interface becoming more continuous with increasing temperature.

9.4.1 Hot Corrosion mechanism

Metallographic evidence showed that narrow pits developed beneath salt deposits. Detailed surface analysis revealed that two general areas developed with time and temperature. Upon further through section analysis, including Elemental X-ray mapping, it was shown that two different corrosion mechanisms were operating in parallel. The first mechanism, occurring at isolated areas, was characteristic of low temperature type two hot corrosion. The second mechanism, resembled the sulphidation mechanism proposed for Ti-45Al-2Mn-2Nb in air/SO_2, occurred more generally. The corrosion mechanisms were categorised into four stages, with each having been defined by the kinetic behaviour of this material. The schematic diagram shown in figure 97 illustrates the two mechanisms.

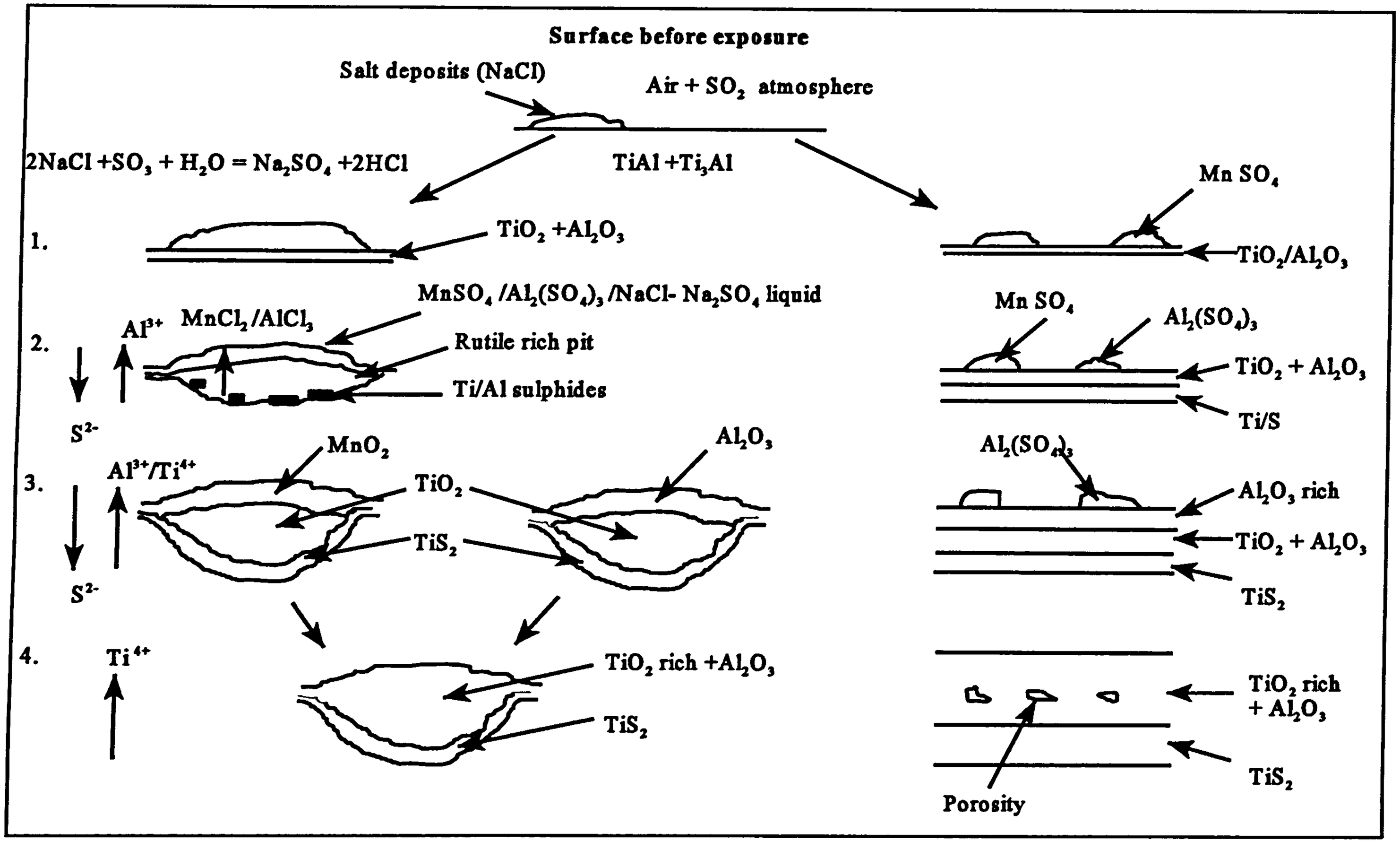

Figure 97: Hot corrosion mechanisms of Ti-45Al-2Mn-2Nb in air plus low pS_2 between 650-800°C

Mechanism 1

This mechanism closely follows a type two hot corrosion model and was usually observed below the melting point of Na_2SO_4. The major characteristic features being the development of pits all be it for γ-TiAl fine pits associated with the preferential attack of α2 beneath salt deposits, and the development of a sulphur rich interface region.

Stage 1

Low concentrations of SO_2 (400-700 ppm) in SO_2/air mixtures were circulated over the specimens surface throughout each test. In order for the gas to reach an equilibrium state SO_3 is generated according to equation 9.4.1a.

$$SO_2(g) + 1/2O_2(g) = SO_3(g) \qquad (9.4.1a)$$

In turn the solid NaCl deposits react with SO_3 in the gas to form Na_2SO_4-NaCl mixtures. Several authors have postulated the most likely reactions that take place. Water vapour has been shown to influence the halide species that are also generated.

$$2NaCl(s) + SO_3(g) + H_2O(g) = Na_2SO_4(s) + 2HCl(g) \qquad (9.4.1b)$$

$$2NaCl(s) + SO_3(g) + 1/2O_2(g) = Na_2SO_4(s) + Cl_2(g) \qquad (9.4.1c)$$

The rapid initial hot corrosion rates suggest that the evolution of chloride species results in the substrate being attacked almost immediately with no incubation periods or the development of protective oxide scales. Three possible halide reactions are shown below;

$$Ti(s) + 2HCl(g) = TiCl_2(s) + H_2(g) \qquad (9.4.1d)$$

$$Al(s) + 3HCl(g) = AlCl_3(s) + 3/2H_2(g) \qquad (9.4.1e)$$

$$Mn(s) + 2HCl(g) = MnCl_2(s) + H_2(g) \qquad (9.4.1.f)$$

From a thermodynamic point of view, discussed in section 9.3.1, $AlCl_3$ and $MnCl_2$ are the more favourable reaction products and therefore more likely to have been incorporated within the salt. These reactions are thermodynamically more favourable than the reactions between oxides and chlorides showing that either these oxides do not form continuous layers or that cracks and pores exist allowing the chlorides access to the substrate. Due to the high partial pressures of oxygen in the atmosphere it must be assumed that even after damage (cracking and spallation) thin rutile and alumina scales form at the scale/substrate interface.

Stage 2

The rate of attack varies depending on the substrate composition. Mn and Al rich areas, associated with S and O develop at the scale/gas interface. Due to the low vapour pressures of the metal chlorides at the surface and the high vapour pressures at the oxide/substrate it is believed that $MnCl_2$ and $AlCl_3$ may have been transported out through pores and reoxidised near the scale/gas interface where the pO_2 is greater.

$$\mathbf{MnCl_2(g) + O_2(g) = MnO_2(s) + Cl_2(g)} \qquad \mathbf{(9.4.1g)}$$

$$\mathbf{2AlCl_3(g) + 3/2O_2(g) = Al_2O_3(s) + 3Cl_2(g)} \qquad \mathbf{(9.4.1h)}$$

Hydrolysis reactions may also account for the formation of these surface oxides generating HCl,

$$\mathbf{MnCl_2(g) + H_2O(g) + 1/2O_2(g) = MnO_2(s) + 2HCl(g)} \qquad \mathbf{(9.4.1i)}$$

$$\mathbf{2AlCl_3(g) + 3H_2O(g) = Al_2O_3(s) + 6HCl(g)} \qquad \mathbf{(9.4.1j)}$$

Following classic type II hot corrosion theory for Ni and Co alloys an alternative mechanism, operating alongside the vapour transport theory, based on the formation of low melting point eutectic phase can be postulated[4]. Low melting point Na_2SO_4-$MnSO_4/Al_2(SO_4)_3$ mixtures could form during this stage through the sulphation of the oxides at the salt/gas interface.

$$MnO_2(g) + SO_2(g) = MnSO_4 \qquad (9.4.1k)$$

$$Al_2O_3(s) + 3SO_3(g) = Al_2(SO_4)_3 \qquad (9.4.1l)$$

Oxides are formed at the salt/substrate interface, in equilibrium with the metal substrate phases, as these are the most stable species in high partial pressures of oxygen. High levels of pSO_2 and pS_2 are then developed at the salt/alloy interface through equations (9.4.1a) and (9.4.1m), as oxide formation lowers the pO_2. The high partial pressures of sulphur result in the development of a TiS_2 rich interface region.

$$SO_3(g) = 1/2S_2(g) + 3/2O_2(g) \qquad (9.4.1m)$$

Slow corrosion rates where observed during this period. This can be attributed to the rutile scale and the thickening sulphate surface layer acting as partial barriers to the diffusion of corrosion species. Stage 3 is initiated when a continuous TiS_2 layer has formed at the scale/substrate interface.

Stage 3

Parabolic growth kinetics operated during this period. Depending on whether the sulphate mixtures were Al or Mn based, discontinuous Al_2O_3 or MnO_2 surface layers developed. The decomposition of the surface sulphates, through the reverse of the reactions shown in equations 9.4.1k and 9.4.1l, releases SO_2 to diffuse back into the scale or to return back into the atmosphere.

The development of discontinuous MnO_2/Al_2O_3 rich surface layers results in further increases in the pS_2/pSO_2 at the scale/substrate interface. During this stage a stable TiS_2 layer develops maintaining rapid corrosion rates.

Stage 4

This stage was characterised by breakaway growth rates caused by scale spallation and

the breakdown of the semi-continuous Al_2O_3/MnO_2 surface layer. Rutile growth dominates accelerating the growth rates, with the result that the scale exceeds a critical scale thickness above which the stresses cause failure. Due to the scale failing and pulling away from the substrate one of two things occur. In the first instance the scale loses contact with the substrate but does not spall. The thick scale acts as a barrier to the inward diffusion of SO_3/O_2. In some cases this allowed a renewal of scale growth at the substrate, with a sulphide layer developing at the substrate and an Al_2O_3 or MnO_2 layer at the surface. The stability of the sulphide layer in the original scale depends on the partial pressure of SO_2 being maintained. If the original scale fails completely and allows the pO_2 to increase to atmospheric pressures at the original sulphide/substrate interface, the sulphides decompose releasing sulphur back into the atmosphere. Thus, where scale adherence was maintained a TiS_2 layer continued to exist at the oxide/substrate interface.

Mechanism 2

Due to the uneven salt coverage a large proportion of the specimens surface were salt free. Hot corrosion requires a salt to accelerate the corrosion rates. A different corrosion mechanism thus operated at salt free areas. This mechanism of attack was characterised by the formation of an outer alumina layer and an inner sulphide layer at the scale/substrate interface. This scale was distinguishable from the previous by the lack of pitting, suggesting slower initial corrosion rates. Of the two mechanisms the first controls the rate of corrosion as the degree of pitting increases with time at low temperatures.

Stage 1

In high pO_2 TiO_2 and Al_2O_3 are the more thermodynamically stable corrosion products. TiO_2 forms at faster growth rates, producing a porous oxide layer through which SO_2/SO_3 is able to diffuse. Sulphate particles form at the oxide/gas interface. $MnSO_4$ was shown in section 9.2.1, which compares phase stability diagrams of the $M-O_2-SO_2$ systems, to be stable at the scale/gas interface in contact with TiO_2, Al_2O_3 and MnO_2.

These areas of low salt concentrations are surrounded by areas of much higher salt concentrations. During stage 1 of the type II hot corrosion mechanism salt was expected to react with the substrate producing vapour metal chlorides, which disrupted the oxide at the scale/substrate interface and escaped out to the surface through short circuit diffusion paths. These vapour chlorides may diffuse along the substrate/scale interface and diffuse out at areas of low salt concentrations. At the surface the chlorides may react with SO_2 or SO_3 in the atmosphere to form the sulphates which were observed at these areas. At low temperatures SO_2 is thermodynamically more stable than SO_3 This may explain the reason why $MnSO_4$ initially formed in preference to $Al_2(SO_4)_3$. It may be for this reason that the initial surface scale developed is a mixture of alumina and rutile.

Stage 2

During this stage a sulphide layer is developed at the oxide/substrate interface as the pSO_2/pS_2 increases and the pQ decreases. In the absence of salt deposits but in an atmosphere of SO_2/SO_3 an external TiQ plus AlQ rich layer forms. Similar surface oxides are developed during this stage. Both environments resulted in the formation of porous oxide/sulphide scales. $MnSO_4$ particles continued to form in the manner described in stage 1. Towards the end of this stage a more continuous TiS_2 interfacial layer is developed at the scale/substrate interface.

Stage 3

During stage 3 a predominantly porous alumina rich layer forms at the scale/gas interface and acts as a partial barrier to the inward diffusion of anions/SO_2. Parabolic corrosion rates during this period show steadily decreasing mass gains consistent with the development of a semi-protective alumina layer. However, at the same time a continuous Titanium sulphide layer is developed at the scale/substrate interface. Fast diffusion rates through this layer maintains the accelerated corrosion rates and the formation of a mixed TiO_2 rich plus Al_2O_3 intermediate layer.

The outward diffusion of chloride species from the surrounding high salt deposits could again explain the formation of an external alumina layer. At higher temperatures SO_3 becomes more thermodynamically stable favouring the sulphidation of alumina, rather than MnO_2, forming $Al_2(SO_3)_3$ which may then decompose to form alumina at the surface.

Stage 4

The porous nature of the scale developed causes rapid corrosion rates and rapidly growing oxide scales. Breakaway growth rates occur when a critical scale thickness is exceeded and cracking occurs along the interface and through the scale Titanium then becomes the dominant corrosion species and this results in the formation of rutile rich scales, with alumina in solution.

Conclusions

1. Ti-45Al-2Mn-2Nb was shown to have excellent oxidation resistance up to 800°C, with logarithmic type kinetics operating after 100 hours at 700°C and up to 13 hours at 750°C. Parabolic kinetics were then followed with a protective intermediate alumina layer forming beneath an external rutile layer. A mixed alumina/rutile layer formed beneath the alumina layer. Niobium concentrated within the oxide layers adjacent to the metal substrate and was believed to promote the formation of the alumina layer. No internal oxidation was observed.

2. Low partial pressures ($<10^{-4}$ atm) of SO_2 accelerated the oxidation rates. Relatively good sulphidation resistance existed at 700°C. The development of a stable sulphide layer at the scale/substrate was supported thermodynamically showing that as the scale thickened sulphide stability increased at this interface. Breakaway growth rates coincided with the development of continuous sulphide layers. This then resulted in the formation of thick non protective mixed rutile/alumina layers.

3. Salt accelerated the corrosion rate of the Ti-45Al-2Mn-2Nb alloy. Its effect was greatest during the first 10 to 20 hours when rapid corrosion rates occurred. Chlorine reacted with the substrate after penetrating the initial oxide layer formed over the surface and depending on the exposure time and temperature either diffused back into the salt or was transported away via a mechanism of vapour phase transport. Preferential substrate degradation occurred down grain boundaries and $\alpha 2$ lathes, up to 40 -50μm in depth, resulting in the development of whiskers over a predominantly rutile layer. Thermodynamic Phase Stability Diagrams supported the vapour transport of $MnCl_2$ and $AlCl_3$. A three stage mechanism was derived kinetically and supported

metallographically. The onset of whisker growth occurred after shorter times as the temperature was increased.

4. A salt saturation level of approximately 0.12mg/cm^2 existed above which no further increases in mass gains were observed after 100 hours at 700°C. Resalting affected the early stages of corrosion increasing the corrosion rate by depositing at areas of no salt. Once saturated the level of salt became irrelevant to the rate of corrosion as this is then controlled by temperature. Thermal cycling may cause spallation exposing the substrate to salt initiating the salt corrosion cycle of vapour phase transport.

5. Environments containing solid salt deposits and bi-oxidant atmospheres caused severe alloy degradation, with the formation of porous oxide/sulphide scales. Two mechanisms of attack were shown to operate. Classic type II hot corrosion developed at salt deposits with the formation of low melting point $MnSO_4$-Na_2SO_4 mixtures with the salt deposits, and of pits at grain boundaries and $\alpha 2$ lathes. The second mechanism followed sulphidation type reactions with mixed oxide/sulphide scales developing. Salt was believed to dominate during the early stages of corrosion disrupting the initial oxide through the production of HCl/Cl_2. During this period sulphides form beneath the external oxide/sulphate scale. The combination of liquid salt at the surface and the development of a continuous sulphide layer at the scale/substrate interface resulted in rapid corrosion rates often leading to severe scale spallation. The early stages of corrosion thus prevent the formation of compact scales, providing diffusion paths for SO_2 accelerating the formation of continuous sulphide layers at the scale/substrate interface.

Future Work

1. Under hot salt corrosion conditions Ti-45Al-2Mn-2Nb +0.8% TiB_2 suffers from severe substrate attack with preferential attack down grain boundaries and $\alpha 2$ lathes. The rapid corrosion rates were attributed to vapour phase transport. One question of importance is whether or not the corrosion rates of this material could be reduced via microstructural modifications at the surface. If the density of preferential sites could be reduced would substrate corrosion proceed at slower rates over a broader area? This may enable higher operating temperatures to be considered. Lamellar microstructures satisfy the bulk material mechanical property requirements. Heat treating the surface to produce thin surface layers of large single phase gamma grains may reduce corrosion rates.

2. Titanium and aluminium were shown to be susceptible to salt attack. Chromium has been shown to be less favourablly attacked by salt in other systems. Investigations are thus needed to determine if tertiary chromium additions would result in Cr_2O_3 being incorporated in the scale reducing corrosion rates.

3. Corrosion resistance can be provided if a suitable coating system is used. One of the requirements for a TiAl coating system is for it to be resistant to salt attack. NiCr coatings have been used successfully on other alloy systems. However, the corrosion behaviour of the coating is only one problem that must be overcome. Properties such as the coatings adhesion, thermal expansion, and brittleness must also be considered. If the coating barrier is compromised and salt gains access to the substrate, high corrosion rates would again be observed. Hence the need for extensive studies to develop a reliable high temperature coating system for γ-TiAl.

4. Modifying the surface composition, through ion implantation techniques, overcomes the problems of barrier integrity associated with coating systems. It may also be possible to develop highly corrosion resistant surface layers. Ion implantation has been shown to be effective in increasing the oxidation resistance of TiAl alloys[49]. Here Niobium was implanted resulting in the formation of continuous alumina scales. For increased hot salt corrosion resistance Chromium could be implanted. This relies on Cr_2O_3 rich scales developing beneath the salt during high temperature exposure. Extensive research would be needed to determine the critical concentration of Chromium which would result in uniform continuous Cr_2O_3 scales. The depth of implantation is another important factor as adequate Chromium reserves are needed to maintain the chromia layer if spallation occurs.

5. The environmental studies have so far looked at the corrosion behaviour of this TiAlNb alloy under atmospheric pressure. The potential corrosion problems have thus been categorised. However, the effect of pressure has of yet not been investigated. High pressures are often encountered in the applications being targeted, presenting the possibility that the corrosion rates may be altered. The problems which have been identified may not be as great as suggested with high pressures having the potential to suppress the effects of salt and SO_2 on the rate of high temperature corrosion.

APPENDIX A

Continuous Thermogravimetric and Discontinuous Mass Gain Curves

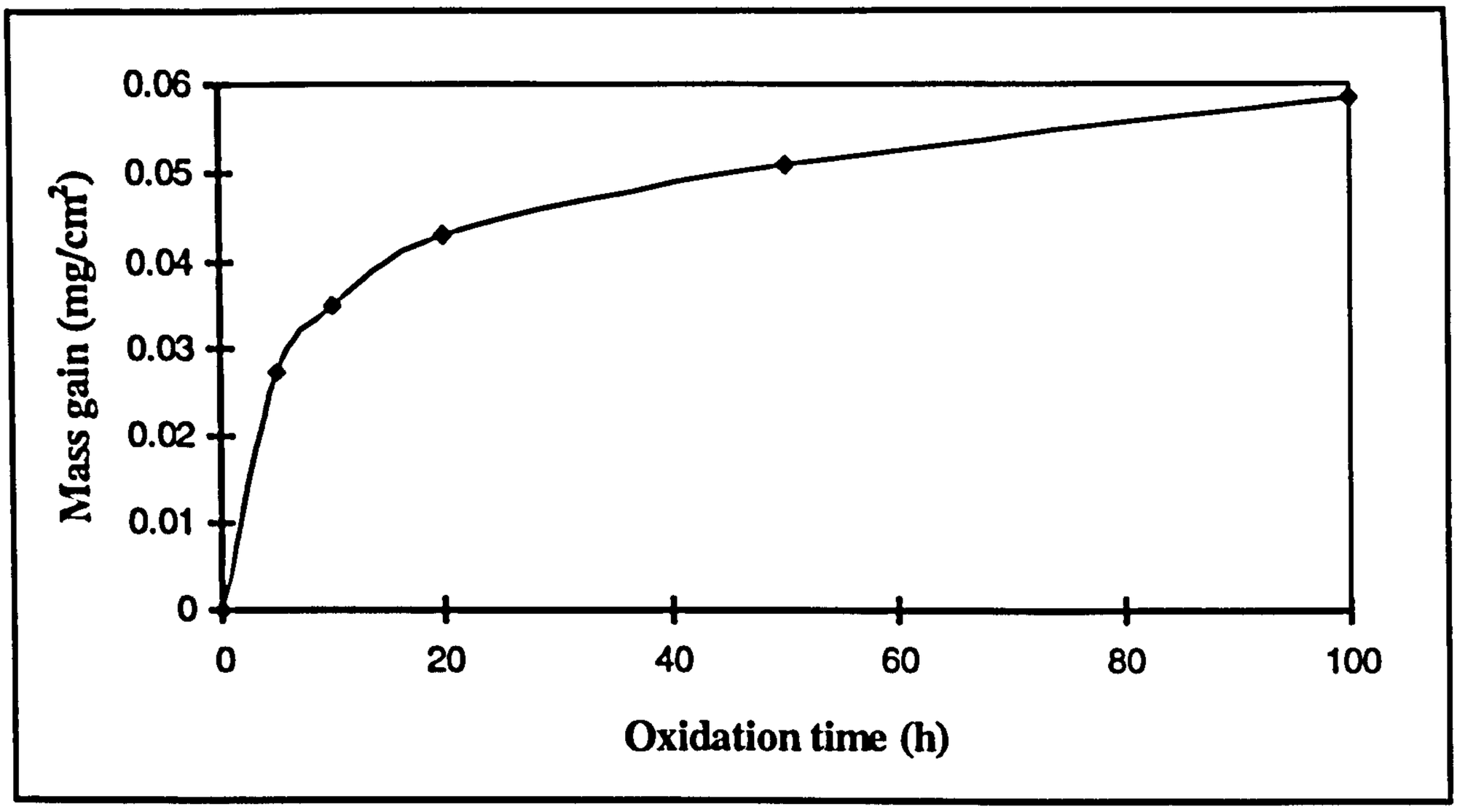

Figure A1: Oxidation behaviour of Ti-45Al-2Mn-2Nb after 100h at 700°C in air

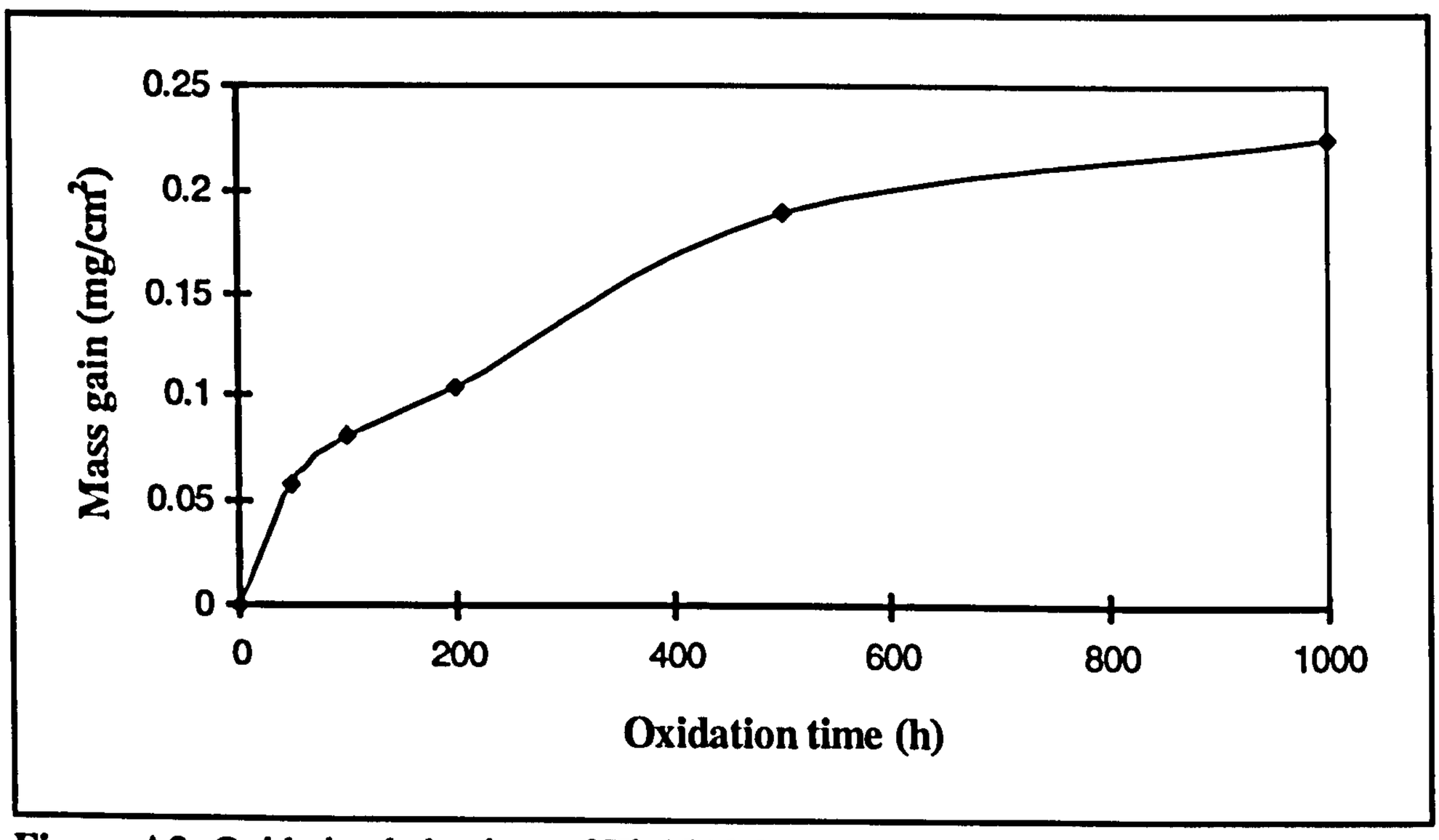

Figure A2: Oxidation behaviour of Ti-45Al-2Mn-2Nb after 1000h at 700°C in air

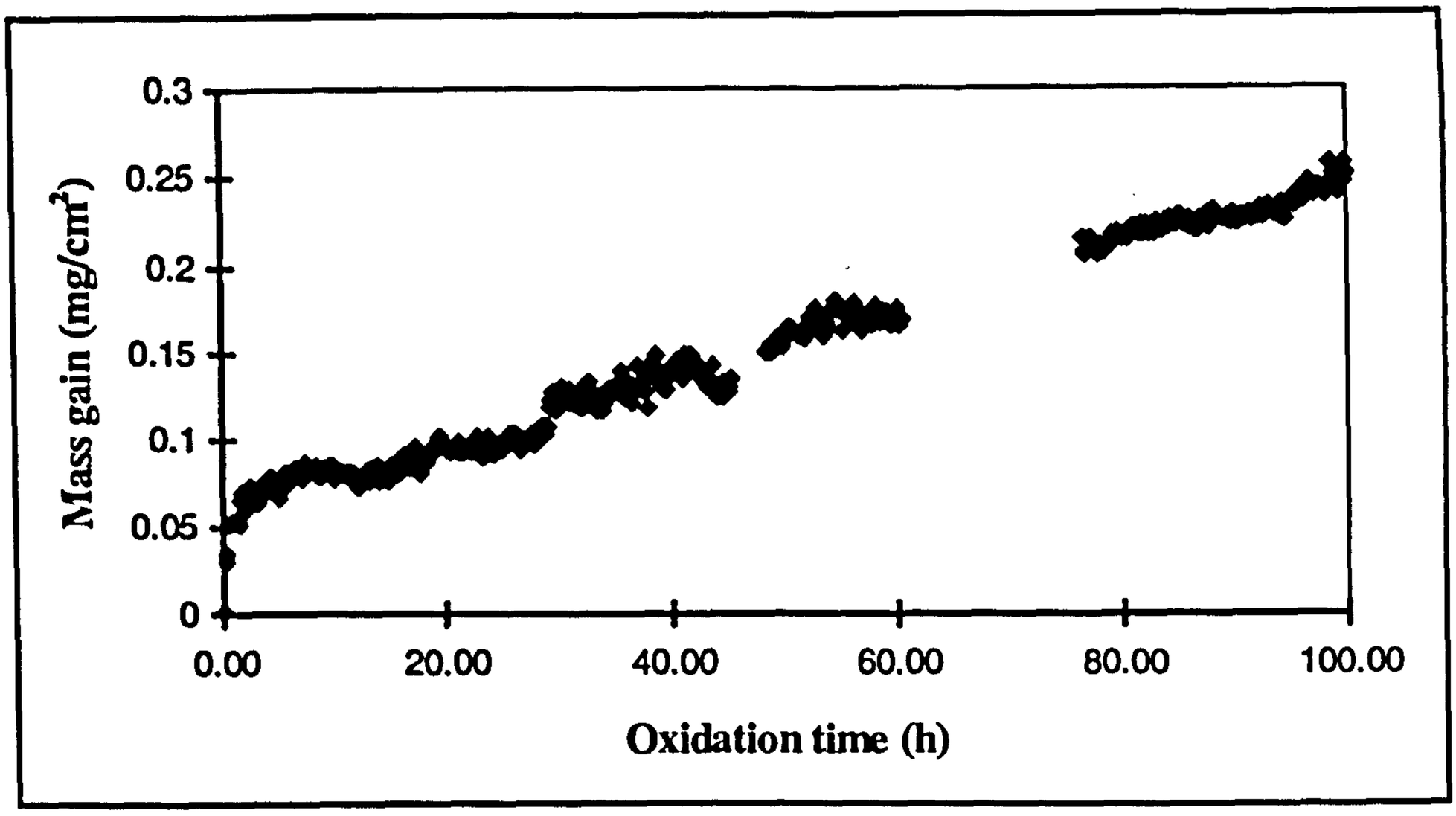

Figure A3: Oxidation behaviour of Ti-45Al-2Mn-2Nb after 100h at 750°C in air

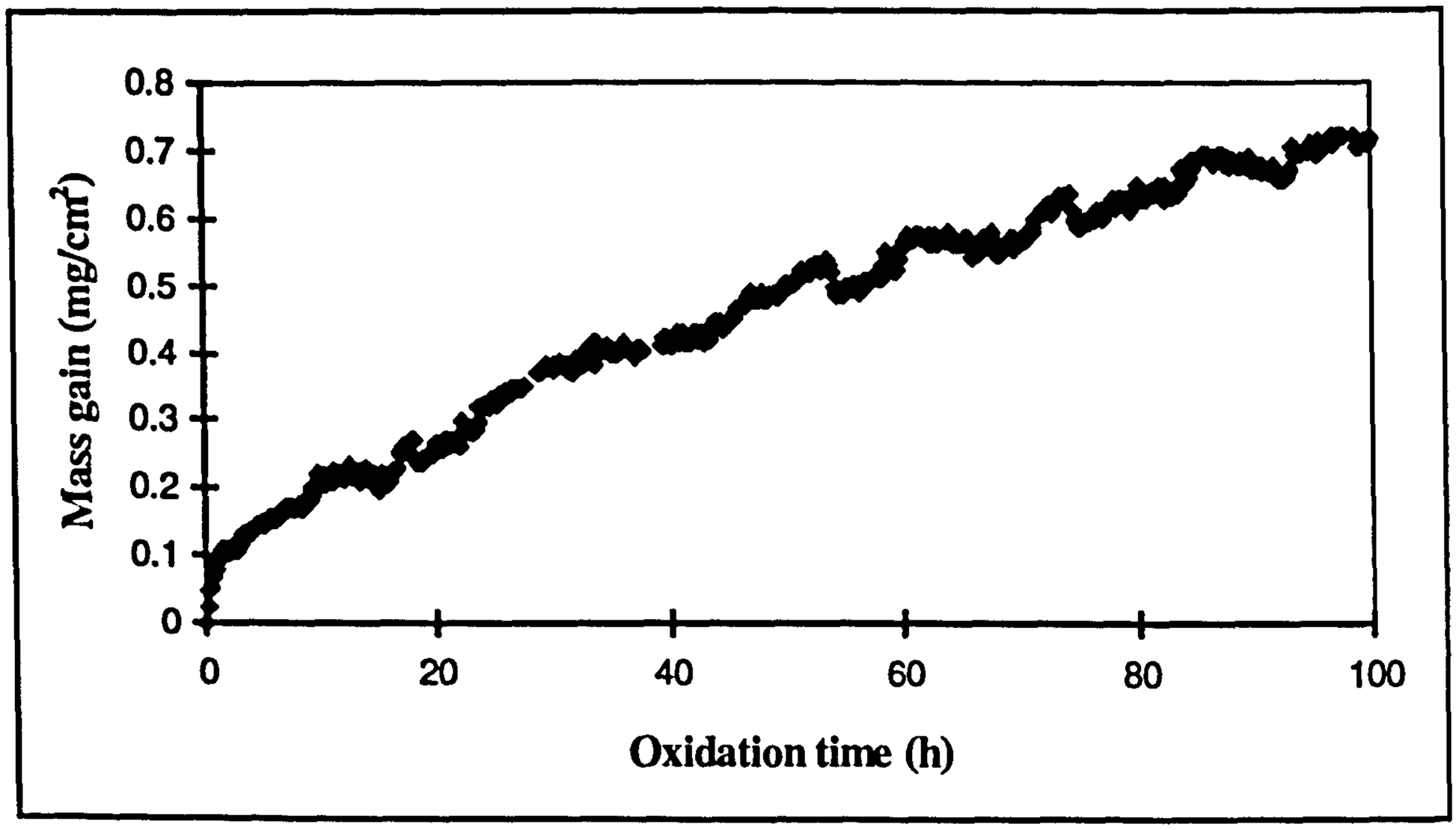

Figure A4: Oxidation behaviour of Ti-45Al-2Mn-Nb after 100h at 800°C in air

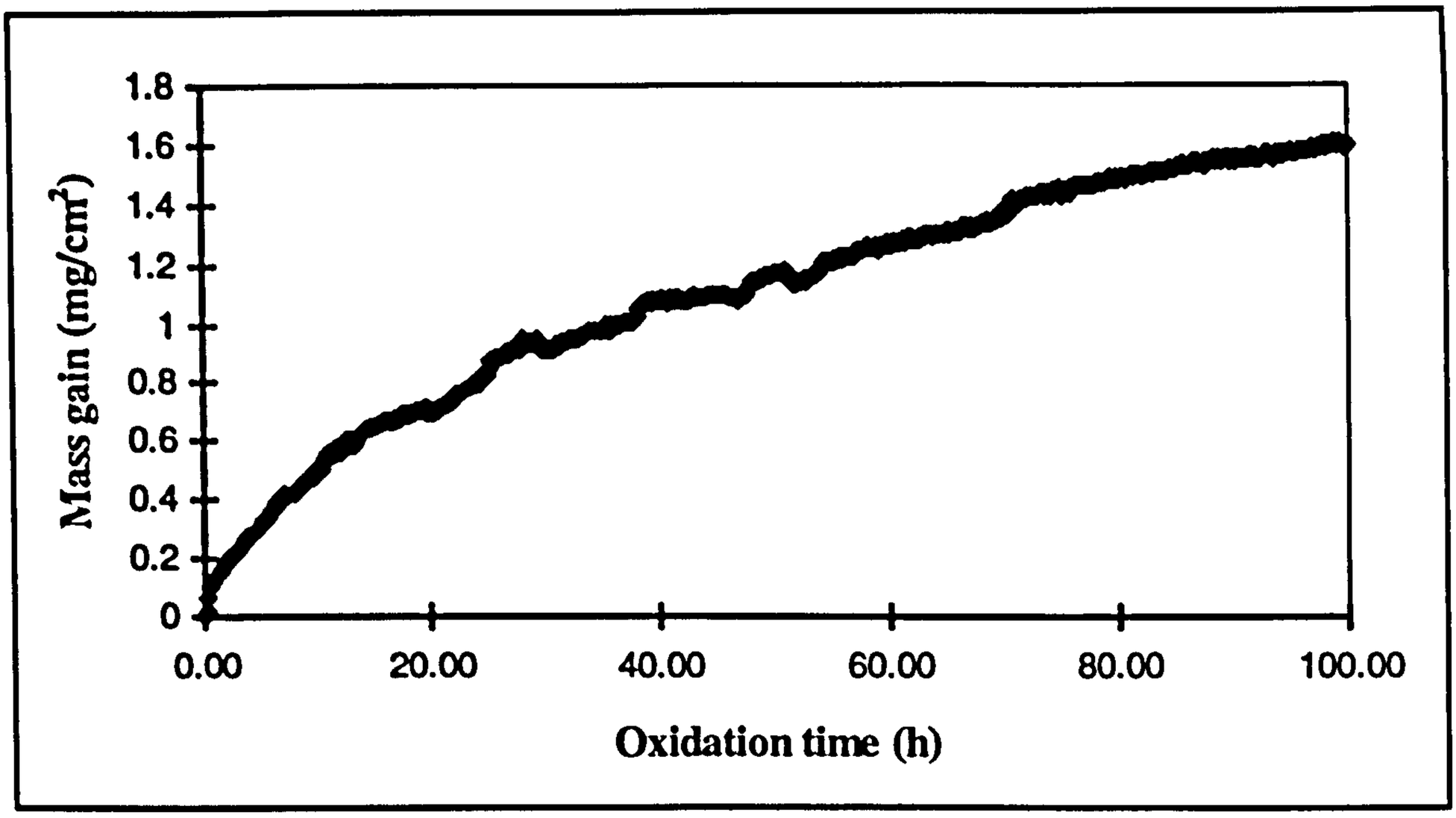

Figure A5: Oxidation behaviour of Ti-45Al-2Mn-2Nb after 100h at 850°C in air

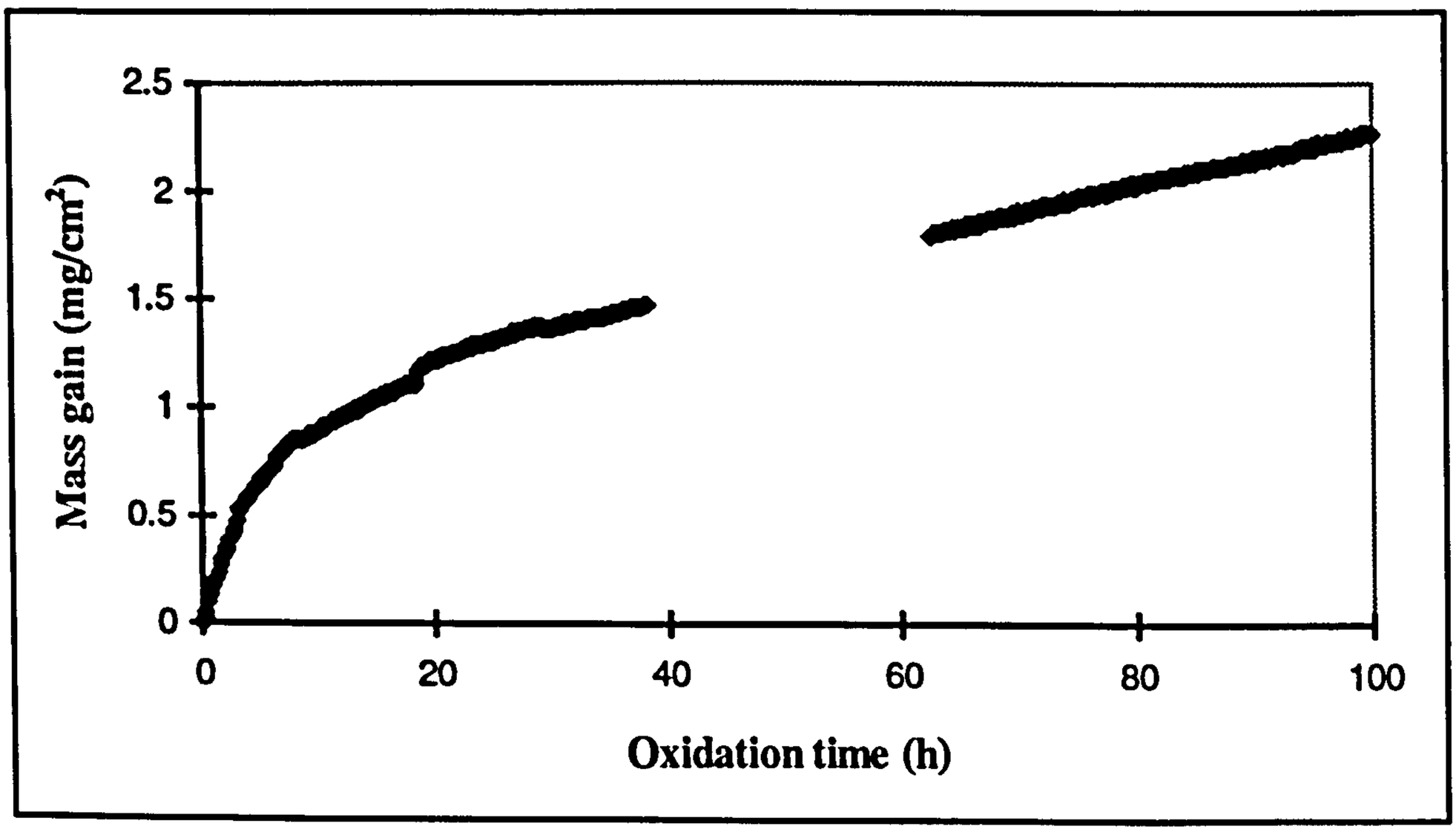

Figure A6: Oxidation behaviour of Ti-45Al-2Mn-2Nb after 100h at 900°C in air

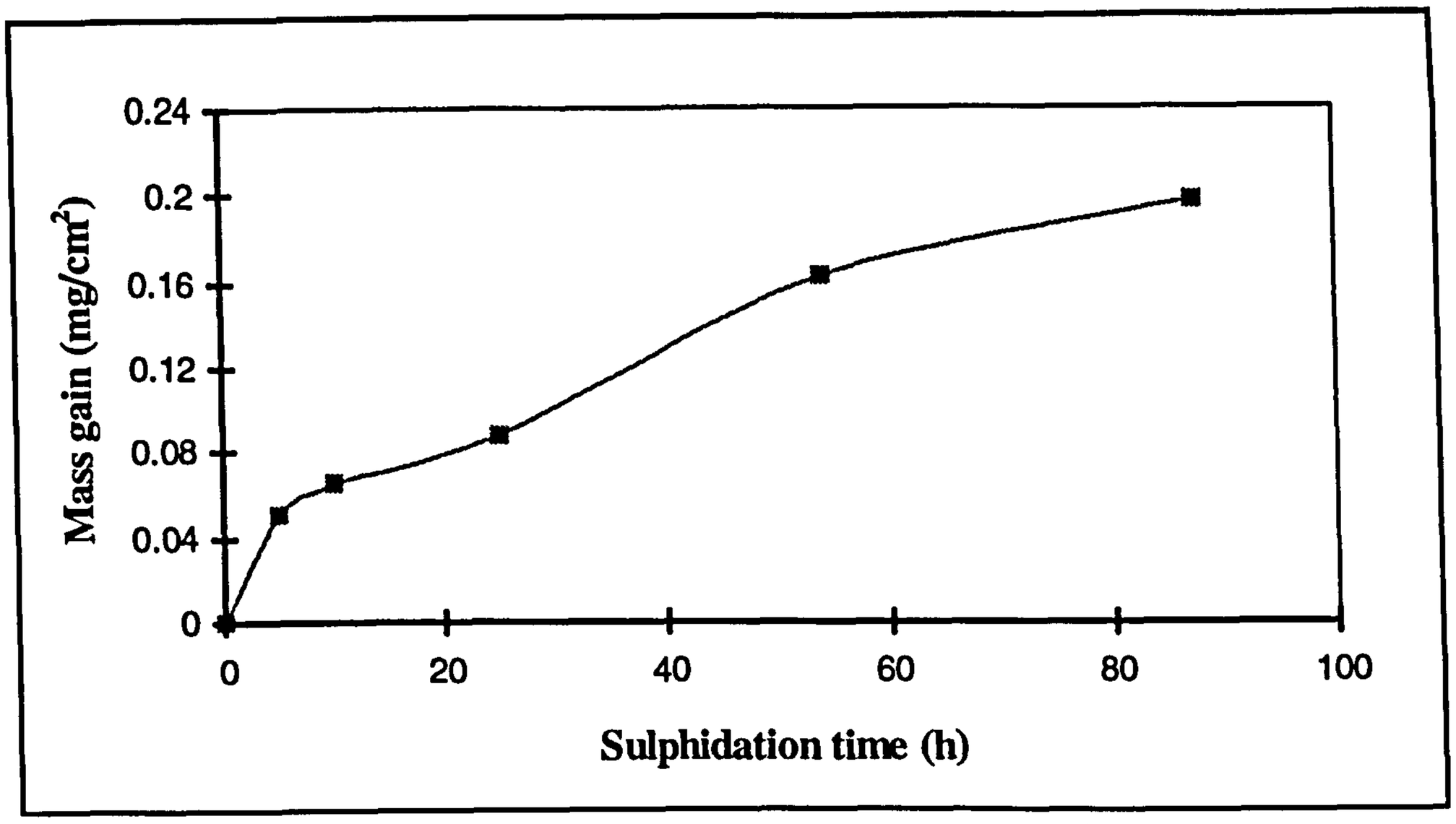

Figure A7: Sulphidation behaviour of Ti-45Al-2Mn-2Nb at 700°C in 450ppm SO_2

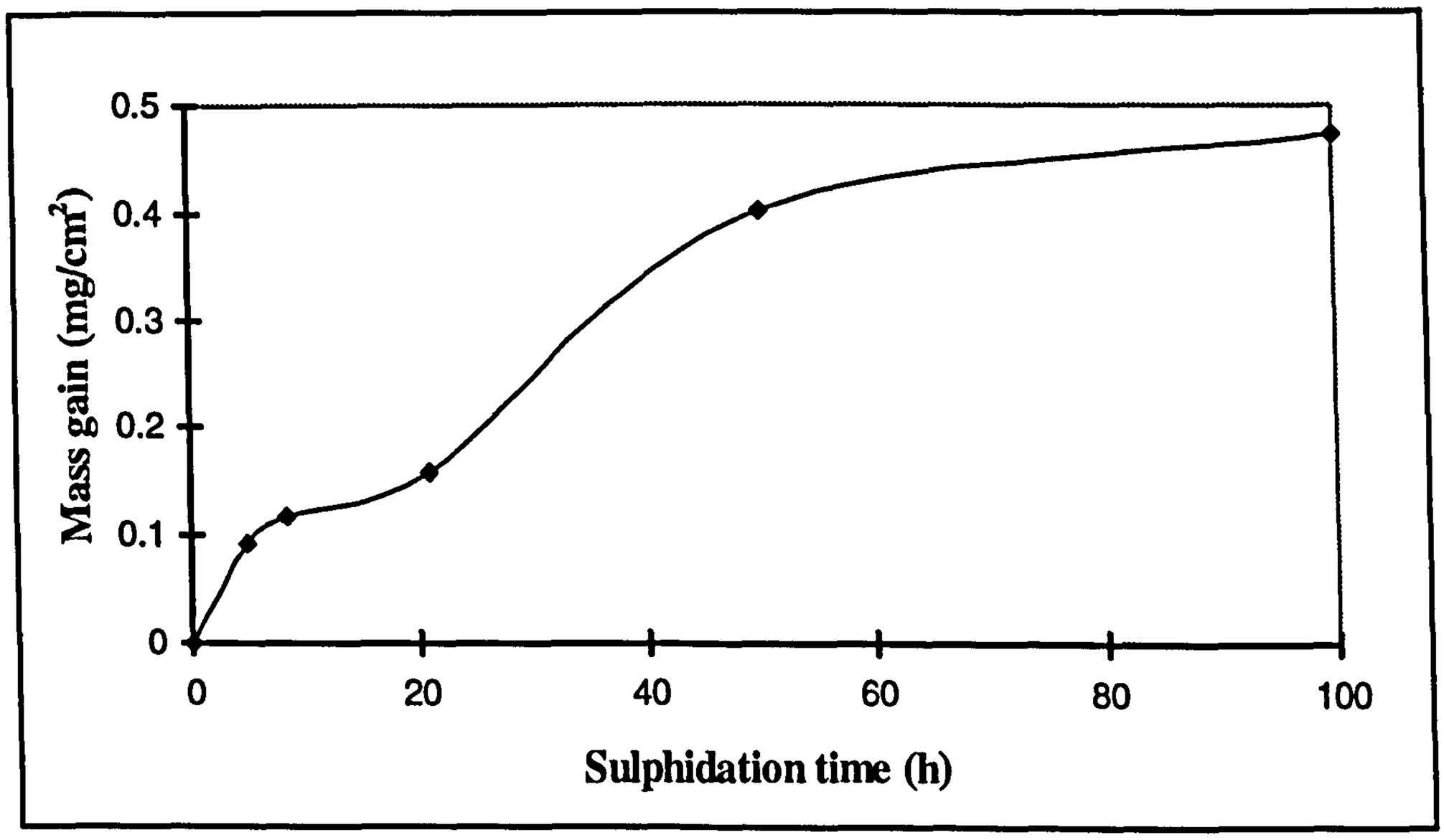

Figure A8: Sulphidation behaviour of Ti-45Al-2Mn-2Nb at 750°C in 590 ppm SO_2

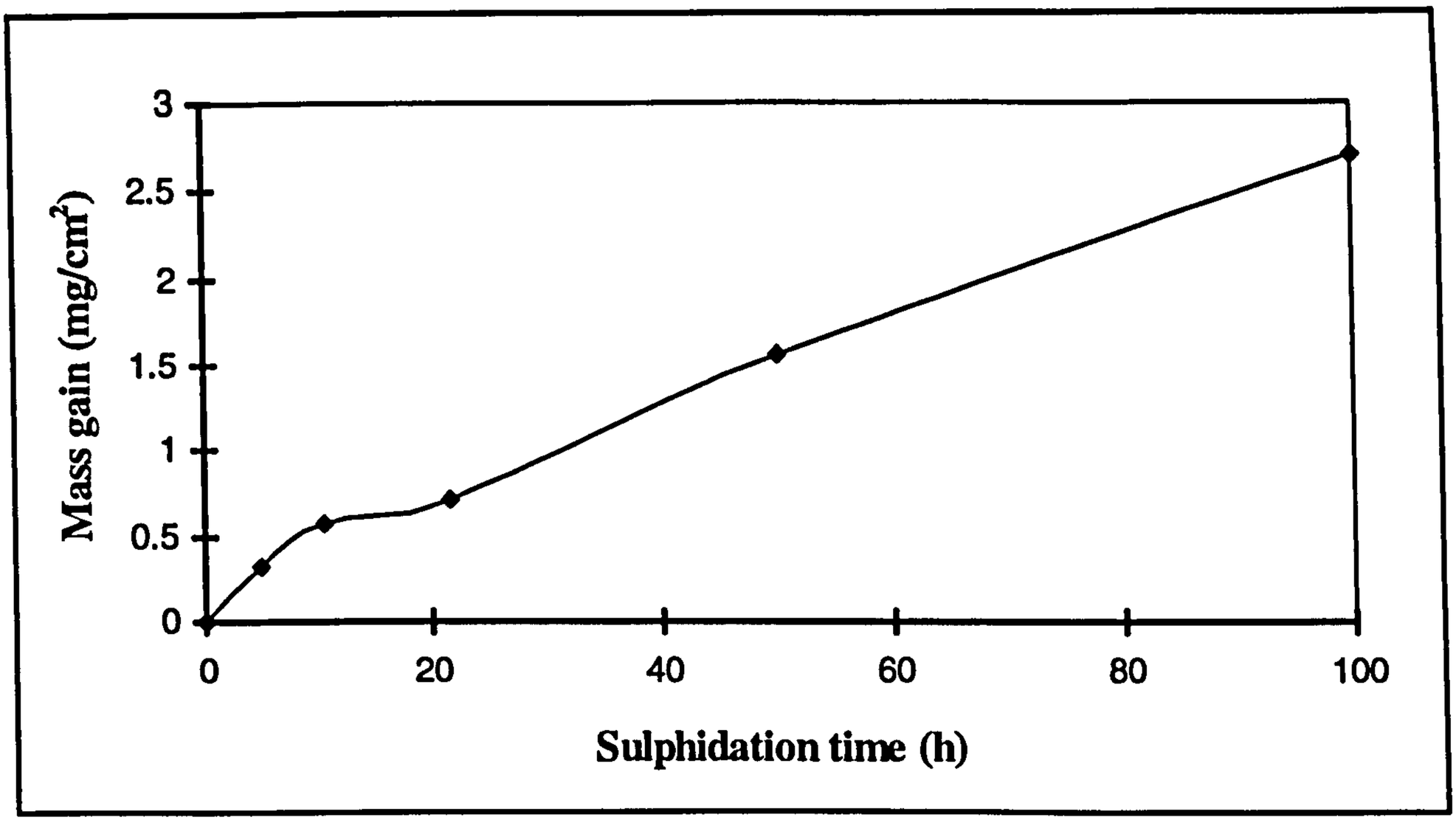

Figure A9: Sulphidation behaviour of Ti-45Al-2Mn-2Nb at 800°C in 650ppm SO_2

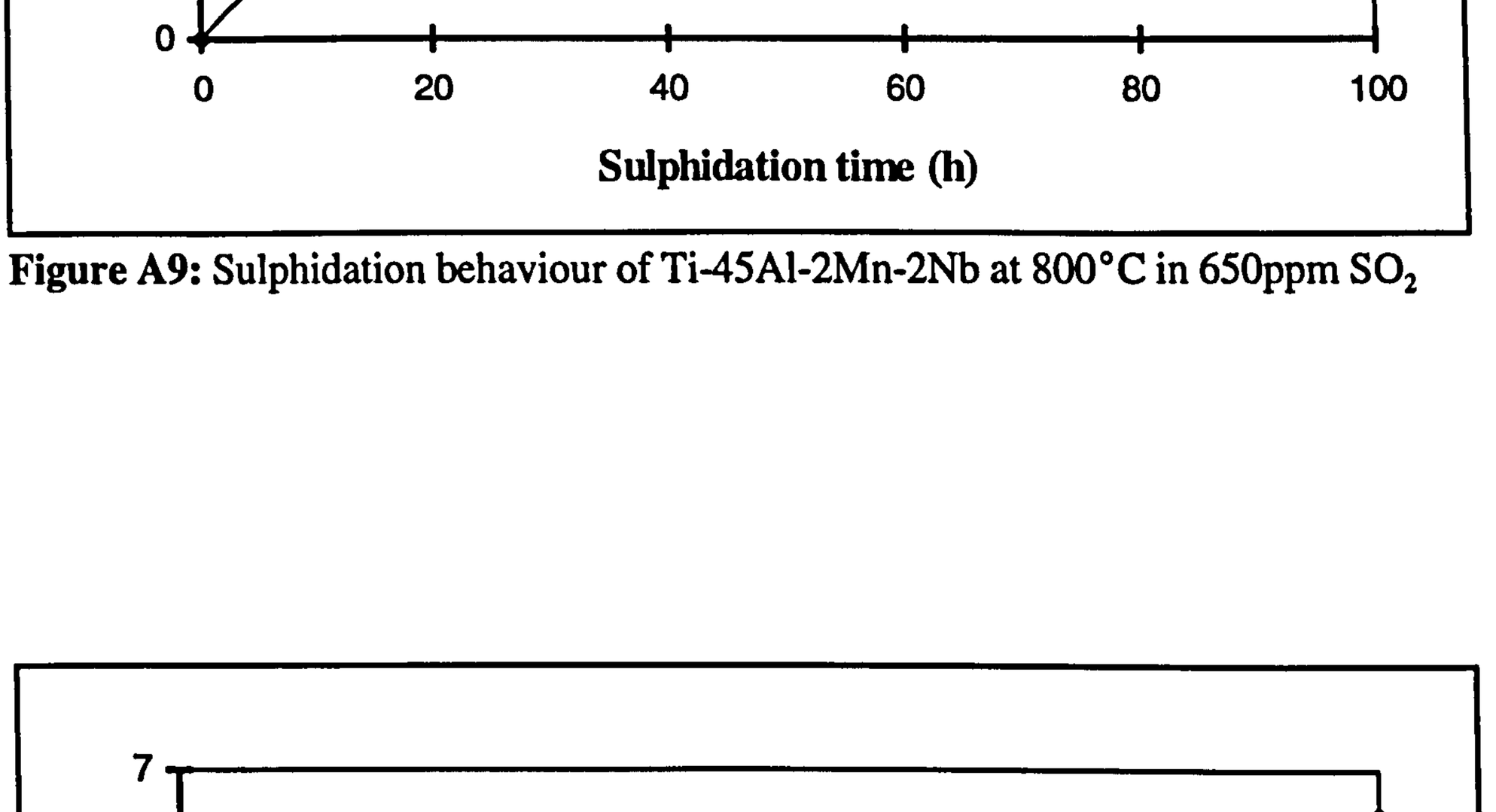

Figure A10: Sulphidation behaviour of Ti-45Al-2Mn-2Nb at 900°C in 660ppm SO_2

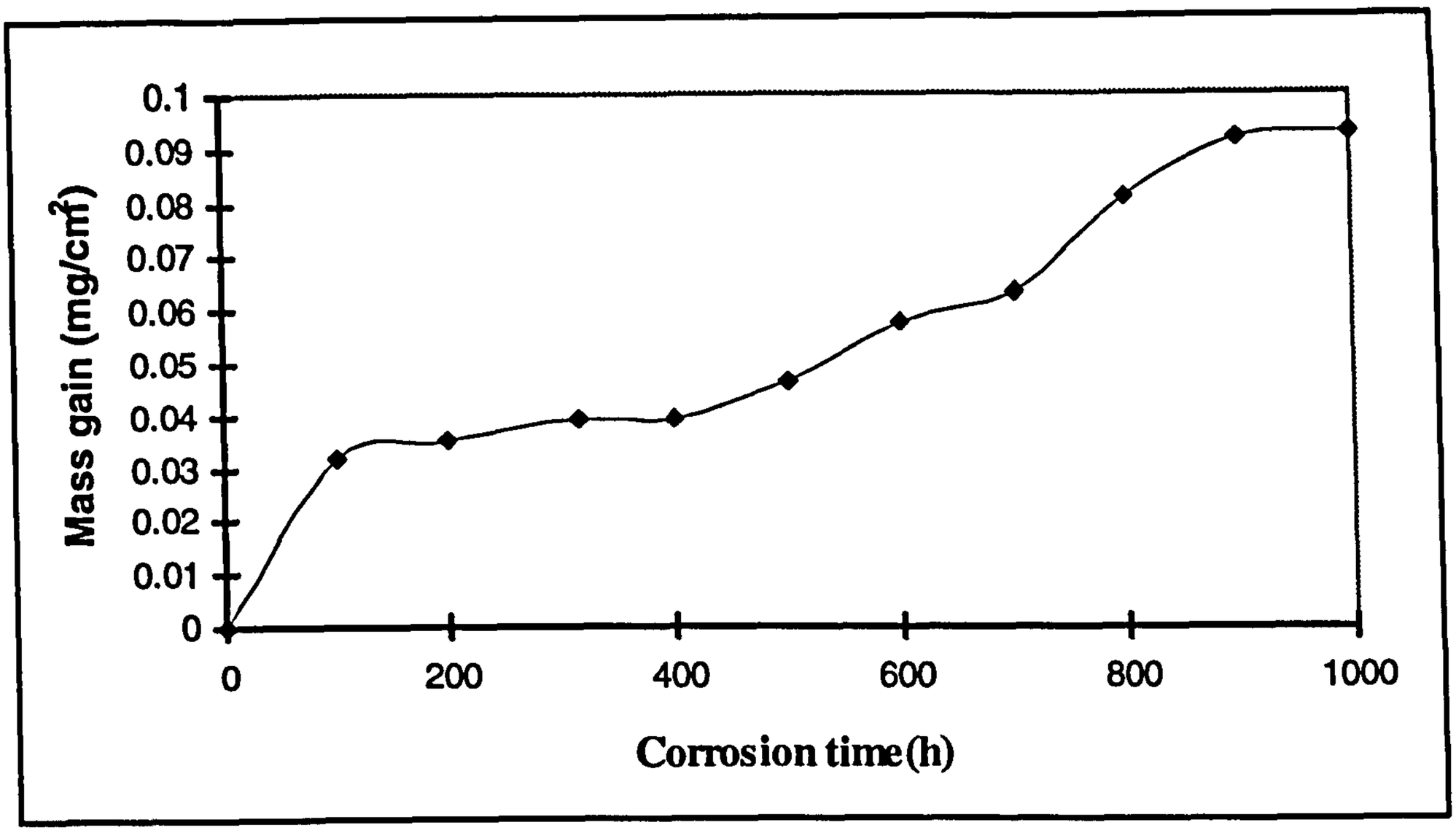

Figure A11: Hot salt corrosion behaviour of Ti-45Al-2Mn-2Nb after 1000h at 450°C in air.[0.0451 mg/cm^2]

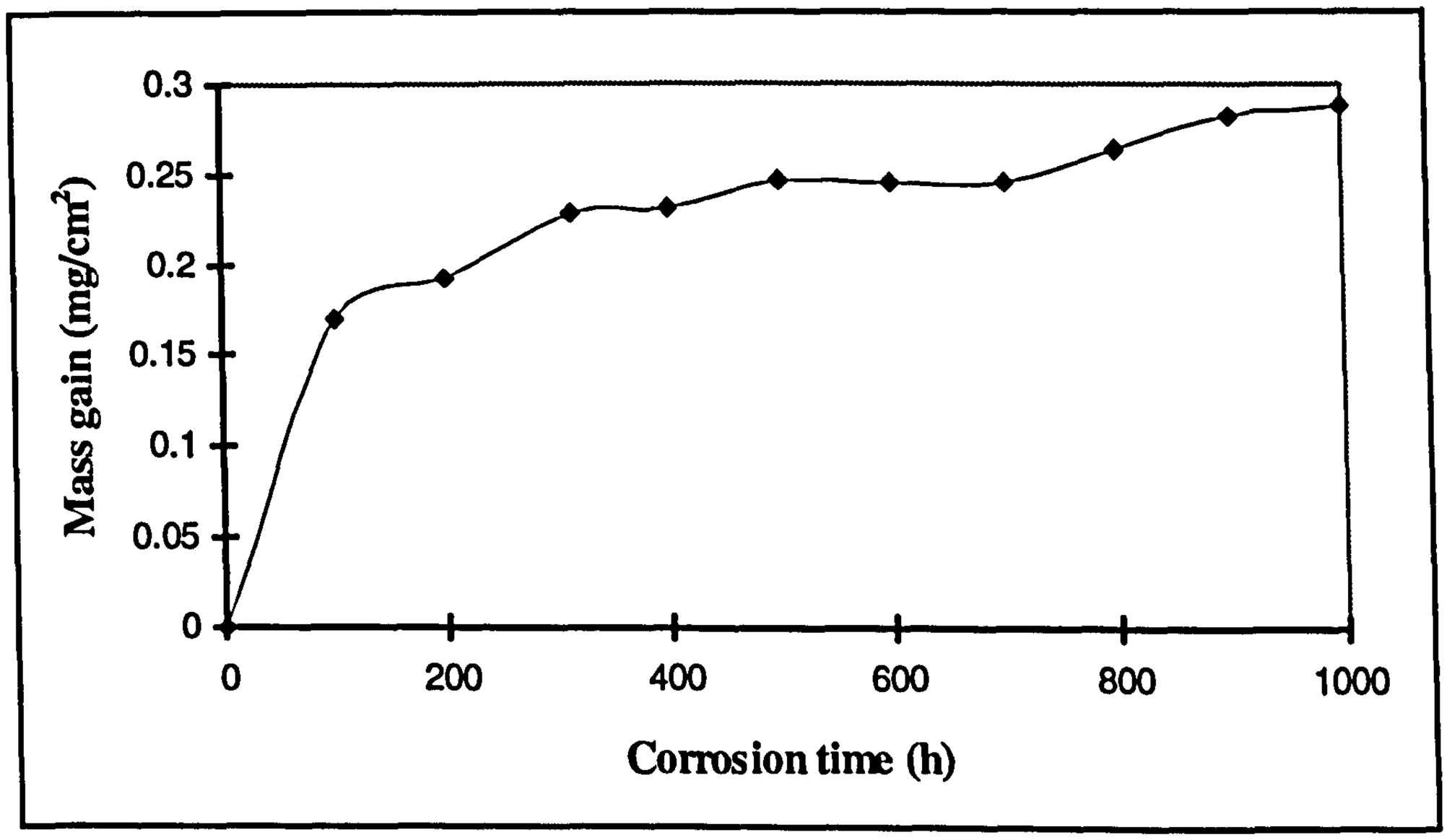

Figure A12: Hot salt corrosion behaviour of Ti-45Al-2Mn-2Nb after 1000h at 500°C in air.[0.0516 mg/cm^2]

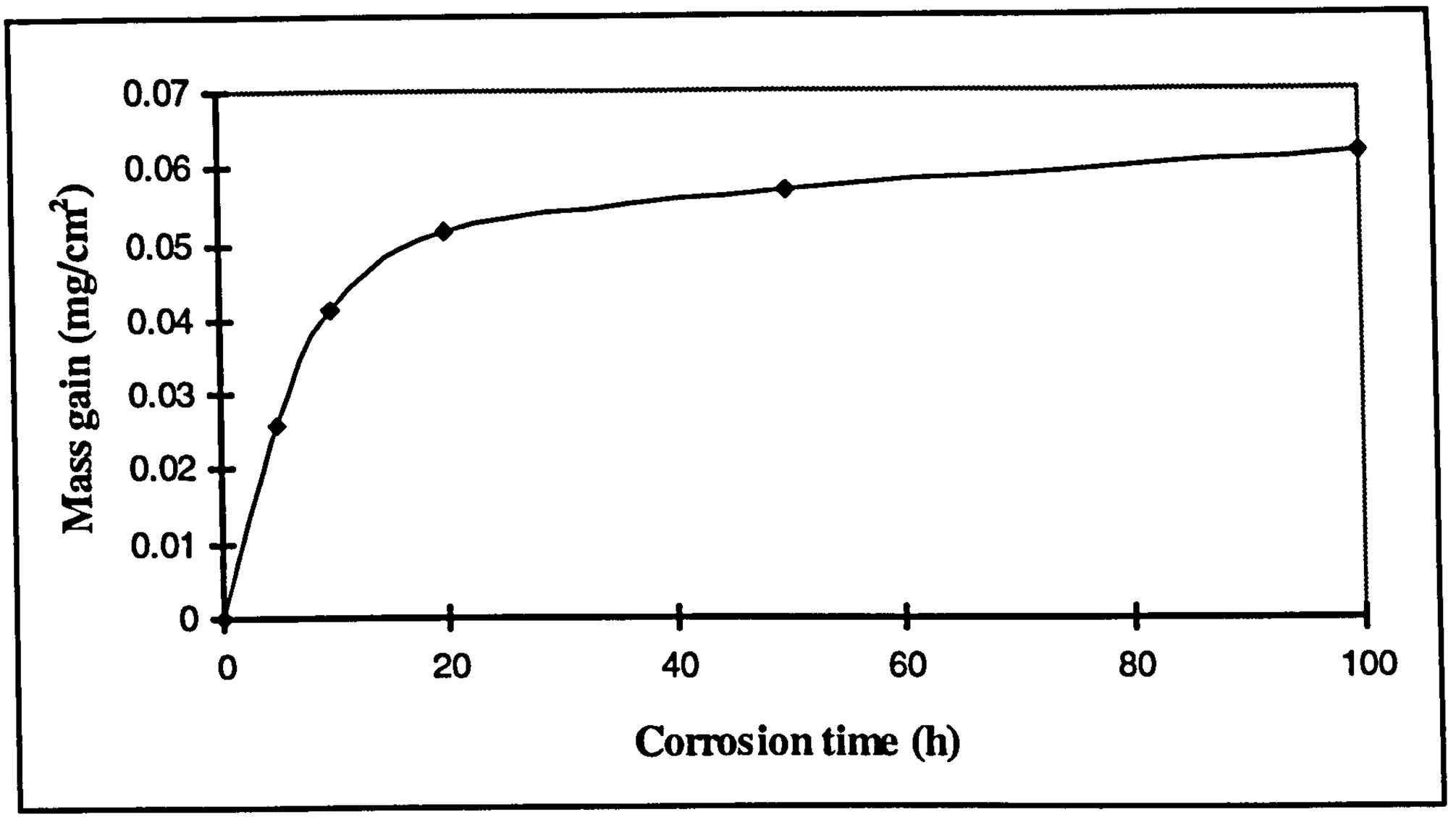

Figure A13: Hot salt corrosion behaviour of Ti-45Al-2Mn-2Nb after 100 h at 500°C in air.

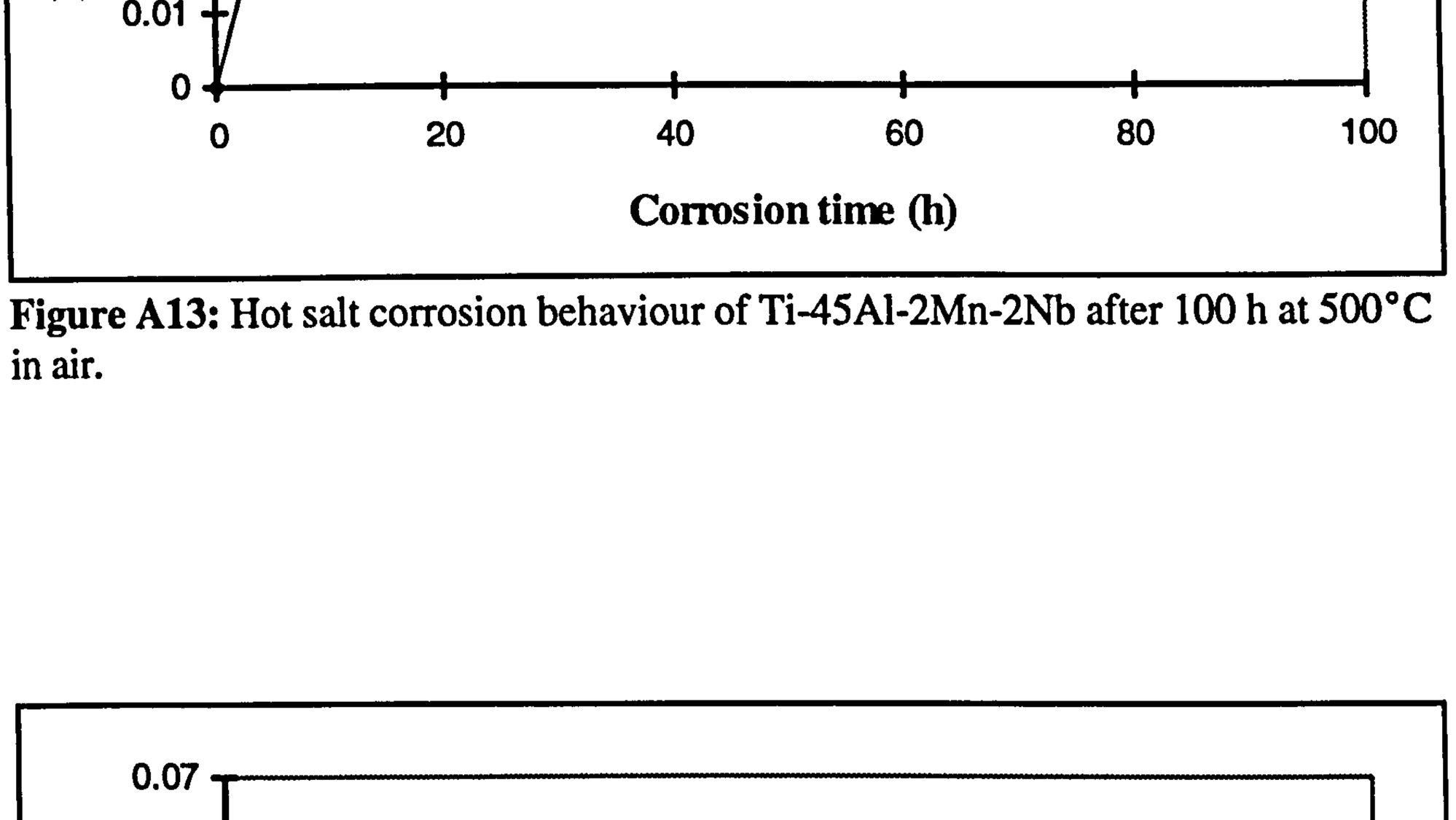

Figure A14: Hot salt corrosion behaviour of Ti-45Al-2Mn-2Nb after 100h at 550°C in air

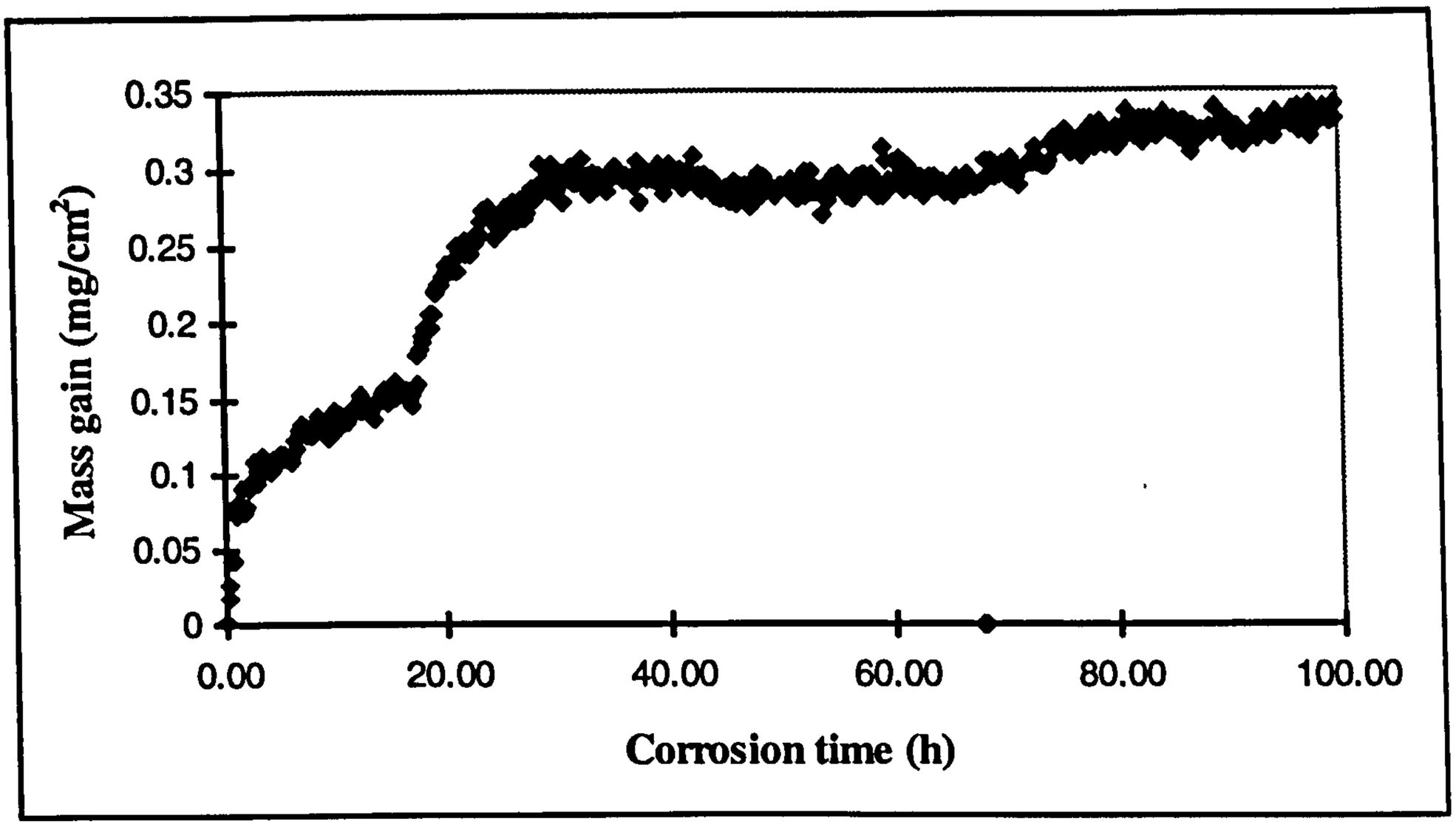

Figure 15: Hot salt corrosion behaviour of Ti-45Al-2Mn-2Nb after 100h at 600°C in air

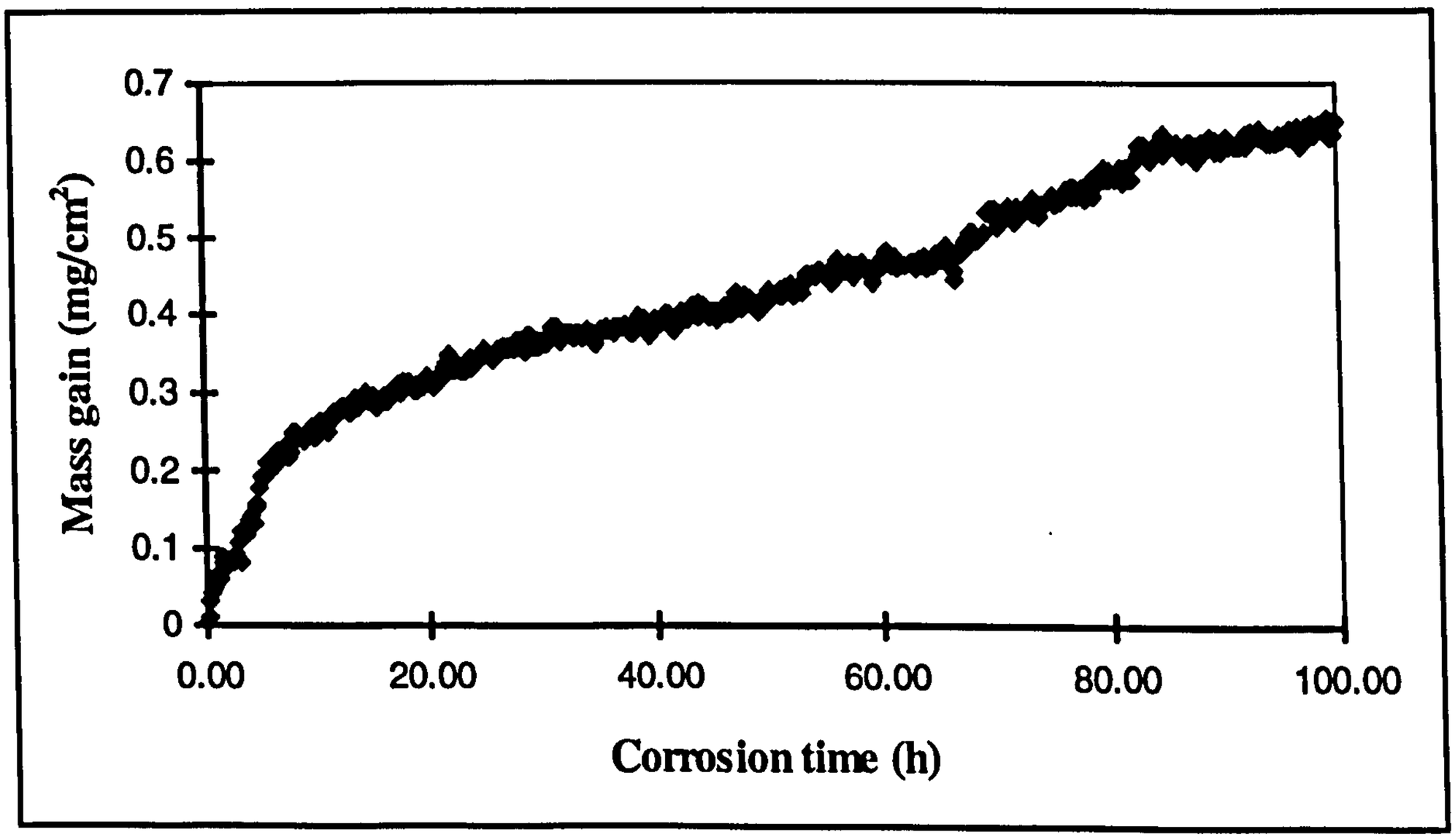

Figure A16: Hot salt corrosion behaviour of Ti-45Al-2Mn-2Nb after 100h at 650°C in air.

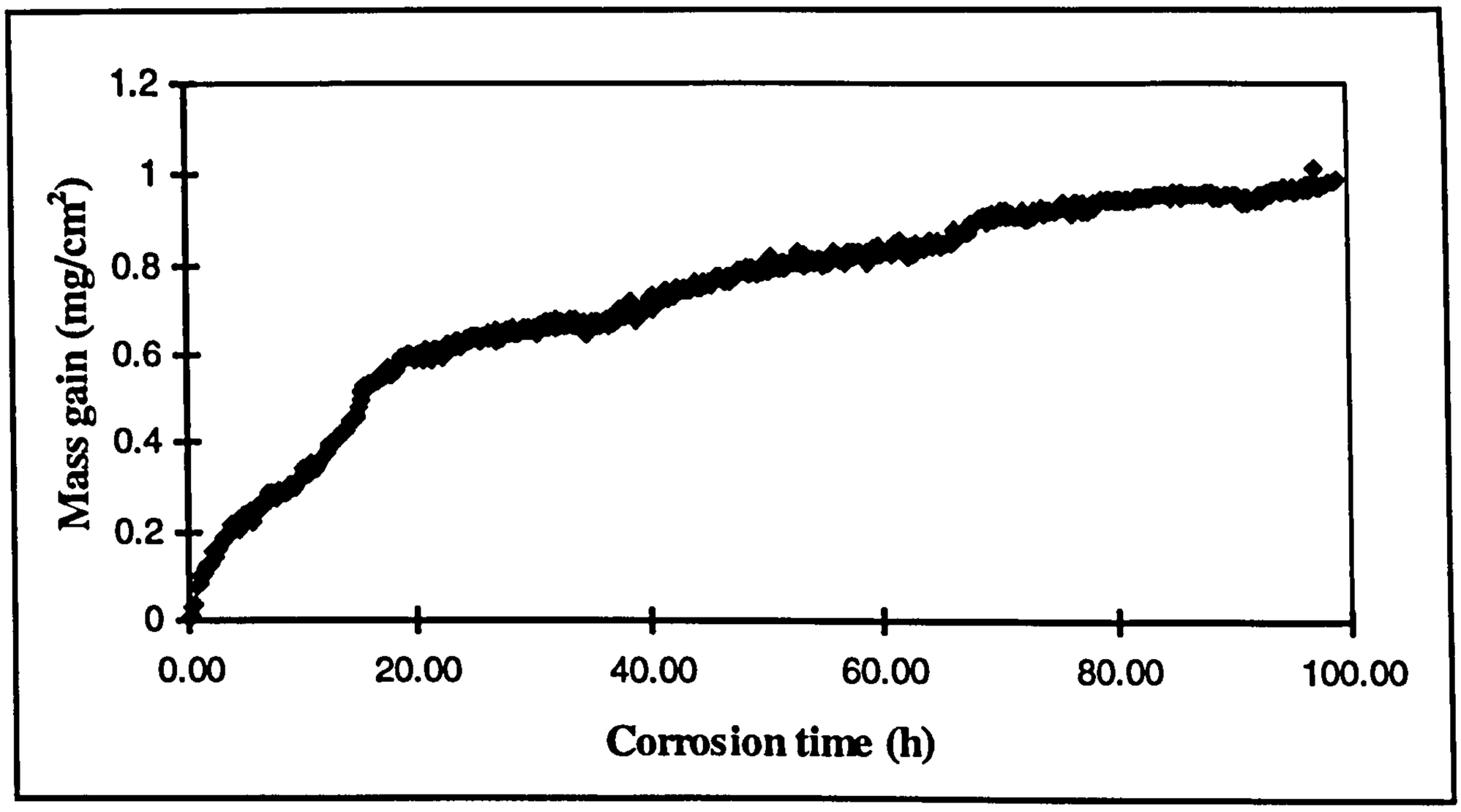

Figure A17: Hot salt corrosion behaviour of Ti-45Al-2Mn-2Nb after100h at 675°C in air.

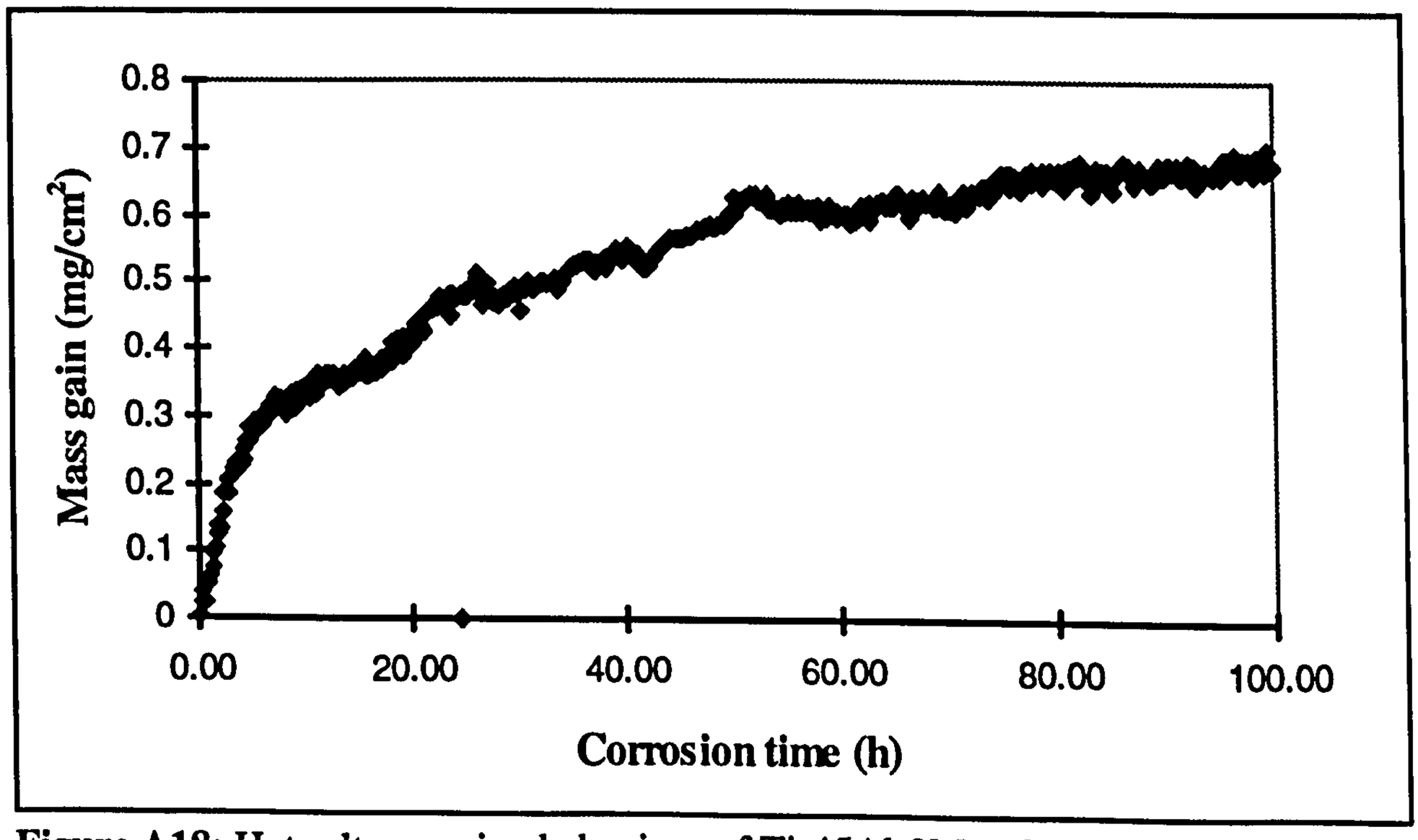

Figure A18: Hot salt corrosion behaviour of Ti-45Al-2Mn after 100h at 700°C in air. Test a

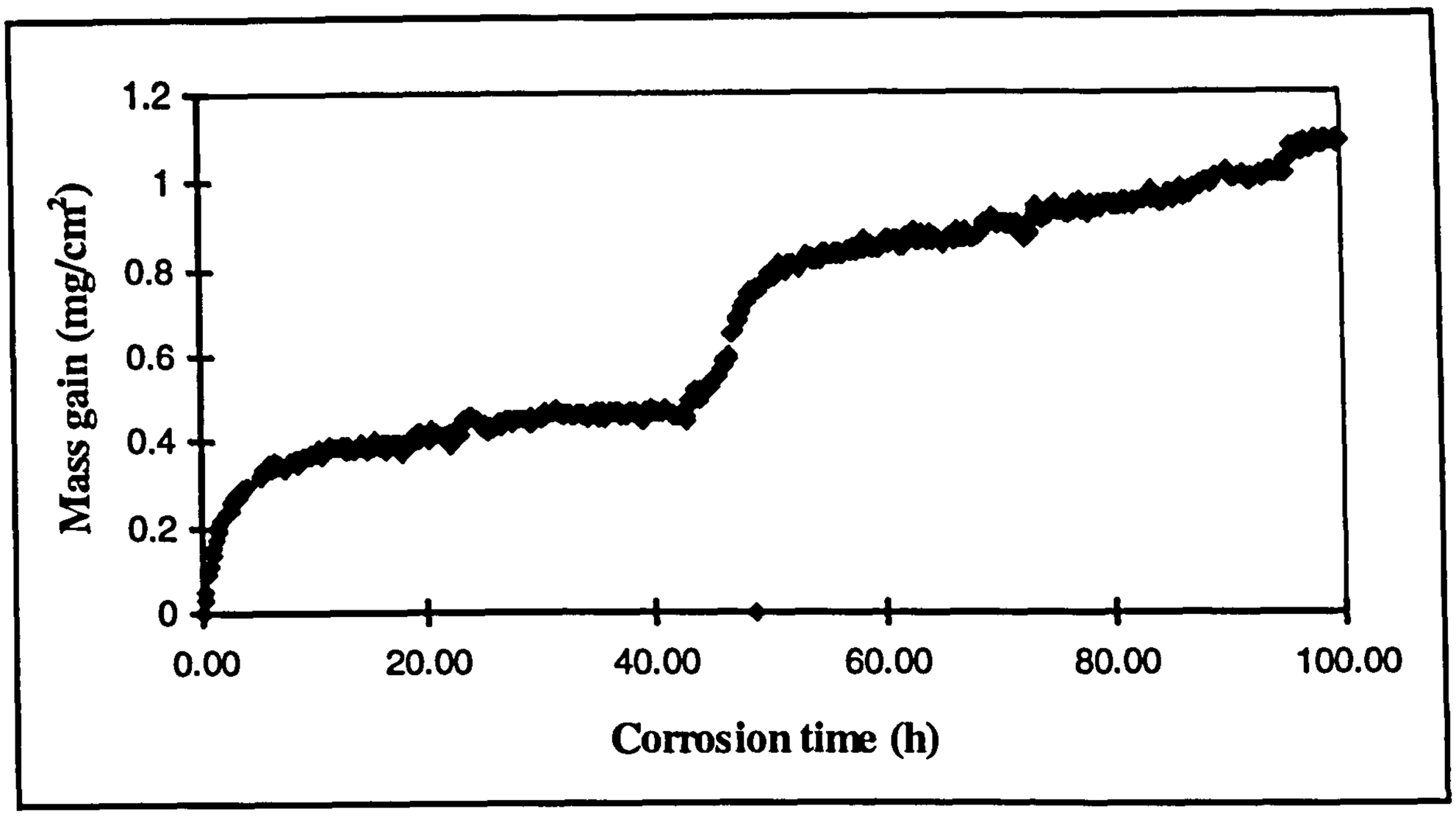

Figure A19: Hot salt corrsion behaviour of Ti-45Al-2Mn-2Nb after 100h at 700°C in air. Test b

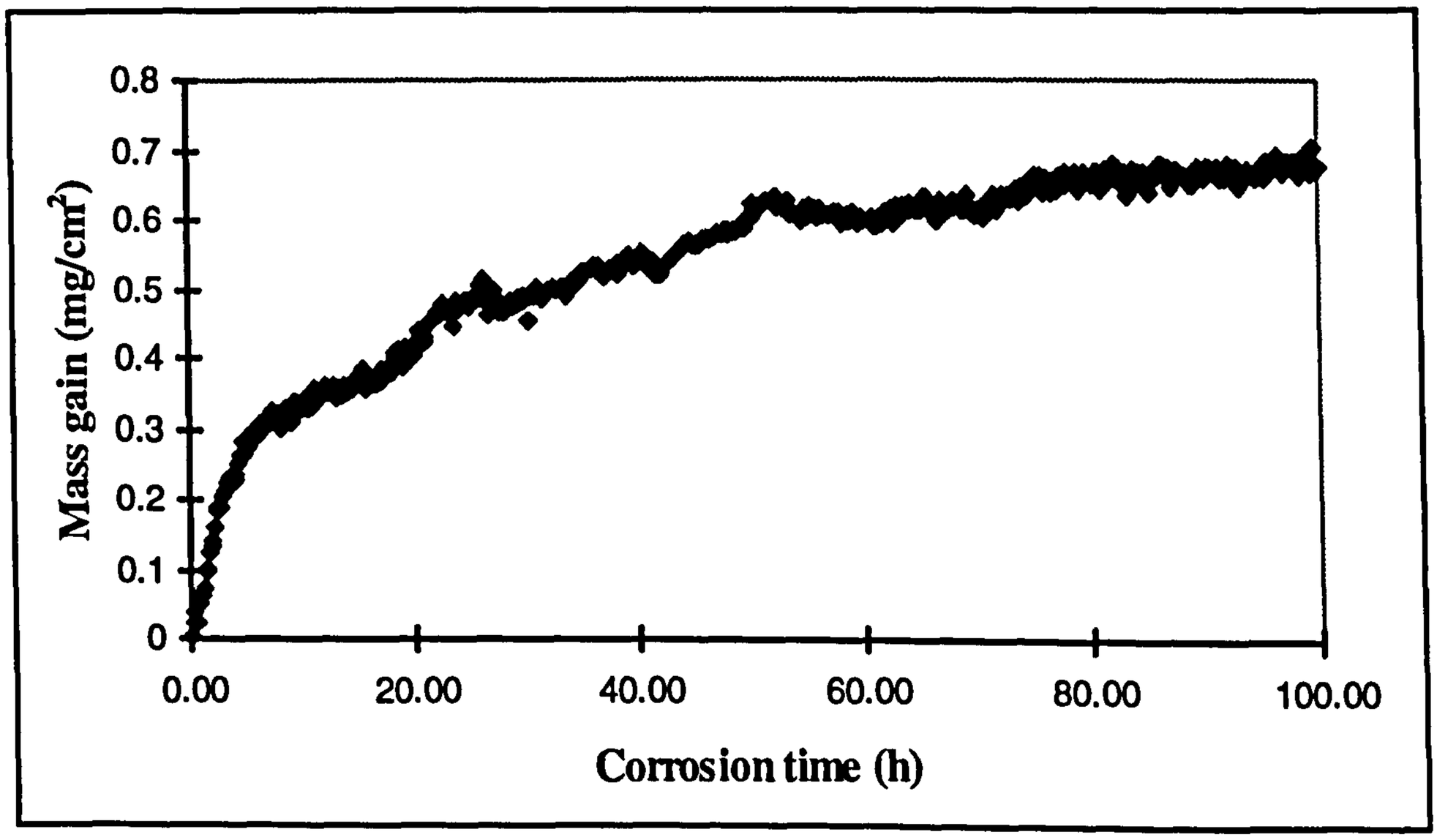

Figure A20: Hot salt corrosion behaviour of Ti-45Al-2Mn-2Nb after 100h at700°C in air. Test c

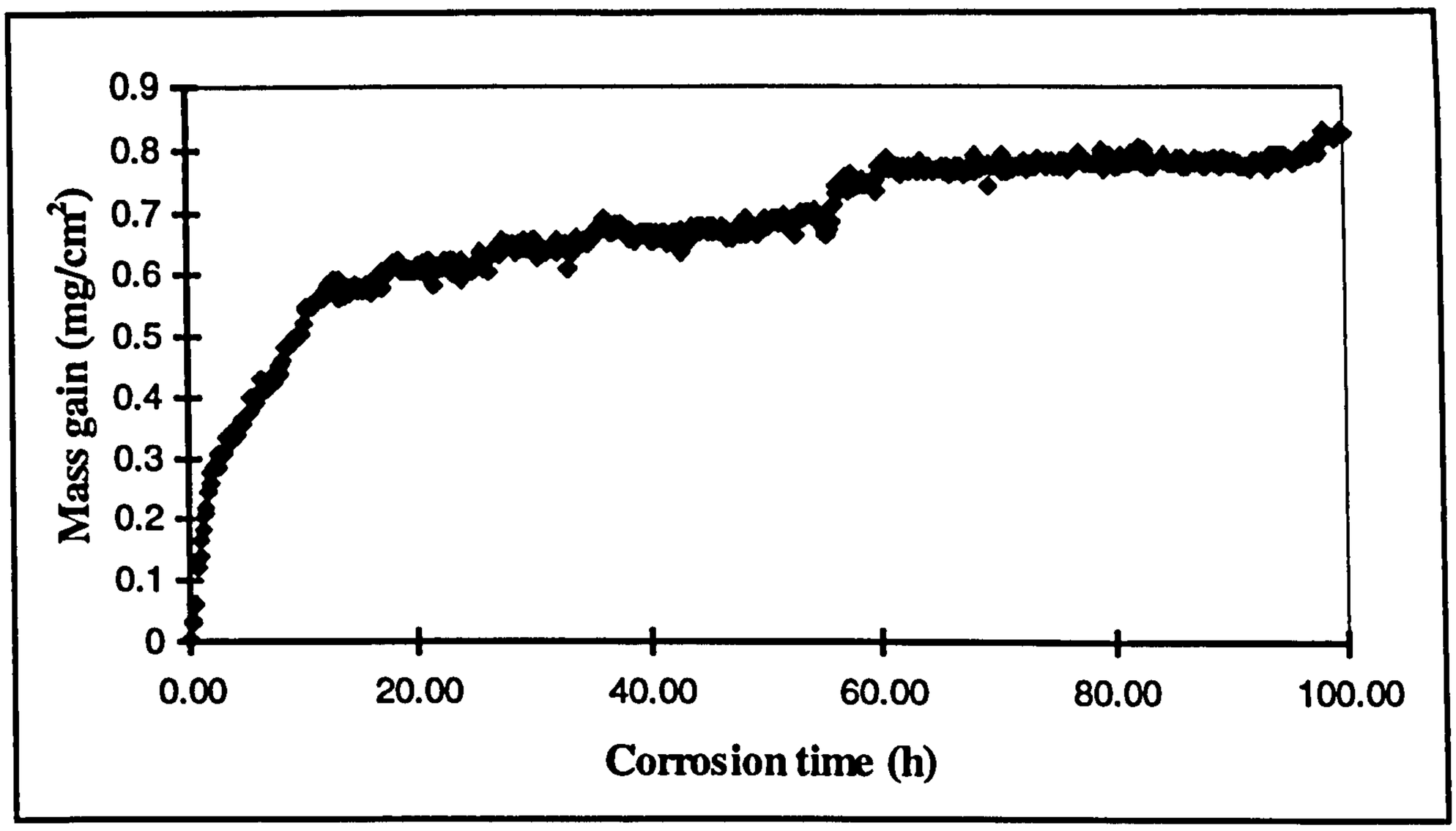

Figure A21: Hot salt corrosion behaviour of Ti-45Al-2Mn-2Mn after 100h at 725°C in air.

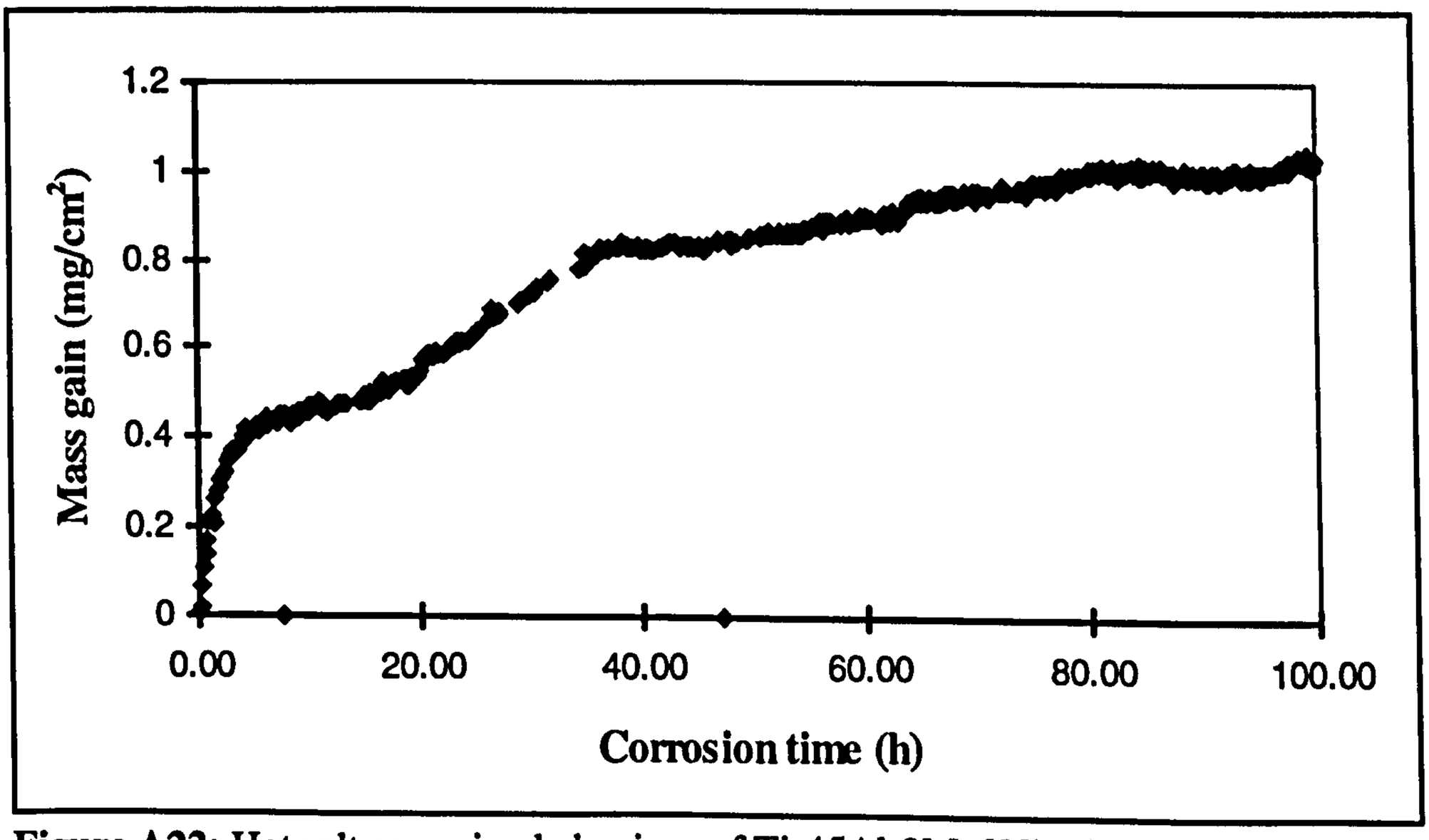

Figure A22: Hot salt corrosion behaviour of Ti-45Al-2Mn2Nb after 100h at 750°C in air.

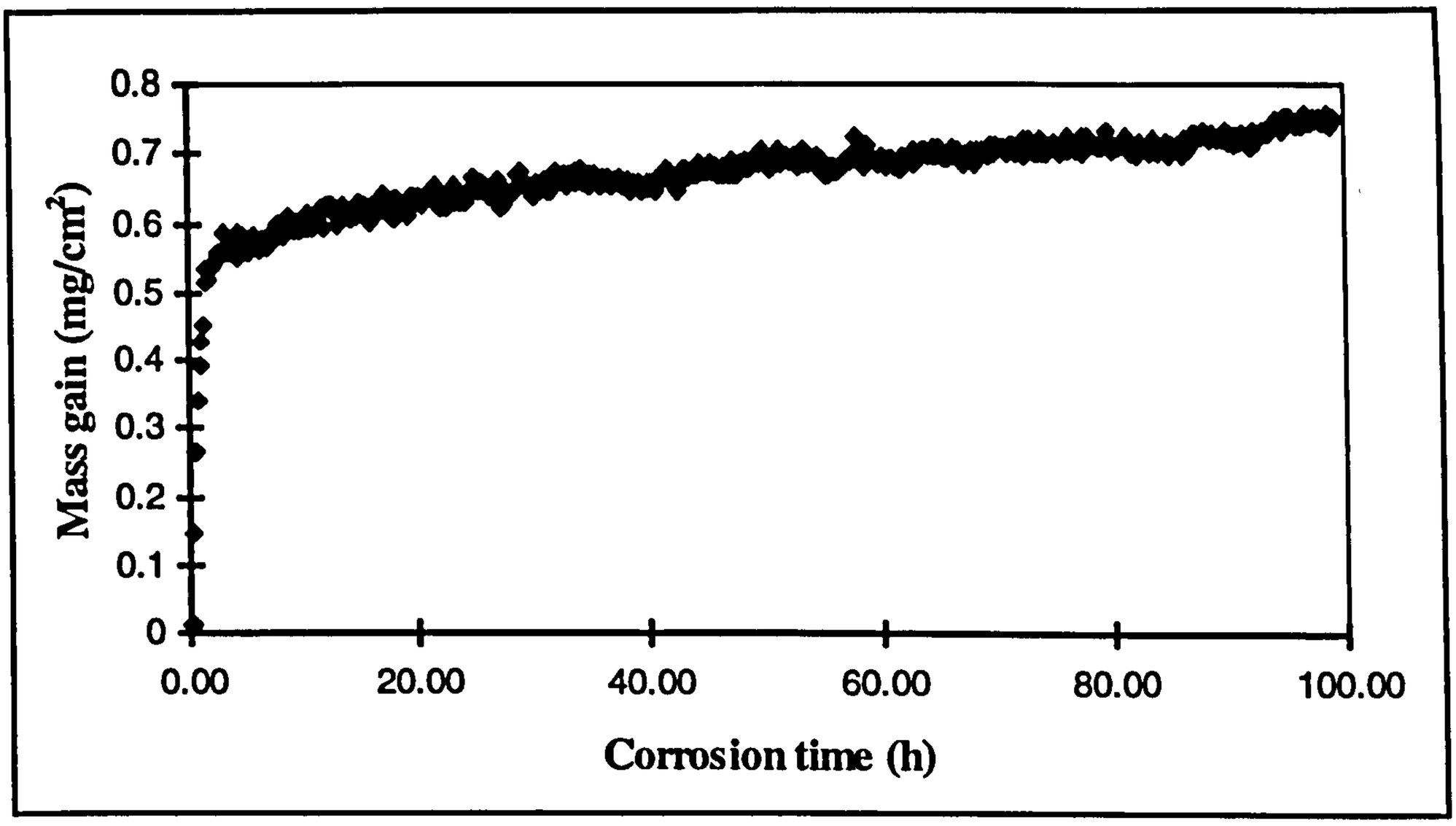

Figure A23: Hot salt corrosion behaviour of Ti-45Al-2Mn-2Nb after 100h at 800°C in air.

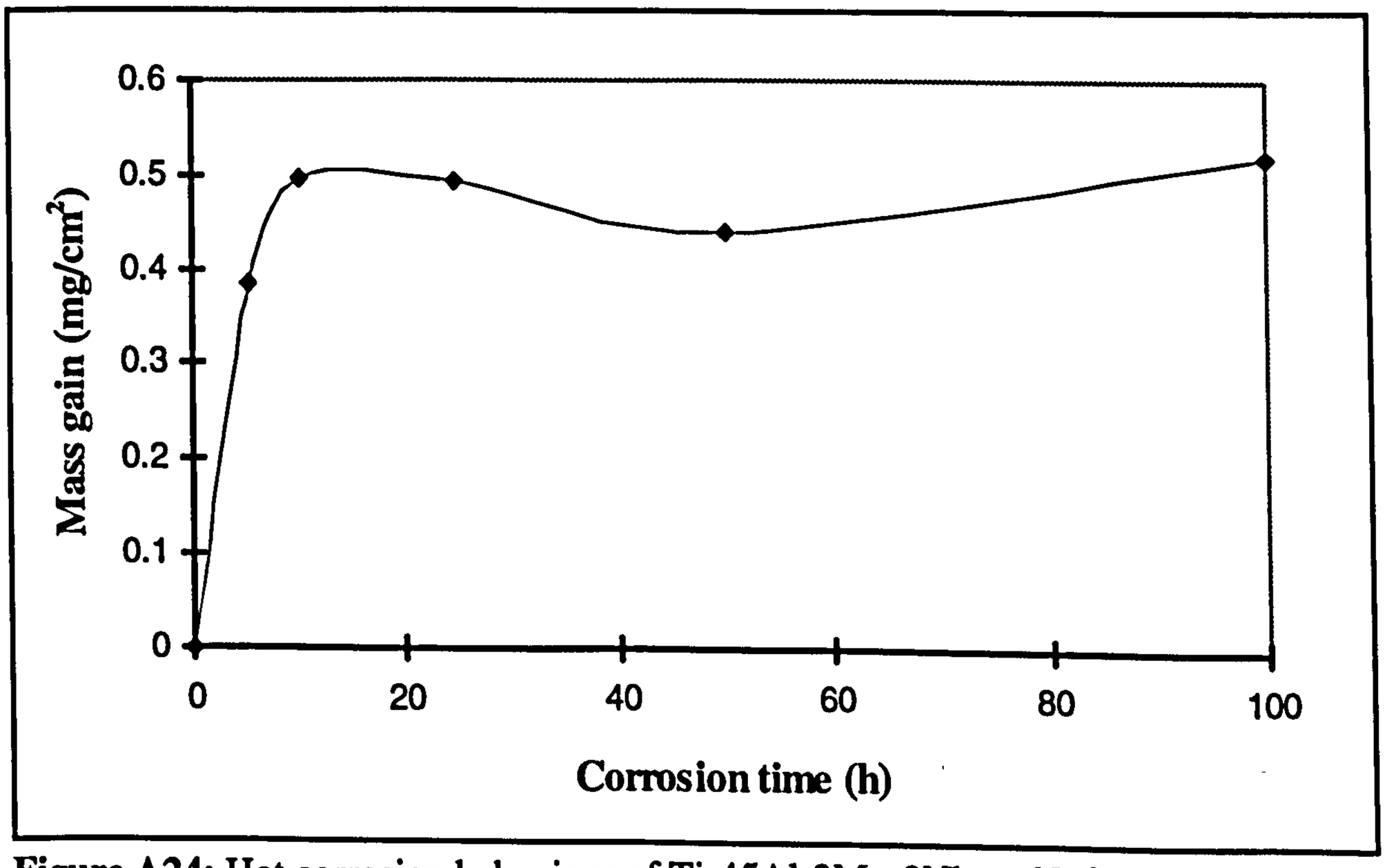

Figure A24: Hot corrosion behaviour of Ti-45Al-2Mn-2Nb at 650°C in air + 400ppm SO_2 .

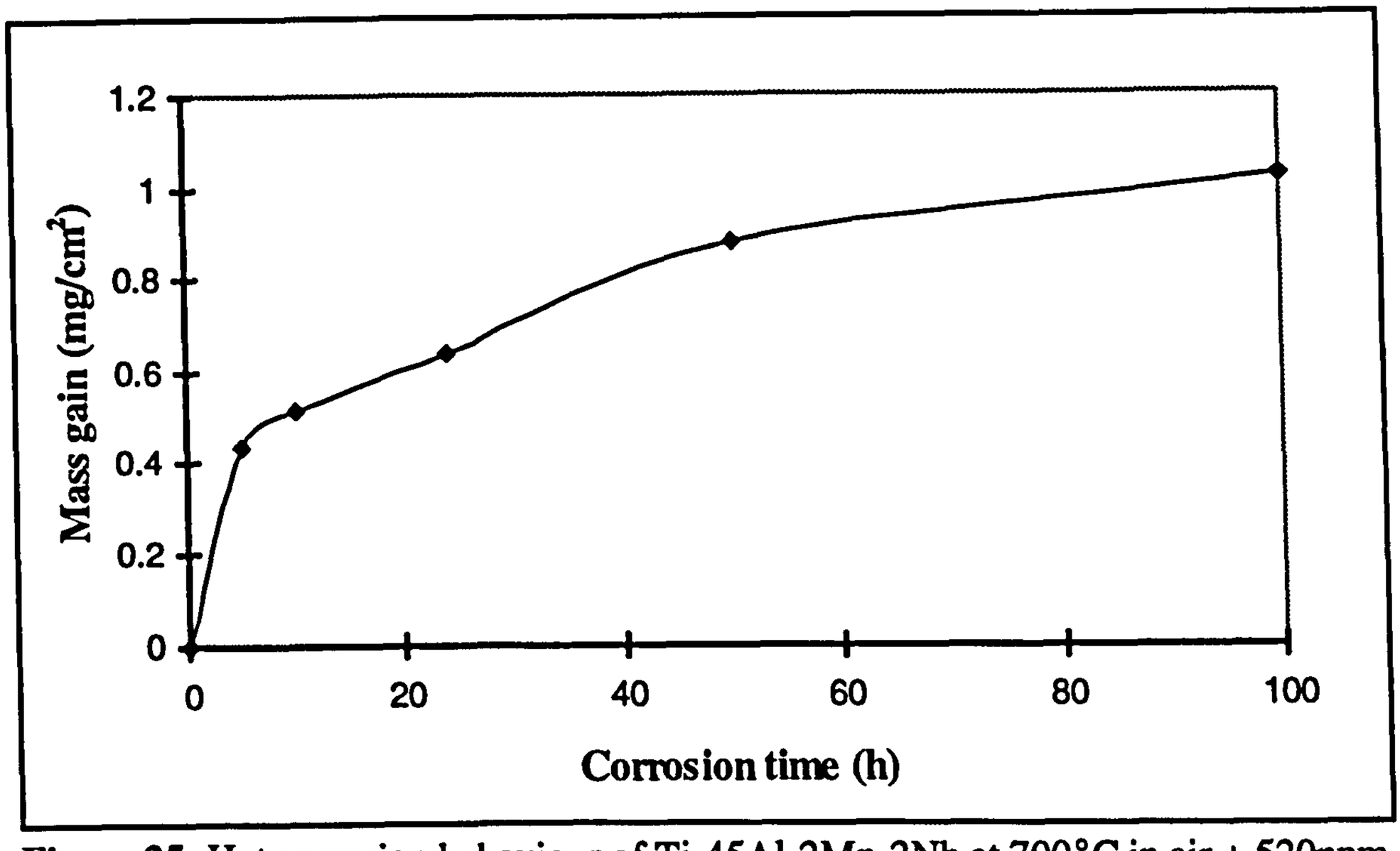

Figure 25: Hot corrosion behaviour of Ti-45Al-2Mn-2Nb at 700°C in air + 520ppm SO_2

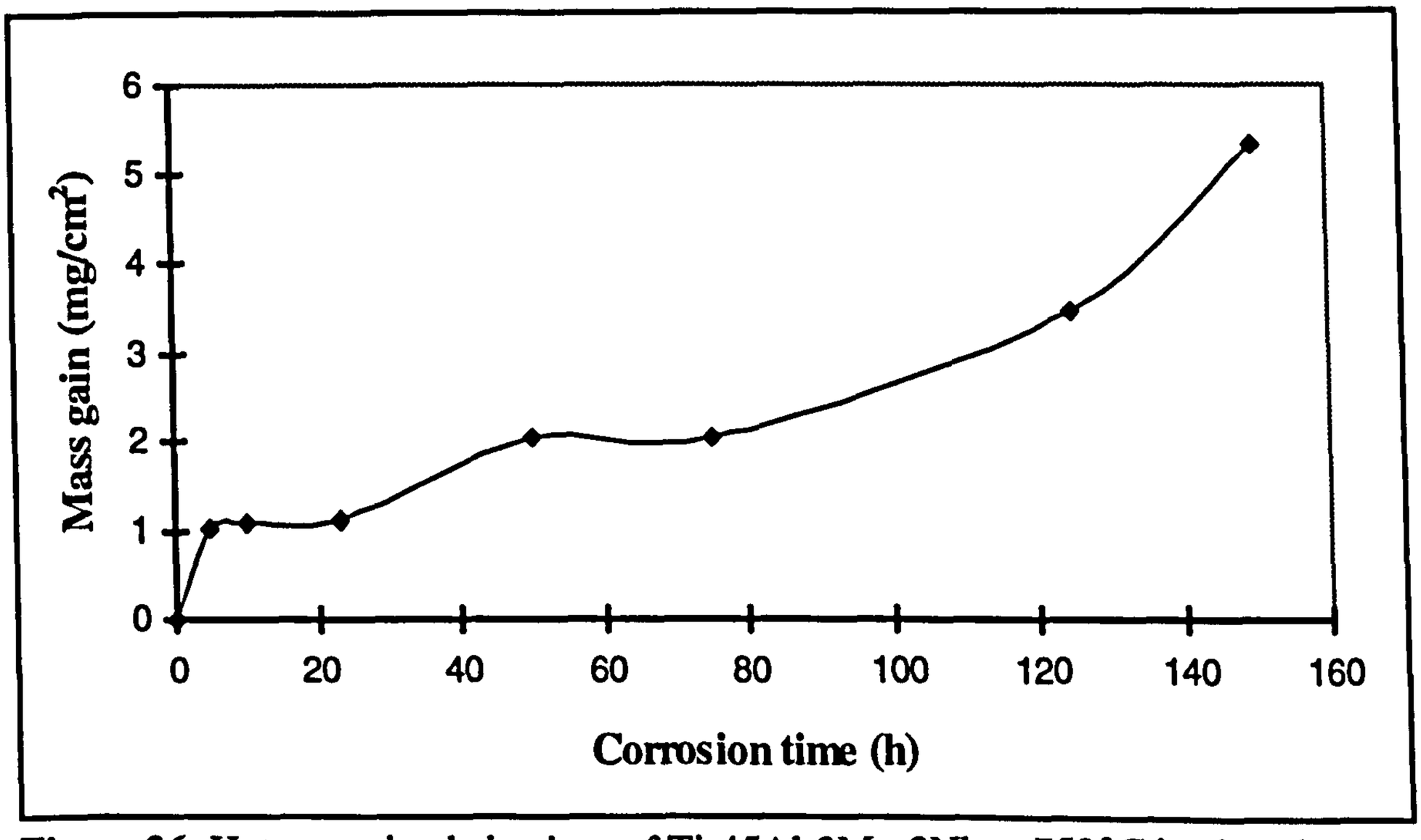

Figure 26: Hot corrosion behaviour of Ti-45Al-2Mn-2Nb at 750°C in air +plus 470ppm SO_2.

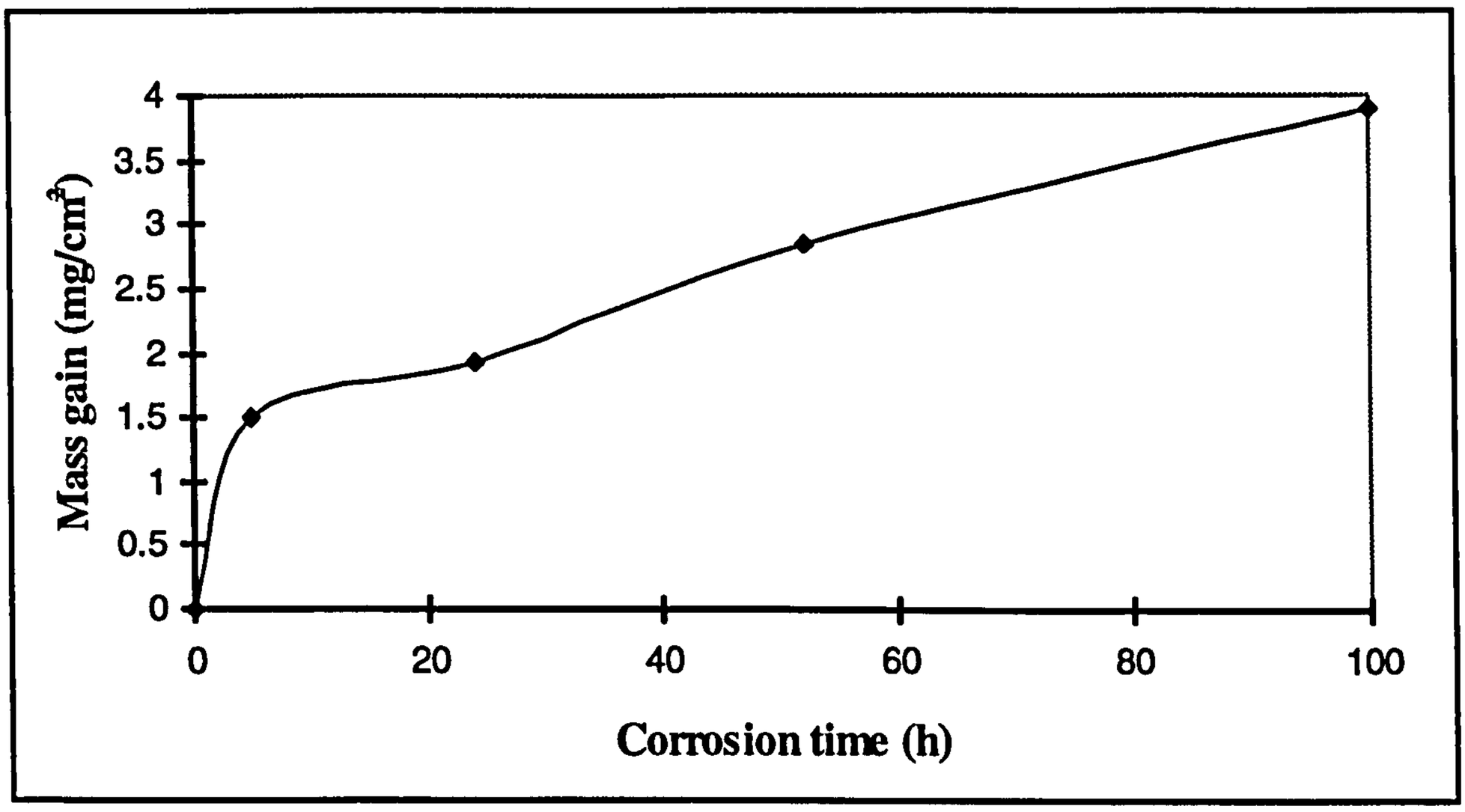

Figure 27: Hot corrosion behaviour of Ti-45Al2Mn-2Nb at 800°C in air + 470ppm SO_2.

References

(1) H.J.Engell, A.Von Keitz, G.Southoff, **Intermetallics-Fundamentals and Prospects,** Advanced Structural and functional Materials Symposium, 1991, p.91

(2) Y.W.Kim, **Ordered Intermetallic Alloys, Part III: Gamma Titanium Aluminides,** YOM, 1994, p.30

(3) S.Becker, M.Schutze, and A.Rahmel, **Cyclic-Oxidation Behaviour of TiAl and of TiAl Alloys,** Oxidation of Metals, Vol. 39, 1992, p.93

(4) G.Southoff, **State of Intermetallics Development,** Materials and Corrosion, Vol.47,1996, p.589

(5) R.Boyer, G.Welsch, E.W.Collins, **Materials Properties Handbook,** ASM International, June 1994

(6) Y-W.Kim, **Intermetallic Alloys Based on Gamma Titanium Aluminide,** JOM, July 1989, p.24

(7) Y-W.Kim, **Recent Advances in Gamma Titanium Aluminide Alloys,** Mat. Res.Symp.Proc., Vol.213, 1991, p.777

(8) H.A.Lipsit, **Titanium Aluminides-An Overview,** Mat.Res.Soc.Symp.Proc., Vol.39, 1985, p.351

(9) H.A.Lipsitt, **Titanium Aluminides-Future Turbine Materials,** Proc.of the Nicholas J.Grant Symposium, Processing and properties of advanced high temperature Alloys, 1985, p.157

(10) F.H.Frooes, C.Suryanarayana, D.Eliezer, **Review Synthesis, Properties and Applications of Titanium Aluminides,** J.Mater. Science, Vol.27, 1992, p.5113

(11) P.Kofstad, **High Temperature Oxidation of Metals,** John Wiley and Sons, Inc, 1966

(12) G.Ehrlich, **On the Kinetics of Chemisorption,** Journal of Physical Chemistry, Vol.59, 1955, p.473

(13) N.Cabrera and N.F.Mott, **Theory of the Oxidation of Metals,** Rept.Prog.Phys., Vol.12, 1948-1949, p.163

(14) N.F.Mott, **A Theory of the Formation of Protective Oxide Films on Metals,** Trans.Faraday Soc., Vol.35, 1939, p.1175

(15) T.B.Grimley and B.M.W.Trappnell, **The Gas/Oxide Interface and the Oxidation of Metals,** Proc.Roy.Soc.(London), Vol.A234,1956, p.405

(16) H.H.Uhlig, **Initial Oxidation Rate of Metals and The Logarithmic Equation,,** Acta Met. Vol. 4, 1956, p.541

(17) D.E.Davies, U.R.Evans, and J.N.Agar, **The Oxidation of Iron at 175 to 350°C,** Proc.Roy.Soc.(London), Vol. A225, 1954, p.443

(18) U.R.Evans, **The Corrosion and Oxidation of Metals,** Edward Arnold Ltd., London, 1960

(19) J.S.Anderson and K.J.Gallagher, in , **Reactivity of Solids,** Proc.4th International Symp. on the reactivity of solids, Edited by J.H.de Boer, Elsevier, Amsterdam, 1961, p.222

(20) C.Wagner, **Atom Movements,** Amer. Soc. Metals, Cleveland, 1951, p.153

(21) A.Atkinson, **Wagner Theory and Short Circuit Diffusion,** The Institute of Materials, 1988, p.1046

(22) E.A. Gulgransen, and T.P.Copan, Proc.European Conf.Electron Microscopy, Delft, Vol.1, 1961, p.225

(23) R.A.Rapp, **The High Temperature Oxidation of Metal forming Cation-Diffusing Scales,** Met. Trans.A, Vol.15A, 1984, p.765

(24) J.Markali, in **Mechanical Properties of Engineering Ceramics,** Edited by W.W.Kriegel and H.Palmour, Interscience, New York, 1963, p.93

(25) G.Pffiekorn, J.Vah, and K.Schur, Z.Elektrochem., Vol.66, 1962, p.717

(26) P.Kofstad, **High Temperature Corrosion of Metals,** Elsevier Pub., 1988

(27) M.P.Silva, **Oxidation of Aluminium-Magnesium Alloys at Elevated Temperatures in the Solid Semi-Solid and Liquid States,** PhD thesis, Brunel University, May 1987

(28) M.Schutze, **Protective Oxide Films and their Breakdown,** The Institute of Corrosion and Wiley, 1997

(29) A.M.Huntz, M.Schutze, **Stresses Generated During Oxidation Sequences and High Temperature Fracture,** Materials at high temperatures, Vol.12, Nos.2-3, 1994, p.151

(30) D.W.Mckee, S.C.Huang, **The Oxidation Resistance of Gamma-Titanium Aluminide Alloys Under Thermal**

Cycling Conditions, Corrosion Science Vol. 33, 1992, p.1899-1914

(31) A. Rahmel, W.J.Quadakkers, M.Schutze, **Fundamentals of TiAl Oxidation - A Critical Review, Materials and Corrosion**, Vol.46, 1995, p.271

(32) G.H.Meier, **Fundamentals of the Oxidation of High Temperature Intermetallics**, Oxidation of high temperature intermetallics, The Minerals, Metals and Materials Society, 1989, p.1

(33) A.Rahmel, P.J.Spencer, **Thermodynamic Aspects of TiAl and $TiSi_2$ Oxidation: The Al-Ti-O and Si-Ti-O Phase Diagrams**, Oxidation of Metals Vol.35, 1991, p.53

(34) S.Taniguchi, **Coatings for TiAl**, MRS Bulletin, 1994, p.31

(35) K.L.Luthra, **Stability of Protective Oxide films on Ti-Base Alloys**, Oxidation of metals, Vol.36, Nos.5/6, 1991, p.475

(36) U.Herold-Schmidt, B.Opolka, S.Schwantes, **The Oxidation Behaviour of TiAl Based High Temperature Materials**, Prakt. Metallogr., 30, 1993, p.344

(37) A.Takasaki, K.Ojima, Y.Taneda, T.Hoshiya, A.Mitsuhashi, **High Temperature Oxidation Process of Intermetallic Compound Ti-42 at% Al**, Journal Of Materials Science, Vol.28, 1993, p.1067

(38) G.Welsch, A.Kaveci, **Oxidation Behaviour of Titanium Aluminide Alloys**, The Minerals, Metals and Matcrials Society, Warrendale, 1988, p.207

(39) R.A.Rapp, K.T.Chiang, **Formation of Alumina on TiAl Alloys**, Scripta Metallurgica, Vol.21, 1987, p.1505

(40) K.E.Wiedemann, S.N.Sankaran, R.K.Clark, T.A.Wallace, **Static and Dynamic Oxidation of Ti-14Al-21Nb and Coatings**, The Minerals, Metals and Materials Society, Warrendale, 1988, p.195

(41) Y.Shida, H.Anada, **The Influence of Ternary Element Addition on the Oxidation Behaviour of TiAl Intermetallic Compound in High Temperature Air**, Corrosion Science, Vol.35, 1993, p.945

(42) G.Chen, Z.Sun, X.Zhou, **Oxidation of Intermetallic Alloys in Ti-Al-Nb Ternary Systems**, Corrosion, Vol.48, 1992, p.939

(43) U.Figge, A.Elschner, N.Zheng, H.Schuster, W.J.Quadakkers, **Surface Analytical Investigations on the Oxidation Behaviour of TiAl-base Intermetallics**, Frensenius J Anal Chem 346, 1993, p.75

(44) C.H.Koo, J.W.Evans, K.Y.Song, T.H.Yu, **High Temperature Oxidation of Ti,Al-Nb Alloys**, Oxidation of Metals, Vol.42, Nos.5/6, 1994, p.529

(45) S.N.Sankaran, R.K.Clark, J.Unnam, **Oxidation Characteristics of Ti-14Al-21Nb Alloy**, Nasa Technical Report (3012), 1990

(46) T.A.Wallace, R.K.Clark, S.A.Sankara, **Oxidation Characteristics of Ti-25Al-10Nb-3V-1Mo Intermetallic Alloy**, Nasa Technical Report (3044), 1990

(47) G.Welsch, S.L.Friedmann, A.I.Kakveci, **24 In Situ TEM Investigations of Titanium Aluminide Alloys**, Microscopy of Oxidation, p.193

(48) M.Bennett, J.A.Desport, P.A.Labun, In Proceedings of 43rd Annual meeting of the electron microscopy society of America, ed. G.W.Bailey, 1985, p.270

(49) R.F.Stroosnijder, N.Zheng, W.J.Quadakkers, R.Hofman, A.Gill, F.Langa, **The Effect of Ion Implantation on the Oxidation Behaviour of a γ-TiAl-based Intermetallic**, Oxidation of metals, Vol.46, Nos.1/2, 1996, p.19

(50) R.A Meier, D.Appalonia, **Oxidation of Titanium Base Alloys**, Oxidation of high Temperature Intermetallics, TMS/AIME publishers, The Minerals, Metals and Materials Society, 1989

(51) D.P.Whittle, **Oxidation Mechanisms for Alloys in Single Oxidant Gases**, International Corrosion conference, High temperature Corrosion, NACE-6, 1983, p.171

(52) S.A.Kekare, D.K.Shelton, P.B.Aswath, **Study of Oxidation Kinetics, Oxide scale, morphology and Composition in Binary TiAl base Alloys, Structural Intermetallics**, The minerals, Metals and Materials Society, 1993, p.325

(53) S.Becker, A.Rahmel, M.Schorr, and M.Schutze, **Mechanism of Isothermal Oxidation of the Intermetallic TiAl and of TiAl Alloys**, Oxidation of Metals 38, 1992, p.425

(54) S.Taniguchi, **Coatings for TiAl** , MRS Bulletin, 1994, p.31

(55) K.Maki, M.Shoda, M.Saayashi, T.Shimizu, S.Isobe, **Effect of Silicon and Niobium on Oxidation Resistance of TiAl Intermetallics**, Materials Science and Engineering, A153, 1992, p.591

(56) E.U.Lee, J.Waldman, **Oxidation of Two Phase (TiAl + Ti_3Al) Alloy**, Scripta Metallurgica, Vol.22, 1988, p.1389

(57) S.Becker, M.Schutze, and A.Rahmel, **Cyclic-Oxidation Behaviour of TiAl and of TiAl Alloys**, Oxidation of Metals 39, 1992, p.93

(58) J.Subrahmanyam, **Cyclic Oxidation of Aluminised Ti-14Al-24Nb Alloy**, Journal of Materials Science, Vol.23, 1988, p.1907

(59) G.Meier, **A Review of Advances in High Temperature Corrosion**, Materials Science and Engineers, A120, 1989, p.1

(60) K.N.Strafford, and P.K.Datta, **Design of Sulphidation Resistant Alloys, Minerals Science and Technology**, Vol.5, 1989, p.765

(61) K.N.Strafford and P.K.Datta, **Progress in the Design of Sulphidation Resistant Alloys**, Corrosion Science, Vol.35, Nos 5-8, 1993, p.1053-1063

(62) S.Mrowec, **The Problem of Sulfur in High-Temperature Corrosion**, Oxidation of Metals, Vol.44, Nos.1/2, 1995, p.177

(63) S.Mrowec and K.Przybylski, **Transient Properties of Sulfide Scales and Sulfidation of Metals and Alloys**, Oxidation of Metals, Vol.23, Nos.3/4, 1985, p.107

(64) S.Mrowec, T.Werber, M.Zastawnik, **The Mechanism of High Temperature Sulphur Corrosion of Nickel-Chromium Alloys**, Corrosion Science, Vol.6, 1966, p.47

(65) K.N.Strafford and K.Upadhya, **The Kinetics and Mechanism of the Attack of MCr-Type Alloys in Oxygen-Sulphur Environments at 700°C**, Proc.JIMIS-3, High Temperature Corrosion Transactions of the Japan Institute of Metals, 1983, p.481

(66) S.Mrowec, **The Function of Sulphur in High Temperature Corrosion of Metals and Alloys**, OCHR.PRZED KOROZ, Vol.24, 1981, p.169

(67) P.Hancock, **The Corrosion of Nickel-Chromium Alloys in Sulphur-containing Atmospheres at High Temperatures**, p.193

(68) M.R.Wootton and N.Birks, **The Oxidation of Nickel Chromium Alloys in the Atmospheres Containing Sulphur Dioxide**, Corrosion Science, Vol.15, 1975, p.1

(69) H.L.Du, P.K.Datta, D.B.Lewis, J.S.Burnell-Gray, **High Temperature Corrosion of Ti and Ti-6Al-4V Alloy**,

Oxidation of Metals, Vol.45., Nos.5/6, 1996, p.507

(70) H.L.Du, P.K.Datta, D.B.Lewis, J.S.Burnell-Gray, **Enhancement of Oxidation/Sulphidation Resistance of Ti and Ti-6Al-4V Alloy by HfN Coating**, Mat.Eng.A, A205, 1996, p.199

(71) F.S.Pettit and C.S.Giggins, in **Supperalloys II, High Temperature Materials for Aerospace and Industrial Power**, C.T.Sims et al.Eds. 1986, p.327-358

(72) V.A.C.Haanappel, T.Fransen, and P.J.Gellings, **High Temperature Material and Processes**, Vol.19, No. 2,1992, p.67-89

(73) M.J.McNallan, W.W.Liang, S.H.Kim, C.T.Kang, **Acceleration of the High Temperature Oxidation of Metals by Chlorine**, High temperature corrosion, NACE-6, International corrosion conference, 1983, p.316

(74) Al-Khjatt, **High Temperature Chloride induced Corrosion of Nickel and Nickel based Alloys, PhD thesis,** Cranfield Institute of Technology, August 1991

(75) M.Yoshiba and O.Miyagawa, **High Temperature Materials for Power Engineering,,** Proceedings of a Conference held in Liege, Belgium, 1990, p.24-27

(76) P.Hancock, **Vanadic and Chloride Attack of Superalloys**, Materials Science and Technology, Vol.3, 1987, p.536

(77) P.Hancock, R.C.Hurst, A.R.Sollars, **Influence of Chloride Contamination of the Atmosphere on the Mechanism of Oxidation of Iron**, Proc.Interat Symposium on Chemical Metallurgy of Iron and Steel, 1973, p.415

(78) P.Dumas, C.St.John, **NaCl-Induced Accelerated Oxidation of a Titanium Alloy**, Oxidation of Metals, 1975, p.127

(79) T. Chevrot, **Pressure Effects on the Hot-Salt Stress-Corrosion Cracking of Titanium Alloys**, PhD Thesis, Cranfield University, March 1994

(80) H.L.Logan, **The Mechanisms of Stress- Corrosion of the Titanium Alloy Ti-1-1 Exposed to Salt Environments at Elevated Temperatures**, National bureau of standards, R-130, May 1964

(81) S.P.Rideout, **The Initiation of Hot-Salt Stress-Corrosion Cracking of Titanium ALloys**, in Applications related phenomena in titanium alloys, ASTM STP432, 1968, p. 205

(82) M.Garfinkle, **An Electrochemical Model for Hot-Salt Stress-Corrosion of Titanium Alloys**, NASA TN D-6779, 1972

(83) S.P.Rideout, R.S.Ondrejcin, M.R.Louthan, D.E.Rawl, **The Role of Moisture and Hydrogen in Hot-Salt Cracking of Titanium Alloys**, Symposium of fundamental aspects of stress corrosion cracking , Ohio State University, September 1967

(84) A.J.Hatch, H.W.Rosenberg, E.F.Erbin, **Effects of Environment on Cracking of Titanium Alloys**, in Stress-Corrosion Cracking in Titanium, ASTM STP397, 1966, p.122

(85) F.A.Crossley, C.J.Reichel, C.R.Simcoe, **The Determination of the Effects of Elevated Temperatures on the Stress-Corrosion Behaviour of Structural Materials**, WADD technical report 60-191, 1960

(86) Z.Yao, **NaCl-Induced Hot Corrosion of a Titanium Aluminide Alloy**, PhD thesis, Georgia Institute of Technology, February 1995

(87) Y.Shinata, **Accelerated Oxidation Rate of Chromium Induced by Sodium Chloride**, Oxidation of Metals, No.27, 1987, p.315

(88) M.DeCrescente, N.S.Bornstein, **Formation and Reactivity Thermodynamics of Sodium Sulphate with Gas Turbine Alloys**, Corrosion, Vol.24, 1968, p.127

(89) P.Hancock, **The Role of Halides in High Temperature Gas Corrosion**, Proceedings of the symposium on high temperature halide chemistry., The electrochemical society, 1978, p.645

(90) C.S.Giggins, F.S.Pettit, **Hot Salt Corrosion Degradation of Metals and Alloys-A Unified Theory**, Pratt and Whitney report FR-11545

(91) J.A.Goebel, F.S.Pettit, G.N.Goward, **Mechanism for the Hot Corrosion of Nickel Based Alloys**, Met.Trans., Vol.4, 1973, p.261

(92) R.A.Rapp, K.S.Goto, **The Hot Corrosion of Metals by Molten Salts, in Molten Salts**, Electrochemical Society, 1981, p.81

(93) R.A.Rapp, K.S.Goto, M.Kawakami, **Accelerated Oxidation (Hot Corrosion) of Alloys by Molten Salts**, Trans.Iron Steel Inst.JPN, Vol.20, 1980, p.646

(94) D.A.Shores, D.W.McKee, K.L.Luthra, **The Effect of SO_2 and NaCl on High Temperature Hot Corrosion**,

Journal of the Electrochemical Society, 1978, p.411

(95) D.A.Shores, **New Perspective on Hot Corrosion Mechanisms**, High Temperature Corrosion, National Association of Corrosion Engineers, 1981, p.493

(96) P.Hancock, R.C.Hurst, J.Johnson, M.Davies, **Deposition and Corrosion in Gas Turbines**, Applied Science publishers, 1978

(97) J.B.Johnson, J.R.Nicholls, R.C.Hurst, P.Hancock, **The Mechanical Properties of Surface Scales on Nickel Base Superalloys -II. Contaminant Corrosion**, Corrosion science, Vol.18, 1978, p. 543

(98) M.K.Hossain, S.R.J.Saunders, **A Microstructural Study of the Influence of NaCl Vapour on the Oxidation of a Ni-Cr-Al Alloy at 850°C**, Oxidation of Metals, Vol.12, No.1, 1978, p.1

(99) M.K.Hossain, J.E.Rhoades-Brown, S.R.J.Saunders, **The Effect of HCl and NaCl on Hot Corrosion**, Proc.Inter. Conf., The metal society, 1979, p.483

(100) R.L.Jones, K.H.Stern, M.L.Deanhardt, J.C.Halle, 4th UK Conf. On gas turbine materials in a marine environment, 1979

(101) D.A.Shores, K.L.Luthra, **A Study of the Mechanism of Hot Corrosion in Environments Containing NaCl**, Final report, Naval Research Laboratory, Contract N00173-77-C-0253, General Electric Research and Development Laboratory, 1979

(102) K.L.Luthra, **Low Temperature Hot Corrosion of Cobalt-base ALloys. Part 1- Morphology of the Reaction Product**, Met.Trans.A., Vol.13A, 1982, p.1843

(103) K.T.Chiang, F.S.Pettit, G.H.Meier, **Low Temperature Hot Corrosion**, International Corrosion Conference on High temperature Corrosion, NACE-6, 1983, p. 519

(104) J.R.Nicholls, **Discontinuous Measurements of High Temperature Corrosion**, in Guidelines for Methods of Testing and Research in High Temperature Corrosion, The Institute of Materials, 1995, p.11

(105) N.Birks and G.H.Meier, **Introduction to High Temperature Oxidation of Metals**, Edward Arnold, London, 1983

(106) H.J.Grabke, W.Auer, M.J.Bennett et al, **Points to be Considered in Thermogravimetry**, Werkstoffe und Korrosion, Vol.44, 1993, p.345

(107) H.J.Grabke, **Thermogravimetry**, in Guidelines for Methods of Testing and Research in High Temperature Corrosion, The Institute of Materials, 1995, p.52

(108) A.Tomasi, S.Gialanella, P.G.Orsini, M.Nazmy, **Oxidation Behaviour of Intermetallic Compounds Based on Ti-Al System**, MRS Fall Meeting, Boston, 1994

(109) M.Bennet, Private comunication, 1996

(110) H.Davies, **MTData program**, constructed Phase Stability Diagrams, National Physics Laboratory, July 1997

(111) V.C.Petersen, H.B.Bomberger, **The mechanism of Salt Attack on Titanium Alloys,** in Stress Corrosion Cracking of Titanium, ASTM, STP397, 1966, p.80

(112) G.Martin, **Investigation of Long-Term Exposure Effects under Stress of two Titanium Structural Alloys,** in Stress Corrosion Cracking of Titanium, ASTM, STP396, 1966, p.95

(113) V.V.Travkin, V.F.Pshirkov, B.A.Kolashev, **Thermodynamic Analysis of the Chemical Mechanism for the Hot Salt Corrosion of Titanium Alloys**, Sov.Mater.Sci., Vol.15, 1979, p.134

(114) S.P.Ridout, S.P.Louthan, C.L.Selby, **Basic Mechanisms of Stress-Corrosion Cracking of Titanium, in Stress-Corrosion Cracking of Titanium**, ASTM, STP397, 1966, p.137

(115) P.Hancock, **The Use of Laboratory and Rig Tests to Simulate Gas Turbine Corrosion Problems**, Corrosion Science, Vol.22, 1982, p.51

(116) J.G.Tschinkel, **Formation of Sodium Sulphate in Gas Turbine Combustors**, Corrosion, Vol.28, 1972, p.161

(117) Bauer, cited in W.K.Boyd, and F.W.Fink, **The Phenomenon of Hot Salt Stress Corrosion of Titanium alloys,** NASA CR-117, 1964

(118) R.L.Ashbrook, **A Survey of Salt Deposits in Compressors of Flight Gas Turbine Engines,** NASA TN D-4999, 1969